Springer Series in Materials Science 166

Richard V. Craster
Sébastien Guenneau *Editors*

Acoustic Metamaterials

Negative Refraction, Imaging, Lensing and Cloaking

Springer

Springer Series in
MATERIALS SCIENCE 166

Springer Series in
MATERIALS SCIENCE

The Springer Series in Materials Science covers the complete spectrum of materials physics, including fundamental principles, physical properties, materials theory and design. Recognizing the increasing importance of materials science in future device technologies, the book titles in this series reflect the state-of-the-art in understanding and controlling the structure and properties of all important classes of materials.

Richard V. Craster • Sébastien Guenneau
Editors

Acoustic Metamaterials

Negative Refraction, Imaging, Lensing and Cloaking

Springer

Editors
Prof. Richard V. Craster
Department of Mathematics
Imperial College
London, UK

Dr. Sébastien Guenneau
Liverpool University
Liverpool, UK

Institut Fresnel CNRS
Marseille, France

ISSN 0933-033X Springer Series in Materials Science
ISBN 978-94-007-4812-5 ISBN 978-94-007-4813-2 (eBook)
DOI 10.1007/978-94-007-4813-2
Springer Dordrecht Heidelberg New York London

Library of Congress Control Number: 2012954244

Printed on acid-free paper

Springer is part of Springer Science+Business Media (www.springer.com)

Foreword
by Prof. Andrew Norris, Rutgers University, USA

What are Acoustic Metamaterials? The term Metamaterial has been in use for a little over a decade, introduced in 2000 by R.M. Walser [1]. His and subsequent definitions emphasize the requirements that metamaterials are artificial, i.e. man-made, heterogeneous devices that display new responses precluded by physical constraints from occurring in the constituent materials. In this sense it is clear that acoustic metamaterials must be capable of performing unusual acoustical feats, whether it is sound in air or water, bulk or surface elastic waves in solids, or other types of mechanical wave motion. Interest in acoustic metamaterials has grown rapidly with the realization that the concepts underlying the wave physics of electromagnetic metamaterials, concepts such as negative index of refraction, sub-wavelength imaging, time reversal techniques, transformation optics, etc., have counterparts in acoustics. The subsequent rapid increase of research activity has resulted in numerous special sessions at acoustics conferences, and several special issues of journals devoted to acoustic metamaterials and related topics. However, it is difficult for the researcher, let alone the newcomer, to keep abreast of developments in this new and fast moving field.

The present volume is therefore especially welcome as it is the first comprehensive survey of the state of the art in acoustic metamaterials research. The book is particularly recommended for scientists, engineers and mathematicians with no prior knowledge of acoustic metamaterials. The twelve chapters, written by some of the best people working in the field, are generally written at the level of review articles. This format allows the reader with some background in theoretical and applied acoustics to quickly appreciate and understand the variety of phenomena, applications, and theory at play. The editors, Richard Craster and Sébastien Guenneau, are deeply involved in the subject, having made significant theoretical and experimental contributions to the development of acoustic metamaterials research. As they themselves became acquainted with this rapidly evolving subject, they realized the need for a single source where the interested scientist could quickly get up-to-speed with the wide range of topics involved, such as dynamic homogenization, sub-wavelength acoustic imaging, and transformation acoustics. Prior to this there was no existing text where one could find all of this information. The editors are to be congratulated

for assembling in one volume survey articles that together provide a fairly thorough overview of current acoustic metamaterials research.

The field of acoustic metamaterials combines a wide variety of disciplines and subjects, providing a wealth of interesting and challenging problems: Take, for instance, the topic of transformation acoustics and its most well known application, cloaking. The problems involve differential geometry, partial differential equations, acoustic experimentation, continuum mechanics, anisotropy, homogenization, multiple scattering, numerical simulation, material fabrication, etc., and researchers with background in any of these areas will find something of interest. I have found breadth of subject matter to be the most stimulating and rewarding aspect of acoustic metamaterials, and I hope the reader will share my enthusiasm for the subject after reading this book.

1. R.M. Walser, Metamaterials: What are they? What are they good for? APS March Meeting Abstracts, p. 5001, 2000

Rutgers University, Piscataway, NJ, USA Prof. Andrew Norris

Foreword
by Prof. Ross McPhedran, The University of Sydney, Australia

The study of metamaterials is often considered to relate only to the construction of devices and systems for controlling in unprecedented ways the propagation of electromagnetic waves and light. Indeed, it was with his radical ideas relating to these types of wave that Sir John Pendry ignited the interest of scientists, mathematicians and engineers worldwide.

However, it has gradually become evident that the new concepts and techniques emerging from the study of metamaterials are not restricted just to electromagnetism: indeed, we are witnessing a revolution in the whole field of wave science. This is no more evident than in this timely book, which is the first comprehensive study of the impact of metamaterial concepts on the control of acoustic and elastic waves.

Those who are already knowledgeable about the interaction of acoustic or elastic waves with structured systems will not need convincing as to the value of this book. For those who are thinking about taking up the field, there are a number of good reasons why they should commence, with *Acoustic Metamaterials* as an indispensable guide. First among these is Sir Edmund Hillary's classic reason: "Because it's there". The field of acoustic metamaterials is relatively underexplored, with compensating rich challenges and opportunities. Secondly, many of the aspects which make optical metamaterials research difficult do not apply to acoustic metamaterials. For example, to achieve strong contrast in optical properties generally requires use of metals, which are accompanied by strong and undesirable dissipation or loss of energy. The combination of strong contrast and weak energy dissipation is easily achieved in acoustics and elastodynamics. Fabrication of acoustic metamaterials can also be much easier than for their optical counterparts. Other motivational reasons abound in the comprehensive chapters comprising this book.

The principal authors and architects of *Acoustic Metamaterials* are internationally-known and respected researchers in this new field. They have used their wide knowledge and excellent range of contacts to assemble a prestigious team of authors. The result is a beautifully written and well illustrated volume, which exposes the reader to the whole range of techniques necessary to comprehend this field and its

emerging applications, ranging from the basic ideas to the latest striking research developments.

Acoustic Metamaterials does more than capture an expanding research field at an exciting stage of its development. Its survey of ideas and techniques will make it an indispensable element of any wave scientist's library for years to come.

CUDOS, School of Physics
The University of Sydney
Sydney, Australia

Prof. Ross McPhedran

Preface

In 1931, on the centennial of Maxwell's birthday, Albert Einstein described the work of the Scottish physicist and mathematician as *the most profound and the most fruitful that physics has experienced since the time of Newton.* Einstein kept a photograph of Maxwell on his study wall, alongside pictures of Michael Faraday and Newton. James Clerk Maxwell is best known for formulating classical electromagnetic theory: This united all previously unrelated observations, experiments and equations of electricity, magnetism and optics into a consistent theory summarized by four partial differential equations. Importantly, Maxwell's equations retain their form under coordinate changes and gave rise to the Einstein field equations of general theory of relativity. Einstein's equations, published in a compact form in 1915, are a set of 10 (coupled and non-linear) equations describing the fundamental interaction of gravitation as a result of spacetime being curved by matter and energy. These tensor equations are also preserved when they undergo geometric transformations. In generalized coordinate systems, e.g. non-Euclidean metrics, they express that light follows curved trajectories along geodesics. In this way, the flow of light in spacetime is detoured around massive cosmological objects such as heavy planets or black holes (in the latter case, light is ultimately absorbed if it enters the so-called event horizon, but that's another story). The *tour de force* of British physicist Sir John Pendry was to recognize in 2006 that one can markedly enhance control of light trajectories on the scale of the human laboratory by designing metamaterials whose permittivity and permeability curve the electromagnetic space, whereby the time variable only plays the role of a parameter. This original proposal opened new vistas in photonics, e.g. with the fast growing field of cloaking.

However, James Clerk Maxwell is also known for other seminal works, such as for presenting the first durable colour photograph (using the principle of three-colour analysis and synthesis, the basis of nearly all subsequent photochemical and electronic methods of colour photography) during an 1861 Royal Institution lecture on colour theory. Moreover, Maxwell is also recognized for his foundational work on the rigidity of rod-and-joint frameworks like those in many bridges. The latter scientific legacy is maybe less well known, but is of foremost importance as it underpins the parallel developments in electromagnetic and acoustic metamaterials. The

foundations of continuum mechanics were lain in Sir Isaac Newton's *Philosophiæ Naturalis Principia Mathematica*, published in 1687, that is over two centuries before Maxwell's work on solid mechanics; it lays the foundations for most of classical mechanics. In this groundbreaking work, Newton described universal gravitation and the three laws of motion. However, Newton was also interested in the theory of light: He built the first practical reflecting telescope and developed a theory of colour based on the observation that a prism decomposes white light into the many colours that form the visible spectrum. In mathematics, Newton shares the credit with Gottfried Leibniz for the development of differential and integral calculus, which are central to modern analysis.

Newton's first Law (the law of inertia) states that an object at rest tends to stay at rest and that an object in uniform motion tends to stay in uniform motion unless acted upon by an external force. The meaning of this law is the existence of reference frames (called inertial frames) where objects not acted upon by forces move in uniform motion (in particular, they may be at rest). This law is central to Galilean and Lorentzian mechanics. In Chap. 1, we draw some useful analogies between governing equations of electromagnetic and mechanical waves allowing for control of their trajectories in transformed coordinates. The field of transformational optics and acoustics is actually a very topical subject and will be further discussed in Chaps. 7–12. The second of Newton's laws further states that a force applied on a particle equals its mass times its acceleration. In the case of a rigid solid, this law is still valid, in which case one considers the center of mass (or gravity) of the solid. In Chap. 1, we stress that it is this very precise law, which bridges electromagnetic and acoustics metamaterials, since it allows one to approximate them as a discrete set of masses connected by springs. The detailed analysis of very unusual dynamic averaged properties of locally resonant structures consisting of split ring resonators (associated with effective negative magnetism or density upon resonance) is carried out using the concept of multi-structures developed by Kozlov, Movchan and Mazy'a in the late nineties. The asymptotic analysis involves Newton's second law at junctions between thin bridges and rigid bodies. Another way to achieve a genuine negative refractive index is to consider a high-contrast in material parameters, modelled using classical low-frequency homogenization. In contradistinction, the origins of all-angle-negative refraction (AANR) in phononic crystals can be seen from the high-frequency homogenization approach recently introduced by Craster and Kaplunov which is also described in this chapter; AANR is based upon negative group velocity of waves propagating along certain crystallographic directions.

Chapter 2 by Khelif, Achaoui and Aoubiza focusses on the numerical analysis (using a finite time difference domain method coupled with Floquet-Bloch conditions to take into account the periodicity in the transverse direction and perfectly matched layers to account for the unbounded domain in the vertical direction) of elastic stop bands associated with periodic arrays of pillars evenly spaced on the surface of a semi-infinite substrate. Elastic waves propagating near the surface are sometimes evanescent in the upper and lower half planes (and therefore reminiscent of Rayleigh waves), and sometimes couple to body (pressure and shear) elastic waves. Depending upon the height of pillars, the physics is associated with either

a locally resonant acoustic metamaterial type behaviour leading to low frequency stop bands (for high enough pillars, which can bend, rotate and so forth), or a phononic crystal behaviour leading to classical Bragg effects (for small pillars). The influence of crystal cladding symmetry upon the position and width of stop bands is used in order to distinguish between metamaterial and phononic crystal effects: In the former case, it is shown that stop bands are robust against symmetry changes, while in the latter case stop bands are wider for hexagonal than square lattices.

In Chap. 3, Gei, Bigoni, Movchan and Bacca investigate the effects of prestress on stop band and filtering properties of flexural waves propagating within periodic and quasi-periodic beams, as well as in periodic plates. In the first part, they model Floquet-Bloch propagation of flexural waves in prestressed periodic beams on an elastic spring foundation (Winkler type) which leads to a fourth order ordinary differential equation. They can then adjust the size of the periodic cell in order to introduce some quasi-periodic patterns (supercell approach), and this in turn leads to localization effects reminiscent of Anderson localization. Band gaps and self-similarity in quasiperiodic beams are also investigated. A transfer matrix model is used with the classical trace condition met in optics (whereas here the focus is on bending waves) in order to locate position of stop bands. In the second part, the authors consider plates prestressed through normal and shearing tractions (tensile prestress), and using a finite element model, the authors investigate tuning of stop band positions by varying prestress.

In Chap. 4, Estrada, de Abajo, Candelas, Uris, Belmar, and Meseguer explore extraordinary transmission of pressure waves through subwavelength holes in periodically perforated plates immersed in a fluid. In order to understand how pressure waves can squeeze into periodically arranged thin channels, the authors first use a scalar wave equation to model pressure waves in a fluid surrounded by rigid walls. But they also compare their numerical results with a full elasto-acoustic theory taking into account the transmission of sound waves from the fluid to the surrounding walls, within which pressure waves do couple to shear waves. Numerics are then shown to be in excellent agreement with experiments. Unlike for light, it is found that sound is transmitted through individual subwavelength holes in a perfectly rigid thin film approximately in proportion to their area. Moreover, hole arrays in perfectly rigid thin films do not exhibit full sound transmission due to the absence of lattice resonances responsible for the extraordinary transmission of light in Ebbesen's experiments. However extraordinary sound screening beyond that predicted by the mass law is observed. The authors also unveil a unique interplay between Wood anomaly minima and intrinsic plate (Lamb) modes.

In Chap. 5, Simonetti makes a very comprehensive survey of recent theoretical and experimental results on high-resolution imaging techniques for ultrasonic waves with fascinating applications in medical imaging, such as breast cancer detection. The author combines beamforming algorithms with inverse scattering theory in order to overcome the Rayleigh criterion, which limits the image resolution to about half the working wavelength, hence does not allow for shape reconstruction of subwavelength objects. His original approach involves the factorization of the far-field operator which encodes information about the subwavelength features of an object

in the far-field pattern of the scattered wave. The basis of this approach is that to unlock the information about the distortion experienced by the probing wavefield as it travels within the object and which is caused by multiple scattering, it is necessary to approach image formation from an inverse scattering perspective. Recent advances in computer sciences underpin the fast and accurate mapping of the perturbation to the free propagation of ultrasound induced by the presence of an object, the maximum achievable resolution being only dictated by the dynamic range of the detector.

In Chap. 6, Fink, Lemoult, de Rosny, Tourin, and Lerosey review recent developments in time reversal techniques applied to subwavelength imaging for electromagnetic and acoustic waves. The authors explain how the time reversal symmetry of the wave equation allows for the refocussing of the far field emitted by a pressure source surrounded by a closed surface filled with transducer elements back onto the source. In this experiment, the heterogeneities of the medium inside the so-obtained time reversal cavity facilitate the imaging effect: the more complex the medium, the better the focussing. The authors come back to their famous broomstick experiment, whereby eight 2 mm long reactive antenna radiating an electromagnetic wave of about 2.5 GHz surrounded by a random collection of 3 cm long copper wires, and placed a distance of about one thirtiest of a wavelength apart are time reversed and refocussed on two antennas. A similar experiment is then devised for pressure waves with a periodic set of soda cans acting as Helmholtz resonators. With time reversal, the focal spots resolution is already one eight of the wavelength, whereas after the refined iterative time reversal technique, the resolution is far beyond.

In Chap. 7, Li, Liang, Zhu and Zhang review theoretical and experimental properties of transformation based acoustic metamaterials. They explain how one can control pressure waves propagating in structured fluids by playing with the effective anisotropic density of a metamaterial immersed in the fluid. This is done using several examples: An acoustic carpet cloak consisting of curved brass plates flattens the wavefront of pressure waves scattered by a ground with a bump. A magnifying hyperlens consisting of 36 brass fins in air spanning 180 degrees radiates a pressure source field along three preferential directions. Finally, a holey structured metamaterial allows for a subwavelength image thanks to very large effective anisotropic density along some acoustic waveguides, which can be seen as the acoustic counterpart of the famous swiss roll experiment designed by the group of Pendry for electromagnetic radio frequencies.

In Chap. 8, Cummer draws analogies between transformation optics and acoustics, with in-depth explanations of what virtual (original medium) and physical (transformed medium) spaces are in terms of material parameters and wave phenomena. A beam shifter and an acoustic cloaking shell are designed through geometric transforms for pressure waves. Some examples of acoustic metamaterial structures are given and an experimental realization of an acoustic carpet based on perforated sheets of thin plastic stacked with thin air gaps in between is finally discussed.

In Chap. 9, Sánchez-Dehesa and Torrent make a survey of homogenization techniques applied to acoustic cloaking. These are based upon multilayered structures alternating fluids of different density and compressibility. The authors also propose to add some structural elements in fluid layers, such as cylindrical objects, thereafter

called sonic crystals. They finally show an experimental realization of a corrugated metamaterial behaving as an anisotropic fluid and they explain what are the physical constraints on acoustic cloaking.

In Chap. 10, Haberman, Guild and Alù explain how one can design acoustic cloaks via scattering cancellation phenomena, based upon plasmonic and anti-resonance cloaking. They manage to cloak the pressure field for an isotropic sphere of stainless steel, aluminum and glass when it is surrounded by a thin shell of fluid. They also investigate such plasmonic shells with multilayers of fluids.

In Chap. 11, Kadic, Farhat, Guenneau, Quidant and Enoch make a survey of theoretical and experimental results on surface liquid and electron wave cloaking. The former is based upon effective anisotropic shear viscosity induced by a structured medium immersed in a fluid. The latter is associated with conformally mapped electromagnetic field at a metallic surface structured with dielectric pillars.

In Chap. 12, Guevara Vasquez, Milton, Onofrei and Seppecher make a very thorough survey of coordinate transformation techniques for Maxwell (electromagnetism), Helmholtz (acoustics) and Navier (elastodynamics) equations. They look at transformed mass-spring networks (what is called discrete transformation elastodynamics) with a Torque effect which could be used in elastic cloaking. They also discuss cloaking via active scattering cancellation devices not completely surrounding the cloaked region (exterior cloaking). The authors use a rich mathematical arsenal for zero frequency (Laplace in 2D) and finite frequency (Helmholtz in 3D) problems. Some theorems are stated for the conductivity equation in 2D making use of conformal transformation with an explicit polynomial solution and for active exterior cloaking for the Helmholtz equation in 3D with a remark on the Green's formula allowing for the explicit form of monopole and dipole sources needed for the cloaking device. The authors finally look at closely packed spherical exterior cloaks.

The twelve chapters constituting this book present an up-to-date survey of many aspects of acoustic metamaterials, including filtering effects, extraordinary transmission, subwavelength imaging via tomography or time-reversal techniques, cloaking via transformation acoustics and elastodynamics and even cloaking via acoustic scattering cancellation and active exterior cloaking. However, we do not claim that the topics covered in this book exhaust the acoustic wave phenomena to which suitably structured surfaces, solids or fluids could lead. Nonetheless, we hope the variety of subjects touched upon in this book, and the way to handle them (theoretically, numerically, experimentally) give a grasp of the richness of the emerging topic of acoustic metamaterials and will contribute to initiate even more research activity and applications in the near future.

The editorial staff at the Springer Verlag Publishing company have our many thanks for their help in producing this book. We are also indebted to Tom Spicer, director of Canopus Academic Publishing LTD for making this project viable.

Finally, we wish to express our deepest gratitude to the authors for the thought and care they put into preparing their contributions, and to Professors Andrew Norris and Ross McPhedran whom kindly agreed to preface this book.

Marseille, France — Sébastien Guenneau
London, UK — Richard V. Craster

Contents

Chapter 1
Fundamentals of Acoustic Metamaterials

Sébastien Guenneau and Richard V. Craster

Abstract This chapter introduces the field of acoustic metamaterials in light of correspondences with related phenomena in electromagnetics. The semantic frontier between phononic/photonic crystals (PCs) and metamaterials is underpinned by low-frequency high-contrast and high-frequency homogenization models for periodic structures, the former being well suited for metamaterials, while the latter unveils the band structure and associated anomalous dispersion of PCs. We find it therefore worthwhile to outline the corresponding asymptotic models for waves propagating in such structured media. The mathematics behind the physical scene are illustrated by numerical simulations including cloaking, lensing and confinement effects via artificial anisotropy (motivated by transformational optics and acoustics), negative refraction and slow waves.

1.1 Introduction

In 1967, the Russian physicist Victor Veselago published a visionary paper in which electromagnetic media with simultaneously negative permittivity (ε) and magnetic permeability (μ) were shown to be characterized by a negative refractive index of refraction [51]. Veselago pointed out using a simple ray analysis that a slab of such a negative refractive index material (NIM) can act as a flat convergent lens that images a source on one side to a point on the other: such a ray analysis also holds for the case of acoustic waves, and is shown in Figs. 1.1 and 1.2. Veselago's lens is unusual: the simplest example of a convergent lens is a curved piece of silica which bends light according to the Snell-Descartes laws of refraction at a curved air/glass interface: a lens with a positive refractive index is necessarily convex.

S. Guenneau (✉)
Institut Fresnel, UMR CNRS 7249, Aix-Marseille Université, Marseille, France
e-mail: sebastien.guenneau@fresnel.fr

R.V. Craster (✉)
Imperial College London, London, UK
e-mail: r.craster@imperial.ac.uk

R.V. Craster, S. Guenneau (eds.), *Acoustic Metamaterials*,
Springer Series in Materials Science 166, DOI 10.1007/978-94-007-4813-2_1,

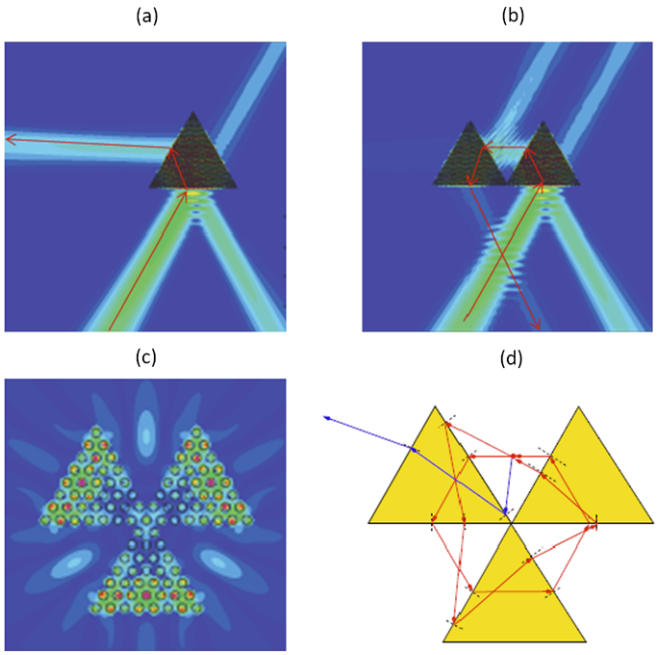

Fig. 1.1 Open resonator via negative refraction: (**a**) Gaussian beam incident from the left on a triangular photonic crystal (PC) consisting of 60 dielectric rods in honeycomb configuration (the *arrows* highlight the negatively refracted beams); (**b**) Same as (**a**) for 2 PCs (*arrows* unveil some beams circling in loop); (**c**) Resonant mode in three triangular PCs sharing a corner and consisting of 34 dielectric rods in honeycomb configuration; (**d**) Schematic diagram for the triangular perfect corner consisting of 3 triangular NIMs with some rays being trapped along closed trajectories (*in red*) around the corner and some rays diverging; Such an open resonator confines light to certain extent. Simulations by G. Tayeb (Institut Fresnel, CNRS/Aix-Marseille University, 2007)

1.1.1 Electromagnetic Meta-Materials and Cloaking via Reaction

However, Veselago's discovery remained an academic curiosity for almost thirty years, until the British physicist John Pendry and co-workers [41, 42] proposed designs of structured materials which would have *effectively*[1] negative ε and μ. The experimental demonstration of a negative refractive index at GHz frequencies by a handful of photonic groups in the United States in 2000 [49] provided a fillip to research in this area, and we direct the reader to [40, 45] for recent comprehensive reviews including a fair historical survey on this subject. Importantly, these materials are structured at subwavelength lengthscales (typically one tenth of the wavelength), hence it is possible to regard them as nearly homogeneous and describe their response by dispersive effective medium parameters.

[1] At this stage, the meaning of the word *effectively* seems to be rather vague, but its definition will be made more precise with specific physical contexts and mathematical models as we proceed.

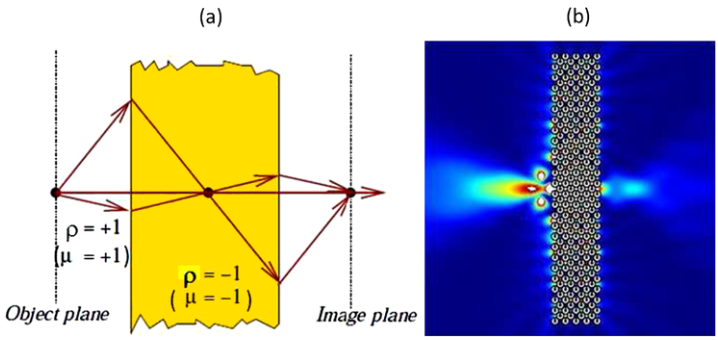

Fig. 1.2 Acoustic lens via negative refraction: (**a**) Schematic diagram depicting the focussing of rays by the acoustic counterpart of the Pendry-Veselago lens (the density ρ and the shear modulus μ for anti-plane shear waves play the role of the electric permittivity and the magnetic permeability—or vice-versa depending upon light polarization—in optics). A point source placed on one side will produce an image on the other side of the slab of negative density. The entire object plane is mapped point-wise onto the image plane; (**b**) Numerical simulation demonstrating the imaging effect for anti-plane shear waves (plot of field intensity). An acoustic source placed on the left side of an array of voids (with cross-sections shaped as split ring resonators (SRRs)) in an isotropic bulk (e.g. silica) is imaged on the right side (with subwavelength resolution, about one third of the incident wavelength). The asymptotic formula (1.1) provides us with the resonant frequency of SRRs at which the effective density of the array turns negative, according to (1.2)

It turns out that a branch of modern applied mathematics known as homogenization theory [24, 30] does this job very well as we shall see later. The term meta-materials (coined by Pendry) actually describes such periodic structures when one can average their properties, which turn out to be strongly dispersive (and anisotropic).

The paradigm of potential applications of the physics of dispersive media and negative refraction is what is known as Pendry's perfect lens: the Veselago slab lens not only involves the propagating waves, but also the evanescent near-field components of a source in the image formation [39], thereby ensuring a resolution beyond the famous Rayleigh criterion (in principle a lens cannot resolve details smaller than half the wavelength of incident light). Negative refraction also allows for cylindrical lenses with high-resolution combined with a magnification effect [35, 43].

More surprisingly, a finite set of dipoles located in the close neighborhood of such NIM lenses is cloaked i.e. made invisible to an external field, as shown in Fig. 1.3. Such an invisibility induced by anomalous resonances of the NIM shell was discovered by Graeme Milton and Nicolae Nicorovici in 2006 [32] and has laid the foundations of cloaking by reaction, a fascinating field of physics attracting the growing attention of researchers as its understanding involves considerations reminiscent of plasmonics, wherein transparency can be achieved thanks to scattering cancellation as chiefly demonstrated by Alu and Engheta [1]. We should not withstand the fact that cloaking by reaction also requires knowledge of indepth mathematics, which makes it all the more attractive. On somewhat a more anecdotal note, it was also shown that two corners of NIM combined in a checkerboard fashion can

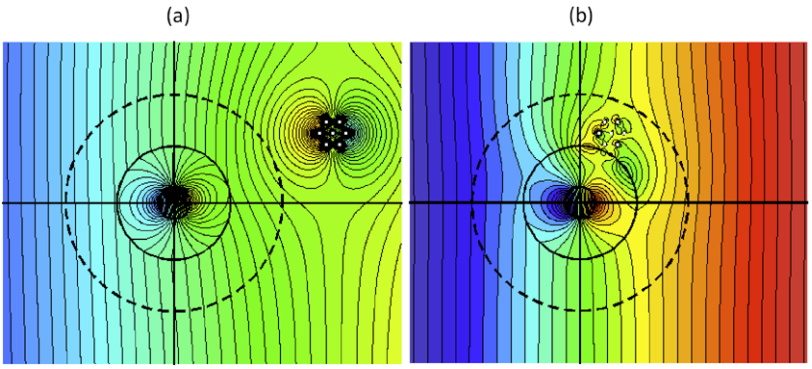

Fig. 1.3 Cloaking by reaction as in Milton and Nicorovici [32]: An electric potential and associated streamlines is computed for a uniform electric field interacting with seven dipoles in a honeycomb configuration: (**a**) the dipoles are located outside the cloaking region (*dark dashed circle*) associated with a coated cylinder filled with NIM; (**b**) the dipoles are located inside the cloaking region. We note that the streamlines outside the cloaking region in (**b**) are nearly flat, showing that the cluster goes unnoticed for the ambient field, unlike for (**a**) where streamlines are obviously distorted around the dipoles. Simulations by N. Nicorovici (CUDOS, University of Sydney, 2010)

act as a unique resonator (ray trajectories are closed loops) [18, 23, 37, 43], which is yet another form of cloaking [22, 46], see Fig. 1.1. Interestingly, such checkerboards also lead to a form of extraordinary transmission [6]. A natural question to ask is whether such unusual phenomena could be reproduced for other types of waves, and this problem lies at the heart of acoustic metamaterials.

1.1.2 Acoustic Meta-Materials and Lensing via Negative Refraction

At the beginning of this millennium, the group of Ping Sheng at the University of Hong-Kong provided the first numerical and experimental evidence of a localized resonant structure for elastic waves propagating in three-dimensional arrays of thin coated spheres [29]. This work paved the way towards acoustic analogues of electromagnetic metamaterials. Alexander Movchan and one of us subsequently proposed to use arrays of cylinders with a split ring cross section as building blocks for 2D localized resonant structures [33]. Li and Chan independently proposed a similar type of negative acoustic metamaterial [28]. In a recent work, Fang *et al.* experimentally demonstrated a dynamic effective negative stiffness for a chain of water filled split ring resonators for ultrasonic waves [12]. Milton, Briane and Willis provided a mathematical framework for such effects including cloaking whereby the elastic response of an obstacle subject to an applied field is suppressed [31].

Interestingly, similar localization effects with a markedly enhanced elastic response have been also observed experimentally by Russell *et al.* at MHz frequencies in sonic band gap crystal fibre preforms with dual core defects in 2003 [47], see Fig. 1.4: trapped modes appear in the stop band of the periodic cladding, and couple

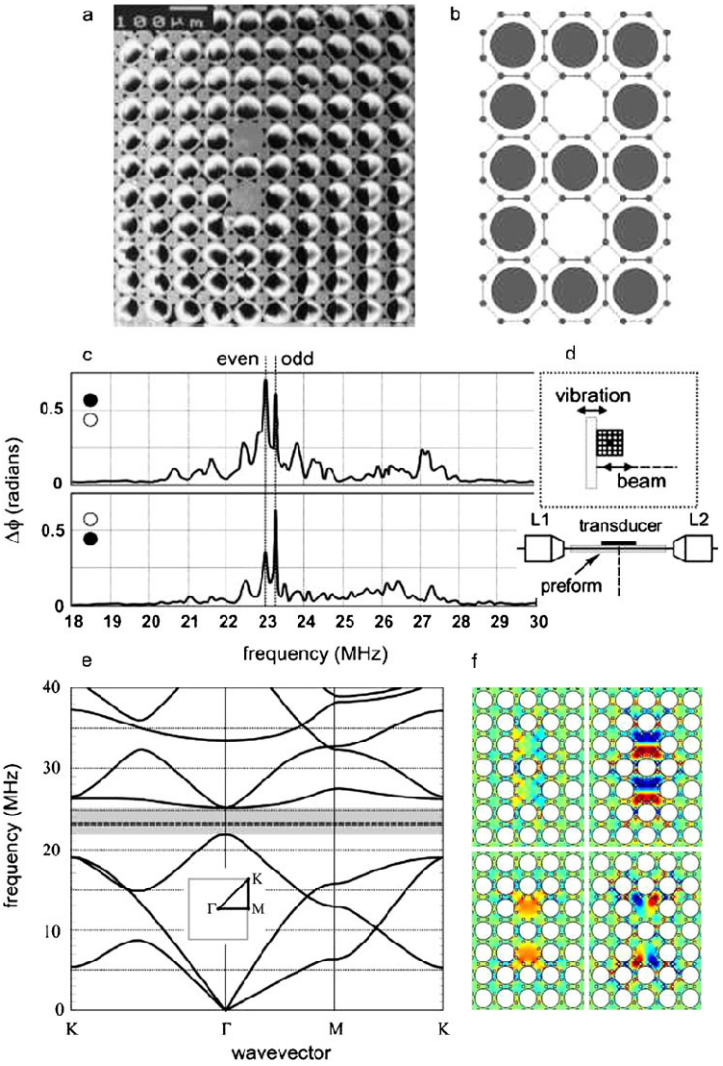

Fig. 1.4 Photonic Crystal Fibre Preform as a locally resonant elastic metamaterial: (**a**) Scanning electron micrograph of the preform used in the experiments of Philip Russell's optoelectronic group at Bath University in 2001–2003. It has two solid core defects, an inter-hole period of 80 μm, a hole diameter of 59 μm, and an interstitial hole diameter of 80 μm; (**b**) A detail of the structure used in the numerical modelling (the lines are guidelines only). (**c**) Phase change of the light propagating in the cores of the PCF preform, induced by the acoustic wave, as a function of frequency. Two sharp resonances are apparent at 23.00 MHz and 23.25 MHz. (**d**) Schematic diagram of the experimental set up. L1 and L2 are microscopic objectives. A piezoelectric transducer was used to create acoustic vibrations. (**e**) Sonic band structure for in-plane mixed-polarized shear and dilatational waves in the sonic crystal, with defects removed (Rayleigh method [20]). The experimentally observed resonances (at 23 and 23.25 MHz—the *dashed lines*) sit near the middle of the sonic band gap, which extends from 21.8 to 25 MHz. (**f**) Field patterns for the acoustic resonances at 23.47 MHz and 24.15 MHz (Finite element simulations with Comsol Multiphysics)

to light via photo-elastic effects in the defects. This suggests that elastic metamaterials are in essence periodic structures within which wave localization occurs, thereby enhancing resonance effects (as well as light and sound interplay).

1.1.3 Correspondences Between Electromagnetic and Acoustic Metamaterials via Locally Resonant Models

Metamaterials are artificially structured composites that can be engineered to have desirable electromagnetic properties, such as focussing via negative refraction [51] or spatially varying, anisotropic, refractive index. The former makes a high resolution flat lens [39] while the latter leads to invisibility cloaks via transformation optics [27, 44]. As such, they offer unique and previously unexplored features. A new branch of physics has emerged in the last decade, following the discovery by John Pendry [41, 42] of new structures that lead to negative refraction of electromagnetic waves [49]. Negative Refractive Index Materials (NRIM) consist of structured metamaterials such as arrays of thin straight wires [41] and split ring resonators (SRRs) [42]. SRRs are cylinders with capacitive splits that respond resonantly to radiation with the magnetic field along the cylindrical axes, see Fig. 1.5(a). Circulating currents around the rings actually tend to shield the interior due to the inductance while the capacitance due to the gaps gives rise to a resonance associated with a negative refractive index, see e.g. [21] for a comprehensive review. This resonant effect creates a narrow low frequency stop band (near normalized frequency 0.5, cf. Fig. 1.10) associated with artificial magnetism in the context of optics. Importantly, the second dispersion curve in Fig. 1.10 displays a negative curvature around the resonant frequency of SRR which physicists interpret as a negative group velocity of the wave: This is the hallmark of negative refraction, which can be used to make a convergent flat lens, as shown in Fig. 1.12.

Using asymptotic methods for fields in multistructures [26], it can be shown that (normalized) resonant frequencies ω_m, $m = 1, 2\ldots$ are given by the transcendental equation [33]:

$$d\cot(\omega_m l) = \text{area}(\Xi)\omega_m, \tag{1.1}$$

where Ξ denotes the region inside a split ring, a the pitch of the array, d the thickness of the slit, see Fig. 1.5 (left panel), and l its width. The analogy with the mass-spring model counterpart of the usual electrical circuit description of electromagnetic metamaterials, see Fig. 1.5 (right panel), first appears in [33].

The effective density ρ_{hom} at a frequency ω is then given in the form [15]:

$$\rho_{hom}(\omega) = 1 - \sum_{m=1}^{\infty} \frac{\omega^2}{\omega^2 - {\omega_m}^2} \|V_m\|^2_{L^2(0,l)}, \tag{1.2}$$

where V_m is the eigenfield within the slit $(0, l)$ of the split ring, and $\|V_m\|^2_{L^2(0,l)} = \int_0^l V_m^2(x)\,dx$. It is clear from (1.2) that $\rho_{hom}(\omega)$ can take negative values near resonances $\omega = \omega_m$. In the context of electromagnetism, the expression for the effective

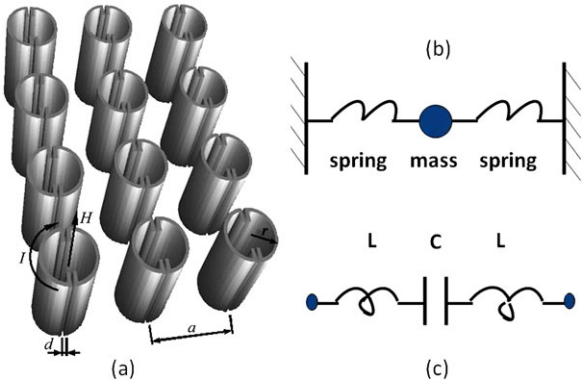

Fig. 1.5 (**a**) Square array of cylinders with capacitive splits (so-called thin bridges of thickness d small compared to the pitch a) that respond resonantly to radiation with the (longitudinal) magnetic field along the cylindrical axes. Circulating currents I around the rings tend to shield the interior due to the inductance while the capacitance due to the gaps gives rise to a resonance, the so-called artificial magnetism (picture adapted from Guenneau and Ramakrishna [21]). (**b**) A split ring acts as a Helmholtz resonator: a mass (counterpart of the capacitance C in electric circuits) is connected to walls via springs (counterparts of inductance L, say in solenoids) [33]. The mechanical interpretation is a negative effective density [15] upon resonance, see (1.2). (**c**) Resonant LC circuit counter part of a Hemholtz resonator

permeability μ_{hom} is the same, and first appears in [42], where ω_m was referred to as plasmon frequency.

Combined together, structural elements such as split ring resonators and thin straight wires (associated with an effective permittivity ε_{hom} described by a similar expression to (1.2) in the optical setting, and a negative stiffness in the acoustical setting [19][2]) can bring about a (complex valued) negative effective refractive index for the Snell-Descartes law and result in negative refraction of radiation [19, 49]. Indeed, a slab of NRIM with $n = -1$ can image both the far-field propagating modes [51] and the near-field modes of a source [39], thus acting as a perfect lens. The resolution of this system is not limited by the wavelength, but only by the dissipation, dispersion and imperfections in the constituent materials. Negative refractive index materials indeed support a host of surface plasmon states for both polarizations of light which conveys the subwavelength details from the source to the image. However, such surface waves also exist in acoustic settings. This opens up new horizons

[2]Kohn and Shipman were the first mathematicians to retrieve Pendry's formula for artificial magnetism via two-scale homogenization of split ring resonators in 2008 [25]. However, Bouchitté and Schweizer obtained a more general form for the tensor of effective permeability in the case of a cubic array of toroidal SRRs with a thin slit of high contrast material in 2010 [3]. In the two-dimensional case, Farhat *et al.* retrieved Pendry's result in 2009, using a three-scale homogenization approach for SRRs with thin slits with Neumann data which model infinite conducting boundaries for transverse electromagnetic waves as in Fig. 1.2 or rigid boundaries in the context of acoustics [15].

such as imaging with subwavelength image resolution through an acoustic counterpart of the Pendry-Veselago slab lens [15], already shown in Fig. 1.2.

In fact, as we mentioned earlier in the case of electromagnetic waves, the negatively refracting slab is only one member of a whole category of systems which satisfy a generalized lens theorem such as cylindrical lenses [35, 43] and two negative corners [18] sharing the same corner which combine to make a system within which rays emanating from a line source are bent around a closed trajectory and are refocused back onto the line source: the latter could make an open resonator that confines sound. Similarly, there is a whole category of systems enhancing the confinement and the control of light, such as metamaterials with a vanishing refractive index (ultra-refraction), leading possibly to three-dimensional highly directive antennae. The question then arises as to whether or not elastic metamaterials of refractive indices $n = -1$ (Veselago's lens) and $n = 0$ (omnidirective antenna) can be built in a similar way to what was done for electromagnetic metamaterials. This leads to the inter-disciplinary research area of numerical and asymptotic analysis combined with optimal design for novel optical and acoustical devices.

1.1.4 Correspondences Between Electromagnetic and Acoustic Metamaterials via Analogies in Governing Equations

Mathematically, electromagnetic waves propagating in complex magneto-dielectric cylindrical media (i.e. invariant along the z direction) are characterized by a permittivity, $\varepsilon(x, y)$, and permeability, $\mu(x, y)$, that are related to the refractive index n through $\varepsilon\mu = n^2$ and to the speed of light in the medium c_L through $\varepsilon\mu = 1/c_L^2$. The electric and magnetic fields $\mathbf{E}(x, y)$, $\mathbf{H}(x, y)$ are solutions of time-harmonic vector Maxwell's equations: Harmonic time dependence, $\exp(-i\omega t)$, with ω as wave frequency is assumed and henceforth suppressed. Such harmonic dependence allows us to work directly in the spectral domain, i.e. with the Maxwell operator: (in the weak sense in $\mathbb{R}^3$):

$$\nabla \times \left(\mu^{-1}\nabla \times \mathbf{E}\right) = \omega^2\varepsilon\mathbf{E}, \quad \text{and} \quad \nabla \times \left(\varepsilon^{-1}\nabla \times \mathbf{H}\right) = \omega^2\mu\mathbf{H}, \tag{1.3}$$

where it should be noted that $\mathbf{E}$ and $\mathbf{H}$ play a symmetric role. Moreover, assuming transverse electromagnetic waves, the problem splits in two polarizations, namely transverse magnetic (TM) which is such that $\mathbf{H} = (H_1, H_2, 0)$ and $\mathbf{E} = (0, 0, E_3)$ (i.e. longitudinal electric field) or transverse electric (TE) which is such that $\mathbf{E} = (E_1, E_2, 0)$ and $\mathbf{H} = (0, 0, H_3)$ (i.e. longitudinal magnetic field). The vector equations (1.3) can then be recast as:

$$\nabla \cdot \left(\mu^{-1}\nabla E_3\right) + \omega^2\varepsilon E_3 = 0 \text{ (TM)}, \quad \text{and} \quad \nabla \cdot \left(\varepsilon^{-1}\nabla H_3\right) + \omega^2\mu H_3 = 0 \text{ (TE)}. \tag{1.4}$$

Importantly, these two partial differential equations have a scalar unknown. However, if electromagnetic waves propagate with certain oblique incidence (e.g. in pho-

tonic crystal fibres), all components of **E** and **H** are inherently coupled through interface or boundary conditions, and one has to deal with the full vector problem.

Let us now draw some analogies with governing equations for acoustic metamaterials. The acoustic counterpart of a split-ring resonator (SRR) is simply a Helmholtz resonator: a mass (counterpart of the capacitance in electric circuits) is connected to walls via springs (counterpart of inductances), as first reported by one of us in 2004 in a paper with Alexander Movchan [33]. This makes acoustic metamaterials with a negative effective density possible upon resonance of SRR, which led to a simple design of convergent flat lens for anti-plane shear waves in 2007 [19]. The fact that electric circuit models mimic resonant mechanical systems and vice-versa is only the visible part of the iceberg: similar designs can also be achieved for linear surface water waves, which are governed, as are anti-plane shear waves in elasticity, by a scalar Helmholtz equation [15]

$$\nabla \cdot (a \nabla v) + \kappa^2 v = 0. \tag{1.5}$$

According to (1.4), we note that v stands for the longitudinal non-vanishing component of the electric or field in optics. As it turns out, v is the longitudinal (shear) component of the displacement field in elasticity and the phase velocity of surface water waves in hydrodynamics; κ is related to the wave frequency and a is related to the material/liquid parameters.

However, in-plane (pressure and shear) elastic waves are inherently coupled, even in a cylindrical domain. In which case, an in-plane elastodynamic wave needs to be represented by the displacement field $\mathbf{u}(x, y) = (u_1, u_2, 0)$ within a cylindrically isotropic elastic medium of spatially varying density ρ, and Lamé parameters $\hat{\lambda}$, $\hat{\mu}$ as described by the vector Navier equation (in the weak sense in $\mathbb{R}^3$):

$$\hat{\mu}\nabla^2\mathbf{u} + \left(\hat{\lambda} + \hat{\mu}\right)\nabla\nabla\cdot\mathbf{u} + \left(\nabla\hat{\lambda}\right)\nabla\cdot\mathbf{u} + 2\nabla\hat{\mu}\cdot\nabla\mathbf{u} + \nabla\hat{\mu}\times(\nabla\times\mathbf{u}) = -\omega^2\rho\mathbf{u}. \tag{1.6}$$

We can use this formulation to consider e.g. the spectrum for an array of inclusions (such as a cross sectional part of phononic crystal fibres) assuming that the stresses and displacements are continuous across interfaces and that Floquet-Bloch conditions hold connecting the ends of the periodic elementary cell; either stress free or clamped conditions hold on the inclusions. The out-of-plane elastic case is identical mathematically to transverse electromagnetic waves and hydrodynamic waves (i.e. governed by (1.5)) and allows for a greater variety in the boundary conditions that are allowable physically compared to electromagnetism: for instance, one can assume mixed Dirichlet (clamped) and Neumann (stress free) data on boundaries of an acoustic material, say a waveguide, whereas in optics one has either Dirichlet or Neumann data, not both of them simultaneously, as these model infinite conducting walls for a specific light polarization: Dirichlet holds for the TM case, while Neumann holds for the TE case. For instance, assuming a combination of these two conditions holds on the wall of a metallic waveguide leads to a vanishing field i.e. no mode is allowed to propagate.

Figure 1.6 is an experimental proof of lensing via negative refraction, which is based on an analogy between acoustics whereby anti-plane shear waves propagate

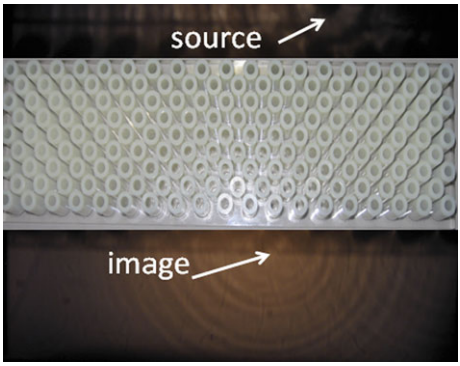

Fig. 1.6 Photograph of a surface liquid wave experiment with a surface wave generated on one side (*dark region*) of an array of rigid cylinders immersed in Methoxynonafluorobutane, which is a liquid that presents the advantage of combining a low viscosity coefficient with a relatively high density. An image appears on the other side of the array, according to the laws of negative refraction, see Fig. 1.2, though it is slightly shifted to the left. It should be noted that the image does not show subwavelength features as the structure works as a phononic crystal rather than an acoustic metamaterial: the wavelength is of the same order as the pitch of the array. Photo courtesy of S. Enoch, CNRS/Institut Fresnel, Aix-Marseille University, 2010

within an array of voids with stress-free conditions (Neumann data), see Fig. 1.2, and surface waves propagating within an array of rigid cylinders immersed in a liquid. The fact that the C-shaped inclusions have been replaced by circular inclusions shifts the frequency up at which negative refraction occurs, and this in turn spoils the subwavelength features of the image: we are in the presence of a phononic crystal rather than an acoustic metamaterial, and the imaging effect is due to multiple scattering between the cylinders (Bragg regime) rather than local resonances (homogenization regime); we return to this question of semantics later.

In conclusion, while it seems that there is a perfect analogy between transverse electromagnetic, hydrodynamic and anti-plane shear waves, and thus many exciting phenomena achieved in photonics should find their counterpart for water and sound waves, the situation is less clear in the case of coupled pressure and shear elastic waves (solutions of vector Navier equations). For instance, we shall see later that focussing effects via negative refraction requires us to have simultaneously negative density, shear and pressure modulus for such waves, which is a further challenge requiring some models of elastodynamic waves with complex microstructure [5].

1.1.5 Cloaking via Refraction: Controlling Electromagnetic and Elastodynamic Fields via Geometric Transforms

It is clear that the governing equations for electromagnetic (1.3) and elastodynamic (1.6) waves are very different. One can however draw some correspondences in specific cases, such as transverse electromagnetic waves, linear surface water waves

and anti-plane shear waves which are all governed by the scalar Helmholtz equation (1.5). More surprisingly, the clearly different vector equations (1.3) and (1.6) can be identified for the case obliquely (out-of-plane) propagating electromagnetic waves and in-plane coupled pressure and shear waves [20]. However, there are major structural differences between (1.3) and (1.6). For instance, (1.3) retains its form under geometric changes, while (1.6) does not. More precisely, it is well known that a change of coordinates amounts to replacing the different materials (often homogeneous and isotropic, which corresponds to the case of scalar piecewise constant permittivities and permeabilities) by equivalent inhomogeneous anisotropic materials in electromagnetism whatever the light polarization, a property used for instance to facilitate the analysis of twisted fibres in computational electromagnetics [53].

Such a property can be most easily derived for a scalar PDE of the form of (1.5), which is central to transversely propagating light, linear surface liquid waves and anti-plane shear waves in cylindrical geometries. In order to give a physical twist to the derivation, we write it for the latter case, but the derivation for (1.5) follows mutatis mutandis. We consider the time-harmonic acoustic equation:

$$\nabla_{(x,y)} \cdot (\underline{\underline{\mu}} \nabla_{(x,y)} u) + \omega^2 \rho u = 0, \tag{1.7}$$

where we assume that the shear parameter is here a rank-2 tensor $\underline{\underline{\mu}}$ for more generality, ρ is a scalar (spatially varying) density, $\nabla^T_{(x,y)} = (\partial/\partial x, \partial/\partial y)$ and $u = u(x, y)$ is the third component of the displacement field.

Multiplying (1.7) by a test function $\bar{\phi}$ and integrating by parts over a domain Ω, we obtain:

$$-\int_\Omega \left(\nabla_{(x,y)} \bar{\phi} \cdot \underline{\underline{\mu}} \nabla_{(x,y)} u\right) dx\, dy + \int_\Omega \left(\omega^2 \rho u \bar{\phi}\right) dx\, dy = 0, \tag{1.8}$$

where we have assumed that the surface term is zero (corresponding to a Dirichlet or Neumann integral over the boundary $\partial\Omega$ i.e. the boundary of the domain is either stress free or clamped, or a mixture of both);[3] Robin boundary conditions can also be incorporated.

We now apply to (1.8) the coordinate change $(x, y) \to (u, v)$ and using the fact that

$$\begin{pmatrix} \frac{\partial}{\partial x} \\ \frac{\partial}{\partial y} \end{pmatrix} = \begin{pmatrix} \frac{\partial u}{\partial x} & \frac{\partial v}{\partial x} \\ \frac{\partial u}{\partial y} & \frac{\partial v}{\partial y} \end{pmatrix} \begin{pmatrix} \frac{\partial}{\partial u} \\ \frac{\partial}{\partial v} \end{pmatrix} \quad \Longleftrightarrow \quad \nabla_{(x,y)} = (\mathbf{J}_{ux})^T \nabla_{(u,v)} \tag{1.9}$$

where $\mathbf{J}_{ux} = (\mathbf{J}_{xu})^{-1} = \partial(u, v)/\partial(x, y)$ is the Jacobian of the transformation $(u, v) \to (x, y)$ and $\nabla^T_{(u,v)} = (\partial/\partial u, \partial/\partial v)$, we are led to

[3] One can also assume that $\Omega = \mathbb{R}^2$, in which case the displacement goes to zero at infinity if it is assumed of finite energy and the surface term naturally vanishes.

$$-\int_{\Omega}\left\{\left(\mathbf{J}_{ux}^{T}\nabla_{(u,v)}\bar{\phi}\cdot\underline{\underline{\mu}}\mathbf{J}_{ux}^{T}\nabla_{(u,v)}u\right)\det(\mathbf{J}_{xu})\right\}du\,dv$$
$$+\int_{\Omega}\left(\det(\mathbf{J}_{xu})\omega^{2}\rho u\bar{\phi}\right)du\,dv=0.$$

This can be expressed in terms of $\mathbf{J}_{ux}$:

$$-\int_{\Omega}\left(\left(\nabla_{(u,v)}\bar{\phi}\right)^{T}\frac{\mathbf{J}_{ux}\underline{\underline{\mu}}\mathbf{J}_{ux}^{T}}{\det(\mathbf{J}_{ux})}\nabla_{(u,v)}u\right)du\,dv$$
$$+\int_{\Omega}\left(\frac{\rho}{\det(\mathbf{J}_{ux})}\omega^{2}u\bar{\phi}\right)du\,dv=0.$$

The new parameters $\underline{\underline{\tilde{\mu}}}$ and $\tilde{\rho}$ after the change of coordinates can be now deduced, and are given by:

$$\begin{cases}\underline{\underline{\tilde{\mu}}}=\mathbf{J}_{ux}\underline{\underline{\mu}}\mathbf{J}_{ux}^{T}/\det(\mathbf{J}_{ux}),\\ \tilde{\rho}=\rho/\det(\mathbf{J}_{ux}).\end{cases}\tag{1.10}$$

This was the property exploited by Pendry, Schurig and Smith in their 2006 theoretical proposal of an invisibility cloak for transverse magnetic waves, in which case one can see from (1.3) and (1.7) that $\underline{\underline{\tilde{\mu}}}\to\mathbf{J}_{ux}^{-T}\mu^{-1}\mathbf{J}_{ux}^{-1}\det(\mathbf{J}_{ux})$ and $\tilde{\rho}\to\varepsilon/\det(\mathbf{J}_{ux})$, where μ and ε are the permeability and the permittivity of an isotropic homogeneous medium before the geometric transform (which leads to an heterogeneous anisotropic medium). At first glance, this does not seem like a great achievement, but Pendry and his co-workers introduced a map [44]

$$r'=r_0+\frac{r_1-r_0}{r_1}r,\quad \theta'=\theta,\quad \text{for } r\le r_1,\tag{1.11}$$

which blows up a point to a sphere of radius r_0 while leaving the sphere of radius r_1 unchanged. Outside the sphere of radius r_1, one assumes that $r'=r$ and $\theta'=\theta$ i.e. the medium is untouched (identity map). This way, one can make a hole in space in which to hide an object, see Fig. 1.7! This map was already known in the context of inverse problems where it served as a paradigm of ill-posed problems [16]. However, its application to a specific problem in photonics, namely the design of an invisibility cloak, can be considered as a breakthrough in 2006. The price to pay for this change of coordinates is that the hole should be surrounded by a coating in the ring $r_0<r\le r_1$ consisting of an exotic material [44]. Noting that $\mathbf{J}_{rr'}=\partial(r,\theta)/\partial(r',\theta')=\mathrm{Diag}(1/\alpha,1,1)$ with $\alpha=(r_1-r_0)/r_1$, we find that in our acoustic case

$$\underline{\underline{\tilde{\mu}}}=\mathrm{Diag}\left(\frac{r'-r_0}{r'},\frac{r'}{r'-r_0}\right),\qquad \tilde{\rho}=\frac{r'-r_0}{\alpha^2 r'}.\tag{1.12}$$

Cummer and Schurig were the first ones to derive such a transformed set of parameters for transverse pressure waves in a fluid in 2007 [11], a route towards

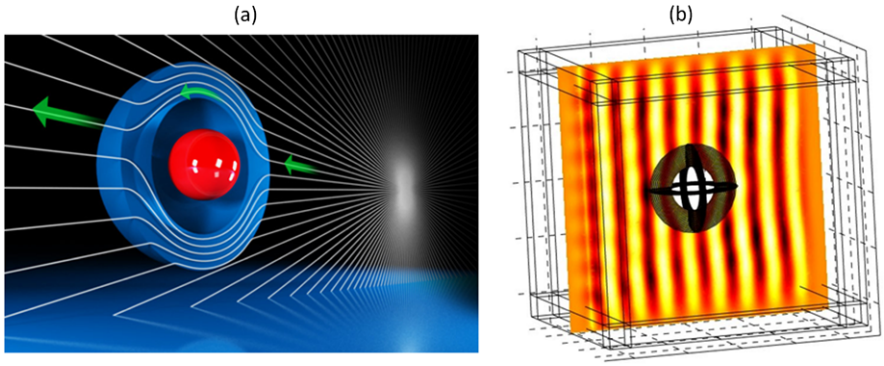

Fig. 1.7 *Acoustic cloak for underwater camouflaging:* (**a**) Schematic diagram depicting trajectories of rays emitted by an acoustic source in presence of a spherical acoustic invisibility cloak (*the blue shell*) surrounding an object (*the red sphere*), for instance a submarine (*left picture* courtesy of Pour La Science, French Edition of Scientific American [17]); (**b**) Finite element computation for a pressure plane wave incident from the right on a multilayered spherical cloak with a rigid spherical obstacle in its center (courtesy of G. Dupont, Institut Fresnel, 2010). Further details can be found in Chap. 9

acoustic cloaking that Torrent and Sanchez-Dehesa furthered with a homogenization study [50], while one of us proposed, together with Alexander Movchan, to use a transversely anisotropic fluid to control linear surface water waves via homogenization of a radially symmetric structured metallic cloak validated at 10 Hertz by M. Farhat and S. Enoch in 2008 [13].

One should note that the parameters in (1.12) become singular on the inner boundary $r' = r_0$ of the cloak as $\underline{\underline{\tilde{\mu}}}$ tends to $\mathrm{Diag}(0, \infty)$ and $\tilde{\rho}$ tends to zero there. Such an extreme behavior is underpinned by the fact that the acoustical path followed by detoured waves around the invisibility region $r \leq r_0$ is longer than if they would travel right through the center of this region, which means that waves need to get infinitely accelerated in the azimuthal direction. Of course, the homogenization approach cannot handle such an extreme set of parameters, which can only be mimicked to certain extend by a strong artificial anisotropy.

Interestingly, the theoretical physicist Ulf Leonhardt independently analyzed conformal invisibility devices using the stationary Schrödinger equation in 2006 [27]. His approach, valid in the geometrical optics limit, only requires spatially varying parameters, which are neither anisotropic, nor singular. As already mentioned, an alternative route to invisibility was proposed in 2005 by Alu and Engheta [1] but it relies on a specific knowledge of the shape and material properties of the object being concealed. In 2006, Milton and Nicorovici proposed to cloak a countable set of line sources using anomalous resonance when it lies in the close neighborhood of a cylindrical coating filled with negative refractive index material [32]. Milton, Briane and Willis further investigated the possibility to cloak objects for elastodynamic waves using geometric transforms, but they ended up with a transformed Navier equation exhibiting rank-3 and rank-4 tensors, whereas the original elasticity equation involves only a rank-4 elasticity tensor [31]. An alternative route towards

cloaking in elastodynamics followed by one of us with Alexander Movchan and Michele Brun leads to a transformed Navier equation which retains its form, but the rank-4 elasticity tensor loses its minor symmetries [4] see also the subsequent work of Norris and Shuvalov [36] and Chap. 12 of the book. One way to achieve such a Cosserat-type elastic material is possibly to play with effective properties of composite structures that may behave in the low frequency regime as neutral coated inclusions as shown by Davide Bigoni, Alexander Movchan and their colleagues in [2].

To exemplify the nature of the challenge of elastodynamic cloaking, let us consider the in-plane propagation of time-harmonic elastic waves governed by the Navier equations

$$\nabla \cdot \mathbb{C} : \nabla \mathbf{u} + \rho \omega^2 \mathbf{u} = \mathbf{0}, \tag{1.13}$$

where $\mathbf{u} = (u_1, u_2)$ is the displacement, ρ the (scalar) density, and $\mathbb{C}$ the 4th-order constitutive tensor of the linear elastic isotropic material which has non-zero cylindrical components

$$\begin{array}{lll} \mathbb{C}_{rrrr} = \lambda + 2\mu, & \mathbb{C}_{\theta\theta\theta\theta} = \lambda + 2\mu, & \mathbb{C}_{rr\theta\theta} = \mathbb{C}_{\theta\theta rr} = \lambda, \\ \mathbb{C}_{r\theta\theta r} = \mathbb{C}_{\theta rr\theta} = \mu, & \mathbb{C}_{r\theta r\theta} = \mu, & \mathbb{C}_{\theta r\theta r} = \mu, \end{array} \tag{1.14}$$

with λ and μ the Lamé moduli characterizing the response of the medium to compressible or shear displacements. Moreover, we assume this equation is valid everywhere except at a point where we apply a harmonic body force $\mathbf{b} = \mathbf{b}(\mathbf{x})$ with ω the wave-frequency and t is time.

By application of the blow-up transformation (1.11) in (1.6), see [4], in the region $r' \in [r_0, r_1]$ the Navier equations (1.6) are mapped into (see also Fig. 1.8):

$$\nabla \cdot \mathbb{C}' : \nabla \mathbf{u} + \rho' \omega^2 \mathbf{u} = \mathbf{0}, \tag{1.15}$$

where the support of the body force is outside the ring of Fig. 1.8, where the stretched density $\rho' = \frac{r - r_0}{r} (\frac{r_1}{r_1 - r_0})^2 \rho$, and the elasticity tensor $\mathbb{C}'$ has non zero cylindrical components

$$\begin{array}{lll} \mathbb{C}'_{r'r'r'r'} = \dfrac{r' - r_0}{r'}(\lambda + 2\mu), & \mathbb{C}'_{\theta\theta\theta\theta} = \dfrac{r'}{r' - r_0}(\lambda + 2\mu), & \mathbb{C}'_{r'r'\theta\theta} = \mathbb{C}'_{\theta\theta r'r'} = \lambda, \\ \mathbb{C}'_{r'\theta\theta r'} = \mathbb{C}'_{\theta r'r'\theta} = \mu, & \mathbb{C}'_{r'\theta r'\theta} = \dfrac{r' - r_0}{r'}\mu, & \mathbb{C}'_{\theta r'\theta r'} = \dfrac{r'}{r' - r_0}\mu, \end{array} \tag{1.16}$$

with λ and μ the Lamé moduli characterizing the isotropic behavior described by $\mathbb{C}$. Note that $\mathbb{C}'$ does not possess the minor symmetries, which is known as a Cosserat-type elastic material. We also note that $\mathbb{C}'$ is singular on the inner boundary of the cloak as some of its entries tend to infinity and some tend to zero when r' tends to r_0.

There is however a special limit case whereby the Navier equation retains its form: (1.6) reduces to a scalar fourth-order PDE in the limit of thin elastic plates. In this case, the out-of-plane displacement $\mathbf{u} = (0, 0, U(r, \theta))$ in (1.15) is such that:

$$\nabla . \big(\underline{\underline{\zeta}}^{-1} \nabla \big(\lambda \nabla . \big(\underline{\underline{\zeta}}^{-1} \nabla U \big) \big) \big) - \lambda^{-1} \beta_0^4 U = 0, \tag{1.17}$$

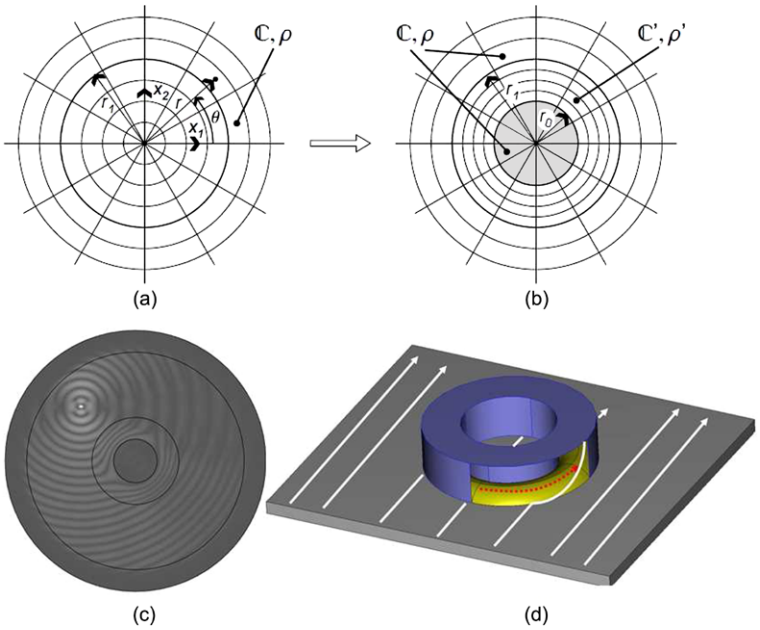

Fig. 1.8 Geometric transform (1.11) from coordinate system (r, θ) (a) to coordinate system (r', θ') (**b**); r_0 and r_1 are the inner and the outer radius of the cylindrical cloak, respectively. Elastic constitutive tensor and density in undeformed and in deformed domains are denoted by $\mathbb{C}$, ρ and $\mathbb{C}'$, ρ', respectively. (**c**) Full wave finite element computation, see [4], for coupled in-plane pressure and shear waves (plot of magnitude of displacement); (**d**) Principle of the anti-earthquake cloak for body elastic waves: a cylindrical coating (shown in *blue*) detours wave trajectories inside the coating (shown in *red*), hence wave trajectories outside the coating (shown in *white*) are unperturbed

with $\beta_0^4 = \omega^2 \rho_0 h / D_0$, where D_0 is the flexural rigidity of the plate, ρ_0 its density and h its thickness. $\underline{\underline{\zeta}}$ is a diagonal rank-2 tensor and λ is a varying coefficient of the material. Physical considerations based on dimensional analysis lead to the choice [14] $\underline{\underline{\zeta}} = \underline{\underline{E}}^{-1/2}$ and $\lambda = \rho^{-1/2}$, where E has the dimension of a Young modulus and ρ of a density. Cloaking further requires that $E_r = (\frac{r-r_0}{r})^2$, $E_\theta = (\frac{r}{r-r_0})^2$ and $\rho = \alpha^4 (\frac{r-r_0}{r})^2$ where $\alpha = r_1/(r_1 - r_0)$; r_0 and r_1 are the interior and the exterior radii of the elastic coat of thickness h. As it turns out, it is fairly easy to achieve such material parameters (except as usual for $r = r_0$), and a workable prototype of an anti-earthquake cloak could be as in Fig. 1.9.

Thus far, we have seen that one can detour waves around finite regions thanks to changes of variables leading to anisotropic (and spatially varying) parameters. Let us now move to another famous paradigm in the control of waves: focussing via negative refraction[4] whereby the parameters take negative values thanks to anomalous dispersion in periodic structures.

[4]Negative refraction can also be seen as some kind of space folding, see for instance [21].

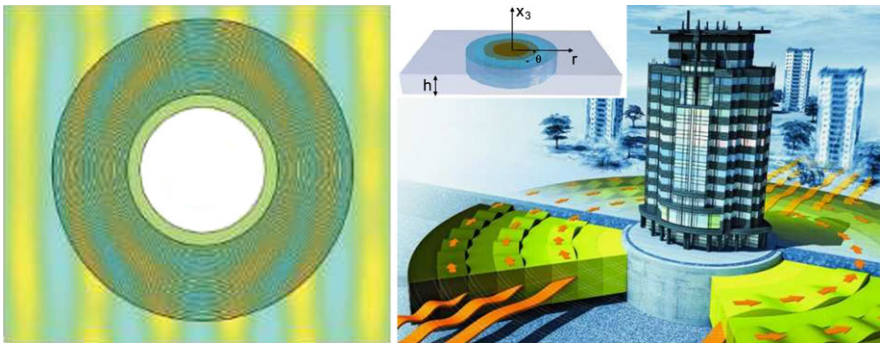

Fig. 1.9 (**a**) Design of an invisibility cloak for bending waves in a thin-elastic plate with concentric rings of homogeneous isotropic materials (here some polymers, see [13]); (**b**) Civil engineering application for anti-earthquake building foundations (courtesy of Popular Science Magazine)

1.2 Asymptotic Modelling of Resonators with a Thin Domain: The Spring-Mass Model Behind Acoustic Metamaterials

In this section, we model the famous split ring resonator (introduced by John Pendry's team in 1998 [42] in order to achieve artificial magnetism) as an acoustic multi-structure [26]. This derivation is taken from [33] (see also [34] for the full mathematical details in the analogous case of transverse electric waves propagating within thin-walled photonic crystal fibres). This derivation unveils the link between the spring-mass model and the split ring resonator, as schematically depicted in Fig. 1.5 i.e. it bridges the discrete and continuous models. Split ring resonators in a perfect doubly periodic arrangement allow for a representation in terms of Bloch waves, the resulting dispersion curves in Fig. 1.10 are useful for interpretation.

We denote by Ω the double-split rings as shown in Fig. 1.5. Formally,

$$\Omega = \left\{ r_0 < \sqrt{x^2+y^2} < r_1 \right\} \setminus \overline{\bigcup_{j=1}^{N} \Pi_\eta^{(j)}} \tag{1.18}$$

where r_0 and r_1 are functions of variables x, y unless the rings are circular and

$$\Pi_\eta^{(j)} = \left\{ (x,y) : 0 < x < l_j,\ |y| < \eta h_j/2 \right\}, \tag{1.19}$$

is a thin ligament of length l_j between the 'ends of the letter C'. Here ηh_j the thickness of the jth bridge, with η a small positive non-dimensional parameter. In our case, we have two thin bridges $\Pi_\eta^{(1)}$ and $\Pi_\eta^{(2)}$.

To derive the asymptotic expansions, we introduce the scaled variable $\xi = y/\eta$ so that $\xi \in (-h_j/2, h_j/2)$ within $\Pi_\eta^{(j)}$, and

$$\frac{\partial^2 v}{\partial y^2} = \frac{1}{\eta^2}\frac{\partial^2 v}{\partial \xi^2}.$$

In $\Pi_1^{(j)}$, the time-harmonic wave equation (1.7) takes the rescaled form

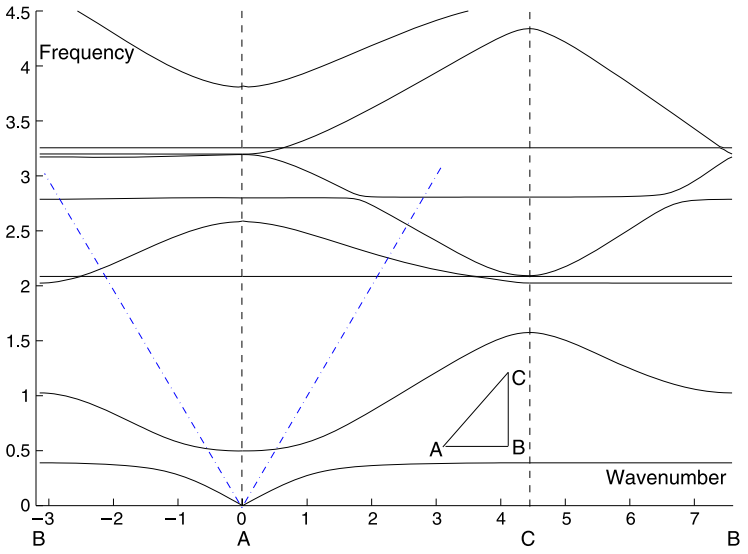

Fig. 1.10 Band diagram corresponding to a square array of split ring resonators as in Fig. 1.5 of center to center spacing 1. The wavenumber is a projection of the Bloch vector which describes the first Brillouin zone ABC with $A = (0, 0)$, $B = (\pi, 0)$ and $C = (\pi, \pi)$. Dispersion curves correspond to frequencies of waves propagating within the array. The resonance associated with a constant longitudinal magnetic field inside each infinite conducting cylinder (resp. anti-plane shear displacement inside each rigid cylinder in the context of acoustics, see Fig. 1.11(a)) creates a low frequency stop band (range of frequencies for which no waves can propagate within the array) near the normalized frequency 0.39 at which the effective permeability (resp. density) displays a negative real part [19] upon resonance

$$\mu\left(\frac{1}{\eta^2}\frac{\partial^2}{\partial\xi^2}+\frac{\partial^2}{\partial x^2}\right)u+\rho\omega^2 u=0, \tag{1.20}$$

where the derivatives are taken in classical sense (μ is constant in the thin bridge). The field u is approximated in the form

$$u\sim U^{(0)}(x,y)+\eta^2 U^{(1)}(x,y). \tag{1.21}$$

Assuming some Neumann (stress-free) boundary conditions hold on the lower and upper edges of the thin-domain,[5] to leading order we obtain (see (1.20) and (1.21))

$$\frac{\partial^2 U^{(0)}}{\partial\xi^2}=0,\qquad |\xi|<h_j/2,\qquad \left.\frac{\partial U^{(0)}}{\partial\xi}\right|_{\xi=\pm h/2}=0. \tag{1.22}$$

Hence, $U^{(0)}=U^{(0)}(x)$ (it is ξ-independent). Assuming that $U^{(0)}$ is given, we derive that the function $U^{(1)}$ satisfies the following model problem on the scaled cross-section of Π_1

[5] If one assumes Dirichlet (clamped) conditions hold on the upper and lower edges of the thin-domain, this kills the field oscillations in the thin bridge, which is of no physical interest.

$$\frac{\partial^2 U^{(1)}}{\partial \xi^2} = -\frac{\partial^2 U^{(0)}}{\partial x^2} + \frac{\rho\omega^2}{\mu} U^{(0)}, \qquad |\xi| < h_j/2$$
$$\left.\frac{\partial U^{(1)}}{\partial \xi}\right|_{\xi=\pm h_j/2} = 0. \tag{1.23}$$

The condition of solvability for the problem (1.24) has the form

$$\frac{d^2 U^{(0)}}{dx^2} + \frac{\omega^2}{c^2} U^{(0)} = 0, \quad 0 < x < l_j, \tag{1.24}$$

where $c = \sqrt{\mu/\rho}$ is the speed of wave. Hence we have shown that to the leading order we can approximate the field u within the thin bridge $\Pi_\eta^{(j)}$ by the function $U^{(0)}$ which satisfies the wave equation in one-space dimension.

We now assume that the field is periodic over each unit cell Y within an array of SRRs: this is a legitimate assumption for a configuration like in Fig. 1.11(a) as the field is localized inside the core region of the SRR. This shows that the average of the eigenfield over the cell vanishes. Indeed, let χ_1 denote the value of the field in the large body Σ of the multi-structure Ω (union of the two C-shaped voids) and let χ_2 (which we normalize to 1) denote the value of the field within the complementary area of the macro-cell $Y \setminus \Omega$ excluding the ligaments. Applying Green's formula, we deduce that

$$\omega^2 \int_Y \rho u \, dx \, dy = \int_{Y\cup\Omega} \mu \nabla \cdot \nabla u \, dx \, dy = \int_{\partial Y \cup \partial\Omega} \mu \frac{\partial u}{\partial n} \, dl = 0, \tag{1.25}$$

since u is periodic on ∂Y (and the normal anti-periodic) and u is traction free on $\partial\Omega$.

This shows that the average of the displacement field u over Y vanishes, hence by neglecting the area of the thin bridges, we obtain

$$\chi_1 \mathscr{S}_\Sigma + \chi_2 \mathscr{S}_{Y\setminus\Omega} = O(\eta). \tag{1.26}$$

Since we have two thin bridges, we have two separate eigensolutions V_j, $j = 1, 2$, corresponding to the vibrations of the thin domains $\Pi_\eta^{(j)}$:

$$\mu V_j''(x) + \rho\omega^2 V_j(x) = 0, \quad 0 < x < l_j, \tag{1.27}$$

$$V_j(0) = \chi_2 = -\chi_1 \frac{\text{meas}(\Xi)}{\text{meas}(Y \setminus \Omega)}, \tag{1.28}$$

$$\mu\eta h_j V_j' l_j = M_j \omega^2 V(l_j), \tag{1.29}$$

where ηh_j and l_j are the thickness and the length of the thin ligament $\Pi_\eta^{(j)}$, and M is the mass of the body Ξ. The bridges are both connected to Ξ, hence $V_1(l_1) = V_2(l_2) = V$, where V is the anti-plane displacement of the rigid body Ξ. We note that $V_j(0)$ is equal to a non-zero constant unlike in [33] (in that case we assumed that

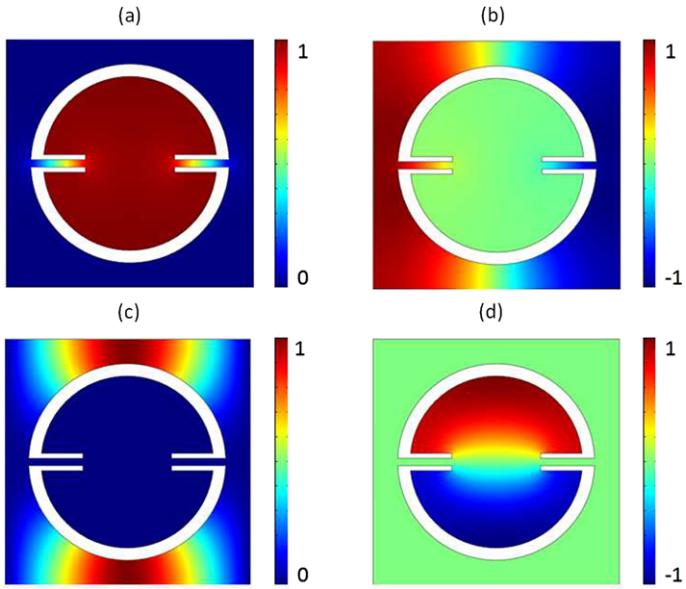

Fig. 1.11 First four Bloch eigenmodes corresponding to Fig. 1.10 at point $C = (\pi, \pi)$. (**a**) Standing wave (monopole localized) mode (monopole) at frequency 0.39; (**b**) Standing wave mode at frequency $\pi/2$; (**c**) Standing wave mode at frequency 2.02; (**d**) Standing wave (dipole localized) mode (monopole) at frequency 2.08. The mechanical interpretation is that in panel (**a**) the core of the cylinder moves like a rigid body whereas in panel (**d**) it wobbles. We note that the field vanishes in the thin bridges in panels (**c**) and (**d**). The only case whereby the field is constant in the core region and oscillating in the thin bridges is in panel (**a**): this is the hallmark of a locally resonant structure

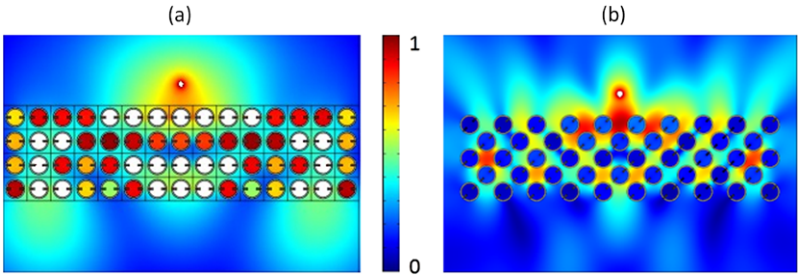

Fig. 1.12 Numerical simulation demonstrating the imaging effect for anti-plane shear waves in an isotropic elastic medium: (**a**) An acoustic source placed on the left side of an array of rigid cylinders (with cross-sections shaped as split ring resonators (SRRs)) is imaged on the right side (with subwavelength resolution). The asymptotic formula (1.1) provides us with the resonant frequency of SRRs at which the effective density of the array turns negative, according to (1.2): The image is most visible around normalized frequency 0.57 i.e. at intersection between *blue dotted lines* (sound cone) and second dispersion curve. (**b**) At normalized frequency 1.45, a lensing effect is also achieved by tilting the array through an angle $\pi/4$, what corresponds to waves propagating with negative group velocity in the CA direction in Fig. 1.10. Note that one can translate the sound cone from point A to point C, to estimate the frequency of such all-angle-negative refraction [9]

$\chi_2 = 0$ i.e. $u = 0$ where the bridges meet the region outside Ω). Here, the constant is chosen in such a way that the average of the field over the basic cell vanishes, as should be expected for a localized (stationary) field.

The solution of the problem (1.27)–(1.29) has the form

$$V_j(x) = -\frac{\chi_2 \cos(\frac{\omega}{c} l_j) - 1}{\sin(\frac{\omega}{c} l_j)} \sin\left(\frac{\omega}{c} x\right) + \chi_2 \cos\left(\frac{\omega}{c} x\right), \tag{1.30}$$

where $c = \sqrt{\mu/\rho}$ and the frequency ω is given as the solution of the following equation

$$\eta\left(h_1 \cot\left(\frac{\omega l_1}{c}\right) + h_2 \cot\left(\frac{\omega l_2}{c}\right) + 2C\right) = \frac{Mc}{\mu}\omega. \tag{1.31}$$

Looking at a first low frequency, we deduce an explicit asymptotic approximation

$$\omega \sim \sqrt{\frac{\eta h_1}{l_1} + \frac{\eta h_2}{l_2}} \sqrt{\frac{\mu}{M}} \left(1 + \frac{\text{meas}(\Xi)}{\text{meas}(Y \setminus \Omega)}\right). \tag{1.32}$$

This estimate actually holds for the frequency of the upper edge of the first phononic band gap of Fig. 1.10. It matches that of a LC resonant circuit as schematically shown in Fig. 1.5(c).

We report in Fig. 1.10 finite element computations for a periodic cell of side length d with a double C-shaped void. The central disk has a radius of $0.3d$ and the two cuts have the same length $0.22d$ and a thickness $0.03d$. Therefore, the frequency estimate is

$$\omega_2^* d/c \sim 0.59, \tag{1.33}$$

which is in reasonably good agreement with the finite element value $\omega_2 d/c = 0.5$ for the lowest value point on the second dispersion curve on Fig. 1.10 occurring at the A point (where the Bloch vector $\mathbf{k}$ vanishes). This provides us with an estimate of the upper-edge frequency of the first gap.

We note that if we take $V(0) = 0$ instead of $V(0) = \text{meas}(\Xi)/\text{meas}(Y \setminus \Omega)$ (*cf.* the original work on acoustic SRRs [33]), we end up with the estimate

$$\omega_1^* d/c = \omega_1^* \sim = 0.37, \tag{1.34}$$

which is in good agreement with the finite element value $\omega_1 d/c = 0.39$ for the lower-edge of the first gap (occurring at the C point when $\mathbf{k} = (\pi, \pi)$). The associated eigenfield is strongly localized inside the SRR, as can be seen in Fig. 1.11(a). In contradistinction, the next two standing waves, see panels (b) and (c), feel the periodicity of the array.

What we should remember of this section is the fact that the lower edge of the low frequency stop band is associated with a localized mode whose amplitude completely vanishes on the cell's boundary (it corresponds to skew symmetric Floquet-Bloch conditions as $\mathbf{k} = (\pi, \pi)$ at the lower edge frequency), and it is therefore

well approximated by (1.34), while the upper edge frequency of the stop band corresponds to a localized mode for which $\mathbf{k} = (0, 0)$, so it is periodic on the cell's boundary, but not vanishing there and it is reasonably well approximated by (1.33).

1.3 Homogenization of Composite Materials

Back in 2002, O'Brien and Pendry developed an effective medium description of a two-dimensional photonic band-gap medium composed of dielectric cylinders of large dielectric constant displaying a negative magnetic permeability for p-polarized wave incidence at microwave frequencies due to single-scatterer (Mie) resonances in the medium [38]. This discovery means that a time harmonic p-polarized magnetic field $\mathbf{H} = u(x_1, x_2)\exp(-i\omega t)\mathbf{e}_3$ within a two-dimensional high-contrast dielectric photonic crystal, with the main axis of fibres along $\mathbf{e}_3$, will be refracted according to the Snell-Descartes laws of negative refraction.

In the sequel, we first expose some homogenization results for such a physical phenomenon known as artificial magnetism, and then we describe a multi-scale mathematical model for the counterpart of this phenomenon in acoustics.

1.3.1 Homogenizing High-Contrast Dielectric Photonic Crystals

The structure under study is basically a 2D photonic crystal depicted in Fig. 1.13, with basic cell Y, the cross-section of a rod is denoted by D (an arbitrary, connected i.e. not holey, cross-section as shown in Fig. 1.13). The rods have a permittivity of ε_r and they are embedded in a host medium of permittivity ε_η. The magnetic field satisfies the following equation:

$$\nabla \cdot \left(\varepsilon^{-1}\nabla u\right) + k^2 u = 0, \tag{1.35}$$

where $k = 2\pi/\lambda = \omega/c$ is the wavenumber in vacuum, with λ the (fixed) wavelength, ω the radian frequency and c the speed of light in vacuum. Here, ε is a piecewise constant function equal to ε_r inside the rods, to ε_e in the host medium and to 1 (air) outside the overall structure. In order to derive the effective parameters of the photonic crystal, we assume that the wavelength λ is large with respect to the period d of the crystal and we denote by the small positive parameter $\eta = d/\lambda$. Equivalently, we might say that ω is small i.e. we are in the quasi-static limit.

As explained by O'Brien and Pendry [38], what is central to the artificial magnetism is the local resonances of the high-contrast rods. We therefore need to scale the permittivity inside the rods in order to model this physical phenomenon. Therefore, the permittivity ε_r of the rods is supposed to be large and their size $r$small compared to the wavelength. Physically, the resonances depend mainly on the optical diameter $r\sqrt{\varepsilon_r}$, therefore, it can be assumed that the existence of a resonance is invariant with respect to a scale transformation. More precisely, if the radius is reduced and the permittivity increased by keeping the optical diameter constant, we expect the physics to be the same. Let us therefore scale the radius as $r \to \eta r$ then

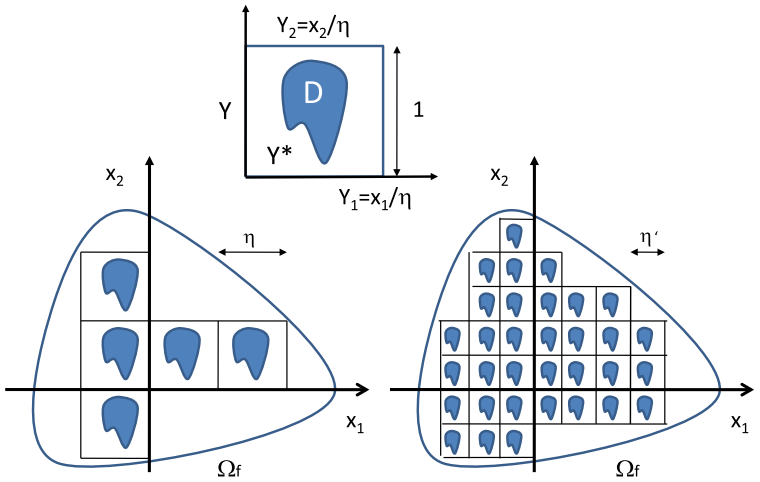

Fig. 1.13 Schematic of the homogenization process: The smaller the positive parameter η, the larger the number of small inclusions of identical cross-section (here $\eta' < \eta$) in the fixed domain Ω_f. In the rescaled coordinate system $(y_1, y_2) = (x_1/\eta, x_2/\eta)$ a unit cell Y contains an inclusion D and Y^* denotes the complementary of D in Y. The wavelength is of the same order as the fixed domain Ω_f, hence very large compared to the small inclusions

if we scale the permittivity as $\mu_r \to \mu_r/\eta^2$, the resonances should not move. Under such a scaling, it can be shown using two-scale convergence that the homogenized equation governing the propagation of p-polarized waves of long wavelengths inside the crystal is given by:

$$\nabla \cdot \left[\underline{\underline{\varepsilon}}_{hom}^{-1} \nabla \left(\mu_{hom}^{-1} u_{hom} \right) \right] + k^2 u_{hom} = 0, \tag{1.36}$$

where it should be noticed that the homogenized permittivity is now matrix valued (artificial anisotropy), and moreover a homogenized permeability has appeared inside the equation (artificial magnetism).

1.3.2 Artificial Anisotropy

Let us first look at the anisotropic features of (1.36). The longitudinal magnetic field is a solution of (1.36) with an anisotropic permittivity matrix given by

$$\underline{\underline{\varepsilon}}_{hom}^{-1} = \frac{1}{\mathscr{A}(Y^*)} \begin{pmatrix} \mathscr{A}(Y^*) - \psi_{11} & \psi_{12} \\ \psi_{21} & \mathscr{A}(Y^*) - \psi_{22} \end{pmatrix}. \tag{1.37}$$

Here, $\mathscr{A}(Y^*)$ denotes the area of the region $Y^* = Y \setminus D$ surrounding a void D in an elementary cell Y of the periodic array, and ψ_{ij} represent corrective terms

$$\forall i, j \in \{1, 2\}, \quad \psi_{ij} = -\int_{\partial D} \Psi_i n_j \, ds, \tag{1.38}$$

where $\mathbf{n}$ is the unit outward normal to the boundary ∂D of the freely vibrating inclusion in the cell Y.

Furthermore, Ψ_j, $j \in \{1, 2\}$, are periodic potentials which are unique solutions (up to an additive constant) of the following two Laplace equations $(\mathscr{L}_j)$:

$$(\mathscr{L}_j) : \nabla^2 \Psi_j = 0 \quad \text{in } Y^*, \tag{1.39}$$

which are supplied with the effective boundary condition $\frac{\partial \Psi_j}{\partial n} = -\mathbf{n} \cdot \mathbf{e}_j$ on the boundary ∂D of the inclusion. Here, $\mathbf{e}_1$ and $\mathbf{e}_2$ denote the vectors of the basis in Cartesian coordinates.

1.3.3 Artificial Magnetic Activity

Thus far, there is no real surprise in the model, as it has been known for over four decades now that the homogenization of periodic structures brings some artificial anisotropy. However, the expression for the effective permeability is less usual:

$$\mu_{hom}(\xi) = \left(\int_Y \beta(\mathbf{y})\, d\mathbf{y} \right)^{-1} \tag{1.40}$$

with $\beta(\mathbf{y})$ is the function which was first introduced in the context of high-contrast homogenization theory by Zhikov in [52]

$$\beta(\mathbf{y}) = 1 + \sum_{j=1}^{\infty} \frac{k^2 \varepsilon_r}{\Lambda_j - k^2 \varepsilon_r} \left(\int_Y \phi_j(\mathbf{y})\, d\mathbf{y} \right)^2. \tag{1.41}$$

Here, Λ_j and ϕ_j are the eigenvalues and orthonormal eigenfunctions of the following Laplace eigenvalue problem with homogeneous Dirichlet boundary conditions:

$$\begin{aligned} \nabla^2 v + k^2 \varepsilon_r v = 0, \quad & \text{in } D, \\ v = 1, \quad & \text{on } \partial D. \end{aligned} \tag{1.42}$$

Importantly, the values of β are negative in the gaps of the periodic structure and positive in its conduction bands. We note that the function β was already well known from the physics community and it underlies the physics of meta-materials as developed by Pendry and his co-authors in the late 90's [41, 42]. It is also worth noting that nothing has been said thus far regarding a negative effective permittivity which is a prerequisite criterion in order to obtain a negative effective refractive index. One way to do this, is to include a small infinitely conducting wire in each unit cell. However, the corresponding homogenization model is beyond the scope of this introductory chapter.

1.4 Homogenization of High-Contrast Phononic Crystals

In a way similar to what has been achieved for transverse electromagnetic waves, we can attribute the existence of a negative mass density to frequencies λ for which $\rho(\xi)\beta(\lambda)$ becomes negative. But it does not seem obvious to explain why μ_{hom} might take some negative values. This does not preclude the possibility to obtain an effective negative refractive index $n_{hom} = \sqrt{\rho_{hom}/\mu_{hom}}$ for acoustic waves, as acknowledged in [19], but such a doubly negative metamaterial requires additional resonant elements.

1.4.1 The Homogenization Result: Anisotropic Shear Modulus and Dispersive Density

The basic principle of homogenization is to perform a scaling analysis of the structured medium: the shear modulus of the rods shall become larger and larger when we refine the mesh i.e. $\mu_\eta = \eta^2\mu_r$ where μ_r denotes the shear modulus inside a rod before scaling. The time-harmonic displacement field satisfies the following governing equation

$$\nabla \cdot (\mu_\eta \nabla u_\eta) + k^2 u_\eta = 0. \tag{1.43}$$

When the acoustic wave penetrates the structured cloak Ω_f, it undergoes fast periodic oscillations: Ω_f $(a \leq |x_i| \leq b,\ i = 1, 2)$, is evenly divided into a large number $N(\eta) \sim \eta^{-2}$ of small sectors ηY, where η is a small positive real parameter. The smaller η, the larger the number of small sectors ηY. The homogenization technique amounts to looking at the limit when η goes to zero, while the wavenumber k in (1.43) remains fixed. To filter these oscillations, we consider an asymptotic expansion of the displacement field solution of (1.43) in terms of a macroscopic (slow) variable $\mathbf{x} = (x_1, x_2)$ and a microscopic (fast) variable $\mathbf{x}/\eta$

$$\forall \mathbf{x} \in \Omega_f, \quad u_\eta(\mathbf{x}) = \sum_{i=0}^{\infty} \eta^i u^{(i)}(\mathbf{x}, \mathbf{x}/\eta), \tag{1.44}$$

where $u^{(i)} : \Omega_f \times Y \longmapsto \mathbb{C}$ is a smooth function of 4 variables, independent of η, such that $u^{(i)}(\mathbf{x}, \cdot)$ is Y-periodic.

Rescaling the differential operator in (1.43) accordingly as $\nabla = \nabla_{\mathbf{x}} + \frac{1}{\eta}\nabla_{\mathbf{y}}$, and collecting terms of same powers of η, we obtain the following homogenized problem in the limit when η tends to zero:

$$(\mathscr{P}_{hom}) : \nabla \cdot \big([\mu_{hom}]\nabla u_{hom}(\mathbf{x})\big) = \rho_{hom} k^2 u_{hom}(\mathbf{x}) \quad \text{in } \Omega_f. \tag{1.45}$$

From (1.45) (where derivatives are understood in weak sense i.e. they include discontinuities), we deduce the effective transmission conditions

$$u^{(-)}_{hom}\big|_{\partial\Omega_f^-} = \text{area}\big(Y^*\big) u^{(+)}_{hom}\big|_{\partial\Omega_f^+}, \tag{1.46}$$

for the values $u_{hom}^{(-)}$ and $u_{hom}^{(+)}$ of the homogenized displacement u_{hom} on the inner and outer boundaries $\partial\Omega_f^-$ and $\partial\Omega_f^+$ of the cloak Ω_f and

$$n \cdot \left([\mu_{hom}]\nabla u_{hom}^{(-)}\right)\big|_{\partial\Omega_f^-} = n \cdot \left(\nabla u_{hom}^{(+)}\right)\big|_{\partial\Omega_f^+}, \tag{1.47}$$

for its normal derivative (the flux).

This result shows that the displacement field is solution of (1.45) with a shear anisotropic matrix given by

$$[\mu_{hom}] = \frac{1}{\mathscr{A}(Y^*)} \begin{pmatrix} \mathscr{A}(Y^*) - \psi_{11} & \psi_{12} \\ \psi_{21} & \mathscr{A}(Y^*) - \psi_{22} \end{pmatrix}. \tag{1.48}$$

Here, $\mathscr{A}(Y^*)$ denotes the area of the region Y^* surrounding a void in an elementary cell Y of the periodic array, and ψ_{ij} represent corrective terms defined as in (1.38) and (1.39).

The form of the effective density is the same as in (1.41)–(1.42) replacing ε_r by μ_r^{-1}.

1.4.2 Multi-Scale Analysis

An elegant way to identify the limit problem is to use some weak formulation of the problem and look at the convergence of a sequence of minimization problems [7]. It is also possible to use some heuristic approach known as multi-scale expansion which can be further validated by a priori estimates. We opt for this second approach here.

Let us recall that the shear modulus in the inclusions D scales as $\mu_\eta = \eta^2\mu_r$, whereas it is remains constant outside the matrix background. We would like to incorporate the ansatz (1.44) of the displacement field into 1.43. To make things simple, we denote $\chi_\eta = \mu_\eta \nabla u_\eta$, so that the Helmholtz equation is now recast into the following coupled system:

$$\begin{aligned} -\nabla \cdot \chi_\eta &= k^2 u_\eta, \\ \mu_\eta \nabla u_\eta &= \chi_\eta. \end{aligned} \tag{1.49}$$

We proceed with the asymptotic analysis by splitting the ansatz (1.44) as per:

$$\begin{aligned} u_\eta(x) &= u_0(x, x/\eta) + \eta u_1(x, x/\eta) + \cdots, \\ \chi_\eta(x) &= \chi_0(x, x/\eta) + \eta \chi_1(x, x/\eta) + \cdots, \end{aligned} \tag{1.50}$$

where the pairs (u_j, χ_j) of successive terms for the ansatz of the displacement field and its gradient depend on two variables: the macroscopic (slow) variable $x = (x_1, x_2)$ and the microscopic (fast) variable x/η. These fields are periodic with respect to the second variable: if d is the pitch of the square array, $(u_j, \chi_j)(x, y+d) = (u_j, \chi_j)(x, y)$.

Remark 1.1 Importantly, we note that the limit field u_0 depends on both macroscopic and microscopic variables, respectively x and y. As a consequence, the homogenized macroscopic field u_{hom} shall be obtained by averaging over Y:

$$u_{hom} = \int_Y u_0(x, y)\, dy. \tag{1.51}$$

This feature is known in the homogenization literature as a double-porosity problem whereby classical homogenization fails [52].

Let us plug the expansions (1.50) into the coupled system (1.49), keeping in mind that the gradient should be rescaled as $\nabla = \nabla_x + \frac{1}{\eta}\nabla_y$.

The identification of the terms of orders $1/\eta$ and $1/\eta^2$ leads to the following two coupled systems:

$$\text{on } Y: \quad \begin{cases} \nabla_x \cdot \chi_0 + \nabla_y \cdot \chi_1 = k^2 u_0, \\ \nabla_y \cdot \chi_0 = 0, \end{cases} \tag{1.52}$$

$$\text{on } Y \setminus D: \quad \begin{cases} \nabla_x u_0 + \nabla_y u_1 = \mu_e^{-1} \chi_0, \\ \nabla_y u_0 = \mathbf{0}, \end{cases} \tag{1.53}$$

$$\text{on } D: \quad \begin{cases} \nabla_y u_0 = \mu_r^{-1} \chi_1, \\ \chi_0 = \mathbf{0}, \end{cases} \tag{1.54}$$

where μ_r is the shear modulus inside each inclusion and μ_e is the shear modulus in the surrounding material.

Remark 1.2 It is important to note that we have obtained three coupled systems on three different domains. Moreover, from the second differential equation in (1.53), we deduce that the leading term of the displacement u_0 does not depend on y on $Y \setminus D$: the fact that u_0 depends on the microscopic variable in D comes from the high-contrast there.

We shall now look at the transmission conditions in order to get more information on the homogenized system.

$$\eta^2 \mu_r \left[\mathbf{n} \cdot \nabla u_\eta^-\right] = \mu_e \left[\mathbf{n} \cdot \nabla u_\eta^+\right] \tag{1.55}$$

where the superscript $\pm$ denotes the value of the displacement field on the inner and outer boundaries of D with $\mathbf{n}$ the corresponding unit outwards normal to ∂D.

Collecting the terms of order η^0 and η^{-1}, we obtain on ∂D:

$$\begin{aligned} \mathbf{n} \cdot \nabla_y u_1^+ + \mathbf{n} \cdot \nabla_x u_0^+ &= 0, \\ \mathbf{n} \cdot \nabla_y u_0^+ &= 0. \end{aligned} \tag{1.56}$$

Let us now take the divergence in both members of the first equation of (1.54):

$$\Delta_y u_0 = \mu_r^{-1} \nabla_y \cdot \chi_1, \tag{1.57}$$

so that making use of the first equation in (1.52) and the second equation in (1.54), we deduce that in the region D:

$$\Delta_y u_0 + \mu_r^{-1} k^2 u_0 = 0. \tag{1.58}$$

Remark 1.3 This microscopic equation is central to the problem of high-contrast homogenization. It is a spectral problem set on the cross-section of high-contrast rods. This problem is fully specified provided we subject it to the specific boundary condition from the second equation in (1.56).

Let us now look for the solutions of the spectral problem:

$$\Delta_y p + \mu_r^{-1} k^2 p = 0 \quad \text{in } D, \qquad p = 1 \quad \text{on } \partial D. \tag{1.59}$$

Here, we have used the boundary condition in (1.56). Assuming that $\rho_{hom} = \int_Y p(y)\, dy$, we can see that $u_0(x, y) = p(y)/\rho_{hom}$ in (1.58).

It remains to derive the homogenized macroscopic equation. For this, we take the divergence in both members of the first equation of (1.53) which together with the second equation of (1.52) leads to

$$\Delta_y u_1 = -\nabla_y \cdot \nabla_x u_0 \quad \text{in } Y \setminus D. \tag{1.60}$$

This equation is supplied with the transmission condition in (1.55). We deduce that $\nabla_y u_1$ depends linearly on $\nabla_x u_0$.

Remark 1.4 The fact $\nabla_y u_1$ is proportional to $\nabla_x u_0$ is a classical result in homogenization theory and allows for an important simplification:

$$\begin{aligned} \nabla_y \cdot \psi_j &= 0 \quad \text{in } Y \setminus D, \\ \mathbf{n} \cdot \nabla_y \psi_j &= -n_j \quad \text{on } \partial D, \end{aligned} \tag{1.61}$$

where $j = 1, 2$ and $\mathbf{n} = (n_1, n_2)$. This annex problem can be solved numerically and provides us with the homogenized matrix

$$A_{hom}(y) = \begin{pmatrix} \frac{\partial \psi_1}{\partial y_1} & \frac{\partial \psi_1}{\partial y_2} \\ \frac{\partial \psi_2}{\partial y_1} & \frac{\partial \psi_2}{\partial y_2} \end{pmatrix}, \tag{1.62}$$

which is such that $\nabla_y u_1 = A_{hom}(y) \nabla_x u_0$.

Averaging the first equation in (1.52) over Y, we obtain:

$$\nabla_x \cdot \int_Y \chi_0\, dy + \int_Y \nabla_y \cdot \chi_1\, dy = k^2 \int_Y u_0\, dy, \tag{1.63}$$

where the second integral in the left-hand side vanishes due to the Green's theorem.

This leads to

$$\nabla_x \cdot \chi_{hom} = k^2 u_{hom}. \tag{1.64}$$

Averaging the first equation in (1.53) over $Y \setminus D$, we obtain:

$$\nabla_x \int_{Y\setminus D} u_0\, dy + \int_{Y\setminus D} \nabla_y u_1\, dy = \mu_e^{-1} \int_{Y\setminus D} \chi_0\, dy. \tag{1.65}$$

This can be recast as:

$$\nabla_x (\rho_{hom} u_{hom}) \int_{Y\setminus D} \big(1 + A_{hom}(y)\big)\, dy + \int_{Y\setminus D} \nabla_y u_1\, dy = \mu_e^{-1} \chi_{hom}. \tag{1.66}$$

Combining (1.64) and (1.66), we deduce the homogenized macroscopic equation

$$\nabla_x \cdot \big[\mu_{hom}(x) \nabla(\rho_{hom} u_{hom})\big] + k^2 u_{hom} = 0, \tag{1.67}$$

where the effective shear modulus can be expressed as:

$$\mu_{hom} = \mu_e \int_{Y\setminus D} \big(1 + A_{hom}(y)\big)\, dy. \tag{1.68}$$

1.4.3 Solving the Spectral Problem in the Rescaled Inclusion

Equation (1.67) clearly shows that the effective medium has both an effective anisotropic shear modulus and an effective scalar density. In order to find a closed form for the effective density, we have to solve the spectral problem (1.59). To do so, we introduce the following spectral problem:

$$-\Delta_y \phi = \Lambda \phi \quad \text{in } D, \qquad \phi = 0 \quad \text{on } \partial D. \tag{1.69}$$

This leads to a family of eigenvalues Λ_p and associated eigenfunctions (possibly degenerate) ϕ_{pl} (the index l accounts for the degeneracy). Then, we can solve for $p(y)$ by expanding it on the Hilbertian basis $\{\phi_{pl}\}$ by noting that $p - 1 = 0$ on $Y \setminus D$, hence

$$p(y) = 1 + \sum_{nl} c_{nl} \phi_{nl}(y). \tag{1.70}$$

By plugging this expression into (1.59), we obtain:

$$p(y) = 1 + \sum_{nl} \frac{-{\mu_r}^{-1} k^2}{{\mu_r}^{-1} k^2 - \Lambda_p} \left(\int_Y \phi_{nl}(y)\, dy \right) \phi_{nl}(y). \tag{1.71}$$

We deduce that

$$\rho_{hom} = \int_Y p(y)\, dy = 1 + \sum_{nl} \frac{-k^2}{k^2 - \mu_r \Lambda_p} \left(\int_Y \phi_{nl}(y)\, dy \right)^2. \tag{1.72}$$

An explicit expression for ρ_{hom} will be derived in the next section for the case of circular rods. Let us however remark that, near a resonance, the effective density is proportional to $k^2/(\mu_r \Lambda_p - k^2)$. This shows that the sign of ρ_{hom} changes when crossing the resonance Λ_p, therefore there exists a band of wavelengths over which the effective density is negative. Let us now turn to some numerical illustration of this theory.

Let us first consider the case of square inclusions of sidelength $a = d/2$, where d is the pitch of the array. The eigenfunctions are $\phi_{nm}(y) = 2\sin(n\pi y_1)\sin(n\pi y_2)$ and the corresponding eigenvalues are $k_{nm}^2 = \pi^2(n^2 + m^2)$. The expansion of p on this basis leads to the effective density:

$$\rho_{hom}^{*} = 1 + \frac{64a^2}{\pi^4} \sum_{(n,m)odd} \frac{k^2}{n^2 m^2 (k_{nm}^2 \mu_r / a^2 - k^2)}. \tag{1.73}$$

This function can be computed numerically for instance with Matlab, see Sect. 1.4.4.

Let us now consider the case of circular inclusions of radius $r = R$. The eigenfunctions are Bessel functions. Let us denote by χ_{nm} the mth zero of the nth Bessel function (i.e. $J_n(\chi_{nm}) = 0$), then the eigenvalues of the spectral problem (1.69) are $\Lambda_{nm} = (\chi_{nm}/R)^2$. These eigenvalues are twice degenerate except for $n = 0$ and the associated normalized eigenfunctions are $\phi_{nm}^{\pm}(y) = |\pi R^2 J_n'(\chi_{nm})|^{-1} J_n(r\chi_{nm}/R)\exp(\pm in\theta)$. Since $\int_Y \phi_{nm}^{\pm}(y)\,dy = 0$ for $n \neq 0$, the only resonance is the fundamental one, and the expansion of p on this basis leads to the effective density:

$$\rho_{hom}^{**} = 1 + \frac{4\pi R^2}{\chi_{00}^2} \frac{k^2}{\chi_{00}^2 \mu_r / R^2 - k^2}, \tag{1.74}$$

where $\chi_{00} \sim 2.405$.

1.4.4 Correspondences Between Zhikov's Function and Floquet-Bloch Diagrams

The aforementioned Zhikov's functions can be computed numerically for instance with Matlab and depending upon the value of μ_r, we can see that the effective density takes some negative values near the resonance for the case of circular cylinders, or square inclusions, as shown in Figs. 1.14 and 1.15. For the frequency 0.61, the effective density is nearly -1. This corresponds to the frequency range for which a negative group velocity appears in the corresponding Bloch diagram, cf. Fig. 1.17. At this frequency, we observe a lensing effect for a finite array of high-contrast cylinders, see Figs. 1.19 and 1.20. We note that the stop bands correspond to Mie resonances of the cylinders, see Fig. 1.18. However, if the contrast is not large enough, the stop bands cannot form as the contrast in shear modulus is only on the order of 10, and the whole theory breaks down, see Fig. 1.16. Similar results hold for

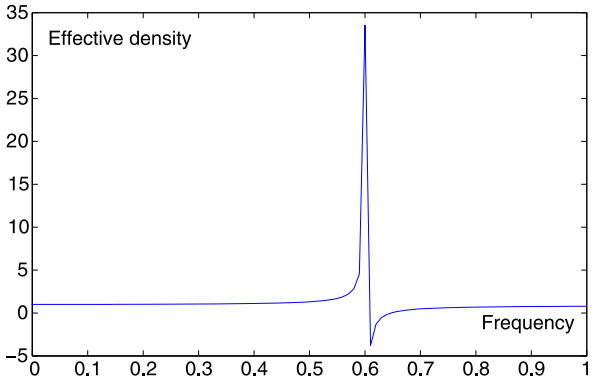

Fig. 1.14 Effective density versus frequency using (1.74) for a circular inclusion with $R = 0.25$ and $\mu_r = 0.01$. Negative values of the density are in the frequency region $[0.609, 0.647]$ whereby the group velocity is negative on the optical band of the low frequency stop band in Fig. 1.17. We numerically obtain an effective density of -1 for frequencies 0.60925 and 0.624

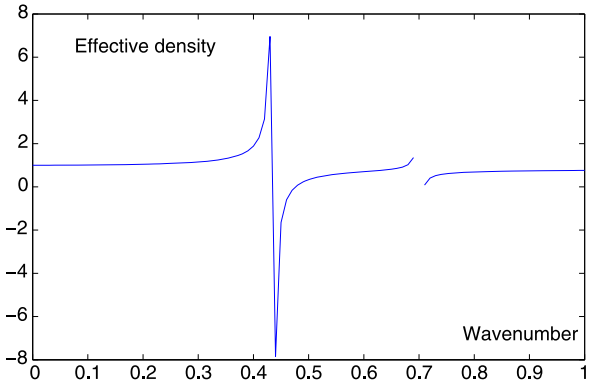

Fig. 1.15 Effective density versus frequency using (1.74) for a square inclusion with $a = 0.5d$ ($d = 0.1$) and $\mu_r = 0.01$. Negative values of the density are in the frequency region $[0.432, 0.534]$ whereby the group velocity is negative on the optical band of the low frequency stop band in Fig. 1.22. The second resonance around frequency 0.7 is much sharper and corresponds to the second (tiny) stop band in Fig. 1.22

square cylinders. In this case, the theory captures nearly all the resonances associated with stop bands, as usually $\int_Y \phi^{\pm}_{nm}(y)\,dy \neq 0$. The first two resonances are shown in Fig. 1.15 and correspond respectively to the low frequency stop band and a very tiny second stop band in Fig. 1.22. Once can clearly see that these kinds of tiny stop bands also occur at higher frequencies in Fig. 1.22. Similarly to the case of circular cylinders, a contrast on the order of 100 is required to achieve such a typical high-contrast band spectrum with many flat bands (standing waves). Indeed, when the contrast in shear modulus is on the order of 10, see Fig. 1.21, dispersion curves do not exhibit such flat bands.

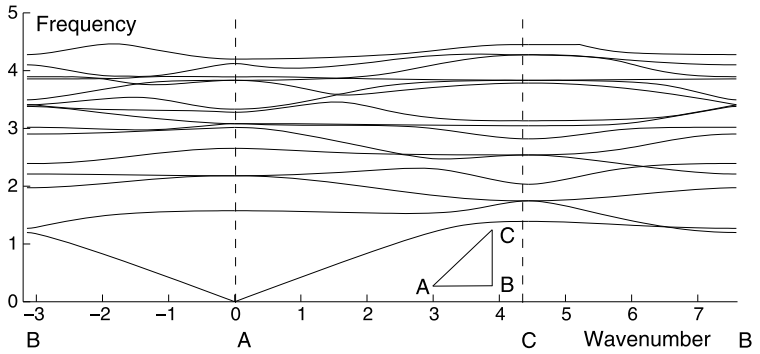

Fig. 1.16 Dispersion curves (normalized frequency versus normalized wavenumber) for an array of cylinders of radius $R = 0.25$ with center-to-center spacing 1 and a relatively high contrast of shear modulus: $\mu_r = 0.1$ inside each inclusion and $\mu_e = 1$ in the matrix. Note that there are no stop bands for the first 15 dispersion curves. However, some upper curves are nearly flat (dispersionless). The acoustic band is non-monotonic and the optical band has a small, but positive, group velocity for vanishing wavenumbers

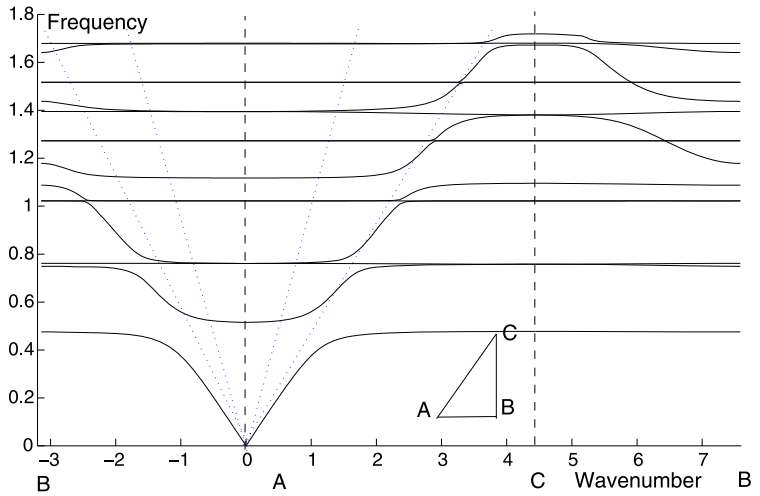

Fig. 1.17 Dispersion curves (normalized frequency versus normalized wavenumber) for an array of circular cylinders of radius $R = 0.25$ with center-to-center spacing 1 and for a high contrast of shear modulus: $\mu_r = 0.01$ inside each inclusion and $\mu_e = 1$ in the matrix. Note that there is a complete low frequency stop band at normalized frequency 0.49 associated with a Mie resonance (the acoustic and optical bands are dispersionless for wavenumbers outside the range $[-1, 1]$ and the optical band has a negative group velocity for wavenumbers in the range $[-1, 1]$). Similar features can be seen for higher bands, but the associated stop bands are very narrow. The dotted lines on either sides of wavenumber A stand for the dispersion of shear waves in a homogeneous matrix with wavespeed 1 (known as light line in the context of optics) and 0.5

It is interesting to note that the homogenized density turns out to be simpler to analyze for circular than for square inclusions, as the latter involves the computation

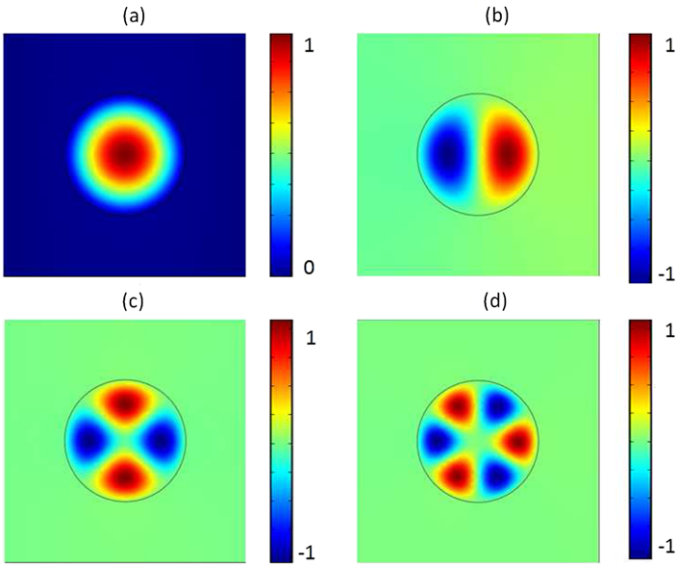

Fig. 1.18 Eigenmodes corresponding to standing waves of dispersion curves in Fig. 1.17. (**a**) Monopole (frequency 0.43 corresponding to the lower edge of the first stop band, see also plot of effective density versus frequency in Fig. 1.14); (**b**) Dipole (frequency 0.78 corresponding to the lower edge of a second (tiny) stop band); (**c**) Quadrupole (frequency 1.02 corresponding to the lower edge of a third (tiny) stop band); (**d**) Sextupole (frequency 1.28 corresponding to a flat band)

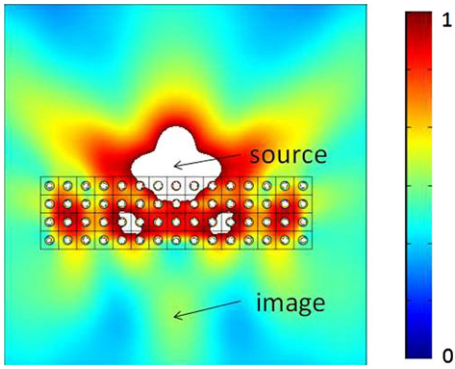

Fig. 1.19 Lensing effect for a line source located close to a finite array of circular cylinders of radius 0.5 and shear modulus $\mu_r = 0.01$ in a matrix of shear modulus $\mu_e = 1$, at normalized frequency 0.61 corresponding to an effective density close to -1 in Fig. 1.14 and a negative group velocity in Fig. 1.18. The density is 1 everywhere

of a series. It is also clear from (1.73) and (1.74) that the larger the inclusion, the larger the negative values of the homogenized density upon resonance.

1.4.5 Dispersive Effective Parameters and Negative Refraction

An important application of the dispersive nature of the effective density for such high-contrast phononic crystals is the possibility to achieve negative refraction and

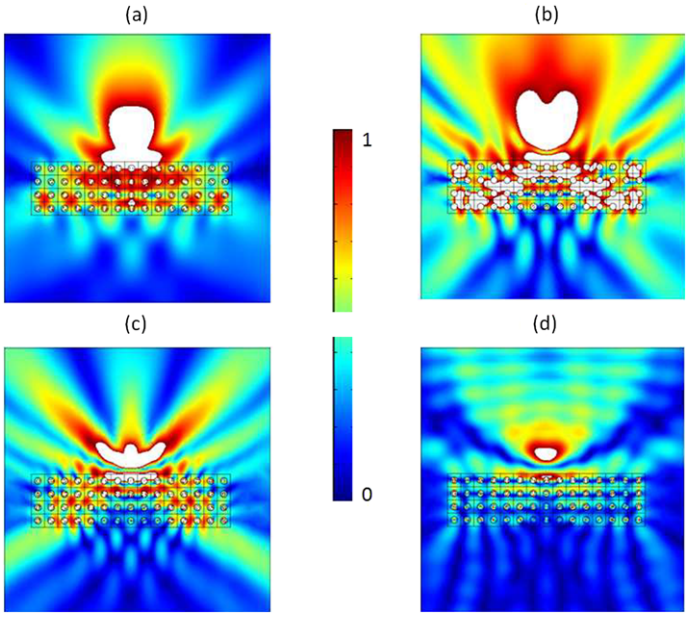

Fig. 1.20 Lensing effect for a line source located close to a finite array of circular cylinders of radius 0.5 and shear modulus $\mu_r = 0.01$ in a matrix of shear modulus $\mu_e = 1$ (**a**, **b**, **c**) and $\mu_e = 2$ (**d**), at normalized frequencies 0.8 (**a**), 1.15 (b) and 1.5 (**c**, **d**) corresponding to a negative group velocity in Fig. 1.17. The density is 1 everywhere. We note that the field in (**d**) undergoes less reflection by the photonic crystal than in (**c**), as it corresponds to the intersection of a dispersion curve of the crystal with the dispersion of sound in the surrounding homogeneous medium, see dotted blue line with lowest slope in Fig. 1.18

thus focussing of acoustic waves by a flat structured lens. Figures 1.19 and 1.23 display the hallmarks of such a spectacular phenomenon. In Fig. 1.20, an attempt has been made at reducing the impedance mismatch between the phononic crystal and the surrounding medium in order to enhance the lensing effect. Moreover, it has been checked numerically that the image resolution is about a third of the wavelength in Fig. 1.19 and respectively a fourth, a third and a half of a wavelength in Figs. 1.20(a), (b), (c) and 1.23(a), (b), (c). The fact that there is less impedance mismatch in (d) than in (c) of Fig. 1.20 does not improve the image resolution which is still about half the wavelength. The key parameter to improve the image resolution seems to be the ratio between the pitch of the array and the frequency.

1.5 High-Frequency Homogenization

Over the past ten years there has been a growing interest in the fabrication and modelling of so-called photonic crystal fibres (PCFs). These fibres guide the light in a unique way: instead of channelling the light by using a stepped refractive index

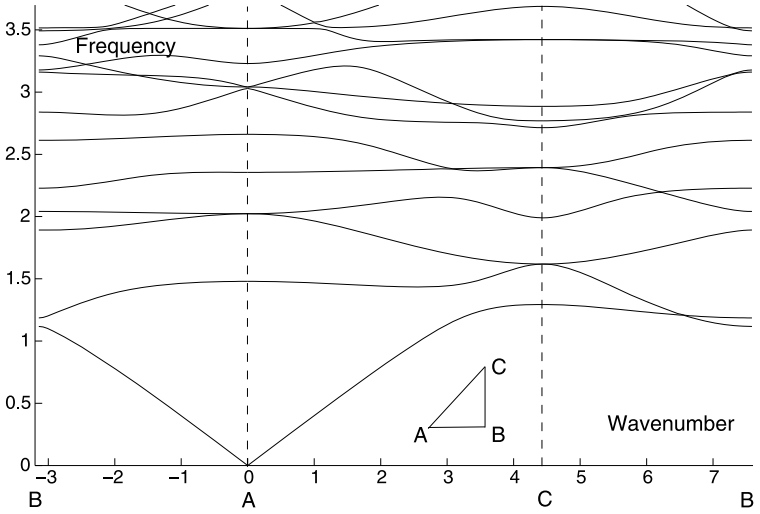

Fig. 1.21 Dispersion curves (normalized frequency versus normalized wavenumber) for an array square cylinders of sidelength $a = 0.5$ with center-to-center spacing 1 and for a high contrast of shear modulus: $\mu_r = 0.1$ inside each inclusion and $\mu_e = 1$ in the matrix. Note that there is a complete low frequency stop band at normalized frequency 0.49 associated with a Mie resonance (the acoustic and optical bands are dispersionless for wavenumbers outside the range $[-1, 1]$ and the optical band has a negative group velocity for wavenumbers in the range $[-1, 1]$. Similar features can be seen for higher bands, but the associated stop bands are very narrow

gradient, the fibre itself contains inhomogeneities which are used to *trap* light in a central core. Materials of this kind are often referred to as photonic band-gap materials, since they suppress the propagation of light over a small band of frequencies, and are the optical analogue of semiconductors. A related question, and one which is attracting steadily more attention, involves the propagation of elastic waves through heterogeneous materials. Such *phononic band-gap materials* would use the spacing of inhomogeneities in the materials to suppress mechanical vibrations (such as sound) in one or all directions. The advantages of being able to model and fabricate these phononic crystal materials are numerous. By adjusting the scale of these materials, they could be used either as the basis for a new generation of audio filters, or to construct earthquake-resistant foundations for buildings. An acoustic band gap could be designed and tuned for the vibration-free operation of high-precision machine systems. In addition, materials with an acoustic band gap in a suitable frequency range might be used to build phononic lasers (*phasers*) as well as acousto-optical switches. Knowledge of the effect of defects on the band-gap phenomenon is essential. Modes which are forbidden to propagate within a band-gap will tend to cluster around a defect in the material, an effect known as localization. Localization can occur at high frequencies, to address this we now turn our attention to an asymptotic scheme that is capable of capturing this even when the wavelength and typical microstructural lengthscales are similar.

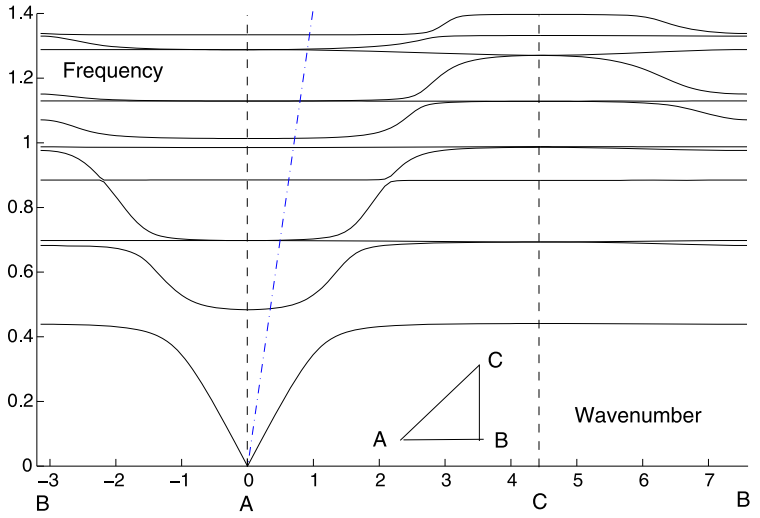

Fig. 1.22 Dispersion curves (normalized frequency versus normalized wavenumber) for an array square cylinders of sidelength $a = 0.5$ with center-to-center spacing 1 and for a high contrast of shear modulus: $\mu_r = 0.01$ inside each inclusion and $\mu_e = 1$ in the matrix. Note that there is a complete low frequency stop band at normalized frequency 0.49 associated with a Mie resonance (the acoustic and optical bands are dispersionless for wavenumbers outside the range $[-1, 1]$ and the optical band has a negative group velocity for wavenumbers in the range $[-1, 1]$. Similar features can be seen for higher bands, but the associated stop bands are very narrow

Returning to Sect. 1.4 on high-contrast homogenization we note that the usual asymptotic procedure proceeds via the introduction of two scales: the slow scale $\mathbf{x}$ and a fast scale (microscopic) $\mathbf{y} = \mathbf{x}\eta$ where $\eta \ll 1$, see Fig. 1.13. This scale separation shrinks the microstructure allowing it to be isolated and averaged; the emphasis is upon the long scale. The frequency of the waves is effectively low and this limits the validity of the usual theory. The more conventional homogenization theory (without high contrast) as in, say [48], is even more limited in its extent with the leading order displacement field eventually independent of the microscale. Both of these existing homogenization theories have limitations.

We now make a subtle change of emphasis beginning with a trivial change in the definition of the two scales i.e. a slow scale $\mathbf{X} = \eta\mathbf{x}$ and a fast scale $\xi = \mathbf{x}$, see Fig. 1.25; the scaling fixes attention upon the micro-scale. The theory expounded in [10] then follows through the logic of this together with an additional idea taken from physics. If one has a perfect lattice then attention can be concentrated upon a simple cell with Bloch conditions set upon its edges, this perfect lattice problem encodes the multiple scattering between cells no matter how high the frequency is. Noting that there exist standing waves at the wavenumbers corresponding to the edges of the Brillouin zone, and that those standing waves have associated standing wave frequencies inspires one to use this information within an asymptotic theory.

The physical interpretation of the modified theory is that close to standing wave frequencies then on the fast scale, even if the overall system is not perfectly pe-

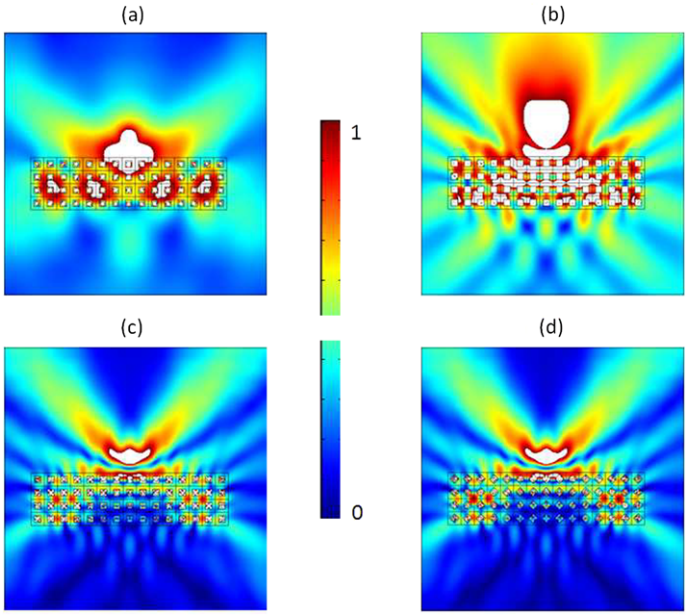

Fig. 1.23 Lensing effect for a line source located close to a finite array of square cylinders of radius 0.5 and shear modulus $\mu_r = 0.01$ in a matrix of shear modulus $\mu_e = 1$, at normalized frequencies 0.57 (**a**), 1.15 (**b**) and 1.41 (**c**, **d**) corresponding to a negative group velocity in Fig. 1.22. The density is 1 everywhere. We note that the field in (**d**) is nearly the same as in (**c**), but the square cylinders have been titled by an angle of $\pi/4$: the localized modes of each cylinder is independent of the orientation of the cylinder with respect to the lattice directions

riodic, but nearly so, each cell feels the effect of its neighbors primarily through these standing wave solutions. However, on the longer scale these rapidly oscillating "fast" solutions are modulated by a long-scale solution. The mathematical details are in [10] but it then enables homogenization to be employed for a far greater range of situations. Mathematically we adopt the ansatz:

$$\begin{aligned} u(\mathbf{X}, \boldsymbol{\xi}) &= u_0(\mathbf{X}, \boldsymbol{\xi}) + \eta u_1(\mathbf{X}, \boldsymbol{\xi}) + \eta^2 u_2(\mathbf{X}, \boldsymbol{\xi}) + \cdots, \\ k^2 &= k_0^2 + \eta k_1^2 + \eta^2 k_2^2 + \cdots \end{aligned} \tag{1.75}$$

This ansatz assumes variation both at the microscale and macroscale even at leading order, as opposed to classical homogenization theory for which $u_0(\mathbf{X}, \boldsymbol{\xi}) \equiv u_0(\mathbf{X})$. This is also contrary to high contrast homogenization from which u_0 has no variation in one of the media. This ansatz also involves expanding the frequency k where k_0 is the frequency associated with the standing waves. Going through the analysis gives the leading order solution as

$$u(\mathbf{X}, \boldsymbol{\xi}) \sim u_0(\mathbf{X}, \boldsymbol{\xi}) = f(\mathbf{X}) U_0(\boldsymbol{\xi}; k_0) \tag{1.76}$$

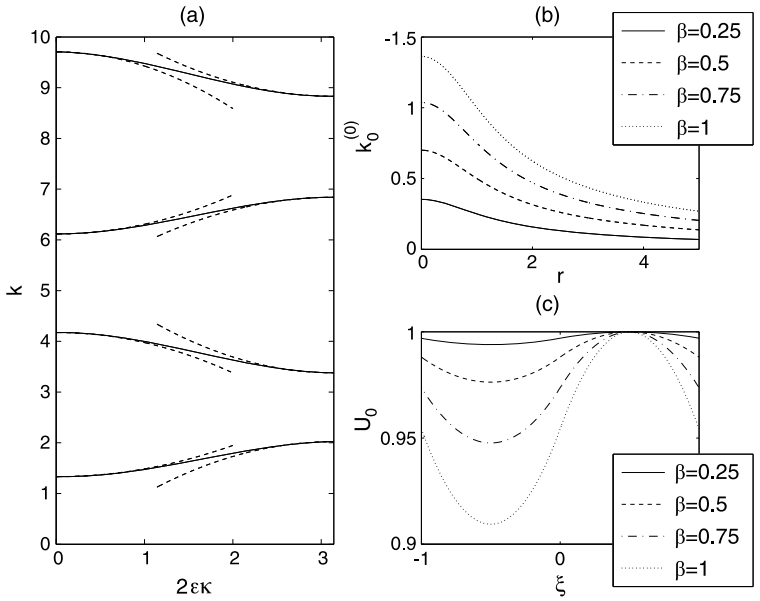

Fig. 1.24 The dispersion curves for the piecewise homogeneous string. Panel (**a**) is for $r = 1/4$, $\beta = 1$ showing the absence of the fundamental mode and the curves from the full numerics (*solid*) versus the asymptotics (*dashed*). Panel (**b**) shows the variation of the lowest frequency cut-off at $\kappa = 0$, namely $k_0^{(0)}$, versus the change in wavespeed r for various values of β. Panel (**c**) shows the variation in the leading order solution, $U_0(\xi, k_0^{(0)})$ as β increases for fixed r: $r = 1.5$ in panel (**c**). [From [10]]

that is it separates into a standing wave solution on the fast scale $U_0(\boldsymbol{\xi}; k_0)$ modulated by a long-scale function $f(\mathbf{X})$. The function $f(\mathbf{X})$ satisfies a PDE

$$T_{ij}\frac{\partial^2 f}{\partial X_i \partial X_j} + \frac{(k^2 - k_0^2)}{\eta^2} f = 0, \tag{1.77}$$

where the spatially constant tensor T_{ij} incorporates the short-scale information associated with the standing wave frequency k_0. This tensor is composed of integrals of the standing wave displacements are related quantities, [10], these are no longer simple averages, that act to capture the influence of the short-scale upon the long-scale.

A simple illustrative example, is that of a one-dimensional string with a periodic variation in wavespeed $c(\xi)$:

$$c(\xi) = \begin{cases} 1/r & \text{for } 0 \le \xi < 1, \\ 1 & \text{for } -1 \le \xi < 0, \end{cases} \tag{1.78}$$

for r a positive constant, an exact solution is readily obtained. For the string we have to solve

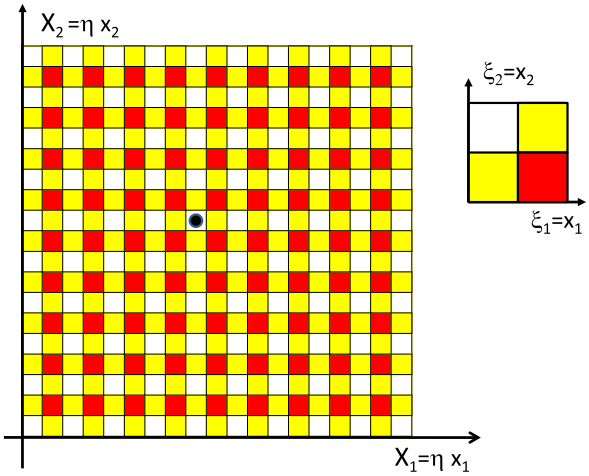

Fig. 1.25 Schematic of the high-frequency homogenization process: A three-phase checkerboard with a source located in one of the cells is infinite periodic. The (x_1, x_2) coordinates are now on the scale of the unit cell, unlike for Fig. 1.13 where they describe the scale of the macroscopic obstacle. This shifts the emphasis from the macroscopic (slow) variable $(X_1, X_2) = (\eta x_1, \eta x_2)$ to the microscopic (fast) variable $(\xi_1, \xi_2) = (x_1, x_2)$ which is of the same order as the wavelength

$$\frac{d^2u}{dx^2} - \beta^2 u + \frac{k^2}{c^2(\xi)}u = 0, \tag{1.79}$$

where the term $-\beta^2 u$ corresponds to a constant elastic restoring parameter in a Winkler model. This example is instructive as it can be solved exactly, it has a zero-frequency stop band (and so homogenization theory is normally of no use) and one can compare easily to the high frequency homogenization asymptotics: the results are shown in Fig. 1.24.

These ideas carry across to two-dimensions too, for instance a checkerboard medium [8, 9] created from cells repeated to fill the plane. The elementary cell being defined with

$$\frac{\partial^2 u}{\partial x_1^2} + \frac{\partial^2 u}{\partial x_2^2} + k^2\big[1 + g_1(x_1) + g_2(x_2)\big]u = 0, \tag{1.80}$$

for $u(x_1, x_2)$ (we use x and y interchangeably for x_1 and x_2 respectively). We take the elementary cell to be the square $-1 < x_1, x_2 < 1$, and in the analytical and numerical work the $g_i(x_i)$ in (1.80) are taken to be piecewise constant

$$g_i(x_i) = \begin{cases} r^2 & \text{for } 0 \le x_i < 1, \\ 0 & \text{for } -1 \le x_i < 0. \end{cases} \tag{1.81}$$

The checkerboard medium is shown in Fig. 1.25. For a perfect checkerboard free from defects and free from forcing one can consider just this elementary cell with

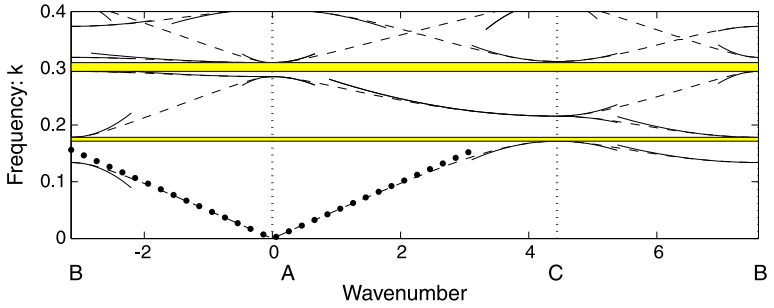

Fig. 1.26 Dispersion curves for high contrast $r = 10$: exact solutions (*dashed*), classical homogenization limit (*dotted*) and high frequency homogenization (HFH) asymptotics (*solid*). Stop-bands, whose edges are accurately predicted by HFH, are shown shaded. [From [8]]

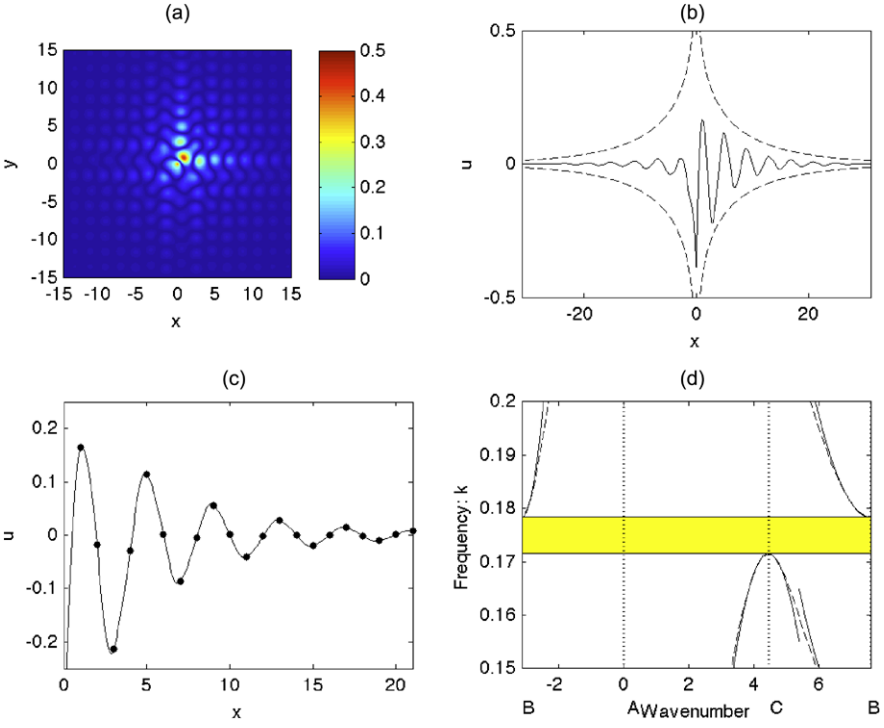

Fig. 1.27 Response to localized line source excitation with frequency $\Omega = 0.172$ for the checkerboard structure with $r = 10$. Panel (**a**) shows $|u|$ as a globally decaying solution modulating an oscillatory behavior. Panel (**b**) gives u along the line $y = 1/2$ as the solid line lying within a dashed envelope given by the asymptotic relation. Panel (**c**) is further detail of the solution along this line with the points marking the cell-edges demonstrating the local out-of-phase oscillations from cell to cell. Panel (**d**) gives a detailed view of the dispersion curves, and stop-band, near the excitation frequency; dashed lines are from the full numerics and the asymptotics are the *solid lines*. [From [8]]

Bloch conditions and extract the dispersion curves as shown in Fig. 1.26; the exact curves are the dashed lines. Also shown in the figure is the only line that conventional homogenization theory finds, that is, the dotted straight line emerging from the origin. The asymptotics from the high frequency homogenization are the solid lines and they capture the local behavior near every edge of the Brillouin zones and reproduce the fine detail such as changes in curvature etc. All of this is encapsulated in the tensor T_{ij}.

Clearly being able to reproduce known results is nice, but one would like a theory to be able to predict something that is not already available. Fortunately it does so, Fig. 1.27 show the response to a forcing at a frequency within the first stop-band, as expected the field decays spatially and full numerical simulations in Fig. 1.27(a) show this. The asymptotic theory nicely reproduces this asymptotically with f giving the decay envelope, further details can be found in [8] where other topical issues such as ultra-refraction and all-angle negative refraction are also covered.

1.6 Concluding Remarks

The subject of acoustic metamaterials, and related topics, relies deeply upon the properties of waves passing through structured media. In particular the mismatch in material scales and properties creates the possibility of apparent unphysical overall properties such as negative density. The purpose of this chapter is to demonstrate that it is possible to formalize how this happens directly from the equations using homogenization theory; extensions of homogenization theory are then illustrated showing how one can use these ideas to move to higher frequencies and model the physics of stop bands and wave localization. The concept of creating effective media from microstructured layers or other media underlies much of what follows in subsequent chapters, such as superlensing and cloaking phenomena in the context of acoustic and elastodynamic waves. A brief introduction to the design of metamaterials via geometric transformations has also been provided, with an emphasis on correspondences between governing equations in electromagnetics, acoustics and elastodynamics which are detailed in following chapters.

References

1. Alú, A., Engheta, N.: Achieving transparency with plasmonic and metamaterial coatings. Phys. Rev. E **72**, 016623 (2005)
2. Bigoni, D., Serkov, S., Valentini, M., Movchan, A.B.: Asymptotic models of dilute composites with imperfectly bonded inclusions. Int. J. Solids Struct. **35**, 3239 (1998)
3. Bouchitté, G., Schweizer, B.: Homogenization of Maxwell's equations in a split ring geometry. Multiscale Model. Simul. **8**(3), 717–750 (2010)
4. Brun, M., Guenneau, S., Movchan, A.B.: Achieving control of in-plane elastic waves. Appl. Phys. Lett. **94**, 061903 (2009)
5. Brun, M., Guenneau, S., Movchan, A.B., Bigoni, D.: Dynamics of structural interfaces: Filtering and focussing effects for elastic waves. J. Mech. Phys. Solids **58**, 1212–1224 (2010)

6. Chakrabarti, S., Ramakrishna, S.A., Guenneau, S.: Finite checkerboards of dissipative negative refractive index. Opt. Express **14**, 12950 (2006)
7. Cherednichenko, K.D., Smyshlyaev, V.P., Zhikov, V.V.: Non-local homogenised limits for composite media with highly anisotropic periodic fibres. Proc. R. Soc. Edinb. A **136**, 87–114 (2006)
8. Craster, R.V., Kaplunov, J., Nolde, E., Guenneau, S.: High frequency homogenization for checkerboard structures: Defect modes, ultra-refraction and all-angle-negative refraction. J. Opt. Soc. Amer. A **28**, 1032–1041 (2011)
9. Craster, R.V., Kaplunov, J., Nolde, E., Guenneau, S.: Bloch dispersion and high frequency homogenization for separable doubly-periodic structures. Wave Motion **49**, 333–346 (2012).
10. Craster, R.V., Kaplunov, J., Pichugin, A.V.: High frequency homogenization for periodic media. Proc. R. Soc. Lond. A **466**, 2341–2362 (2010)
11. Cummer, S.A., Schurig, D.: One path to acoustic cloaking. New J. Phys. **9**, 45 (2007)
12. Fang, N., Xi, D., Xu, J., Ambati, M., Srituravanich, W., Sun, C., Zhang, X.: Ultrasonic metamaterials with negative modulus. Nature **5**, 452 (2006)
13. Farhat, M., Enoch, S., Guenneau, S., Movchan, A.B.: Broadband cylindrical acoustic cloak for linear surface waves in a fluid. Phys. Rev. Lett. **101**, 134501 (2008)
14. Farhat, M., Guenneau, S., Enoch, S., Movchan, A.: Cloaking bending waves propagating in thin plates. Phys. Rev. B **79**, 033102 (2009)
15. Farhat, M., Guenneau, S., Enoch, S., Movchan, A.B.: Negative refraction, surface modes, and superlensing effect via homogenization near resonances for a finite array of split-ring resonators. Phys. Rev. E **80**, 046309 (2009)
16. Greenleaf, A., Lassas, M., Uhlmann, G.: On nonuniqueness for Calderon's inverse problem. Math. Res. Lett. **10**, 685–693 (2003)
17. Guenneau, S., Enoch, S., McPhedran, R.C.: L'invisibilite en vue. Pour Sci. (French edn. of Sci. Am.) **382**, 42–49 (2009)
18. Guenneau, S., Gralak, B., Pendry, J.B.: Perfect corner reflector. Opt. Lett. **30**, 1204–1206 (2005)
19. Guenneau, S., Movchan, A.B., Ramakrishna, S.A., Petursson, G.: Acoustic meta-materials for sound focussing and confinement. New J. Phys. **9**, 399 (2007)
20. Guenneau, S., Poulton, C.G., Movchan, A.B.: Oblique propagation of electromagnetic and elastic waves for an array of cylindrical fibres. Proc. R. Soc. Lond. A **459**, 2215–2263 (2003)
21. Guenneau, S., Ramakrishna, S.A.: Negative refractive index, perfect lenses and checkerboards: Trapping and imaging effects in folded optical spaces. C. R. Phys. **10**, 352–378 (2009)
22. Guenneau, S., Vutha, A.C., Ramakrishna, S.A.: Negative refraction in 2d checkerboards related by mirror anti-symmetry and 3d corner lenses. New J. Phys. **7**, 164 (2005)
23. He, S., Jin, Y., Ruan, Z., Kuang, J.: On subwavelength and open resonators involving metamaterials of negative refraction index. New J. Phys. **7**, 210 (2005)
24. Jikov, V.V., Kozlov, S.M., Oleinik, O.A.: Homogenization of Differential Operators and Integral Functionals. Springer, New York (1994)
25. Kohn, R.V., Shipman, S.P.: Magnetism and the homogenization of micro-resonators. Multiscale Model. Simul. **7**, 62–92 (2008)
26. Kozlov, V., Mazya, V., Movchan, A.B.: Asymptotic Analysis of Fields in Multistructures. Oxford Science Publications, Oxford (1999)
27. Leonhardt, U.: Optical conformal mapping. Science **312**, 1777 (2006)
28. Li, J., Chan, C.T.: Double negative acoustic metamaterial. Phys. Rev. E **70**, 055602 (2004)
29. Liu, Z.Y., Zhang, X.X., Mao, Y.W., Zhu, Y.Y., Yang, Z.Y., Chan, C.T., Sheng, P.: Locally resonant sonic materials. Science **289**, 1734 (2000)
30. Milton, G.W.: The Theory of Composites. Cambridge University Press, Cambridge (2002)
31. Milton, G.W., Briane, M., Willis, J.R.: On cloaking for elasticity and physical equations with a transformation invariant form. New J. Phys. **8**, 248 (2006)
32. Milton, G.W., Nicorovici, N.A.: On the cloaking effects associated with localized anomalous resonances. Proc. R. Soc. Lond. A **462**, 3027 (2006)

33. Movchan, A.B., Guenneau, S.: Localised modes in split ring resonators. Phys. Rev. B **70**, 125,116 (2004)
34. Movchan, A.B., Movchan, N.V., Guenneau, S., McPhedran, R.C.: Asymptotic estimates for localized electromagnetic modes in doubly periodic structures with defects. Proc. R. Soc. A **463**, 1045 (2007)
35. Nicorovici, N.A., McPhedran, R.C., Milton, G.W.: Optical and dielectric properties of partially resonant composites. Phys. Rev. B **49**, 8479–8482 (1994)
36. Norris, A., Shuvalov, A.L.: Elastic cloaking theory. Wave Motion **48**, 525–538 (2011)
37. Notomi, N.: Superprism phenomena in photonic crystals. Opt. Quantum Electron. **34**, 133 (2002)
38. O'Brien, S., Pendry, J.B.: Photonic band-gap effects and magnetic activity in dielectric composites. J. Phys. Condens. Matter **14**, 4035–4044 (2002)
39. Pendry, J.B.: Negative refraction makes a perfect lens. Phys. Rev. Lett. **85**, 3966–3969 (2000)
40. Pendry, J.B.: Negative refraction. Contemp. Phys. **45**, 191 (2004)
41. Pendry, J.B., Holden, A.J., Robbins, D.J., Stewart, W.J.: Extremely low frequency plasmons in metallic mesostructures. Phys. Rev. Lett. **76**, 4763 (1996)
42. Pendry, J.B., Holden, A.J., Stewart, W.J., Youngs, I.: Magnetism from conductors and enhanced nonlinear phenomena. IEEE Trans. Microw. Theory Tech. **47**, 2075–2084 (1996)
43. Pendry, J.B., Ramakrishna, S.A.: Focussing light with negative refractive index. J. Phys. Condens. Matter **15**, 6345 (2003)
44. Pendry, J.B., Schurig, D., Smith, D.R.: Controlling electromagnetic fields. Science **312**, 1780–1782 (2006)
45. Ramakrishna, S.A.: Physics of negative refractive index materials. Rep. Prog. Phys. **68**, 449 (2005)
46. Ramakrishna, S.A., Guenneau, S., Enoch, S., Tayeb, G., Gralak, B.: Light confinement through negative refraction in photonic crystal and metamaterial checkerboards. Phys. Rev. A **75**, 063830 (2007)
47. Russell, P.S., Marin, E., Diez, A., Guenneau, S., Movchan, A.B.: Sonic band gap PCF preforms: enhancing the interaction of sound and light. Opt. Express **11**, 2555 (2003)
48. Sanchez-Palencia, E.: Non-homogeneous Media and Vibration Theory. Springer, Berlin (1980)
49. Smith, D.R., Padilla, W.J., Vier, V.C., Nemat-Nasser, S.C., Schultz, S.: Composite medium with simultaneously negative permeability and permittivity. Phys. Rev. Lett. **84**, 4184 (2000)
50. Torrent, D., Sanchez-Dehesa, J.: Acoustic cloaking in two dimensions: A feasible approach. New J. Phys. **10**, 063015 (2008)
51. Veselago, V.G.: The electrodynamics of substances with simultaneously negative values of ε and μ. Sov. Phys. Usp. **10**, 509–514 (1968)
52. Zhikov, V.V.: On an extension of the method of two-scale convergence and its applications. Sb. Math. **191**, 973–1014 (2000)
53. Zolla, F., Renversez, G., Nicolet, A., Kuhlmey, B., Guenneau, S., Felbacq, D.: Foundations of Photonic Crystal Fibres. Imperial College Press, London (2005)

Chapter 2
Locally Resonant Structures for Low Frequency Surface Acoustic Band Gap Applications

Abdelkrim Khelif, Younes Achaoui, and Boujemaa Aoubiza

Abstract In this chapter we investigate the propagation of acoustic waves in a two-dimensional array of cylindrical pillars on the surface of a semi-infinite substrate. Through the computation of the acoustic band diagram and transmission spectra of periodic pillars arranged in different symmetries, we show that these structures possess acoustic metamaterial features for surface acoustic waves. The pillars on the top of the surface introduce new guided modes in the non-radiative region of the substrate outside the sound cone. The modal shape and polarization of these guided modes are more complex than those of classical surface waves propagating on a homogeneous surface. Significantly, an in-plane polarized wave and a transverse wave with sagittal polarization appear that are not supported by the free surface. In addition, the band diagram of the guided modes defines band gaps that appear at frequencies markedly lower than those expected from the Bragg mechanism. We identify them as originating from local resonances of the individual cylindrical pillar and we show their dependence on the geometrical parameters, in particular with the height of the pillars. The frequency positions of these band gaps are invariant with the symmetry, and thereby the period, of the lattices, which is unexpected in band gaps based on Bragg mechanism. However, the role of the period remains important for defining the non-radiative region limited by the slowest bulk modes and influencing the existence of new surface modes of the structures. The surface acoustic wave transmission across a finite array of pillars corroborates the signature of

A. Khelif (✉)
International Joint Laboratory, GeorgiaTech-CNRS UMI 2958, 2-3 Rue Marconi, 57070 Metz, France
e-mail: abdelkrim.khelif@femto-st.fr

Y. Achaoui
Institut FEMTO-ST, Université de Franche-Comté, CNRS, 32 avenue de l'Observatoire, 25044 Besançon, France
e-mail: younes.achaoui@femto-st.fr

B. Aoubiza
Laboratoire de Mathématiques, Université de Franche-Comté, route de Gray, 25030 Besançon Cedex, France
e-mail: boujamaa.aoubiza@univ-fcomte.fr

R.V. Craster, S. Guenneau (eds.), *Acoustic Metamaterials*,
Springer Series in Materials Science 166, DOI 10.1007/978-94-007-4813-2_2,

the locally resonant band gaps for surface modes and their link with the symmetry of the source and its polarization. Numerical simulations based on an efficient finite element method and considering Lithium Niobate pillars on a Lithium Niobate substrate are used to illustrate the theory.

2.1 Introduction

The propagation of acoustic and elastic waves in inhomogeneous media has attracted a lot of interest during the last two decades. Usually presented as periodic structures with spatially modulated elastic moduli and mass density, the so-called phononic crystals have a number of important features such as the occurrence of frequency band gaps [13, 19]. In the frequency band gap ranges, sound and acoustic vibrations are strictly prohibited to propagate within these media resulting in a significant attenuation in their transmission spectra regardless of the direction of propagation. In order to widen these acoustic band gaps, different combinations of materials using solid/solid, solid/fluid and fluid/fluid phononic crystals have been put forward [11, 15, 20]. Using the band gap principle, phononic crystals allow the propagation of elastic or acoustic waves to be regulated. In other words, they play the role of perfect mirrors for elastic or acoustic waves in the frequency range of the band gap. The fundamental interest in controlling the elastic energy, and the potential applications, of phononic crystals are thus well established. These first studies of bulk, surface and Lamb waves have paved the way in establishing the fundamental physics in terms of controlling acoustic waves by trapping, guiding and demultiplexing them through single and linear defects [10, 12, 17].

Basically, band gaps can originate from Bragg reflections due to the periodicity of the structure. In this case, the spatial period of the crystal is of the same order of magnitude as the acoustic wavelength at the central frequency of the gap and, as a consequence, the lattice constant has generally been the key parameter to scale band gaps. A shortcoming of this principle was identified early in the context of low frequency acoustic applications for sound isolation, as well as earthquake shielding, which has long been regarded as a pernicious form of environmental pollution and a dangerous natural issue. In fact, complete sound attenuation for a low frequency range (10 Hz–10 KHz) needs a feature-sized structure of a few meters in order to ensure a spectral band gap with classical phononic crystals.

Another approach to realize low frequency acoustic band gaps, while utilizing lattice constants much shorter than the acoustic wavelength, is to use an acoustic metamaterial. More generally, these acoustic metamaterials are defined as an arrangement of artificial structural elements, designed to achieve advantageous and unusual acoustic properties and have an inhomogeneity scale that is much smaller than the wavelength of interest. Their acoustic response can be expressed in terms of homogenized material parameters. Various artificially engineered metamaterials are now demonstrating unprecedented acoustic proprieties that are not observed in naturally occurring materials. Among them are negative refraction, super-prism resolution, sub-wavelength acoustic imaging and acoustic cloaking. The structural

units of metamaterials can be tailored in shape and size, their composition and morphology can be artificially tuned, and inclusions can be designed and placed in a predetermined manner to achieve prescribed functionalities.

The first acoustic metamaterials appearing in the literature were so-called locally resonant sonic crystals [14] with acoustic resonators built into individual unit cells. The development of these acoustic metamaterials has led to groundbreaking demonstrations of the mass density law, often used in sonic shielding. Particularly, a broad frequency (10 Hz–10 KHz) sonic band gap with lattice constants two orders much shorter than the acoustic wavelength. The physical interpretation of locally resonance band gaps can result from the Fano resonance of a localized state with a continuum of propagation modes [5, 16]: at resonance, the energy of waves propagating in the matrix can be efficiently stored and delayed, while at anti-resonance, wave propagation becomes prohibited. In addition, the local resonance can be tuned by using intrinsic material features such as silicon rubber for which the sound velocity is two orders of magnitude lower than the one of the host matrix. For such composites, polarization-dependent frequency band gaps were reported for bulk waves [21] and complete band gaps were reported for Lamb waves [6]. A local resonance can also be altered using shape-design as in the case of Helmholtz resonators [4].

In this chapter, we consider a two-dimensional distribution of a periodic array of the pillars on the surface of a semi-infinite medium with different symmetries. The pillars are acting as local acoustic resonances interacting with the substrate continuum [1, 8, 18] and lead to the possibility of finding a low-frequency band gap for acoustic waves guided by the surface. In addition, we study the effect of square, triangular and honeycomb lattices on the band gaps. We highlight the role of the pitch, where it can be fundamental in controlling the dispersion of guided modes by defining the non radiative region and its non influence on the band gaps. The exhibition of these two features—the subwavelength low frequency band gaps and invariance with the lattice symmetries—makes the proposed structure an acoustic metamaterial. The numerical results presented here are related to the case of Lithium Niobate pillars on a Lithium Niobate substrate, but the conclusions remain valid for other materials and compositions as well. The chapter is organized in three sections. Section 2.2 deals briefly with model and method of calculation. In Sect. 2.3, we expose and discuss the main results of new surface modes and low frequency band gaps of different symmetry arrays. The conclusion is presented in Sect. 2.3.4.

2.2 Model and Method of Calculation

As illustrated in Fig. 2.1, we consider square, triangular and honeycomb lattice arrays of cylindrical pillars on the surface of a semi-infinite substrate. The z axis is chosen to be perpendicular to the surface and parallel to the cylinder axis. The lattice parameter of the acoustic periodic structure is a for square and triangular lattices and $\sqrt{3}a$ for honeycomb lattice. The filling fractions in the case of a square, triangular and honeycomb lattices, are respectively defined as: $F = \pi r^2/a^2$, $F = 4\pi r^2/\sqrt{3}a^2$

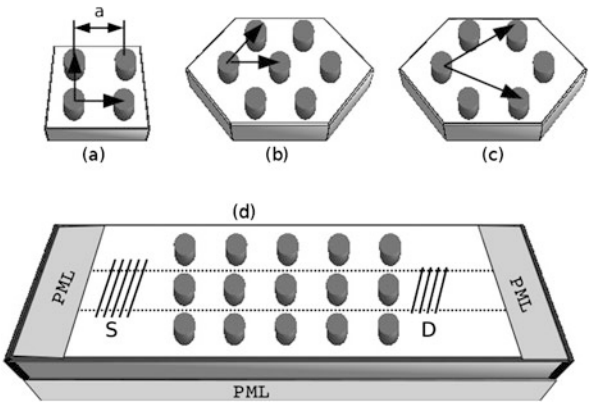

Fig. 2.1 Phononic periodic structure composed of cylindrical pillar arrays on a substrate with different symmetries: (**a**) square, (**b**) triangular and (**c**) honeycomb lattice. The lattice parameter is a for square and triangular lattices and $\sqrt{3}a$ for the honeycomb lattice. The pillars have height h and radius r. (**a**) The unit cell domains used for band structure calculations are meshed in three dimensions and Bloch-Floquet periodic boundary conditions are applied in both the x and the y directions. (**b**) The domain used for transmission computations has periodic boundary conditions along the y direction and a finite extent along the x direction. Perfectly matched layers are used to prevent reflections from the domain boundaries. A line S generates waves propagation in the (x, y) plane including surface acoustic waves. A line D detects the surface waves traveling through the finite size structure

and $F = (8\pi/3)r^2/\sqrt{3}a^2$. Here r is the radius of the cylinder and the height of the cylinders is h. Dispersion curves are calculated for the infinite system by using a finite element method in which only the unit cell is meshed and Bloch-Floquet conditions are implemented via periodic boundary conditions [9]. A three-dimensional mesh is used and the structure is assumed to be infinite and periodic in both the x and y directions (Fig. 2.1a). A phase relation is applied on the lateral sides of the mesh, defining boundary conditions between adjacent cells. This phase relation is related to the Bloch wave number of the modes of the periodic structure. By varying the wave vector in the first Brillouin zone and solving a spectral problem, the eigenfrequencies are obtained. The eigenvectors represent the modal displacement fields.

To simulate the transmission spectra through a finite size structure (finite number of periods), we use the model depicted in Fig. 2.1b. An incident surface acoustic wave with a specific polarization (u_x, u_z, u_y) is modelled by applying a line source vibrating on the surface. We apply in the y direction a periodic boundary condition that renders the line source infinitely long. The line source thus generates waves propagating in the (x, z) plane with uniform phase fronts along the y direction. In the far field of the source, the generated waves can be either bulk waves propagating away inside the substrate or surface waves propagating along the surface in the x direction. We assume that a few wavelengths from the source, the displacements at the surface are only caused by surface waves and not by bulk waves. To prevent reflections caused by the scattering of waves from the domain boundaries, perfectly

matched layers (PMLs) [2] are applied as illustrated in Fig. 2.1d. PMLs have the property that the mechanical disturbances are gradually absorbed in the layers before they can reach the outer boundaries [3]. Indeed, we can write the governing equation as

$$\frac{1}{\gamma_j}\frac{\partial T_{ij}}{\partial x_j} = -\rho\omega^2 u_i, \tag{2.1}$$

where ρ is the mass density of the material and ω is the angular frequency. Summation over repeated indices is implicitly assumed. T_{ij} is the stress tensor, the u_i are the displacements and the x_j are the coordinates ($x_1 = x, x_2 = y, x_3 = z$). The functions $\gamma_j(\mathbf{r})$ are the artificial damping along axis x_j at an arbitrary position $\mathbf{r}$ inside the PML. As PMLs are added to attenuate acoustic waves propagating in the (x, z) plane, only γ_1 and γ_3 are different from 1. γ_1 is for instance given by

$$\gamma_1(x_1) = 1 - i\sigma_1(x_1 - x_l)^2, \tag{2.2}$$

where x_l is the coordinate of the interface between the regular domain and the PML and σ_1 is a suitable constant. There is no damping outside the PMLs and here $\gamma_j = 1$ is assumed. A suitable thickness of the PML as well as the value of σ_j must be found by trial calculations such that mechanical disturbances are absorbed before reaching the outer boundaries. However, the absorption variation must also be sufficiently slow so that reflections occurring at the interface between the regular domain and the PML are kept minimal. The mechanical stresses T_{ij} further depend on the strains as

$$T_{ij} = C_{ijkl}S_{kl}, \tag{2.3}$$

where the C_{ijkl} are the elastic stiffness constants. Strains are related to the displacements according to

$$S_{ij} = \frac{1}{2}\left(\frac{1}{\gamma_j}\frac{\partial u_i}{\partial x_j} + \frac{1}{\gamma_i}\frac{\partial u_j}{\partial x_i}\right). \tag{2.4}$$

2.3 Results and Discussion

In this section, we discuss the effect of locally resonant modes of the pillars on surface waves of the substrate and the appearance of band gaps. These band gaps for the surface guided modes are restricted in a similar manner to those of photonic crystal slabs. Indeed, there is a continuum of radiation states that are extended infinitely in the region outside the slab [7]. Guided modes, which are states localized to the plane of the slab, can only exist in the regions of the band diagram that are outside the sound cone. Similarly, since the array of pillars we consider sits on top of a semi-infinite medium, the continuum of radiation states in this medium forms a sound cone. Guided acoustic waves, localized in the pillar array and the immediate vicinity of the substrate surface, can only exist in the regions of the band diagram that are outside the sound cone. However, this situation is unlike acoustic band

gaps of phononic crystal slabs, which may not be obvious at first sight. Phononic crystals slabs surrounded by a vacuum provide a naturally perfect confinement of waves in the vertical direction and their in-plane band gaps are similar to those of three-dimensional phononic crystals [14]; these band gaps are very sensitive to the existence of additional branches originating from the finite thickness of the slab [9]. In the following, we restrict our definition of band gaps to a range of frequencies in which no guided modes exist.

2.3.1 Band Diagram of Locally Resonant Surface Guided Modes

Obviously, the first parameter which can play an important role on the discrete acoustic modes of the pillars is their height. In order to investigate its influence, we have calculated the band diagram, for the guided modes, with a square lattice of the phononic crystal depicted in Fig. 2.1a. Propagation is in the (x, y) plane, and band structures are generated along the high symmetry axes of the first Brillouin zone. Both the substrate and the pillars are made from $Ycut$ Lithium Niobate. A low filling fraction $F = 32$ % $(r/a = 0.32)$ and different relative heights of the cylinders ($h/a = 0.32$, 0.5 and 1.0) were considered for square lattice in Fig. 2.2. The gray region on the band structure is the sound cone representing the radiative zone of the Lithium Niobate substrate. The sound line limiting the sound cone is computed from the smallest phase velocity in the substrate as a function of the propagation direction. Due to the anisotropy of bulk acoustic wave propagation in Lithium Niobate, the sound line varies continuously along the XM direction of the first Brillouin zone. These particular choices for h/a ensure the existence of several absolute band gaps for guided modes. Particularly, in Fig. 2.2a when h/a is equal to 0.32, two branches exist in the non radiative zone starting from zero frequency. The quasi-linear behavior of the mode dispersion is close to that of the classical surface acoustic waves except at the first limit of the Brillouin zone. Indeed, at the X point of the reduced wave vector the two branches are folded back due to the array period and their interaction induced the first band gap operating from $fa = 1600$ to 1700 m/s. The frequency positions of the band gap are very close to those expected from Bragg interferences related to the pitch period. Which means that the pillars act here to slow the surface wave velocity as is usual in phononic crystals and their discrete acoustic modes do not erupt in the non radiative zone. When the height of the pillars is increased, the branches shift down towards low frequencies and other kinds of band gaps show up. In fact, for $h/a = 0.5$, we find two band gaps extending, respectively, from $fa = 1000$ to 1100 m/s and a very narrow band gap appearing around the radiation limit in ΓX direction, i.e. $fa = 1700$ m/s. Moreover, with equality of height and period $h/a = 1.0$ as a condition, the first band gap occurs at a central frequency of $fa = 400$ m/s and its relative bandwidth reaches 22 %. A wider second band gap appears around $fa = 1550$ m/s. The first band gap (low frequency) is bounded from below by flat branches, which induce zero group velocities and space confinement of the acoustic energy. This effect outlines the role

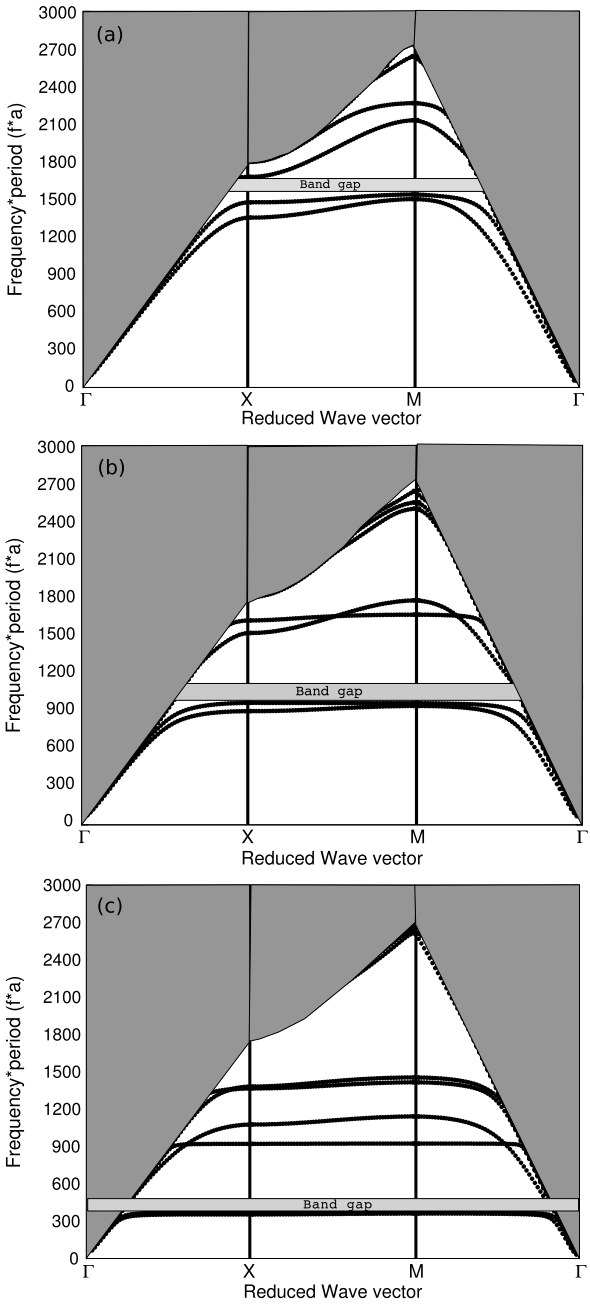

Fig. 2.2 Band structure of a square array of cylindrical pillars on a Lithium Niobate substrate, calculated along high symmetry directions of the first irreducible Brillouin zone. The lattice parameter is a and the filling fraction $F = 0.3$. The relative height of the cylinders h/a equals (**a**) 0.32, (**b**) 0.5, and (**c**) 1.0. The *gray region* represents the sound cone of the substrate. The sound line limiting the sound cone is given by the smallest phase velocity in the substrate for every propagating direction

of the locally resonant modes of the pillars. The frequency position of the first band gap is markedly lower, and the wavelength propagating in the surface is one order

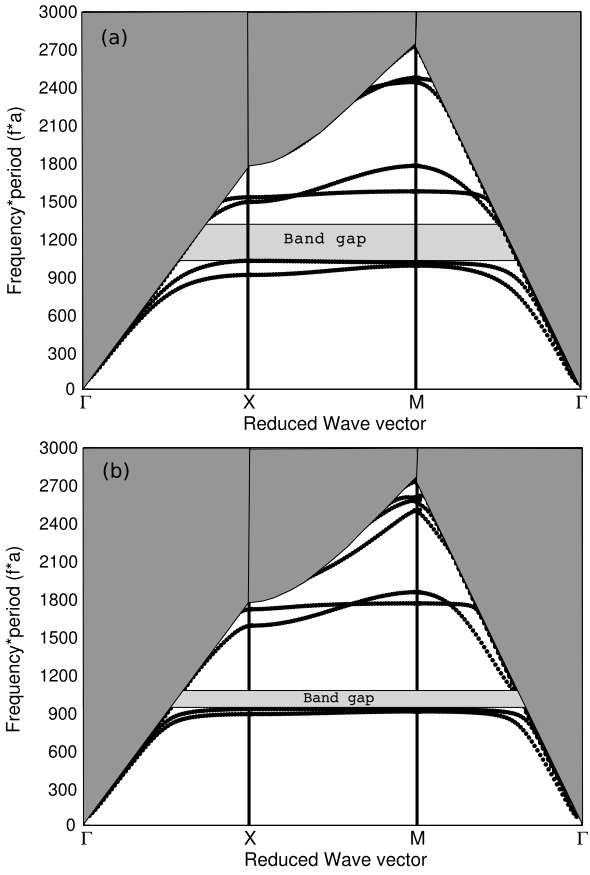

Fig. 2.3 Same parameters as Fig. 2.2, but instead two values of the filling fraction are compared: (**a**) $F = 0.4$ and (**b**) $F = 0.25$

greater, than the period of the structure. Finally, the pitch period and the filling fraction are kept fixed in Fig. 2.2, which clearly shows that the origin of the band gaps is not related to Bragg interferences, as in classic phononic crystals, but is rather related to the result of resonant modes of the structure.

Usually the other important geometrical parameter in the process of opening band gaps and controlling their bandwidths is the filling fraction F. We plot in Fig. 2.3 the band diagram for two values of filling fraction $F = 0.25$ and 0.4. The relative height h/a is fixed to 0.5 which allows us to compare the results with those of Fig. 2.2b. The increase of the filling fraction to $F = 0.4$, as compared to $F = 0.32$, induces a relative widening of the band gap. In fact, when the filling fraction is increased, or the space between adjacent pillars is reduced, the interaction between locally resonant modes can be enhanced through surface coupling and can lead to wider band gaps. Besides, we observe that the second and the fourth bands are more sensitive to the filling fraction. In the opposite case, decreasing the filling fraction, the band gap becomes smaller. However, the central frequency position is not very sensitive to the filling fraction as is usual in any phononic crystal systems.

In general, if h/a is smaller than 0.3, the acoustic modes of the pillars appear at well separated frequencies within the sound cone and thus radiate into the bulk. However, when h/a is increased, the acoustic modes of the pillars shift down in frequency. They are then in a position to interact and form collective propagating surface modes, whereby acoustic energy can be guided along the surface of the substrate. Concurrently, this interaction opens band gaps inside which guided surface acoustic waves are forbidden to propagate. The band gaps shown in Fig. 2.2 are complete and omnidirectional for guided modes at the surface of the substrate. Such guided waves exist only under the sound cone such as, for instance, the Rayleigh surface wave of the homogeneous surface. This means that when a standard Rayleigh surface wave propagating on the free surface of the substrate is incident on the pillar array, it will be either converted to the existing surface-pillar modes at the same frequency, or reflected from the array if the frequency is within a band gap for guided waves. Naturally, a fraction of the surface wave energy can be converted to radiation modes of the substrate at the phononic crystal boundary in both cases, but this does not preclude that no energy is propagated along the surface within a band gap for guided waves. This exhibition of band gaps makes the pillars a very appealing structure in achieving low frequency applications with lattice constants much shorter than the acoustic wavelength.

2.3.2 Wave Transmission of Locally Resonant Surface Guided Modes

It is well known that the study of wave transmission in finite size systems is crucial in understanding the size effect (number of periods) on the band gap attenuations, insertion loss and reflection spectra; this is especially so when the structures possess a radiation condition, which is the case in 1D and 2D periodic systems. For instance, in our case the radiative zone allows the surface waves to leak into the bulk. However, the evaluation of the leaks is not obvious from the band diagram. In the following, we describe the wave transmission properties through a finite number of pillars on the substrate.

The wave transmission spectra were simulated for propagation along the x direction, using the three dimensional domain depicted in Fig. 2.1d. The domain is finite along x with seven rows of pillars sandwiched between the incoming and the outgoing media and infinitely periodic along y. A line source is applied on the surface of the Lithium Niobate substrate just in front of the first pillar. This source vibrates at a monochromatic frequency and can have two different polarizations: either (i) (u_x, u_z) sagittal displacements, which can excite the Rayleigh surface wave of the homogeneous surface or (ii) u_y transverse displacements which can be considered as a shear horizontal wave source. Basically, most elastic materials with free surface (i.e., without phononic crystal) do not support the propagation of the shear horizontal surface wave. Nevertheless, the periodic array of pillars can support surface modes with such a polarization, as discussed in the following.

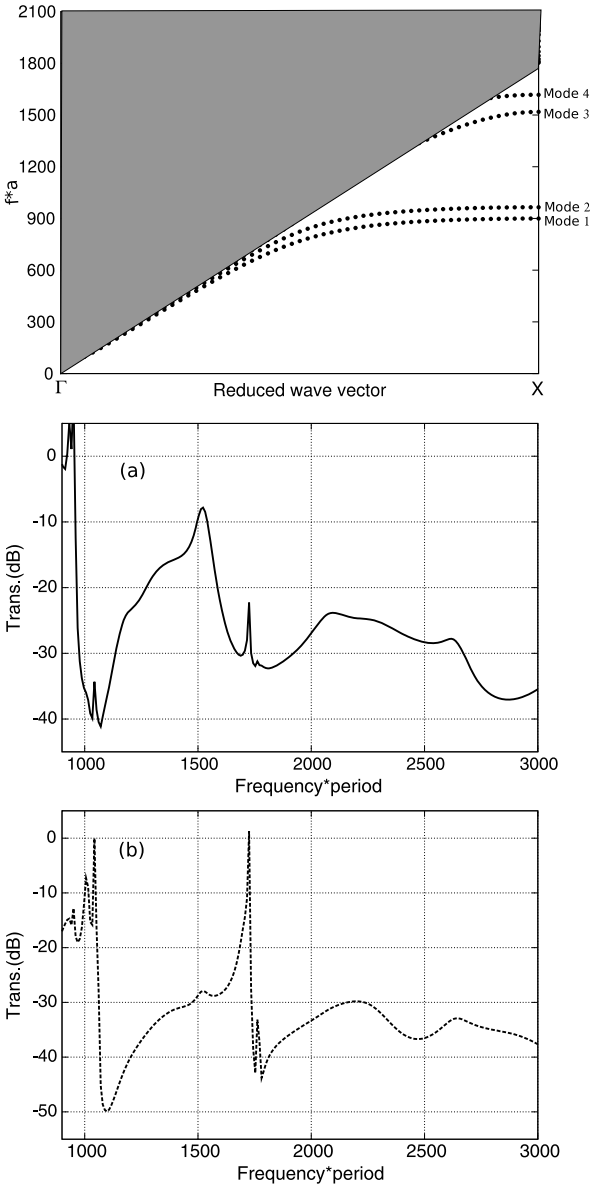

Fig. 2.4 Band diagram for surface guided waves propagating along the ΓX direction with a square-lattice phononic crystal composed of cylindrical Lithium Niobate pillars on a Lithium Niobate substrate. The filling fraction is equal to $F = 0.3$ and the relative height is fixed to $h/a = 0.5$. Transmission of surface waves through 7 rows: ((**a**) *straight line*) Computed transmission spectrum with a sagittally polarized excitation line source. ((**b**) *dashed line*) Computed transmission spectrum with a shear horizontally polarized excitation line source. Transmissions represent an average of all displacement components, $|u_x| + u_z| + |u_y|$, as a function of frequency. The average is collected along a line D (see Fig. 2.1) located after the seventh period of pillars

Figure 2.4 display the computed transmissions for the sagittal and the shear horizontal line sources. The band diagram is added to the transmission to help in interpretation of the results. The filling fraction is fixed to $F = 0.32$ and the relative height of the pillars is $h/a = 0.5$. Transmissions are computed for the ΓX direction of the band diagram. The transmission in Fig. 2.4a is for the total displacement, but is however related to the sagittal (u_x, u_z) excitation. Two attenuations are apparent in the transmission. The first drop is centered at $fa = 1050$ m/s corresponding to

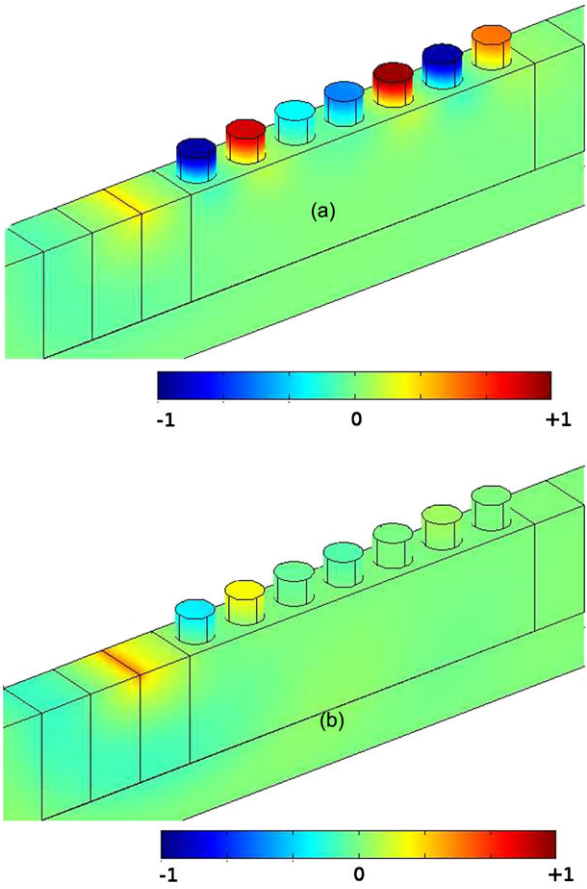

Fig. 2.5 Computed displacement field $|u_y|$ with a shear horizontal polarized excitation line source. (**a**) displacement field at resonance frequency. (**b**) displacement field at anti-resonance frequency

the first and the third band limits in the band diagram. The second drop centered at $fa = 1700$ m/s is related to the third band and the limit of the non radiative zone. Besides, the computed transmission for the shear horizontal line source in Fig. 2.4c displays two narrow pass bands occurring at $fa = 1050$ m/s and 1700 m/s. These frequency positions correspond to the deep attenuations of sagittal excitation shown in Fig. 2.4b. The response of the different excitations allows us to suggest that the second and the fourth branches are deaf to the sagittal source while the first and the third bands are deaf to the shear horizontal source.

In addition, the shape of the transmission for the shear horizontal source around the frequencies where the second and fourth bands reach the X point is typical of a linear response function proportional to $1/(f_0^2 - f^2)$, when a wave with frequency f interacts with a medium supporting a localized excitation with frequency f_0. Such an effect is manifest, for instance, in the electromagnetic frequency response of materials with optical resonances or more generally the so-called Fano resonances of a localized state interacting with a continuum of propagating modes. In order to have a physical interpretation of these local resonances, we display in Figs. 2.5a and 2.5b

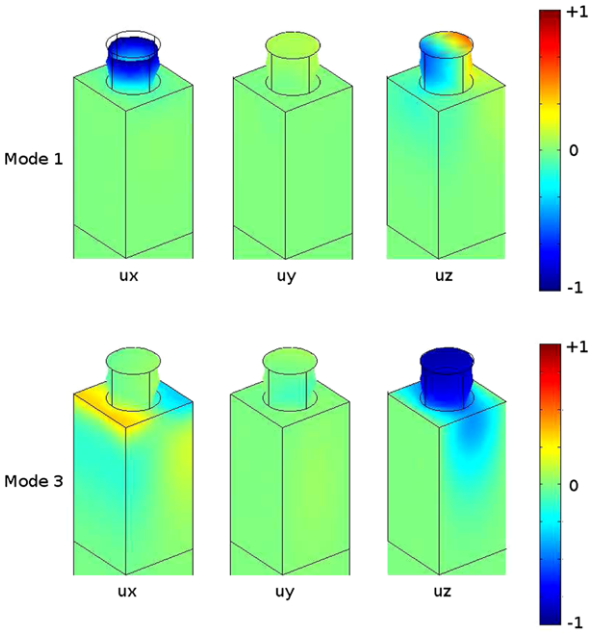

Fig. 2.6 Eigenmode of mode 1 and mode 3 analysis close to the point X of the Brillouin zone. They represent the displacement field of the three components u_x and u_z and u_y. These modes have mostly in-plane polarization

the displacement field $|u_y|$ of the transmission for two significative frequencies—resonance and anti-resonance—occurring at $fa = 1042$ m/s and $fa = 1100$ m/s. In Fig. 2.5a, the energy of waves propagating in the matrix can be efficiently stored in the pillars and delayed at the resonance frequency $fa = 1042$ m/s corresponding to the maximum transmission in Fig. 2.4c. However, at the anti-resonance frequency $fa = 1100$ m/s which corresponds to a strong attenuation in the transmission spectra, the wave propagation becomes prohibited and the pillars act as an obstacle for the guided wave in Fig. 2.5b. Naturally, a fraction of the surface wave energy can be converted to radiation modes of the substrate at the structure boundary in both cases, but this does not preclude that no energy is propagated along the surface within a band gap for guided waves.

To corroborate the previous observations of deaf bands, we plot in Figs. 2.6 and 2.7 the modal displacements of the first and the third bands, and on the second and fourth bands, respectively. The wavevector k_x selected for these illustrations is close to the point X of the first Brillouin zone. We emphasize that the acoustic energy is mostly distributed between u_x and u_z for the eigenmodes in Fig. 2.6. Those modes have mostly sagittal polarization. The displacement u_y is not equal to zero but is very small in comparison. We notice that the same scale has been used in all displacements to give a good appreciation of each polarization. This observation explains the significant transmission magnitude of the first and the third bands with the a sagittal source.

As Fig. 2.7 shows, the acoustic energy is mostly distributed between u_z and u_y for the second band and between u_x and u_y for the fourth band. We observe that the u_z displacement for the second band and the u_x displacement for the fourth band

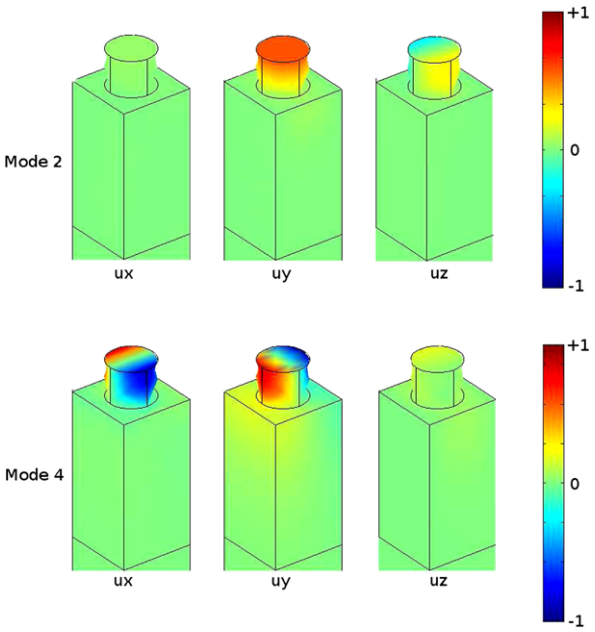

Fig. 2.7 Same as Fig. 2.6 for mode 2 and mode 4, these modes have mostly sagittal polarization with transverse propagation

have an antisymmetric character with respect to the sagittal mid plane (x, z) of the structure. The sagittal excitation is symmetric with respect to the same mid-plane, which means that the energy cannot be transferred to the second and the fourth bands. This explains the absence of a signature of these modes in the transmission spectra with the sagittally polarized source. Conversely, the u_y displacement is symmetric with respect to the sagittal mid plane and can thus be excited by the shear horizontally polarized source.

2.3.3 Lattice Symmetry Effect on the Locally Resonant Surface Acoustic Band Gaps

Basically, in metamaterial structures the observed phenomena are not linked to the period pitch or to the lattice symmetries and can appear in disordered systems, on the strict condition that the local resonances are not affected. Aiming to highlight this effect, we describe in this section the effect of the surface acoustic wave propagation properties of pillars on semi-infinite substrate with square, triangular and honeycomb lattices. Especially, we focus on the position of the locally resonant band gap in respect to these symmetry lattices. In other words, we wish to demonstrate that the sub-wavelength band gaps are not sensitive to the period pitch—which can be found in conventional phononic crystals—and reinforce the position of this structure as an acoustic metamaterial element. However, the considered pitch will

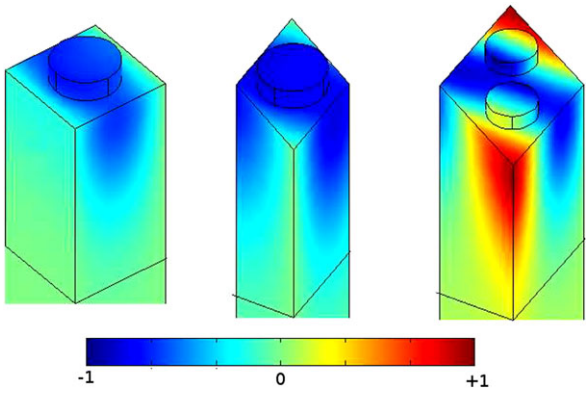

Fig. 2.8 Eigenmode of the lowest frequency mode analysis close to the limit of the first Brillouin zone for the square, triangular and honeycomb symmetries. These are the total displacement field of the three component u_x and u_z and u_y. The relative radius is $r/a = 0.32$ and the relative height of the cylinders h/a equals 0.2

play a fundamental role in controlling the dispersion of guided modes and will define the non radiative zone which is a key condition to obtain guided modes.

As discussed in Sect. 2.2, when the discrete acoustic resonances of the pillars are not able to appear in the non-radiative zone due to the small value of the pillars height h/a, we still have two major effects coming from the presence of pillars: the existence of two surface waves propagating in the substrate with different polarizations and a slowing down of the classical wave velocity of the substrate. The latter effect is less pronounced in the case of the honeycomb structure. In fact, the pitch is larger than the other symmetries ($\sqrt{3}a$) which decreases its filling fraction, and therefore reduces the slowing down effect of the classical surface wave. Figs. 2.8a, b and c show the field distribution of the total displacement close to the limit of the first Brillouin zone for the square, triangular and honeycomb symmetries respectively. The relative radius is $r/a = 0.32$ and the relative height of the cylinders h/a equals 0.2. These modes have different shape for the three symmetries and cover both the pillar and the surface of the substrate. Consequently, the period pitch will affect the wave propagation properties through the phase condition that can be applied in each different symmetry lattice.

Actually, the relative height of the pillars is fixed at $h/a = 0.6$ to ensure the presence of pillars vibration modes in the non radiative zone. As shown in Fig. 2.9, several bands appear below the sound cone and low frequency band gaps show up. We observe the existence of two band gaps appearing around $fa = 1150$ m/s and $fa = 2200$ m/s for square and triangular lattices (Figs. 2.9a and 2.9b). In the case of honeycomb lattice, only one complete band gap for guided modes opens around $fa = 1150$ m/s Fig. 2.9c. Although, there is a large difference between lattice pitch of square or triangular (a) and honeycomb ($\sqrt{3}a$), we highlight that the first band gaps appear at the same frequency position in the three different lattice symmetries. This means, that the physical phenomena behind the opening of the band gap is clearly not due to the Bragg interference of waves linked to the period, but to the signature of the locally resonance acoustic vibration of the pillars. The expectation of the same position of the band gap occurring in any other ordered or disordered structures is presumably upon condition that keeping the same geometry of pillars, which ensures the resonance frequency positions.

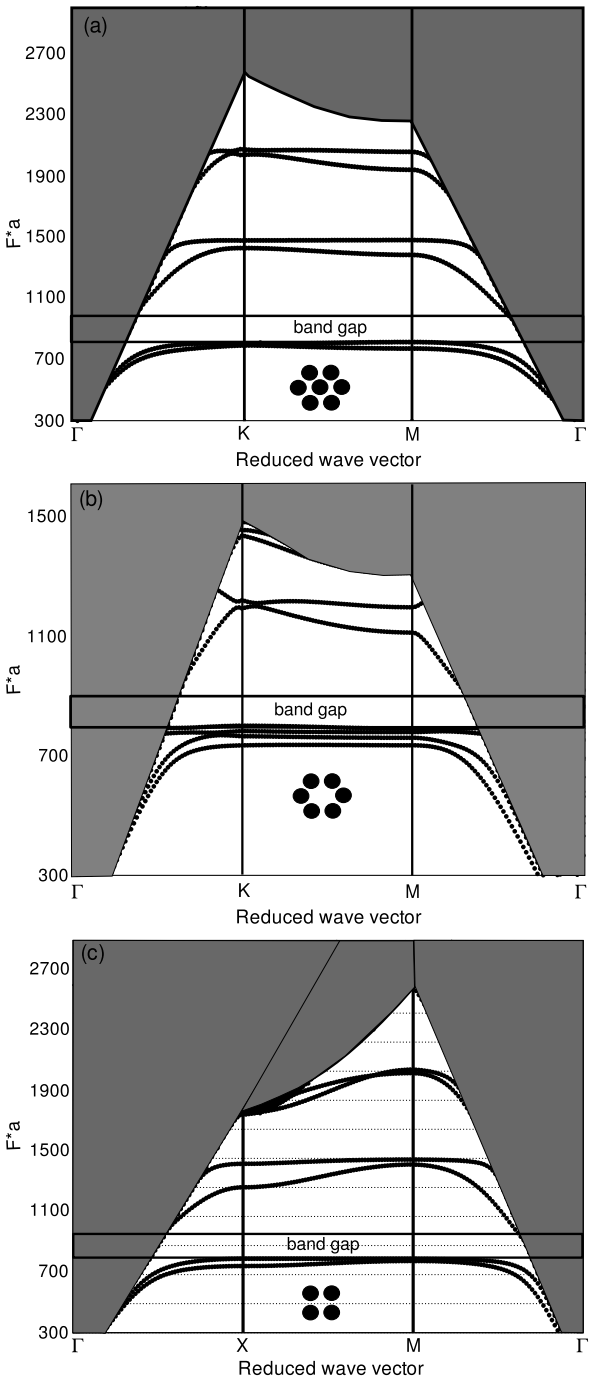

Fig. 2.9 Band structure of a phononic crystal composed of cylindrical lithium niobate pillars on a lithium niobate substrate, calculated along high symmetry directions of the first irreducible Brillouin zone for: (**a**) square; (**b**) triangular; (**c**) honeycomb. The lattice parameter is a for triangular and square lattice and $(\sqrt{3}a)$ for the honeycomb lattice. The radius is $r/a = 0.32$ and the relative height of the cylinders h/a equals 0.6. The *gray region* represents the sound cone of the substrate. The sound line limiting the sound cone is given by the smallest phase velocity in the substrate for every propagation direction

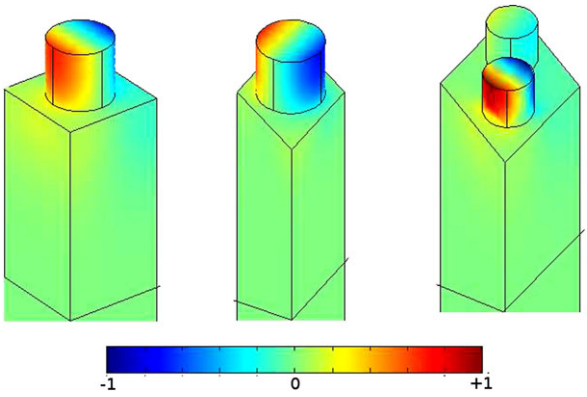

Fig. 2.10 Eigenmode of the lowest frequency mode analysis close to the limit of the first Brillouin zone for the square, triangular and honeycomb symmetries. These are the total displacement field of the three component u_x and u_z and u_y. These modes have mostly the same shape for the three symmetries. The relative radius is $r/a = 0.32$ and the relative height of the cylinders h/a equals 0.6

To corroborate this effect, we display in Fig. 2.10 the mode shapes of the lowest frequency solutions for the three lattices. The wave vectors of the eigenmodes are chosen close to the limit of the first Brioullin zone. These mode shapes, which represent the total displacement field of the three components u_x and u_z and u_y, have mostly the same shape for the three symmetries and demonstrate that the flat bands observed in their band diagrams are related to the discrete acoustic mode of the pillars.

2.3.4 Conclusion

In summary, the study of the locally acoustic resonances with different periodic arrays of cylindrical pillars deposited on a semi-infinite substrate is presented. The band structures of square, triangular and honeycomb arrays show that they possess the characteristics of acoustic metamaterials. Precisely, the presence of pillars introduce new surface propagating modes. The period defines the non-radiative region limited by the slowest bulk modes and influences the existence of these new modes. In addition, with a specific geometrical value of pillars, guided modes define a first band gap that appears at frequencies markedly lower than those expected from the Bragg condition and it does not depend on the symmetry of the arrays. This band gap originates from local resonances of the individual cylindrical pillars and is sensitive to their geometrical parameters, in particular to the height of the pillars. The transmission calculation corroborates very well with the band structure and highlights the major role of the local resonance of a single pillar in the opening of the low frequency band gap. In this case, we expect the same band gap position to occur in any other ordered or disordered structures.

Acknowledgements The authors thank Prof. Vincent Laude and Dr. Sarah Benchabane for fruitful discussions.

References

1. Achaoui, Y., Khelif, A., Benchabane, S., Robert, L., Laude, V.: Experimental observation of locally-resonant and Bragg band gaps for surface guided waves in a phononic crystal of pillars. Phys. Rev. B **83**, 104201 (2011)
2. Berenger, J.P.: A perfectly matched layer for the absorption of electromagnetic waves. J. Comput. Phys. **114**, 185 (1994)
3. Dühring, M.B., Laude, V., Khelif, A.: Energy storage and dispersion of surface acoustic waves trapped in a periodic array of mechanical resonators. J. Appl. Phys. **105**, 093504 (2009)
4. Fang, N., Xi, D., Xu, J., Ambati, M., Srituravanich, W., Sun, C., Zhang, X.: Ultrasonic metamaterials with negative modulus. Nat. Mater. **5**, 452 (2006)
5. Goffaux, C., Sánchez-Dehesa, J., Levy Yeyati, A., Khelif, A., Lambin, P., Vasseur, J.O., Djafari-Rouhani, B.: Evidence of Fano-like interference phenomena in locally resonant materials. Phys. Rev. Lett. **88**, 225502 (2002)
6. Hsu, J.C., Wu, T.T.: Lamb waves in binary locally resonant phononic plates with two dimensional lattices. Appl. Phys. Lett. **90**, 201904 (2007)
7. Johnson, S.G., Fan, S., Villeneuve, P.R., Joannopoulos, J.D., Kolodziejski, L.A.: Guided modes in photonic crystal slabs. Phys. Rev. B **60**, 5751–5758 (1999)
8. Khelif, A., Achaoui, Y., Benchabane, S., Laude, V., Aoubiza, B.: Locally resonant surface acoustic wave band gaps in a two-dimensional phononic crystal of pillars on a surface. Phys. Rev. B **81**, 214303 (2010)
9. Khelif, A., Aoubiza, B., Mohammadi, S., Adibi, A., Laude, V.: Complete band gaps in two-dimensional phononic crystal slabs. Phys. Rev. E **74**, 046610 (2006)
10. Khelif, A., Choujaa, A., Benchabane, S., Djafari-Rouhani, B., Laude, V.: Guiding and bending of acoustic waves in highly confined phononic crystal waveguides. Appl. Phys. Lett. **84**(22), 4400–4402 (2004)
11. Khelif, A., Choujaa, A., Djafari-Rouhani, B., Wilm, M., Ballandras, S., Laude, V.: Trapping and guiding of acoustic waves by defect modes in a full-band-gap ultrasonic crystal. Phys. Rev. B **68**, 214301 (2003)
12. Khelif, A., Wilm, M., Laude, V., Ballandras, S., Djafari-Rouhani, B.: Guided elastic waves along a rod-defect of a two-dimensional phononic crystal. Phys. Rev. E **69**, 067601 (2004). doi:10.1103/PhysRevE.69.067601
13. Kushwaha, M.S., Halevi, P., Dobrzynski, L., Djafari-Rouhani, B.: Acoustic band structure of periodic elastic composites. Phys. Rev. Lett. **71**(13), 2022–2025 (1993). doi:10.1103/PhysRevLett.71.2022
14. Liu, Z., Zhang, X., Mao, Y., Zhu, Y.Y., Yang, Z., Chan, C.T., Sheng, P.: Locally resonant sonic materials. Science **289**, 1734 (2000)
15. Martínez-Sala, R., Sancho, J., Sanchez, J.V., Gomez, V., Llinares, J., Meseguer, F.: Sound attenuation by sculpture. Nature **378**, 241 (1995)
16. Miroshnichenko, A.E., Flach, S., Kivshar, Y.S.: Fano resonances in nanoscale structures. Rev. Mod. Phys. **82**(3), 2257 (2010). doi:10.1103/RevModPhys.82.2257
17. Pennec, Y., Djafari-Rouhani, B., Vasseur, J.O., Larabi, H., Khelif, A., Choujaa, A., Benchabane, S., Laude, V.: Acoustic channel drop tunneling in a phononic crystal. Appl. Phys. Lett. **87**(26), 261912 (2005). doi:10.1063/1.2158019
18. Robillard, J.F., Devos, A., Roch-Jeune, I.: Time-resolved vibrations of two-dimensional hypersonic phononic crystals. Phys. Rev. B **76**(9), 092301 (2007). doi:10.1103/PhysRevB.76.092301
19. Sigalas, M.M., Economou, E.N.: Band structure of elastic waves in two dimensional systems. Solid State Commun. **86**(3), 141–143 (1993)
20. Vasseur, J.O., Deymier, P.A., Chenni, B., Djafari-Rouhani, B., Dobrzynski, L., Prevost, D.: Experimental and theoretical evidence for the existence of absolute acoustic band gaps in two-dimensional solid phononic crystals. Phys. Rev. Lett. **86**(14), 3012–3015 (2001)
21. Wang, G., Wen, X., Wen, J., Shao, L., Liu, Y.: Two dimensional locally resonant phononic crystals with binary structures. Phys. Rev. Lett. **93**, 154302 (2004)

Chapter 3
Band-Gap Properties of Prestressed Structures

M. Gei, D. Bigoni, A.B. Movchan, and M. Bacca

Abstract The design of periodic and quasiperiodic structures possessing innovative filtering properties for elastic waves opens the way to the realization of elastic metamaterials. In these structures prestress has a strong influence, 'shifting' in frequency, but also 'annihilating' or 'nucleating' band gaps. The effects of prestress are demonstrated with examples involving flexural waves in periodic and quasiperiodic beams and periodic plates. Results highlight that prestress can be employed as a 'tuning parameter' for continuously changing vibrational properties of elastic metamaterials.

3.1 Introduction

By analogy with their electromagnetic counterpart, 'elastic metamaterials' are designed to become innovative filters for mechanical waves. The design is focussed on vibrational properties connected with the periodicity of a structure, which can be engineered to provide special effects, such as: band gaps (frequency ranges where the waves are evanescent [17, 22, 36, 39]), localized or defect modes (an exponentially localized waveform located near a periodicity-breaking element [2, 30]), negative refraction (refraction occurring on the same side of the normal to the interface where the incoming wave is incident [15, 32, 34, 40, 41]), and effective negative

M. Gei (✉) · D. Bigoni · M. Bacca
Department of Civil, Environmental and Mechanical Engineering, University of Trento, via Mesiano 77, 38123 Trento, Italy
e-mail: massimiliano.gei@unitn.it

D. Bigoni
e-mail: davide.bigoni@unitn.it

M. Bacca
e-mail: mattia.bacca@unitn.it

A.B. Movchan
Department of Mathematical Sciences, University of Liverpool, Liverpool L69 3BX, UK
e-mail: abm@liv.ac.uk

R.V. Craster, S. Guenneau (eds.), *Acoustic Metamaterials*,
Springer Series in Materials Science 166, DOI 10.1007/978-94-007-4813-2_3,

mass effects (corresponding to an exponential decay of vibrational modes, rather than sinusoidal propagation [24, 29, 35]).

Wave propagation within elastic structures is strongly influenced by the pre-existing state of stress, the so-called 'prestress'. This effect is well-known in structural engineering [7, 23, 26–28], in two-dimensional boundary-value problems of prestressed solids [3, 4, 9, 11, 13, 14, 31, 37] and finds simple experimental demonstrations, so that for instance prestress plays a chief role in the vibrational behaviour of stringed musical instruments: in the absence of the strong compression induced by ribs a piano soundboard would not vibrate properly. It is therefore not surprising that prestress can have a determinant influence on dynamical properties of periodic structure, as demonstrated in [5, 12, 33].

Our purpose is to review results by Gei et al. [12] and Gei [10] relative to vibrating periodic and quasiperiodic beams and extending these to vibrating periodic plates. We will show that prestress can: (i.) change the dispersion properties of Floquet-Bloch elastic waves, (ii.) shift the frequency range of band gaps towards high (low) frequency, when tensile (compressive) prestress is applied (iii.) 'annihilate' or (iv.) 'nucleate' band gaps.

For periodic prestressed structures, we will use the Floquet-Bloch technique directly (analytically in the case of beams and numerically in the case of plates), while for the quasiperiodic case the transmission matrix of the elementary cell is obtained, so that applying the Floquet-Bloch conditions a set of eigenvalue problems for the circular frequency is derived. In the case of quasiperiodic beams (generated employing the Fibonacci sequence), flexural waves are considered and the following aspects are analyzed: (i.) the number of stop/pass bands and (ii.) the self-similarity of dispersion diagrams as functions of the generation index i of the elementary cell; (iii.) the role of an invariant function which governs the scaling of stop/pass band structure; and (iv.) the possibility of shifting and broadening the stop/pass bands.

3.2 Band Gaps for Periodic Beams on a Spring Foundation

Floquet-Bloch propagation of flexural waves is investigated within prestressed periodic beams on an elastic 'spring' foundation (so-called 'Winkler type') which models a typical design problem of Microelectromechanical systems (MEMS) technology, namely, vibrations of a relatively stiff elastic layer bonded to a thick elastic layer. The geometry of the problem under consideration is shown in Fig. 3.1, where the period is equal to d and N denotes the constant longitudinal prestress applied at infinity.

We will also consider a perturbation to the periodicity by addition of a mass into the central cell of the structure, as shown in Fig. 3.1(b). This perturbation does not affect the physical characteristics of the other cells and we will show that an exponentially localized wave form will become possible, within a certain frequency range.

The structure is made up of two phases, $m = 1$ and $m = 2$, so that the time-harmonic flexural displacement $w_m(z)$ satisfies the following differential equation (a prime denotes differentiation with respect to the longitudinal coordinate z)

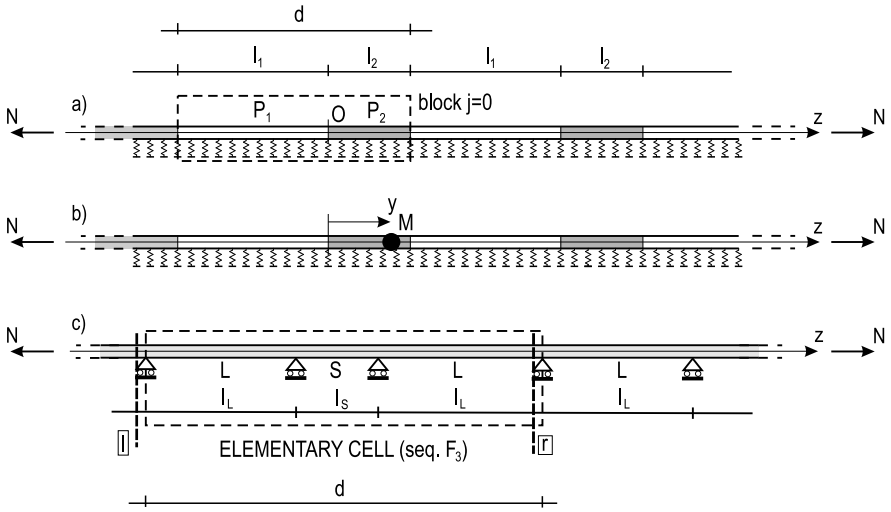

Fig. 3.1 Periodic and quasiperiodic beam systems. (**a**) Piecewise homogeneous beam on an elastic 'spring' foundation; (**b**) same as (**a**), but with an additional mass M placed at $z = y$ to investigate 'band-gap localized modes'; (**c**) quasiperiodic multisupported beam with the elementary cell generated by the Fibonacci sequence F_3. N represents the longitudinal prestress. (**a**), (**b**) are reprinted from [12] with permission [Copyright (2010) American Institute of Physics]. (**c**) is reprinted from [10] with permission from Elsevier. Copyright (2010) American Institute of Physics

$$B_m w_m'''' - N w_m'' + \left(S - \rho_m \omega^2\right) w_m = 0 \quad (m = 1, 2), \tag{3.1}$$

where ρ_m is the piecewise-constant mass density, $B(z) = I(z)E(z)$ the bending stiffness [with the second-order moment $I(z)$ and the Young modulus $E(z)$] and the stiffness of the elastic foundation is denoted by S (see [38] for details).

Note that the bending stiffness $B(z)$ could be easily made dependent on the longitudinal prestress N acting on the beam, a dependency neglected in the following for simplicity.

The solution for flexural displacements is sought in the form

$$w_m = \xi_m \exp\left(i k^{(m)} z\right) \quad (m = 1, 2), \tag{3.2}$$

so that a substitution of (3.2) into (3.1) yields the following equation for the circular frequency ω

$$\left(k^{(m)} r_m\right)^4 + \overline{N}_m \left(k^{(m)} r_m\right)^2 + \overline{S}_m - P_m \omega^2 = 0 \quad (m = 1, 2), \tag{3.3}$$

where the following dimensionless parameters have been introduced

$$\overline{N}_m = \frac{N r_m^2}{B_m}, \qquad \overline{S}_m = \frac{S r_m^4}{B_m} \quad (m = 1, 2), \tag{3.4}$$

in which r_m are the radii of inertia of the beam cross-section, while

$$P_m = \frac{\rho_m r_m^4}{B_m} \quad (m = 1, 2) \tag{3.5}$$

have the dimension of a squared time. The parameters r_m are related to the second-order moments I_m and the cross-sectional areas A_m of the two phases of the beam by

$$r_m = \sqrt{I_m / A_m} \quad (m = 1, 2). \tag{3.6}$$

Equation (3.3) admits eight solutions

$$k_{1,2,3,4}^{(m)} = \pm \frac{1}{r_m} \sqrt{-\frac{\overline{N}_m}{2} \pm \sqrt{\frac{\overline{N}_m^2}{4} + P_m \omega^2 - \overline{S}_m}} \quad (m = 1, 2), \tag{3.7}$$

so that the transverse displacements w_1, w_2 become a linear combination of the following four terms

$$w_1(z) = \sum_{p=1}^{4} \xi_1^p \exp\left(i k_p^{(1)} z\right), \qquad w_2(z) = \sum_{p=1}^{4} \xi_2^p \exp\left(i k_p^{(2)} z\right), \tag{3.8}$$

where the eight constants ξ_1^p and ξ_2^p $(p = 1, \ldots, 4)$ can be obtained by imposing the interface conditions at the internal interface of the elementary block; these are: continuity of displacement, rotation, bending moment and shear force. Therefore, for the block $j = 0$ the interface is located at $z = 0$ and the corresponding interface conditions for the functions w_1, w_2 and their derivatives are

$$\begin{aligned} &w_1(0) = w_2(0), && w_1'(0) = w_2'(0), \\ &B_1 w_1''(0) = B_2 w_2''(0), && B_1 w_1'''(0) = B_2 w_2'''(0), \end{aligned} \tag{3.9}$$

while the remaining four equations follow from the imposition of the *Floquet-Bloch conditions*, linking fields at the boundaries of the elementary block

$$w_2\left(l_2^-\right) = w_1\left(-l_1^+\right) \exp(i K d), \qquad w_2'\left(l_2^-\right) = w_1'\left(-l_1^+\right) \exp(i K d), \tag{3.10}$$

$$B_2 w_2''\left(l_2^-\right) = B_1 w_1''\left(-l_1^+\right) \exp(i K d), \qquad B_2 w_2'''\left(l_2^-\right) = B_1 w_1'''(-l_1^+) \exp(i K d), \tag{3.11}$$

where K is the Bloch parameter.

The vanishing of the determinant of the matrix associated with (3.9)–(3.11) yields the dispersion equation of the beam system. Note that if ω is taken to be zero in (3.1) and (3.7), the system (3.9)–(3.11) provides the buckling load of the structure [8].

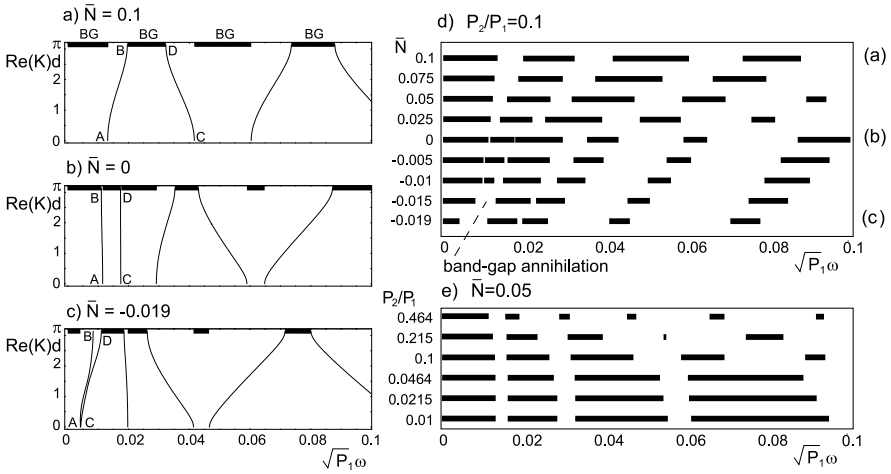

Fig. 3.2 Dispersion diagrams [circular frequency $\sqrt{P_1}\omega$ versus Bloch parameter $\mathrm{Re}(K)d$] and band gap/pass band distribution for a beam on an elastic foundation with piecewise constant mass density [Fig. 3.1(a)] and homogeneous flexural stiffness, $B_1 = B_2$ ($P_2/P_1 = 0.1$, $\overline{S} = 0.0001$, $r/d = 0.015$, $l_1 = l_2 = d/2$). Dispersion diagrams: (**a**) tensile prestress: $\overline{N} = 0.1$; (**b**) null prestress: $\overline{N} = 0$; (**c**) near-buckling ($\overline{N}_{buckl} = -0.02$) compressive prestress: $\overline{N} = -0.019$. BG denotes a band gap. Note that the compressive stress in part (**c**) induces the annihilation of the second band gap (between branches AB and CD). Band gap/pass band distribution (**d**) in terms of prestress $\overline{N}$ ($P_2/P_1 = 0.1$); (**e**) in terms of the contrast parameter P_2/P_1 (logarithmic scale) ($\overline{N} = 0.05$). The band-gap annihilation induced by a compressive force is highlighted. Reprinted from [12] with permission. Copyright (2010) American Institute of Physics

3.2.1 Dispersion Diagrams and Band-Gap Shift

The dispersion equation is solved in Fig. 3.2 for the beam sketched in Fig. 3.1(a) (without defects) and with piecewise constant mass density ($\rho_1 \neq \rho_2$), but uniform bending stiffness ($B_1 = B_2$, yielding $\overline{N}_1 = \overline{N}_2 = \overline{N}$). The case $P_2/P_1 = 0.1$, $\overline{S} = 0.0001$, $r/d = 0.015$, $l_1 = l_2 = d/2$, is considered for three different levels of prestress $\overline{N}$ [tensile, null and compressive, in parts (a), (b) and (c), respectively]. For the beam under consideration, the buckling force corresponds to $\overline{N}_{buckl} = -0.02$, while the cutoff frequency of the homogeneous counterpart (which can be recovered if $P_1 = P_2$) is $\sqrt{P_1}\omega_0 = 0.01$.

In general, at a given dimensionless circular frequency $\sqrt{P_1}\omega$, four complex values of the Bloch parameter K can be found from the dispersion equation. In particular, a propagating mode [like those displayed in Figs. 3.2(a), (b), (c)] corresponds to a pure real K, while a monotonic decaying mode is found when K is purely imaginary; for complex conjugate Bloch parameters, the mode also does not propagate and decays, with a sinusoidal decaying. Diagrams displayed in Figs. 3.2(a), (b), (c) are symmetric with respect to the vertical axis $K = 0$, so that only the positive ranges have been plotted. The band gap ('BG') frequency ranges are marked with black segments.

The band-gap distribution is reported as a function of the prestress for fixed contrast parameter $P_2/P_1 = 0.1$ in Fig. 3.2(d), while a fixed, small and tensile prestress is assumed in Fig. 3.2(e), for varying P_2/P_1. The latter figure makes evident that the cutoff region is not strongly influenced by the contrast parameter P_2/P_1, and that the range where the increase in the size of the BG zones is more pronounced occurs for $0.0464 < P_2/P_1 < 0.464$.

Let us consider now the two lower frequency band gaps in Figs. 3.2(a), (b), (c), one of which is present also in a homogeneous beam on an elastic foundation. The prestress strongly modifies the band gap intervals (shifting these toward higher frequencies for tensile loading) and, when this becomes compressive, the higher frequency band gap (between branches AB and CD in Fig. 3.2) is reduced in size and *annihilated already before the buckling load is attained.*

3.3 Band-Gap Localized Defect Modes

A 'band-gap localized defect mode' is a vibration mode associated with a single mass placed along the beam at a frequency within a band gap in the dispersion diagram. The influence of prestress N on those modes is demonstrated for an infinite piecewise uniform beam on an elastic foundation, making use of a Green's function formulation. While for a homogeneous beam on an elastic foundation localized modes available below the cut-off frequency can be computed analytically (see [12]), for a piecewise homogeneous beam the Green's function is not immediately available (although—in principle—it can be obtained analytically), so that we prefer pursuing an approximate calculation, where a 'sufficiently long', but finite, beam (seven elementary cells of length d in our examples) is solved, with a unit force applied at the central cell (the fourth cell in our examples).

The properties of localized modes are very interesting for a piecewise beam as: (i) the dispersion diagrams exhibit several band gaps (not only one as in the uniform case); (ii) the concentrated mass can be placed at different positions within the cell, thus providing different responses; (iii) the vibration modes of the mass can be made more or less localized in the vicinity of the defect depending of the frequency (an effect shown in [30]).

Results pertinent to the seven-cell structure are reported in Fig. 3.3. Here the ranges of frequencies where localized modes associated with the concentrated mass are possible are reported as functions of the position y (normalized through division by d) of the mass in the central cell, for two levels of prestress, namely, $\overline{N} = 0.025$ in Fig. 3.3(a) and $\overline{N} = 0$ in Fig. 3.3(b).

In both parts (a) and (b) of Fig. 3.3 the first three band gaps have been investigated, placing masses at discrete distances multiple of $d/20$. Results depend on the dimensionless frequencies $\sqrt{P_1}\omega$, to generate localized modes associated with $\overline{M} = 1$ (denoted with black dots) and 10 (denoted with black squares), where the dimensionless concentrated mass $\overline{M}$ is defined now with respect to the mass density and radius of inertia of part 1, namely,

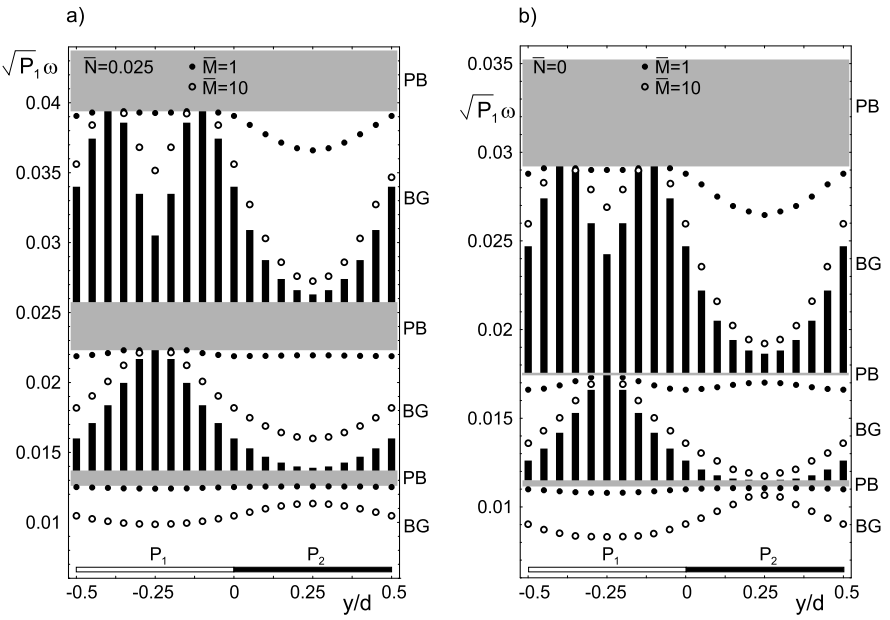

Fig. 3.3 Dimensionless frequency $\sqrt{P_1}\omega$ at which a localized mode connected to a concentrated point mass located at y [Fig. 3.1(b)] exists for $\bar{M} = 1$ (*black dots* in the figure) and $\bar{M} = 10$ (*open circles*) (the following values of constants have been taken: $P_2/P_1 = 0.1$, $l_1 = l_2 = d/2$, $r/d = 0.015$, $\bar{S} = 0.0001$). (**a**) Tensile prestress: $\bar{N} = 0.025$; (**b**) null prestress: $\bar{N} = 0$. BG denotes a band gap, PB a pass band (see Fig. 3.2). A *black vertical segment* in the band-gap zone indicates a frequency range where localized modes are not possible. Reprinted from [12] with permission. Copyright (2010) American Institute of Physics

$$\bar{M} = \frac{M}{2\rho_1 r_1}. \tag{3.12}$$

The black vertical segments crossing the band gaps indicate frequency ranges where *localized modes (and effective negative mass effects) cannot be generated just by inserting a single concentrated mass*, being the displacement of the point of application of the unit force out of phase with respect to the force itself. We note that at certain locations y/d within the second and third band gap these vertical segments cross the entire range (for instance at $y = 0.25d$, within the second band gap, and at $y = 0.2d$, $0.8d$, within the third band gap), so that *in these cases localized modes cannot be obtained for an applied finite and positive concentrated mass*.

3.4 Periodic Plates Under Tensile Prestress

Wave propagation in two-dimensional structures becomes more complicated, but more interesting, than propagation in beam elements. We address transversal vibration of infinite and periodic Kirchhoff plates, prestressed with tensile forces, and we

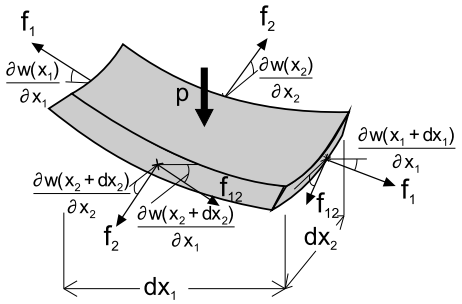

Fig. 3.4 An element of a prestressed elastic Kirchhoff plate, subject to a transversal dead load p and displacement w. The prestress has normal components f_1 and f_2 and shearing component f_{12}

will show that the prestress can induce anisotropy effects that, 'added' to effects associated with the periodicity, can create privileged propagation directions as related to the presence of 'directional' band gaps. Note that a two-dimensional plate model provides an accurate approximation only for the lower-frequency modes, while correct computations at high-frequency would require a model of Mindlin plate, or a fully three-dimensional analysis.

With reference to Fig. 3.4, the differential equations governing dynamics of an elastic Kirchhoff plate of thickness h, prestressed through two normal f_1 and f_2 and shearing f_{12} tractions, are

$$B\nabla^4 w - f_1\frac{\partial^2 w}{\partial x_1^2} - f_2\frac{\partial^2 w}{\partial x_2^2} - 2f_{12}\frac{\partial^2 w}{\partial x_1 \partial x_2} = -\rho h\ddot{w} + p, \tag{3.13}$$

where w is the transversal displacement, ρ is the mass density per unit volume, p the transversal dead load, a superimposed dot means time-derivative, and B is the flexural rigidity, which can be related to the elastic modulus E, the Poisson's coefficient ν of the material, and the thickness of the plate h as

$$B = \frac{Eh^3}{12(1-\nu^2)}. \tag{3.14}$$

Assuming that the shearing component of the prestress is null, $f_{12} = 0$, the time-harmonic free oscillations are ruled by the equation

$$B\nabla^4 w - \rho h\omega^2 w - f_1\frac{\partial^2 w}{\partial x_1^2} - f_2\frac{\partial^2 w}{\partial x_2^2} = 0, \tag{3.15}$$

where ω is the circular frequency. Equation (3.15) holds at every point of the domain Ω defining the plate. A weak formulation of dynamics of a plate can be obtained transforming (3.15) into

$$\int_{\Omega^*} (\boldsymbol{\chi}\cdot\boldsymbol{C}\boldsymbol{\chi})\, d\Omega^* - \rho h\omega^2 \int_{\Omega^*} w^2\, d\Omega^* - \int_{\Omega^*}\left[f_1\left(\frac{\partial w}{\partial x_1}\right)^2 + f_2\left(\frac{\partial w}{\partial x_2}\right)^2\right] d\Omega^* = 0, \tag{3.16}$$

holding for every subdomain Ω^* of Ω, in which

$$\boldsymbol{\chi} = \left(\frac{\partial^2 w}{\partial x_1^2}, \frac{\partial^2 w}{\partial x_2^2}, \frac{\partial^2 w}{\partial x_1 \partial x_2} \right)^T, \qquad \boldsymbol{C} = B \begin{pmatrix} 1 & \nu & 0 \\ \nu & 1 & 0 \\ 0 & 0 & (1-\nu)/2 \end{pmatrix}. \tag{3.17}$$

A finite element discretization of the domain Ω is now introduced through the shape functions (collected into the row vector $\boldsymbol{\Phi}$), so that the transversal displacement and the rotation can be expressed as

$$w = \boldsymbol{\Phi} \cdot \boldsymbol{u}^e, \tag{3.18}$$

where $\boldsymbol{u}^e$ is the vector collecting the nodal displacements and rotations of the eth element.

Using (3.18) in $(3.17)_1$, we obtain

$$\boldsymbol{\chi} = \boldsymbol{D}\boldsymbol{u}^e, \qquad \frac{\partial w}{\partial x_1} = \frac{\partial \Phi}{\partial x_1}\boldsymbol{u}^e, \qquad \frac{\partial w}{\partial x_2} = \frac{\partial \Phi}{\partial x_2}\boldsymbol{u}^e, \tag{3.19}$$

three equations holding in the domain of the eth element, in which

$$\boldsymbol{D} = \left(\frac{\partial^2 \boldsymbol{\Phi}^T}{\partial x_1^2}, \frac{\partial^2 \boldsymbol{\Phi}^T}{\partial x_2^2}, \frac{\partial^2 \boldsymbol{\Phi}^T}{\partial x_1 \partial x_2} \right)^T. \tag{3.20}$$

If we substitute (3.19) into (3.16) and identify Ω^* with the domain of the eth element Ω^e, we obtain the eigenvalue problem governing time-harmonic vibration of a finite element

$$\boldsymbol{u}^e \cdot \left(\boldsymbol{K}_e + \boldsymbol{K}_{fe} - \omega^2 \boldsymbol{M}_e \right) \boldsymbol{u}^e = 0, \tag{3.21}$$

where, for the eth elements, $\boldsymbol{M}_e$ is the mass matrix, $\boldsymbol{K}_e$ is the stiffness matrix, while $\boldsymbol{K}_{fe}$ keeps into account the effect of the prestress. Their expressions are

$$\begin{aligned} \boldsymbol{M}_e &= \int_{\Omega^e} \rho h \boldsymbol{\Phi} \boldsymbol{\Phi}^T \, d\Omega^e, \\ \boldsymbol{K}_e &= \int_{\Omega^e} \boldsymbol{D}^T \boldsymbol{C} \boldsymbol{D} \, d\Omega^e, \\ \boldsymbol{K}_{fe} &= \int_{\Omega^e} \boldsymbol{D}_f \cdot \boldsymbol{C}_f \boldsymbol{D}_f \, d\Omega^e, \end{aligned} \tag{3.22}$$

where

$$\boldsymbol{D}_f = \left(\boldsymbol{\Phi}^T, \frac{\partial \boldsymbol{\Phi}^T}{\partial x_1}, \frac{\partial \boldsymbol{\Phi}^T}{\partial x_2} \right)^T, \qquad \boldsymbol{C}_f = \begin{pmatrix} 0 & 0 & 0 \\ 0 & f_1 & 0 \\ 0 & 0 & f_2 \end{pmatrix}. \tag{3.23}$$

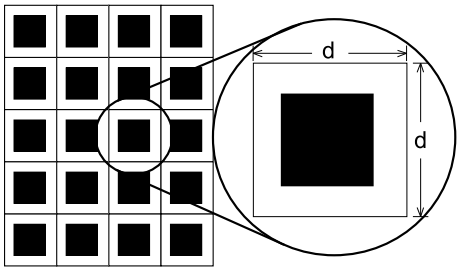

Fig. 3.5 The periodic plate analyzed in the examples. Inclusions are marked black and will be identified with an elastic material less stiff, but heavier, than the matrix

Applying (3.21) to the whole domain Ω of the plate and assembling the matrix of the finite elements, we obtain the mass matrix and the stiffness matrix of the whole cell,

$$\boldsymbol{M} = \sum_e \boldsymbol{M}_e, \qquad \boldsymbol{K} = \sum_e \boldsymbol{K}_e, \qquad \boldsymbol{K}_f = \sum_e \boldsymbol{K}_{fe}, \tag{3.24}$$

where $\boldsymbol{M}_e$, $\boldsymbol{K}_e$ and $\boldsymbol{K}_{fe}$ are the expanded matrices of the element, so that we finally arrive at the eigenvalue problem governing time-harmonic vibrations of the discretized plate

$$\boldsymbol{u} \cdot \left(\boldsymbol{K} + \boldsymbol{K}_f - \omega^2 \boldsymbol{M}\right)\boldsymbol{u} = 0, \tag{3.25}$$

where $\boldsymbol{u}$ is the vector collecting the nodal displacements and rotations of the whole cell.

The Floquet-Bloch condition for a cell of a periodic system made up of square cells of edge d (Fig. 3.5) can be written in terms of transverse displacement w as

$$w(x_1 + md, x_2 + nd) = w(x_1, x_2) e^{i(k_1 md + k_2 nd)}, \tag{3.26}$$

where m and n are integers indexing a node of the cell lattice and $\boldsymbol{k} = (k_1, k_2)$ is the Bloch vector. Note that (3.26) imposes also periodicity restrictions on rotations (and consequently on bending moments and shearing forces).

Using the finite element technique, only one cell is analyzed, so that condition (3.26) has to be imposed on its boundary, where it becomes

$$\begin{aligned} u(d, x_2) &= u(0, x_2) e^{i k_1 d}, \quad 0 \le x_2 \le d, \\ u(x_1, d) &= u(x_1, 0) e^{i k_2 d}, \quad 0 \le x_1 \le d, \end{aligned} \tag{3.27}$$

expressed in terms of generalized displacements (displacements and rotations).

Condition (3.27) imposes a linear dependence between some components of the generalized displacement vector $\boldsymbol{u}$, so that we assume that the linearly independent components $\tilde{\boldsymbol{u}}$ of displacement along the boundary of the periodicity cell can be written as

$$\boldsymbol{u} = \boldsymbol{T}(\boldsymbol{k}) \tilde{\boldsymbol{u}}, \tag{3.28}$$

and therefore the eigenvalue problem (3.25) takes the final form

$$\left(\widetilde{\boldsymbol{K}} + \widetilde{\boldsymbol{K}}_f - \omega^2 \widetilde{\boldsymbol{M}}\right)\tilde{\boldsymbol{u}} = 0, \tag{3.29}$$

where

$$\widetilde{\boldsymbol{K}} = \boldsymbol{T}(\boldsymbol{k})^T \boldsymbol{K} \boldsymbol{T}(\boldsymbol{k}), \qquad \widetilde{\boldsymbol{K}}_f = \boldsymbol{T}(\boldsymbol{k})^T \boldsymbol{K}_f \boldsymbol{T}(\boldsymbol{k}), \qquad \widetilde{\boldsymbol{M}} = \boldsymbol{T}(\boldsymbol{k})^T \boldsymbol{M} \boldsymbol{T}(\boldsymbol{k}). \tag{3.30}$$

The eigenvalue problem (3.29) can be numerically solved (we have used Matlab R2007b©). In a dimensionless form, (3.29) becomes

$$\left(\boldsymbol{K}^* + \Xi \boldsymbol{K}_f^* - \widetilde{\omega}^2 \boldsymbol{M}^*\right)\tilde{\boldsymbol{u}} = 0, \tag{3.31}$$

where $\boldsymbol{K}_f^*$ depends on the dimensionless ratio f_2/f_1, while

$$\Xi = \frac{f_1 d^2}{h^3 E}, \qquad \widetilde{\omega} = \frac{d^2}{h}\sqrt{\frac{\rho}{E}}\omega. \tag{3.32}$$

Examples of dispersion diagrams, calculated through solution of the eigenvalue problem (3.31), are reported in Figs. 3.6 and 3.7, where the inclusions have been taken of square shape (as sketched in Fig. 3.5), with an area equal to 0.36 d^2, a stiffness and density contrast respectively equal to $E_{matrix}/E_{inclusion} = 100$ and to $\rho_{matrix}/\rho_{inclusion} = 1/100$.

The dimensionless frequency $\widetilde{\omega}/(2\pi)$ is plotted

- for Fig. 3.6, which refers to the case of isotropic prestress $f_1 = f_2 = f$, along the right-handed triangle $\Gamma M X$, with vertices at $\Gamma = (0, 0)$, $M = (\pi, 0)$ and $X = (\pi, \pi)$, see the inset in the figure;
- for Fig. 3.7, which refers to the case of uniaxial prestress $f_2 = 0$, along the right-handed square $\Gamma M X N$, with vertices at $\Gamma = (0, 0)$, $M = (\pi, 0)$, $X = (\pi, \pi)$, and $N = (0, \pi)$, see the inset in the figure.

Note that there are, say, 'complete' and 'partial' band gaps, so that the former correspond to grey rectangles crossing completely Figs. 3.6 and 3.7, while the latter only extend to an edge of the triangle $\Gamma M X$ or of the square $\Gamma M X N$. A partial band gap means that there is only a limited angular range of wave propagation direction, while other directions are forbidden within a certain range of frequencies. The presence of a partial band gap can exploited to design special vibrational characteristics. Our results presented in Figs. 3.6 and 3.7 indicate that the global and partial band gaps are strongly influenced by the prestress, so that they can be (i.) shifted in frequency (towards high frequency for tensile prestress), (ii.) reduced or enlarged in size, (iii.) annihilated or (iv.) nucleated.

We can note the different role played by prestress in Fig. 3.6 (where the prestress state is isotropic) and in Fig. 3.7 (where the prestress state is anisotropic), so that for anisotropic (isotropic) prestress there is a progressive reduction (increase) in the number of band gaps, related to the increase in the tensile prestress, so that one complete band gap is nucleated in Fig. 3.6 and one is annihilated in Fig. 3.7.

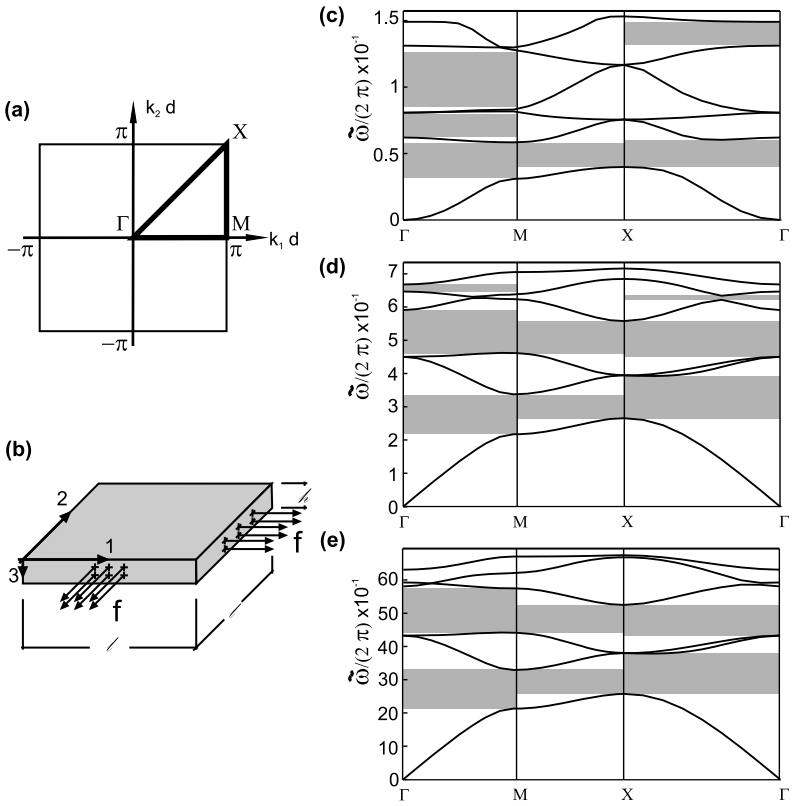

Fig. 3.6 A prestressed plate with an isotropic tensile prestress in the x_1–x_2 plane, so that $f_1 = f_2 = f$. (**a**) the First Irreducible Brillouin Zone; (**b**) the prestressed plate. Dispersion curves of the periodic plate at different values of the prestress f: (**c**) null prestress, $f = 0$; (**d**) moderate prestress, $f = Eh^3/d^2$; and (**e**) high prestress, $f = 10^2 Eh^3/d^2$. The *grey zones* identify the band gaps; note the difference between 'complete' (extending along $\Gamma M X$) and'partial' band gaps

Moreover, we see from Fig. 3.7 that there are a number of partial band gaps along the ΓM (the $N\Gamma$) direction that are annihilated (are nucleated) at increasing prestress.

An anisotropy effect related to the prestress is visible in Fig. 3.7, where only the band gaps in the direction of the prestress are annihilated. This effect is important, since we can exploit it to create a waveguide operating in a specific frequency range and controlling the vibration direction, as sketched in Fig. 3.8, where the vibration of a point-source is channelled along a certain direction, tuned by prestress.

3.5 Band Gaps and Self-Similarity in Quasiperiodic Beams

We consider now flexural vibrations of a quasiperiodic multisupported infinite beam. Structures analyzed in this section are formed by a set of—typically two—

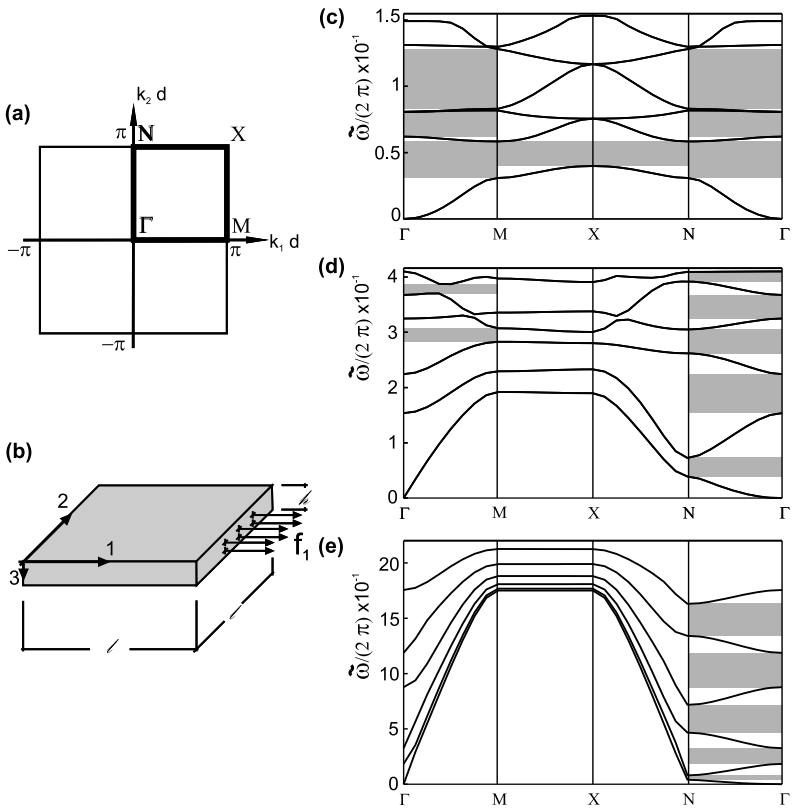

Fig. 3.7 A prestressed plate under a tensile prestress aligned parallel to the x_1-axis. (**a**) The First Irreducible Brillouin Zone; (**b**) the prestressed plate. Dispersion curves of the periodic plate at different values of uniaxial prestress f_1: (**c**) null prestress, $f_1 = 0$; (**d**) moderate prestress, $f_1 = Eh^3/d^2$; and (**e**) high prestress, $f_1 = 10^2 Eh^3/d^2$. The *grey zones* identify the band gaps; note the difference between 'complete' (extending along $\Gamma M X N$) and'partial' band gaps

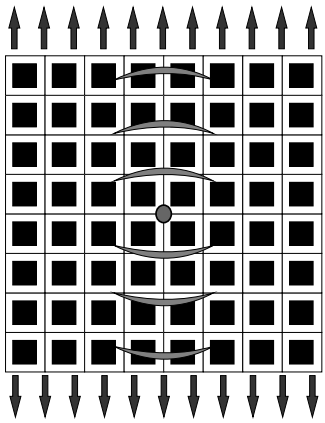

Fig. 3.8 Sketch of a wave guide effect created by prestress and periodicity. Vibrations induced by a pulsating force within a given frequency range are 'channelled' along a privileged direction, set by the prestress

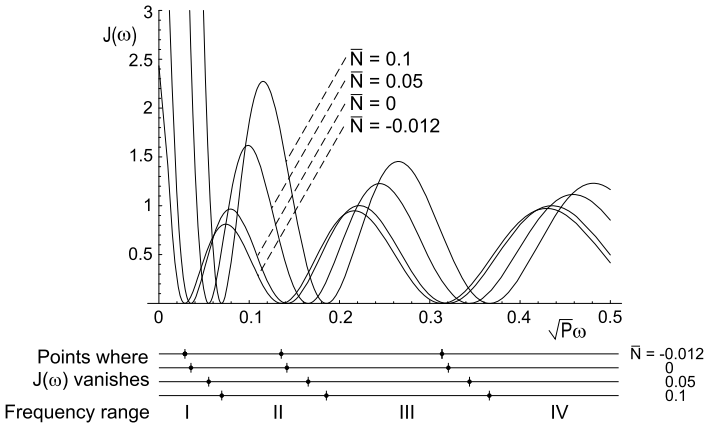

Fig. 3.9 Plots of the invariant $J(\omega)$, (3.46), for different prestress values $\overline{N}$ (for $l_S = l_L/2$). Frequency ranges set by null points of $J(\omega)$ are highlighted. Reprinted from [10] with permission from Elsevier

homogeneous parts combined to create a one-dimensional quasicrystalline pattern such as the Fibonacci sequence (other generation rules do exist, see e.g. the Thue-Morse sequence [25]) and subjected to an axial prestress. The goal is to extend to the domain of structural systems the features of phononic quasiperiodic crystals (see, e.g., [1, 6, 16, 18]). We refer to [10] for more details on the problem.

The elementary cell (Fig. 3.1(c)) of the structure is generated placing the supports at relative distances such that they follow a Fibonacci sequence. Introducing the notation $F_0 = (S)$, $F_1 = (L)$, where S ('short') and L ('long') identify two segments, the Fibonacci sequence obeys the recursive rule $F_i = (F_{i-1}F_{i-2})$ $(i \geq 2)$, where i is the *generation index*, so that $F_2 = (LS)$, $F_3 = (LSL)$ and so on. The number of elements of F_i is equal to $n_i = n_{i-1} + n_{i-2}$ $(i \geq 2, n_0 = n_1 = 1)$, with $\lim_{i\to\infty} n_{i+1}/n_i = \phi$, where ϕ represents the golden ratio $[\phi = (\sqrt{5}+1)/2]$.

The beam is homogeneous, with bending stiffness denoted by B and subjected to a constant prestress N, so that the equation governing transverse displacements $w(z)$ in the harmonic problem is

$$Bw'''' - Nw'' - \rho\omega^2 w = 0. \tag{3.33}$$

The solution can be sought in the form $w(z) = C\exp(ikz)$, yielding the characteristic equation

$$(kr)^4 + \overline{N}(kr)^2 - P\omega^2 = 0, \tag{3.34}$$

where r is the radius of inertia of the cross section and, as in the previous problem,

$$\overline{N} = \frac{Nr^2}{B}, \qquad P = \frac{\rho r^4}{B}. \tag{3.35}$$

Equation (3.34) provides four solutions k, namely

$$k_{1,2} = \pm\frac{1}{r}\sqrt{-\frac{\overline{N}}{2} + \sqrt{\frac{\overline{N}^2}{4} + P\omega^2}}, \qquad k_{3,4} = \pm\frac{1}{r}\sqrt{-\frac{\overline{N}}{2} - \sqrt{\frac{\overline{N}^2}{4} + P\omega^2}}, \tag{3.36}$$

which allow to build the general integral of (3.33) and where the first index is associated with sign '+'.

The dispersion diagram will be obtained through the concept of transmission matrix $\boldsymbol{M}_i$ of the elementary cell (relative to the sequence F_i), which relates the characteristic kinematical quantities of the cell evaluated on the two boundaries. In our case, we note that the configuration of the beam is defined once the rotation $\varphi(z)$ and its derivative $\varphi'(z)$ at each constrained point are known (see Fig. 3.1(c)). Then, we can write formally

$$\boldsymbol{V}_r = \boldsymbol{M}_i \boldsymbol{V}_l, \tag{3.37}$$

where $\boldsymbol{V}_j = [\varphi_j \quad \varphi'_j]^T$ and subscripts r and l denote the right-hand and left-hand boundary of the elementary cell, respectively. The matrix $\boldsymbol{M}_i$ can be assembled multiplicating the matrices of receptances ($\boldsymbol{M}^X$, $X \in \{L, S\}$) associated with all spans within the elementary cell, [10], namely

$$\boldsymbol{M}_i = \prod_{p=1}^{n_i} \boldsymbol{M}^X, \tag{3.38}$$

where $\boldsymbol{M}^X$ is given by

$$\boldsymbol{M}^X = \begin{bmatrix} \frac{\psi^X_{bb}}{\psi^X_{ab}} & \psi^X_{ba} - \frac{\psi^X_{bb}\psi^X_{aa}}{\psi^X_{ab}} \\ \frac{1}{\psi^X_{ab}} & -\frac{\psi^X_{aa}}{\psi^X_{ab}} \end{bmatrix}. \tag{3.39}$$

The entries of the matrix can be calculated from

$$\psi^X_{aa} = \frac{k_1 \cot(k_1 l_X) - k_3 \cot(k_3 l_X)}{k_3^2 - k_1^2}, \qquad \psi^X_{bb} = \frac{k_1 \cot(k_1 l_X) - k_3 \cot(k_3 l_X)}{k_1^2 - k_3^2}, \tag{3.40}$$

$$\psi^X_{ab} = \frac{k_1 \mathrm{cosec}(k_1 l_X) - k_3 \mathrm{cosec}(k_3 l_X)}{k_1^2 - k_3^2}, \qquad \psi^X_{ba} = \frac{k_1 \mathrm{cosec}(k_1 l_X) - k_3 \mathrm{cosec}(k_3 l_X)}{k_3^2 - k_1^2}, \tag{3.41}$$

that depend on circular frequency and prestress N through k_1 and k_3 [see (3.36)].

Transmission matrices $\boldsymbol{M}_i$ have some important properties that can be exploited in the analysis of quasiperiodic structures:

- they follow the recursion rule $\boldsymbol{M}_{i+1} = \boldsymbol{M}_{i-1}\boldsymbol{M}_i$, with $\boldsymbol{M}_0 = \boldsymbol{M}^S$ and $\boldsymbol{M}_1 = \boldsymbol{M}^L$;
- they are unimodular, i.e. $\det \boldsymbol{M}_i = 1$, so that writing down the trace of the equation

$$\boldsymbol{M}_{i+1} + \boldsymbol{M}_{i-2}^{-1} = \boldsymbol{M}_{i-1}\boldsymbol{M}_i + \boldsymbol{M}_{i-1}\boldsymbol{M}_i^{-1},$$

we obtain that the half trace $y_i = \mathrm{tr}\boldsymbol{M}_i/2$ follows the recursive rule [19]

$$y_{i+1} = 2y_i y_{i-1} - y_{i-2}, \tag{3.42}$$

with initial conditions $y_0 = \mathrm{tr}M^S/2$, $y_1 = \mathrm{tr}M^L/2$, $y_2 = \mathrm{tr}(M^S M^L)/2$.

The Bloch-Floquet condition requires that $\boldsymbol{V}_r = \exp(iK)\boldsymbol{V}_l$, so that, combining this with (3.37), the dispersion equation takes the form

$$\left|\boldsymbol{M}_i - \exp(iK)\boldsymbol{I}\right| = 0, \tag{3.43}$$

or

$$K = \arccos\left(\frac{\mathrm{tr}\boldsymbol{M}_i}{2}\right), \tag{3.44}$$

that is a real quantity if $|\mathrm{tr}\boldsymbol{M}_i/2| \leq 1$.

3.5.1 Dispersion Diagrams and Distribution of Pass Bands and Band Gaps

Dispersion diagrams and stop/pass band distributions are now illustrated in terms of dimensionless quantities for $l_S = l_L/2$. An invariant function similar to that introduced by Kohmoto et al. [19] (used to analyze certain solutions of the Schrödinger equation in the presence of quasiperiodic potentials), and employed in [21] to investigate the transmission properties of photonic crystals, can help in the understanding of their properties. Since the recursion rule (3.42) is satisfied, it can be shown [19] that the following quantity is independent of the index i

$$J(\omega) = y_{i+1}^2 + y_i^2 + y_{i-1}^2 - 2y_{i+1}y_i y_{i-1} - 1. \tag{3.45}$$

The explicit expression for $J(\omega)$ turns out to be

$$\begin{aligned} J(\omega) = {} & \frac{k_1^2 k_3^2}{[k_3\sin(k_1 l_L) - k_1\sin(k_3 l_L)]^2[k_3\sin(k_1 l_S) - k_1\sin(k_3 l_S)]^2} \\ & \times \left\{\sin(k_1 l_L)\sin(k_3 l_L)\left[1 - \cos(k_1 l_S)\cos(k_3 l_S)\right]\right. \\ & \left. + \sin(k_1 l_S)\sin(k_3 l_S)\left[\cos(k_1 l_L)\cos(k_3 l_L) - 1\right]\right\}^2, \end{aligned} \tag{3.46}$$

which is a modulated periodic function, sketched in Fig. 3.9 for four different values of the dimensionless prestress $\overline{N}$. The function $J(\omega)$ is identically null for $l_L = l_S$,

which corresponds to the case of a beam resting on equidistant supports. In Fig. 3.9 we have also reported the ranges of frequencies comprised between two null points of the function for different prestresses $\overline{N}$. In particular, the second range will be considered later on.

Single dispersion diagrams for different generation sequences are displayed in Figs. 3.10(a) and 3.10(b) which display cut-off frequencies associated with the discrete distribution of supports. Ranges set by null values of the invariant $J(\omega)$ (Fig. 3.9) are reported to facilitate the analysis of the different cases. Assuming an elementary cell built according to the sequence F_i, in the first range ($0 < \sqrt{P}\omega < 0.03553$ for $\overline{N} = 0$) the number of stop and pass bands equals n_i, while in all other intervals it corresponds to n_{i+1}. In Fig. 3.10(c), the global dispersion diagram combining solutions relative to problems where the elementary cell is generated by sequences F_0 to F_7 is reported. It is interesting to note that the various branches of single diagrams localize within certain ranges of frequencies and stop bands common to all F_i's emerge. The position of these common stop bands is therefore a characteristic of the Fibonacci sequence and can be controlled by changing the ratio l_S/l_L and the space between supports.

The distribution of pass bands follows a self-similar law when the index i of the generation sequence F_i increases. This property can be recognized looking at the rectangular boxes in Fig. 3.11. Here the second frequency range (for which $0.03553 < \sqrt{P}\omega < 0.14212$) is investigated in detail. All rectangles enclose a number of pass bands that, starting from the top, follows the Fibonacci recursion rule: 1, 1, 2, 3, ... However, differently from the axial-wave problem addressed in [10], the relative positions of pass bands with respect to those of the preceding row strongly change, depending on their position on the spectrum.

The function $J(\omega)$ controls also the scaling of pass-band widths changing the sequence F_i. In quantum mechanics, Kohmoto and Oono [20] established that the ratio between the widths of two pass bands (F_i and F_{i+3}, $\forall i$) centered at the same frequency is given by the factor $f(\omega)$, which depends on $J(\omega)$ through the relationship

$$f(\omega) = \sqrt{1 + 4\big[J(\omega) + 1\big]^2} + 2\big[1 + J(\omega)\big]. \tag{3.47}$$

Compared to the case investigated by Kohmoto and Oono, where $J(\omega)$ was a constant, here f depends on ω, however its role in setting the scaling remains essentially the same. The function $f(\omega)$ is sketched in Fig. 3.12(a) for four values of $\overline{N}$. Denoting by $q_k(F_i)$ the width of the pass band for F_i at a frequency corresponding to the index k, f describes exactly their scaling, namely the ratio $q_k(F_i)/q_k(F_{i+3})$, only when the generation index i is relatively high, as shown in Fig. 3.12(b) for two cases (for $\sqrt{P}\omega = 0.060$, $k = 1$, and 0.0956, $k = 2$).

The self-similarity properties show that periodic structures built with a quasiperiodic elementary cell can display very narrow stop and pass bands and therefore can be exploited, in principle, to conceive very sensitive filters.

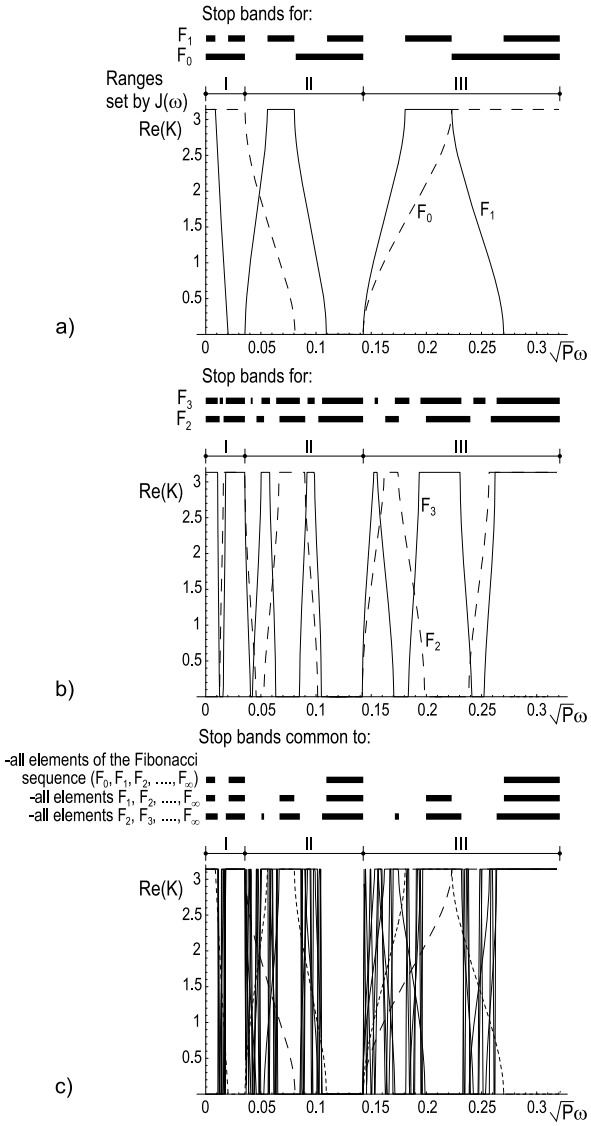

Fig. 3.10 Dispersion diagrams for flexural waves for beams generated by elementary cells given by sequences (**a**) F_0 and F_1, (**b**) F_2 and F_3; (**c**) global dispersion diagram for beams generated by elements F_i ($i = 0, \ldots, 7$) and stop bands common to all elements of the Fibonacci sequence (frequency intervals where waves cannot propagate in any structure generated by a generic F_i with $i = 0, \ldots, \infty$), to all elements F_i with $i = 1, \ldots, \infty$, and to all elements F_i with $i = 2, \ldots, \infty$; *long-dashed line*: solutions for F_0; *short-dashed line*: solutions for F_1; *solid lines*: cumulated diagram for cases F_2 to F_7. In all plots $l_S = l_L/2$ and $\overline{N} = 0$. Reprinted from [10] with permission from Elsevier

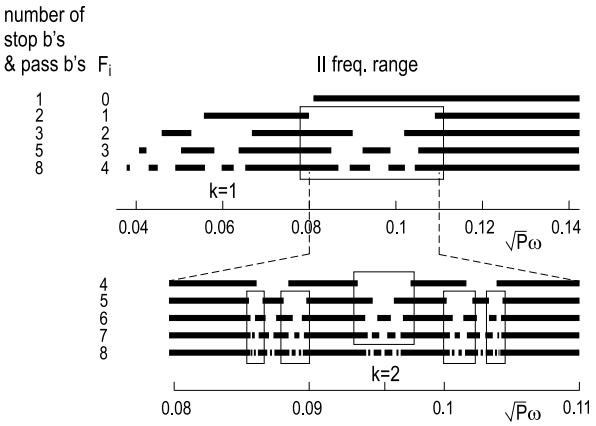

Fig. 3.11 Stop-band structure in the second frequency range ($0.03553 < \sqrt{P}\omega < 0.14212$, see Fig. 3.10) for beams generated by sequences F_0 to F_8, for $l_S = l_L/2$ and $\overline{N} = 0$. Indices k's identify the values of the dimensionless frequency $\sqrt{P}\omega = 0.06$ ($k = 1$) and 0.0956 ($k = 2$) (see Fig. 3.12). All rectangles contain the same self similar, recursive band structure. Reprinted from [10] with permission from Elsevier

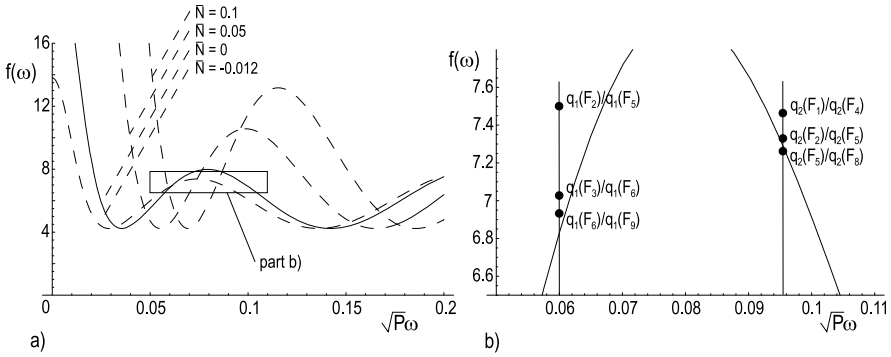

Fig. 3.12 Function $f(\omega)$ (3.47) describing the scaling factor of pass-band widths between F_i and F_{i+3} for the flexural problem. In part (**b**), the plot of $f(\omega)$ for $\overline{N} = 0$ is reported (*solid line*) and the scaling is verified for pass bands at $\sqrt{P}\omega = 0.060$ ($k = 1$, see Fig. 3.11) and at $\sqrt{P}\omega = 0.0956$ ($k = 2$). In both cases the relevant value of f describes the pass-band width scaling $q_k(F_i)/q_k(F_{i+3})$ at high index i. Reprinted from [10] with permission from Elsevier

3.5.2 Effect of the Prestress

We want to explore now how the prestress affects the positions of stop and pass bands in the dispersion diagram for flexural waves of a quasiperiodic, multisupported beam. We note that under compression the structure can buckle at a load that

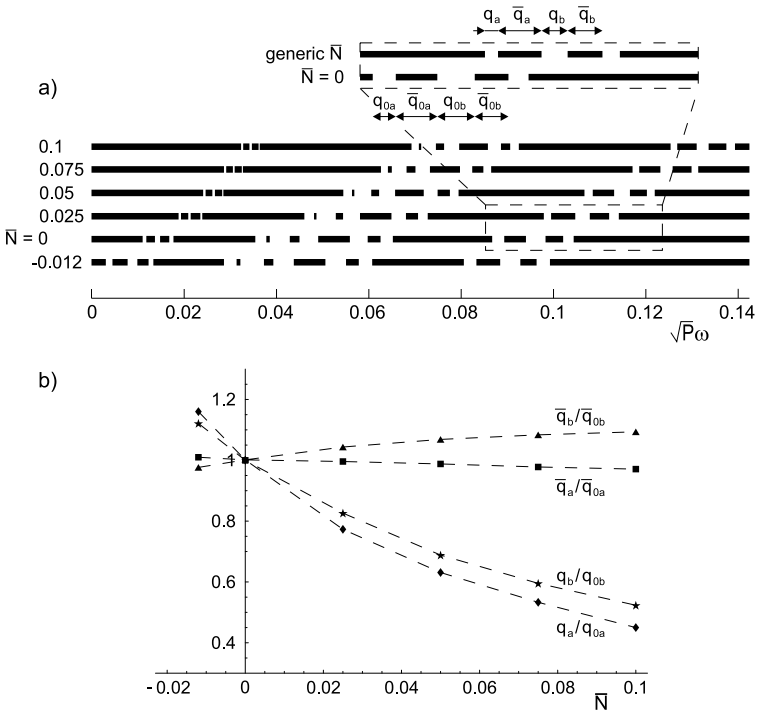

Fig. 3.13 (**a**) Effect of prestress $\overline{N}$ on stop/pass band distribution for flexural waves of a multi-supported quasiperiodic beam generated by sequence F_4; (**b**) influence of $\overline{N}$ on pass-band widths (represented by quantities q_1/q_{01}, q_2/q_{02}) and on stop-band widths (represented by quantities $\bar{q}_1/\bar{q}_{01}$, $\bar{q}_2/\bar{q}_{02}$). Subscript '0' denotes values for $\overline{N} = 0$. Reprinted from [10] with permission from Elsevier

can be easily obtained imposing $\omega = 0$ in (3.33) and treating N as the eigenvalue of (3.43).[1]

In Fig. 3.13(a), the stop/pass band distribution of a beam generated by sequence F_4 as functions of the axial load $\overline{N}$ (for $\sqrt{P}\omega < 0.1421$) is reported. Six values of $\overline{N}$ are investigated: $\overline{N} = -0.012$, a value slightly lower in absolute value than the buckling load, that corresponds to $\overline{N}_{buckl} = -0.01304$ (see footnote 1), $\overline{N} = 0, 0.025, 0.05, 0.075$, and 0.1. It is clear that a tensile stress shifts toward higher frequencies the bands, almost in a linear fashion, while in compression they move to lower frequencies, similarly to the problem analyzed in the previous section. Here it has been verified that no band-gap annihilation occurs.

The axial load has also an influence on the width of stop/pass bands. In Fig. 3.13(b), the stop/pass bands that in part (a) lie within the range $0.08 < \sqrt{P}\omega <$

[1] In terms of generation sequence F_i dimensionless buckling loads are $\overline{N}_{buckl}(F_0) = -0.03553$, $\overline{N}_{buckl}(F_1) = -0.00888$, $\overline{N}_{buckl}(F_2) = -0.01579$, $\overline{N}_{buckl}(F_3) = -0.01233$, $\overline{N}_{buckl}(F_4) = -0.01305$, $\overline{N}_{buckl}(F_5) = -0.01269$, $\overline{N}_{buckl}(F_6) = -0.01276$.

0.11 for $\overline{N} = 0$ (see the inset in Fig. 3.13(a)) are investigated. In particular, the ratios between their widths at different $\overline{N}$ and that at $\overline{N} = 0$ are reported in the plot. We note that stop-band widths (see the behaviour of ratios $\bar{q}_a/\bar{q}_{0a}$, $\bar{q}_b/\bar{q}_{0b}$) are weakly influenced by the prestress, while pass bands reduce (increase) considerably their lengths when a tensile (compressive) stress is applied (see q_a/q_{0a}, q_b/q_{0b}).

Acknowledgements M.G. and M.B. gratefully acknowledge the support of Italian Ministry of Education, University and Research (PRIN grant No. 2009XWLFKW); D.B. and A.B.M. gratefully acknowledge the support from the European Union FP7 under contract No. PIAP-GA-2011-286110-INTERCER2.

References

1. Aynaou, H., El Boudouti, E.H., Djafari-Rouhani, B., Akjouj, A., Velasco, V.R.: Propagation and localization of acoustic waves in Fibonacci phononic circuits. J. Phys. Condens. Matter **17**, 4245–4262 (2005)
2. Bacon, M.D., Dean, P., Martin, J.L.: Proc. Phys. Soc. **80**, 174 (1962)
3. Bigoni, D., Capuani, D., Bonetti, P., Colli, S.: A novel boundary element approach to time-harmonic dynamics of incremental non-linear elasticity: The role of pre-stress on structural vibrations and dynamic shear banding. Comput. Methods Appl. Mech. Eng. **196**, 4222 (2007)
4. Bigoni, D., Capuani, D.: Time-harmonic Green's function and boundary integral formulation for incremental nonlinear elasticity: Dynamics of wave patterns and shear bands. J. Mech. Phys. Solids **53**, 1163 (2005)
5. Bigoni, D., Gei, M., Movchan, A.B.: Dynamics of a prestressed stiff layer on an elastic half space: filtering and band gap characteristics of periodic structural models derived from long-wave asymptotics. J. Mech. Phys. Solids **56**, 2494–2520 (2008)
6. Chen, A.L., Wang, Y.S.: Study on band gaps of elastic waves propagating in one-dimensional disordered phononic crystals. Physica B **392**, 369–378 (2007)
7. Cremer, L., Leilich, H.O.: Zur theorie der biegekettenleiter. Arch. Elektr. Übertrag. **7**, 261 (1953)
8. Feynman, R.: The Feynman Lectures on Physics, vol. 2. Addison-Wesley, Reading (1965)
9. Gei, M.: Elastic waves guided by a material interface. Eur. J. Mech. A, Solids **27**, 328–345 (2008)
10. Gei, M.: Wave propagation in quasiperiodic structures: Stop/pass band distribution and prestress effects. Int. J. Solids Struct. **47**, 3067–3075 (2010)
11. Gei, M., Bigoni, D., Franceschini, G.: Thermoelastic small-amplitude wave propagation in nonlinear elastic multilayer. Math. Mech. Solids **9**, 555–568 (2004)
12. Gei, M., Movchan, A.B., Bigoni, D.: Band-gap shift and defect induced annihilation in prestressed elastic structures. J. Appl. Phys. **105**, 063507 (2009)
13. Gei, M., Ogden, R.W.: Vibration of a surface-coated elastic block subject to bending. Math. Mech. Solids **7**, 607–629 (2002)
14. Gurtin, M.E., Murdoch, A.I.: A continuum theory of elastic material surfaces. Arch. Ration. Mech. Anal. **57**, 291–323 (1975)
15. Hladky-Hennion, A.-C., Vasseur, J., Dubus, B., Djafari-Rouhani, B., Ekeom, D., Morvan, B.: J. Appl. Phys. **104**, 094206 (2008)
16. Hou, Z., Wu, F., Liu, Y.: Acoustic wave propagating in one-dimensional Fibonacci binary composite systems. Physica B **344**, 391–397 (2004)
17. John, S.: Strong localization of photons in certain disordered dielectric superlattices. Phys. Rev. Lett. **58**, 2486–2489 (1987)
18. King, P.D.C., Cox, T.J.: Acoustic band gaps in periodically and quasiperiodically modulated waveguides. J. Appl. Phys. **102**, 014908 (2007)

19. Kohmoto, M., Kadanoff, L.P., Tang, C.: Localization problem in one dimension: Mapping and escape. Phys. Rev. Lett. **50**, 1870–1872 (1983)
20. Kohmoto, M., Oono, Y.: Cantor spectrum for an almost periodic Schroedinger equation and a dynamical map. Phys. Lett. A **102**, 145–148 (1984)
21. Kohmoto, M., Sutherland, B., Iguchi, K.: Localization in optics: Quasiperiodic media. Phys. Rev. Lett. **58**, 2436–2438 (1987)
22. Kushwaha, M.S., Halevi, P., Dobrzynski, L., Djafari-Rouhani, B.: Acoustic band structure of periodic elastic composites. Phys. Rev. Lett. **71**, 2022–2025 (1993)
23. Lin, Y.K.: Free vibrations of a continuous beam on elastic supports. Int. J. Mech. Sci. **4**, 409–423 (1962)
24. Liu, Z., Chan, C. T, Sheng, P.: Analytic model of phononic crystals with local resonances. Phys. Rev. B **71**, 014103 (2005)
25. Liu, Z., Zhang, W.: Bifurcation in band-gap structures and extended states of piezoelectric Thue-Morse superlattices. Phys. Rev. B **75**, 064207 (2007)
26. Mead, D.J.: Wave propagation in continuous periodic structures: Research contributions from Southampton. J. Sound Vib. **190**, 495 (1996)
27. Mead, D.J.: Wave propagation and natural modes in periodic systems. II. Multi-coupled systems, with and without damping. J. Sound Vib. **40**, 19 (1975)
28. Miles, J.W.: Vibrations of beams on many supports. J. Eng. Mech. **82**, 1–9 (1956)
29. Milton, G.W., Willis, J.R.: On modifications of Newton's second law and linear continuum elastodynamics. Proc. R. Soc. Lond. A **463**, 855 (2007)
30. Movchan, A.B., Slepyan, L.I.: Band gap Green's functions and localized oscillations. Proc. R. Soc. Lond. A **463**, 2709 (2007)
31. Ogden, R.W., Steigmann, D.J.: Plane strain dynamics of elastic solids with intrinsic boundary elasticity, with application to surface wave propagation. J. Mech. Phys. Solids **50**, 1869–1896 (2002)
32. Page, J.H., Sukhovich, A., Yang, S., Cowan, M.L., Van Der Biest, F., Tourin, A., Fink, M., Liu, Z., Chan, C.T., Sheng, P.: Phys. Status Solidi B **241**, 3454 (2004)
33. Parnell, W.J.: Effective wave propagation in a prestressed nonlinear elastic composite bar. IMA J. Appl. Math. **72**, 223–244 (2007)
34. Pendry, J.B.: Negative refraction makes a perfect lens. Phys. Rev. Lett. **85**, 3966 (2000)
35. Sheng, P., Zhang, X.X., Liu, Z., Chan, C.T.: Physica B **338**, 201 (2003)
36. Sigalas, M.M., Economou, E.N.: Elastic and acoustic-wave band-structure. J. Sound Vib. **158**, 377–382 (1992)
37. Steigmann, D.J., Ogden, R.W.: Plane deformations of elastic solids with intrinsic boundary elasticity. Proc. R. Soc. Lond. A **453**, 853–877 (1997)
38. Timoshenko, S.P., Weaver, W., Young, D.H.: Vibration Problems in Engineering. Wiley, New York (1974)
39. Yablonovitch, E.: Inhibited spontaneous emission in solid-state physics and electronics. Phys. Rev. Lett. **58**, 2059–2062 (1987)
40. Yang, S., Page, J.H., Liu, Z., Cowan, M.L., Chan, C.T., Sheng, P.: Phys. Rev. Lett. **93**, 024301 (2004)
41. Zhang, X., Liu, Z.: Appl. Phys. Lett. **85**, 341 (2004)

Chapter 4
Ultrasound Transmission Through Periodically Perforated Plates

Héctor Estrada, F. Javier García de Abajo, Pilar Candelas, Antonio Uris, Francisco Belmar, and Francisco Meseguer

Abstract We study sound transmission through plates perforated with subwavelength holes. Experimental results are analyzed in the light of both a rigid solid model as well as a full elasto-acoustic theory. A discussion comparing sound and optics is given based upon an analytical framework. We show that, unlike light, sound is transmitted through individual subwavelength holes, in a perfectly rigid thin film approximately in proportion to their area. Moreover, hole arrays in perfectly rigid thin films do not exhibit full sound transmission due to the absence of lattice resonances. Therefore, the resonant full transmission observed in hole arrays is not extraordinary in the case of sound. However extraordinary sound screening well beyond that predicted by the mass law is observed. Finally, we find a strong interplay between Wood anomaly minima and intrinsic plate modes (Lamb modes), which results in fundamentally unique behavior of sound as compared to light.

H. Estrada · P. Candelas · A. Uris · F. Belmar · F. Meseguer
Centro de Tecnologías Físicas, Unidad Asociada ICMM-CSIC/UPV, Universidad Politécnica de Valencia, Av. Naranjos s/n. 46022 Valencia, Spain

P. Candelas
e-mail: pcandelas@fis.upv.es

A. Uris
e-mail: auris@fis.upv.es

F. Belmar
e-mail: fbelmar@fis.upv.es

F. Meseguer (✉)
e-mail: fmese@fis.upv.es

F.J. García de Abajo
Instituto de Óptica CSIC, Unidad Asociada CSIC-Universidade de Vigo, Serrano 121, 28006 Madrid, Spain
e-mail: J.G.deAbajo@csic.es

H. Estrada · F. Meseguer
Instituto de Ciencia de Materiales de Madrid (CSIC), Cantoblanco, 28049 Madrid, Spain

H. Estrada
e-mail: hector.estrada@icmm.csic.es

R.V. Craster, S. Guenneau (eds.), *Acoustic Metamaterials*,
Springer Series in Materials Science 166, DOI 10.1007/978-94-007-4813-2_4,

4.1 Introduction

Periodically perforated plates or membranes are ubiquitous in technological applications in today's world. They constitute an important element in the toolbox of an acoustic engineer [31], and therefore, their acoustical properties are well known when the size of the aperture is quite small compared to the wavelength λ. Furthermore, periodically patterned structures have received great attention in the last ten years as a result of the discovery of extraordinary optical transmission (EOT) [16]. Some of the phenomena observed at atomic scales, typically using electron waves [53] in ordered systems, are mimicked by light and sound at larger scales. The concepts of phononic [48, 64] and photonic [32] metamaterials are now well-established areas of research, which consist in the combination of two or more structured constituent materials having macroscopic properties that are largely dependent on their detailed structure. The interest in these materials is that some of the resulting properties cannot be achieved by means of conventional materials, thus revealing fundamentally new ways of controlling optical and acoustic waves. Band-gaps [60, 78], localized states [34, 67], waveguiding [36, 49], cloaking [15, 42], and negative refraction [63, 65] have been achieved by means of metamaterials. In this context, periodically perforated plates (PPP), which are already used in many acoustic applications, appear to be good candidates to exhibit new properties and hence be used for new applications.

The study of sound interactions with periodic structures originates at the end of the XIX century with the work of Lord Rayleigh [58], who studied the reflection coefficient of one-dimensional gratings. More recently, full reflection was reported by Norris and Luo [51] in 1987 for a two-dimensional array of circular holes of period a in a semi infinite rigid-solid when $\lambda = a$. The problem received more attention after the experimental report of EOT through a periodically perforated membrane [16] and the evidence of analogies between photonic and phononic metamaterials [60]. Ebbesen et al. [16] demonstrated experimentally that periodic arrays of subwavelength holes drilled on a metal film transmit much more light per hole than expected from Bethe's theory [5]. This effect occurred at specific wavelengths strongly correlated with the periodicity. EOT has been reported in one- and two-dimensional gratings in numerous theoretical and experimental studies [3, 25, 54, 66, 68, 79] and over a wide range of wavelengths [26, 61]. Several mechanisms have been identified to contribute to EOT, such as surface plasmon resonances [4, 47], cavity resonances [23], and dynamical diffraction [68], all of them describable using a simple analytical formulation [23].

The wave nature of sound can then be exploited to produce effects that are similar to EOT. Sound collimation through a corrugated plate with a central aperture was proposed by Christensen et al. [10], following some ideas from Barnes et al. [4], and experimentally verified recently [82] for a steel corrugated plate in air. In an attempt to deal with a perforated plate, Zhang [80] studied numerically the sound transmission through a one-dimensional array of steel cylinders in air using a multiple-scattering method, leaving a very narrow air-gap between the cylinders to mimic a slit array. Resonant transmission and a dip corresponding to the Wood

anomaly [76] have been reported. Zhou and Kriegsman [81] predicted complete transmission through two-dimensional subwavelength hole-arrays by means of the scattering matrix technique for the first mode of the cavity. Experimental confirmation of complete transmission has been reported by two groups [30, 46], for a perforated brass plate immersed in water and for a slit array made of steel in air, respectively. This full transmission has been called extraordinary acoustic transmission (EAT) [46] by analogy to EOT. However, Fabry-Pérot resonances in the hole produce the main contribution to the full transmission peaks. Also, the existence of a cutoff-free mode in the holes is a major difference with respect to the electromagnetic case. The situation is complex, because evanescent waves and diffractive surface-waves can produce significant deviation of the transmission peaks from the Fabry-Pérot condition. Moreover, it has been argued [30] that the existence of a full transmission peak near to the Wood anomaly is due to an array resonance. Christensen et al. [11, 13] reported theoretical results in the rigid-solid limit for one- and two-dimensional arrays of square holes, for which they derived the dispersion relation of leaky and non-leaky surface modes. It has been pointed out that hybridization occurs between these modes and the Fabry-Pérot resonances. Wang [71, 72] obtained an impedance description of full sound transmission by assuming piston-like behavior at the hole apertures. In this way, the full transmission near to the Wood anomaly can be understood as induced by the singularity of the radiation impedance of the hole array. High transmission has been also observed by He et al. [27] for a corrugated brass plate immersed in water without the need of any opening due to the fluid-solid resonant coupling attributed to a non-leaky elastic surface mode. Two layers of periodically perforated plates [12, 45] have also been proposed for sound blocking in the rigid solid limit. In addition, Liu and Jin [44] have predicted a suppression of the full transmission peaks due to phase resonances when the hole array basis is asymmetric.

In this chapter, we show that perforated plates do not only exhibit high transmission, but also hydrodynamic short-circuiting leading to extraordinary sound screening well beyond that predicted by the mass law [17]. Perforated plates can shield sound more effectively than non-perforated ones for aluminum (Al) plates immersed in water at ultrasonic frequencies. Hydrodynamic short-circuit shielding is found to be more effective than that obtained by means of two periodically perforated PMMA (Polymethyl methacrylate) plates in water as proposed in [43]. The role of the filling fraction of holes and the lattice geometry in the transmission features of perforated plates is also reported here, showing that both the position and the width of the transmission peak can be tuned by changing geometrical parameters (see [19]). At variance to previous results [29], where a simple effective fluid model is proposed to describe the behavior of a periodically perforated brass plate immersed in water, a high complexity was observed for periodically perforated Al plates immersed in water. Leaky surface waves (Lamb modes) coming from the vibration of the plate become important and they interact with Wood anomaly minima [18, 21], as we will show on both theoretical and experimental grounds. Finally, we summarize some results for the transmission properties of individual holes and hole arrays for light, electrons, and sound, as shown in [24]. We analyze differences in the transmission of these types of waves.

4.2 Background

4.2.1 Homogeneous Plate

The problem of sound transmission through an homogeneous solid has been extensively studied in the past [40, 41, 70]. Several textbooks deal with wave and ultrasound propagation in solids [39, 59]. A simple fluid-solid-fluid geometry can be used to study the transmission of incident plane waves and the coefficient of sound transmission power τ as shown in Fig. 4.1.

Regions of high transmission are observed, which reveal a complex dispersion. For this case, three kinds of modes can be distinguished [52]: the Scholte-Stoneley mode, symmetric leaky Lamb modes S_n, and antisymmetric leaky Lamb modes A_n. The Scholte-Stoneley mode propagates across the fluid-solid interface with a phase velocity slightly below that of sound in water. At low frequencies, this mode is mixed with the A_0 mode and slowly converges to the sound line as ω increases.

Leaky Lamb modes are produced due to multiple reflections of longitudinal and out of-plane transverse modes at both plate-fluid interfaces. The inset in Fig. 4.1 shows the different shapes of the symmetric (S_n) and antisymmetric (A_n) modes. The two cutoff-free modes, A_0 and S_0, show different transmission properties. The antisymmetric mode has a broader transmission peak and smaller phase velocity than the symmetric mode, but both of them converge at higher frequencies to the phase velocity of Rayleigh waves. The higher order Lamb modes exhibit many interesting features like negative and zero group velocity (see mode S_1), mode splitting (see S_1 and S_2), and mode crossing (see A_2 and S_2).

We can obtain more insight into the plate displacement by considering a wave traveling along the x direction. Since we are interested in modes of the system, we exclude the incident wave. Then, applying the boundary conditions for sound and elastic waves, we obtain a condition for the existence of such modes, the so-called dispersion relation [39, 52, 59, 70]. The dispersion equations are quite complex and can only be solved using numerical methods for nonlinear systems. Thus, despite its

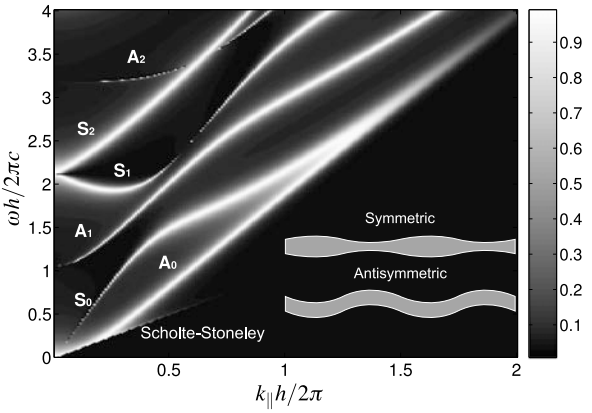

Fig. 4.1 Transmitted sound power coefficient τ (*gray linear scale*) calculated for an homogeneous aluminum plate immersed in water as a function of the parallel wavevector $k_{\|}$ and the frequency ω, both of them normalized by the plate thickness h. The different modes are labeled according to their symmetry, as shown in the inset

simplicity, the transmission approach produces the correct dispersion relation. Lamb waves are widely used for nondestructive evaluation at ultrasonic frequencies in plate-like structures. For example, internal defects in large plates can be detected by means of Lamb waves. Not only isotropic plates, but also anisotropic or multilayered structures can be inspected. In addition, material characterization can be performed by means of Lamb waves because the elastic constants of the plate can be retrieved by studying their propagation [22]. Most applications use water-coupled Lamb wave excitation and detection, although some techniques make use of zero group velocity [28] for nondestructive testing of airborne plates in order to increase the fluid-solid coupling.

4.2.2 Single Hole

As a part of the sound transmission through plates perforated with many holes, we will analyze the case of a single hole. The problem of sound transmission through a circular hole has been studied at different levels of detail and using several methods. In the late nineteenth century, Rayleigh [55, 56] pioneered these studies by considering scalar waves (appropriate for sound, but also for the later discovered electrons) assuming plates of zero thickness. An exact solution to the three dimensional diffraction problem was found by Bouwkamp [6] in 1941, who later in 1954 wrote a review [7] comprising not only scalar, but also vectorial waves (for light), also assuming zero-thickness screen, and summarizing the knowledge on the problem at that time.

Although the same equation must be satisfied for sound, electrons, and light in homogeneous regions, namely the wave equation $(\nabla^2 + k^2)\phi = 0$, the boundary conditions lead to severe differences in their scattering characteristics. In order to unify criteria regarding the perfectness of the boundary conditions, we consider a completely rigid screen for sound, infinite-potential boundaries for electrons, and a perfect conductor for light. Sound and electrons show complementary behavior via Babinet's principle, which is a rigorous result [24]. The diffraction of sound (electrons) by a disc is essentially identical to the diffraction by the complementary aperture for electrons (sound). However, a small hole in a perfect screen is quite permeable to sound while for electrons and light it is nearly opaque. A more technical way of expressing this idea is that a subwavelength aperture transmits sound approximately in proportion to its area, whereas electrons are nearly blocked and they are transmitted in proportion to the fourth power of the ratio of its diameter to the wavelength. Using the noted Babinet relation, one infers that a subwavelength scatterer will produce very little scattering of sound, but its scattering cross section towards electrons must be comparable to its physical cross section.

Finite-thickness screens were worked out for sound by Nomura and Inawashiro [50], who developed an exact solution, but this was difficult to implement. Afterwards, Wilson and Soroka [75] derived an approximate solution for normal incidence and found very good agreement with measurements. However, a more rigorous and exact method relying on modal expansions has been derived in [35]. New

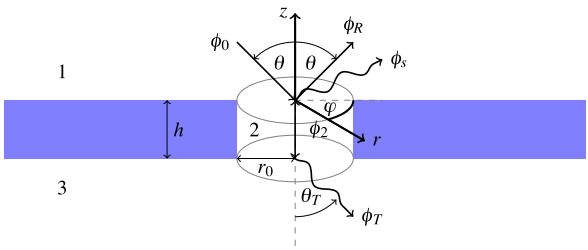

Fig. 4.2 Schematic of the elements used to study sound transmission through a circular hole of radius r_0 in a rigid plate of thickness h. As the sound field does not penetrate into the solid, the same fluid is used in the three regions $j = 1, 2, 3$. Cylindrical coordinates (r, φ, z) are used

developments [62, 69] have dealt with diffuse-field incidence and compared different methods both theoretically and experimentally. Some of the authors of this chapter have contributed to this field by presenting a diacritical study comparing the behavior of light, electrons, and sound when transmitted through an individual hole or a hole array drilled in membranes of arbitrary thickness [24] using a unified framework presented elsewhere [23].

Here the modal expansion method described in [35] will be used to show the transmission properties through a circular aperture. A comparison between the flat piston approximation of [75] and the modal expansion method will also be given.

Following the method described in [35], the geometry of the problem is depicted in Fig. 4.2, where cylindrical coordinates are used to take advantage of the hole symmetry. For simplicity, harmonic time excitation is assumed through this report, and thus a time dependence $\exp(-\mathrm{i}\omega t)$ is understood in what follows, although it is not explicitly shown. The incident sound pressure ϕ_0 and the specularly reflected sound pressure ϕ_R are plane waves, whereas the backscattered (ϕ_s) and the transmitted (ϕ_T) sound pressures are described using plane wave expansions. Under the rigid-solid approximation, there is no field inside the solid, whereas the field inside the hole ϕ_2 consists of circular eigenmodes in the polar plane together with backward and forward components in the z direction. Thus, the pressure field in the three regions can be written as follows:

$$\phi_1 = \left(\exp(\mathrm{i}q_0 z) + \exp(-\mathrm{i}q_0 z)\right) \sum_{m=-\infty}^{\infty} i^m J_m(Q_0 r)\mathrm{e}^{\mathrm{i}m\varphi} + \sum_{m=-\infty}^{\infty} \mathrm{e}^{\mathrm{i}m\varphi} \int_0^{\infty} \beta_{Qm}^{+} J_m(Qr)\mathrm{e}^{\mathrm{i}qz}\, Q\, \mathrm{d}Q, \tag{4.1}$$

$$\phi_2 = \sum_{m=-\infty}^{\infty} \sum_{n=1}^{\infty} J_m(Q_{mn} r)\mathrm{e}^{\mathrm{i}m\varphi} \Psi_{mn}^{+}(z), \tag{4.2}$$

$$\phi_3 = \phi_T = \sum_{m=-\infty}^{\infty} \mathrm{e}^{\mathrm{i}m\varphi} \int_0^{\infty} \beta_{Qm}^{-} J_m(Qr)\mathrm{e}^{-\mathrm{i}q(z+h)}\, Q\, \mathrm{d}Q, \tag{4.3}$$

with

$$\Psi_{mn}^{\pm}(z) = \left[\alpha_{mn}^{+} \exp(\mathrm{i}q_{mn}z) \pm \alpha_{mn}^{-} \exp(-\mathrm{i}q_{mn}z)\right], \tag{4.4}$$

where $Q_0 = k_0 \sin\theta$ and $q_0 = k_0 \cos\theta$ are the projections of the incident wavevector. The wavenumbers in the z direction satisfying the Helmholtz equation outside and inside the hole are $q = \sqrt{k_0^2 - Q^2}$ and $q_{mn} = \sqrt{k_0^2 - Q_{mn}^2}$, respectively. The Bessel function of the first kind and order m is denoted $J_m(x)$. Note that $\phi_1 = \phi_0 + \phi_R + \phi_s$ and the components of the incident and reflected plane waves parallel to the plate are represented using the Jacobi-Anger expansion (see [1]). At both hole openings, the field must satisfy the continuity of the pressure and the normal velocity. However, at the solid surface, the normal particle velocity is zero. Therefore, at the hole walls $J_m'(Q_{mn}r_0) = 0$. The boundary conditions at $z = 0, -h$ are given by

$$\partial_z\phi_1|_{z=0} = \partial_z\phi_2|_{z=0} \quad \text{if } r < r_0, \qquad \partial_z\phi_1|_{z=0} = 0 \quad \text{if } r > r_0, \tag{4.5}$$

$$\partial_z\phi_3|_{z=-h} = \partial_z\phi_2|_{z=-h} \quad \text{if } r < r_0, \qquad \partial_z\phi_3|_{z=-h} = 0 \quad \text{if } r > r_0, \tag{4.6}$$

$$\phi_1|_{z=0} = \phi_2|_{z=0}, \qquad \phi_3|_{z=-h} = \phi_2|_{z=-h}, \quad \text{if } r < r_0. \tag{4.7}$$

Taking advantage of the orthogonality of the Bessel functions (see [1]) by applying Hankel transforms in (4.5) and (4.6), we obtain

$$\beta_{Qm}^{+} = \sum_{n=0}^{\infty} \frac{q_{mn}}{q} \Psi_{mn}^{-}(0) I(Q_{mn}, Q), \tag{4.8}$$

$$\beta_{Qm}^{-} = -\sum_{n=0}^{\infty} \frac{q_{mn}}{q} \Psi_{mn}^{-}(-h) I(Q_{mn}, Q), \tag{4.9}$$

and then [1]

$$\begin{aligned} I(Q_{mn}, Q) &= \int_0^{r_0} J_m(Q_{mn}r) J_m(Qr) r\, dr \\ &= \begin{cases} \frac{r_0}{Q_{mn}^2 - Q^2}[Q J_m(Q_{mn}r_0) J_{m-1}(Qr_0) \\ \quad - Q_{mn} J_m(Qr_0) J_{m-1}(Q_{mn}r_0)] & \text{if } Q_{mn} \neq Q, \\ \frac{r_0^2}{2} J_m^2(Q_{mn}r_0)[1 - \frac{m^2}{(Q_{mn}r_0)^2}] & \text{if } Q_{mn} = Q. \end{cases} \end{aligned} \tag{4.10}$$

Similarly, substituting (4.8) and (4.9) into (4.7), multiplying by $J_m(Q_{mn'}r)r$, and integrating with respect to r from 0 to r_0 yields

$$2i^m I(Q_0, Q_{mn'}) + \sum_{n=0}^{\infty} \Psi_{mn}^{-}(0) \mathbf{I}_{nn'}^{m} = \sum_{n=0}^{\infty} \Psi_{mn}^{+}(0) I(Q_{mn}, Q_{mn'}), \tag{4.11}$$

$$-\sum_{n=0}^{\infty} \Psi_{mn}^{-}(-h) \mathbf{I}_{nn'}^{m} = \sum_{n=0}^{\infty} \Psi_{mn}^{+}(-h) I(Q_{mn}, Q_{mn'}), \tag{4.12}$$

where

$$\mathbf{I}^m_{nn'} = \int_0^\infty \frac{q_{mn}}{q} I(Q_{mn}, Q) I(Q_{mn'}, Q) Q \, dQ, \tag{4.13}$$

which we calculate numerically. Truncating the sums in (4.11) and (4.12) over n, n', and m up to N, N, and M, respectively, a linear system of equations of size $2(M+N) \times 2(M+N)$ is obtained with the variables $\alpha^{\pm}_{mn}$ as unknowns. More precisely,

$$\begin{bmatrix} \mathbf{A}_{11} & \mathbf{A}_{12} \\ \mathbf{A}_{21} & \mathbf{A}_{22} \end{bmatrix} \begin{bmatrix} \alpha^+_{mn} \\ \alpha^-_{mn} \end{bmatrix} = \begin{bmatrix} 2i^m I(Q_0, Q_{mn'}) \\ 0 \end{bmatrix}, \tag{4.14}$$

where

$$\mathbf{A}_{11} = I(Q_{mn}, Q_{mn'}) - \mathbf{I}^m_{nn'}, \tag{4.15}$$

$$\mathbf{A}_{12} = I(Q_{mn}, Q_{mn'}) + \mathbf{I}^m_{nn'}, \tag{4.16}$$

$$\mathbf{A}_{21} = \left[I(Q_{mn}, Q_{mn'}) + \mathbf{I}^m_{nn'} \right] \exp(-\mathrm{i} q_{mn} h), \tag{4.17}$$

$$\mathbf{A}_{22} = \left[I(Q_{mn}, Q_{mn'}) - \mathbf{I}^m_{nn'} \right] \exp(\mathrm{i} q_{mn} h). \tag{4.18}$$

However, we still have to calculate β^-_{Qm} from (4.9) and evaluate the integral in (4.3). In order to get the far-field and overcome the complexity of this integral, the stationary-phase approximation [74] is used. The final expression after applying this approximation is

$$\phi_3 \approx \Phi_3 = i q_T \exp(-\mathrm{i} q_T h) \frac{\exp(-i k_0 R)}{R} \sum_m i^m \beta^-_{Q_T m} \mathrm{e}^{\mathrm{i} m \varphi}, \tag{4.19}$$

where $r = R \sin\theta_T$, $z = R \cos\theta_T$, $Q_T = k_0 \sin\theta_T$, and $q_T = k_0 \cos\theta_T$. Notice that R is the radial distance in spherical coordinates. Then, the transmitted sound power coefficient τ can be calculated as

$$\tau = \frac{\Pi_T(\omega, \theta)}{\Pi_0(\omega, \theta)}, \tag{4.20}$$

$$\Pi_0(\omega, \theta) = \frac{1}{2} \mathscr{R}e \left\{ \int_0^{2\pi} \int_0^{r_0} \phi_0 \left(\frac{i \partial_z \phi_0}{\omega \rho} \right)^*, r \, dr \, d\varphi \right\} = \frac{\pi r_0^2 \cos\theta}{2\rho c}, \tag{4.21}$$

where the asterisk denotes complex conjugation and $\mathscr{R}e$ refers to the real part. The expression (4.21) corresponds to the time-averaged intensity of the incident wave integrated through the aperture area. The radiated sound power can be calculated either following [35] as

$$\Pi_T(\omega, \theta) = \frac{1}{2} \mathscr{R}e \left\{ \int_0^{2\pi} \int_0^{r_0} \phi_2|_{z=-h} \left(\frac{i \partial_z \phi_2|_{z=-h}}{\omega \rho} \right)^* r \, dr \, d\varphi \right\}, \tag{4.22}$$

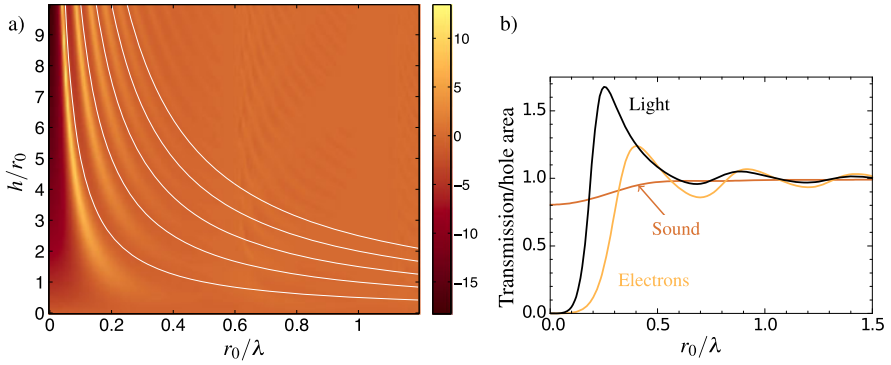

Fig. 4.3 (**a**) Transmitted sound power coefficient τ in (dB) through a circular hole as a function of r_0/λ and h/r_0 for normal incidence. The white dashed curves correspond to the $h = n\lambda/2$ Fabry-Pérot resonance condition for an open tube. (**b**) Normal-incidence transmission as a function of r_0/λ for light, electrons, and sound through a circular hole drilled in perfect conductor, infinite-potential, and rigid-solid membrane, respectively. Zero-thickness is assumed in all three cases

or using the far-field pressure Φ_3 and numerically integrating over θ_T and φ_T as

$$\Pi_T(\omega,\theta) = \frac{1}{2\rho c}\int_0^{\pi/2}\int_0^{2\pi} |\Phi_3|^2 R^2 \sin(\theta_T)\, d\varphi_T\, d\theta_T. \tag{4.23}$$

Although numerical integration is involved, the last alternative has been chosen due to its simplicity. In fact, since normal incidence selects only $m = 0$ components, the integrand in (4.23) yields $q_T^2 |\beta^-_{Q_T 0}|^2 \sin\theta_T$.

The results of this model under normal incidence are plotted in Fig. 4.3(a) for different h/r_0 proportions as a function of r_0/λ. For comparison, white dashed curves corresponding to the $h = n\lambda/2$ ($n \in \mathbb{N}$) Fabry-Pérot resonance condition for an open tube are shown. As the thickness increases, more resonances are found in the transmission spectrum. The resonances are always at larger wavelengths than those predicted by the open tube resonances. This discrepancy is usually corrected by means of an equivalent thickness or end correction [37]. When $h = 0$ the transmission converges to $8/\pi^2$ for very large wavelengths [6] (see point $(0, 0.8)$ in Fig. 4.3). Figure 4.3(b) summarizes the comparison between sound, electrons, and light when transmitted through a single hole as reported in [24]. In contrast to electron and electromagnetic waves, sound scattered by the hole shows a monopolar behavior (4.19) instead of dipolar response. Another difference between sound, electrons, and light is the existence of a cutoff-free mode in the acoustical case, where the whole fluid inside the hole moves in phase like an acoustic mass. Both fluid half-spaces are always connected through the hole and the limiting factor for the transmission of sound from one side to the other in the long-wavelength regime is the radiation efficiency of the aperture. This is clearly shown in Fig. 4.3(b) for a zero thickness screen. While almost all the sound is transmitted over the area of the hole, even at large wavelengths, light and electrons undergo a strong cutoff in their transmission spectra. Figure 4.4 shows a comparison between the approximation of Wilson and

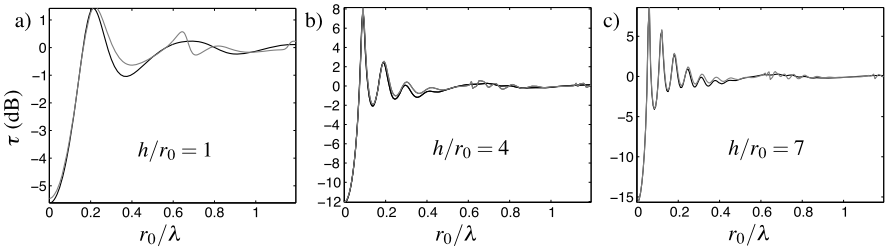

Fig. 4.4 Comparison between the approximation of Wilson and Soroka [75] (*black*) and the model described here (*gray*) for three different values of h/r_0

Soroka [75] and the model derived here for normal incidence. For the three different h/r_0 ratios under consideration, the agreement is excellent when $r_0/\lambda < 0.5$ and the differences for $r_0/\lambda > 0.5$ can be explained as originating in the lack of higher-order circular modes in the approximation that assumes planar piston behavior at the hole openings. Therefore, the modal model method has been chosen because it provides an exact solution for a larger range of frequencies, in contrast to the planar-piston approximation.

4.3 Theory of Periodically Perforated Plates

In this section, we describe a theoretical model that we have developed to understand the experimental results. First, some notation and geometrical facts regarding two-dimensional arrays are briefly given. Afterwards, the rigid-solid theory is derived.

4.3.1 Geometry

The geometry is of holes drilled periodically in a plate to form two-dimensional structures. To characterize two-dimensional periodic structures we borrow some ideas and nomenclature from solid-state physics [2, 38], which deals with ordered structures at atomic scales, because some geometrical results obtained at that tiny scale are also useful for this study. The key parameters to describe the arrays of holes are the radius of the hole r_0 and the distance a between them, as shown in Fig. 4.5. Also in order to characterize the plate we need the thickness h.

A more global parameter that involves not only the hole size but also the array period is the filling fraction of holes f, which is defined as the ratio between the hole area and the unit cell area. Then, the filling fraction of holes in the square lattice is $f_\square = \pi r_0^2/a^2$, whereas in the case of the triangular lattice it becomes $f_\triangle = 2\pi r_0^2/\sqrt{3}a^2$. Figure 4.6 shows the filling fraction of holes for both lattices depending on the geometrical proportions $2r_0/a = d/a$ and h/a of the perforated

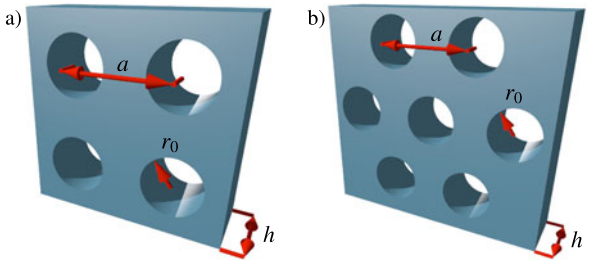

Fig. 4.5 Diagram of the geometrical parameters of the PPP where r_0 is the hole radius, a is the array period, and h is the plate thickness for (**a**) square and (**b**) triangular lattices

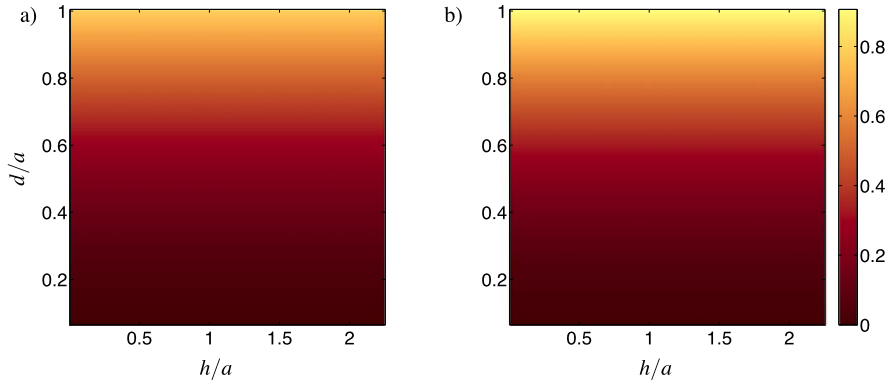

Fig. 4.6 Parameter spaces of the PPP for (**a**) square and (**b**) triangular lattices. $d = 2r_0$ is the hole diameter, a is the array period, and h is the plate thickness. The *color scale* corresponds to the filling fraction of the holes (Color figure online)

plate. This geometrical parameter space is very useful in the study of the transmission characteristics of the plate, as it helps to retain a global picture of the phenomena. The main difference between both parameter spaces is the fact that $f_{\triangle}\max > f_{\square}\max$, as can be clearly seen in Fig. 4.6 comparing both colors at $d/a = 1$.

The position of every hole can be written as $\mathbf{r_n} = n_1\mathbf{a}_1 + n_2\mathbf{a}_2$, where $\mathbf{a}_i$ are the so-called primitive cell vectors and n_i are integers. For the square lattice we have

$$\mathbf{a}_1 = a\hat{\mathbf{x}}, \qquad \mathbf{a}_2 = a\hat{\mathbf{y}}, \tag{4.24}$$

whereas for the triangular lattice one can take

$$\mathbf{a}_1 = \frac{a}{2}\left(\hat{\mathbf{x}} + \sqrt{3}\hat{\mathbf{y}}\right), \qquad \mathbf{a}_2 = \frac{a}{2}\left(\hat{\mathbf{x}} - \sqrt{3}\hat{\mathbf{y}}\right). \tag{4.25}$$

The area S of the unit cell is $S = a^2$ for the square lattice and $S = \sqrt{3}a^2/4$ for the triangular lattice. The entire array can be seen as infinite series of periodically distributed Dirac-delta functions

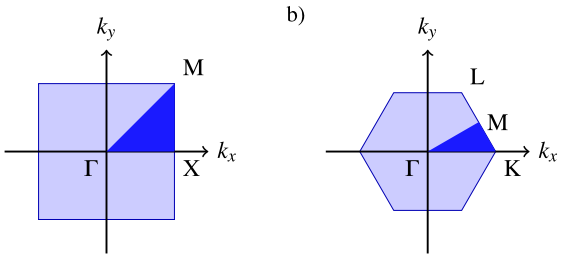

Fig. 4.7 Diagram of the first Brillouin zone in reciprocal space for (**a**) square and (**b**) triangular lattices. The irreducible Brillouin zone is depicted in dark

$$\Delta(\mathbf{r_n}) = \sum_{\mathbf{n}=-\infty}^{\infty} \delta(\mathbf{r} - \mathbf{r_n}), \tag{4.26}$$

whose Fourier transform

$$\mathscr{F}_x \mathscr{F}_y \{\Delta(\mathbf{r_n})\} = \frac{4\pi^2}{S} \sum_{\mathbf{m}=-\infty}^{\infty} \delta(\mathbf{k} - \mathbf{G}), \tag{4.27}$$

is also an infinite set of periodically distributed delta functions, but in the reciprocal space instead of real space (note that $\mathscr{F}_x\{\}$ and $\mathscr{F}_y\{\}$ denotes the Fourier transform along x and y directions, respectively). This gives rise to the reciprocal lattice, where

$$\mathbf{G} = m_1 \mathbf{b}_1 + m_2 \mathbf{b}_2 \tag{4.28}$$

denotes the reciprocal lattice vector, $\mathbf{b}_i$ are the primitive vectors of the reciprocal lattice, and the integers m_i are called Miller indices. For the square array, we have

$$\mathbf{b}_1 = \frac{2\pi}{a}\hat{\mathbf{x}}, \qquad \mathbf{b}_2 = \frac{2\pi}{a}\hat{\mathbf{y}}, \tag{4.29}$$

and for the triangular array

$$\mathbf{b}_1 = \frac{2\pi}{a}\left(\hat{\mathbf{x}} + \frac{\hat{\mathbf{y}}}{\sqrt{3}}\right), \qquad \mathbf{b}_2 = \frac{2\pi}{a}\left(\hat{\mathbf{x}} - \frac{\hat{\mathbf{y}}}{\sqrt{3}}\right). \tag{4.30}$$

Due to this periodicity in reciprocal space, some physical quantities become redundant if they are studied along a large area. To avoid this redundancy, the analysis is performed inside the first Brillouin zone [9], which is depicted in Fig. 4.7(a) for the square lattice and in Fig. 4.7(b) for the triangular lattice. Moreover, as the Brillouin zone is symmetric, one can restrict further the region of study to the irreducible Brillouin zone, showed in dark in Fig. 4.7.

4.3.2 Rigid-Solid Theory

In a way similar to the single hole, sound transmission through periodically arranged holes can be studied using the rigid-solid approximation, taking advantage

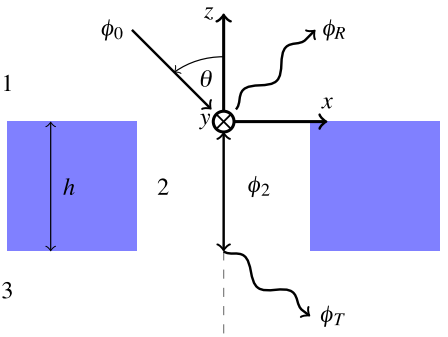

Fig. 4.8 Diagram of the unit-cell cross-section of the periodically perforated plate. Due to the circular symmetry of the holes, we use polar coordinates (r, φ) together with Cartesian coordinates. The dimensions of the holes and the plate are depicted in Fig. 4.5. The sound field is divided into three fluid regions $j = 1, 2, 3$

of periodicity. The problem also started with Rayleigh's work, who in the second, 1896 edition of his book "The Theory of Sound" [58] deals with the problem of a plane wave scattering on a periodic surface using a rigorous approach then called Rayleigh's hypothesis. Later [57] he extended his study to electromagnetic waves, trying to explain the Wood anomaly [76]. In words of Wood [77]:

> Lord Rayleigh showed that, in the case of sound waves passing, at normal incidence, through very narrow parallel slits, the passage of energy through any slit might be prevented by the cooperative action of the other slits, under the condition that the distance between the slits was an integral multiple of the wave-length.

Nearly a century later, this result was also found by Norris and Luo [51], dealing with a two-dimensional semi-infinite perforated rigid solid. The same method used by Norris and Luo was further extended to the case of a two-dimensional periodically perforated slab by Zhou and Kriegsman [81]. They found complete transmission through narrow holes using only the cutoff-free mode inside the hole. Very recently, several groups have also found similar full transmission peaks in PPP [11, 30, 46]. To calculate sound transmission we use Rayleigh's hypothesis, whose validity for gratings remained under discussion until recently [73] for the electromagnetic case, extending Takakura's model [66] for light in a slit array as described in [20].

A diagram with the description of the geometry is shown in Fig. 4.8. An incident plane wave of pressure ϕ_0 impinges in the perforated plate. The reflected pressure field ϕ_R is plane wave expanded, as well as the transmitted sound pressure ϕ_T. The pressure field inside the cavity is described by guided waves in the same manner as the single-hole case (4.2). Separating the entire space in three regions, we can write the pressure field as

$$\phi_1 = \exp\big(\mathrm{i}(\mathbf{Q}_0\mathbf{r}_\parallel - q_0 z)\big) + \iint_{-\infty}^{\infty} \beta^+(\mathbf{Q}) \mathrm{e}^{i(\mathbf{Q}\mathbf{r}_\parallel + qz)}\, d^2\mathbf{Q}, \tag{4.31a}$$

$$\phi_2 = \sum_{m=-\infty}^{\infty} \sum_{n=1}^{\infty} J_m(Q_{mn} r) \mathrm{e}^{\mathrm{i}m\varphi} \Psi_{mn}^+(z), \tag{4.31b}$$

$$\phi_3 = \iint_{-\infty}^{\infty} \beta^-(\mathbf{Q}) \mathrm{e}^{i(\mathbf{Q}\mathbf{r}_\parallel - q(z+h))}\, d^2\mathbf{Q}, \tag{4.31c}$$

with

$$\Psi_{mn}^{\pm}(z) = \left[\alpha_{mn}^{+} \exp\left(\mathrm{i}q_{mn}(z+h)\right) \pm \alpha_{mn}^{-} \exp(-\mathrm{i}q_{mn}z)\right], \tag{4.32}$$

where $\mathbf{k}_0 = (\mathbf{Q}_0, q_0)$ is the incident wave vector, $\mathbf{r}_\parallel = (x, y) = (r, \varphi)$, and $q = \sqrt{\mathbf{k}_0^2 - \mathbf{Q}^2}$ and $q_{mn} = \sqrt{\mathbf{k}_0^2 - Q_{mn}^2}$ are the wavenumbers in the z direction satisfying the Helmholtz equation outside and inside the hole, respectively. Also, $\beta^{+}(\mathbf{Q})$, $\beta^{-}(\mathbf{Q})$ correspond to the coupling coefficients between the holes and the semi-infinite space. As the sound does not penetrate into the solid, the polar eigenfunctions inside the hole must satisfy $J_m'(Q_{mn}r_0) = 0$, which is equivalent to assuming zero normal velocity at the hole walls. From the plane wave expansion, we can relate the coefficients $\beta^{\pm}(\mathbf{Q})$ to the particle velocity at both sides of the plate. As the particle velocity is periodic along the plate directions, and based on the Rayleigh hypothesis, one can perform Fourier series expansion on either side of the film thus yielding

$$\beta^{+}(\mathbf{Q}) = \delta(\mathbf{Q} - \mathbf{Q}_0) + \sum_{\mathbf{G}} \beta_{\mathbf{G}}^{+} \delta(\mathbf{Q} - \mathbf{Q}_{\mathbf{G}}), \tag{4.33}$$

$$\beta^{-}(\mathbf{Q}) = \sum_{\mathbf{G}} \beta_{\mathbf{G}}^{-} \delta(\mathbf{Q} - \mathbf{Q}_{\mathbf{G}}), \tag{4.34}$$

where $\mathbf{Q}_{\mathbf{G}} = \mathbf{Q}_0 + \mathbf{G}$, and $\mathbf{G}$ is the reciprocal lattice vector defined in (4.28). Thus, (4.31a) and (4.31c) can be rewritten as

$$\phi_1 = 2\exp(\mathrm{i}\mathbf{Q}_0\mathbf{r}_\parallel)\cos(q_0 z) + \sum_{\mathbf{G}} \beta_{\mathbf{G}}^{+} \exp\left(i\left(\mathbf{Q}_{\mathbf{G}}\mathbf{r}_\parallel + q_{\mathbf{G}}z\right)\right), \tag{4.35}$$

$$\phi_3 = \sum_{\mathbf{G}} \beta_{\mathbf{G}}^{-} \exp\left(i\left(\mathbf{Q}_{\mathbf{G}}\mathbf{r}_\parallel - q_{\mathbf{G}}(z+h)\right)\right). \tag{4.36}$$

Imposing the continuity of the particle velocity at both hole openings, multiplying by $\exp(-\mathrm{i}\mathbf{Q}_{\mathbf{G}'}\mathbf{r}_\parallel)$, and integrating along a unit cell it yields

$$\beta_{\mathbf{G}}^{+} = \frac{1}{S} \sum_{mn} \frac{q_{mn}}{q_{\mathbf{G}}} \Psi_{mn}^{-}(0) I_n^m(\mathbf{Q}_{\mathbf{G}}), \tag{4.37}$$

$$\beta_{\mathbf{G}}^{-} = -\frac{1}{S} \sum_{mn} \frac{q_{mn}}{q_{\mathbf{G}}} \Psi_{mn}^{-}(-h) I_n^m(\mathbf{Q}_{\mathbf{G}}), \tag{4.38}$$

where S is the unit-cell area and the term $I_n^m(\mathbf{Q}_{\mathbf{G}})$ denotes the following integral:

$$I_n^m(\mathbf{Q}_{\mathbf{G}}) = \int_0^{2\pi} \int_0^{r_0} J_m(Q_{mn}r) \mathrm{e}^{\mathrm{i}m\varphi} \exp(-\mathrm{i}\mathbf{Q}_{\mathbf{G}}\mathbf{r}_\parallel) r \, dr \, d\varphi$$

$$= 2\pi i^m \exp(\mathrm{i}m\varphi_{\mathbf{G}}) \begin{cases} \frac{|\mathbf{Q}_{\mathbf{G}}|r_0}{|\mathbf{Q}_{\mathbf{G}}|^2 - Q_{mn}^2} J_m(Q_{mn}r_0) J_m'(|\mathbf{Q}_{\mathbf{G}}|r_0) \\ \quad \text{if } Q_{mn} \neq |\mathbf{Q}_{\mathbf{G}}|, \\ \frac{r_0^2}{2} J_m^2(Q_{mn}r_0)[1 - \frac{m^2}{(Q_{mn}r_0)^2}] \\ \quad \text{if } Q_{mn} = |\mathbf{Q}_{\mathbf{G}}|. \end{cases} \tag{4.39}$$

Here, $\varphi_{\mathbf{G}} = \arcsin(\mathbf{Q}_{\mathbf{G}y}/\mathbf{Q}_{\mathbf{G}x})$. The continuity of the sound pressure at the hole openings requires

$$2\exp(\mathrm{i}\mathbf{Q}_0\mathbf{r}_\parallel) + \sum_{\mathbf{G}} \beta_{\mathbf{G}}^+ \exp(\mathrm{i}\mathbf{Q}_{\mathbf{G}}\mathbf{r}_\parallel) = \sum_{mn} J_m(Q_{mn}r)\mathrm{e}^{\mathrm{i}m\varphi} \Psi_{mn}^+(0), \tag{4.40}$$

$$\sum_{\mathbf{G}} \beta_{\mathbf{G}}^- \exp(\mathrm{i}\mathbf{Q}_{\mathbf{G}}\mathbf{r}_\parallel) = \sum_{mn} J_m(Q_{mn}r)\mathrm{e}^{\mathrm{i}m\varphi} \Psi_{mn}^+(-h). \tag{4.41}$$

Substituting (4.37) and (4.38) into (4.40) and (4.41), respectively, multiplying by $rJ_m(Q_{mn'}r)\exp(-\mathrm{i}m'\varphi)$, and integrating over the hole area yields

$$\delta_{mm'}\Psi_{mn}^+(0) I(Q_{mn}, Q_{mn'}) = \frac{1}{S}\sum_{mn} q_{mn}\Psi_{mn}^-(0) \sum_{\mathbf{G}} \frac{I_n^m(\mathbf{Q}_{\mathbf{G}})(I_{n'}^{m'}(\mathbf{Q}_{\mathbf{G}}))^*}{q_{\mathbf{G}}} + 2\big(I_{n'}^{m'}(\mathbf{Q}_0)\big)^*, \tag{4.42}$$

$$\delta_{mm'}\Psi_{mn}^+(-h) I(Q_{mn}, Q_{mn'}) = -\frac{1}{S}\sum_{mn} q_{mn}\Psi_{mn}^-(-h) \sum_{\mathbf{G}} \frac{I_n^m(\mathbf{Q}_{\mathbf{G}})(I_{n'}^{m'}(\mathbf{Q}_{\mathbf{G}}))^*}{q_{\mathbf{G}}}, \tag{4.43}$$

where $\delta_{mm'}$ denotes the Kronecker delta. A set of linear equations involving only $\alpha_{mn}^{\pm}$ is then obtained. We truncate the sums to include only a finite number of hole modes and reciprocal lattice vectors. In matrix form, (4.42) and (4.43) can be written

$$\begin{bmatrix} \mathbf{D}_{11} & \mathbf{D}_{12} \\ \mathbf{D}_{21} & \mathbf{D}_{22} \end{bmatrix} \begin{bmatrix} \alpha_{mn}^+ \\ \alpha_{mn}^- \end{bmatrix} = \begin{bmatrix} 2(I_{n'}^{m'}(\mathbf{Q}_0))^* \\ 0 \end{bmatrix}, \tag{4.44}$$

where

$$\mathbf{D}_{11} = \left[\delta_{mm'} I(Q_{mn}, Q_{mn'}) - \frac{1}{S} q_{mn} \mathbf{M}_{nn'}^{mm'}(\mathbf{Q}_{\mathbf{G}})\right] \mathrm{e}^{\mathrm{i}q_{mn}h}, \tag{4.45}$$

$$\mathbf{D}_{12} = \delta_{mm'} I(Q_{mn}, Q_{mn'}) + \frac{1}{S} q_{mn} \mathbf{M}_{nn'}^{mm'}(\mathbf{Q}_{\mathbf{G}}), \tag{4.46}$$

$$\mathbf{D}_{21} = \delta_{mm'} I(Q_{mn}, Q_{mn'}) + \frac{1}{S} q_{mn} \mathbf{M}_{nn'}^{mm'}(\mathbf{Q}_{\mathbf{G}}), \tag{4.47}$$

$$\mathbf{D}_{22} = \left[\delta_{mm'} I(Q_{mn}, Q_{mn'}) - \frac{1}{S} q_{mn} \mathbf{M}_{nn'}^{mm'}(\mathbf{Q}_{\mathbf{G}})\right] \mathrm{e}^{\mathrm{i}q_{mn}h}, \tag{4.48}$$

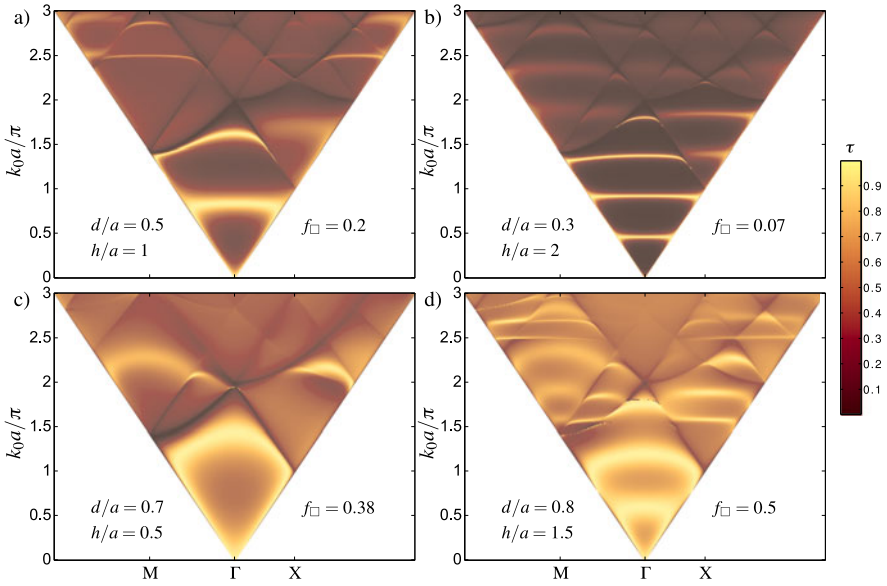

Fig. 4.9 Transmitted sound power coefficient τ (*color scale*) through plates with a square array of holes as a function of the normalized frequency k_0a/π and the wavevector $\mathbf{Q}_0$ along the MΓX directions of the irreducible Brillouin zone (see Fig. 4.7). Four different cases are showed with their geometrical parameters indicated in the lower parts of the plots (Color figure online)

and

$$\mathbf{M}_{nn'}^{mm'}(\mathbf{Q_G}) = \sum_{\mathbf{G}} \frac{I_n^m(\mathbf{Q_G})(I_{n'}^{m'}(\mathbf{Q_G}))^*}{q_{\mathbf{G}}}. \tag{4.49}$$

We have thus calculated the coefficients $\alpha_{mn}^{\pm}$, whereas the coefficients $\beta_{\mathbf{G}}^{\pm}$ can be easily obtained by substituting back in (4.37) and (4.38).

As the perforated plate is assumed to have an infinite extension in the $\mathbf{r}_\parallel$ plane, the radiated sound power [74] is given by

$$\Pi(\omega) = \frac{\rho c k_0}{8\pi^2}\mathscr{R}e\left\{\iint_{-\infty}^{\infty} \frac{|V(\mathbf{Q})|^2}{\sqrt{k_0^2 - \mathbf{Q}^2}}\, d^2\mathbf{Q}\right\}, \quad V(\mathbf{Q}) = \mathscr{F}_x\mathscr{F}_y\left\{\frac{i\partial_z\phi}{\omega\rho}\bigg|_{z=0,-h}\right\}, \tag{4.50}$$

which when applied to the incident and radiated sound power yields

$$\tau = \frac{\Pi_T(\omega)}{\Pi_0(\omega,\theta,\varphi)} = \sum_{\mathbf{G}} \mathscr{R}e\left\{\frac{q_{\mathbf{G}}}{q_0}\right\}\left|\beta_{\mathbf{G}}^{-}\right|^2. \tag{4.51}$$

To gain further insight into these phenomena, we calculate sound transmission for a square array of holes under angle-dependent incidence. Convergence is achieved for ∼20 hole modes in the cases explored throughout this report. Figure 4.9 shows

results of four different plates, whose geometrical parameters are shown in the lower side corners of the panels. The transmission τ is represented in linear color scale as a function of the normalized frequency $k_0 a/\pi$ and the parallel-to-the-plate wavevector $\mathbf{Q}_0$ along the MΓ and ΓX symmetry directions of the irreducible Brillouin zone. The effect of $f_\square$ is reflected in the transmission dispersion. We conclude that the smaller the filling fraction, the narrower the peaks. It is remarkable that all spectra share the same position of the minima, because they correspond to similar Wood anomalies. The number of transmission peaks depends on the plate thickness, but also on the periodicity, due to their interaction via the periodic lattice. It is interesting to note the existence of full transmission peaks that are independent of the angle of incidence, presumably originating in single-hole Fabry-Pérot resonances. This can be seen in Figs. 4.9(a), (b), and (d). A more detailed analysis is given in Sec. 4.5, where these results are compared to the experimental measurements.

4.4 Experimental Setup

In order to measure the transmission through a perforated plate, the ultrasonic range has been chosen due to two major advantages:

- As the plate is immersed in water, plate samples having the size of an A4 paper sheet can be used at ultrasonic frequencies.
- The acoustic impedance $Z_{water} = \rho c$ of the water is relatively high. Therefore, it is possible to vary the impedance contrast between the plate and the water using common solid materials.

The experimental setup is based on the well-known ultrasonic immersion transmission technique (Fig. 4.10). This technique utilizes a couple of transmitter/receiver ultrasonic transducers, which in our case are centered at 250 kHz (Imasonic immersion transducers with 32 mm in active diameter), with a frequency range between 155 and 350 kHz. A pulser/receiver generator (Panametrics model 5077PR) produces a pulse that is applied to the emitter transducer and launches the signal through the inspected plate. Then, the signal is detected by the receiving transducer, acquired by the pulser/receiver, post amplified, and digitized by a digital PC oscilloscope (Picoscope model 3224). Time-domain data are finally analyzed after averaging 100 different measures and deleting unwanted reflections by means of a time window. The transmission spectrum is then calculated as $T(\omega)|^2 = |H(\omega)|^2/|H_0(\omega)|^2$ from the power spectrum of the signal $H(\omega)$ normalized to the reference signal power spectrum $H_0(\omega)$, measured without the sample plate.

The measurements were made using aluminum plates of 200 mm in width and 350 mm in length ($\rho = 2700$ kg/m^3, $c_l = 6500$ m/s, $c_t = 3130$ m/s) immersed in water ($\rho = 1000$ kg/m^3, $c_l = 1480$ m/s). Also brass ($\rho = 8560$ kg/m^3, $c_l = 4280$ m/s, $c_t = 2030$ m/s) and PMMA ($\rho = 1190$ kg/m^3, $c_l = 2700$ m/s, $c_t = 1330$ m/s) plates were measured. Each transducer was located at a distance from the plate larger than that of its near-field extension (43 mm) and aligned with respect to the plate.

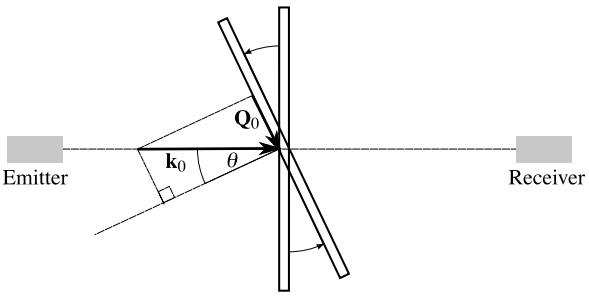

Fig. 4.10 Diagram of the experimental setup. This setup allows us to explore the transmission coefficient at different angles of incidence. $\mathbf{Q}_0$ corresponds to the component, that is parallel to the plate, of the incident wavevector $\mathbf{k}_0$

Measurements using Synthetic Aperture Technique (SAT) [33] were made to avoid finite size effects. In this technique, several measurements were performed for different receiver positions. The post-processing of the data is such that the results obtained are equivalent to those measured with a transducer array. Only small differences were observed between SAT and single point measurements for the geometrical parameters of the plates under study and the size of the transducers.

4.5 Results

In this section, experimental results obtained by means of the technique described above are presented and discussed in light of our theoretical models. From the results we derive conclusions concerning fundamentals of applied acoustics like the well known mass-law. When no holes are drilled, the sound transmission for normal incidence can be approximated using the mass-law [14] given by

$$\tau \approx \left(\frac{2\rho c}{m''\omega} \right)^2, \tag{4.52}$$

where $m'' = \rho_s h$ is the mass per unit area of the plate. This law states that heavier walls shield sound better than lighter ones. Thus, an increase in plate mass produces a decrease in sound transmission. However, in contrast to both common intuition and the mass law, PPP can transmit less sound than homogeneous plates. Figure 4.11(a) shows the transmission spectra under normal incidence of several perforated plates with different thicknesses h and periods a. Perforated plates can shield sound much better than non-perforated ones when $\lambda \approx a$. For wavelengths larger than the period, hole resonances show up, leading to high-transmission values. The transmission dip appears at similar wavelengths for both plates with $a = 5$ mm, while the plate with $a = 6$ mm shows the dip at larger wavelengths.

A crucial role of the impedance mismatch can be observed in Fig. 4.11(b). The transmission spectra of PPP made of different materials, but having the same square lattice, are compared with the rigid solid theory for normal incidence. The impedance ratio relative to water is 25 for brass, 11.8 for Al, and 2.1 for PMMA. The transmission curve for brass follows quite closely the prediction of the rigid-solid

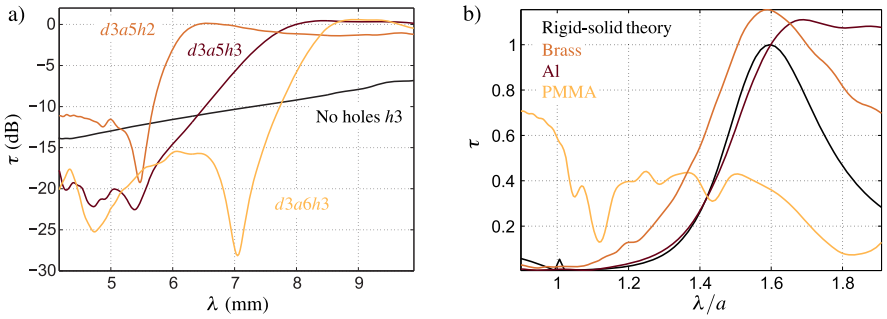

Fig. 4.11 (**a**) Measured transmission spectra of PPP immersed in water at normal incidence for Al plates with different geometrical parameters, as indicated by labels (in millimeters). (**b**) Comparison between measurements and rigid solid theory. The perforated plates are made of different materials (brass, Al, and PMMA), but they share the same geometrical parameters, namely $d = 3$ mm, $a = 5$ mm, and $h = 3$ mm. Reprinted with permission from [17]. Copyright 2008 by the American Physical Society

theory. In the case of Al, it also agrees rather well with the theory, except at long wavelengths, where the transmission is still large above the resonance compared with the theory and the case of brass. This step-like behavior found for perforated Al plates can be attributed to the lower impedance mismatch. A completely different picture from those of the brass and the Al plates is observed for the PMMA. The very strong coupling of the PMMA plate and the water result in a larger amount of energy passing through the bulk plate. Moreover, 60 % transmission is obtained instead of the Wood anomaly dip when $\lambda \approx a$.

An extended comparison between the rigid-solid theory and the measurements is shown in Figs. 4.12(a)–(f) for different plate proportions and lattices. Good agreement can be observed between measurements for Al plates and the rigid-solid theory. The main differences can be explained by the finite impedance mismatch between Al and water, in particular the high transmission values above the resonance in Figs. 4.12(a), (b), (d), and (e), which is not predicted by the theory as mentioned above. Transmission values slightly above unity in the resonances can be attributed to finite-size effects of both transducers and perforated plates. The Wood anomaly minima are placed in at positions that depend on the lattice geometry. In contrast to the $\lambda/a = 1$ position for the square lattice, we find $\lambda/a = \sqrt{3}/2 \approx 0.87$ for the triangular lattice. When increasing the plate thickness h, the transmission peak shifts, in both lattices, towards larger wavelengths. Although this statement could seem to be invalid when $h = 5$ mm, this peak is actually related to the first-order Fabry Pérot resonance instead of the zero-order Fabry-Pérot resonance, which is out of the measurement range. Both zero- and first-order resonance-related peaks appear together in Fig. 4.12(e), where the very narrow peak near to the Wood anomaly can be traced back to the first-order resonance. A similar case should be observed in Fig. 4.12(b), as predicted by theory, but in this case the peak is so narrow that it cannot be resolved in the measurements. Small losses from the water and in the holes could mask the detection of these very narrow peaks.

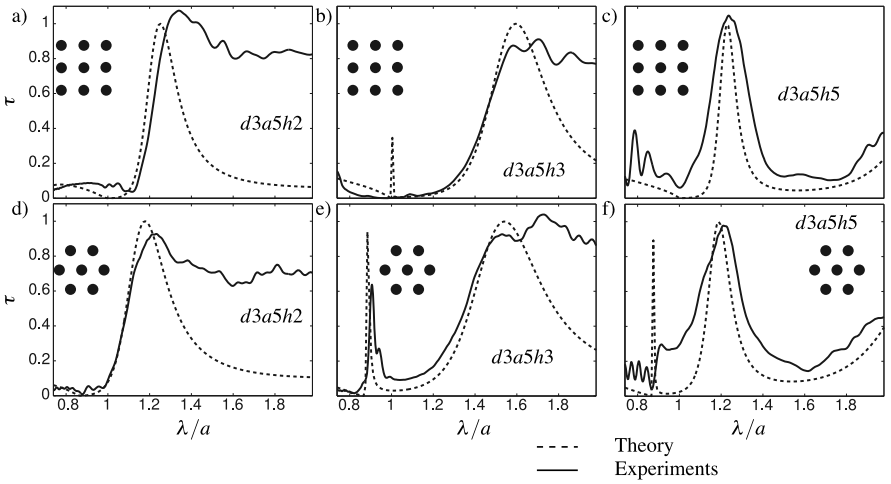

Fig. 4.12 Comparison between measured and calculated sound power transmission of PPP at normal incidence. Different plate thicknesses and lattice geometries are showed, keeping d and a constant as indicated by labels. The measurements correspond to perforated Al plates immersed in water, whereas the calculations were performed with the rigid-solid model. Reprinted with permission from [18]. Copyright 2009, American Institute of Physics

The dependence of the transmission coefficient τ on the geometrical parameters of the plate and the hole array under normal incidence was calculated using the rigid-solid model and is showed in Fig. 4.13. Each contour plot corresponds to one line in the parameter space of Fig. 4.13(a), related to four different d/h values. The filling fraction is then varied through a, keeping d/h constant. A first examination of Fig. 4.13 reveals full transmission in all cases. The number of peaks is directly related to the thickness, as they depend on the Fabry-Pérot resonances inside the hole. However the position of the peaks is highly influenced by the array periodicity. For an open tube, the Fabry-Pérot resonances appear at $\lambda/h = 2/j$ (here, j is an integer) which is very close to the condition of full transmission for high filling fractions, but the transmission peak for an individual hole is actually placed at larger wavelengths, as show by the white vertical dashed lines in Figs. 4.13(b)–(e). Thus, the resonant peak can be tuned only within the open tube resonance position and the single hole transmission resonance position. As the filling fraction decreases, the peak moves to larger wavelengths, following the $\lambda = a$ minima, and it becomes narrower. While for a single hole the transmission peak is higher for the lower order Fabry Pérot modes (see Fig. 4.4), in the periodic case each Fabry Pérot mode reaches nearly full transmission. The influence of the filling fraction of the holes [19] via variations in the periodicity reveals strong inter-hole interaction, which translates into peak narrowing when the filling fraction decreases, also accompanied by a shift in peak position towards longer wavelengths.

A more global picture is obtained when the angle of incidence is varied for two different lattices, as shows Fig. 4.14. The color scale corresponds to τ in dB as a function of both parallel wavevector within the irreducible Brillouin zone and the

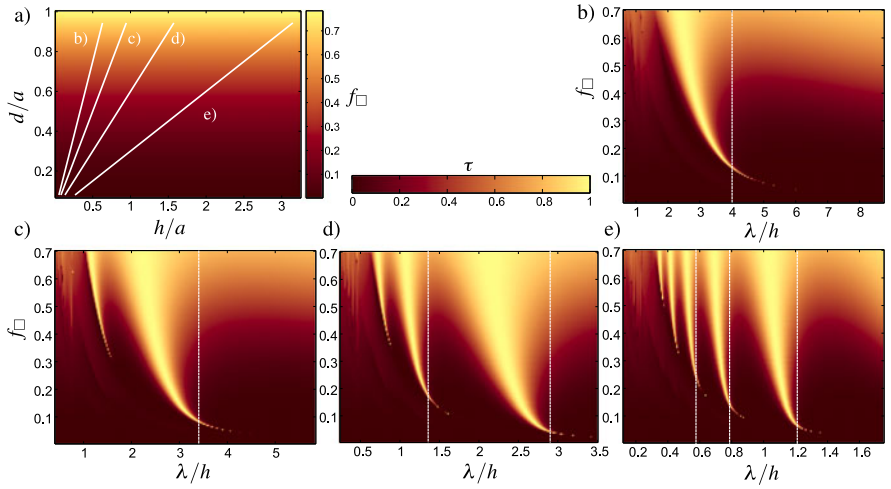

Fig. 4.13 Transmitted sound power coefficient τ through PPP as a function of λ/h and the filling fraction for a square array $f_\square$ calculated with the rigid-solid model for normal incidence. The parameter space (**a**) shows the possible proportions of the perforated plate and their corresponding $f_\square$ value (*color scale*). Each contour plot represents a line in (**a**) for (**b**) $d/h = 1.5$, (**c**) $d/h = 1$, (**d**) $d/h = 0.6$, and (**e**) $d/h = 0.3$. The *vertical white dashed lines* correspond to the position of the resonances calculated for an individual hole

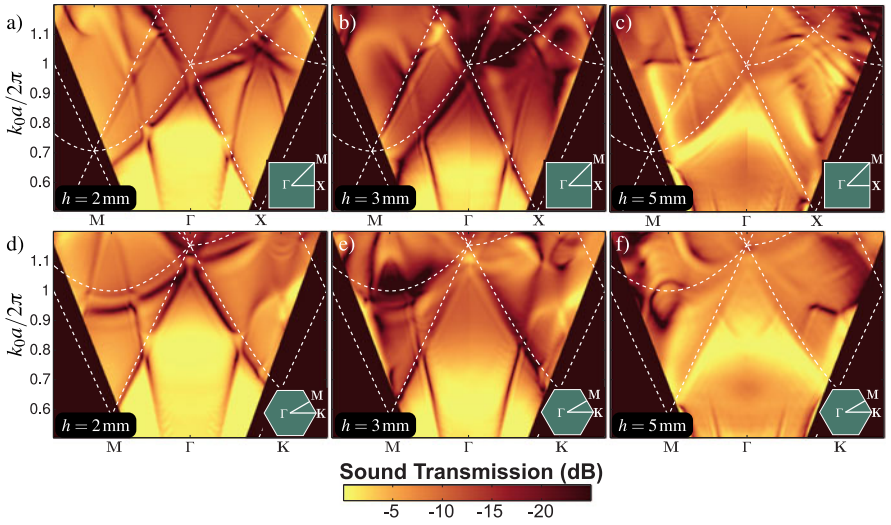

Fig. 4.14 Measured sound transmission as a function of parallel wavevector $\mathbf{Q}_0$ and the normalized incident wavenumber $k_0a/2\pi$ for periodically perforated Al plates with square (**a**)–(**c**) and triangular (**d**)–(**f**) lattice symmetry (see *insets*), and for different plate thicknesses h. The period is $a = 5$ mm and the hole diameter is $d = 3$ mm in all cases. White dashed curves correspond to Wood-anomaly minima. Reprinted with permission from [18]. Copyright 2009, American Institute of Physics

normalized incident wavenumber $k_0 a/2\pi$. Three different plate thicknesses were measured for square and triangular arrays drilled in Al plates. Complex interaction between minima and maxima is observed in the spectra and it makes clear that the symmetry of the array results in a marked angular dependence of the spectra [21]. In Figs. 4.14(a)–(f), Wood anomalies are depicted in the transmission dispersion as white dashed curves. These minima were also observed by Wood in terms of sharp reflection maxima when light impinges in a diffraction grating [76]. As predicted by Rayleigh, the minimum is produced by the coherent interference between holes. The Wood anomaly is given by the following condition:

$$k_0 = |\mathbf{Q}_0 + \mathbf{G}|, \tag{4.53}$$

that is, when a diffracted beam becomes grazing to the array plane. Therefore, it only depends on the array symmetry. Equation (4.53) can be explicitly written as

$$\frac{\omega}{c} = |\mathbf{Q}_0 + \mathbf{G}| = \sqrt{\left(Q_{0x} + \frac{2\pi}{a} m_1\right)^2 + \left(Q_{0y} + \frac{2\pi}{a} m_2\right)^2} \tag{4.54}$$

for a square array and as

$$\frac{\omega}{c} = |\mathbf{Q}_0 + \mathbf{G}| = \sqrt{\left(Q_{0x} + \frac{2\pi}{a}(m_1 + m_2)\right)^2 + \left(Q_{0y} + \frac{2\pi}{a\sqrt{3}}(m_1 - m_2)\right)^2} \tag{4.55}$$

for a triangular array. The transmission vanishes right when this condition is satisfied. Different values of the Miller indices (m_1, m_2) produce the various white dashed curves represented in the figure. Like in the optical case, these transmission minima are driven by lattice-sum singularities originating in cumulative in-phase scattering among the holes of the array. There is excellent agreement between the measured position of the minima and the prediction of (4.54) and (4.55) when the thickness of the plates is small. However, the dips emerging at the bottom part of the figures are not predicted by the Wood anomaly and can be related to surface modes, whose phase velocity can be measured. Indeed, it has been found that the geometrical anisotropy of the arrays leads to anisotropy of the modes phase-velocity [18]. This surface modes resemble leaky Lamb modes observed in the homogeneous plate (see Fig. 4.1) arising from the plate vibration and the solid-fluid coupling. Therefore, one can suspect the validity of the rigid-solid assumption for the case of Al in water medium, particularly because no trace of such surface modes is found in Fig. 4.9. A theory that takes into account the plate vibrations and the solid-fluid coupling is then needed. One option is the use of the Full Elasto Acoustic Theory (FEAT), which involves the following steps:

1. The displacement field $\mathbf{u}$, the plate density ρ, and the Lamé coefficients λ, μ, are Fourier-expanded along directions parallel to the periodic plate.
2. The eigenstates of a 2D crystal formed by infinitely-long holes with the same periodicity as the plate are obtained when solving the inhomogeneous elastic wave equation (see [8, p. 12]) leading to a quadratic eigenvalue problem.

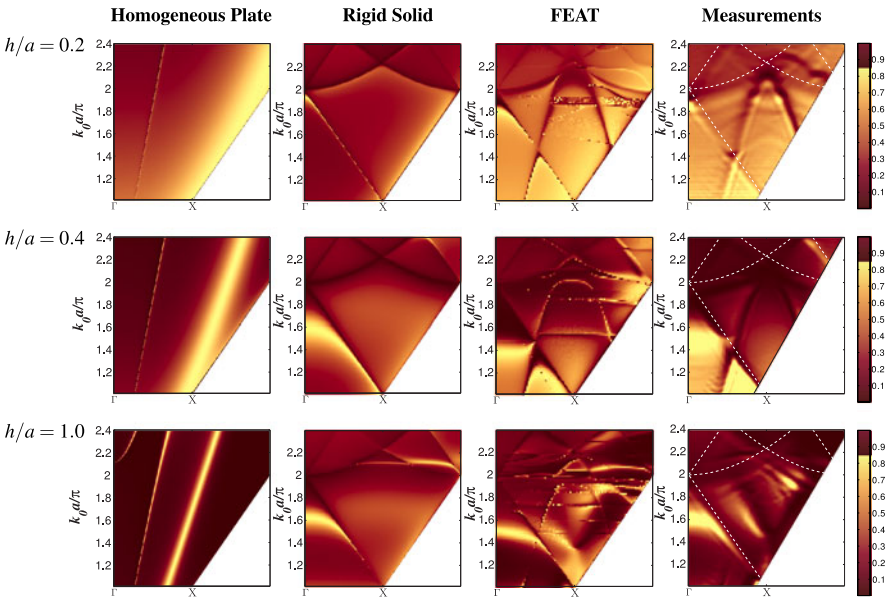

Fig. 4.15 Comparison of the transmitted sound power coefficient τ between the different theoretical models and the measurements for square arrays ($f_{\square} = 0.28$) in the ΓX direction. Empty-lattice conditions are depicted as white dashed curves in the measurements column. Reprinted with permission from [21]. Copyright 2009 by the American Physical Society

3. Rayleigh expansions are used for the displacement in the water outside the plate, whereas the displacement field inside the plate is expanded in terms of its eigenstates calculated previously from the inhomogeneous elastic wave equation.
4. The continuity of the displacement and the stress in the plate boundaries leads to a set of linear equations that are solved to yield the coefficients of these expansions. This method of solution gives a rigorous expansion for finite plates, in which the thickness enters through the boundary conditions matching the internal 2D modes to the Rayleigh expansions outside the film.

Comparing the results of the three theories, namely the homogeneous plate, the rigid-solid, and the FEAT, with the experimental results we obtain Fig. 4.15. The sound power transmission coefficient τ is depicted in color scale as a function of the parallel wavevector along the ΓX direction and the normalized incident wavenumber $k_0 a/\pi$. Plates having three different h/a ratios but sharing the same filling fraction ($f_{\square} = 0.28$) are shown. In the homogeneous-plate calculations, the normalization by the lattice period a in both axes is only used to have the same scale as the other contour plots. The first column shows the transmission dispersion for the homogeneous plate, dominated by the cutoff-free symmetric and antisymmetric leaky Lamb modes, the latter mixed with the Scholte-Stoneley mode for $h/a = 0.2, 0.4$ near the $\omega = ck_{\parallel}$ line (c is the sound phase velocity in water). Each of this three images represents a magnified version of the complete behavior for Al plates im-

mersed in water given in Fig. 4.1, which is valid for plates of any thickness. Higher-order modes enter our frequency range when the plate thickness in increased (see $h/a = 1.0$). The second column contains the sound transmission dispersion calculations of PPP under the rigid solid assumption. Full transmission peaks arising from the hole resonances and hybridized with the empty-lattice dips are observed. The peak is quite narrow when $h/a = 0.2$ and it is placed immediately below the Wood anomaly. The transmission peak is then moved to lower frequencies by increasing the h/a ratio and higher order Fabry-Pérot resonances enter into the frequency range. The third column shows the calculations obtained with the FEAT, which includes the hole resonances, coherent scattering due to the hole array, and the elastic vibrations of the plate. These three phenomena are shown to be responsible for the complex transmission dispersion obtained in the measurements, shown in the fourth column. In despite of the numerical instabilities observed in the results of the FEAT, the main features regarding the finite impedance mismatch between solid and fluid can be appropriately resolved. When $h/a = 0.2$, the FEAT correctly predicts a dip arising from the bottom of the dispersion plot reaching zero group velocity at the X point and falling down again due to symmetry around X. Adding the rigid-solid results to the comparison enable us to infer that this dip correspond to a surface mode similar to Lamb modes, i.e., caused by the plate vibrations. The high transmission values measured at low frequencies at the left of the X point are also properly predicted by the FEAT, in contrast to the rigid-solid model. A similar landscape is obtained for $h/a = 0.4$. The crossing between the Wood anomaly and the surface mode can be clearly seen in both measurements and FEAT results. This crossing is particularly interesting because it involves the surface mode, the Wood anomaly condition, and the transmission peak, all of them hybridized. The high transmission found below this crossing is connected to the step-like behavior observed at normal incidence (see Figs. 4.12(a), (b), (d), and (e)). This behavior has been correctly attributed to the effect of finite impedance mismatch, which is taken into account in the FEAT model. The full transmission peak is also affected by the plate vibration with a small shift towards lower frequencies. For thicker plates ($h/a = 1.0$) the interaction between surface modes, coherent scattering among holes, and hole resonances are all stronger, thus producing a rich and complex scenario, and further investigation is needed to scrutinize it.

In order to clarify the key role of symmetry in the transmission properties of perforated plates we can compare a periodic lattice with a random lattice, both having the same filling fraction (average hole filling fraction $\bar{f}$ for the random array) and sharing the same plate thickness. This comparison is shown in Fig. 4.16, where the upper subfigures (a) and (b) correspond to transmission dispersions while the lower subfigures (c) and (d) represent the two-dimensional Fourier transforms of both lattices. The rich interplay between lattice modes and intrinsic plate modes in the ordered array (Fig. 4.16(a)) is completely absent in the random sample. However, the latter displays a feature resembling the surface mode coming from the plate vibration without the fall due to the array symmetry around the X point. Interestingly, the Fourier transform of the 2D distribution of geometrical openings in random arrays shows a broad annular maximum with a radius close to $|\mathbf{Q}_0| = \pi/a$. This maximum gives rise to a broad dark region near normal incidence, close to the Wood

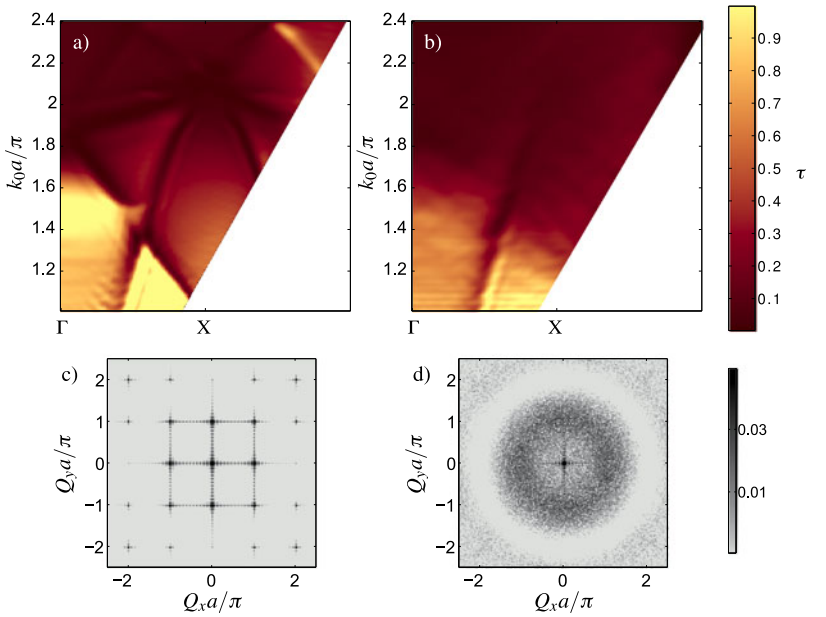

Fig. 4.16 Measured transmitted sound power coefficient τ (*color scale*) through perforated plates as a function of the normalized frequency k_0a/π and $\mathbf{Q}_0$ along the ΓX symmetry direction of the irreducible Brillouin zone for square (**a**) and random (**b**) lattices. (**c**), (**d**) 2D Fourier transforms (*contour plots in log scale*) of the film openings for the (**c**) periodic and (**d**) random arrays. Reprinted with permission from [21]. Copyright 2009 by the American Physical Society

anomaly of the ordered array. Regarding the transmission peak, it is reduced nearly to one half for the random lattice at normal incidence, while the high transmission observed near the X point at low frequencies is mainly due to the plate vibration and not to the hole resonance.

Finally, Wood anomalies can be analyzed from another point of view following [23] as the divergence of the structure factor of the array. Under the zero-thickness and small-hole approximations, one can relate via Babinet's principle the reflection coefficient of a disk array for electrons with the transmission coefficient of the complementary hole array for sound [24]:

$$T = \frac{1}{1 + i\frac{Sq_0}{2\pi}\mathscr{R}e\{\frac{1}{\alpha} - \mathscr{G}(\mathbf{Q}_0)\}}, \tag{4.56}$$

where

$$\mathscr{G}(\mathbf{Q}_0) = \sum_{\mathbf{n}} \exp(-\mathrm{i}\mathbf{Q}_0\mathbf{r}_\mathbf{n})\frac{\exp(ik_0R)}{R} \tag{4.57}$$

corresponds to the inter-hole interaction and $\mathscr{R}e\{\alpha\} = -r_0/\pi$, $\mathscr{I}m\{\alpha^{-1}\} = -2k_0$ is the scattering coefficient of a single hole. When $\mathscr{R}e\{\mathscr{G}(\mathbf{Q}_0)\}$ diverges, the transmission becomes zero. The condition for the divergence [23] of $\mathscr{G}(\mathbf{Q}_0)$ is

Table 4.1 Subwavelength transmission (ST) of individual small holes, extraordinary transmission (ET) of arrayed small holes, and surface-bound modes in arrays. The acoustic transmission of individual holes is proportional to their area, whereas arbitrarily small-hole arrays can trap light and produce full optical transmission

Type of wave	One-hole ST	Hole-array ET	Hole-array bound states
Sound	Yes	No	No
Electrons	No	No	No
Light	No	Yes	Yes

$$\mathscr{G}(\mathbf{Q}_0) \propto \frac{1}{\sqrt{|\mathbf{Q}_0 + \mathbf{G}|^2 - k_0^2}}, \tag{4.58}$$

which is the same condition given before for the Wood anomaly. This approach also facilitates the analysis of full transmission peaks, which are subject to the condition $\mathscr{R}e\{\alpha^{-1} - \mathscr{G}(\mathbf{Q}_0)\} = 0$. This condition cannot be fulfilled in the case of sound because $\mathscr{R}e\{\alpha\} < 0$ and $\mathscr{R}e\{\mathscr{G}(\mathbf{Q}_0)\} > 0$, similarly to electrons and in contrast to light [24], where full transmission occurs for arbitrarily small holes. Therefore, in the acoustic case no full transmission peaks can be produced associated to lattice resonances; full transmission in the acoustic case are directly originating from Fabry-Pérot resonances instead.

In summary, we reach the results showed in Table 4.1, where the existence of different transmission properties is stated against the different kinds of waves. We find very different behavior between light and sound, in contrast to the similarities emphasized by several groups [11, 30, 46]. Whereas subwavelength transmission takes place for sound through a single hole, this is neither the case for electrons nor for light (see Fig. 4.3(b)). Extraordinary transmission and surface-bound states exist exclusively for light and not for sound or electrons associated to lattice resonances, although full transmission can occur in the acoustic case due to Fabry-Pérot resonances.

4.6 Summary and Conclusions

In summary, the transmission of ultrasound through periodically perforated plates has been studied theoretically and experimentally. Different array geometries including square, triangular, and random lattices have been measured for Al plates immersed in water. The following conclusions can be drawn:

(A) It has been found that the transmission features of periodically perforated plates involve three different physical phenomena, namely Fabry Pérot resonances of the holes, coherent scattering due to the hole array, and elastic surface-modes of the plate. The interaction of these phenomena results in the following transmission features: (a) Full transmission peaks, (b) Wood anomaly minima, and

(c) minima and maxima associated with intrinsic surface modes. While (a) and (b) depend mostly on the geometrical parameters, (c) depends strongly on the physical properties of the constituent materials.

(B) The key role of Fabry-Pérot resonances in the full transmission peaks has been demonstrated. The periodicity adds an extra element of complexity to coherently add the amplitudes of different holes. The position and the width of the peaks can be tuned by changing the hole filling fraction. The number of peaks depends on both the plate thickness and the hole filling fraction.

(C) It has been observed that perforated plates can transmit much less sound than homogeneous plates of the same thickness due to the hydrodynamic short-circuit. Thus, a higher transmission loss can be achieved using lighter barriers. Sound screening by means of a hydrodynamic short-circuit could have interesting applications in underwater acoustics.

(D) Two theoretical models have been discussed. As they differ only in the behavior of the plate, it allows us to extract the role of the plate vibration and its interaction with the modes derived from the period distribution of holes. The rigid-solid model showed good agreement with experiment at normal incidence, whereas the FEAT resolved properly the key transmission features for arbitrary angle of incidence.

(E) It has been pointed out that full acoustic transmission should not be called extraordinary transmission. In contrast to light, there is a lack of true lattice resonances in sound [23, 24], and moreover, there is a cutoff-free mode at each hole connecting both sides of the plate, thus making full transmission an expected rather than an extraordinary phenomenon in plates with holes.

We hope that our study can contribute to a better understanding of the acoustic properties of perforated plates over a wider frequency range and for a larger number of materials.

Acknowledgements The authors wish to acknowledge financial support from projects MICINN MAT2010-16879, Consolider Nanolight.es CSD-2007-0046 of the Spanish Education and Science Ministry, and project PROMETEO/2010/043 of Generalitat Valenciana. H.E. acknowledges a CSIC-JAE scholarship.

References

1. Abramowitz, M., Stegun, I.A.: Handbook of Mathematical Functions with Formulas, Graphs, and Mathematical Tables, 9th Dover printing, 10th GPO printing edn. Dover, New York (1964)
2. Ashcroft, N.W., Mermin, N.D.: Solid State Physics. Harcourt Brace, Orlando (1976)
3. Barbara, A., Quémerais, P., Bustarret, E., Lopez-Rios, T.: Optical transmission through subwavelength metallic gratings. Phys. Rev. B **66**(16), 161403 (2002). doi:10.1103/PhysRevB.66.161403
4. Barnes, W.L., Dereux, A., Ebbesen, T.W.: Surface plasmon subwavelength optics. Nature **424**, 824–830 (2003). http://dx.doi.org/10.1038/nature01937
5. Bethe, H.A.: Theory of diffraction by small holes. Phys. Rev. **66**(7–8), 163–182 (1944). doi:10.1103/PhysRev.66.163

6. Bouwkamp, C.J.: Theoretische en numerieke behandeling van de buiging door een ronde opening. Ph.D. thesis, University of Groningen (1941)
7. Bouwkamp, C.J.: Diffraction theory. Rep. Prog. Phys. **17**(1), 35–100 (1954). http://stacks.iop.org/0034-4885/17/35
8. Brekhovskikh, L.M., Godin, O.A.: Acoustics of Layered Media. Springer Series on Wave Phenomena, vol. I, 2nd edn. Springer, Berlin (1998)
9. Brillouin, L.: Wave Propagation in Periodic Structures. Dover, New York (1953)
10. Christensen, J., Fernandez-Dominguez, A.I., de Leon-Perez, F., Martin-Moreno, L., Garcia-Vidal, F.J.: Collimation of sound assisted by acoustic surface waves. Nat. Phys. **3**, 851–852 (2007). doi:10.1038/nphys774, http://dx.doi.org/10.1038/nphys774
11. Christensen, J., Martin-Moreno, L., Garcia-Vidal, F.J.: Theory of resonant acoustic transmission through subwavelength apertures. Phys. Rev. Lett. **101**(1), 014301 (2008). doi:10.1103/PhysRevLett.101.014301, http://link.aps.org/abstract/PRL/v101/e014301
12. Christensen, J., Martín-Moreno, L., García-Vidal, F.J.: All-angle blockage of sound by an acoustic double-fishnet metamaterial. Appl. Phys. Lett. **97**(13), 134106 (2010). doi:10.1063/1.3491289, http://link.aip.org/link/?APL/97/134106/1
13. Christensen, J., Martín-Moreno, L., García-Vidal, F.J.: Enhanced acoustical transmission and beaming effect through a single aperture. Phys. Rev. B **81**(17), 174104 (2010). doi:10.1103/PhysRevB.81.174104
14. Cremer, L., Möser, M.: Technische Akustik, 5th edn. Springer, Berlin (2003)
15. Cummer, S.A., Schurig, D.: One path to acoustic cloaking. New J. Phys. **9**(3), 45 (2007). http://stacks.iop.org/1367-2630/9/45
16. Ebbesen, T.W., Lezec, H.J., Ghaemi, H.F., Thio, T., Wolff, P.A.: Extraordinary optical transmission through sub-wavelength hole arrays. Nature **391**(6668), 667–669 (1998). http://dx.doi.org/10.1038/35570
17. Estrada, H., Candelas, P., Uris, A., Belmar, F., García de Abajo, F.J., Meseguer, F.: Extraordinary sound screening in perforated plates. Phys. Rev. Lett. **101**(8), 084302 (2008). doi:10.1103/PhysRevLett.101.084302, http://link.aps.org/abstract/PRL/v101/e084302
18. Estrada, H., Candelas, P., Uris, A., Belmar, F., García de Abajo, F.J., Meseguer, F.: Influence of lattice symmetry on ultrasound transmission through plates with subwavelength aperture arrays. Appl. Phys. Lett. **95**(5), 051906 (2009). doi:10.1063/1.3196330, http://link.aip.org/link/?APL/95/051906/1
19. Estrada, H., Candelas, P., Uris, A., Belmar, F., Meseguer, F., García de Abajo, F.J.: Influence of the hole filling fraction on the ultrasonic transmission through plates with subwavelength aperture arrays. Appl. Phys. Lett. **93**(1), 011907 (2008). doi:10.1063/1.2955825, http://link.aip.org/link/?APL/93/011907/1
20. Estrada, H., Candelas, P., Uris, A., Belmar, F., Meseguer, F., García de Abajo, F.J.: Sound transmission through perforated plates with subwavelength hole arrays: A rigid-solid model. Wave Motion **48**(3), 235–242 (2011). doi:10.1016/j.wavemoti.2010.10.008, http://www.sciencedirect.com/science/article/B6TW5-51D7HPV-1/2/fa69698be2a24bb62629931deab14e4f
21. Estrada, H., García de Abajo, F.J, Candelas, P., Uris, A., Belmar, F., Meseguer, F.: Angle-dependent ultrasonic transmission through plates with subwavelength hole arrays. Phys. Rev. Lett. **102**(14), 144301 (2009). doi:10.1103/PhysRevLett.102.144301, http://link.aps.org/abstract/PRL/v102/e144301
22. Fei, D., Chimenti, D.E., Teles, S.V.: Material property estimation in thin plates using focused, synthetic-aperture acoustic beams. J. Acoust. Soc. Am. **113**(5), 2599–2610 (2003). doi:10.1121/1.1561496, http://link.aip.org/link/?JAS/113/2599/1
23. García de Abajo, F.J.; Colloquium: Light scattering by particle and hole arrays. Rev. Mod. Phys. **79**(4), 1267 (2007). doi:10.1103/RevModPhys.79.1267, http://link.aps.org/abstract/RMP/v79/p1267
24. García de Abajo, F.J., Estrada, H., Meseguer, F.J.: Diacritical study of light, electrons, and sound scattering by particles and holes. New J. Phys. **11**(9), 093013 (2009). http://stacks.iop.org/1367-2630/11/i=9/a=093013

25. Genet, C., Ebbesen, T.W.: Light in tiny holes. Nature **445**, 39–46 (2007). http://dx.doi.org/10.1038/nature05350
26. Gómez Rivas, J., Schotsch, C., Haring Bolivar, P., Kurz, H.: Enhanced transmission of the radiation through subwavelength holes. Phys. Rev. B **68**(20), 201,306 (2003). doi:10.1103/PhysRevB.68.201306
27. He, Z., Jia, H., Qiu, C., Peng, S., Mei, X., Cai, F., Peng, P., Ke, M., Liu, Z.: Acoustic transmission enhancement through a periodically structured stiff plate without any opening. Phys. Rev. Lett. **105**(7), 074301 (2010). doi:10.1103/PhysRevLett.105.074301
28. Holland, S.D., Chimenti, D.E.: Air-coupled acoustic imaging with zero-group-velocity lamb modes. Appl. Phys. Lett. **83**(13), 2704–2706 (2003). doi:10.1063/1.1613046, http://link.aip.org/link/?APL/83/2704/1
29. Hou, B., Mei, J., Ke, M., Liu, Z., Shi, J., Wen, W.: Experimental determination for resonance-induced transmission of acoustic waves through subwavelength hole arrays. J. Appl. Phys. **104**(1), 014909 (2008). doi:10.1063/1.2951457, http://link.aip.org/link/?JAP/104/014909/1
30. Hou, B., Mei, J., Ke, M., Wen, W., Liu, Z., Shi, J., Sheng, P.: Tuning Fabry-Perot resonances via diffraction evanescent waves. Phys. Rev. B **76**(5), 054303 (2007). doi:10.1103/PhysRevB.76.054303, http://link.aps.org/abstract/PRB/v76/e054303
31. Ingard, U., Bolt, R.H.: Absorption characteristics of acoustic material with perforated facings. J. Acoust. Soc. Am. **23**(5), 533–540 (1951). http://link.aip.org/link/?JAS/23/533/1
32. Joannopoulos, J.D., Meade, R.D., Winn, J.N.: Photonic Crystals: Molding the Flow of Light. Princeton University Press, Princeton (1995)
33. Jocker, J., Smeulders, D.: Minimization of finite beam effects in the determination of reflection and transmission coefficients of an elastic layer. Ultrasonics **46**, 42–50 (2007). http://www.sciencedirect.com/science/article/B6TW2-4MBCGB5-1/2/f117c6f285ef0f4f621c6bd2eddb3912
34. John, S.: Strong localization of photons in certain disordered dielectric superlattices. Phys. Rev. Lett. **58**(23), 2486–2489 (1987). doi:10.1103/PhysRevLett.58.2486
35. Jun, K.H., Eom, H.J.: Acoustic scattering from a circular aperture in a thick hard screen. J. Acoust. Soc. Am. **98**(4), 2324–2327 (1995). doi:10.1121/1.414404, http://link.aip.org/link/?JAS/98/2324/1
36. Khelif, A., Choujaa, A., Benchabane, S., Djafari-Rouhani, B., Laude, V.: Guiding and bending of acoustic waves in highly confined phononic crystal waveguides. Appl. Phys. Lett. **84**(22), 4400–4402 (2004). doi:10.1063/1.1757642, http://link.aip.org/link/?APL/84/4400/1
37. Kinsler, L.E.: Fundamentals of Acoustics, 4th edn. Wiley, New York (2000)
38. Kittel, C.: Introduction to Solid State Physics, 7th edn. Wiley, New York (1996)
39. Kundu, T.: Ultrasonic Nondestructive Evaluation. CRC, Boca Raton (2004)
40. Lamb, H.: On waves in an elastic plate. Proc. R. Soc. Lond., a Contain. Pap. Math. Phys. Character **93**(648), 114–128 (1917). http://www.jstor.org/stable/93792
41. Lamb, H.: On the vibrations of an elastic plate in contact with water. Proc. R. Soc. Lond., a Contain. Pap. Math. Phys. Character **98**(690), 205–216 (1920). http://www.jstor.org/stable/93996
42. Leonhardt, U.: Optical conformal mapping. Science **312**(5781), 1777–1780 (2006). doi:10.1126/science.1126493, http://www.sciencemag.org/cgi/content/abstract/312/5781/1777
43. Liu, F., Cai, F., Ding, Y., Liu, Z.: Tunable transmission spectra of acoustic waves through double phononic crystal slabs. Appl. Phys. Lett. **92**(10), 103504 (2008). doi:10.1063/1.2896146, http://link.aip.org/link/?APL/92/103504/1
44. Liu, Z., Jin, G.: Resonant acoustic transmission through compound subwavelength hole arrays: The role of phase resonances. J. Phys. Condens. Matter **21**(44), 445,401 (2009). http://stacks.iop.org/0953-8984/21/i=44/a=445401
45. Liu, Z., Jin, G.: Acoustic transmission resonance and suppression through double-layer subwavelength hole arrays. J. Phys. Condens. Matter **22**(30), 305003 (2010). http://stacks.iop.org/0953-8984/22/i=30/a=305003
46. Lu, M.H., Liu, X.K., Feng, L., Li, J., Huang, C.P., Chen, Y.F., Zhu, Y.Y., Zhu, S.N., Ming, N.B.: Extraordinary acoustic transmission through a 1d grating with very narrow

apertures. Phys. Rev. Lett. **99**(17), 174301 (2007). doi:10.1103/PhysRevLett.99.174301, http://link.aps.org/abstract/PRL/v99/e174301
47. Martín-Moreno, L., García-Vidal, F.J., Lezec, H.J., Pellerin, K.M., Thio, T., Pendry, J.B., Ebbesen, T.W.: Theory of extraordinary optical transmission through subwavelength hole arrays. Phys. Rev. Lett. **86**(6), 1114–1117 (2001). doi:10.1103/PhysRevLett.86.1114
48. Martinez-Sala, R., Sancho, J., Sanchez, J.V., Gomez, V., Llinares, J., Meseguer, F.: Sound attenuation by sculpture. Nature **378**, 241 (1995). http://dx.doi.org/10.1038/378241a0
49. Mekis, A., Chen, J.C., Kurland, I., Fan, S., Villeneuve, P.R., Joannopoulos, J.D.: High transmission through sharp bends in photonic crystal waveguides. Phys. Rev. Lett. **77**(18), 3787–3790 (1996). doi:10.1103/PhysRevLett.77.3787
50. Nomura, Y., Inawashiro, S.: On the transmission of acoustic waves through a circular channel of a thick wall. Res. Inst. Elec. Commun. **2**, 57–71 (1960)
51. Norris, A.N., Luo, H.A.: Acoustic radiation and reflection from a periodically perforated rigid solid. J. Acoust. Soc. Am. **82**(6), 2113–2122 (1987). doi:10.1121/1.395656, http://link.aip.org/link/?JAS/82/2113/1
52. Osborne, M.F.M., Hart, S.D.: Transmission, reflection, and guiding of an exponential pulse by a steel plate in water. I. Theory. J. Acoust. Soc. Am. **17**(1), 1–18 (1945). http://link.aip.org/link/?JAS/17/1/1
53. Pendry, J.B.: Low Energy Electron Diffraction: The Theory and Its Application to Determination of Surface Structure. Academic Press, London (1974)
54. Porto, J.A., García-Vidal, F.J., Pendry, J.B.: Transmission resonances on metallic gratings with very narrow slits. Phys. Rev. Lett. **83**(14), 2845–2848 (1999). doi:10.1103/PhysRevLett.83.2845
55. Rayleigh, L.: On the incidence of aerial and electric waves upon small obstacles in the form of ellipsoids or elliptic cylinders, and on the passage of electric waves through a circular aperture in a conducting screen. Philos. Mag. **44**, 28–52 (1897)
56. Rayleigh, L.: On the passage of waves through apertures in plane screens, and allied problems. Philos. Mag. **43**, 259–272 (1897)
57. Rayleigh, L.: On the dynamical theory of gratings. Proc. R. Soc. A **79**, 399–416 (1907)
58. Rayleigh, L.: The Theory of Sound, vol. II, 2nd edn. Courier Dover Publications (1945)
59. Royer, D., Dieulesaint, E.: Elastic Waves in Solids, vol. I. Springer, Berlin (2000)
60. Sánchez-Pérez, J.V., Caballero, D., Mártinez-Sala, R., Rubio, C., Sánchez-Dehesa, J., Meseguer, F., Llinares, J., Gálvez, F.: Sound attenuation by a two-dimensional array of rigid cylinders. Phys. Rev. Lett. **80**(24), 5325–5328 (1998). doi:10.1103/PhysRevLett.80.5325
61. Selcuk, S., Woo, K., Tanner, D.B., Hebard, A.F., Borisov, A.G., Shabanov, S.V.: Trapped electromagnetic modes and scaling in the transmittance of perforated metal films. Phys. Rev. Lett. **97**(6), 067403 (2006). doi:10.1103/PhysRevLett.97.067403, http://link.aps.org/abstract/PRL/v97/e067403
62. Sgard, F., Nelisse, H., Atalla, N.: On the modeling of the diffuse field sound transmission loss of finite thickness apertures. J. Acoust. Soc. Am. **122**(1), 302–313 (2007). doi:10.1121/1.2735109, http://link.aip.org/link/?JAS/122/302/1
63. Shelby, R.A., Smith, D.R., Schultz, S.: Experimental verification of a negative index of refraction. Science **292**(5514), 77–79 (2001). doi:10.1126/science.1058847, http://www.sciencemag.org/cgi/content/abstract/292/5514/77
64. Sigalas, M., Kushwaha, M.S., Economou, E.N., Kafesaki, M., Psarobas, I.E., Steurer, W.: Classical vibrational modes in phononic lattices: theory and experiment. Z. Kristallogr. **220**(9–10), 765–809 (2005). http://www.atypon-link.com/OLD/doi/abs/10.1524/zkri.2005.220.9-10.765
65. Sukhovich, A., Jing, L., Page, J.H.: Negative refraction and focusing of ultrasound in two-dimensional phononic crystals. Phys. Rev. B **77**(1), 014301 (2008). doi:10.1103/PhysRevB.77.014301, http://link.aps.org/abstract/PRB/v77/e014301
66. Takakura, Y.: Optical resonance in a narrow slit in a thick metallic screen. Phys. Rev. Lett. **86**(24), 5601–5603 (2001). doi:10.1103/PhysRevLett.86.5601

67. Torres, M., Montero de Espinosa, F.R., García-Pablos, D., García, N.: Sonic band gaps in finite elastic media: surface states and localization phenomena in linear and point defects. Phys. Rev. Lett. **82**(15), 3054–3057 (1999). doi:10.1103/PhysRevLett.82.3054
68. Treacy, M.M.J.: Dynamical diffraction in metallic optical gratings. Appl. Phys. Lett. **75**(5), 606–608 (1999). doi:10.1063/1.124455, http://link.aip.org/link/?APL/75/606/1
69. Trompette, N., Barbry, J.L., Sgard, F., Nelisse, H.: Sound transmission loss of rectangular and slit-shaped apertures: Experimental results and correlation with a modal model. J. Acoust. Soc. Am. **125**(1), 31–41 (2009). doi:10.1121/1.3003084, http://link.aip.org/link/?JAS/125/31/1
70. Viktorov, I.A.: Rayleigh and Lamb Waves. Plenum Press, New York (1967)
71. Wang, X.: Acoustical mechanism for the extraordinary sound transmission through sub-wavelength apertures. Appl. Phys. Lett. **96**(13), 134104 (2010). doi:10.1063/1.3378268, http://link.aip.org/link/?APL/96/134104/1
72. Wang, X.: Theory of resonant sound transmission through small apertures on periodically perforated slabs. J. Appl. Phys. **108**(6), 064903 (2010). doi:10.1063/1.3481434, http://link.aip.org/link/?JAP/108/064903/1
73. Wauer, J., Rother, T.: Considerations to Rayleigh's hypothesis. Opt. Commun. **282**, 339–350 (2009). doi:10.1016/j.optcom.2008.10.023
74. Williams, E.G.: Fourier Acoustics: Sound Radiation and Nearfield Acoustical Holography. Academic Press, San Diego (1999)
75. Wilson, G.P., Soroka, W.W.: Approximation to the diffraction of sound by a circular aperture in a rigid wall of finite thickness. J. Acoust. Soc. Am. **37**(2), 286–297 (1965). http://link.aip.org/link/?JAS/37/286/1
76. Wood, R.W.: Philos. Mag. **4**, 396 (1902)
77. Wood, R.W.: Anomalous diffraction gratings. Phys. Rev. **48**(12), 928–936 (1935). doi:10.1103/PhysRev.48.928
78. Yablonovitch, E., Gmitter, T.J.: Photonic band structure: the face-centered-cubic case. Phys. Rev. Lett. **63**(18), 1950–1953 (1989). doi:10.1103/PhysRevLett.63.1950
79. Yang, F., Sambles, J.R.: Resonant transmission of microwaves through a narrow metallic slit. Phys. Rev. Lett. **89**(6), 063901 (2002). doi:10.1103/PhysRevLett.89.063901
80. Zhang, X.: Acoustic resonant transmission through acoustic gratings with very narrow slits: Multiple-scattering numerical simulations. Phys. Rev. B **71**(24), 241102 (2005). doi:10.1103/PhysRevB.71.241102
81. Zhou, L., Kriegsmann, G.A.: Complete transmission through a periodically perforated rigid slab. J. Acoust. Soc. Am. **121**(6), 3288–3299 (2007). doi:10.1121/1.2721878, http://link.aip.org/link/?JAS/121/3288/1
82. Zhou, Y., Lu, M.H., Feng, L., Ni, X., Chen, Y.F., Zhu, Y.Y., Zhu, S.N., Ming, N.B.: Acoustic surface evanescent wave and its dominant contribution to extraordinary acoustic transmission and collimation of sound. Phys. Rev. Lett. **104**(16), 164301 (2010). doi:10.1103/PhysRevLett.104.164301

Chapter 5
Novel Ultrasound Imaging Applications

Francesco Simonetti

Abstract Routine applications of ultrasound imaging combine array technology and beamforming (BF) algorithms for image formation. Although BF is very robust, it discards a significant proportion of the information encoded in ultrasonic signals. Therefore, BF can reconstruct some of the geometrical features of an object but with limited resolution due to the diffraction limit. Inverse scattering theory offers an alternative approach to BF imaging that has the potential to break the diffraction limit and extract quantitative information about the mechanical properties of the object. High-resolution, quantitative imaging is central to modern diagnostic technology to achieve cost-effective detection through high sensitivity and limited false positive rate. This chapter lays out a framework encompassing theoretical and experimental results, and in which inverse scattering and modern array technology can be combined together to achieve super-resolution, quantitative imaging.

5.1 Introduction

Whether the aim is to detect a cancer mass in the human body, a precursor of damage in a metal, or to monitor CO_2 sequestration in an oil reservoir, the complexity of the host medium can result in a very challenging process. As an example, the different spatial scales that characterize the structure of the human body from molecular to organ system level and which in turn determine life functions, result in an extraordinarily complex system where discriminating between a state of disease, especially at an early stage, and normal function, poses a fundamental challenge.

The extent of the detection challenge is better understood by considering the final stage of the detection process when the diagnosis is formulated. In this context, the most basic form of detection is based on the analysis of signals such as the one shown in the diagram in Fig. 5.1(a). To illustrate the underpinning principles we consider the problem of damage detection in NDE although similar observations apply to other fields. This signal contains a signature that is related to the presence

F. Simonetti (✉)
College of Engineering and Applied Science, School of Aerospace Systems,
University of Cincinnati, 726 Rhodes Hall, P. O. Box 210070, Cincinnati, OH 45221, USA
e-mail: f.simonetti@uc.edu

R.V. Craster, S. Guenneau (eds.), *Acoustic Metamaterials*,
Springer Series in Materials Science 166, DOI 10.1007/978-94-007-4813-2_5,

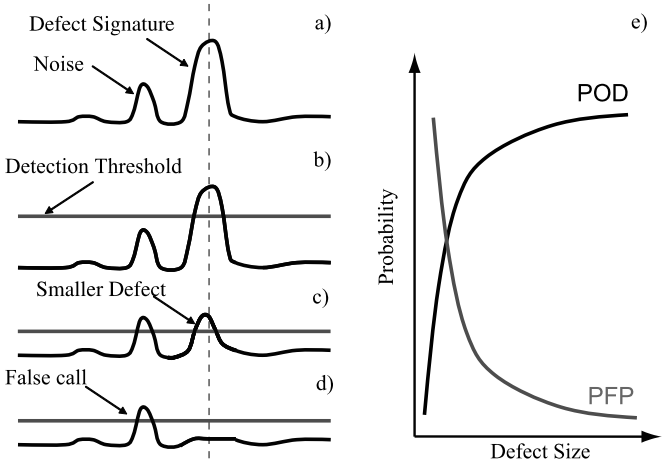

Fig. 5.1 The detection problem. (**a**) A signal contains signatures due to noise and features of interest; (**b**) to differentiate between noise and features a detection threshold is introduced; (**c**) lowering the threshold enables the detection of smaller features (**d**) but leads to false positives; (**e**) typical trends of probability of detection (POD) and false positives (PFP) as a function of feature size

of damage and some *nuisance* signatures that do not bear any direct relationship to damage and arise from the complexity of the host medium. Here, we refer to the nuisance signatures as noise. The key challenge in diagnostics is to decide whether a particular signature is due to noise or to the feature of interest. For this purpose an inspector sets a threshold level, Fig. 5.1(b), and decides that damage is present if somewhere in the signal the amplitude of one of the signatures rises above the threshold. Since the choice of the threshold level is somehow arbitrary, this approach is reliable only if the amplitude of the signature from damage is larger than the amplitude of noise, i.e. the signal to noise ratio (SNR) is high. In fact, if the damage is smaller in size, the amplitude of its signature can drop below the threshold and the flaw would go undetected. To detect the smaller flaw it is then necessary to lower the threshold, Fig. 5.1(c); however, now also noise intersects the threshold level leading to a false positive when damage is not present, Fig. 5.1(d).

The tradeoff between the detection of weak signatures, hence small features, and the occurrence of false positives is very important when assessing the cost-effectiveness of a diagnostic technology. In particular, the cost associated with false positives can be far more important than the direct cost of the diagnostic test. For instance, x-ray based mammography is the gold standard for breast cancer detection. However, it is known that in dense breast it leads to a 80 % false positive rate which results in unnecessary biopsies [22]. As a result, most of the more than $ 2 billion spent annually on biopsies and follow up ultrasound in the USA is spent on benign lesions.

To characterize the cost-effectiveness of a diagnostic method two key metrics are used: sensitivity and specificity [43]. The former refers to the rate of true positives whereas the latter gives the rate of true negatives. In NDE, sensitivity is more

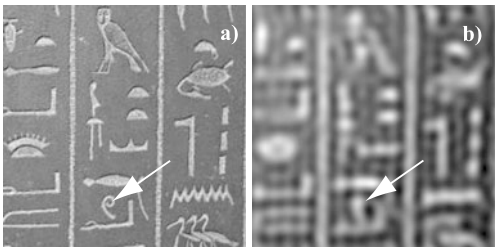

Fig. 5.2 Images of a photograph of the hieroglyphics on a sarcophagus in the British Museum: (**a**) High and (**b**) low resolution. The *arrows* point at a feature shaped like the number 9, as resolution decreases it is no longer possible to detect individual features

often referred to as probability of detection (POD). Under ideal conditions, a detection technology should achieve 100 % sensitivity and 100 % specificity. However, real values of sensitivity and specificity tend to be lower and vary depending on the characteristics of the feature of interest. Figure 5.1(e) illustrates typical trends of the POD and probability of false positive (PFP) as a function of damage size for a typical NDE inspection technique (PFP = 1-specificity). As damage size decreases the POD decreases while the PFP increases due to the need for lowering the detection threshold. The POD and PFP curves can be combined in a single curve resulting in the Receiver-Operating Characteristic (ROC) which summarizes the performance of a diagnostic system [43].

Detection of small features is becoming increasingly more important in a number of fields. Examples include early stage detection of cancer, which is known to reduce mortality rates, and detection of damage precursors that allows life extension of complex engineering systems such as jet engines.

Imaging technology offers the potential to improve the sensitivity of diagnostic methods whilst limiting or even lowering the PFP. This is possible because an image is the synthesis of the information contained in multiple measurements recorded by sensors deployed at different positions along an aperture. This spatial diversity yields complementary information that enhances the SNR of individual signals when they are combined together to form an image.

Although image-based detection could use threshold levels applied to the image, in a similar fashion to conventional detection (Fig. 5.1), thresholding would not make full use of the information available in the image. In fact, an image provides geometrical information about the structures within an object which allows target features to be discriminated from other nuisance features, thus detecting a target even in the presence of a highly complex background.

The metric used for quantifying the amount of information contained in an image is resolution. As an example Fig. 5.2 shows the high and low resolution versions of a photograph of the hieroglyphics on a sarcophagus. From the high resolution image it is possible to conclude that the sarcophagus contains a hieroglyphic that resembles the number 9 (pointed to by the arrow). On the other hand, the same conclusion cannot be reached from the low resolution image, thus illustrating how a loss of resolution results in a loss of information.

While resolution is important to discriminate between the different geometrical features of an image, it is not sufficient to characterize the full amount of information

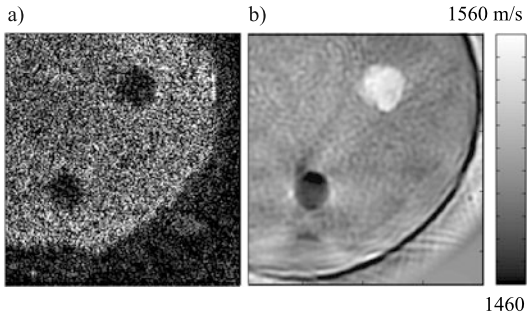

Fig. 5.3 Comparison between a structural (**a**) and a quantitative image of a three-dimensional object. (**a**) Features can be detected thanks to speckle contrast; (**b**) grey levels provide a spatial map of sound speed throughout the object

that is contained in the image. For instance, Fig. 5.3 shows two experimental images of a complex three-dimensional breast phantom. Figure 5.3(a) is obtained using ultrasound based sonography and is characterized by a granular appearance due to the speckle phenomenon [1]. Thanks to the speckle contrast it is possible to detect two circular dark inclusions inside the phantom. Next, is an ultrasound tomography image of the same phantom obtained with the method introduced in [37]. The image shows how the speed of sound, which is related to the mechanical properties of the materials in the phantom, varies in space with each grey level corresponding to a numerical value of sound speed. While the sonogram provides a *structural* image containing geometrical information, the tomogram in Fig. 5.3(b) is a *quantitative* image that blends together the geometrical and material properties of the probed object. Importantly, thanks to the sound-speed contrast in Fig. 5.3(b) it is possible to observe that the two inclusions are different in nature whereas, they appear to be the same on the sonogram. The sound-speed information is critical to increase specificity (lower the PFP). As an example, in human tissue it is known that cancer masses tend to be stiffer and have higher sound-speed than healthy tissue [17]. As a result, by examining the image in Fig. 5.3(b) it would be possible to conclude that the bright inclusion, which has high sound speed, is a cancer mass while the dark one could be a cyst of simply fat. Therefore, although the two images in Fig. 5.3 have comparable level of spatial resolution, the quantitative image yields additional information that leads to higher specificity and hence to a superior diagnostic technology.

To meet the requirements of high sensitivity and specificity of modern diagnostics, imaging methods have to provide quantitative information with high spatial resolution. However, the resolution of classical imaging methods is dictated by the diffraction limit that leads to a minimum resolvable size of the order of the wavelength, λ, of the probing wave (see, for instance, Ref. [16]). This has important practical implications in subsurface imaging. In fact, to achieve high resolution short wavelengths need to be propagated. However, as λ decreases the penetration depth of the probing wave decreases due to increasing absorption and scattering. As a result, the higher the resolution the shallower the volume of the object that can be imaged, this being the major limitation of conventional ultrasonic imaging systems.

This chapter provides an overview of recent progress on acoustic imaging methods that can break the diffraction limit to achieve super resolution as well as recon-

structing spatial maps of material properties. Therefore, the imaging problem is formulated in Sect. 5.2 which also introduces the classical diffraction limit. Section 5.3 links acoustic scattering to the imaging problem using a general wave-matter interaction model. Section 5.4 introduces beamforming that is used in routine ultrasound imaging and shows its connection to diffraction tomography. Section 5.5 presents the approach to subwavelength resolution imaging which is based on nonlinear inverse scattering as discussed in Sect. 5.6. To support the inverse scattering approach, experimental results are presented in Sect. 5.7 which is followed by conclusions in Sect. 5.8.

5.2 The Imaging Problem

Modern imaging technology builds on recent progress in solid state electronics and micromachining that have led to the rapid development of ultrasound arrays.

Scattering experiments can be performed with sensors arranged under different configurations. If the entire surface of the volume is accessible, they can be distributed in a full-view configuration (Fig. 5.4(a)) whereas in the limited view case, data can be collected by using an array interrogating the accessible surface (Fig. 5.4(b)). Array elements can be excited individually, launching a wave which propagates in the background medium and is scattered by the features contained in it. The scattered field is detected by all the transducers and recorded individually. Therefore, for an array with N elements, N^2 signals can be measured.

The general imaging problem can be formulated in terms of reconstructing the spatial distribution of one or more physical parameters characterizing the structure of an object from a set of scattering experiments performed with an array. Let us assume that scattering can be described by a scalar wavefield, ψ, solution to

$$\widehat{H}\psi(\mathbf{r}, k\hat{\mathbf{r}}_0, \omega) = -4\pi O(\mathbf{r}, \omega)\psi(\mathbf{r}, k\hat{\mathbf{r}}_0, \omega), \tag{5.1}$$

where $\widehat{H}$ is the Helmholtz operator, $(\nabla^2 + k^2)$, k is the background wavenumber $(2\pi/\lambda)$, $\hat{\mathbf{r}}_0$ specifies the direction of the incident plane wave which illuminates the object and ω is the angular frequency. The object is described by the *Object Function*, $O(\mathbf{r}, \omega)$, of support D corresponding to the volume occupied by the object

$$O(\mathbf{r}, \omega) = \frac{1}{4\pi}\left(\frac{\omega}{c_0(\omega)}\right)^2\left[\left(\frac{c_0(\omega)}{c(\mathbf{r}, \omega)}\right)^2 - 1\right] - \frac{1}{4\pi}\rho^{1/2}(\mathbf{r})\nabla^2\rho^{-1/2}(\mathbf{r}), \tag{5.2}$$

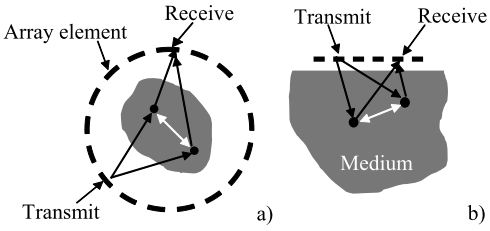

Fig. 5.4 Diagram of typical transducer arrangements for acoustic imaging. Signals are collected for each permutation of transmitter and receiver element pairs in the array: (**a**) full view; (**b**) limited view

where, c_0 is the sound speed in the homogeneous background and $c(\mathbf{r})$, and $\rho(\mathbf{r})$ are the local sound speed and mass density inside the object [27]. The analysis performed in the rest of this chapter will consider monochromatic wavefields, therefore the explicit dependence on ω is omitted.

Equations (5.1) and (5.2) provide an accurate representation of the acoustic scattering problem where elastic effects can be neglected. Therefore, while this model is suitable to describe the propagation of ultrasound in human tissue it is less accurate when studying ultrasonic NDE of solids or seismic wave scattering in the earth. Despite these limitations, the acoustic model underpins most of the imaging methods used in NDE and seismic imaging, therefore it will be adopted as the basic model for the theory presented in the following sections.

To obtain a quantitative image of the object, the spatial function $O(\mathbf{r})$ needs to be reconstructed from the set of scattering experiments. Spatial maps of sound speed and density can then be obtained by inverting (5.2) [23]. Structural imaging on the other hand, only reconstructs the boundaries of sudden variations of $O(\mathbf{r})$ as in the case of the sonogram shown in Fig. 5.3(a).

Even with the most advanced quantitative imaging method, it is not possible to reconstruct $O(\mathbf{r})$ exactly as this would require unlimited resolving power. A rigorous definition of resolution can be based on the representation of the object function in the spatial frequency domain, Ω, obtained by performing the three-dimensional Fourier transform of $O(\mathbf{r})$

$$\widetilde{O}(\Omega) = \int_{-\infty}^{\infty} d^3 r\, O(\mathbf{r}) e^{-i\Omega\cdot\mathbf{r}}. \tag{5.3}$$

The resolution of an imaging system is then determined by the largest spatial frequency, $|\Omega|$, that the system can reconstruct.

5.2.1 The Diffraction Limit

While a homogeneous medium does not support the propagation of monochromatic wavefields oscillating over a spatial scale smaller than λ, subwavelength oscillations can occur on the surface and within the interior of the probed object [16]. The subwavelength oscillations are described by evanescent fields that are trapped on the object's surface and do not radiate energy into the far field. The interplay between radiating and evanescent fields can be seen by considering the scattering of a plane wave incident on a planar surface. Let $\psi^s(\mathbf{r}_\parallel, 0)$ be the resulting complex scattered field, measured along an aperture close ($\ll \lambda$) to the surface. By means of the angular spectrum method [16], the spectrum of the field along a parallel aperture at distance z from the first is $\tilde{\psi}^s(k_\parallel, z) = \tilde{\psi}^s(k_\parallel, 0)\exp(ik_\perp z)$ where $\tilde{\psi}^s(\mathbf{k}_\parallel, 0)$ is the spectrum of $\psi^s(\mathbf{r}_\parallel, 0)$ and $k_\parallel$ and $k_\perp$ are related to the medium wavenumber, k

$$k_\perp = \begin{cases} \sqrt{k^2 - k_\parallel^2} & \text{if } |k_\parallel| \le k, \\ i\sqrt{k_\parallel^2 - k^2} & \text{if } |k_\parallel| > k. \end{cases} \tag{5.4}$$

The condition, $|k_{\|}| \leq k$, corresponds to propagating waves that can travel from the object to a remote detector placed in the far field. In this case, $k_{\|}$ and $k_{\perp}$ are the projections of the wavenumber vector $\mathbf{k}$ along the plane of the aperture and in the direction perpendicular to it. Since $|k_{\|}| \leq k$, propagating waves oscillate over a spatial scale larger than λ ($k = 2\pi/\lambda$). In contrast, $|k_{\|}| > k$ corresponds to evanescent waves that decay exponentially in the direction perpendicular to the aperture, thus making their detection increasingly more difficult as the detector moves away from the surface of the object. Evanescent waves can oscillate over a subwavelength scale along the surface of the object and the smaller their spatial period, the more rapid their exponential decay is. As a result, if detectors are placed many wavelengths away from the object, the contribution from the evanescent fields is negligible and the wavefield is effectively bandlimited with bandwidth $\mathscr{B} = 2k$ [16].

Classical imaging methods, from microscopy to sonography, are based on a linear, one-to-one mapping between the spatial frequencies contained in a radiating wavefield and the spatial frequencies, Ω, of the object function $\widetilde{O}(\Omega)$ [4]. Since the wavefield is bandlimited to $2k$, the largest object bandwidth that can be retrieved is also $2k$ leading to the classical Rayleigh limit [16].

In 1928 Synge suggested that subwavelength resolution could be achieved by probing the evanescent fields directly. The premise of this approach is that evanescent waves encode information about the subwavelength properties of the object due to their super-oscillatory behavior. Synge's original idea has led to the development of Near-field Scanning Optical Microscopy (NSOM) where resolution in the order of $\lambda/100$ has been reported (for an overview of the topic see [11]). However, a major limitation of NSOM is that to access the evanescent fields a probe has to be scanned close ($< \lambda$) to the surface to be imaged. This is not feasible in a number of subsurface imaging problems where the surface or volume of interest are many wavelengths away from the sensors. This chapter explores the possibility of achieving super resolution when all the sensors are in the far field ($\gg \lambda$).

5.3 Acoustic Scattering and the Far-Field Operator

The link between the spatial frequencies of the object function and those of the radiating scattered field is dictated by the scattering mechanism describing how waves interact with matter. In this section this link is considered further based on the theory of acoustic scattering. For this purpose, it can be observed that the potential ψ in (5.1) is also a solution to the Lippman-Schwinger equation

$$\psi(\mathbf{r}, k\hat{\mathbf{r}}_0) = \exp(ik\hat{\mathbf{r}}_0 \cdot \mathbf{r}) + \int_D d^3r'\, G(\mathbf{r}, \mathbf{r}')O(\mathbf{r}')\psi(\mathbf{r}', k\hat{\mathbf{r}}_0), \tag{5.5}$$

where $\exp(ik\hat{\mathbf{r}}_0 \cdot \mathbf{r})$ is an incident plane wave and $G(\mathbf{r}, \mathbf{r}')$ is the free-space Green's function solution to $\widehat{H}G(\mathbf{r}, \mathbf{r}') = -4\pi\delta(|\mathbf{r} - \mathbf{r}'|)$. Using the far-field approximation, $|\mathbf{r} - \mathbf{r}'| \to r[1 - (\mathbf{r} \cdot \mathbf{r}')/r^2]$, (5.5) leads to the asymptotic expression of ψ

$$\lim_{r\to\infty} \psi(\mathbf{r}, k\hat{\mathbf{r}}_0) = e^{ik\hat{\mathbf{r}}_0\cdot\mathbf{r}} + f(k\hat{\mathbf{r}}, k\hat{\mathbf{r}}_0)\frac{e^{ikr}}{r}, \tag{5.6}$$

where $f(k\hat{\mathbf{r}}, k\hat{\mathbf{r}}_0)$ is the scattering amplitude defined as

$$f(k\hat{\mathbf{r}}, k\hat{\mathbf{r}}_0) = \int_D d^3r'\, e^{-ik\hat{\mathbf{r}}\cdot\mathbf{r}'} O(\mathbf{r}')\psi(\mathbf{r}', k\hat{\mathbf{r}}_0). \tag{5.7}$$

We now introduce the T-matrix or transition amplitude [41]

$$T(\alpha\hat{\mathbf{u}}, k\hat{\mathbf{r}}_0) = \int_D d^3r'\, e^{-i\alpha\hat{\mathbf{u}}\cdot\mathbf{r}'} O(\mathbf{r}')\psi(\mathbf{r}', k\hat{\mathbf{r}}_0), \tag{5.8}$$

so that $T(\alpha\hat{\mathbf{u}}, k\hat{\mathbf{r}}_0) = f(k\hat{\mathbf{r}}, k\hat{\mathbf{r}}_0)$ for $\alpha\hat{\mathbf{u}} = k\hat{\mathbf{r}}$. As shown in [32] the scattering amplitude can be related to the spectral representation of the object function $\widetilde{O}(\Omega)$ and the transition matrix according to

$$f(k\hat{\mathbf{r}}, k\hat{\mathbf{r}}_0) = \widetilde{O}\big[k(\hat{\mathbf{r}} - \hat{\mathbf{r}}_0)\big] + \frac{1}{2\pi^2}\int_{-\infty}^{+\infty} d^3\alpha \frac{\widetilde{O}[k\hat{\mathbf{r}} - \alpha\hat{\mathbf{u}}]T(\alpha\hat{\mathbf{u}}, k\hat{\mathbf{r}}_0)}{k^2 - \alpha^2 + i\varepsilon}, \tag{5.9}$$

where ε is an infinitesimal introduced to remove the singularity at $k = \alpha$. Equation (5.9) links the spectrum of $O(\mathbf{r})$ to the measurements and is central to super resolution imaging as explained in Sect. 5.5.

5.3.1 Born Approximation

Under the Born approximation, the total field under the integral sign in (5.5) is approximated to the incident field which causes the integral term in (5.9) to vanish [32]. As a result, the Born approximation leads to a one-to-one mapping between the measured scattering amplitude $f(k\hat{\mathbf{r}}, k\hat{\mathbf{r}}_0)$ and $\widetilde{O}(\Omega)$ at the spatial frequency $\Omega = k(\hat{\mathbf{r}} - \hat{\mathbf{r}}_0)$, i. e.

$$f(k\hat{\mathbf{r}}, k\hat{\mathbf{r}}_0) \approx \widetilde{O}\big[k(\hat{\mathbf{r}} - \hat{\mathbf{r}}_0)\big]. \tag{5.10}$$

To illustrate the physical implications of the one-to-one mapping, Fig. 5.5 depicts a two-dimensional scattering problem. If the object is probed with a circular array consisting of N transducers, the scattering amplitude can be measured for N^2 combinations of the illumination, θ, and scattering, ϕ, angles through (5.6). The measurements can be arranged into a $N \times N$ matrix, known as the *multistatic matrix*, whose i–j entry is the scattering amplitude measured under the scattering angle ϕ_i when the object is illuminated in the direction θ_j. Due to (5.10), the entries of the multistatic matrix map into a subset of the Ω-space which coincides with a disk (sphere in 3-D) of radius $2k$ known as the Ewald limiting disk [4]. This also implies that under the Born approximation, measurements are independent of the spatial frequencies of the object larger than $2k$ or in other words the spatial periodicities

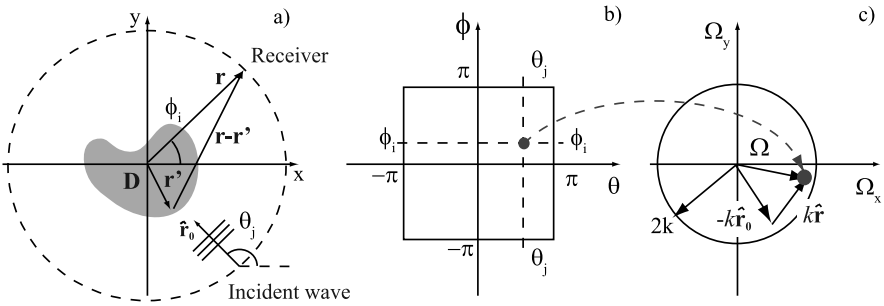

Fig. 5.5 (**a**) Diagram of scattering experiments showing a transmitter, T_x, launching a plane wave and a receiver, R_x detecting the scattered field. (**b**) The multistatic matrix—a discrete representation of the T_∞ operator. (**c**) The spatial frequency domain showing how measurements map onto the Ewald limiting disk

of the object function that vary over a spatial scale shorter than $\lambda/2$ do not affect the far-field measurements. Therefore, since the measurements are independent of the sub-$\lambda/2$ structures, any imaging method consistent with the Born approximation will not be able to achieve sub-$\lambda/2$ resolution.

For the Born approximation to be valid the object should have low contrast relative to the background. Moreover, its size should be comparable to λ so that the phase delay accumulated by the incident field as it travels inside the object is less than π [19]. These are very stringent conditions for most practical applications and are in common with other linear approximations such as Rytov [24]. Finally, it is observed that the Born approximation violates energy conservation [18].

5.3.2 *Factorization of the Far-Field Operator T_∞*

Here, we follow the approach proposed by Kirsch [20, 21]. Central to any imaging method is the far-field operator, $T_\infty : L^2(\mathbb{S}) \to L^2(\mathbb{S})$ defined as

$$T_\infty \big| g(\hat{\mathbf{r}}) \big\rangle = \int_{\mathbb{S}} ds(\hat{\mathbf{r}}_0)\, f(k\hat{\mathbf{r}}, k\hat{\mathbf{r}}_0) g(k\hat{\mathbf{r}}_0), \tag{5.11}$$

where we have made use of the Dirac notation[1] and $\mathbb{S}$ is the unit shell in $\mathbb{R}^3$. The physical significance of T_∞ can be understood by observing that $T_\infty|g\rangle$ is the far-field pattern of the scattered field, $|u_s\rangle$, due to a linear combination of incident plane waves, $\exp(ik\hat{\mathbf{r}}_0 \cdot \mathbf{r})$, with relative complex amplitude $g(k\hat{\mathbf{r}}_0)$, i.e.

$$|u_s\rangle = T_\infty |g\rangle. \tag{5.12}$$

[1]This is a convenient way of describing both the continuous and discrete cases. For instance, $|v(\mathbf{r})\rangle$ can refer to a continuous function of space, $v(\mathbf{r})$, or a vector field, $\mathbf{v}$, whose entries correspond to the values of $v(\mathbf{r})$ at the nodes of a discrete representation of space. Similarly, an operator becomes a matrix such as the multistatic matrix representing T_∞. Note that $\langle v(\mathbf{r})|$ is the transpose conjugate of the vector $|v(\mathbf{r})\rangle$ [2].

Therefore, T_∞ describes how any arbitrary incident field is scattered by the object. From a functional analysis perspective, T_∞ maps the space of the functions $|g\rangle$ that define the incident field into the space of the far-field scattering patterns $|u_s\rangle$.

The definition of T_∞ allows the scattering process to be expressed as the combination of three consecutive events: 1) the propagation of an incident field from the far-field (or array of transducers) to the object; 2) the interaction of the incident field with the object physical properties and the resulting local perturbation to the incident field; 3) the radiation of the perturbation from the object to the far field.

The three scattering events can be described by three separate mathematical operators that combined together result in T_∞. To show this, let us introduce the illumination operator $H : L^2(\mathbb{S}) \to L^2(D)$ which maps the illumination functions $|g\rangle$ into the incident field $|\phi\rangle$ inside the object

$$|\phi\rangle = H|g\rangle = \int_{\mathbb{S}} ds(\hat{\mathbf{r}}_0) \exp(ik\hat{\mathbf{r}}_0 \cdot \mathbf{r}) g(k\hat{\mathbf{r}}_0). \tag{5.13}$$

Similarly, it is possible to define a radiation operator $H^\dagger : L^2(D) \to L^2(\mathbb{S})$ that maps a continuous distribution of point sources in D with strength defined by the continuous function $|\sigma\rangle$ into the radiated far-field pattern

$$|u_s\rangle = H^\dagger|\sigma\rangle = \int_D dr^3 \exp(-ik\hat{\mathbf{r}}_0 \cdot \mathbf{r})\sigma(\mathbf{r}). \tag{5.14}$$

By definition $H^\dagger$ is the adjoint operator of H. Crucially, both H and $H^\dagger$ depend on the geometry of the scatterer but are independent of its mechanical properties.

Finally we introduce the interaction operator $S : L^2(D) \to L^2(D)$ that transforms the incident field inside the object, $|\phi\rangle$, into the source distribution $|\sigma\rangle$ characterizing the perturbation to the incident field. This operator accounts for the wave-matter interaction and can take different forms depending on the scattering model under consideration. As an example, under the Born approximation it is assumed that each point inside the scatterer acts as an independent point scatterer. Therefore, the equivalent source distribution coincides with the incident field multiplied by the object function and S is a diagonal operator defined as

$$|\sigma\rangle = S|\phi\rangle = O(\mathbf{r})\phi(\mathbf{r}). \tag{5.15}$$

The expression of S in the case of multiple scattering can be found in [21].

We are now able to decompose the far-field operator into the three main steps of the scattering process. In particular, from the diagram in Fig. 5.6 it is clear that $|u_s\rangle = T_\infty|g\rangle = H^\dagger SH|g\rangle$, which leads to the factorization

$$T_\infty = H^\dagger SH. \tag{5.16}$$

The factorization of T_∞ suggests a formal approach to imaging. In particular, we have already observed that only S depends on $O(\mathbf{r})$. Therefore, to reconstruct $O(\mathbf{r})$ from T_∞, it is necessary to isolate the contribution of S from H and $H^\dagger$.

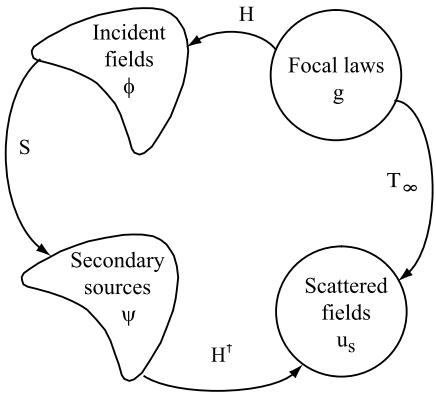

Fig. 5.6 The mapping of the space of the illumination laws $|g\rangle$ into the space of scattered fields $|u_s\rangle$ can be described by three operators. In anticlockwise order: the space of illumination functions $|g\rangle$ maps onto the space of incident fields inside the object $|\phi\rangle$ via H. The space of incident fields then maps onto the space of secondary sources $|\sigma\rangle$ through S. Finally the secondary sources radiate into the space of the scattered fields $|u_s\rangle$ as described by $H^\dagger$

5.4 Beamforming and Diffraction Tomography

Beamforming (BF) is the image formation method underpinning current commercial imaging technology. Fields of application include: sonar [3], medical diagnostics [42], and non-destructive testing [13].

Although several hardware and software implementations of BF have been proposed, the general working principle consists of two stages as illustrated in Fig. 5.7. In the first stage and for each point in the image space, **z**, a focal law is defined. This sets the relative time delays between the input signals fed into each array transducer so that the acoustic waves excited by the array elements interfere coherently with each other only when they reach **z**. For this purpose, the transducer that is at the greatest distance from **z** is fired first while the closest transducer is fired last. The field resulting from the superposition of the waves radiating from the array elements is an acoustic beam focused at **z**. If a point scatterer is present at **z**, the beam is scattered into a spherical wave radiating from **z**. The scattered wave is subsequently detected by the array elements that measure wavepackets arriving at different times depending on the element relative distance from **z**. The signals are again time shifted using the same focal law used in transmission and summed coherently. This ensures that maximum weight is given to the energy scattered from **z** and represents the second stage of BF imaging. This two-stage process shares the same physical principle used in confocal microscopy where two separate lenses are used to achieve the two focusing stages. To form an image, the BF process is repeated for all points in the volume to be imaged assuming that the scattering event at a particular location **z** is independent of the scattering events occurring at neighboring points, i.e. multiple scattering effects are neglected. Therefore, BF makes use of the Born approximation.

The two stages of the BF process aim at isolating the interaction operator S from H and $H^\dagger$ in the factorization of T_∞. To illustrate this, we first consider an ideal

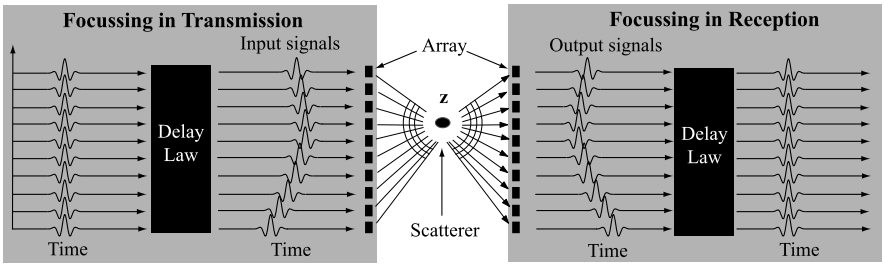

Fig. 5.7 The two stages of beamforming imaging. In the transmission stage, the array elements are phased according to a delay law that results in a focused beam at a prescribed point **z**. In the reception stage, the signals received by different array elements are again time shifted with the same delay law to isolate the energy scattered from **z**. For illustration purposes two separate arrays are shown; however, in practice the two operations are performed by a single array

scenario where it is possible to focus a beam at a point in space, **z**, with unlimited resolution, or in other words there exists an illumination law $|g_z\rangle$ such that

$$H|g_z\rangle = \delta\big(|\mathbf{r} - \mathbf{z}|\big). \tag{5.17}$$

By reciprocity, this also means that it is possible to '*see*' a secondary source at the same position **z** with unlimited resolution

$$\langle g_z|H^{\dagger}|\sigma\rangle = \sigma(\mathbf{z}). \tag{5.18}$$

Using properties (5.17) and (5.18) and the factorization of T_∞ in (5.16) one obtains

$$\langle g_z|T_\infty|g_z\rangle = S(\mathbf{z},\mathbf{z}). \tag{5.19}$$

Under the Born approximation, (5.15) and (5.19) then lead to

$$\langle g_z|T_\infty|g_z\rangle = O(\mathbf{z}), \tag{5.20}$$

which is the object function reconstructed with unlimited resolution. However, the ideal focusing in (5.17) and (5.18) is not physically possible. Symmetry considerations imply that in a homogeneous medium with transmitters placed far away from the focal point, the sharpest acoustic beam is obtained by using the focal law

$$|g_{\mathbf{z}}\rangle = \exp(-ik\hat{\mathbf{r}}_0 \cdot \mathbf{z}), \tag{5.21}$$

which is also known as the steering function. This function produces a relative phasing between the sources that is equivalent to the time delays between the elements of an array in BF imaging. Therefore, properties (5.17) and (5.18) now become

$$H|g_z\rangle = 4\pi j_0\big(k|\mathbf{z} - \mathbf{r}|\big), \tag{5.22}$$

$$\langle g_z|H^{\dagger}|\sigma\rangle = 4\pi \int_D dr^3\, O(\mathbf{r})\, j_0\big(k|\mathbf{z} - \mathbf{r}|\big), \tag{5.23}$$

where j_0 is the zero-order spherical Bessel function of the first kind. Under the Born approximation, the finite spatial extent of the focal spot now implies that the object function reconstructed with BF, $R_{BF}(\mathbf{z})$, is[2]

$$R_{BF}(\mathbf{z}) = \langle g_z | T_\infty | g_z \rangle = \int_D dr^3 \, O(\mathbf{r}) h_{BF}\big(|\mathbf{r}-\mathbf{z}|\big), \tag{5.24}$$

which is the spatial convolution of the object function with the point spread function (PSF) $h_{BF}(|\mathbf{r}-\mathbf{z}|)$ defined as

$$h_{BF}\big(|\mathbf{r}-\mathbf{z}|\big) = \langle g_z | I | g_z \rangle = 16\pi^2 j_0^2\big(k|\mathbf{r}-\mathbf{z}|\big). \tag{5.25}$$

In the spatial frequency domain the convolution in (5.24) is equivalent to

$$\widetilde{R}_{BF}(\Omega) = \widetilde{O}(\Omega)\tilde{h}_{BF}(\Omega), \tag{5.26}$$

where, $\tilde{h}_{BF}(\Omega)$ is the Fourier transform of (5.25)

$$\tilde{h}_{BF}(\Omega) = \begin{cases} \frac{16\pi^3}{k^2}\frac{1}{|\Omega|} & \text{if } |\Omega| \le 2k, \\ 0 & \text{if } |\Omega| > 2k. \end{cases} \tag{5.27}$$

From (5.26) and (5.27) it follows that the BF process leads to a reconstruction of the object function which is a low-pass filtered version of $O(\mathbf{r})$ with a cutoff at $2k$ consistent with the diffraction limit. However, BF also introduces a distortion caused by the factor $1/|\Omega|$ in (5.27) which tends to amplify the low spatial frequencies of the object at the expense of the higher ones. Because of this distortion, the use of BF is limited to structural imaging as in the case of sonography. Diffraction tomography (DT) algorithms rectify the distortion while retaining the same resolution level producing a PSF with a flat spectrum $\tilde{h}_{DT}(\Omega) = 1$ within the ball $|\Omega| < 2k$ and zero outside it [4]. The reconstructed object function is therefore low-pass filtered

$$\widetilde{R}_{DT}(\Omega) = \widetilde{O}(\Omega)\tilde{h}_{DT}(\Omega), \tag{5.28}$$

with

$$h_{DT}(\mathbf{r}) = \frac{4k^3}{\pi^2}\left[\frac{j_1(2k|\mathbf{r}-\mathbf{z}|)}{2k|\mathbf{r}-\mathbf{z}|}\right], \tag{5.29}$$

where, $j_1(\cdot)$ is the spherical Bessel function of the first order.

From (5.26) and (5.28) it is clear that the DT image can be obtained from the BF image by deconvolving the latter with the BF PSF in (5.27). Similar considerations apply to the two dimensional problem [33].

[2] In practice BF is performed in the time domain according to the procedure illustrated in Fig. 5.7. This is equivalent to integrating (5.24) over the frequency bandwidth of the input signal and including the negative frequencies.

5.5 Subwavelength Imaging

Equation (5.9) describes the encoding of subwavelength information into the far field. In fact, the integral term in (5.9) which is due to multiple scattering, links the entire spectrum of $O(\mathbf{r})$ to a single scattering measurement $f(k\hat{\mathbf{r}}, k\hat{\mathbf{r}}_0)$ since the integral spans the entire $\mathbb{R}^3$ domain rather than being limited to a point inside the Ewald limiting sphere. Therefore, far-field measurements are sensitive to the spatial frequencies larger than $2k$ and hence to the subwavelength structures of the object. This is a key observation because if the measurements are sensitive to the subwavelength structure of the object then it should be possible to retrieve them. The encoding mechanism for the simple case of two point scatterers has been studied in [29, 36].

In order to extract this information from the far field, the inverse scattering problem needs to be solved. While the forward scattering problem predicts the scattered field for a prescribed object function [solving (5.1)], the inverse problem attempts to retrieve $O(\mathbf{r})$ from the measured T_∞. The former is well posed whereas the latter is ill-posed in the sense of Hadamard, because although the solution exists and is unique (at least under full view conditions), it is unstable [9].

From a mathematical perspective, the uniqueness of the solution to the inverse problem implies that the object function could be reconstructed with unlimited resolution, since only the exact object function is the solution to the inverse problem. However, the problem is also unstable, which means that small measurement errors (e.g. noise) can be amplified in the reconstructed image leading to significant artifacts or even causing the non-existence of the solution. As a result, central to the imaging problem is the solution of the inverse scattering problem in a stable fashion.

The solution of the inverse problem is further complicated by its nonlinear nature. In fact, while the forward problem is linear with respect to the incident field, it is nonlinear relative to the object function due to the presence of multiple scattering. On the other hand, under the Born approximation the problem becomes linear because multiple scattering is neglected. As a result, DT and hence BF are solutions to the linearized inverse scattering problem. This implies that even if real measurements are affected by multiple scattering, both DT and BF are not able to decode the subwavelength information that is encoded by multiple scattering.

To extract subwavelength information it is therefore necessary to account for the actual physical mechanism that describes the interaction of the incident field with the object and solve the fully nonlinear inverse problem.

5.5.1 The Information Capacity of Noisy Measurements

Before discussing methods to solve the inverse scattering problem it is important to consider the extent of information available in noisy measurements. According to the definition introduced in Sect. 5.2 a super resolved image of $O(\mathbf{r})$, $R(\mathbf{r})$, is characterized by a spatial bandwidth $B > 4/\lambda$. Since the bandwidth of $R(\mathbf{r})$ will

be finite, a complete representation of $R(\mathbf{r})$ can be obtained by calculating $R(\mathbf{r})$ at the nodes of a regular grid where the nodes are spaced $1/B$ apart. If the object is contained in a cubic field of view with dimensions L, $R(\mathbf{r})$ is fully characterized by $N_R = (1 + LB)^3$ nodal values; here, we refer to N_R as the number of degrees of freedom (DOF) of the reconstruction. The N_R nodal values of $R(\mathbf{r})$ are obtained by solving the inverse scattering problem which uses as an input the discrete number of measurements contained in the matrix representation of T_∞. On the other hand, if the measurements are performed with an array with N transducers, the number of independent measurements after performing all the possible transmit-receive experiments is $M = N(N + 1)/2$, since some of the measurements are redundant by reciprocity. If the number of measurements is kept constant, the inverse problem becomes increasingly more ill-posed as we try to increase resolution—a larger number of DOF needs to be determined from the same number of measurements, M. This would suggest that to increase resolution whilst limiting ill-posedness one should increase the number of measurements, e.g. by increasing the number of transducer elements. However, in the presence of noise only a finite number of measurements are truly independent. To show this, let us consider an object contained in a ball of radius R_0 probed with an ideal spherical array of radius $R \gg R_0$ concentric with the ball. The scattered field measured by the array when one transducer is excited is

$$\psi^s(k\hat{\mathbf{r}}_0, r, \theta, \phi) = \sum_{n=0}^{\infty} \sum_{m=-n}^{n} a_{mn}(k\hat{\mathbf{r}}_0) \frac{h_n^{(1)}(kr)}{h_n^{(1)}(kR_0)} Y_n^m(\theta, \phi), \tag{5.30}$$

where the position of the receiving array element is expressed in spherical coordinates $\{r, \theta, \phi\}$. The coefficients $a_{mn}(k\hat{\mathbf{r}}_0)$ depend on the distribution of the scattered field over the sphere of radius R_0, vary with the illumination direction $\hat{\mathbf{r}}_0$, and encode information about the properties of the object. Even if the field does not contain evanescent waves, the coefficients a_{nm} can be non-zero for any order.[3] The functions $h_n^{(1)}$ are the spherical Hankel functions of the first kind and order n representing outgoing waves, $Y_n^m(\theta, \phi)$ are the spherical harmonics of order n and degree m [2]. By considering the asymptotic case $r \to \infty$, $h_n^{(1)}(kr) \approx (-i)^{n+1} \exp(ikr)/r$, the scattering amplitude can be written as

$$f(k\hat{\mathbf{r}}_0, \theta, \phi) = \sum_{n=0}^{\infty} \sum_{m=-n}^{n} (-i)^{n+1} \frac{a_{mn}(k\hat{\mathbf{r}}_0)}{h_n^{(1)}(kR_0)} Y_n^m(\theta, \phi). \tag{5.31}$$

Equation (5.31) shows that any order n of the scattered field on the sphere of radius R_0 radiates into the far field. All the spherical waves decay at the same rate, $1/r$; therefore, the possibility of measuring a particular a_{mn} coefficient depends on the *efficiency* with which the corresponding spherical wave radiates from the object.

[3] Consider, for instance, the spherical wave expansion of a plane wave [39].

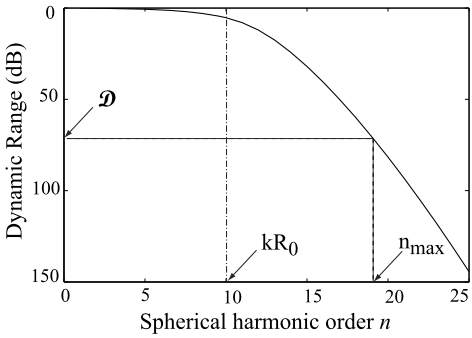

Fig. 5.8 Required dynamic range as a function of the order of the spherical harmonics to be detected when $kR_0 = 10$. If the dynamic range of the array system is $\mathscr{D}$, only harmonics up to n_{max} can be detected

This is determined by the factor $1/h_n^{(1)}(kR_0)$ in (5.31) which for $n \gg kR_0$ has the asymptotic form

$$\frac{1}{h_n^{(1)}(kR_0)} \approx \exp\left(-n \ln \frac{2n}{ekR_0}\right). \tag{5.32}$$

From this expression it is clear that for high order spherical waves $n \gg kR_0$, the radiation efficiency rapidly decays as the order n increases. In other words, the radiation mechanism leads to a greater attenuation of the higher order spherical waves, thus making their detection more challenging. In particular, there exists an upper bound to the maximum order, n_{max}, of the spherical waves that can be detected by an array system. This is dependent upon the noise characteristic and dynamic range of the array system. The latter refers to the capability of the detector to measure large signals, as well as small ones and is defined as $\mathscr{D} = 20\log(S_{max}/S_{min})$ where S_{min} is the amplitude of the smallest signal that can be detected.

Assuming that all the coefficients a_{mn} have comparable magnitude, the amplitude of the corresponding spherical waves reaching the detectors would only be dependent on their radiation efficiency which for $n > kR_0$ decays according to (5.32). As a result, for large orders ($n > kR_0$) the minimum dynamic range, $\mathscr{D}(n_{max})$, required to detect the orders up to n_{max} is

$$\mathscr{D}(n_{max}) \propto n_{max} \ln \frac{2n_{max}}{ekR_0}. \tag{5.33}$$

Figure 5.8 shows the dynamic range for increasing orders n when $kR_0 = 10$. For $n > kR_0$, the dynamic range increases rapidly with the order to be detected.

Since any detector will have a finite dynamic range, the wavefield is bandlimited by the maximum order that the system can sense, i.e. $B = n_{max}$ where B is the effective bandwidth. The spatial sampling criterion for a bandlimited field sampled over a spherical surface was given by Driscoll and Healy [14] and states that the wavefield can be represented by B^2 sampling points distributed over an equiangular grid of points (ϕ_i, θ_j), $i, j = 0, \ldots, 2B-1$, where $\phi_i = \pi i/2B$ and $\theta_j = \pi j/B$. Therefore, the number of sampling points is n_{max}^2; a larger number of detectors would yield redundant information. For detectors with low dynamic range, it can be

assumed that the maximum order is kR_0; therefore it is sufficient to sample the field with an array that contains

$$N \approx \begin{cases} k^2 R_0^2 & \text{in } 3D, \\ 2kR_0 & \text{in } 2D, \end{cases} \tag{5.34}$$

elements [5, 34]. By reciprocity, it can be shown that the number of independent illumination directions is also limited by the dynamic range of the array system and the number of independent scattering experiments is still $M = N(N+1)/2$, where N is limited by the effective bandwidth as discussed earlier.

So far it has been assumed that scattering experiments are performed at a single frequency. However, ultrasound imaging utilizes broadband signals from which it is possible to extract measurements at different frequencies by means of Fourier analysis. Therefore, it can be expected that measurements at different frequencies yield complementarity information. From an information theory perspective, this is understood in terms of information capacity of an imaging system. As an example, in an optical system such as a microscope, the number of DOF necessary to describe the wavefield in the image plane is

$$N_F = 2(1 + L_x B_x)(1 + L_y B_y)(1 + T B_T), \tag{5.35}$$

where B_x and B_y are the spatial bandwidth determined by the optics of the system, L_x and L_y are the widths of the rectangular image area in the x and y directions, respectively. T is the observation time and B_T is the temporal bandwidth of the signals, and the factor 2 accounts for two possible states of polarization. According to the invariance theorem [25] and in the absence of noise, one of the spatial bandwidths in (5.35) can be extended at the expense of the others—provided that N_F remains constant. The invariance theorem can be extended to the case of noisy measurements by introducing the concept of information capacity defined as

$$N_C = (1 + 2L_x B_x)(1 + 2L_y B_y)(1 + 2T B_T) \log(1 + \mathscr{S}/\mathscr{N}), \tag{5.36}$$

where $\mathscr{S}$ and $\mathscr{N}$ are the average signal and noise power. By applying the invariance theorem to N_C, it is possible to extend the spatial bandwidth at the expense of other parameters, including the noise level, provided that some *a priori* knowledge is available [12]. For the acoustic problem considered throughout this chapter it is realistic to assume that the object to be imaged is finite in size and that its properties do not vary with time. The latter assumption implies that the spatial bandwidths can be extended at the expense of the temporal bandwidth whilst maintaining the same SNR and leads to so-called time multiplexing [30]. We now observe that an ultrasonic array can be thought of as the image plane of a particular optical system without lenses, therefore the spatial bandwidths in (5.36) correspond to the spatial bandwidth B of the array (as determined by its characteristic dynamic range). As a result, in principle it is possible to increase B from B_T, or in other words to increase the number of independent data by using measurements at different frequencies.

5.6 Nonlinear Inverse Scattering

Since the introduction of regularization methods for ill-posed problems by Tikhonov, the nonlinear inverse scattering problem has attracted considerable interest across a number of disciplines. It is possible to discriminate between two main streams of research depending on whether the inversion is performed directly or by means of multiple iterations.

Iterative inverse scattering methods fall within the category of optimization methods and nonlinear filters. A variety of methods have been therefore proposed and the reader is referred to [8] for a general overview. Common to all iterative techniques is the use of a forward model that allows the output of scattering experiments to be predicted if the object function is known. The key idea of these methods is then to update the object function in the forward model until a cost function defined by the residual between the measured and predicted scattered field is minimized. The use of numerical solvers for the forward problem allows for accurate wave-matter interaction models to be used. In particular, it is possible to model multiple scattering effects that are central to achieving super resolution. Iterative techniques require an initial model for the object function to be assumed at the beginning of the iterations. This is a very critical step because if the model is not sufficiently close to the true object function, several iterations are required to achieve convergence and most importantly the iterations could converge to a local rather than the global minimum. To address this problem, frequency hopping techniques can be used. The key idea is to perform a frequency sweep, using the image produced at a lower frequency as the initial model for the next higher frequency. The premise is that at lower frequencies the resolution is lower and therefore the accuracy of the initial model is less critical. In addition, the use of multiple frequencies allows the limited bandwidth of the detection system to be expanded from the temporal one. This method has been implemented in geophysics [28] and optical and microwave imaging leading to the experimental super-resolved reconstructions in [6, 7].

Although iterative methods are extremely versatile they do not allow a direct representation of the link between measurements and reconstruction. Therefore, direct inverse scattering methods are considered in greater detail next.

5.6.1 Sampling Methods

Here, the nonlinear inverse problem is replaced with a linear integral equation of the first kind whilst still accounting for multiple scattering. However, while the iterative methods can reconstruct the object function, these methods can only reconstruct its support D, i.e. the shape of the object.

The sampling methods are based on the factorization of T_∞ and use two main results: 1) If the $H^\dagger$ operator is known, the shape of the object can be reconstructed exactly; 2) $H^\dagger$ can be characterized from T_∞ by means of the factorization in (5.16).

It can be shown [9] that if we select a point $\mathbf{z}$ in the image space and consider the far-field pattern of a point source at $\mathbf{z}$, $g_z = \exp(-ik\hat{\mathbf{r}} \cdot \mathbf{z})$, the solution to

$$H^{\dagger}|a\rangle = |g_z\rangle, \tag{5.37}$$

exists if and only if $\mathbf{z} \in D$. In other words, if $\mathbf{z}$ belongs to D there exists a continuous source distribution, $|a\rangle$ inside D that produces a far-field pattern equal to the pattern of a single point source at $\mathbf{z}$. On the other hand, such a source distribution does not exist if $\mathbf{z}$ is outside D. Therefore, the shape of the object is the locus of all points $\mathbf{z}$ for which (5.37) is solvable. In functional analysis this condition (solvability) is expressed by saying that g_z is in the range of the operator $H^{\dagger}$.

The second result is based on the fact that the range of $H^{\dagger}$ can be evaluated from T_{∞} without knowing $H^{\dagger}$. In particular, Kirsch [20, 21] has demonstrated that the range of $H^{\dagger}$ is equal to that of the operator $\sqrt{T_{\infty}}$. As a result, the condition of existence of the solution to (5.37) can be assessed by considering the equation

$$\sqrt{T_{\infty}}|a\rangle = |g_z\rangle. \tag{5.38}$$

The condition can be verified by using the singular value decomposition of T_{∞} $\{\mu_n, |p_n\rangle, |q_n\rangle\}$ where μ_n are the singular values (real) so that

$$T_{\infty}|p_n\rangle = \mu_n|q_n\rangle \quad \text{and} \quad T_{\infty}^{\dagger}|q_n\rangle = \mu_n|p_n\rangle. \tag{5.39}$$

According to Picard's theorem, the solution to $T_{\infty}|x\rangle = |y\rangle$ exists if and only if

$$\sum_{n=1}^{\infty} \frac{1}{\mu_n^2} \left|\langle y|q_n\rangle\right|^2 < \infty. \tag{5.40}$$

By Silvester's theorem the singular value decomposition of $\sqrt{T_{\infty}}$ is $\{\sqrt{\mu_n}, |p_n\rangle, |q_n\rangle\}$; therefore, the condition of existence in (5.37) via (5.40) leads to the central result of the sampling methods

$$\mathbf{z} \in D \quad \Longleftrightarrow \quad \sum_{n=1}^{\infty} \frac{1}{\mu_n} \left|\langle g_z|q_n\rangle\right|^2 < \infty, \tag{5.41}$$

which means that the series converges only inside the scatterer. An image of the shape of the object can be formed by plotting the functional

$$F(z) = \left(\sum_{n=1}^{\infty} \frac{1}{\mu_n} \left|\langle g_z|q_n\rangle\right|^2 \right)^{-1}, \tag{5.42}$$

which is non-zero inside the object and vanishes outside it. Equation (5.42) defines the Factorization Method (FM) [20]; slightly different expressions have been given for the Linear Sampling Method [8] and Time Reversal and MUSIC [26].

In the absence of noise, condition (5.41) leads to the reconstruction of the object shape with unlimited resolution since the condition is exact. However, in the presence of noise the resolution degrades. In fact, T_{∞} is a compact operator with a countable number of singular values accumulating at zero. In other words, when

$n \to \infty$, $\mu_n \to 0$ with the singular values following a similar trend to that shown in Fig. 5.8 with a cutoff order at $n = kR_0$ [10]. Therefore, as the order of the terms in the series in (5.41) increases, errors in the estimation of the singular functions $|q_n\rangle$ are amplified by the small singular values at the denominator.

The limited resolution of BF can also be explained in terms of the singular value decomposition of T_∞ [33]

$$R_{BF}(\mathbf{z}) = \langle g_z | T_\infty | g_z \rangle = \sum_{n=1}^{\infty} \mu_n \langle g_z | q_n \rangle \langle p_n | g_z \rangle. \tag{5.43}$$

Due to the rapid decay of the singular values of orders larger than kR_0 only the first $n \approx kR_0$ terms in the series contribute to R_{BF}. As a result, the information contained in the higher order singular functions is lost due to the small weight given by the corresponding singular values μ_n.

5.7 Experimental Examples

To illustrate how the inverse scattering approach is applied to experimental data this section outlines methods and results that have been reported in previous communications. We start with full-view experiments that have been performed with a prototype array system for breast ultrasound tomography (BUST) [15]. BUST produces tomographic slices of the breast using ultrasound rather than the ionizing radiation used in CT. The basic measurement setup is shown in Fig. 5.9(a). The patient lies prone on a table with a breast suspended in a water bath through an aperture in the table. A toroidal ultrasound array encircles the breast and scans it vertically from the chest wall to the nipple region. The array consists of 256 transducers, which are mounted on a 200 mm diameter ring, and can measure the multistatic matrix in around 0.1 seconds. A total of 65536 signals is recorded within this time and the data is stored in around 100 MBytes of RAM. Similar systems with more array elements have been built, e.g. [40].

The signals are wideband therefore, the $i-j$ entry of the multistatic matrix at a particular frequency ω, is obtained by performing the Fourier transform of the $i-j$ signal and selecting the complex value of the spectrum at the frequency ω. This leads to the amplitude and phase of the multistatic matrix shown in Fig. 5.9(b), (c) which have been measured for the complex three-dimensional breast phantom shown in the CT image in Fig. 5.9(d) at 750 kHz.

Figure 5.9(e) is the sound-speed map obtained from the data shown in Fig. 5.9(b), (c) with the inverse scattering approach introduced in [37]. The sound-speed reconstruction shows striking similarities with the CT image revealing, for instance, the irregular contour of the bright inclusion on the right. Some artifact outside the phantom boundary is due to aliasing caused by spatial undersampling.[4]

[4]For a phantom diameter of 120 mm and $\lambda = 2$ mm the sampling criterion given in (5.34) requires 377 sensors while the array has 256 only.

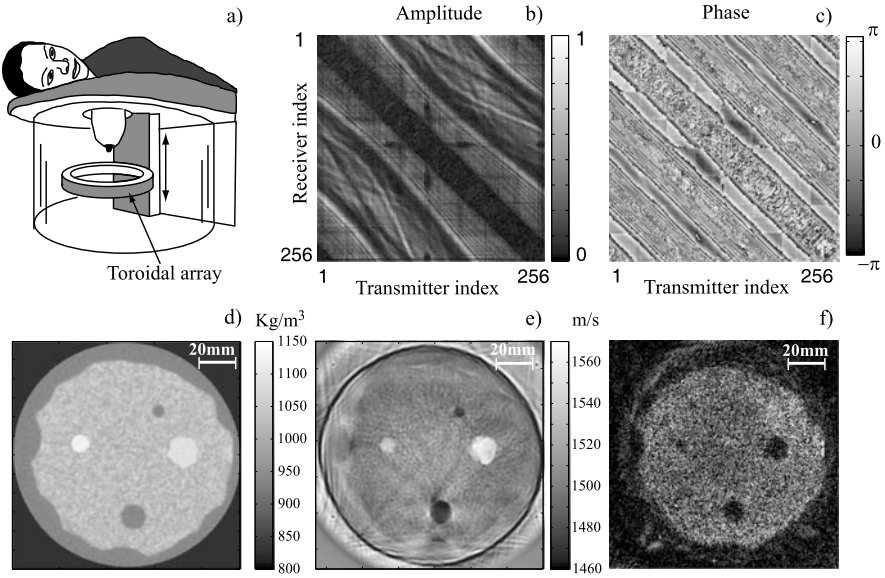

Fig. 5.9 Example of quantitative imaging under a full-view configuration. (**a**) Diagram of the BUST setup for cancer detection; (**b**) amplitude and (**c**) phase of the multistatic matrix at 750 kHz; (**e**) X-ray CT of a complex 3-D breast phantom showing density distribution; (**f**) sound-speed map obtained with the inverse scattering approach; (**g**) BF reconstruction representative of sonography

Another important characteristic of the reconstruction in Fig. 5.9(e) is that it is relatively free of speckle. Speckle is instead dominant in the reflection image shown in Fig. 5.9(f) which is obtained with BF [38]. Thanks to speckle contrast, the irregular outline of the glandular tissue and three of the four inclusions are revealed. At the same time, speckle masks the presence of the smallest inclusion, thus affecting the sensitivity of BF to the smaller lesions. These results show that current ultrasound array technology is sufficiently mature to achieve high resolution tomographic images of complex 3-D objects, comparable to those obtained with X-ray CT.

The super resolving capabilities of the inverse scattering approach can be demonstrated using the sampling methods. As an example Fig. 5.10 refers to an experiment performed with two 0.25 mm diameter nylon wires immersed in the water bath perpendicularly to the plane of the array (the experimental setup is detailed in [35]). Due to the small diameter of the wires compared to λ, the reflected signal is very weak as can be seen from Fig. 5.10(a). The reflections are buried in the background noise and the SNR is lower than 0 dB.

Figure 5.10(b) is a monochromatic image of the wires obtained at 1 MHz ($\lambda = 1.5$ mm) with the FM over an area $\lambda \times \lambda$ around the wires; the BF image is shown in Fig. 5.10(c) for comparison. While BF cannot resolve the two wires, FM clearly resolve them despite of their $\lambda/4$ spacing. Moreover, FM provides a well defined reconstruction of the shape of the scatterers revealing features which are even smaller than $\lambda/4$. Note that the diameter of the wires is $\lambda/6$. This is a re-

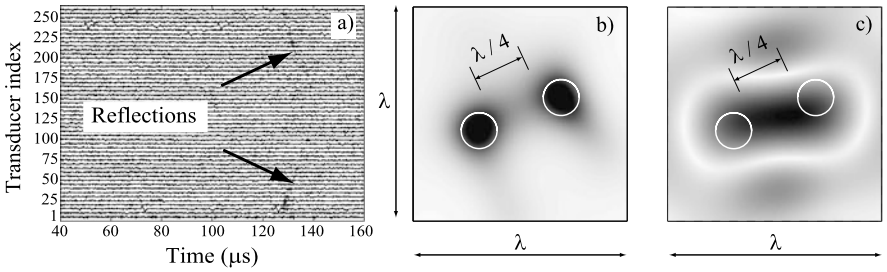

Fig. 5.10 (**a**) Pulse-echo signals showing the reflection (between 120 and 140 μs) from two 0.25 mm diameter nylon wires immersed in water; (**b**) monochromatic image obtained with the FM at 1 MHz ($\lambda = 1.5$ mm); (**c**) monochromatic image at 1 MHz obtained with BF

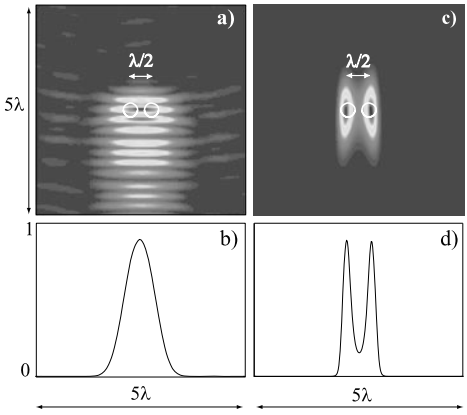

Fig. 5.11 Experimental demonstration of super resolution imaging under limited view. The images show an area of 15 × 15 mm centered in between two holes in a block of steel, the circles representing the position and actual size of the holes. (**a**) Image obtained with commercial BF technology; (**b**) cross-section of (**a**); (**c**) super resolved image obtained with the methods; (**d**) cross-section of (**c**)

markable result given the low SNR and the large distance between the wires and the sensors, ∼70λ.

Finally we consider a limited view configuration [Fig. 5.4(b)] in which a mild steel block is probed with a 32 element linear array. The block contains two parallel through-thickness holes 1 mm diameter, 1.5 mm apart, and at a 46 mm depth from the array (see, for more details, [31]). Figure 5.11(a) is a BF image of the two holes at 2 MHz obtained with a commercial BF system from Technology Design. The image reveals the presence of the scatterers but is not able to resolve them. This is better shown in Fig. 5.11(b) which is a cross section of Fig. 5.11(a) along the direction joining the two hole centers. The lack of resolution is predicted by the Rayleigh criterion [16] which, for the aperture of the array and the depth of the holes, predicts a minimum resolvable distance $d = 0.61\lambda/\sin(\theta) = 1.32\lambda$. Since $\lambda = 3$ mm, $d = 4$ mm which is well above the actual distance between the holes (1.5 mm).

Figures 5.11(c), (d) show the reconstructions obtained with the sampling methods at 2 MHz [31]. By contrast with BF the two holes are completely resolved and the image is very sharp as better seen in Fig. 5.11(d). The resolved distance is more than 2.5 times smaller the minimum resolvable distance predicted by the Rayleigh

criterion. This means that in order to achieve the same resolution with BF, a frequency of 5 MHz would be required, thus resulting in a much higher attenuation (in metals the attenuation due to grain scattering increases with the square of the frequency).

5.8 Conclusion

The detection of small features in complex background media is a recurrent problem across a number of application areas, medical diagnostics and non-destructive testing being two important examples. In this context, imaging techniques offer significant potential for achieving cost-effective detection through high sensitivity and limited false positive rate. However, to fully realize this potential, it is crucial to extract all the information encoded in the physical signals that are used to form the image. Current, off-the-shelf ultrasound imaging technology is underpinned by the beamforming (BF) method, which although very robust, discards a significant proportion of the information carried by ultrasonic signals. Therefore, BF reconstructs some of the geometrical features of the object but with a resolution limited by the wavelength of the probing signals according to the diffraction limit.

This chapter has introduced the notion that scattering measurements encode more information about the object's structure than BF can extract. In particular, the distortion experienced by the probing wavefield as it travels within the object and which is caused by multiple scattering, encodes information about the subwavelength features of the object in the far-field pattern of the scattered wave. To unlock this information, it is necessary to approach image formation from an inverse scattering perspective. By accounting for multiple scattering effects when solving the inverse problem, it is then possible to obtain subwavelength resolution beyond the diffraction limit. Moreover, the inverse scattering approach introduces a shift of paradigm from the structural imaging of BF that is limited to the geometrical features of an object, to quantitative imaging that reveals complementary information about the mechanical properties of the object.

The use of advanced inverse scattering techniques is now possible thanks to progress in computer power and advances in ultrasound array technology and the front-end electronics used to drive them. These technologies enable a fast and accurate mapping of the perturbation to the free propagation of ultrasound induced by the presence of an object. The dynamic range of the array system, which measures the ability of the system to detect large signals as well as small ones, is a limiting factor in measurement accuracy. Importantly, the maximum achievable resolution is dictated by the dynamic range of the detector and is not an intrinsic physical limitation of wave propagation and scattering mechanisms.

Acknowledgements The author is grateful to the UK Engineering and Physical Sciences Research Council (EPSRC) for supporting this work under grant EP/F00947X/1.

References

1. Abbott, J.G., Thurstone, F.L.: Acoustic speckle: Theory and experimental analysis. Ultrason. Imag. **1**, 303–324 (1979)
2. Arfken, G.B., Weber, H.J.: Mathematical Methods for Physicists. Academic Press, London (2001)
3. Baggeroer, A.B.: Sonar arrays and array processing. In: Thompson, D.O., Chimenti, D.E. (eds.) Rev. Prog. Quant. NDE, vol. 760, pp. 3–24 (2005)
4. Born, M., Wolf, E.: Principles of Optics. Cambridge University Press, Cambridge (1999)
5. Bucci, O.M., Insernia, T.: Electromagnetic inverse scattering: Retrievable information and measurement strategies. Radio Sci. **32**, 2123–2137 (1997)
6. Chaumet, P., Belkebir, K., Sentenac, A.: Experimental microwave imaging of three-dimensional targets with different inversion procedures. J. Appl. Phys. **106**, 034901 (2009)
7. Chen, F.C., Chew, W.C.: Experimental verification of super resolution in nonlinear inverse scattering. Appl. Phys. Lett. **72**, 3080–3082 (1998)
8. Colton, D., Coyle, J., Monk, P.: Recent developments in inverse acoustic scattering theory. SIAM Rev. **42**, 369–414 (2000)
9. Colton, D., Kress, R.: Inverse Acoustic and Electromagnetic Scattering Theory, vol. 93. Springer, Berlin (1992)
10. Colton, D., Kress, R.: Eigenvalues of the far field operator for the Helmholtz equation in an absorbing medium. SIAM J. Appl. Math. **55**, 1724–1735
11. Courjon, D.: Near-field Microscopy and Near-field Optics. Imperial College Press, London (2003)
12. Cox, I.J., Sheppard, C.J.R.: Information capacity and resolution in an optical system. J. Opt. Soc. Am. A **3**, 1152–1158 (1986)
13. Drinkwater, B., Wilcox, P.: Ultrasonic arrays for non-destructive evaluation: A review. NDT E Int. **39**, 525–541 (2006)
14. Driscoll, J.R., Healy, D.M.: Computing Fourier transforms and convolutions on the 2-sphere. Adv. Appl. Math. **15**, 202–250 (1994)
15. Duric, N., Poulo, L.P., et al.: Detection of breast cancer with ultrasound tomography: first results with the computed ultrasound risk evaluation (CURE) prototype. Med. Phys. **34**, 773–785 (2007)
16. Goodman, J.W.: Introduction to Fourier Optics. McGraw-Hill, New York (1996)
17. Huang, S., Ingber, D.E.: Cell Tension, Matrix Mechanics and Cancer Development. Cancer Cell **8**, 175–176 (2005)
18. Jackson, W.D.: Classical Electrodynamics. Wiley, New York (1999)
19. Kak, A.C., Slaney, M.: Principles of Computerized Tomographic Reconstruction. IEEE Press, New York (1998)
20. Kirsch, A.: Characterization of the shape of a scattering obstacle using the spectral data of the far field operator. Inverse Probl. **14**, 1489–1512 (1998)
21. Kirsch, A.: The MUSIC algorithm and the factorization method in inverse scattering theory for inhomogeneous media. Inverse Probl. **18**, 1025–1040 (2002)
22. Kolb, T.M., Lichy, J., Newhouse, J.H.: Comparison of the performance of screening mammography, physical examination, and breast us and evaluation of factors that influence them: an analysis of 27,825 patient evaluation. Radiology **225**, 165–175 (2002)
23. Lavarello, R.J., Oelze, M.L.: Density imaging using inverse scattering. J. Acoust. Soc. Am. **125**, 793–802 (2009)
24. Lin, F.C., Fiddy, A.: The Born-Rytov controversy: I. Comparing analytical and approximate expressions for the one-dimensional deterministic case. J. Opt. Soc. Am. A **9**, 1102–1110 (1992)
25. Lukosz, W.: Optical systems with resolving powers exceeding the classical limit. J. Opt. Soc. Am. **56**, 932–941 (1966)
26. Marengo, E.A., Gruber, F.K., Simonetti, F.: Time-reversal music imaging of extended targets. IEEE Trans. Image Process. **16**, 1967–1984 (2007)

27. Morse, P.M., Ingard, K.U.: Theoretical Acoustics. McGraw-Hill, New York (1968)
28. Pratt, G.R.: Seismic waveform inversion in the frequency domain, part 1: Theory and verification in a physical scale model. Geophysics **64**, 888–901 (1999)
29. Sentenac, A., Guerin, C.A., Chaumet, P.C., et al.: Influence of multiple scattering on the resolution of an imaging system: A Cramer-Rao analysis. Opt. Express **15**, 1340–1347 (2007)
30. Shemer, A., Mendlovic, D., Zalevsky, Z., et al.: Superresolving optical system with time multiplexing and computer encoding. Appl. Opt. **38**, 7245–7251 (1999)
31. Simonetti, F.: Localization of point-like scatterers in solids with subwavelength resolution. Appl. Phys. Lett. **89**, 094105 (2006)
32. Simonetti, F.: Multiple scattering: The key to unravel the subwavelength world from the far-field pattern of a scattered wave. Phys. Rev. E **73**, 036619 (2006)
33. Simonetti, F., Huang, L.: From beamforming to diffraction tomography. J. Appl. Phys. **103**, 103110 (2008)
34. Simonetti, F., Huang, L., Duric, N.: On the sampling of the far-field operator with a circular ring array. J. Appl. Phys. **101**, 083103 (2007)
35. Simonetti, F., Huang, L., Duric, N., Rama, O.: Imaging beyond the Born approximation: An experimental investigation with an ultrasonic ring array. Phys. Rev. E **76**, 036601 (2007)
36. Simonetti, F.: Illustration of the role of multiple scattering in subwavelength imaging from far-field measurements. J. Opt. Soc. Am. A **25**, 292–303 (2008)
37. Simonetti, F., Huang, L., Duric, N.: A multiscale approach to diffraction tomography of complex three-dimensional objects. Appl. Phys. Lett. **95**, 067904 (2009)
38. Simonetti, F., Huang, L., Duric, N., Littrup, P.: Diffraction and coherence in breast ultrasound tomography: A study with a toroidal array. Med. Phys. **36**, 2955–2965 (2009)
39. Stratton, J.A.: Electromagnetic Theory. McGraw-Hill, New York (1941)
40. Waag, R.C., Fedewa, R.J.: A ring transducer system for medical ultrasound research. IEEE Trans. Ultrason. Ferroelectr. Freq. Control **53**, 1707–1718 (2006)
41. Waterman, P.C.: New formulation of acoustic scattering. J. Acoust. Soc. Am. **45**, 1417–1429 (1968)
42. Wells, P.N.T.: Ultrasonic imaging of the human body. Rep. Prog. Phys. **62**, 671–722 (1999)
43. Zweig, M.H., Campbell, G.: Receiver-operating characteristics (ROC) plots: A fundamental evaluation tool in clinical medicine. Clin. Chem. **39**, 561–577 (1993)

Chapter 6
Subwavelength Focussing in Metamaterials Using Far Field Time Reversal

Mathias Fink, Fabrice Lemoult, Julien de Rosny, Arnaud Tourin, and Geoffroy Lerosey

Abstract Time reversal is a physical concept that allows focussing of waves both spatially and temporally regardless of the complexity of the propagation medium. Time reversal mirrors have been demonstrated first in acoustics, then with electromagnetic waves, and are being intensively studied in many fields ranging from underwater communications to sensing.

In this chapter we review the principles of time reversal and in particular its ability to focus waves in complex media. We show that this focussing effect depends on the complexity of the propagation medium rather than on the time reversal mirror itself. A modal approach is utilized to explain the results and grasp the physical mechanisms underlying the concept.

A particular focus is given to the possibility of overcoming the diffraction barrier from the far field using time reversal. With this aim, we return to the first proof of concept of this original approach. Those results are explained in terms of the coherent excitation of subwavelength modes. In particular, we show that a finite size medium consisting of coupled subwavelength resonators, which we call a resonant metalens, supports modes which radiate spatial information of the near field of a source efficiently in the far field. We show that such a process, due to reversibility, enables us to beat the diffraction limit using far field time reversal, and especially that this result occurs due to the inherent broadband nature of time reversal. We then generalize the concept to other types of media, and finally show experimentally that it is also valid for acoustic waves, demonstrating deep subwavelength focal spots obtained within an array of soda cans.

6.1 Introduction

The reversibility of the equations governing the propagation of waves, whether acoustic or electromagnetic, is of major interest in many fields of wave physics. This property is quite intriguing from a fundamental point of view and has also led

M. Fink · F. Lemoult · J. de Rosny · A. Tourin · G. Lerosey (✉)
Institut Langevin, ESPCI ParisTech – CNRS, 10 rue Vauquelin, 75005 Paris, France
e-mail: geoffroy.lerosey@espci.fr

R.V. Craster, S. Guenneau (eds.), *Acoustic Metamaterials*,
Springer Series in Materials Science 166, DOI 10.1007/978-94-007-4813-2_6,

to many fascinating discoveries within the last years. Among them, Time Reversal (TR) has been a major subject of studies in various fields such as ultrasound acoustics, seismology, microwave or more recently in the optical domain.

In a typical TR experiment, a source emits a short pulse in a medium, which generates a wavefield that propagates away from it. Then this wavefield is measured at a set of locations by an array of sensors, the so-called time reversal mirror (TRM). The measured signals are digitized, memorized and time reversed, that is, flipped in time. This first step, called the "learning step", results in the knowledge of a collection of impulse responses between the source and the TRM, which are broadband Green's functions. In the second step, the time reversal one, these time reversed signals are sent back into the medium by the sensors, which results in a spatio-temporal focussing of the generated wavefield onto the initial source position, and at a specific time named the "collapse time" [10, 11, 18].

It has been shown that the temporal focussing of the wave depends on the medium, as well as on the bandwidth used, and the number of sensors constituting the TRM [10–12]. From a spatial point of view, in a homogeneous medium, time reversed waves converge toward the focal point on a spot whose width is limited by the numerical aperture of the TRM, similar to the way conventional lenses focus light [18, 22]. In heterogeneous media, however, TRM behave very differently than regular lenses, and it has been proved that the numerical aperture of the TRM does not play any role when the complexity of the medium is increased [10]. In the extreme case of TR in a chaotic closed cavity, it has even been shown that a single channel TRM can focus waves on spots as small as half a wavelength, i.e. the diffraction limit, provided that broadband signals are used [16].

TR, which was first demonstrated with ultrasound, has been studied quite intensively in acoustics, and has led to interesting concepts such as TR underwater communications [28], interactive objects [25] or acoustic bazookas [20]. Then, the concept was transposed to the electromagnetic waves, in the microwave range, and it was shown that TR experiments can be done at very high frequency using modulated signals, since in this case only the low frequency complex envelope of the signals has to be time reversed [35, 37]. Since then, TR of electromagnetic waves has been studied in various areas such as sensing [9, 62], wireless communications [36, 48, 53, 56] or medical imaging and therapy [24, 27].

One of the most astonishing results obtained using TR of electromagnetic waves is the fact that one can break the diffraction barrier using a TRM and a microstructured material, or in other words, that one can focus electromagnetic waves on deep subwavelength spots and from the far-field, using TR [15, 21, 38]. This opens up very promising avenues in various fields such as telecommunications [48], imaging [27], or therapy [24] in microwaves, but also lithography and sensing at higher frequencies [2, 50].

The goal of this chapter is to review the most recent works dealing with subwavelength focussing using TR, to explain this concept, generalize this approach and propose new media for this purpose in light of the proposed theory. We will first explain the basic principles of TR of waves, and in particular we will show that

the broadband nature of TR experiments is of fundamental interest, hence distinguishing it from phase conjugation methods. Second, we will focus on the specific case of electromagnetic waves and demonstrate analytically the outcome of a TR focussing experiment. We will present the original proof of concept that introduced the possibility of focussing electromagnetic waves on a deep subwavelength scale inside a random collection of metallic scatterers using far-field TR. A link will be made with the theory of TR focussing in Sect. 6.4, and a study will be proposed that explains those results in terms of subwavelength Bloch modes in periodic arrays of subwavelength resonators called resonant metalenses; we will also generalize the concept to other types of media. Finally, in Sect. 6.5 we demonstrate the great generality of the concept through translation to acoustic waves; using time reversal we obtain focal spots as thin as $1/25$th of a wavelength, for sound waves in the audible range, using a simple array of soda cans.

6.2 Basic Principles of Time Reversal Focussing

The principle of TR is based on the fact that the equations governing the propagation of waves, neglecting absorption, contain only derivatives of second order with respect to the time variable. This property is known as reversibility. It implies that changing the time variable t into a $-t$ for a given field which is solution of the wave equation, produces another field which is also solution of the same equation. In other words, if within a given medium there exists a solution of the wave equation denoted $S(t)$, then another dual solution, namely the time reversed one $S(-t)$, necessarily exists as well. For instance if one is able to record the entire field created by a diverging source placed inside a reversible medium, time reversing and reemitting the latter generates a wavefield that converges toward the initial source. Such an ideal TR experiment, however, requires the knowledge of the field throughout the medium, which is impossible in most practical environments. In practice, TR is made possible thanks to the Helmholtz-Kirchoff integral theorem. The latter states that a wavefield and its normal derivative known on the boundaries of a closed surface holds the knowledge of the field inside the whole volume contained by the surface. Hence, a more realistic TR experiment can be imagined as follows (Fig. 6.1); a source generates a brief pulse inside a heterogeneous medium that is surrounded by sensors which record the corresponding time varying fields until all the energy has exited the closed surface. In a second step, the sensors play the recorded fields in a reversed chronology, which generates the time reversed wavefield on the boundary of the closed surface.

This conceptual TR experiment, named the "Time Reversal Cavity", has been theoretically studied in acoustics [7, 19]. Using a monochromatic approach, it has been shown that it produces, at a point r and for a given frequency, a field that is proportional to the imaginary part of the Green's function between the initial source point r_0 and r.

$$\phi_{TR}(r,\omega) \propto \mathrm{Im}\big\{G(\omega, r_0, r)\big\}. \tag{6.1}$$

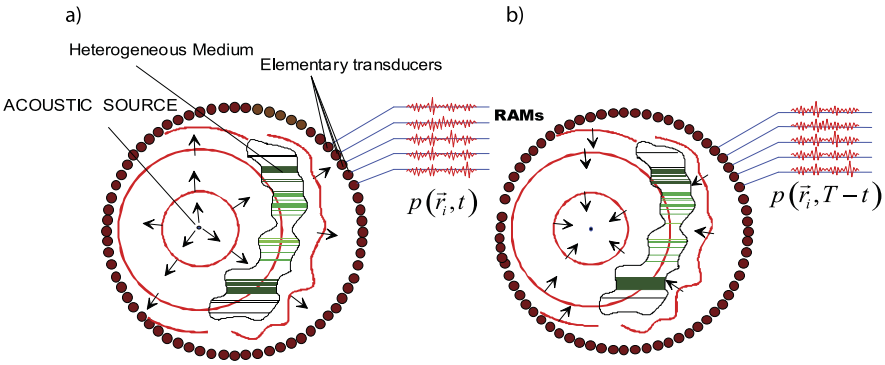

Fig. 6.1 (**a**) Recording step: A closed surface is filled with transducer elements. A point like source generates a wave front which is distorted by heterogeneities. The distorted pressure field is recorded on the cavity elements. (**b**) Time-reversed or reconstruction step: The recorded signals are time-reversed and reemitted by the cavity elements. The time-reversed pressure field back-propagates and refocuses exactly on the initial source

Covering a whole surface with a collection of sensors respecting the Nyquist criterion, though, requires an enormous amount of electronics and is evidently not suitable for an experiment. In practice, closed TRMs are difficult to realize and the TR operation is usually performed on a limited angular area, thus apparently limiting the focussing quality. A TRM consists typically of a small number of elements, or time reversal channels. The major interest of TRM, compared to classical focussing devices (lenses and beam forming) is certainly the relation between the medium complexity and the size of the focal spot. A TRM acts as an antenna that uses complex environments to appear wider than it is, resulting in a refocussing quality that does not depend on the TRM aperture.

The reference experiment using a small aperture TRM is the following [10–12]; a multiple scattering medium is placed between a point like sensor and a TRM which are separated by a distance much larger than a wavelength (Fig. 6.2(a)). A short pulse is emitted by the point source, and the set of impulse responses from this point to the array of sensors constituting the TRM is acquired. Those responses are then flipped in time and sent back by the TRM now acting as a source. It is then possible to scan the field produced by this TR focussing by translating the point source sensor parallel to the output surface of the multiple scattering media. In doing so, one obtains a focal spot whose width is not limited by the numerical aperture of the TRM, but rather by that of the multiple scattering medium, which can be much larger. The temporal and spatial signal to noise ratios of such focussing experiments have been shown to depend linearly on the total number of degrees of freedom of the medium, i.e. the number of uncorrelated sensors in the array times the number of uncorrelated frequency in the bandwidth [10, 11]. Very interestingly, the optics community has recently realized that such experiments can be performed in the visible range, by means of spatial light modulators. Focussing well below the Rayleigh limit of conventional lenses has been demonstrated by inserting a multiple

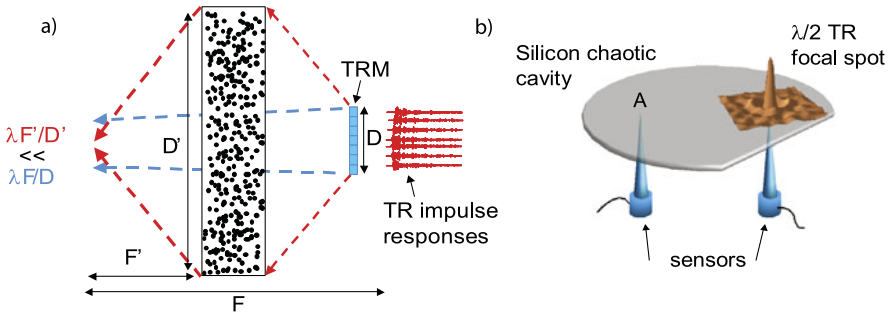

Fig. 6.2 (**a**) Typical focussing experiment using TR. A multiple scattering medium is placed between the TRM and a point like sensor. The size of the focal spot obtained with TR is no longer limited by the aperture of the TRM but rather by that of the multiple scattering medium. (**b**) Simplified view of a single channel TR focussing experiment realized in a silicon cavity. The field produced by TR at the collapse time is scanned using a heterodyne interferometer, and its map is superimposed on the cavity: A diffraction limited spot is obtained using only one emitter

scattering medium (a layer of paint) between a SLM and a CCD camera using this concept [1, 26, 45, 46, 57, 58].

What happens when the number of sensors of the TRM is reduced down to a single one? Regarding the optical experiments mentioned earlier, the answer is quite obvious: a single laser source that is shone through a multiple scattering medium gives rise to a so-called speckle pattern, i.e. a random interference pattern. It is clear that no focussing can occur whatsoever in this case since changing the phase of this single source only changes the phase of the output speckle, hence precluding any focussing effect. The solution to this problem lies in the use of interference between statistically independent speckles, or equivalently between speckle patterns at frequencies which are uncorrelated. This is where TR strongly differs from its monochromatic ancestor, namely, phase conjugation. In fact, our students in acoustics see this everyday experiment during their practical classes: a single sensor is used as the TRM and a multiple scattering medium is placed between the latter and a movable wavelength wide sensor. After TR, they can observe that the waves are tightly focused on the original source position with a spot size limited by the diffraction limit when the numerical aperture of the multiple scattering medium is larger than unity.

This very simple yet fascinating experiment is easier to understand considering the setup of Fig. 6.2(b) taken from [16]. An aluminium cone coupled to a transducer generates waves at one point (A) of a non-symmetrical and ergodic silicon cavity. A second transducer is used as a receiver. The central frequency f_0 of the transducers is set to 1 MHz and their relative bandwidth to 100 % ($\Delta f = 1$ MHz). The source is considered point-like and isotropic because the cone tip is much smaller than the central wavelength. A heterodyne laser interferometer measures the displacement field as a function of time at different points on the cavity, resulting in a spatio-temporal mapping of the field propagating in the cavity. In the learning step, the impulse response is acquired between points A and B, digitized and time reversed.

Then the time reversed signal is sent from point A and the field generated by TR is scanned using the interferometer around point B. At the collapse time, the field, represented in the figure, is focused onto a spot whose width is about half a wavelength, limited by the diffraction limit. In other words, thanks to TR, in this cavity, it is possible to reach the diffraction limit using a single sensor.

This can actually be explained through a simple physical picture. Such a cavity can indeed be described in terms of modes, which are eigenmodes of the propagation and whose eigenvalues are their resonant frequencies. When a point source emits a short pulse in this medium (at point A), it excites all the modes that are non-zero at this location, each one at its resonant frequency, analogous to when a guitar cord is slapped. Measuring the field at point B then simply consists of acquiring the phases and amplitudes of the relative eigenmodes of the cavity at this specific position, at every resonance frequency, and with the condition that all those modes are in phase at point A because of the pulsed excitation. The TR focussing naturally comes out considering that time reversing an impulse response is equivalent to phase conjugating the signal at every frequency of the bandwidth: $S(t)$ to $S(-t) \Leftrightarrow S(\omega)$ to $S^*(\omega)$. Indeed, sending the time reversed impulse response from point A, cancels the phase of each eigenmode at point B. This, in turn, insures that all eigenmodes within the bandwidth interfere constructively at this point and at a specific time, the collapse time. From this very simple approach, one can also infer the signal to noise ratio of this focussing operation. This ratio is defined as the TR peak energy divided by the standard deviation of the field measured away from B and at a time different than the collapse one; at this specific time and at point B, all the modes interfere coherently while everywhere else and at any other time they add up incoherently: the SNR roughly equals the number of eigenmodes of the cavity within the bandwidth. As expected, the focal spot width is given by the average correlation length of the modes, around half of the central wavelength.

At this point it is worth making the link between this modal approach and the results of the time reversal cavity [7] linking the TR produced field to the imaginary part of the Green's functions of the medium. This result, independent of the complexity of the medium, was a monochromatic one which can easily be integrated over the bandwidth in order to obtain the spatially varying field after TR and at the collapse time:

$$\phi_{TR}(r, t = 0) \propto \int_{Bandwidth} \mathrm{Im}\big\{G(\omega, r_0, r)\big\}\, d\omega. \tag{6.2}$$

Within a cavity or a complex medium where a modal analysis can be used, and if there is no degenerated modes (which is the case for a high enough quality factor chaotic cavity), Green's functions are proportional to the eigenmodes. Hence integrating (6.1) is formally equivalent to adding coherently at point r_0 the eigenmodes of the cavity that resonate in the bandwidth. We will see in the next part of the paper that these principles also hold for electromagnetic waves, notwithstanding the polarization of photons which implies the use of dyadic Green's functions.

6.3 Time Reversal of Electromagnetic Waves and First Evidence of Far Field Subwavelength Focussing

6.3.1 Basic Principles

Electromagnetic waves differ from acoustic ones since they are polarized, like elastic waves. Therefore one has to take into account the orientation of the sources. In a typical time reversal scheme, a dipole source oriented along a given axis emits a short pulse. The wavefield propagates and is recorded with one antenna or a set of antennas, namely, the time reversal mirror. Second, the recorded signals are digitized, flipped in time and transmitted back by the same set of antennas. An ideal TRM, "an electromagnetic time reversal cavity" should cover a closed surface that totally surrounds the source, should respect Nyquist criterion, and should also be able to measure the three polarizations of the waves. Such a cavity, from the Helmholtz-Kirchoff theorem, would then give the electromagnetic field inside the whole volume contained within the closed surface. Because the equations governing the propagation of electromagnetic waves are also reversible, if one could realize such a time reversal experiment, the generated wavefield should converge back to the initial source, just as for acoustic waves as seen in the previous part.

The theory of such an electromagnetic time reversal cavity has been done recently. When considering electromagnetic waves, the Green's functions have to be replaced by dyadic Green's functions. For a narrowband signal of oscillating pulsation ω, the time reversal focussing on position r_0 is equivalent to phase conjugation, and it can be demonstrated, starting from the Lorentz reciprocity theorem, that the electric field generated at position r is simply [5, 34]:

$$E_{TR}(r,\omega) = -2i\mu_0\omega^2 \,\mathrm{Im}\left\{\overleftrightarrow{G}(r_0,r,\omega)\right\}.P^*. \tag{6.3}$$

Where μ_0 is the permeability of vacuum, the tensor $\overleftrightarrow{G}$ stands for the dyadic Green's function of the medium and P represents the initial vector dipole source. When the dyadic Green's function is the free space one, it results in a sinc function: the focal spot is diffraction limited to $\lambda/2$ as shown experimentally in [37]. Only when the time reversal mirror is placed in the near field of the initial source do the Green's functions take into account the evanescent component of the field generated by the source, which can lead to smaller focal spots [14]. Note that the field amplitude at the focal point is proportional to the imaginary part of the Green's function which is itself proportional to the so-called local density of states [42] (LDOS).

Again, considering that time reversal uses broadband excitation, the resulting field takes advantage of the frequency diversity. For an excitation with a flat bandwidth, all frequencies add up in phase at a given time, the collapse time ($t = 0$). At this specific time, the time reversed field is [21]:

$$E_{TR}(r,t=0) \propto \mu_0\omega^2 \int_{Bandwidth} \mathrm{Im}\left\{\overleftrightarrow{G}(r_0,r,\omega)\right\}.P^*\,d\omega. \tag{6.4}$$

At this stage, two remarks can be made. The first one is that compared to scalar waves, polarized waves offer more degrees of freedom using TR focussing: the polarization is conserved in a TR experiment. This can be of interest when trying to focus energy or in wireless communications issues, for instance for multiple-input multiple-output communications (MIMO). The second thing that one can notice is that for electromagnetic waves as well, the TR field created at the collapse time in a medium where a modal analysis can be done, can simply be understood as a sum of all the modes within the bandwidth interfering coherently at the original source position.

6.3.2 Experimental Demonstration of Subwavelength Focussing Using Far Field TR

Having the ability to focus waves on dimensions much smaller than the wavelength and from the far-field, i.e. while controlling the field at the scale of the wavelength, has always been a major field of study. Indeed, such a concept has many potential applications in various fields such as sensing, lithography, wireless communications using MIMO compact antennas or more generally in any domain where energy has to be deposited onto narrow focal spots. There exists, however, a very solid barrier that prevents waves from being focused on a subwavelength scale in homogeneous media. The latter, known as the diffraction barrier or the Abbe's limit, can be explained physically as follows:

A source field placed in a given medium, whether extended or point-like, possesses a spatial profile that can vary much faster than the wavelength at which it radiates. For instance, this can occur for a small dipole, whose near field contains fast varying components that decay as the distance cubed, or of a rough surface illuminated by a plane wave which scatters the incoming wavevector into many others, some of them being much larger than the wavenumber in the medium k_0. If one wants to study the propagation of any wavefield in a given direction, one convenient way to do it is to perform a Fourier transform of this field on a plane perpendicular (transverse) to the considered propagation direction. The spatial components of the source field which vary faster than the wavelength have, in this transverse plane, wavevectors k_t whose norm exceed the wavenumber in the medium k_0. Since the norm of any wavevector must equal k_0, those subwavelength spatial variations must present a purely imaginary wavevector k_p in the direction of propagation ($k_p = i\sqrt{k_t^2 - k_0^2}$ for $k_t^2 > k_0^2$). Those waves are evanescent waves and, due to their imaginary propagation constant, they decay exponentially from the source in the considered direction of propagation. This explains why, from the far-field, it seems impossible to focus onto subwavelength spots: all the waves that carry spatial information smaller than the wavelength are lost during propagation. Goodman describes this diffraction limit in other words: he characterizes the propagation from one plane to another as a spatial low pass filter whose cutoff wavelength is that of the waves in the medium [22].

One way though, in order to circumvent this diffraction limit, is to make use of so called near field techniques. The idea of near field imaging dates back to the beginning of the 20th century with a proposal that Synge made during an epistolatory conversation with Einstein about ways to beat Abbe's limit [54]. The proposed method consists of illuminating a very small portion of an object using an opaque screen perforated with a deep subwavelength hole. The point like source is then scattered by the object into a wave that radiates in free space, hence carrying local and subwavelength information about the object. Since this proposal, the concept has been declined in many different ways, and has led to the development of near field scanning optical microscopes, that are based on aperture or aperture-less probes, and whose principles are sensibly identical [4, 39, 44, 63]. Basically, the probe, for instance the elongated tip of an optical fiber, is brought in the very near field of the object to be imaged. This very subwavelength apex scatters locally the evanescent field that is present at the surface of the object to be imaged, some of it being scattered as propagating waves. A conventional imaging system collects the light radiated by the probe, and the information of the object's near field at the specific position of the tip is then extracted. Scanning the tip over the object point by point allows one to reconstruct the near field pattern of the object, and resolutions well below the diffraction limit have been reached using such microscopes.

Such methods, however, appear quite limited from a focussing point of view. Indeed, while dealing with focussing issues, the aim is to be able to focus a wave on several points without the need of any mechanical moving stage. The tip used in near field scanning methods being point like, focussing onto such an object would be quite useless since it would not enable positional control over the focussing without a mechanical part, not even mentioning the issue of multiple foci. Nevertheless this method has inspired us, since it makes use of the fascinating concept of evanescent to propagating wave conversion that is necessary in order to focus waves on a subwavelength scale and from the far field. The concept that we have imagined is the following: suppose that we construct a medium that is able to convert the evanescent field created by a source into propagating waves that can be recorded in the far field. Then, using TR from the far field, because the wave equations are reversible, we should be able to focus back the wave on its initial position, and since the evanescent to propagating wave conversion is reciprocal [6], we should be able to obtain a subwavelength resolved focal spot. If we place a bunch of those sources at a distance much smaller than the wavelength in the fabricated medium and learn the impulse response from those sources to a TRM, then we should be able to focus independently on each of them, hence demonstrating that the diffraction limit is overcome.

This is exactly the idea we exploit here to create focal spots much thinner than the wavelength. In a recent experiment [38] we consider 8 possible focussing points placed in a strong reverberating chamber (Fig. 6.3(a)). Eight electromagnetic sources are placed at these 8 locations to be used in the learning step of the TR process. These sources consist of very short wire antennas (2 mm long, reactive only). The experiments are performed at a central frequency of 2.45 GHz (i.e., $\lambda = 12$ cm),

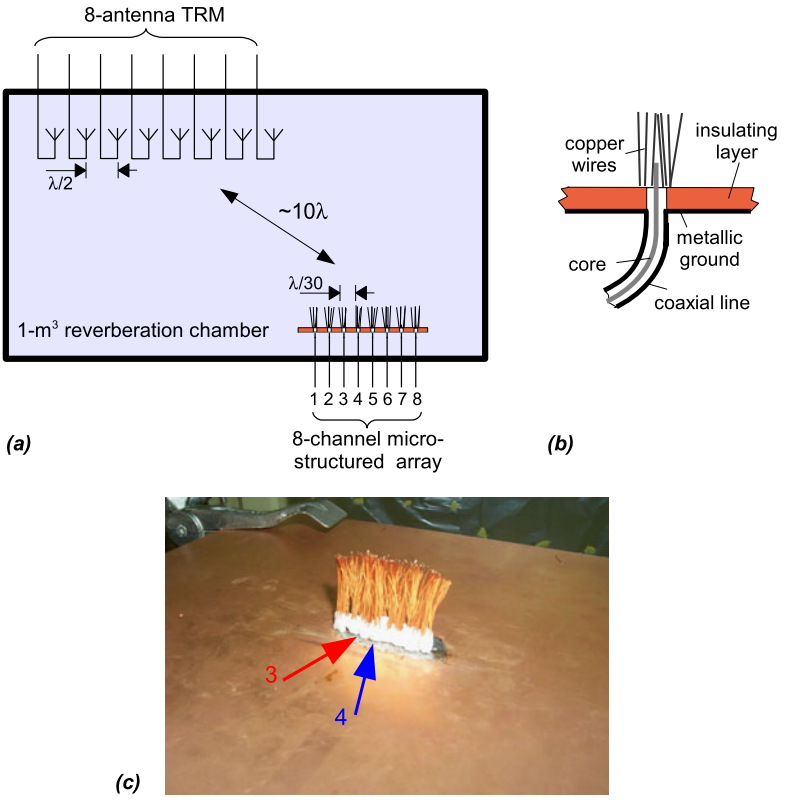

Fig. 6.3 (**a**) A Time Reversal Mirror (TRM) is placed in a 1 m^3 reverberating chamber. Ten wavelengths away from the TRM is placed a subwavelength receiving array. (**b**) Details of one microstructured antenna: a 2 mm long reactive antenna surrounded by a random collection of 3 cm long copper wires. (**c**) Photo of the 8-element subwavelength array. Antennas #3 and #4 are indicated by the *arrows*. Reproduced from [38] with permission from AAAS

with a bandwidth of 100 MHz. The pitch between these sources is $\lambda/30$. These eight antennas form an array which will be referred to as the receiving array. Each antenna in this array is surrounded by a microstructure consisting here of a random distribution of almost parallel thin copper wires that are used to scatter the evanescent field into propagating waves (Fig. 6.3(b)). The mean distance between the thin copper wires is of the order of 1 mm and their length around 3 cm. A TRM made of eight commercial dipolar antennas is placed in the far-field, ten wavelengths apart from the receiving array. The set "reverberant chamber/TRM" acts as a virtual far-field time-reversal cavity. When the antenna marked #3 in Fig. 6.3(c) sends a short electromagnetic pulse (10 ns), the 8 signals received at the TRM are much longer than the initial pulse due to strong reverberation in the chamber (typically 500 ns). As an example the signal received at one of the antennas of the TRM is shown in Fig. 6.4(a). When the antenna marked #4 is now used as a source, it is remarkable to point out that now the signal received at the same antenna in the TRM (shown in

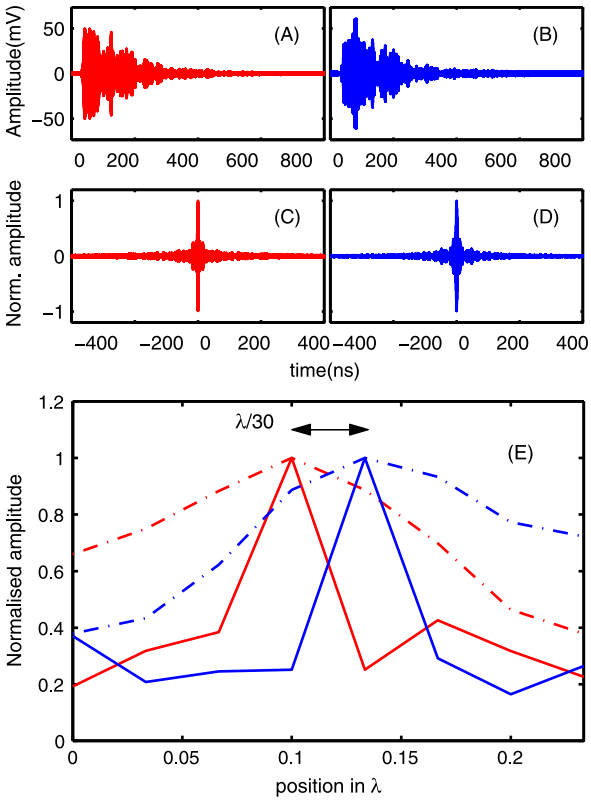

Fig. 6.4 In (**a**) (respectively (**b**)) signal received at one antenna of the TRM when a 10-ns pulse is sent from antenna #3 (resp. #4). The signals in (**a**) and (**b**) look significantly different although antenna #3 and antenna #4 are distant from $\lambda/30$. In (**c**) (resp. (**d**)) is shown the time compression obtained at antenna #3 (resp. #4) when the eight signals coming from antenna #3 (resp. antenna #4) are time-reversed and sent back from the TRM. In (**e**) are shown the focussing spots obtained around antenna #3 and #4. Their width is $\lambda/30$. Thus antenna #3 and #4 can be addressed independently. Reproduced from [38] with permission from AAAS

Fig. 6.4(b)) looks significantly different although sources #3 and #4 are $\lambda/30$ apart from each other.

When these signals are time-reversed and transmitted back, the resulting waves converge respectively to antenna #3 and #4 where they recreate pulses as short as the initial ones (Figs. 6.4(c) and 6.4(d)). Measuring the signal received at the other antennas of the receiving array gives access to the spatial focussing around antennas #3 and #4 (Fig. 6.4(e)). The remarkable result is that the two antennas can be addressed independently since the focussing spots created around them have a size much smaller than the wavelength (here typically $\lambda/30$): the diffraction limit is overcome although the focussing points are in the far-field of the TRM.

In this first very convincing experimental demonstration, our interpretation was that the high spatial frequency components of the field are created upon scattering off the disordered structure. Reciprocity ensures that the time-reversed scattering process creates a subwavelength focus around the source location [6]. In other words, the initial evanescent waves created around the initial wire are converted into propagating waves by the random distribution of wires. In the time-reversed step, these propagating waves are played back from the far field in a reversed chronology. Spatial reciprocity and reversibility ensure that each propagating wave interacts with

the random distribution of wires to recreate the initial evanescent waves around the focus.

However, many points are still obscure concerning the physical interpretation of this experiment. Indeed, the mechanism of the conversion from evanescent to propagating waves is totally opaque, and hence it hampers any generalization of the phenomenon to different systems, with different frequencies or types of waves. Furthermore, there remain a lot of open questions at this stage. The first one could be about the role of the bandwidth: in other words, can this experiment be realized using monochromatic waves? Is such a medium efficient for the purpose of subwavelength focussing, or can we find better ones? Can waves be focused on subwavelength scales without limit, as it appears in this experiment, or are there certain factors that will set a lower bound to the width of the TR focal spots? What is the link between this approach and the Green's function relation of (6.2) and (6.4)?

The aims of the next sections are to explore those questions and give answers through first, a deep analysis of a simplified version of the medium used here, and next a generalization of the concept in light of the developed principles.

6.4 Far Field Subwavelength Focussing Using Time Reversal in an Array of Resonant Wires

One point that was not obvious in the experiments of [38], using the random collection of metallic scatterers creating the micro structured medium, was that the wires were all approximately of equal length. Considering this microstructured medium through this new prism, they can be visualized as an array of resonant wires. Indeed, they are all around a quarter wavelength long, and placed on top of a copper ground plane (i.e. resonant monopole). Such an array of resonators should behave as a matrix of coupled oscillators, similar to a system of N coupled mass/spring systems. This is the idea that we have explored in order to grasp the physics of such a medium and infer the links with the results of TR focussing on a subwavelength scale.

In order to study far field TR in such an array of resonant unit cells, we have simplified the system; the medium (Fig. 6.5(a)) is composed of a periodic array of $N = 20 \times 20$ equal length copper wires (length $L = 40$ cm, period $a = 1.2$ cm, wire diameter $d = 3$ mm). The wires are oriented along the z direction and periodically spaced in the (x, y) plane. Furthermore we perform all our measurements and simulations in free space, or in an anechoic chamber, in order to decouple the effect of the medium from those of the reverberating chamber used in [38]. Leaving the random medium for a periodic array of identical resonators presents two major advantages: first, a Bloch mode analysis can be performed, which greatly simplifies the study, and second, the medium can be analyzed within the framework of wire media that has been deeply studied in the past for different purposes [3, 51].

We have realized an in-depth study of this array of wires from which we will give the principal results in order to explain the principles of TR in such a medium. Part of this study has been published in a short letter and the rest in two longer

articles [30–32]. We mention first that obviously, since this system is analogous to an array of coupled mass/spring systems, we expect that the system can be described in terms of eigenmodes and eigenfrequencies. Lattice modes appear due to the strong coupling between the wires since they are very densely packed. Indeed, the first resonance f_0 of a wire is around 375 MHz, and they are therefore organized on a very deep subwavelength at the equivalent resonant wavelength $\lambda_0 = 80$ cm, i.e. a period equals $\lambda/70$. The very difference between such a medium and a wavelength scaled one, for example a classical photonic crystal, is that in our case the Bloch modes can present very deep subwavelength spatial periods. In such a system, the Bloch theorem imposes that we find N modes if we have N oscillators. Those modes possess wavevectors k_t in the (x, y) plane (which we will be thereafter referred to as the transverse plane) whose norm is within the interval $[0, \pi/a]$. Hence, the spatial variation of the modes supported by the deep subwavelength array of resonant wires ranges from the transverse size of the system for the fundamental mode towards the period of the system for the highest mode. Here we start to understand a very important feature of the system used in [38] and studied deeper in [30–32]: such a medium supports deep subwavelength modes that will be able to couple to the evanescent components created by a source placed either inside or in the very near field of the medium. Let us now look at the dispersion relation of such modes, or equivalently the relation between their eigenvectors and eigenfrequencies.

Such a system of N periodic resonators should be analyzable within the frame of classical coupled oscillators: a set of N equations is written modelling the behaviour of the current in each wire, and including coupling coefficients linking a specific wire to its neighbours. This approach, however, requires the knowledge of the coupling matrix, and some computation; there is actually a much more elegant way to obtain the desired results. The idea of this analysis is to start from an infinite wire medium of the same periodicity and wire diameter as the one used here. Such a medium, known as the wire medium, supports only transverse electromagnetic modes (TEM modes similar to those propagating in coaxial lines), since TE and TM modes turn out to be evanescent due to the very subwavelength period [3, 51]. Those TEM modes are known to be dispersionless: their longitudinal wavevectors k_z are independent of the transverse ones k_t and equal to ω/c, where ω is the pulsation of the wave and c its celerity in the host medium. When a set of TEM modes, each one presenting a complex phase (the decomposition of a point source for instance) propagates inside this medium, it remains unchanged independently of the distance of propagation in the z direction, which explains part of the phenomenon called canalization [3, 51].

If we start by cutting the wires along the z direction so that they now are of a finite length L (placing the wire medium between the $z = -L/2$ and $z = L/2$ planes), things become quite different. Indeed, the dispersionless TEM modes are trapped inside the medium and they propagate back and forth along the z direction: they experience a Fabry-Perot like cavity. Interestingly, the properties of this Fabry-Perot cavity depend on the transverse wavevector of the modes k_t, which in turn induces dispersion. Very naively, one can understand this in the following manner; the TEM

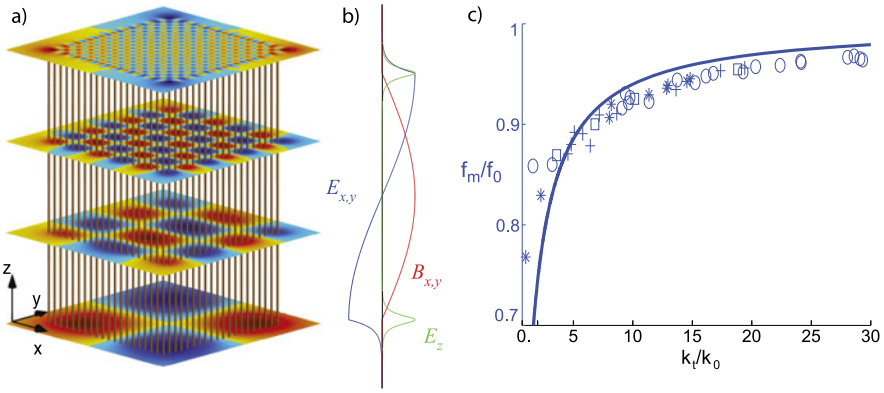

Fig. 6.5 (**a**) The experimentally and numerically studied resonant metalens wire array. The 20×20 wires are 1.2 cm periodically spaced on a square grid, are 3 mm in diameter and 40 cm long. Superimposed are mapped the electric field of 4 Bloch modes out of the 400 that are supported by the structure. (**b**) Shape of the TEM field inside the structure. The transverse magnetic (electric) field is maximum (null) in the middle of the medium of the structure and null (maximum) at the interfaces with air. Only an electric evanescent component exists outside of the medium in the z direction. (**c**) Dispersion relation linking the transverse wavevectors k_t (normalized to π/a) of the modes to their resonant frequencies f_m (normalized to the resonant frequency of a single wire f_0). The *solid curve* is analytical (6.5) while the symbols represent various modes obtained numerically. This *curve* shows that the Bloch modes which are evanescent in the z direction (the *curve* is under the *light line*) show a dispersive behaviour. Reproduced from [30]. Copyright (2010) by the American Physical Society

modes are all evanescent outside the medium in the z direction at the $z = \pm L/2$ interfaces (Fig. 6.5(b)) since they are subwavelength, or equivalently, since their resonant frequencies lie below the light line. It is well known that when a wave impinges from a medium 1 onto an interface with a medium 2 and gives rise in the latter to an evanescent wave, it adds a phase term to the reflection coefficient at the interface. This effect, responsible notably of the Goos-Hänchen shift [23], depends on the penetration depth of the evanescent wave inside medium 2: the longer this penetration depth, the larger the phase shift. Taking this effect into account, it is pretty easy to obtain a relation between the TEM modes transverse wavevector k_t and their eigenfrequencies:

$$\tan\left(\frac{kL}{2}\right) = \frac{\sqrt{k_t^2 - k^2}}{k} \tag{6.5}$$

where k denotes the host medium wavenumber, and hence the frequency (in our case the host medium is air and $k = k_0 = \omega/c$).

This dispersion relation is plotted in Fig. 6.5(c) alongside simulation results obtained from CST Microwave Studio. From now on it is clear that the TEM modes are no longer dispersionless inside the medium, which will have many implications. Indeed, if one uses an electrically small source in the near field of the medium at the

$z = \pm L/2$ interfaces, the field created by the latter decomposes onto the eigenmodes of the system. The modes are dispersive, namely each mode possesses a different resonant frequency. If now the source is broadband and covers all the dispersion relation, then the Fourier decomposition of the source onto the modes is transposed into the spectrum of the field inside the structure. This means that the spatial information of the source on a subwavelength scale (down to the period of the structure) can be converted into a temporal waveform or a complex spectrum thanks to the dispersion that occurs inside this subwavelength scaled resonant medium. This aspect constitutes the first out of the two fundamental concepts that permit us to beat the diffraction limit using time reversal focussing from the far field.

We have shown that a subwavelength source placed in the near field of one interface of a finite length wire medium can decompose onto the subwavelength modes of the system provided that it is broadband and can excite all of the resonant frequencies of the modes. But up to now the medium still remains infinite in the (x, y) plane. Cutting the system in the (x, y) plane in order to obtain the finite size medium that we have studied (Fig. 6.5(a)) has major consequences. First of all, evidently, when we restrict the medium to $N = 20 \times 20$ wires, the dispersion relation is no longer continuous, but the transverse wavenumbers k_t become discrete on the interval $[0, \pi/a]$, since we have only N modes. But there exists a much more important outcome of the finite transverse dimensions of the structure: the modes become leaky in free space due to finite size effects. Of course, the efficiency of the conversion from those subwavelength modes to free space radiation is quite poor, and the more subwavelength the modes, the less efficient the conversion.

What seems to be very limiting though, is actually not a problem, but rather, a solution. Indeed, since the array of wires is resonant, energy is accumulated over time inside the structure. This implies that the modes which cannot exit the structure easily, the most subwavelength ones, are trapped inside the medium for a much longer time: they present a much higher quality factor. Hence, from a monochromatic point of view, their amplitude inside the medium is much higher than that of the source due to resonant amplification, or equivalently to the Purcell effect [47]. From energy conservation, one can easily infer that if the materials are lossless, even though the conversion of the modes to free space radiation is very weak, due to this resonant effect, all the modes radiate equally efficiently in free space! This represents the second fundamental aspect of such finite size subwavelength scaled resonant media: the very low conversion of subwavelength modes to free space radiations is totally counterbalanced by the resonant enhancement of the modes. This explains why those modes actually radiate efficiently in free space, even though they are deeply subwavelength inside the medium (due to the period of the medium).

Together with the first principle, the physical mechanism of our resonant metalens concept can be summarized as follows. First, a source placed in the near field of our medium emits a broadband field that decomposes onto the eigenmodes of the latter. Due to dispersion, the spatial decomposition is converted into a temporal/frequency signature, which resonates inside the medium, the quality factor of the resonance being higher for the most subwavelength modes. Then, due to the finite

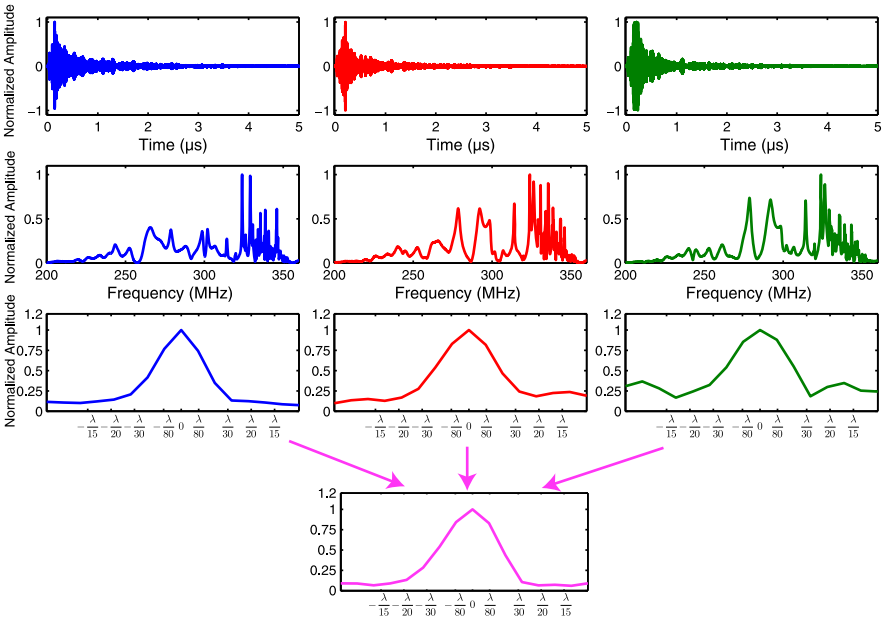

Fig. 6.6 Experimental results in an anechoic chamber: temporal waveforms (*first row*), frequency spectrum (*second row*) and focal spots obtained by TR (*third row*), for the 3 antennas placed in the far field of the structure at relative angles 0°, 45° and 90°. In each case, the signals are very elongated due to the resonant nature of the medium, the spectrum displays increasing quality factors for frequencies approaching f_0, and focal spots $\lambda/25$ wide are measured. The last row presents a focal spot obtained using TR with the 3 antennas at a time. The focal spot is again $\lambda/25$ wide and the sidelobes are lowered. Reproduced from [32] with permission from Taylor & Francis

size effects and the resonant enhancement of the modes, each mode radiates with an equal efficiency in free space. This explains the efficient conversion of the subwavelength information into free space radiations of [38], and the fact that TR can give subwavelength resolution in this medium; indeed, if the conversion is possible from the source to free space, then the time reversed operation is possible due to reversibility and reciprocity. Examples of such subwavelength modes are plotted superimposed on the studied structure in Fig. 6.5(a).

We have verified experimentally and numerically those principles. Numerical simulations, using lossless metal, have shown with a 20×20 wire medium that all the spatial information of a source is radiated in the far field with equal efficiency regardless of its subwavelength nature [30–32]. We have also repeated the TR experiments of [38] using our periodic system in an anechoic chamber. As can be seen in Fig. 6.6, we have recorded the field produced by a small monopole placed in the near field of the medium using 3 antennas in the far field of the structure. Those three antennas are placed at 0°, 45° and 90° around the medium, and we record the impulse response between these antennas and the monopole placed in the near field of the medium. The emitted signal is a 10 ns pulse centered at 300 MHz. It is clear from the temporal signals that even though placed in an anechoic chamber,

the impulse responses between the monopole and the three antennas are very long (1.5 μs rms, i.e. 150 times the original pulse). This means that the array of resonant wires itself constitutes a very high Q cavity for the TEM modes that resonate inside it. Next, considering the spectrum of the recorded impulse responses, it is clear that our analysis is correct, since we can see that the modes that are closer to the resonant frequency of a single wire (375 MHz) show increasing quality factors.

We have also performed TR focussing using the three far field antennas; the impulse responses from each one of the three far field antennas were time reversed and sent back using a single antenna at a time. Measuring the field received on an array of monopoles placed around the initial source position in the near field of the wire medium, we can measure the temporal signal obtained after TR. Clearly, TR focussing gives a focal spot that is deeply subwavelength (around $\lambda/25$) using any of the three far field antennas, that is, using a single antenna and in free space (anechoic chamber), while the sum of the three antennas gives a similar focal spot, with lower sidelobes.

A brief letter of this detailed study can be found in [30] and the rest of it was published elsewhere [31, 32]. In [30] we call such a system a resonant metalens since it can project the image of an object with subwavelength details in the far field, coded in a temporal/frequency signature. We prove in these papers both TR focussing under the diffraction limit and imaging from the far field with subwavelength resolution based on the same concepts. Here we did not discuss the effect of material losses. Obviously, losses diminish all the quality factors, which impacts most upon the most subwavelength modes propagating in the structure. This reduces their resonant enhancement and finally their radiation efficiency. This, in turn, sets a limit to the resolution of the system, whether used for TR focussing under the diffraction limit or for purposes of subwavelength imaging from the far field.

Finally, it is worth making a link between the results obtained here and the formula (6.4) linking the field created by TR at the collapse time and the dyadic Green's functions of the medium. Indeed, in such a periodic system, the Green's functions of the medium are the modes that exist in the latter at each frequency. Equation (6.4) states that the result of TR focussing at the collapse time is the integral of the dyadic Green's functions projected on the dipole vector of the initial source. Very practically, if one's aim is to focus using TR on a deep subwavelength scale, the idea is to sum a lot of independent subwavelength modes in phase at the focal spot and at the collapse time. This is exactly what TR does, since it compensates the phase of the modes excited in the structure from the far field, such that they focus on the initial source position at a definite time. From this approach, it is clear that such results can be obtained provided that we are able to construct a resonant metalens: a finite size medium supporting subwavelength resonant modes, which must be independent (that is, the medium must be dispersive), and must present ohmic losses as low as possible. We will show in the next part that resonant wires, even though they are very common for this purpose due to their small transverse dimensions, are not the only candidates.

6.5 Generalization of the Concept and Transposition to Acoustic Waves

6.5.1 Using Any Subwavelength Resonator for Subwavelength Focussing of Waves Using Far Field Time Reversal

From the results of the last part, it appears that any medium of finite size supporting subwavelength modes, consisting of resonant unit cells and displaying dispersion can be used for the sake of subwavelength focussing from the far field using TR. Very conveniently, many such media have been studied recently in the field of metamaterials. Basically, metamaterials are engineered materials made out of a periodic array of unit cells which exhibit interesting properties that can be tailored [49]. Most metamaterials are designed with a unit cell that is resonant and of subwavelength size. Examples of such unit cells include Split-Ring resonators (SRR), parallel cut wires, complementary SRR, etc. Usually such materials are analyzed within the framework of effective medium theory and effective parameters are obtained through an averaging of the field across one unit cell. Materials with negative permeabilities and permittivities can be obtained, those possessing a band with double negative parameters falling into the class of negative index media [52].

In our case, we are not interested in averaging procedures in order to extract effective parameters since our focus is on finite size media. Such finite size media necessarily support modes which can be calculated using the Bloch formalism. Provided that its unit cell is subwavelength and resonant, a medium should behave just like the medium made out of resonant wires that we have studied before. Indeed, the modes supported by the medium for the first band should be evanescent since their dispersion relation, in analogy with polaritons, lies under the light line. Hence, such modes should be once again trapped inside the medium which then acts as a cavity for those trapped modes. Provided the unit cells are coupled, which should be the general case since subwavelength resonators arranged in a dense array will strongly interact with each other, the medium will also have dispersive behaviour. This should permit us to transpose the subwavelength spatial information of a source into the temporal/frequency signature of the field inside the medium. Finally, because we consider only finite size media, finite size effects should also ensure conversion from the subwavelength modes to free space radiation whose weak efficiency should be compensated by the resonant enhancement of the modes in the medium.

Therefore we argue that if one designs a resonator of subwavelength size and builds up an array of such resonators, the latter being closely spaced, focussing using TR should produce subwavelength spots in such media. The focal spot size will, in the best case, be limited by the period of the medium, but may be limited to larger sizes depending on the losses of the system. We have verified our assertions with various unit cells such as high index dielectric cubes, spiral resonators, loaded wires and Split-Ring resonators. The results obtained totally agree with our statement, and in all cases, at least numerically, TR focussing resulted in subwavelength focal

spots. Here, for the sake of space limitations, we will not show the latter. Instead, we will generalize the concept even further by transposing it to the case of acoustic waves.

6.5.2 *Beating the Diffraction Limit for Sound Using an Array of Soda Cans and Time Reversal*

There have been a few proposals for subwavelength focussing in acoustics. Some focussing techniques were demonstrated, based on an acoustic analog of the "Bull's eye" structure in optics [8, 40] as well as demonstrations of ultrasound focussing using a negative index material [64] and phononic crystals [60]. If some of those methods demonstrated sub-diffraction focal spots from the near field, no experimental demonstration of far field subwavelength focussing has been given so far. The only experimental evidence of far field subwavelength focussing of acoustic waves required the use of an acoustic sink [13]. In order to focus acoustic waves on a subwavelength scale, we want to make use of subwavelength acoustic resonators. Some resonant and subwavelength unit cells have been reported [41, 61]. Yet a simple subwavelength resonator was introduced more than a century ago and reported recently to be a very good candidate for negative modulus and negative index ultrasonic materials [17, 64]: the Helmholtz resonator [59].

In this section we prove that broadband audible range sound can be manipulated and focused on a subwavelength scale, that is on a scale much smaller than the wavelength in air, and from the far field using such Helmholtz resonators. We use for this purpose a collection of simple everyday objects: an array of soda cans. The concept is based on our theoretical proposal of a resonant metalens, which was presented in previous sections [30, 33, 38]. We show that the strong coupling between neighbouring soda cans induces a splitting of the resonant frequency of a single Helmholtz resonator. We demonstrate that monochromatic diffraction limited waves emitted by commercial computer loudspeakers excite efficiently in the array of cans resonant periodic modes of spatial period much smaller than the wavelength in air. Those subwavelength Bloch modes have different resonant frequencies and radiation patterns depending on their wavevectors. Harnessing those sub-diffraction wavefields using broadband sounds, we are able to experimentally obtain from the far field subwavelength focussing of sound onto spots as small as $1/25$th of a wavelength in air, with a position resolution of $1/15$th of the wavelength, i.e. the center to center distance between soda cans. Finally we establish that subwavelength focussing of sound results in strong enhancements of the acoustic displacements, and we show it experimentally through a visual experiment.

A Helmholtz resonator, the acoustic equivalent of an electric LC resonator, is a subwavelength open cavity. As we observe in everyday life, bottles and cans exhibit a Helmholtz resonance in the audible range of the spectrum. We work with soda cans for two reasons; first they possess a truly subwavelength diameter of 6.6 cm at the resonance frequency of 420 Hz, corresponding to $\lambda_R = 0.8$ m. But moreover, its dimensions make it relatively low loss.

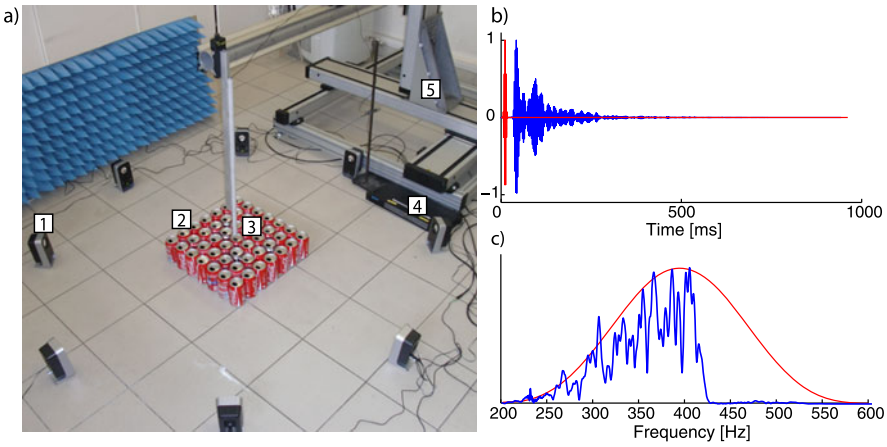

Fig. 6.7 Experimental setup. (**a**) A picture of the setup utilized in the experiment. 8 Commercial computer speakers (1) are controlled using a multi-channel soundcard (4) and create sounds that excite an array of Helmholtz resonators (i.e. soda cans) (2). Mounted on a 3D moving stage (5), a microphone (3) records the pressure over the array of cans. (**b**) Typical emitted pulse (*red*) and measured pressure (*blue*) on top of one can. (**c**) Spectrum of the original pulse (*red*) and average spectrum of the pressure measured every can of the array (*blue*). Reproduced from [33]. Copyright (2011) by the American Physical Society (Color figure online)

First we demonstrate that an array of cans constitutes a good evanescent to propagating wave converter. In other words, we show that harmonic sounds emitted from the far field excite efficiently in the array subwavelength resonant modes with spatial variations as small as the diameter of a can. We present the experimental setup in Fig. 6.7(a). We study a periodic ensemble of 7×7 soda cans (2) arranged on a square matrix of period 6.6 cm, that is, the width of a single can, and placed in the xy-plane. Around it we arrange 8 computer speakers (1), 1 meter (more than one wavelength) away so that only propagating waves reach the cans [22]. The speakers are connected to a multi-channel soundcard (4) controllable via Matlab. We measure the pressure at any location above the soda cans with a 1 cm wide microphone (3) mounted on a 3D moving stage (5).

As an initial step we acquire the time domain Green's functions between the 8 speakers and the top of the 49 cans, using a 10 ms pulse centered around 400 Hz. A typical recorded sound is plotted in Fig. 6.7(b)–(c). It presents resonance peaks spanning roughly from 340 Hz up to the resonance frequency of a single soda can, 420 Hz. Those peaks, which are much thinner than the resonance of a single can, are associated with periodic modes which possess spatial variations ranging from the dimension of the can array down to the period of the structure. Due to the finite size of the can array, only 49 modes with discrete frequencies and wavevectors exist whose dispersion relation is analogous to that of the wires, presented in Fig. 6.5(c). One can understand their origin as follows: similarly to an ensemble of coupled mass spring oscillators, the system of N coupled resonators supports N modes that present N different resonant frequencies. Here, because the resonators are much

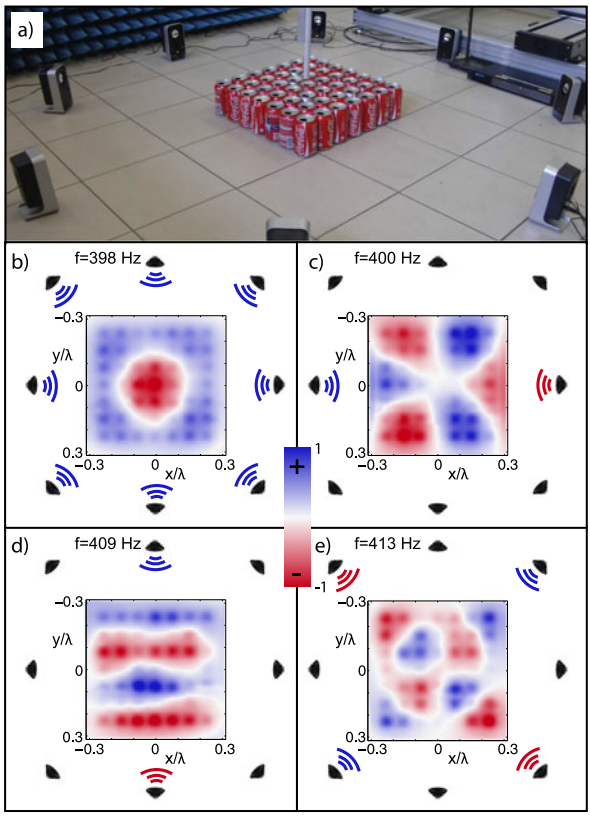

Fig. 6.8 Subwavelength modes. (**a**) A close view of the array of cans surrounded by the 8 computer speakers. The speakers are placed more than one wavelength away from the cans so that evanescent waves are negligible at this distance. (**b**) A subwavelength mode measured at 398 Hz when the speakers are used to generate a monopolar radiation pattern, this modes is already subwavelength, with a $\lambda/4$ spatial period. (**c**) A mode corresponding to a horizontal dipolar pattern at 400 Hz. (**d**) A vertical dipolar wavefield created with the speakers results in a $\lambda/3$ spatial period mode at 409 Hz. (**e**) A quadrupolar far field pattern excites a deep subwavelength mode at 413 Hz. Reproduced from [33]. Copyright (2011) by the American Physical Society

smaller than the wavelength, those modes are subwavelength. Stated differently, the resonance of the cans hybridize with the air continuum, which creates a surface wave polariton. Contrary to intuition, the cans couple to each other via air rather than mechanically despite being compactly packed.

In order to verify the subwavelength nature of the resonant excited modes, we measure the pressure field on top of the collection of Helmholtz resonators at various frequencies. To that end, we evaluate using our set of temporal Green's functions the resonant frequencies of the modes. Due to its square symmetry and subwavelength period, a mode can be scattered in the far field into four different patterns depending on its number of nodes, that is, its parity. Monopolar radiation patterns are obtained for even-even modes, X and Y oriented dipolar fields are generated by even-odd modes, and odd-odd modes scatter into quadrupolar far field radiations.

With our setup, we generate monochromatic wavefields approximating the radiation patterns of the modes at their resonant frequencies. Then, using the microphone and the moving stage, we measure the pressure for the desired mode. In Fig. 6.8(a) we first show the array of cans surrounded by the speakers in close view. Then we exemplify the far field generation of resonant modes in the collection of Helmholtz

resonators, sketching the created wavefield with schematized speakers and wavefronts. We represent the fields generated in the array of cans at four different frequencies and with wavefronts approximating the four possible radiation patterns of the subwavelength modes. The field of Fig. 6.8(b), measured at 398 Hz and corresponding to a Monopolar radiation pattern, already presents a subwavelength spatial period since it presents two nodes within about 0.6 wavelengths at this frequency. Conversely, Figs. 6.8(c), 6.8(d), 6.8(e) show pressure fields that all present subwavelength spatial periods from 0.5λ down to 0.3λ, and whose symmetries are consistent with the generated wavefronts.

We point out here that measuring experimentally the most subwavelength modes, those at the edge of the 1st Brillouin zone, is very challenging because of dissipation. Indeed, since the most subwavelength resonant modes scatter less efficiently into propagating waves, they resonate longer inside the array of cans. Without viscous and thermic losses, all the modes should be resolved because their linewidth decreases as the dispersion relation flattens [30]. Here, however, even though soda cans present acceptable amounts of dissipation, the higher frequency, or most subwavelength modes, are unresolved and cannot be excited independently. Nevertheless we will see that this does not hamper our ability to control sound on a scale even smaller than the period of the medium.

We have shown that incident diffraction limited and monochromatic sound fields generate sub-diffraction resonant modes that extend over the entire collection of cans. Now we want to harness those modes in order to create subwavelength focal spots. This becomes possible if instead of utilizing the usual monochromatic approach of metamaterials, a broadband one is preferred. Indeed, one very simple solution for focussing waves in a medium presenting modes consists in adding them coherently at a specific time and a given location, while they add up incoherently at other positions and other times. This can be realized using time reversal (TR). Indeed, as we have proven it in the previous sections, achieving TR from an array of sensors toward one point literally amounts to summing all the modes with zero relative phase at this specific position hence creating a spatio-temporally focused wave.

We have performed this experiment on several locations on top of the ensemble of Helmholtz resonators using the 8 computer speakers. We present two maps of the acoustic intensities obtained after time reversal on two positions of the array (respectively $(2, 2)$ and $(3, 5)$, Figs. 6.9(c) and 6.9(d)). Clearly the focal spots obtained, which display similar widths at half maximum, prove that the diffraction limit was overcome by a factor of 4. Although we only show two maps because of space limitation, we stress that those foci can be placed at will on any can of the array by changing the sounds emitted with the speakers. As a control experiment, we also plot in Figs. 6.9(a) and 6.9(b) the maps of the acoustic intensities measured after TR in our laboratory without the soda cans and on the same locations. This map unambiguously proves that the subwavelength focussing arises from the ensemble of resonators, since here we obtain typical $\lambda/2$ wide diffraction limited foci. We underline that focussing sound in the array of cans results in much thinner foci than with a single can.

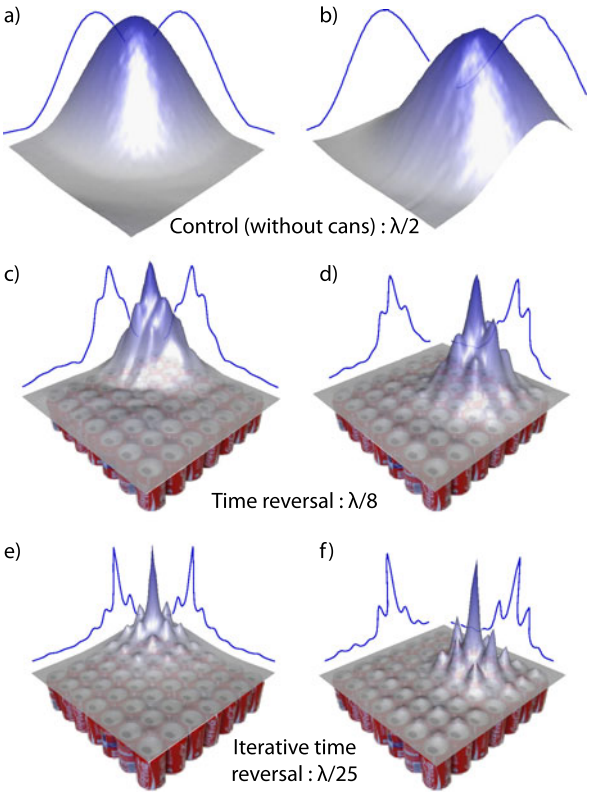

Fig. 6.9 Sub-diffraction focussing of sound. All surfaces are pressure intensities normalized. (**a**), (**b**) Focal spots obtained using time reversal in the laboratory room and without the array of cans, typical diffraction limited spots are displayed. (**c**), (**d**) The foci obtained using time reversal onto the same locations with the array of Helmholtz resonators show $\lambda/8$ width, 4 times smaller than the diffraction limit. (**e**), (**f**) The experiment is realized in the same conditions with an iterative time reversal scheme, demonstrating focal spots as thin as $\lambda/25$. The peak acoustic intensities for equal emitted energies are around 6.3 AU (arbitrary units) for (**a**)–(**b**), 3.5 for (**c**)–(**d**) and 1.9 for (**e**)–(**f**). Reproduced from [33]. Copyright (2011) by the American Physical Society

Even though TR is a very simple and powerful method for subwavelength control of sound, its performances can be surpassed using more elaborate methods. Indeed, TR is optimal in non-dissipative media because it does not modify the relative amplitudes of the spectrum of a signal, and simply acts on its phases. However, we have shown that the more subwavelength a mode, the higher the impact of dissipation. As a consequence, waves can be controlled onto sharper foci provided that highly attenuated modes are compensated at emission. We use a modified version of TR [29, 43, 55] to generate a bank of sounds which can focus onto any point of the collection of cans. Again, the 8 speakers emit the calculated sounds and we measure the intensity on top of the array of resonators. We have repeated the operation for several locations and we map here the intensities obtained for two chosen ones, respectively $(2, 2)$ and $(3, 5)$, in Figs. 6.9(e) and 6.9(f). Now, measuring the width at half maximum of the acoustic intensity, we obtain focal spots as thin as $1/25$th of the wavelength, corresponding roughly to the size of the opening of a can. Of course, because we cannot focus waves in between cans, the focussing resolution is limited by the period of the medium. Overall, we prove that we can beat the diffraction limit by a factor of 12 with a positioning accuracy of $\lambda/15$. Moreover, the acoustic intensities obtained with and without cans are of the same order of magnitude, hence demonstrating the efficiency of the approach (see caption of Fig. 6.9).

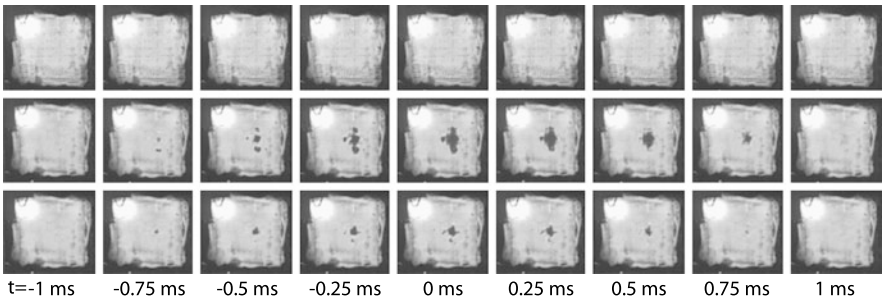

Fig. 6.10 *2nd and 3rd rows*: Subwavelength enhanced acoustic displacements obtained with TR and iterative TR in the array of cans and filmed with a high speed camera. Without cans no movement is observed (*1st row*). Reproduced from [33]. Copyright (2011) by the American Physical Society

Apart from its obvious interest in terms of energy deposition, the obtained subwavelength focussing of pressure fields has a direct consequence. Analogous to the enhancement of the electric field in subwavelength varying potentials, it leads to a strong enhancement of the acoustic displacement, a key property for efficient actuators and sensors. We show this in the last part of this section.

To do so, we perform a visual experiment that recalls the works of Chladni, using a high speed camera. We suspend a 20 micron thin sheet of metallized Mylar on top of the array of cans. A white light projector illuminates the sheet of Mylar, oriented a few degrees off its normal, while the camera is placed exactly at normal incidence. Because of the small angle between the projector and the camera, the Mylar sheet appears dark except for the direct image of the projector's bulb. Now, we deposit one layer of glass beads (diameter around 120 μm) on top of the Mylar sheet, and take another picture with the camera: the Mylar sheet appears very shiny due to the glass beads. This effects occurs thanks to the retro-reflection of the light on the glass beads placed on top of the metallized surface.

It is widely known that Mylar is transparent to sound especially at low frequencies: a sheet of Mylar follows the displacement of a sound field. We use a trick to film this displacement using the high speed camera and the retroreflective effect of the glass beads. When the upward displacement of the sound field is large enough, the glass beads have too much kinetic energy to follow the downward displacement of the Mylar sheet, and they dissociate from it. This, in turn, cancels the retroreflective effect, which darkens the related area of the Mylar sheet. This way we can image the acoustic displacement generated by the array of Helmholtz resonators with a good optical contrast.

We have used this experimental procedure to make movies of the field created when we focus onto various locations on top of the collection of cans. Figure 6.10 shows pictures taken from films obtained using time reversal (2nd row) and our modified time reversal scheme (3rd row). We verify that the beads were lifted from the Mylar sheet onto areas of subwavelength sizes. Utilizing the same experimental procedure without the soda cans, we did not observe any movement of the glass beads despite some reverberation of sound in the room (1st row of Fig. 6.10). This

means that even though the deposited pressures are of the same order of magnitude with and without the cans, our approach results in much higher displacements of the acoustic field. Indeed, since the displacement depends on the gradient of the pressure, subwavelength pressure fields induce strong exaltations of the latter. In our case, focussing on the soda cans, for the same emitted energy and the aforementioned acoustic intensities at foci, we get 7.4 (TR) and 5.4 (modified time reversal scheme) times the acoustic displacement obtained without the cans. This entails that our approach can be exploited for the design of efficient subwavelength size actuators and MEMs.

Our experiment is of fundamental interest and its main results can be reproduced easily. Using subwavelength coupled acoustic resonators offers three tremendous advantages. First, it introduces the possibility of engineering a matrix of actuators or sensors that are arranged on a subwavelength scale. Second, because our approach takes advantage of dispersion, it allows us to independently address many sensors using their temporal signature and a few sources. Third, subwavelength pressure fields create enhanced acoustic displacements with numerous potential applications. This approach is valid for a broad range of resonators throughout the spectrum and can easily be generalized to elastic waves in solids. We believe this opens up many avenues in the audible domain for sound control, generation and engineering but also at any frequency for the design of arrays of actuators, micro-mechanical actuators in general and by reciprocity, of sensors.

6.6 Conclusion

The goal of this chapter was to introduce TR as a method for focussing below the diffraction limit from the far field in designed subwavelength scaled and resonant media. To that aim, we have introduced the basic principles of TR through a brief review of some results obtained using acoustic waves. We have shown that a TR focal spot can be explained in terms of a sum over the bandwidth of the Green's functions of the medium, which happen to be the modes of the medium if the latter can be analyzed within a modal approach. Starting from these original results, we have underlined how they can be transposed to electromagnetic waves. More specifically, we have shown that in terms of focal spot, TR behaves identically with both electromagnetic waves and acoustics, notwithstanding the polarized nature of the latter which must be accounted for through the use of dyadic Green's functions. We have introduced our first experimental proof of concept of subwavelength focussing using far field TR in a random collection of metallic scatterers. This experiment has been explained in terms of conversion of evanescent waves to propagating ones, and linked to the reciprocity of evanescent waves. Then we have given evidence that this initial demonstration could be analyzed within the simplified model of a subwavelength periodic array of resonant wires. The main characteristics of such a medium have been presented: dispersion allows the evanescent components of a source to couple to the subwavelength Bloch modes supported by the structure

while the weak conversion to propagating waves of the latter is counterbalanced by the resonant enhancement of the modes. We have verified that TR in such a medium indeed provides deep subwavelength focal spots whose width are limited by the losses of the structure to $\lambda/25$ in our experimental demonstration. In light of this new approach, we have generalized the concept and argued that any dense and finite-size array of subwavelength resonators constitutes a medium which can be utilized to break the diffraction barrier using TR focussing. This has been shown through a transposition of the approach to the domain of acoustics. We have, in that regard, demonstrated that it is possible to focus audible sound onto focal spots as thin as $\lambda/25$ using an array of simple everyday life objects: soda cans.

We believe that this approach, because of its generality and simplicity, will have very interesting applications in various fields, for various types of waves, and throughout their spectra. Finally, we would like to add that such media, which we have called "resonant metalens" for their capability to project on the far field the near field information of a source regardless of its spatial variations, can also be utilized as imaging systems with subwavelength resolution.

References

1. Aulbach, J., et al.: Control of light transmission through opaque scattering media in space and time. Phys. Rev. Lett. **106**, 103901 (2011)
2. Bartal, G., Lerosey, G., Zhang, X.: Subwavelength dynamic focusing in plasmonic nanostructures using time reversal. Phys. Rev. B **79**, 201103 (2009)
3. Belov, P.A., Hao, Y., Sudhakaran, S.: Subwavelength microwave imaging using an array of parallel conducting wires as a lens. Phys. Rev. B **73**, 33108 (2006)
4. Betzig, E., Trautman, J.: Near-field optics: Microscopy, spectroscopy, and surface modification beyond the diffraction limit. Science **257**, 189–195 (1992)
5. Carminati, R., et al.: Theory of the electromagnetic time reversal cavity. Opt. Lett. **32**, 3107–3109 (2007)
6. Carminati, R., Nieto-Vesperinas, M., Greffet, J.J.: Reciprocity of evanescent electromagnetic waves. J. Opt. Soc. Am. A **15**, 706–712 (1998)
7. Cassereau, D., Fink, M.: Time-reversal of ultrasonic fields—Part III: Theory of the closed time reversal cavity. IEEE Trans. Ultrason. Ferroelectr. Freq. Control **39**, 579 (1992)
8. Christensen, J., et al.: Collimation of sound assisted by acoustic surface waves. Nat. Phys. **3**, 851–852 (2007)
9. Dehong, L., et al.: Electromagnetic time-reversal imaging of a target in a cluttered environment. IEEE Trans. Antennas Propag. **53**, 3058 (2005)
10. Derode, A., Roux, P., Fink, M.: Robust acoustic time reversal with high-order multiple scattering. Phys. Rev. Lett. **75**, 4206–4209 (1995)
11. Derode, A., Tourin, A., Fink, M.: Random multiple scattering of ultrasound. II. Is time reversal a self-averaging process? Phys. Rev. E **64**, 036606 (2001)
12. Derode, A., et al.: Taking advantage of multiple scattering to communicate with time-reversal antennas. Phys. Rev. Lett. **90**, 014301 (2003)
13. de Rosny, J., Fink, M.: Overcoming the diffraction limit in wave physics using a time-reversal mirror and a novel acoustic sink. Phys. Rev. Lett. **89**, 124301 (2002)
14. de Rosny, J., Fink, M.: Focusing properties of near-field time reversal. Phys. Rev. A **76**, 065801 (2007)
15. de Rosny, J., Lerosey, G., Fink, M.: Theory of electromagnetic time reversal mirrors. IEEE Trans. Antennas Propag. **58**, 3139–3149 (2010)

16. Draeger, C., Fink, M.: One-channel time reversal of elastic waves in a chaotic 2D-silicon cavity. Phys. Rev. Lett. **79**, 407–410 (1997)
17. Fang, N., et al.: Ultrasonic metamaterials with. Negative modulus. Nat. Mater. **5**, 452 (2006)
18. Fink, M.: Time reversed acoustics. Phys. Today **50**, 34–40 (1997)
19. Fink, M., et al.: Time reversed acoustics. Rep. Prog. Phys. **63**, 1933 (2000)
20. Fink, M., Montaldo, G., Tanter, M.: Time reversal acoustics in biomedical engineering. Annu. Rev. Biomed. Eng. **5**, 465 (2003)
21. Fink, M., et al.: Time reversal in metamaterials. C. R. Phys. **10**, 447 (2009)
22. Goodman, J.: Introduction to Fourier Optics. Roberts & Company, Greenwood Village (2005)
23. Goos, F., Hänchen, H.: Ann. Phys. **436**, 333 (1947)
24. Guo, B., Xu, L., Li, J.: Time reversal based microwave hyperthermia treatment of Breast. In: Proc. Conf. Cancer, Signal, Systems and Computers 29th Asilomar, vol. 290 (2005)
25. Ing, R.K., et al.: In solid localization of finger impacts using acoustic time-reversal process. Appl. Phys. Lett. **87**, 204104 (2005)
26. Katz, O., Small, E., Bromberg, Y.: Focusing and compression of ultrashort pulses through scattering media. Nat. Photonics **5**, 372–377 (2011)
27. Kosmas, P., Rappaport, C.M.: Time reversal with the FDTD method for microwave breast cancer detection. IEEE Trans. Microw. Theory Tech. **53**, 2317 (2005)
28. Kuperman, W.A., et al.: Phase conjugation in the ocean: Experimental demonstration of an acoustic time-reversal mirror. J. Acoust. Soc. Am. **103**, 25–40 (1998)
29. Lemoult, F., et al.: Manipulating spatiotemporal degrees of freedom of waves in random media. Phys. Rev. Lett. **103**, 173902 (2009)
30. Lemoult, F., et al.: Resonant metalenses for breaking the diffraction barrier. Phys. Rev. Lett. **104**, 203901 (2010)
31. Lemoult, F., Lerosey, G., Fink, M.: Revisiting the wire medium: An ideal resonant metalens. Waves in Random and Complex Media **21**, 591–613 (2011)
32. Lemoult, F., Lerosey, G., Fink, M.: Far field subwavelength imaging and focusing using a wire medium based resonant metalens. Waves Random Complex Media **21**, 614–627 (2011)
33. Lemoult, F., Fink, M., Lerosey, G.: Acoustic resonators for far field control of sound on a subwavelength scale. Phys. Rev. Lett. **107**, 064301 (2011)
34. Lerosey, G.: Ph.D. thesis, Université Paris VII (2006)
35. Lerosey, G., et al.: Time reversal of electromagnetic waves. Phys. Rev. Lett. **92**, 193904 (2004)
36. Lerosey, G., et al.: Time reversal of electromagnetic waves and telecommunication. Radio Sci. **40**, RS6S12 (2005)
37. Lerosey, G., et al.: Time reversal of wideband microwaves. Appl. Phys. Lett. **88**, 154101 (2006)
38. Lerosey, G., et al.: Focusing beyond the diffraction limit with far-field time reversal. Science **315**, 1120–1122 (2007)
39. Lewis, A., et al.: Development of a 500Å resolution microscope. Ultramicroscopy **13**, 227–231 (1984)
40. Lezec, H.J., et al.: Beaming light from a subwavelength aperture. Science **297**, 820 (2002)
41. Liu, Z., et al.: Locally resonant sonic materials. Science **289**, 1734 (2000)
42. Mc Phedran, R.C., et al.: Density of states functions for photonic crystals. Phys. Rev. E **69**, 016609 (2004)
43. Montaldo, G., Tanter, M., Fink, M.: Real time inverse filter focusing through iterative time reversal. J. Acoust. Soc. Am. **115**, 768–775 (2004)
44. Pohl, D.W., Denk, W., Lanz, M.: Optical stethoscope: Image recording with resolution $\lambda/20$. Appl. Phys. Lett. **44**, 651–653 (1984)
45. Popoff, S.M., et al.: Measuring the transmission matrix in optics: An approach to the study and control of light propagation in disordered media. Phys. Rev. Lett. **104**, 100601 (2010)
46. Popoff, S., et al.: Image transmission through an opaque material. Nat. Commun. **1**, 81 (2010). doi:10.1038/ncomms1078

47. Purcell, E.: Spontaneous transition probabilities in radio-frequency spectroscopy. Phys. Rev. **69**, 681 (1946)
48. Qiu, R.C., et al.: Time reversal with MISO for ultrawideband communications: Experimental results. IEEE Antennas Wirel. Propag. Lett. **5**, 269 (2006)
49. Sarychev, A., Shalaev, V.: Electrodynamics of Metamaterials. World Scientific, London (2007)
50. Sentenac, A., Chaumet, P.: Subdiffraction light focusing on a grating substrate. Phys. Rev. Lett. **101**, 013901 (2008)
51. Shvets, G., et al.: Guiding, focusing, and sensing on the subwavelength scale using metallic wire arrays. Phys. Rev. Lett. **99**, 53903 (2007)
52. Smith, D.R., et al.: Composite medium with simultaneously negative permeability and permittivity. Phys. Rev. Lett. **84**, 4184–4187 (2000)
53. Strohmer, T., et al.: Application of time-reversal with MMSE equalizer to UWB communications. In: Proc. GLOBECOM '04 IEEE, vol. 5, p. 3123 (2005)
54. Synge, E.: A suggested method for extending microscopic resolution into the ultramicroscopic region. Philos. Mag. **6**, 356–362 (1928)
55. Tanter, M., Thomas, J.L., Fink, M.: Time reversal and the inverse filter. J. Acoust. Soc. Am. **108**, 223–234 (2000)
56. Tourin, A., et al.: Time reversal telecommunications in complex environments. C. R. Phys. **7**, 816 (2006)
57. Vellekoop, I.M., Mosk, A.P: Focusing coherent light through opaque strongly scattering media. Opt. Lett. **32**, 2309–2311 (2007)
58. Vellekoop, I.M., Lagendijk, A., Mosk, A.P.: Exploiting disorder for perfect focusing. Nat. Photonics **4**, 320–322 (2010)
59. von Helmholtz, H.: On the Sensations of Tone as a Physiological Basis for the Theory of Music. Longmans, Green, New York (1885)
60. Yang, S., et al.: Focusing of sound in a 3D phononic crystal. Phys. Rev. Lett. **93**, 024301 (2004)
61. Yang, Z., et al.: Membrane-type acoustic metamaterial with negative dynamic mass. Phys. Rev. Lett. **101**, 204301 (2008)
62. Yavuz, M.E., Texeira, F.L.: Space-frequency ultrawideband time reversal imaging. IEEE Trans. Geosci. Remote Sens. **46**, 1115 (2008)
63. Zenhausern, F., Martin, Y., Wickramasinghe, H.: Scanning interferometric apertureless microscopy. Science **269**, 1083–1085 (1995)
64. Zhang, S., et al.: Focusing ultrasound with an acoustic metamaterial network. Phys. Rev. Lett. **102**, 194301 (2009)

Chapter 7
Anisotropic Metamaterials for Transformation Acoustics and Imaging

Jensen Li, Zixian Liang, Jie Zhu, and Xiang Zhang

Abstract Metamaterials are becoming a prominent class of artificial materials that allow us to have very precise and specific optical properties. Its associated engineering flexibility opens up a wide range of applications and provides an effective route in molding the flow of energy. By drawing analogies between electromagnetic and acoustic wave frameworks, many concepts like invisibility cloaking and subwavelength imaging can be transplanted from electromagnetic to acoustic waves easily. However, we need quite different ways of constructing the artificial materials and devices for acoustics. Here, we show how anisotropic metamaterials can be constructed to control the constitutive parameters of the effective medium through positioning hard plates in different preferred directions. We will then use them to construct an acoustic carpet cloak, an acoustic hyperlens and a superlens as examples.

7.1 Introduction

Acoustic metamaterials are bringing new opportunities to control sound waves in ways which are previously considered difficult. For example, an effectively homogeneous medium built with locally resonating elements can manipulate the dynamic effective density and the dynamic modulus [17, 39]. This flexibility gives rise to interesting phenomena like negative refractive indices, surface resonant states and acoustic superlensing [1, 3, 7, 8, 13, 15, 19, 24, 28, 33, 34, 41, 64]. By controlling these effective material properties in a spatially varying manner, the metamaterial can act as a transformation medium which paves the way to achieve broadband acoustic cloaking and subwavelength acoustic imaging. This is similar to the corre-

J. Li (✉) · Z. Liang
Department of Physics and Materials Science, City University of Hong Kong, Hong Kong SAR, The People's Republic of China
e-mail: jensen.li@cityu.edu.hk

J. Zhu · X. Zhang
NSF Nanoscale Science and Engineering Center (NSEC), 5130 Etcheverry Hall, University of California, Berkeley, CA 94720-1740, USA

R.V. Craster, S. Guenneau (eds.), *Acoustic Metamaterials*,
Springer Series in Materials Science 166, DOI 10.1007/978-94-007-4813-2_7,

sponding development in electromagnetism [32, 47, 49, 51] except that the designs of the metamaterials building blocks have to be adapted to acoustic waves.

The working principle of the cloak depends on the transformation approach which relies on the form invariance of the wave equation upon coordinate transformation. Milton and co-workers found that such a form-invariance does not apply to full elastic waves for a general elastic medium [44]. For the simpler case of acoustic waves in fluids, the transformation approach is still valid and has been proposed in [4, 6, 11, 21, 22]. Several schemes of acoustic cloaking have been considered [12, 18, 23, 45, 48, 58]. However, their implementations have been hampered by the limited availability of suitable materials. Actually, contrary to optics, materials in acoustics are quite limited, even for constructing a simple lens. We therefore have to rely on artificial acoustic materials.

In many applications based on the transformation approaches, the medium is transformed and distorted in its constitutive parameters. We will therefore need to control the anisotropy and the indexes of the artificial medium in a flexible way. In this chapter, we will first investigate a scheme of constructing the anisotropic acoustic metamaterials by blocking waves in different preferred directions. Then, in the rest of this chapter, we will apply the principle to construct and design an acoustic carpet cloak, an acoustic hyperlens and an acoustic superlens.

7.2 Anisotropic Metamaterials by Blocking Sound Waves

The wave equations for a continuous compressible fluid can be summarized by the Newton's second law and the continuity equation (with harmonic dependence $\exp(-i\omega t)$ considered understood):

$$\nabla p' - i\omega\rho'\mathbf{v}' = 0, \tag{7.1}$$

$$\nabla \cdot \mathbf{v}' - \frac{i\omega}{B'} p' = 0, \tag{7.2}$$

where ω is the angular frequency, p' is the pressure field deviated from equilibrium, $\mathbf{v}'$ is the velocity field. ρ' represents the mass density and B' represents the bulk modulus of the fluid medium. The two equations can then be reduced to a single scalar equation:

$$\nabla \cdot \frac{1}{\rho'} \nabla p' + \frac{\omega^2}{B'} p' = 0. \tag{7.3}$$

By considering the plane wave solution $\exp(i\mathbf{k}' \cdot \mathbf{r}')$ inside a homogeneous fluid, we can obtain the dispersion relationship by

$$\omega^2 = k'^2 B'/\rho'. \tag{7.4}$$

Now, if we apply a general coordinate transformation to the above wave equation and follow the philosophy of transformation optics in electromagnetism [4, 11], the

new system of equations is form-invariant (still behaving as a fluid system having a bulk modulus profile and a density profile) except that the density profile now becomes a tensor instead of a scalar number. Also, the induced density and the induced modulus are in general varying from location to location in the transformed coordinate system. The new set of equations is therefore written as

$$\nabla \cdot \left[\rho[\mathbf{r}]\right]^{-1} \nabla p + \frac{\omega^2}{B(\mathbf{r})} p = 0, \tag{7.5}$$

where

$$\left[\rho[\mathbf{r}]\right]^{-1} = \mathbf{A}\left[\rho'(\mathbf{r}')\right]^{-1} \mathbf{A}^T / \det \mathbf{A}, \tag{7.6}$$

$$B(\mathbf{r}) = B'(\mathbf{r}') \det \mathbf{A}, \tag{7.7}$$

and

$$A_{ij} = \partial x_i / \partial x'_j. \tag{7.8}$$

We have defined the primed system before transformation as the virtual system while the unprimed or transformed one is the physical system. It means that if we can find materials fulfilling the transformed density and modulus profile in the physical system, any field patterns in the virtual system occur in a similar way through rewriting the coordinates in the physical system. Also the energy flow will follow the transformed paths in the physical system and it provides us with a way to manipulate the flow of sound (energy). Our strategy here is to find a simple way to construct an effective fluid medium that can fulfill the transformed density and modulus. We will embed additional structures (plates in our case) to block waves in preferred directions. If possible, we should allow the embedding fluid to percolate freely through the structures in order to avoid the usage of another kind of fluid different to the background one. Otherwise, we will need thin and light membranes to separate between different fluids. Our scheme defines the acoustic properties by its internal subwavelength structures rather than the substances from which it is manufactured. There are also some other schemes for constructing the materials from resonating elements and phononic crystals [33, 59]. In fact, the structures we are going to employ are independent of frequency of the sound and allow the following applications to operate in a broadband of frequencies.

A conventional fluid has a scalar value for its isotropic density (7.1). Now, we introduce the hard-plates structure shown in Fig. 7.1 to block the fluid flow along the z-direction. The fluid is forced to follow a long winding path so more force must be applied to affect the fluid movement along this direction. The fluid will appear to be more dense along the z-direction while in the x- and y-direction, the fluid is allowed to move freely and the fluid medium is least affected. The introduced structure can be made subwavelength in its features and it serves as an acoustic metamaterial. Because of the directional nature in the response, the density of the artificial material naturally becomes anisotropic, showing different values of components in different directions of the density tensor.

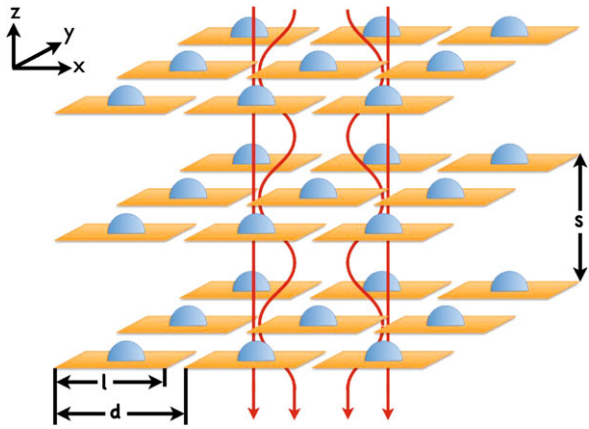

Fig. 7.1 Hard plates normal to the z-axis increase the pressure gradient needed for flow of fluid in the z-direction whilst leaving flow in the xy-plane nearly unaffected. The anisotropic density tensor has a large density in the z-direction. The hemispheres represent sacks of airs attached to each plate which modifies the bulk modulus

Suppose the background fluid is water (density 1000 kg m^{-3}, bulk modulus 2.2×10^9 Pa) and the hard plates are made of steel (density 7860 kg m^{-3}, bulk modulus 1.6×10^{11} Pa). In the x- or y-direction, the metamaterial has the effective density ρ_{xx} and ρ_{yy} and is nearly the same value as the density of water since the fluid motion is least affected. In the z-direction, the water flow is blocked and the effective density appears to be larger. We have done full-wave simulations using COMSOL Multiphysics (with the Acoustic module) to obtain the effective density ρ_{zz}. The transmission and reflection coefficients of a section of the acoustic metamaterial can be calculated and then the effective density and effective bulk modulus can be extracted at the same time. We vary the size of the square steel plate (l) of thickness 10 μm for fixed periodicity $d = 167$ μm and $s = 100$ μm. The enhancements to ρ_{zz}/ρ_{xx} are shown in solid line in Fig. 7.2. Significant enhancements relative to an isotropic fluid are found. Now, we can have an acoustic metamaterial being anisotropic and the anisotropy can be tuned by controlling the degree of blockage in the water flow in particular directions.

Apart from the anisotropy, we can also control the bulk modulus by introducing fluids with different bulk modulus into the metamaterial. For example, we can attach a sack of gas (e.g. air) to each of the plates. The effective modulus of the metamaterial is then a weighted average of those of the gas and the liquid by

$$B^{-1} = B_0^{-1}(1 - f) + B_g^{-1} f \approx B_g^{-1} f, \tag{7.9}$$

where f is the volume filling ratio of the gas in the whole system, B_g is the bulk modulus of the gas introduced and B_0 is the bulk modulus of the background water. Since a gas is so much more compressible than a liquid (water has a bulk modulus 10^4 greater than that of air), only a small volume fraction of gas would be required to reduce the bulk modulus of the metamaterial. On the other hand, if we want to increase the bulk modulus instead of decreasing it, we can introduce incompressible materials into the system in a similar way by volume averaging the reciprocal of the bulk modulus of different components. As an example, for the metamaterial (steel plates in water) we have discussed, the bulk modulus is around that of water

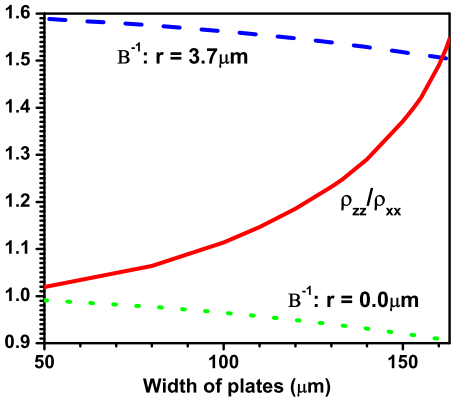

Fig. 7.2 The enhancement ρ_{zz}/ρ_{xx} (*solid line*) as a function of (l) for fixed $d = 167$ μm and $s = 100$ μm. The schematic of the structure is shown in Fig. 7.1. The plates are assumed to be steel of thickness 10 μm with density of 7860 kg m^{-3} and bulk modulus of 1.6×10^{11} Pa. The fluid is water with density of 1000 kg m^{-3} and bulk modulus of 2.2×10^9 Pa. Also shown is the effect of including a small hemisphere of air, radius $r = 3.7$ μm, which is attached to each of the steel sheets. The hemisphere has negligible impact on ρ_{zz}/ρ_{xx} while the relative bulk modulus (with respect to water) without/with the hemisphere of air is shown in *dotted/dashed lines* ($B^{-1} : r = 0.0$ μm/$B^{-1} : r = 3.7$ μm)

as shown in the dotted lines in Fig. 7.2. The bulk modulus decreases for a thicker steel plate since steel is more incompressible than water. On the other hand, if we attach hemispheres of air with radius $r = 3.7$ μm to every steel plate (a sack of air is modeled as a hemisphere on the steal plate), the bulk modulus can be decreased enormously. In this case, it is decreased to nearly 1.7 times of the bulk modulus of water.

7.3 Acoustic Carpet Cloaking

Up to this point, we have already established a scheme of controlling the anisotropy in the effective density of an acoustic metamaterial by blocking wave motion in particular directions and the bulk modulus of an acoustic metamaterial by introducing a sack of gas or incompressible materials. In this following example, we would like to demonstrate the usage of the anisotropic metamaterial in controlling the flow of sound energy to obtain acoustic cloaking in this section and acoustic subwavelength imaging in the next section.

An invisibility cloak is a metamaterial shell to guide waves around an object hidden inside the cloak. An observer outside the cloak will find the cloak with the object disappears, as if the whole system becomes purely free space [49]. However, this approach in general induces metamaterials which require large and extreme anisotropy and which require a large range of refractive indices. In fact, from topological considerations, there are actually three different ways to make an object invisible. They

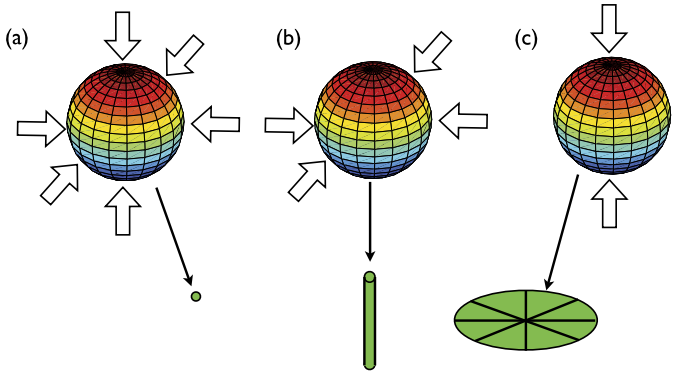

Fig. 7.3 Three topological ways to make an object invisible: **(a)** to compress an object to an infinitesimally small point; **(b)** to compress an object to an infinitesimally thin wire; and **(c)** to compress an object to an infinitesimally thin plate. **(a)** corresponds to a spherical complete cloak, **(b)** corresponds to the cylindrical cloak experimentally realized for microwave, and **(c)** is called the carpet cloak

are summarized in Fig. 7.3. The first two ways (Fig. 7.3(a) and (b)) correspond to the mentioned cloak. The cloak compresses an object to an infinitesimally small point or thin wire using the metamaterial shell. It effectively lowers the scattering cross section of the object to a small value negligible to the observer. However, for both cases, the topology before and after compression are different. Mathematically, the coordinate transformation is unavoidably singular and the coordinate transformation induces metamaterials with extreme anisotropy and refractive indices, appearing as singular values in the density tensor. In fact, the third way (Fig. 7.3(c)), by compressing the object into a thin plate, has the advantage that the coordinate transformation is not singular. It induces metamaterials with only moderate requirements. It has a disadvantage at the same time: the compressed thin plate is still visible with considerable scattering cross-section unless it sits on an infinite background of similarly dense material. Then, when the carpet cloak is covering an object sitting on a plane, the cloak will cancel out the scattering of the object and the observer will think the whole system is just a flat plane. We note that a similar scheme has been proposed in the electromagnetic context [35]. Reference [35] proposed a design for a carpet cloak by using isotropic materials with an inhomogeneous profile of refractive indices to guide light since low-loss isotropic dielectrics are common at optical frequencies. It serves as an easy way to demonstrate cloaking at optical frequencies. Actually, the cloak has been experimentally verified at both microwave and optical frequencies [14, 20, 40, 43, 60]. Later developments also showed that there can be another scheme of a carpet cloak by using a homogeneous yet anisotropic metamaterials profile for realization [5, 42]. It will be appropriate in situations where moderate anisotropy can be achieved, like the acoustic carpet cloaking we are going to explore. We will show that only moderate anisotropic density tensor is required while the bulk modulus can be kept as a constant value very similar to the original background fluid.

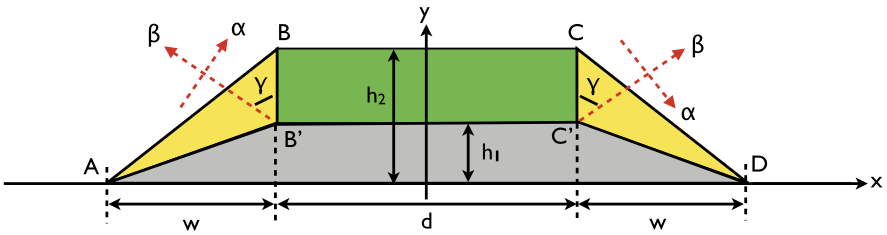

Fig. 7.4 The three structural components of the acoustic carpet cloak, the central rectangular part (BB'C'C), the *left* (*right*) *triangular part*. h_1 is the height of the hidden object region, h_2 is the height of the carpet cloak with object, d is the width of the *central rectangle* and w is the width of the *left* (*right*) *triangular part*. α and β are the principal axes of the acoustic metamaterial in *left* (*right*) *triangular region*. γ is the angle between the principal β-axis and the y-axis

For simplicity and ease of discussion, we will confine wave propagation to the x–y plane in a two-dimensional setting only and consider cloaking within a water background. Figure 7.4 shows the schematic of the carpet cloak. To construct the carpet cloak in water, we lift the flat boundary, straight line AD, of the ground (assumed to be an incompressible infinitely dense surface) upwards to AB'C'D. It creates a hidden tunnel shown as trapezoid AB'C'D in Fig. 7.4. The cloak is composed of three parts, two symmetric triangular parts (ABB', CC'D) and the central part shown as a rectangle (BB'C'C). The coordinate transformation compresses the trapezoid ABCD into the region of the cloak (AB'C'DCB). In the schematic, we have also indicated the various dimensions of the cloak. The cloak has a total width of $2w + d$ and the height is compressed from a original value h_2 to $h_2 - h_1$.

The central part of the cloak (rectangle BB'C'C) can be obtained by the following coordinate transformation:

$$y = \frac{h_2 - h_1}{h_2}\left(y' - h_2\right) + h_2, \qquad x = x', \quad \text{and} \quad z = z'. \tag{7.10}$$

The left part of the cloak (triangle ABB') can be obtained by coordinate transformation:

$$y = \frac{h_2 - h_1}{h_2} y' + \frac{x' + w + \frac{d}{2}}{w} h_1, \qquad x = x', \quad \text{and} \quad z = z', \tag{7.11}$$

while the coordinate transformation in getting the right triangular part of the cloak can easily be obtained from the mirror symmetry of the left portion. Based on the transformation approach, we can now get the induced density tensor $[\rho]$ and modulus B from the coordinate transformation of each part, according to (7.6) and (7.7). We first begin with the central region of the cloak. After some simple algebra, they are given by

$$[\rho] = \begin{pmatrix} \rho_{xx} & \rho_{xy} \\ \rho_{yx} & \rho_{yy} \end{pmatrix} = \begin{pmatrix} \frac{h_2 - h_1}{h_2} & 0 \\ 0 & \frac{h_2}{h_2 - h_1} \end{pmatrix} \rho_0, \tag{7.12}$$

and

$$B = \frac{h_2 - h_1}{h_2} B_0, \tag{7.13}$$

where ρ_0 and B_0 are the density and modulus of the water background. We can also define the corresponding anisotropic refractive indices normalized to the background fluid by

$$n_x = \sqrt{\frac{\rho_{xx}}{B}} / \sqrt{\frac{\rho_0}{B_0}} = 1, \quad \text{and} \quad n_y = \sqrt{\frac{\rho_{yy}}{B}} / \sqrt{\frac{\rho_0}{B_0}} = \frac{h_2}{h_2 - h_1}. \tag{7.14}$$

The coordinate transformation is just a simple compression in the y-direction. Therefore, the refractive index n_x is just the same as the background fluid while the refractive index n_y is increased by the area compression ratio $h_2/(h_2 - h_1)$. This requirement can be easily understood by keeping the elapsed phase the same before and after transformation in the two orthogonal x- and y-directions. Note that the effective medium is homogeneous due to the simplicity of the compression.

For the left triangular part (ABB'), the effective bulk modulus is in fact governed by the same (7.13) for the bulk modulus. It can be easily derived by looking at the transformation rule (7.7). The rule simply means that the transformed bulk modulus is always proportional to the area being transformed through the coordinate transformation. If the transformation compresses the virtual space to the physical space by a certain area compression ratio bigger than one, the bulk modulus is lowered by this compression ratio. In our example, this area compression ratio is always $h_2/(h_2 - h_1)$ in every part of the cloak. It implies that the effective bulk modulus is homogeneous within the whole cloak. On the other hand, the effective density tensor of the cloak can be obtained through (7.6) and is given by

$$[\rho] = \begin{pmatrix} \frac{h_1^2 h_2}{w^2(h_2 - h_1)} + \frac{h_2 - h_1}{h_2} & \frac{h_1}{w}\frac{h_2}{h_1 - h_2} \\ \frac{h_1}{w}\frac{h_2}{h_1 - h_2} & \frac{h_2}{h_2 - h_1} \end{pmatrix} \rho_0. \tag{7.15}$$

The density tensor has non-zero off-diagonal elements since the x- and y-axis are not the principal axes anymore. To facilitate the consideration in constructing this density tensor using acoustic metamaterials, we can diagonalize the tensor to obtain the directions of the principal axes and the associated principal values $(\rho_\alpha, \rho_\beta)$, where

$$\rho_\alpha = \frac{1}{2}\left[\rho_{xx} + \rho_{yy} - \sqrt{4\rho_{xy}\rho_{yx} + (\rho_{xx} - \rho_{yy})^2}\,\right], \tag{7.16}$$

$$\rho_\beta = \frac{1}{2}\left[\rho_{xx} + \rho_{yy} + \sqrt{4\rho_{xy}\rho_{yx} + (\rho_{xx} - \rho_{yy})^2}\,\right]. \tag{7.17}$$

The principal axes α and β are indicated by the arrows in Fig. 7.4. The angle between the β-axis and y-axis is defined by

$$\gamma = \text{acos}\left(\sqrt{\frac{\rho_{yy} - \rho_\alpha}{\rho_\beta - \rho_\alpha}}\right). \tag{7.18}$$

Then we can again obtain the corresponding refractive indices along the principal axes (n_α, n_β) normalized to the background fluid by

$$n_\alpha = \sqrt{\frac{\rho_\alpha}{B}}/\sqrt{\frac{\rho_0}{B_0}}, \quad \text{and} \quad n_\beta = \sqrt{\frac{\rho_\beta}{B}}/\sqrt{\frac{\rho_0}{B_0}}. \tag{7.19}$$

For the right triangular part of the cloak, the effective density tensor can be obtained similarly. The principal values are the same (7.16) and (7.17) while the direction of the β-axis is just the mirror symmetry of the β-axis of the left portion, also shown in Fig. 7.4.

From the above results, we know that the bulk modulus is a constant in the whole cloak while the density tensor is a constant in each part of the cloak. In the following example, we would like to discuss the effect of the various geometric parameters on the anisotropy of the cloak (i.e. the anisotropic refractive indices). It will affect how we construct the carpet cloak using acoustic metamaterials. For the central part of the cloak (BB'C'C), the anisotropic refractive indices are simply affected by the area compression ratio and is governed by (7.14). For the left or the right triangular part (ABB'/CC'D), the anisotropy of the acoustic carpet cloak is described by n_α, n_β, which depend on all the geometric parameters of the cloak, h_1, h_2, and w, according to (7.19). To be more specific, we set $h_2/h_1 = 6$ and we can plot the indices n_α and n_β against w/h_1. The results are shown in blue color (in dashed and solid lines) in Fig. 7.5. As the width w increases to allow slower ramping up of the cloak region, the anisotropy decreases with larger n_α and smaller n_β as expected. They approach the value one and area compression ratio $h_2/(h_2 - h_1)$ for very large w, which is very similar to the case for the central region of the cloak, i.e. coordinate transformation (7.11) becoming (7.10). Moreover, if we decrease/increase the size of cloak through a larger/smaller h_2/h_1, the curve n_β shifts upwards/downwards in having a larger/smaller anisotropy while the curve n_α stays essentially the same. We can also plot the anisotropy factor n_β/n_α when h_2 and w vary at the same time, as shown in Fig. 7.5. The result is shown in Fig. 7.6. From the figure, we see that both a larger h_2 or a larger w favors a smaller anisotropy. In other words, for a given achievable anisotropy (e.g. from acoustic metamaterials from the last section), a particular contour with fixed anisotropy can be picked.

As an example, we choose the contour with anisotropy factor 1.235 and further pick $h_2 = 6h_1$ and $w = 10h_1$ on the contour as the geometric parameters so that both h_2 and w are reasonably small to have a small size of the carpet cloak. It corresponds to $n_\beta = 1.22$ and $n_\alpha = 0.985$ from Fig. 7.5. For our configuration, we have also set $d = 2h_1$ as the width of the center part of the cloak. To test the effectiveness of our design of acoustic carpet cloak, we have employed full wave simulation (COMSOL Multiphysics with acoustic module) by launching a Gaussian beam at 60 degrees towards the cloak. The wavelength in water is set as $1.15h_1$. The total pressure field pattern with only the curved reflecting surface without the presence of the cloak is

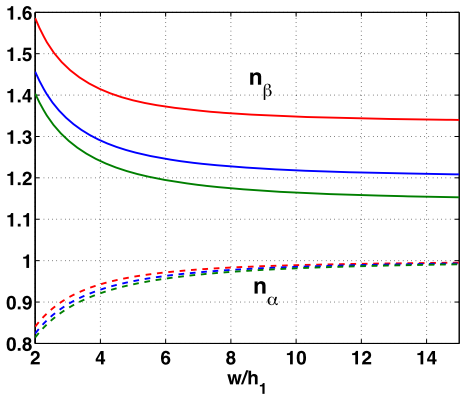

Fig. 7.5 Principal refractive indices of the carpet cloak (*yellow region*) against w/h_1. *Solid lines* show the index n_β and *dashed lines* show the index n_α. Three different cases of $h_2/h_1 = 4$, 6, and 8 are shown in *red*, *blue* and *green colors*. The corresponding indices for the central part of the cloak are the limiting values for $w \to \infty$ (Color figure online)

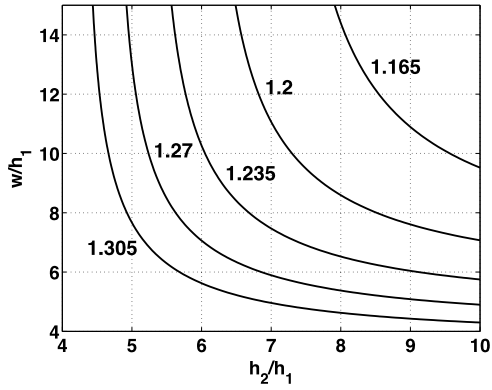

Fig. 7.6 The contours of anisotropy factor n_β/n_α against different h_2 and w of the cloak

shown in Fig. 7.7(a). The curved reflecting surface scatters the incident beam into one upper beam which reflects at roughly 50 degrees (which satisfies reflection law of the left slanted surface of the cloak instead of the original flat ground) and also another part scattered in the forward direction. Now, the situation with the presence of the cloak is simulated and the corresponding pressure field is shown in Fig. 7.7(b). In the simulation, the cloak is composed of the effective medium described from (7.12) to (7.19) except that we have incorporated the bulk modulus into the density tensor by $\rho_\alpha \to \rho_\alpha B_0/B$, $\rho_\beta \to \rho_\beta B_0/B$ and $B \to B_0$. This is called the reduced parameter approximation. It has the advantage that we can concentrate on constructing the density tensor from acoustic metamaterials without considering the bulk modulus. Although there is such an approximation (which introduces an impedance mismatch between the background fluid and the cloak), there is only little spurious reflection from the boundary of the cloak in the simulation. As a whole, the cloak cancels out the scattering of the object in a way that the cloak with the object just looks like a flat hard surface in reflecting the incident Gaussian beam also at 60 degrees without additional scattering. Moreover, the field inside the cloak shows interference pattern between the incident and the reflected beam. The interference pattern is simply squeezed upwards, comparing to the field when only a flat hard surface is present.

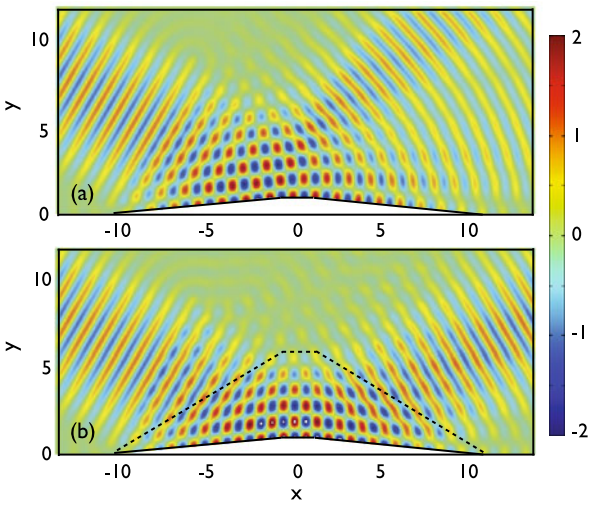

Fig. 7.7 **(a)** Pressure field pattern when only the object (a raised reflecting hard surface) is present without the cloak. **(b)** Pressure field pattern with the carpet cloak bounded by the dashed line. All length scales are normalized to h_1. A Gaussian beam of width $9.2h_1$ at 60 degrees impinges on the surface from the left at a wavelength of $1.15h_1$ in background water

Now, we would like to apply the principle developed in the last section in constructing our optimized carpet cloak. Instead of three dimensional analysis, we only need to construct two-dimensional anisotropic acoustic metamaterials for the current configuration of a carpet cloak. To make the analysis even simpler, we can simply block the waves in the β directions. In our design, it can be achieved by stacking 1D layers of solid brass and water in the β direction. Such a scheme in constructing acoustic metamaterials has also been used for other purposes, e.g. in constructing a focusing lens and in achieving extraordinary transmission and screening [3, 15, 41]. The effective medium of this simple acoustic metamaterial is governed by:

$$\frac{1}{\rho_\alpha} = \frac{f}{\rho_b} + \frac{1-f}{\rho_0} \approx \frac{1-f}{\rho_0}, \tag{7.20}$$

$$\rho_\beta = f\rho_b + (1-f)\rho_0, \tag{7.21}$$

$$\frac{1}{B} = \frac{f}{B_b} + \frac{1-f}{B_0} \approx \frac{1-f}{B_0}, \tag{7.22}$$

where f is the volume filling ratio of brass, ρ_b and ρ_0 are the density of brass and background water, B_b and B_0 are the bulk modulus of brass and background water. Then, in the α direction, the water can easily flow and $n_\alpha \approx 1$, actually a value a bit smaller than 1, from (7.20) and (7.22). In the β direction, the waves are blocked and has a larger density ρ_β and hence a larger index n_β obtained from (7.21) and (7.22). From the required $n_\beta = 1.22$, we can solve the filling ratio which should be set as 0.08. We note that our configuration requires $n_\alpha = 0.985$ which is near enough to the value one given by our acoustic metamaterial. Moreover, we can also obtain the directions of the β-axis according to (7.18). The analysis can be done for all the three parts of the cloak. Hence, we have already obtained a microscopic scheme in constructing the carpet cloak and the layered structure is also outlined in Fig. 7.8(a)

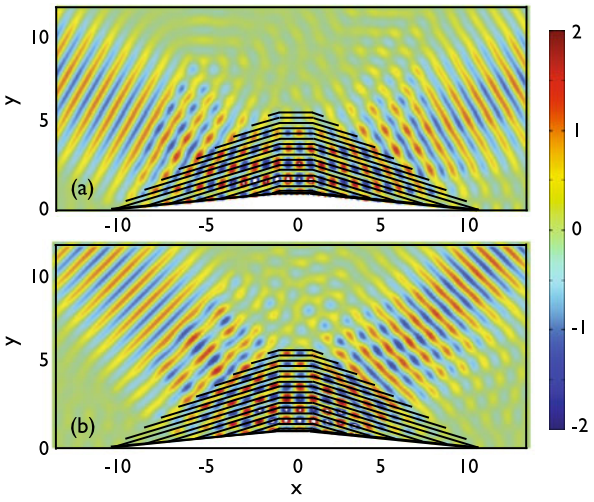

Fig. 7.8 Pressure field pattern of the acoustic carpet cloak constructed by microstructures. The *thin black lines* represent the brass plates with a filling ratio of 0.08, and the periodicity is chosen as $0.3h_1$. β axis is perpendicular to the brass layers and the α axis is parallel to the layers. All length scales are normalized to h_1. A Gaussian beam of width $9.2h_1$ at **(a)** 60 degrees and **(b)** 45 degrees impinges on the cloak from the left at a wavelength of $1.15h_1$ in background water

as thin black lines. The periodicity is chosen as $0.3h_1$, a value a few times smaller than the wavelength of background water in the β direction.

Figure 7.8(a) simulates the cloak with microstructures, the same situation in Fig. 7.7(b) except that the cloak is now simulated with all the microstructures. With the required n_α and n_β, γ can be solved and is set as 17.04°. Therefore we set the brass layers with the angle γ inclined with x-axis. In Fig. 7.8(a), the pressure filled pattern shows that the same Gaussian beam at 60 degrees impinging to the microstructured cloak which also cancels out the scattering of the object, and the Gaussian beam is also reflected at 60 degrees without additional scattering. In fact, as we expect from transformation optics, the cloak should work regardless of the form of excitation. Here, we have changed the incident angle from 60 to 45 degrees and the cloak still works. In Fig. 7.8 (b), a Gaussian beam with the same width as Fig. 7.8(a) impinges on the microstructure cloak at 45 degrees. A reflected beam at 45 degrees results and the same cloak also cancels out the scattering of the object at this incident angle.

7.4 Acoustic Subwavelength Imaging

Similar to the invisibility cloak, we can construct other acoustic devices using the same strategy. In particular, magnifying optical hyperlens [27, 38, 50] have shown the ability to overcome the diffraction limit in electromagnetic waves. The hyperlens can image objects with resolution significantly smaller than half the wavelength. By employing carefully engineered dispersion surfaces obtained using metamaterials, these hyperlenses not only carry the subwavelength information contained in evanescent waves across the lens, but also magnify it. In essence, the hyperlens converts the evanescent waves to propagating waves so that the information travels

to the far field outside the lens. The first demonstrated optical hyperlenses utilized 2-D metamaterials consisting of deep subwavelength layers of metals and dielectrics alternating in the radial directions, to constitute a largely negative effective permittivity along the propagation (radial) direction, and at the same time small effective permittivity at the transverse (angular) direction [27, 38, 50]. For such anisotropic material properties, the 2-D dispersion curves are hyperbolic and nearly flat over a wide range of angular wave vectors, indicating that high angular momentum optical modes are supported as propagating waves, allowing the sub-wavelength information to propagate in the material. The successful demonstration has motivated the search for new forms of magnifying lens with sub-wavelength resolution. These include plasmonic or TEM modes propagating among tapered wires [26, 30, 52], which can sample an image with subwavelength features pixel-by-pixel to create the magnified image at the lens output. As the diffraction limit is intrinsic to all kinds of wave phenomena, conventional acoustic imaging is also limited by the wavelength of the sound wave. Therefore, if we can realize an acoustic hyperlens, it will readily benefit applications in nondestructive testing and medical imaging.

In this section, we design and demonstrate an acoustic hyperlens, that can work in a broadband frequency range. Again, the principle of the acoustic hyperlens will be very similar to its electromagnetic counterpart, except that we have to develop the corresponding acoustic metamaterial designs which are particularly suitable for acoustics instead of electromagnetic waves, i.e. not the mentioned metal-dielectric layers stacking in the radial direction anymore. In fact, in acoustics, there are already some related research works. Recent studies have already shown that acoustic focusing can be achieved by using phononic crystal slabs [10, 25, 31, 55, 56, 61] and acoustic metamaterials [63]. Also, a recent theory of acoustic metamaterial hyperlens has proposed a design utilizing alternating layers of positive and negative dynamic density, with locally resonant acoustic elements to achieve the negative density and flat dispersion curve [2]. Although the negative dynamic density [39, 62] can occur only at a narrow band of frequencies when these elements oscillate resonantly, introducing excessive losses and limiting the maximum propagation distance to magnify the image, it serves as a starting point in constructing the anisotropic acoustic metamaterials.

Here, we utilize again the design of the anisotropic acoustic metamaterial in the last section to construct the acoustic hyperlens. Such a design allows us to image objects with deep-subwavelength resolution in a broadband frequency range with low loss because it does not employ local resonance. Figure 7.9 shows how our anisotropic acoustic metamaterials are used in implementing the acoustic hyperlens. The hyperlens consists of 36 brass fins which are 3 mm tall and extend from 2.7 cm to 21.8 cm from the center of a half-cylinder. Each brass or air fin occupies 2.5 degrees in the angular direction. The lens can be interpreted as a metamaterial made from stacking brass and air layers in the angular direction. The subwavelength spacing of the layers throughout the hyperlens allows the use of effective medium properties described by (7.20) to (7.22). The background medium (subscript 0) is now air. The α and β directions in the equations now indicate the radial and the angular directions. Figure 7.9 is actually the photograph of our finished hyperlens

Fig. 7.9 The acoustic hyperlens sample. The lens is made of 36 brass fins in air (running from radius 2.7 to 21.8 cm in the radial direction). The fins, spanning 180 degrees, are sitting on a brass substrate. The cover sheet has been removed to expose the microstructure for this view. Reproduced from [34] with permission of Nature Publishing Group

sample. The fabrication was done using a two-axis computer numerical controlled vertical mill. The hyperlens was milled off from a 0.5-inch thick brass plate, resulting in the brass fins on the remaining substrate of 9.7 mm in thickness, more than sufficient to prevent wave leakage. To confine sound propagation region to two dimensions for the imaging experiment, a 0.25-inch thick aluminium plate covers the top of the fins.

In our design, we have chosen brass as the fins which have a density much larger than that of the fluid (air) in between. From the effective medium equations, it follows immediately that the effective radial density is close to that of air while the effective angular density is close to that of brass. This large anisotropy resembles the large anisotropy in electromagnetic hyperlens. However, unlike the case in electromagnetism where the large ratio between permittivities in the two perpendicular directions comes from resonance (e.g. with plasmonic constituents), the acoustic anisotropy here comes from perforation and it can be easily extended to the three-dimensional case for acoustic waves [64]. Because of this large anisotropy, the acoustic hyperlens has a similar function to its electromagnetic counterpart to image objects beyond the classical diffraction limit. The information of the fine details of the object is originally stored by the evanescent waves which usually decay and diminish as they travel away from the object. Through the hyperlens, we compress these evanescent waves into propagating waves as they travel down the lens. As a result, the hyperlens magnifies the image progressively with fine details. The originally subwavelength features of the object can be then magnified to an image with feature size comparable or larger than a wavelength of the sound waves.

To demonstrate the effectiveness of the acoustic hyperlens, we have conducted experiments and full-wave simulations to confirm that the hyperlens is able to image objects with subwavelength resolution. The source in the experiment is an arrangement of three speakers as the input object shown in Fig. 7.10. Such an arrangement can show the generality in the imaging process. Two of the speakers were kept at the same 1.2 cm center-to-center separation but offset to one side, and a third source was added 2 cm center-to-center from the centermost speaker. A picture of the sources can be seen in Fig. 7.10(c). The experimentally measured pressure field outside the hyperlens is shown in Fig. 7.10(a). The source distances from the hyperlens edge were varied so that the strength of the three resultant beams also vary. All three

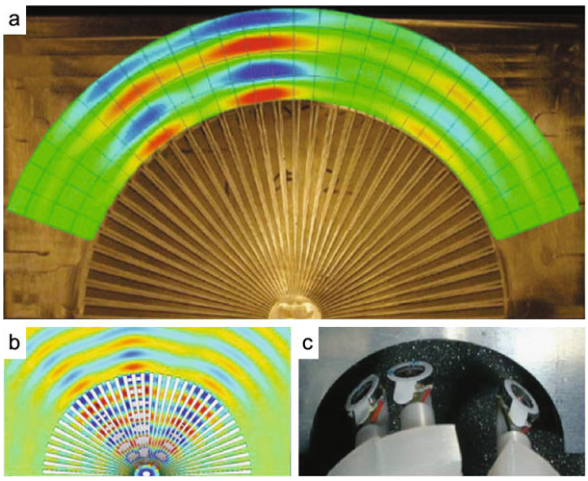

Fig. 7.10 **(a)** Experimental results showing three distinct beams propagating away from the hyperlens. **(b)** Simulation of the three source system with the fins modeled as elastic brass elements. **(c)** Speakers used in 3 source experiment. The speakers have been raised from the testing height for clarity. Reproduced from [34] with permission of Nature Publishing Group

beams can be clearly seen at the output of the hyperlens when the source is fired at 6.6 kHz. Owing to the large ratio between the outer and the inner radii, the hyperlens compresses a significant portion of the evanescent components into the band of propagating waves so that the image is magnified eight times. For example, the two left subwavelength sources (separated by 0.23λ at the input plane) themselves radiate at the lens outer edge as if they are larger than the diffraction limit. The separation is converted to 1.85λ and the sources are magnified to be larger than one wavelength at the hyperlens exit so that it can also be observed in the far field as two distinct beams for the left two sources. The corresponding full-wave simulation of the pressure field is shown in Fig. 7.10(b) which agrees very well with the experimental results. The same experiment is repeated for the case without the hyperlens and the two sources cannot be differentiated as a sharp contrast. As our design does not involve any local resonance, it can operate over a broad band of frequencies without significant loss. Figure 7.11(a) shows the measured broad-band response of the hyperlens. In this case, two in-phase 1-cm-diameter sound sources transmitting at 4.2–7.0 kHz with separation of 1.2 cm (corresponding to a sub-wavelength resolution of $\lambda/6.8$–$\lambda/4.1$) are placed in front of the inner edge of the lens while the pressure intensity is measured at the outer edge of the lens. The corresponding theoretically simulated pressure intensity is plotted in Fig. 7.11(b) to confirm the sub-wavelength resolution in the frequency range.

Apart from the acoustic hyperlens, there are recent works on another subwavelength-imaging device, namely the acoustic superlens. The superlens can be realized by an array of parallel slits for a 2D sample [28] or by an array of hollow cylinders for a 3D sample [64]. Discoveries [16, 37, 46, 53, 54, 57] in the optical field have suggested that a thin slab of metamaterial can act as a superlens and restore all the evanescent components. For our 3D acoustic superlens, we developed a different holey metamaterial that presents a very anisotropic structure which allows wave propagation in the direction perpendicular to the interfaces, so the evanescent waves scattered from imaging object can excite the Fabry-Perot resonant modes presented

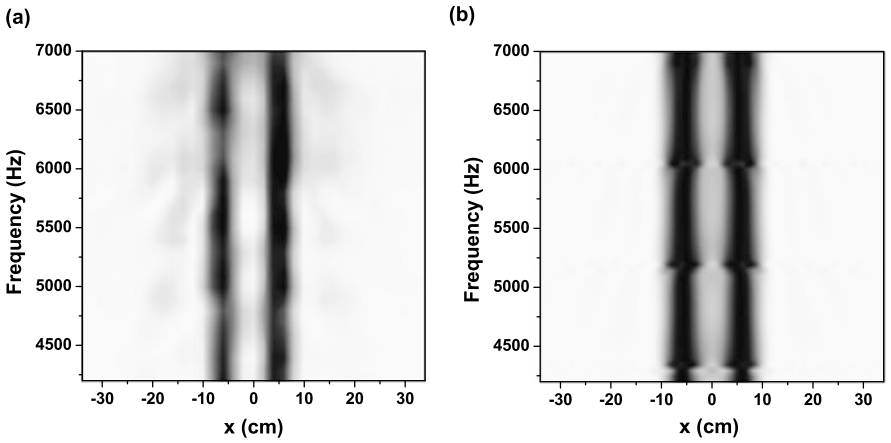

Fig. 7.11 **(a)** Experimental measurement of the pressure intensity against position and frequency, measured at the outer edge of the lens. The frequency ranges from 4.2–7.0 kHz, corresponding to a $\lambda/6.8$–$\lambda/4.1$ resolution. The intensity profile at each frequency is scaled so the two peaks can be clearly resolved throughout the frequency range. **(b)** Theoretical pressure intensity with the microstructures included in the full-wave simulations. *Black/white colors* indicate high/low values

within the cylinders. As a result, deep-subwavelength information is successfully transmitted through this holey metamaterial superlens and contributes in restoring an image with deep sub-diffraction-limit features. It is difficult to demonstrate optical subwavelength imaging with such a structure due to the requirement of filling the cylinders with very high dielectric constant material [29]. But in the case of an acoustic superlens, propagation of acoustic waves inside those deep subwavelength sized cylinders is possible because of the absence of a cutoff frequency. Therefore, the ability of this superlens to resolve subwavelength information can be optimized by downsizing the period of cylinders array.

Figure 7.12 shows the actual sample we built to establish the functionality of an acoustic superlens. This sample can be treated as a metamaterial of thick rigid block perforated with deep-subwavelength square holes to form a periodic array (in x–y plane). Its major part is a combination of 1600 (40×40) square metal tubes, with the geometrical parameters of each tube being: inside diameter l is 0.79 mm, outside diameter and period of array d is 1.58 mm, tube length L is 158 mm (in z-direction). Similar to the acoustic hyperlens, we choose brass alloy as the material for the tubes due to its much larger density compared to the fluid (air) inside. All the brass tubes are clamped firmly in parallel together into a 4-inch-wide square aluminum tube. We applied super glue between the tubes to prevent any possible movement or vibration under pressure. Both experiments and full 3D numerical calculations using a modal expansion technique are performed on this holey structured metamaterial to demonstrate its' effect on deep subwavelength imaging. A 20 mm diameter speaker is chosen as the sound source to produce continuous sinusoidal plane waves. We place this speaker at 20 cm before the imaging object which is a letter "E" with a linewidth 3.18 mm perforated on a ultra thin brass plate. The acoustic superlens is

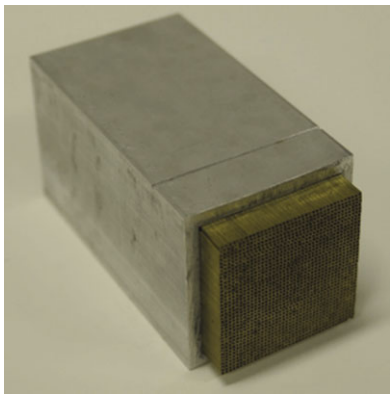

Fig. 7.12 Holey-structured acoustic metamaterial for deep-subwavelength imaging

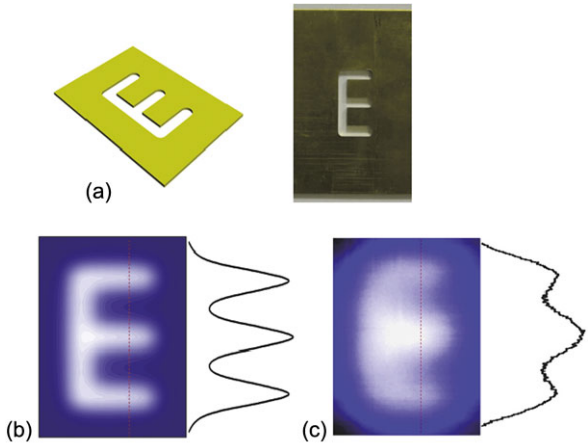

Fig. 7.13 Imaging object is letter 'E' perforated in ultrathin brass plate **(a)**. Operating frequency is 2.18 kHz ($\lambda = 158$ mm). Measured image at $d = 1.58$ mm from the output plane, and the acoustic field distribution along the cross-section indicated by the *dashed line* **(c)** match well with the simulation results **(b)**

placed immediately behind the imaging object so that the evanescent waves scattered from the object can reach the lens. Also a microphone is used to measure the 3D acoustic field distribution on the output side. The whole experimental setup is surrounded by sound absorbing foam to prevent external noise penetration. From the pictures shown in Fig. 7.13, it can be seen that the experimental image is in good agreement with the simulation result. A linewidth feature of 3.18 mm ($\lambda/50$) can be clearly resolved. Despite some mild blurring at the edge and joint points, the shape of whole letter "E" remains intact, subwavelength details at the corners are also well reproduced.

The capability of this holey structured metamaterial to resolve deep subwavelength spatial information can be explained with the effective medium approach. In the limit that all diffraction effects can be safely neglected and the transmission process inside the cylinders is dominated by the fundamental propagating mode, the zero order transmission coefficient of parallel momentum $\mathbf{k}_{||} = (k_x, k_y)$ being transferred to a diffracted plane wave can be expressed as Ref. [9]:

$$t^{00}(\lambda, \mathbf{k}_{||}) = \frac{4|S_{00}|^2 Y \exp(iq_z L)}{(Y|S_{00}|^2+1)^2 + (Y|S_{00}|^2-1)^2 \exp(2iq_z L)}, \tag{7.23}$$

where $q_z = k_0 = 2\pi/\lambda$, $S_{00} = l/d$, $Y = k_0/\sqrt{k_0^2 - k_{||}^2}$, k_0 is the wavenumber in free space. Therefore, at resonance conditions in which a standing wave is excited inside the cylinders ($q_z L = m\pi$, m is integer), the transmission coefficient has unity modulus for all parallel momentum, including evanescent waves. This suggests that, the acoustical image of object placed at the input side can be perfectly transferred to the output side at the Fabry-Perot resonance frequencies.

If we discuss the problem from the point-of-view of multiple scattering, (7.23) can be rewritten in terms of two-media scattering coefficients:

$$t^{00}(\lambda, \mathbf{k}_{||}) = \frac{\tau_{12}\tau_{23} \exp(iq_z L)}{1 - \eta^2 \exp(2iq_z L)}, \tag{7.24}$$

where $\tau_{12} = 2S_{00}/(1 + Y|S_{00}|^2)$ denotes the incident wave coupled with the fundamental mode inside the cylinders. $\tau_{23} = 2S_{00}Y/(1 + Y|S_{00}|^2)$ denotes the waveguide mode that transmits into the zero-order diffraction beam at output side. $\eta = (Y|S_{00}|^2 - 1)/(Y|S_{00}|^2 + 1)$ denotes the reflection of fundamental mode inside the cylinders at two ends. When $|\mathbf{k}_{||}| \gg k_0$, which means the deep-subwavelength situation, η gets closer to 1, $|\tau_{23}| \approx 2S_{00}k_0/|\mathbf{k}_{||}| \ll 1$, therefore the transmission of fundamental mode inside the cylinders into the outgoing plane wave is very weak, and the Fabry-Perot resonance stems from multiple scattering events from the two interfaces that behave as quasi-perfect mirrors. Therefore, the equation resembles the transmission coefficient of a homogeneous slab using the transfer matrix approach. Actually, the effective acoustic impedance of this holey structured metamaterial can be extracted from it. From (7.24), the reflection of a normally-incident acoustic plane wave can be expressed as $R = (1 - |S_{00}|^2)/(1 + |S_{00}|^2)$. And classic acoustic told us that the reflection coefficient of an acoustic wave at the interface of two homogeneous media in terms of acoustic impedance is $R = (Z_2 - Z_1)/(Z_2 + Z_1)$, where Z_1 and Z_2 is the impedance of the input and the output interface of the superlens. From those two expressions, it is obvious that the effective acoustic impedance of this metamaterial superlens with respect to that of air is $Z = Z_{air}/|S_{00}|^2$.

As discussed above, the effective transmission of deep-subwavelength image through the acoustic metamaterial superlens relies on the Fabry-Perot resonances excited inside the cylinders. The scattered evanescent wave components with large wavenumbers are consequently coupled and carried over to the output side for imaging. Although the superlens is not magnifying the image by converting the near field information to the far field, it can resolve very deep-subwavelength features through the Fabry-Perot resonances.

However, there exists a very interesting observation between the superlens and the hyperlens on the working bandwidth. We found that the working bandwidth for the hyperlens is broadband in nature while the one for the superlens is narrow band in nature. In the following, we will investigate the mechanism resulting in the very different behavior on the bandwidth. To explain this difference, it is essential to discuss both the superlens and the hyperlens in a common language using a transfer

matrix, as in the case of superlens [36]. For comparison, we focus on the superlens and the hyperlens systems in 2D. It can clearly show the main difference between hyperlens and superlens, which causes the different working frequency bandwidth of the two lens. To discuss the hyperlens using a transfer matrix, we first transform the hyperlens from a cylindrical to a rectangular shape by using the coordinate transformation approach. The coordinate transformation can be described by the following formulas:

$$x = R_1\theta', \qquad y = r', \quad \text{and} \quad z = z', \tag{7.25}$$

where R_1 is the inner radius of the cylindrical hyperlens, (r', θ', z') are the cylindrical coordinates of the original system containing the cylindrical hyperlens where $\theta' \in [-\pi, \pi]$ and $r' \in (0, \infty)$. (x, y, z) are the coordinates of the transformed system containing the hyperlens now in rectangular shape. Based on the transformation approach, we can obtain the induced density tensor $[\rho(x, y)]$ and bulk modulus $B(x, y)$ in the transformed system, according to (7.6) and (7.7). They are given by:

$$\left[\rho(x, y)\right] = \begin{pmatrix} \rho_{xx} & \rho_{xy} \\ \rho_{yx} & \rho_{yy} \end{pmatrix} = \begin{pmatrix} \frac{y}{R_1} & 0 \\ 0 & \frac{R_1}{y} \end{pmatrix} \rho'\left(r', \theta'\right), \tag{7.26}$$

and

$$B(x, y) = \frac{R_1}{y} B'\left(r', \theta'\right), \tag{7.27}$$

where $\rho'(r', \theta')$ and $B'(r', \theta')$ are the density and the bulk modulus of the system before transformation. We note that ρ' depends on the polar coordinate r' and θ'. It equals to ρ_b if the coordinate falls into the region of the brass fins, otherwise it equals to background density of air ρ_0. B' describes the bulk modulus profile in a similar way.

Figure 7.14 shows the transformation of the hyperlens constructed with microstructures from the cylindrical to the rectangular shape. In Fig. 7.14(a), the cylindrical hyperlens with inner radius $R_1 = 2.7$ cm and outer radius $R_2 = 21.8$ cm is constructed by brass fins and air whose density and modulus are ρ_b, ρ_0, B_b and B_0. Based on the coordinate transformation approach, the fin microstructures in air background for the cylindrical hyperlens are transformed to the layered microstructures (shown in Fig. 7.14(b)) with density tensor and bulk modulus now varying in y-direction, according to (7.26) and (7.27). The corresponding periodicity (in θ' direction) $\Delta\theta' = \pi/36$ for the fin microstructures of the cylindrical hyperlens is transformed to periodicity $a = \frac{\pi}{36} R_1$ in x-direction for the transformed rectangular hyperlens. The thick dashed line in Fig. 7.14(a) is considered as a virtual periodic boundary which is mapped to $x = R_1\pi$ and $x = -R_1\pi$ in the rectangular system as the periodic boundaries (thick dashed lines) shown in Fig. 7.14(b). The interfaces of the cylindrical hyperlens at $r' = R_1, R_2$ are mapped to the transformed rectangular hyperlens at $y = R_1, R_2$.

In Fig. 7.15, we have plotted the simulated pressure field intensity for both systems when we have two sources (with separation 1.2 cm) at a frequency of 6.6 kHz,

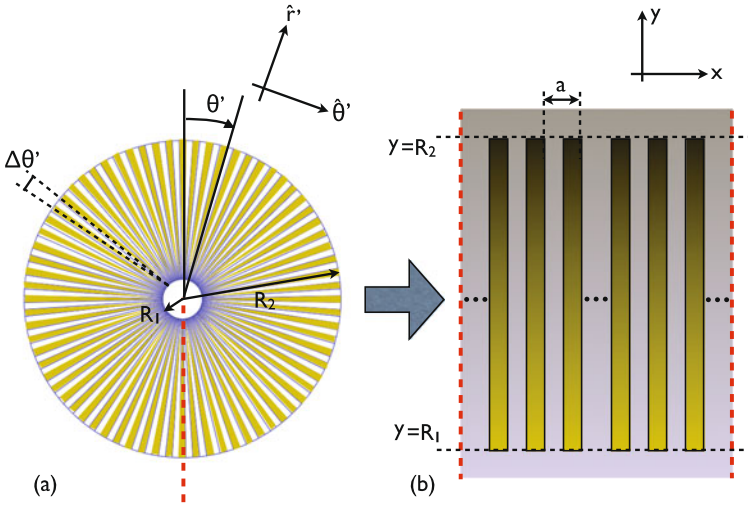

Fig. 7.14 The microstructures of **(a)** the cylindrical hyperlens and **(b)** the transformed rectangular hyperlens. The *thick dashed line* in **(a)**, the virtual periodic boundary, is mapped to the *thick dashed lines* in **(b)** as periodic boundaries. The inner ($r' = R_1$) and outer ($r' = R_2$) interface of the cylindrical hyperlens in **(a)** are mapped to the bottom ($y = R_1$) and top ($y = R_2$) interface of the transformed rectangular hyperlens in **(b)**. $R_1 = 2.7$ cm, and $R_2 = 21.8$ cm. Adapted from [36]. Copyright (2011) American Institute of Physics

fired at the inner interface of the hyperlens. Note that the field intensities before and after transformation have been multiplied by r' and y respectively for clarity of presentation. From the two field patterns, it can be seen that they can both resolve sub-wavelength details (showing two peaks at the outer-interface of the lens) and both field patterns are equivalent to each other simply through rewriting coordinates. Therefore, the simulations validate our approach in representing the original cylindrical hyperlens using the transformed rectangular one as a mathematical measure. From now on, we will use the transformed rectangular hyperlens to represent the original cylindrical one.

Now, since the transformed hyperlens is in the rectangular system with transverse symmetry, we can use the transfer matrix approach (7.24) to decompose the input wave by using plane waves of different transverse wave numbers. Such an approach has an advantage that we can discuss the hyperlens and a superlens on a common footing. Figure 7.16(a) shows the pressure intensity distribution when two sources with separation 1.2 cm are fired at the input interface of the lens for different frequencies. The pressure intensity is calculated at 1 cm away from the outer interface ($y = R_2$) of the transformed rectangular hyperlens. The results resemble the one using full-wave simulation in Fig. 7.11(b) as expected. On the other hand, if we drop the y-dependence of the constitutive parameters of the transformed hyperlens, it becomes the superlens, i.e. simply parallel slits (brass and air with filling fraction 0.5) in the y-direction with the same lattice constant a. Since there is no conversion from the near to the far field, the corresponding pressure intensity is cal-

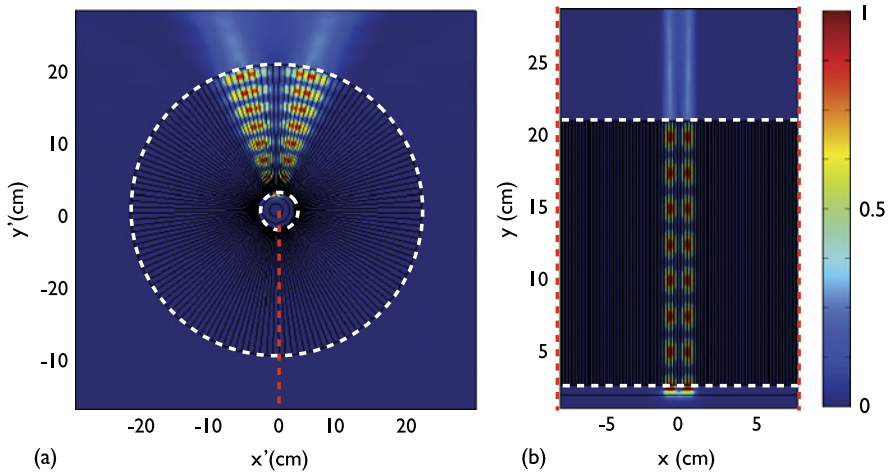

Fig. 7.15 The pressure field pattern at frequency 6.6 kHz of **(a)** the cylindrical hyperlens and **(b)** the transformed rectangular hyperlens when two sources with subwavelength separation 1.2 cm are fired at the input interface. The *white circles* in **(a)** are the inner ($r' = R_1$) and outer ($r' = R_2$) interface of the cylindrical hyperlens. The *white horizontal lines* are the bottom ($y = R_1$) and the top ($y = R_2$) interface of the transformed rectangular hyperlens. Reproduced from [36]. Copyright (2011) American Institute of Physics

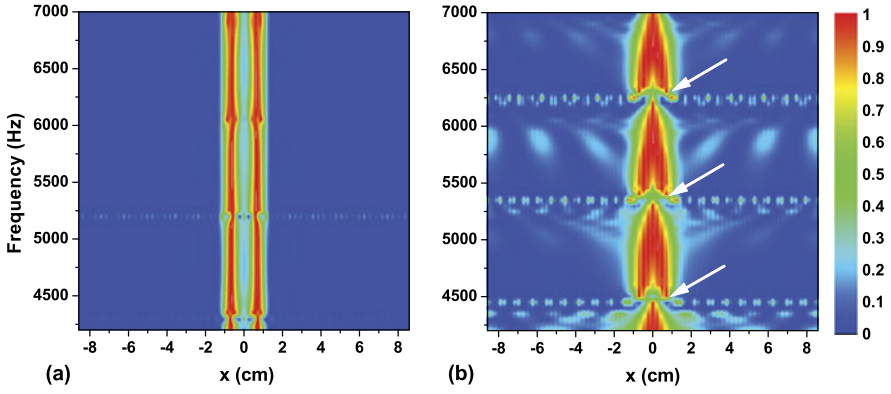

Fig. 7.16 The pressure intensity distribution for frequencies from 4.2 kHz to 7 kHz when two sources with separation 1.2 cm are fired at the input interface of the lens. The intensity profile is calculated at 1 cm away from the outer interface for the **(a)** transformed rectangular hyperlens and at the proximity of the outer interface for the **(b)** superlens. Distance x for the hyperlens is defined according to (7.25). See text for details of the configuration of the superlens in comparison. Adapted from [36]. Copyright (2011) American Institute of Physics

culated at the close proximity of the exit interface of the superlens to conserve the possible subwavelength resolution and is shown in Fig. 7.16(b). The white arrows in Fig. 7.16(b) indicate the several frequencies where the superlens can work well

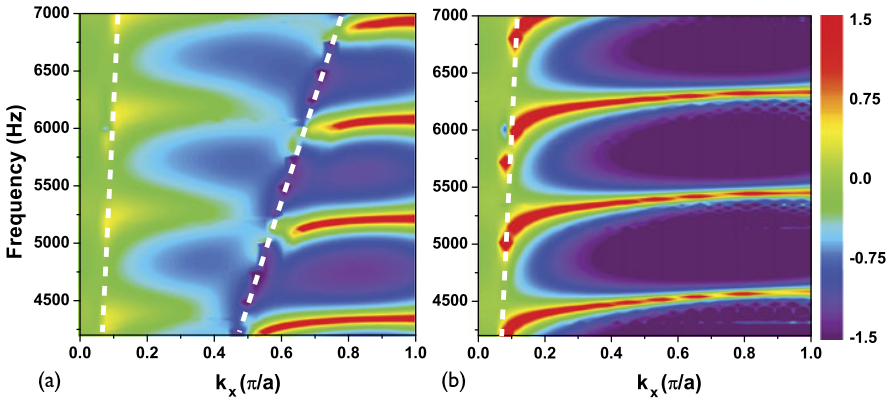

Fig. 7.17 Transmission coefficient T versus parallel momentum $k_x/(\frac{\pi}{a})$ and frequency in logarithmic scale (log 10) of **(a)** transformed 2D hyperlens and **(b)** 2D superlens in comparison. Adapted from [36]. Copyright (2011) American Institute of Physics

and they correspond to the frequencies where Fabry-Perot resonances occur, as discussed above and pointed out in Ref. [28]. On the other hand, the hyperlens can work in broadband except a few frequencies shown in Fig. 7.16(a), e.g. at 5.2 kHz, where some noises come in to contaminate on the two peaks. Such noises, still stored in the near-fields at the exit interface of the hyperlens, will further diminish when the pressure intensity is recorded farther away from the hyperlens.

To further explore the underlying physics, we have plotted the transmission coefficient T (in logarithmic scale, log 10) of the 2D hyperlens (as the coordinate system is rectangular now) and the 2D superlens against transverse wavenumber k_x at different frequencies in Fig. 7.17. Since both the (transformed rectangular) hyperlens and the superlens are constructed by layered structure with the same periodic constant a, we use $\frac{\pi}{a}$ to normalize all the wavenumbers. The transmission coefficient T is defined by

$$T = \left| \frac{Z_2}{Z_1} \frac{|p_2|^2}{|p_1|^2} \right|, \tag{7.28}$$

where Z_i and p_i $(i = 1, 2)$ are the surface impedance and the input$(i = 1)$/output$(i = 2)$ pressure at the interface $(y = R_1, R_2)$ of the lens at different transverse wavenumbers.

Figure 7.17 gives a clear physical picture to understand the difference between the hyperlens and the superlens. In Fig. 7.17(a), there are two sound lines on the hyperlens transmission. The layered structure medium of the hyperlens is y-dependent and so, the first sound line (the one with larger slope, $k_x = k_0$) shows the properties of the input interface $y = R_1$, and the second sound line (the one with smaller slope, $k_x = (R_2/R_1)k_0$) shows the properties of the output interface $y = R_2$. The two sound lines together show how the hyperlens converts the near-field information into the far-field. The transverse wavenumber components to the left-hand side of the first sound line represent the propagating wave components input to the hy-

perlens, and that to the right-hand side represents the evanescent wave components of the input which contain the near field information. The transverse wavenumber components between the two sound lines represent the propagating wave components converted from the evanescent waves at the input of the lens, which are considered as the far field information. The transverse wavenumber components to the right-hand side of the second sound line represent the evanescent wave components exiting from the outer interface of the hyperlens. So the components between the two sound lines are just the near field information which the hyperlens can convert to the far field. From the transmission spectrum in Fig. 7.17 (a), the transmissions of these components are actually large enough (ranging from 0.2 to 1). It induces an effective transmission of these Fourier components contributing to the subwavelength image resolution for the hyperlens. This generally happens in the whole frequency range of our consideration. Therefore, the hyperlens is broadband in nature except for several frequencies corresponding to the guiding modes propagating in the angular direction of the hyperlens. At these frequencies, there are resonant transmission inducing the noises to influence the images, as an example, shown in Fig. 7.16(a) at the frequency 5.2 kHz. These noises will decrease at a distance away from the output interface of the hyperlens. So the hyperlens can still have good subwavelength resolution. In Fig. 7.17(b), the transmission spectrum of the superlens is shown, there is only one sound line where the propagating wave components and the evanescent wave components are separated. There are no evanescent wave components input to the superlens that can be converted to the propagating wave components. From the transmission spectrum in Fig. 7.17(b), the transmission coefficients of most evanescent wave components are very small except for several frequencies of Fabry-Perot resonances (the flat red region), just like the 3D superlens case we discussed before. Only the Fourier components near the Fabry-Perot resonant frequencies can be transmitted, therefore the superlens is narrow band in nature. Nevertheless, the superlens can achieve a very deep sub-wavelength resolution through the resonances.

The transformed hyperlens with Fig. 7.17(a) also gives an alternative picture to understand the angular momentum conservation of the cylindrical hyperlens. The dispersion relation of the hyperlens can be expressed using its effective densities $(\rho'_{r'}, \rho'_{\theta'})$ and effective bulk modulus (B') by

$$\frac{k'^2_{r'}}{\rho'_{r'}/B'} + \frac{k'^2_{\theta'}}{\rho'_{\theta'}/B'} = \omega^2, \tag{7.29}$$

where $k'_{r'}$ is the longitudinal wavenumber, $k'_{\theta'} = \frac{m}{r'}$ is the transverse wavenumber, $m = 0, 1, 2, \ldots$ is the order of the transverse wavenumber in the cylindrical system. It is known that angular momentum conservation means that for a large value of m, $k'_{r'}$ will change from an imaginary number to a real number with r' increasing. It represents the evanescent wave being converted to the propagating wave in the cylindrical system. On the other hand, in the transformed system containing the hyperlens, the dispersion relation can also be formulated along the x- and y- directions. According to (7.6) and (7.7), we can substitute the constitutive parameters $[\rho]$ and B into the dispersion equation and obtain

$$\frac{k_y^2}{\rho'_{r'}/B'} + \frac{R_1^2 k_x^2}{y^2 \rho'_{\theta'}/B'} = \omega^2, \tag{7.30}$$

where k_y is the longitudinal wavenumber in the transformed system (now it is rectangular). The equation with $y = R_1$ and $y = R_2$ for background air gives the two sound lines for the transformed hyperlens. As an example, when y increases and changes from the inner interface to the outer interface of the transformed hyperlens, k_y for the region between the two sound lines in Fig. 7.17(a) changes from an imaginary number to a real number. Therefore the evanescent wave can be converted to the propagating wave in the transformed system. Instead of the angular momentum conservation, the varying medium supplies the conversion mechanism. In other words, the angular momentum conservation of the waves in cylindrical system is equivalent to the waves propagates in a corresponding rectangular medium with varying constitutive parameters.

7.5 Conclusion

In conclusion, we have investigated a scheme for constructing anisotropic acoustic metamaterials by simply blocking waves in different directions. The anisotropy allows us to manipulate the flow of sound energy in preferred ways. In one example, we control the flow of sound energy around an object sitting on a hard surface. An acoustic carpet cloak is constructed and acoustic invisibility can be achieved by just inserting thin solid plates at preferred directions around the object. In another two examples, the hyperlens and the superlens, we control the flow of sound energy across the well designed perforated structures to minimize diffraction. A transformation approach is used to compare the two subwavlength imaging lenses on the same footing. The broadband subwavelength image information can be transported and magnified from evanescent to propagating fields through the acoustic hyperlens, while the deep subwavelength imaging happened when the FP resonances occur in the superlens.

Acknowledgements JL and ZL thank the support from the City University of Hong Kong (SRG grant number 7002598). JZ and XZ acknowledge support from the Office of Naval Research (grant number N00014-07-1-0626).

References

1. Ambati, M., Fang, N., Sun, C., Zhang, X.: Surface resonant states and superlensing in acoustic metamaterials. Phys. Rev. B **75**, 195447 (2007)
2. Ao, X., Chan, C.T.: Far-field image magnification for acoustic waves using anisotropic acoustic metamaterials. Phys. Rev. E **77**, 025601(R) (2008)
3. Cai, F., Liu, F., He, Z., Liu, Z.: High refractive-index sonic material based on periodic subwavelength structure. Appl. Phys. Lett. **91**, 203515 (2007)

4. Chen, H., Chan, C.T.: Acoustic cloaking in three dimensions using acoustic metamaterials. Appl. Phys. Lett. **91**, 183518 (2007)
5. Chen, X., Luo, Y., Zhang, J., Jiang, K., Pendry, J.B., Zhang, S.: Macroscopic invisibility cloaking of visible light. Nat. Commun. **2**, 176 (2011)
6. Cheng, Y., Yang, F., Xu, J.Y., Liu, X.J.: A multilayer structured acoustic cloak with homogeneous isotropic materials. Appl. Phys. Lett. **92**, 151913 (2008)
7. Christensen, J., Fernandez-Dominguez, A.I., de Leon-Perez, F., Martin-Moreno, L., Garcia-Vidal, F.J.: Collimation of sound assisted by acoustic surface waves. Nat. Phys. **3**, 851–852 (2007)
8. Christensen, J., Huidobro, P.A., Martin-Moreno, L., Garcia-Vidal, F.J.: Confining and slowing airborne sound with a corrugated metawire. Appl. Phys. Lett. **93**, 083502 (2008)
9. Christensen, J., Martin-Moreno, L., Garcia-Vidal, F.J.: Theory of resonant acoustic transmission through subwavelength apertures. Phys. Rev. Lett. **101**, 014301 (2008)
10. Cervera, F., Sanchis, L., Sanchez-Perez, J.V., Martinez-Sala, R., Rubio, C., Meseguer, F.: Refractive acoustic devices for airborne sound. Phys. Rev. Lett. **88**, 023902 (2002)
11. Cummer, S.A., Schurig, D.: One path to acoustic cloaking. New J. Phys. **9**, 45 (2007)
12. Cummer, S.A., Popa, B.-I., Schurig, D., Smith, D.R., Pendry, J.B., Rahm, M., Starr, A.: Scattering theory derivation of a 3D acoustic cloaking shell. Phys. Rev. Lett. **100**, 024301 (2008)
13. de Rosny, J., Fink, M.: Overcoming the diffraction limit in wave physics using a time-reversal mirror and a novel acoustic sink. Phys. Rev. Lett. **89**, 124301 (2002)
14. Ergin, T., Stenger, N., Brenner, P., Pendry, J.B., Wegener, M.: Three-dimensional invisibility cloak at optical wavelengths. Science **328**, 337 (2010)
15. Estrada, H., Candelas, P., Uris, A., Belmar, F., Garcia de Abajo, F.J., Meseguer, F.: Extraordinary sound screening in perforated plates. Phys. Rev. Lett. **101**, 084302 (2008)
16. Fang, N., Lee, H., Sun, C., Zhang, X.: Sub-diffraction-limited optical imaging with a silver superlens. Science **308**, 534 (2005)
17. Fang, N., Xi, D., Xu, J., Ambati, M., Srituravanich, W., Sun, C., Zhang, X.: Ultrasonic metamaterials with negative modulus. Nat. Mater. **5**, 452–456 (2006)
18. Farhat, M., Guenneau, S., Enoch, S., Movchan, A., Zolla, F., Nicolet, A.: A homogenization route towards square cylindrical acoustic cloaks. New J. Phys. **10**, 115030 (2008)
19. Fok, L., Zhang, X.: Negative acoustic index metamaterial. Phys. Rev. B **83**, 214304 (2011)
20. Gabrielli, L.H., Cardenas, J., Poitras, C.B., Lipson, M.: Silicon nanostructure cloak operating at optical frequencies. Nat. Photonics **3**, 461 (2009)
21. Greenleaf, A., Lassas, M., Uhlmann, G.: On nonuniqueness for Calderon's inverse problem. Math. Res. Lett. **10**, 685 (2003)
22. Greenleaf, A., Lassas, M., Uhlmann, G.: Anisotropic conductivities that cannot be detected by EIT. Physiol. Meas. **24**, 413 (2003)
23. Greenleaf, A., Kurylev, Y., Lassas, M., Uhlmann, G.: Full-wave invisibility of active devices at all frequencies. Commun. Math. Phys. **275**, 749–789 (2007)
24. Guenneau, S., Movchan, A., Petursson, G., Ramakrishna, S.A.: Acoustic metamaterials for sound focusing and confinement. New J. Phys. **9**, 399 (2007)
25. He, Z., Cai, F., Ding, Y., Liu, Z.: Subwavelength imaging of acoustic waves by a canalization mechanism in a two-dimensional phononic crystal. Appl. Phys. Lett. **93**, 233503 (2008)
26. Ikonen, P., Simovski, C.R., Tretyakov, S., Belov, P., Hao, Y.: Magnification of subwavelength field distributions at microwave frequencies using a wire medium slab operating in the canalization regime. Appl. Phys. Lett. **91**, 104102 (2007)
27. Jacob, Z., Alekseyev, L.V., Narimanov, E.: Optical hyperlens: Far-field imaging beyond the diffraction limit. Opt. Express **14**, 8247–8256 (2006)
28. Jia, H., Ke, M., Hao, R., Ye, Y., Liu, F., Liu, Z.: Subwavelength imaging by a simple planar acoustic superlens. Appl. Phys. Lett. **97**, 173507 (2010)
29. Jung, J., Garcia-Vidal, F.J., Martin-Moreno, L., Pendry, J.B.: Holey metal films make perfect endoscopes. Phys. Rev. B **79**, 153407 (2009)
30. Kawata, S., Ono, A., Verma, P.: Subwavelength colour imaging with a metallic nanolens. Nat. Photonics **2**, 438–442 (2008)

31. Ke, M., Liu, Z., Cheng, Z., Li, J., Peng, P., Shi, J.: Flat superlens by using negative refraction in two-dimensional phononic crystals. Solid State Commun. **142**, 177–180 (2007)
32. Leonhardt, U.: Optical conformal mapping. Science **312**, 1777 (2006)
33. Li, J., Chan, C.T.: Double-negative acoustic metamaterial. Phys. Rev. E **70**, 055602(R) (2004)
34. Li, J., Fok, L., Yin, X., Bartal, G., Zhang, X.: Experimental demonstration of an acoustic magnifying hyperlens. Nat. Mater. **8**, 931 (2009)
35. Li, J., Pendry, J.B.: Hiding under the carpet: A new strategy for cloaking. Phys. Rev. Lett. **101**, 203901 (2008)
36. Liang, Z., Li, J.: Bandwidth and resolution of super-resolution imaging with perforated solids. AIP Adv. **1**, 041503 (2011)
37. Liu, Z., Durant, S., Lee, H., Pikus, Y., Fang, N., Xiong, Y., Sun, C., Zhang, X.: Far-field optical superlens. Nano Lett. **7**, 403 (2007)
38. Liu, Z., Lee, H., Xiong, Y., Sun, C., Zhang, X.: Far-field optical hyperlens magnifying sub-diffraction-limited objects. Science **315**, 1686 (2007)
39. Liu, Z., Zhang, X., Mao, Y., Zhu, Y.Y., Yang, Z., Chan, C.T., Sheng, P.: Locally resonant sonic materials. Science **289**, 1734–1736 (2000)
40. Liu, R., Ji, C., Mock, J.J., Chin, J.Y., Cui, T.J., Smith, D.R.: Broadband ground-plane cloak. Science **323**, 366 (2009)
41. Lu, M., Liu, X., Feng, L., Li, J., Huang, C., Chen, Y., Zhu, Y., Zhu, S., Ming, N.: Extraordinary acoustic transmission through a 1D grating with very narrow apertures. Phys. Rev. Lett. **99**, 174301 (2007)
42. Luo, Y., Zhang, J., Chen, H., Ran, L., Wu, B.-I., Kong, J.A.: A rigorous analysis of plane-transformed invisibility cloaks. IEEE Trans. Antennas Propag. **57**, 3926 (2009)
43. Ma, H.F., Cui, T.J.: Three-dimensional broadband ground-plane cloak made of metamaterials. Nat. Commun. **1**, 21 (2010)
44. Milton, G.W., Briane, M., Willis, J.R.: On cloaking for elasticity and physical equations with a transformation invariant form. New J. Phys. **8**, 248 (2006)
45. Norris, A.N.: Acoustic metafluids. J. Acoust. Soc. Am. **125**, 839–849 (2009)
46. Pendry, J.B.: Negative refraction makes a perfect lens. Phys. Rev. Lett. **85**, 3966 (2000)
47. Pendry, J.B., Holden, A.J., Robbins, D.J., Stewart, W.J.: Magnetism from conductors and enhanced nonlinear phenomena. IEEE Trans. Microw. Theory Tech. **47**, 2075 (1999)
48. Pendry, J.B., Li, J.: An acoustic metafluid: Realizing a broadband acoustic cloak. New J. Phys. **10**, 115032 (2008)
49. Pendry, J.B., Schurig, D., Smith, D.R.: Controlling electromagnetic fields. Science **312**, 1780 (2006)
50. Salandrino, A., Engheta, N.: Far-field subdiffraction optical microscopy using metamaterial crystals: Theory and simulations. Phys. Rev. B **74**, 075103 (2006)
51. Schurig, D., Mock, J.J., Justice, B.J., Cummer, S.A., Pendry, J.B., Starr, A.F., Smith, D.R.: Metamaterial electromagnetic cloak at microwave frequencies. Science **314**, 977 (2006)
52. Shvets, G., Trendafilov, S., Pendry, J.B., Sarychev, A.: Guiding, focusing, and sensing on the subwavelength scale using metallic wire arrays. Phys. Rev. Lett. **99**, 053903 (2007)
53. Smith, D.R., Pendry, J.B., Wiltshire, M.C.K.: Metamaterials and negative refractive index. Science **305**, 788 (2004)
54. Soukoulis, C.M., Linden, S., Wegener, M.: Negative refractive index at optical wavelengths. Science **315**, 47 (2007)
55. Sukhovich, A., Jing, L., Page, J.H.: Negative refraction and focusing of ultrasound in two-dimensional phononic crystals. Phys. Rev. B **77**, 014301 (2008)
56. Sukhovich, A., Merheb, B., Muralidharan, K., Vasseur, J.O., Pennec, Y., Deymier, P.A., Page, J.H.: Experimental and theoretical evidence for subwavelength imaging in phononic crystals. Phys. Rev. Lett. **102**, 154301 (2009)
57. Taubner, T., Korobkin, D., Urzhumov, Y., Shvets, G., Hillenbrand, R.: Near-field microscopy through a SiC superlens. Science **313**, 1595 (2006)
58. Torrent, D., Sanchez-Dehesa, J.: Acoustic cloaking in two dimensions: A feasible approach. New J. Phys. **10**, 063015 (2008)

59. Torrent, D., Sanchez-Dehesa, J.: Anisotropic mass density by two-dimensional acoustic metamaterials. New J. Phys. **10**, 023004 (2008)
60. Valentine, J., Li, J., Zentgraf, T., Bartal, G., Zhang, X.: An optical cloak made of dielectrics. Nat. Mater. **8**, 568 (2009)
61. Yang, S., Page, J.H., Liu, Z., Cowan, M.L., Chan, C.T., Sheng, P.: Focusing of sound in a 3D phononic crystal. Phys. Rev. Lett. **93**, 024301 (2004)
62. Yang, Z., Mei, J., Yang, M., Chan, N.H., Sheng, P.: Membrane-type acoustic metamaterial with negative dynamic mass. Phys. Rev. Lett. **101**, 204301 (2008)
63. Zhang, S., Yin, L., Fang, N.: Focusing ultrasound with an acoustic metamaterial network. Phys. Rev. Lett. **102**, 194301 (2009)
64. Zhu, J., Christensen, J., Jung, J., Martin-Moreno, L., Yin, X., Fok, L., Zhang, X., Garcia-Vidal, F.J.: A holey-structured metamaterial for acoustic deep-subwavelength imaging. Nat. Phys. **7**, 52 (2011)

Chapter 8
Transformation Acoustics

Steven A. Cummer

Abstract In this chapter we review the development of the concept of transformation acoustics, through which sound fields can be arbitrarily manipulated by complex acoustic materials. We describe the theory and the design equations in several different forms, and we present several explicit design examples using transformation acoustics. After briefly describing some theoretical offshoots from the original idea, we conclude with a summary of approaches for engineering composite materials with the smoothly inhomogeneous and anisotropic properties needed for many transformation acoustics devices.

8.1 Introduction

Suppose you can imagine an acoustic device that manipulates sound waves in a specific way. Let us be more specific: let us suppose you can imagine an acoustic device that manipulates sound waves by stretching or squeezing or shifting or in other ways operating on an incident sound field. Perhaps this device takes that sound field and bends it perfectly around a corner with no reflection. Or suppose this device bends incident sound energy around a central object so that it does not scatter or cast a shadow (see Fig. 8.1).

Visualizing the device is the easy part. The hard part is determining the properties of the material or materials required to realize such a device. If you are given a configuration of defined materials, there are any number of analytical or numerical techniques that will enable you to calculate how a sound wave interacts with and is operated on by these materials. But the problem we have posed is the much more challenging one in which we know the output, i.e. the desired new sound field configuration, and we want to know the acoustic medium that would have such an effect. There are very few techniques to apply to such a problem. In fact, there is no guarantee that a medium that produces the desired effect even exists.

Transformation acoustics is technique that solves this problem in a surprisingly straightforward way. More generally, it is a paradigm for the creation of sound-

S.A. Cummer (✉)
Department of Electrical and Computer Engineering, Duke University, Durham, NC 27708, USA
e-mail: cummer@ee.duke.edu

R.V. Craster, S. Guenneau (eds.), *Acoustic Metamaterials*,
Springer Series in Materials Science 166, DOI 10.1007/978-94-007-4813-2_8,

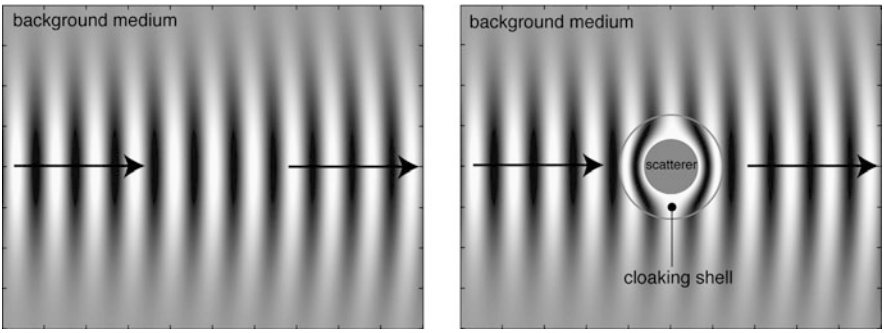

Fig. 8.1 Example of what the coordinate transformation approach can do. *Left*: A simulated field distribution for an electromagnetic beam traveling from left to right in empty space. *Right*: A simulated field distribution for an electromagnetic beam interacting with a metal cylinder surrounded by an ideal electromagnetic cloaking shell, marked by the *solid lines*. Outside the shell, the two distributions are identical, indicating zero scattering from the cloaked cylinder. Inside the shell, the fields are deformed as they would be from the coordinate transformation used to design the shell properties

manipulating materials and devices that are either difficult or impossible to derive through other theoretical approaches. It is based on the idea of a coordinate transformation of an arbitrary initial sound field. If the device you imagine can be defined in terms of a coordinate transformation, by squeezing, stretching, and/or displacing the sound field in a finite region, then transformation acoustics provides the mathematics for taking this coordinate transformation and deriving the properties of a material in that same finite region that will have exactly the same effect on the sound field as the coordinate transformation.

The theory is remarkably powerful, simple to apply, and general. However, few things in life are free, and transformation acoustics is not an exception. In most cases the materials required to physically realize these devices have very complex properties. The usual outcome of a transformation acoustics design is a material that has continuously varying properties and is also anisotropic. Such materials are not usually obtainable off-the-shelf. But many of these properties can be engineered into well-designed composite materials using the techniques from the field of acoustic metamaterials. To be sure, fabricating functional transformation acoustics devices will be a challenge. But basic ideas for how it can be done are in place, and the payoff in realizing truly novel acoustic devices is substantial.

In this chapter we review the development of the concept of transformation acoustics, through which sound fields can be arbitrarily manipulated by complex acoustic materials. We describe the theory in detail, summarize the design equations in several different forms, and briefly describe some theoretical offshoots from the original idea. We present several explicit design examples using transformation acoustics, and we conclude with a summary of approaches for engineering composite materials with the smoothly inhomogeneous and anisotropic properties needed for many transformation acoustics devices.

8.2 The Original Idea: Transformation Electromagnetics

The development of transformation acoustics actually began with the development of transformation electromagnetics, a related idea that linked coordinate transformations on electromagnetic fields to specific electromagnetic material properties. Given that all of this theoretical development occurred within five years of this writing, it is both interesting and instructive to review the sequence of the development of these profound ideas.

8.2.1 Transformation Electromagnetics Theory

Although the concept of equating coordinate transformations with physical material properties in electromagnetics has a long history [27, 38], the modern application of the idea originated quite recently [26]. It should be noted that closely related work developed a similar concept for electric current flow and applied it to electrical impedance tomography [14].

Again, the transformation electromagnetics concept is based on the finding that the specific distortion or modification of an electromagnetic field distribution by a coordinate transformation can also be created by a specific set of electromagnetic material properties in the region of the transformed fields. This transformation-material equivalence is a direct consequence of the coordinate transformation invariance of the dynamical equations describing electromagnetic fields, in this case the well-known Maxwell equations. This invariance is an integral part of general relativity and has been known for a long time. The fantastic insight of Pendry et al. was that this invariance could be interpreted in terms of physical electromagnetic materials.

At this point it will be useful to see show some of the details of how transformation electromagnetics works. Although Pendry et al. presented their version of transformation electromagnetics in terms of basis vectors and scale factors, it can be reformulated more compactly using Jacobian matrices [37]. Let us impose an arbitrary coordinate transformation on the Maxwell equations, or equivalently, on any electromagnetic field distribution that satisfies the Maxwell equations. This function F contains all of the stretching, squeezing, and displacing we might want to impose on the fields. After the transformation, the field equations are in exactly the same form but with new material parameter tensors (electric permittivity $\bar{\bar{\varepsilon}}_r$ and magnetic permeability $\bar{\bar{\mu}}_r$) expressed in matrix form (in terms of the original medium parameters $\bar{\bar{\varepsilon}}'_r$ and $\bar{\bar{\mu}}'_r$) as [37]

$$\bar{\bar{\varepsilon}}_r = \frac{A\bar{\bar{\varepsilon}}'_r A^T}{\det(A)}, \qquad \bar{\bar{\mu}}_r = \frac{A\bar{\bar{\mu}}'_r A^T}{\det(A)}, \tag{8.1}$$

where the matrix A is the Jacobian matrix of the transformation (see Sect. 8.3.1 for a more explicit description of A in the context of transformation acoustics).

In other words, the Maxwell equations are coordinate transformation invariant, and the coordinate transformation manifests itself through a change in the material parameters defined above. This invariance has been long understood, but (8.1) has traditionally been interpreted as a representation of the original material parameters in a new coordinate system or space. Pendry realized this could equally well represent new material parameters in the original space. The first, and perhaps still most interesting, application of this idea was to making an object invisible by surrounding it with a cylindrical or spherical shell that bends, without reflection, any incident wave energy smoothly around the interior of the shell so that the wave energy exits the shell with exactly the same phase and amplitude that it would have had without any object present at all.

Figure 8.1 shows, for demonstration purposes, the resulting field distribution inside and outside of such a cloaking shell with electromagnetic material parameters defined from the original work in the field [26]. One can see that, outside the shell, the field distribution is exactly the same as it would be with no object at all. This means that there is no wave scattering in any direction, including the difficult-to-control forward scatter or shadow region, and any object in the interior of the shell is effectively invisible to electromagnetic waves. Note too that the resulting field distribution *inside* the shell is exactly what one would expect if the original fields in empty space in a circle are compressed into the annulus defined by the shell, which is the coordinate transformation that yielded the desired material properties.

This finding has resulted in an explosion of literature describing complex materials capable of many exotic manipulations of electromagnetic fields [33, 34] that are just beginning to be physically realized in simulation [8] and experiment [21, 36]. In general the electromagnetic parameters that result from transformation electromagnetics are anisotropic and complicated to create, but the concept of electromagnetic metamaterials [25] lends itself well to the design and fabrication of such complex materials.

8.2.2 Can Transformation Electromagnetics Be Extended to Other Waves?

An important question that followed the development of transformation electromagnetics was whether transformation electromagnetics could be extended to other wave systems. The first work to address this issue [22] analyzed the coordinate transformation invariance of the equations of elastodynamics. These equations proved not to be coordinate-transformation invariant, implying that coordinate transformations could not in general be realized through complex elastodynamic media. Importantly, this work suggested that acoustics, as a subset of elastodynamics, could not be manipulated via the transformation approach. However, as described below, it was eventually shown that transformation acoustics is valid under conditions slightly different than those considered in this work.

8.3 Transformation Acoustics

The first work to show that the concept of transformation acoustics was at least partially valid [10] found that the 2D acoustic equations with anisotropic tensor mass density take the same form as the 2D single polarization Maxwell equations with anisotropic permittivity or permeability. Thus, by analogy, any 2D transformation electromagnetics device or material could be translated directly into a 2D transformation acoustics device. Soon after, the analogy approach was applied in a slightly different form [3] and showed that the fully 3D acoustic equations with anisotropic tensor mass density take the same form as the electric conductivity equation with embedded sources, which was already known to have transformation-type solutions [14].

Transformation acoustics at this point was thus shown to be conceptually valid. Any complex manipulation of sound fields that can be described by a coordinate transformation can be realized through complex acoustic materials defined by the transformation itself. We explore and demonstrate this idea in some detailed examples below, but first we derive the basic equations in a simple form that enables us to explore the unusual material properties needed to physically realize transformation acoustics devices.

8.3.1 A Succinct Derivation of Transformation Acoustics

While the original derivations of transformation acoustics were based on analogies with other wave systems [3, 10], useful insight and understanding comes from a direct derivation of the underlying equations of transformation acoustics. Such a derivation was presented in [9], which employed the unit vector-based approach used in the original work on transformation electromagnetics [26]. A more concise derivation comes through the direct use of Jacobian matrixes, and we present such a derivation of transformation acoustics here.

Figure 8.2 articulates the basic transformation idea. We begin with the original coordinate system, sound field distribution, and material parameters (left panel) denoted with the primed ($'$) designation. This describes the virtual space that we want the wave to "see" as it propagates in the physical space that will contain the complex materials. The coordinate transformation $(x, y, z) = F(x', y', z')$ then deforms the space, and the fields and materials contained in it, as shown in the right panel of Fig. 8.2. This leads to a notation in which everything about the virtual space (i.e., coordinates, fields, and material parameters) is primed, and everything about the physical space that contains the complex materials that deform the fields as we want them deformed is unprimed.

In this case we have chosen to alter the coordinates inside a finite region (a circle of $r < 0.5$) by compressing the radius, but this is meant simply to be an illustrative example. After the transformation the right panel represents the physical space and the deformed physical sound field distribution we will obtain with the complex material parameters determined through the transformation acoustics formalism. These new materials will reside inside the region of the coordinate transformation, which

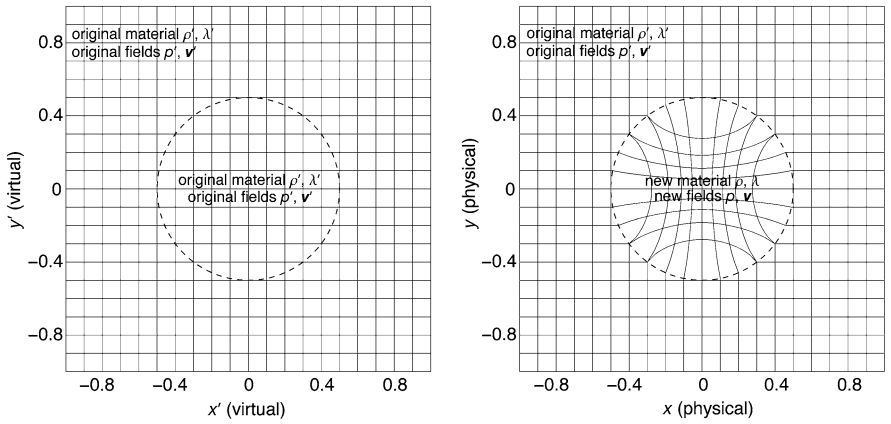

Fig. 8.2 Illustration of how transformation acoustics works. *Left*: The original, "virtual" space represented by a simple Cartesian coordinate system and filled with a simple, homogeneous fluid. *Right*: Inside the circle of $r < 0.5$, the coordinates are transformed by shrinking the radius. The sound field inside the *circle* can be deformed in exactly this way inside this transformed region by complicated acoustic material parameters derived through the transformation acoustics formalism

in this case is again a circle of $r < 0.5$. Outside this circle, the coordinates are unchanged, and thus the material is unchanged by the transformation.

We now derive expressions for the new material properties needed to physically realize the coordinate transformation. We begin the derivation with the time harmonic equations of linear acoustics in a simple inviscid fluid, namely

$$\nabla' p' = i\omega\rho' \mathbf{v}', \tag{8.2}$$

$$i\omega p' = \lambda' \nabla' \cdot \mathbf{v}', \tag{8.3}$$

where p' is pressure, $\mathbf{v}'$ is velocity, λ' is bulk modulus, and ρ' is mass density. Note that the harmonic time convention $\exp(-i\omega t)$ is employed here and throughout this chapter. These fields and material parameters are the fields and materials in virtual space (x', y', z') that usually contain simple material parameters and a simple sound field distribution.

We wish to impose a coordinate change described by new curvilinear coordinates x, y, and z on these equations. The Jacobian matrix A of the transformation from (x', y', z') to (x, y, z) is given by

$$A = \begin{bmatrix} \frac{\partial x}{\partial x'} & \frac{\partial x}{\partial y'} & \frac{\partial x}{\partial z'} \\ \frac{\partial y}{\partial x'} & \frac{\partial y}{\partial y'} & \frac{\partial y}{\partial z'} \\ \frac{\partial z}{\partial x'} & \frac{\partial z}{\partial y'} & \frac{\partial z}{\partial z'} \end{bmatrix}, \tag{8.4}$$

where it is implicitly assumed that each new coordinate (e.g., x) is a function of the three original coordinates (x', y', z'). In terms of A, the gradient operation can be expressed in terms of the new unprimed coordinates as (for example, [15])

$$\nabla' p' = A^T \nabla p' = A^T \nabla p, \tag{8.5}$$

where ∇ denotes the gradient operator in the new coordinate system, and the pressure in the new coordinate system p is simply the original pressure p' translated or dragged to the new coordinates. In other words, the new pressure p reflects the coordinate transformation as in the right panel of Fig. 8.2, but it is not rescaled by the transformation.

Similarly, the divergence operation can be expressed in the new coordinates as

$$\nabla' \cdot \mathbf{v}' = \det(A) \nabla \cdot \frac{A}{\det(A)} \mathbf{v}' = \det(A) \nabla \cdot \mathbf{v}, \tag{8.6}$$

where $\nabla\cdot$ denotes the divergence operator in the new coordinates, and the velocity vector after the transformation is given by

$$\mathbf{v} = \frac{A}{\det(A)} \mathbf{v}'. \tag{8.7}$$

Thus, in contrast to the scalar pressure, the vector velocity is translated and rescaled by the coordinate transformation. In the most general case, this rescaling can involve both a rotation and a magnitude change determined by the matrix A.

With these expressions the original system of equations in (8.2)–(8.3) can be written in the new coordinates as

$$\nabla p = i\omega \left[\det(A) \left(A^T \right)^{-1} \rho \left(A^{-1} \right) \right] \mathbf{v}, \tag{8.8}$$

$$i\omega p = \left[\lambda \det(A) \right] \nabla \cdot \mathbf{v}. \tag{8.9}$$

Note that this set of equations is in exactly the same fundamental form as the original acoustic equations in (8.2)–(8.3)but with new material parameters

$$\bar{\bar{\rho}} = \det(A) \left(A^T \right)^{-1} \rho' \left(A^{-1} \right), \tag{8.10}$$

$$\lambda = \lambda' \det(A). \tag{8.11}$$

That the fundamental structure of the equations remains unchanged after this spatial coordinate transformation is the essence of transformation acoustics. This means that if the original pressure p' and velocity $\mathbf{v}'$ fields are solutions to the acoustic equations in a medium defined by the original mass density ρ' and bulk modulus λ', then the transformed p (which has been dragged through space according to the transformation but is otherwise unmodified) and v (which has been both dragged and rescaled according to (8.7) are *also* solutions to the acoustic equations in a new medium defined by the transformed and anisotropic mass density $\bar{\bar{\rho}}$ and bulk modulus λ given above.

Transformation acoustics is thus a very powerful tool for problems of acoustic design or synthesis. While there are plenty of techniques that can tell you how sound waves interact with a certain material distribution, there are very few (if any) general purpose tools for determining the material properties and spatial distribution

required to execute a specific operation on sound waves. Transformation acoustics is just such a tool—it tells you the precise material properties needed to manipulate sound waves in a certain way, provided that manipulation can be described in terms of a coordinate transformation. Section 8.4 below demonstrates this concept in two concrete examples.

8.3.2 *Some Initial Comments on the Materials Needed for Transformation Acoustics*

Equations (8.10) and (8.11) describe the materials needed to physically realize a transformation acoustics device. These materials are not, in general, simple, and a few comments about their properties might be helpful at this point. How one can realize these kinds of materials is described in more detail in Sect. 8.5, although it should be noted that figuring out how to create such materials is a very active area of research at the time of this writing.

For smooth transformations, which are commonly used in practice, $\det(A)$ will be a smooth and continuous function of position defined by the new coordinates (x, y, z). According to (8.11), this means that the bulk modulus of the needed medium must vary smoothly with position. Importantly, the resulting material is still described by a scalar bulk modulus, and is thus fundamentally still an inviscid fluid. Although smoothly-varying bulk modulus is not a property common in real fluids, one can imagine that composite materials can be designed with spatially varying composition that mimics this property. For example, it has long been known that under some conditions the effective bulk modulus of a mixture of fluids and solids is simply the volume-weighted average of the bulk modulus of the components [41]. This suggests that a fluid with solid inclusions of continuously increasing concentration can behave like a material with smoothly-varying bulk modulus.

In contrast, (8.10) indicates that a general transformation acoustics material must exhibit some properties that are dramatically different from the original fluid. In most cases the original fluid filling the original, virtual space will have a simple, isotropic mass density. The physical material required to mimic the coordinate transformation, however, is described by a mass density tensor or matrix. This means that the fluid needs to behave for acoustic waves as if it has a different mass density for oscillatory fluid motion in different directions. In other words, the effective dynamic mass density of the fluid must be anisotropic.

This is not as crazy a concept as it might sound at first. Obviously a parcel of fluid by itself will not exhibit mass anisotropy. If you grab that parcel and apply a steady force to it, it will accelerate according to Newton's second law of motion or $F = ma$. And if you apply a steady force in a different direction, say perpendicular to that original direction, it will still accelerate as if it has the same mass m. However, oscillatory motion is not the same as steady motion, and for manipulating sound waves we definitely wish to control the response to oscillatory forces.

A relatively simple conceptual model for a material that exhibits anisotropic dynamic mass has been described in the literature [22], namely a hollow shell containing a spring-loaded mass in which the springs attaching the mass to the shell have different spring constants in different directions. The mass inside the shell will exhibit a resonance at a specific frequency that, because of the different spring constants, varies with the direction of the motion. If one applies an oscillatory force to the shell at a frequency far from a resonance frequency, then the dynamic effective mass of the shell will be close to its total static mass. However, if an oscillatory force is applied close to the resonance frequency, the resonant motion of the interior mass will strongly change the dynamic effective mass of the shell. The different resonance frequencies for different directions of motion means that this object exhibits anisotropic dynamic effective mass.

Another possibility for creating anisotropic effective mass density is a composite material made of alternating thin layers two or more different background fluids. It has been shown analytically [35] that sound waves traveling normal to these layers, provided they are sufficiently thin compared to a wavelength, experience a different effective mass than do sound waves traveling parallel to these layers. Simulations have shown that transformation acoustics devices can in principle be realized physically by these alternating thin fluid layers [5, 40]. These conceptual models are primarily meant to show how anisotropic effective dynamic mass density is not an inconceivable concept. More details of how transformation acoustic materials can be physically realized are described in Sect. 8.5, particularly with structures that are simpler to physically construct.

8.4 Application Examples

Through the equations above, transformation acoustics enables any modification of sound fields that can be described by a coordinate transformation to be physically realized with a specific, and admittedly often quite complex, medium. At this stage it will be helpful to demonstrate several concrete examples of applying transformation acoustics to derive the material parameters required for specific applications. Obviously the universe of possible transformations and thus possible transformation acoustics devices is enormous, and these analytically tractable examples are meant to demonstrate these possibilities and illustrate the mathematical mechanics of applying transformation acoustics.

8.4.1 An Acoustic Beam Shifter

We first describe in detail a beam shifter, or a material that laterally shifts an acoustic beam traveling through it. The material properties for such a device were first described for electromagnetics in [32] and for acoustics in [9]. Although not necessarily the most exciting device, it is described naturally in Cartesian coordinates,

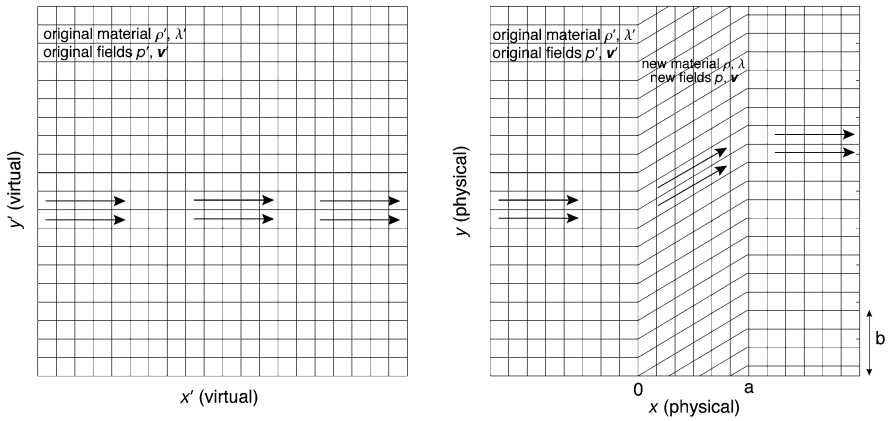

Fig. 8.3 Illustration of the design of an acoustic beam shifter. *Left*: The original, virtual space represented by a simple Cartesian coordinate system and filled with a simple, homogeneous fluid. *Right*: For $0 < x < a$, the coordinates are transformed by linearly shifting the y coordinate with distance such that the total vertical shift is b. The sound field inside the *slab* can be deformed in exactly this way inside this transformed region by acoustic material parameters derived here. The result is that a sound beam that travels from left to right in the virtual space, as in the *arrows* in the *left panel*, will follow the deformed path marked by the *arrows* in the *right panel*

and the Jacobian contains off-diagonal elements that make it useful in illustrating the transformation acoustics concept.

Figure 8.3 illustrates the original virtual space (x', y') and the transformed physical space (x, y). For $x = [0, a]$, the y coordinate is shifted as a linear function of x, yielding the distorted grid in the right panel of the figure. If the space $x = [0, a]$ is filled with material defined by (8.10)–(8.11), then the resulting sounds fields will be distorted in exactly the way shown by the distorted grid. An acoustic beam propagating along the x direction will be laterally shifted as it propagates through this medium, as illustrated by the arrows in the figure, so that it exits the $x = [0, a]$ region at a different y position than it entered.

In the $x = [0, a]$ domain of the coordinate transformation, the transformation itself is given by

$$x = x', \qquad y = y' + \frac{b}{a}x', \qquad z = z'. \tag{8.12}$$

According to (8.10)–(8.11), the key matrixes are the inverse of the Jacobian A^{-1} and $(A^T)^{-1}$, which according to (8.4) are given by

$$A^{-1} = \begin{bmatrix} 1 & 0 & 0 \\ \left(-\frac{b}{a}\right) & 1 & 0 \\ 0 & 0 & 1 \end{bmatrix} \tag{8.13}$$

and

$$\left(A^T\right)^{-1} = \begin{bmatrix} 1 & \left(-\frac{b}{a}\right) & 0 \\ 0 & 1 & 0 \\ 0 & 0 & 1 \end{bmatrix}. \tag{8.14}$$

Since $\det(A) = (\det(A))^{-1} = 1$, (8.11) says directly that

$$\lambda = \lambda', \tag{8.15}$$

or the fluid modulus in the transformed region required for the beam shifter is the same as the background fluid. The effective mass density required is more complicated. Applying (8.10) gives

$$\bar{\bar{\rho}} = \det(A)\left(A^T\right)^{-1}\rho'\left(A^{-1}\right) = \begin{bmatrix} 1+\left(\frac{b}{a}\right)^2 & \left(-\frac{b}{a}\right) & 0 \\ \left(-\frac{b}{a}\right) & 1 & 0 \\ 0 & 0 & 1 \end{bmatrix}\rho'. \tag{8.16}$$

Thus the effective mass density in the transformed region needed to make the beam shifter is strongly anisotropic with off-diagonal elements in a Cartesian coordinate system. Note, however, that this matrix can be diagonalized and thus there is a rotated (x, y) coordinate system in which the mass density has no off-diagonal elements.

And this concludes the transformation acoustics design procedure. We have determined the properties of the fluid in the region $0 < x < a$ that are required to yield the device illustrated in Fig. 8.3, in which a sound beam traveling in the x direction is deflected, without any reflections, to exit the material at $x = a$ with its position in y shifted by an amount b. Note that the more aggressive the beam shifting (denoted by a larger (b/a)), the more anisotropic is the required material. This is a general characteristic of transformation acoustics design: the more extreme the manipulation of the fields (via bending, shifting, squeezing, etc.), the more extreme the material parameters needed to manipulate those fields.

It would be satisfying to confirm via numerical simulations that the derived material parameters in (8.15)–(8.16) really do manipulate sound waves as expected from the original coordinate transformation. Doing so obviously requires the simulation of acoustic waves in materials with anisotropic mass density. Such a capability is not common in commercial simulation tools. Thus, to test the idea, we invoke the equivalence of acoustic and electromagnetic waves in two dimensions [10]. We convert the acoustic material parameters to electromagnetic material parameters, and use the commercial software package COMSOL Multiphysics to compute what is the equivalent of the pressure field distribution in such a material.

Figure 8.4 shows the results of these calculations. After mapping the solution back to the acoustic fields, the left panel shows the resulting pressure field distribution for a beam normally incident on the beam-shifting material of (8.15)–(8.16) with $b/a = 1$. It is clear that the sound field behaves exactly as predicted by the

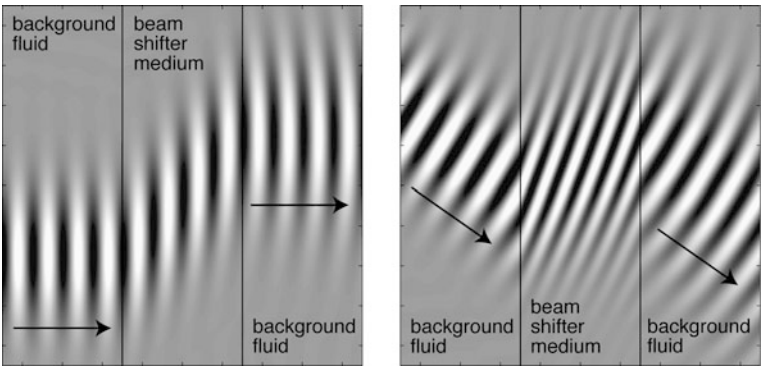

Fig. 8.4 Simulated performance of an acoustic beam shifter. *Left*: A time snapshot of the pressure field resulting from an acoustic beam normally incident on the beam shifting material. The beam is manipulated in precisely the way that is expected from the original transformation. *Right*: Even for off-normal incidence, an incident beam is shifted by the anisotropic acoustic material and exits the slab offset by the expected amount and at the same angle it was incident. The beam propagation direction outside the beam shifting medium is marked by *arrows* in both images

original transformation and illustrated in Fig. 8.3. It is interesting to note that the lines of constant phase of the incident wave are not distorted by the material. This means that although the acoustic wave power is traveling along a direction different from x, the phase fronts and wave normal vector k do point in the x direction. This is a consequence of the anisotropy of the material.

The right panel of Fig. 8.4 shows what happens when an acoustic beam is obliquely incident on the same material. The end result is exactly the same, i.e. the beam exits the material at a location that is offset in y from where it entered the material by a distance equal to the thickness of the material (since we chose $b/a = 1$), and it does so without reflection at either material interface because of the continuity of the coordinate transformation. Note that in this case the wave front behavior is a bit more complicated because they are not parallel to a coordinate direction. Nevertheless, the device performance is exactly what is expected from the original transformation. As the theory says, the designed material manipulates the sound fields as specified by the original coordinate transformation. This is the essence of transformation acoustics.

8.4.2 An Acoustic Cloaking Shell

The most interesting device thus far described in the transformation acoustics literature is an acoustic cloaking shell, i.e. a material shell that can surround an object and render the composite object (the shell plus the object) completely free of acoustic scattering. Below we derive the properties of and demonstrate via simulation the performance of this device.

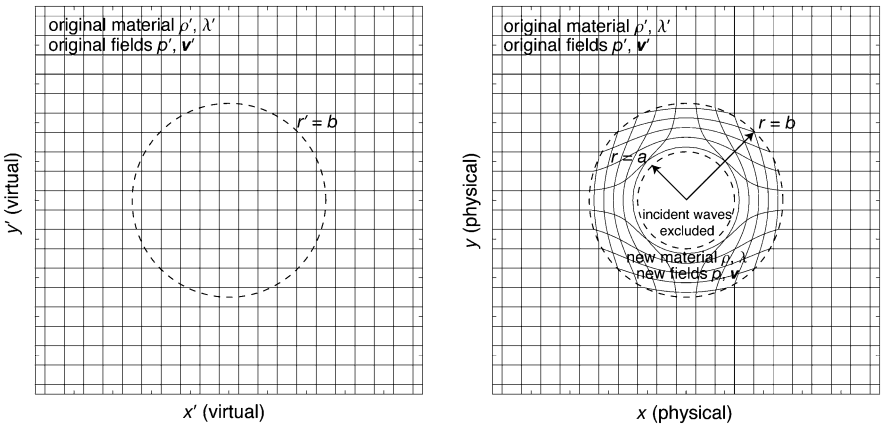

Fig. 8.5 Illustration of the design of an acoustic cloaking shell. *Left*: The original, virtual space represented by a simple Cartesian coordinate system and filled with a simple, homogeneous fluid. *Right*: The transformation opens a hole in space to map the original disk ($r' < b$) to an annulus ($a < r < b$). This squeezes the original fields into that annulus and also creates a region ($r < a$) in the interior of the annulus that does not map to virtual space. The result is that any incident sound beam is smoothly bent, without scattering or reflections, around the interior region, and any object hidden in that interior does not interact with any wave incident from the outside

Figure 8.5 illustrates the idea behind an acoustic cloaking shell. A two-dimensional cloaking transformation is the mapping of a disk in virtual space, defined by $0 < r' < b$, to an annulus in physical space, defined by $a < r < b$ [26]. This transformation squeezes the original sound fields that filled the disk into the annulus and effectively removes the interior of the annulus from the domain of the problem in physical space because there are no fields in the virtual space that map to the center of the annulus. This isolation means that, ideally, no fields are able to enter the interior, and thus any object placed in the interior cannot interact with fields incident from the outside. Equally importantly, the continuity of the transformation at $r = b$ ensures that the fields outside the annulus ($r > b$) are completely undisturbed. Consequently there is no wave scattering of any kind from the annulus, and its presence is (again ideally) undetectable from any wave measurements made outside of it.

The Jacobian-based approach for transformation acoustics derived in Sect. 8.3.1 can be used to derive the parameters of the acoustic cloaking shell. However, it is tricky (at least in the opinion of the author) to use cylindrical or spherical coordinates with this approach. Consequently we derive here the cloaking material parameters using the unit vector-scale parameter approach that was used in the original derivation of transformation electromagnetics [26] and has been outlined for transformation acoustics in several papers [4, 9] that we follow here.

The cloaking transformation is most naturally dealt with in cylindrical coordinates, and is given by

$$r = \frac{(b-a)}{b} r' + a, \qquad \phi = \phi', \qquad z = z'. \tag{8.17}$$

Note that this is not the only way to map $0 < r' < b$ to $a < r < b$, and other functional forms for the transformation result in different material parameters that, ideally, result in identical cloaking performance. In practice, different mapping functions can result in material parameters that are harder or easier to realize in practice, and the exploration of these design space degrees of freedom is a topic of active research at the time of this writing. For illustration purposes we focus only on this particular transformation.

This transformation is particularly simple in that it only squeezes r in an r' dependent way. In this case the material parameters can be more easily derived (in the opinion of the author) through the scale function approach [4, 9, 26] than by a direct calculation of the Jacobian matrix in cylindrical coordinates. These scale functions describe how much the transformation alters distances in each coordinate direction, and are defined by

$$Q_r = \frac{dr'}{dr}, \qquad Q_\phi = \frac{r'\,d\phi'}{r\,d\phi}, \qquad Q_z = \frac{dz'}{dz}. \tag{8.18}$$

For the transformation in (8.17) the specific expressions in terms of the physical (unprimed) coordinates are

$$Q_r = \frac{b}{b-a}, \qquad Q_\phi = \frac{b}{(b-a)}\frac{(r-a)}{r}, \qquad Q_z = 1. \tag{8.19}$$

Since we are effectively transforming from cylindrical to cylindrical coordinates, there is no change in the basis vectors and the ensuing complications that result from changed basis vectors [9, 26] are not needed.

Following [4, 9], and assuming the initial (primed) material is a uniform isotropic fluid with density ρ_0' and bulk modulus λ_0', the material parameters (relative to those of the background medium) that result from this transformation are, in terms of these scale functions,

$$\rho^{-1} = \left(\rho_0'\right)^{-1} Q_r Q_\phi Q_z \begin{bmatrix} Q_r^{-2} & 0 & 0 \\ 0 & Q_\phi^{-2} & 0 \\ 0 & 0 & Q_z^{-2} \end{bmatrix} \tag{8.20}$$

and

$$\lambda = \lambda_0'(Q_r Q_\phi Q_z)^{-1}. \tag{8.21}$$

Plugging in the specific values from (8.19) and rearranging (8.20), we find that

$$\rho_r = \rho_0'\frac{r}{r-a}, \qquad \rho_\phi = \rho_0'\frac{r-a}{r}, \qquad \rho_z = \rho_0'\frac{(b-a)^2}{b^2}\frac{r}{r-a} \tag{8.22}$$

and

$$\lambda = \lambda_0'\frac{(b-a)^2}{b^2}\frac{r}{r-a}. \tag{8.23}$$

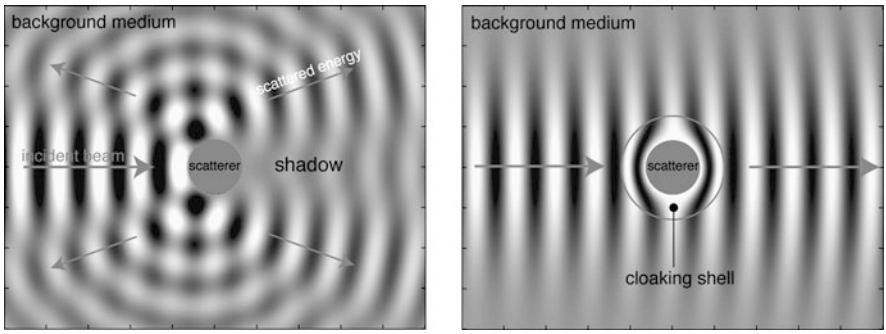

Fig. 8.6 Simulated performance of a 2D acoustic cloak. *Left*: A time snapshot of the pressure field resulting from an acoustic beam normally incident on a rigid scatterer. This object produces scattering in most directions and strong scattering in the forward direction (*shadow*) and several other directions. *Right*: When the same object is surrounded by the acoustic cloaking shell, the acoustic scattering is essentially eliminated. The pressure field outside the object is basically identical to that if there were no object at all (see the left panel of Fig. 8.1), indicating no scattering, and the field inside the cloaking shell is deformed as prescribed by the coordinate transformation used to design the material (see the right panel of Fig. 8.5)

The above expressions define the effective mass density tensor components and the bulk modulus of a 2D acoustic cloaking shell. The resulting medium has a strongly anisotropic mass density (although it is diagonal in cylindrical coordinates), and both the bulk modulus and the density tensor components are smoothly inhomogeneous in radius (but uniform in polar angle ϕ). These are not simple material parameters to realize physically, but if these complex material properties can be created, then so can an acoustic cloaking shell.

To confirm that these material properties yield the desired wave behavior, we use the same simulation approach used in Sect. 8.4.1, namely exploiting the equivalence of acoustic and electromagnetic waves in two dimensions [10] and using the electromagnetic simulation capabilities of COMSOL Multiphysics. Figure 8.6 shows a fixed time snapshot of the pressure field that results when a rigid scattering object is illuminated from the left by a time-harmonic acoustic wave beam, with and without a shell of material described by (8.22)–(8.23). Without the shell, as shown in the left panel, the wave scattering from the object is substantial, as expected. The object casts a strong shadow, which indicates the expected strong forward scattering, and also produces strong backscattering and specular scattering in several different directions. Clearly this object would be acoustically visible from measurements of the scattered sound field.

But when the same rigid object is surrounded by the acoustic cloaking shell, as shown in the right panel, the pressure field outside the composite object made of the shell and scatterer is essentially identical to the field of the beam in empty space (refer back to the left panel of Fig. 8.1. This means that all scattering, including the difficult-to-eliminate forward scattering (i.e. the shadow) is effectively eliminated, and this cloaked object would not be detectable from measurements of the scattered sound field. Note also that the pressure field inside the shell is deformed

exactly as prescribed by the coordinate transformation used to design the material, as illustrated in the right panel of Fig. 8.5.

8.5 Realizing Materials for Transformation Acoustics

As evident from the examples above, the material properties that result from transformation acoustics device design are complex. Equations (8.10)–(8.11) show that, for a general design, the bulk modulus needs to be smoothly inhomogeneous, while the effective mass density not only needs to be smoothly inhomogeneous but also anisotropic, i.e. exhibiting different effective mass densities in different directions. In Sect. 8.3.2 above, we briefly described several simple approaches from the literature that have shown how one might engineer a material that exhibits an inhomogeneous anisotropic effective mass. Neither of these approaches, however, yield designs that are easy to fabricate.

Here we will briefly describe simulations and measurements of composite structures that can exhibit anisotropic mass but that are easier to fabricate, and thus are some initial steps that show that at least some transformation acoustics devices can be physically realized and their performance tested. It should be emphasized that, at the time of this writing, developing approaches for designing and fabricating materials for transformation acoustics design is a very active area of research that is still in its very early stages. Because of this, few practical constraints such as mass, mechanical robustness, visual appearance, etc., are being addressed. The goal is simply to design a structure that achieves the needed effective material parameters and that can be measured under laboratory conditions. We will focus on passive structures that do not contain resonant components and thus exhibit broadband effective properties [29, 39, 45].

It should be mentioned that the design of composite materials that achieve desired complex acoustic properties, which is to be sure an old field, has been given the modern name of acoustic metamaterials. The field of acoustic metamaterials encompasses an effort to achieve a wide variety of effective material properties in composite materials, including negative dynamic density, in which net material motion opposes the applied force [17, 19], and negative bulk modulus, in which the net material strain is opposite the applied stress [11, 18]. These negative properties do arise in some rather exotic applications of transformation electromagnetics and transformation acoustics, such as making one object appear to be another [16], but in most cases the transformation approach generates the need for materials with positive properties.

One approach for physically realizing composite materials with smoothly inhomogeneous properties and/or anisotropic mass involves layers of solid material with gaps embedded in a host fluid or, alternately, arrangements of solid scatterers in a host fluid [29, 39, 45], as illustrated in Fig. 8.7. The gaps serve two purposes. They ensure that the background fluid permeates the entire metamaterial, and the gap dimensions can easily be tuned from point to point to tune the effective properties

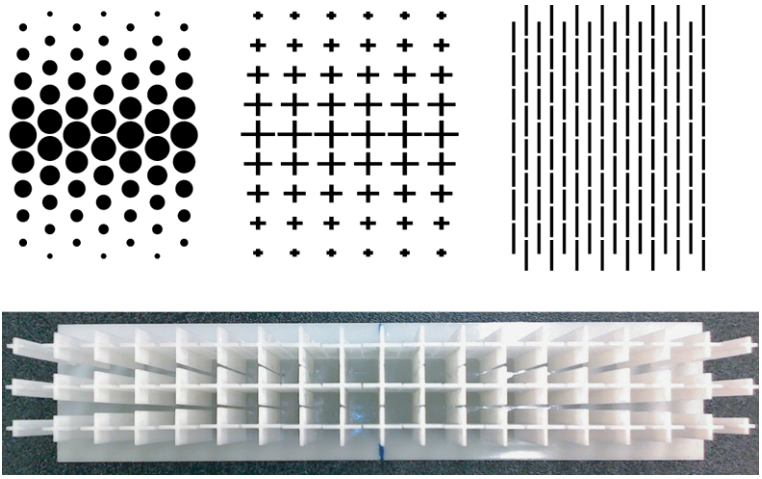

Fig. 8.7 Examples of acoustic metamaterial structures. *Top left*: An array of solid circular cylinders of varying size surrounded by a host fluid can be used to create an isotropic and inhomogeneous material (adapted from [6]). *Top middle*: An array of more complex shapes of varying size can also be used to create a similar inhomogeneous material with less mass and a better impedance match to the background fluid (adapted from [44]). *Top right*: An array of thin solid plates, or alternately perforated thin solid sheets, can be used to create an anisotropic acoustic metamaterial (adapted from [45]). *Bottom*: A photograph of a fabricated acoustic metamaterial sample based on the structure shown in the *top middle*, and experimentally demonstrated in [44]

of the medium. This approach has been applied to tune the effective properties of isotropic acoustic metamaterials to create smoothly inhomogeneous materials for devices such as gradient index sonic lenses [6, 29, 44].

Rotationally symmetric solid inclusions yield isotropic material properties that do not vary with direction. In contrast, rotational asymmetry can yield anisotropic material properties. Asymmetry in the lattice of symmetric inclusions can be used to create acoustic metamaterials with modestly anisotropic effective mass [39]. In contrast, asymmetry in the inclusions themselves can be used to create strongly anisotropic acoustic metamaterials [29]. This concept has been demonstrated experimentally through reflection and transmission measurements of the same metamaterial under two different orientations [45]. At the time of this writing, the most sophisticated device fabricated using this general approach is a two-dimensional acoustic cloak in which a water background permeates an aluminum structure [43].

Conceptually it is fairly easy to understand how this kind of composite medium results in a material with an anisotropic effective mass. For sound waves traveling parallel to the thin plates, there is minimal interaction between the sound pressure and the plate, and the wave travels as if it is in a material with properties close to the background fluid. But sound waves that travel perpendicular to the plates interact strongly with the plates and can result in waves that behave as if they are traveling in a fluid with properties very different to that of the background fluid. This anisotropy turns out to be identical to that produced by a fluid with anisotropic effective mass

[29], which is not surprising because the fluid permeating the entire volume ensures that the material has an isotropic and fluid-like stiffness.

Most applications of transformation acoustics envisioned at this point involve acoustic metamaterials either in air or in water. There are some interesting differences between these two host media in the kinds of effective material properties that can be easily realized that are worth mentioning. Air is obviously a very low density and very compressible material compared to almost all materials one might use as metamaterial inclusions. This means that large effective mass (relative to that of air) can be created in such a material, and very high levels of mass anisotropy can be achieved. However, for the same reasons, it is difficult to create an acoustic metamaterial that is lighter or more compressible than air. This limits the range of acoustic metamaterial properties that can be realized in air.

In contrast, water is only a little bit less dense and more compressible than most solid inclusions. This means that it is difficult to achieve high effective mass and high effective stiffness relative to the water background. However, it is possible to use gas-filled materials that exhibit masses less than that of the water background. One possibility that has been identified in the literature is closed-cell metal foam [30].

These differences between water and air mean that the achievable effective parameters are fundamentally different for air and water applications. For example, the challenges of trying to create a material that exhibits the acoustic cloak parameters of (8.10)–(8.11) are different for these two host fluids. The ideal parameters contain one density component (ρ_r) that is very large at the inner edge of the shell and one component (ρ_ϕ) that is very small. In air, the former is straightforward to realize but the latter is difficult, while in water, large values of ρ_r are the bigger challenge.

In light of these limitations, an active area of research is designing approximations of devices that still perform reasonably well but can be fabricated with material parameters that are physically realizable for a given host fluid. This idea has been more fully explored in transformation electromagnetics than transformation acoustics, but the concepts from one are immediately applicable to the other. Concepts that have been demonstrated, at least theoretically, include using different coordinate transformations that yield different material properties [2, 7], and numerical optimization of device performance given material property constraints [1, 28].

8.6 Recent Experimental Results in Transformation Acoustics

At the time of this writing, the authors' research group had just completed and published [31] an experimental effort to demonstrate one version of acoustic cloaking in air using transformation acoustics design concepts. The goal of this effort was to design, fabricate, and test a material shell that is capable of hiding from acoustic scattering an object in the vicinity or on top of a reflecting plane. This kind of cloak is referred to as a "carpet cloak", and also a ground-plane cloak or a reflecting plane

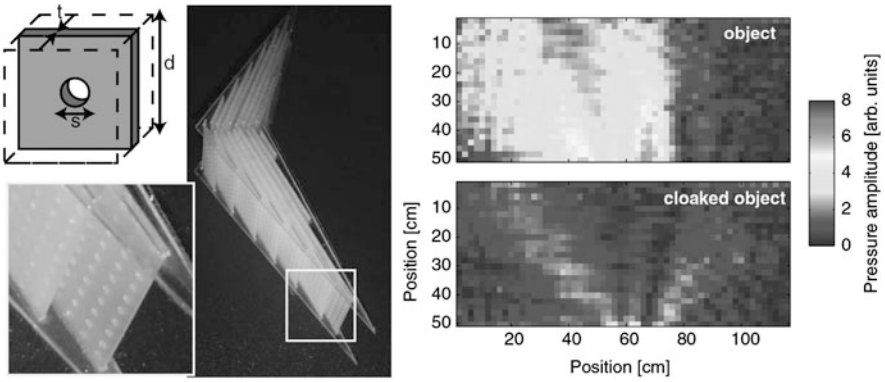

Fig. 8.8 Summary of experimentally demonstrated acoustic cloaking in air reported in [31]. *Left panels*: Photographs of the fabricated acoustic cloaking shell based on perforated sheets of thin plastic stacked with thin air gaps in between. This material provides the effective mass anisotropy needed for the device to function. *Right panels*: Measurements of the acoustic scattering from the uncloaked and cloaked object. The sound reflections from the object by itself are dramatically reduced when it is covered with the shell, rendering it hidden from sound waves. Figures adapted from [31]

cloak. This problem was first considered in the context of electromagnetics [20], and has become a common test problem in transformation electromagnetics because the material properties needed to realize the cloaking shell are much simpler to realize than for a free space cloaking shell.

Applying a relatively straightforward transformation that effectively opens a hole underneath the reflecting plane in which an object can hide results in material parameters not dramatically different from the background fluid, which in this case was air. The effective mass density of the cloaking shell is anisotropic, with a mass density about 5 times higher in one direction than the other [31]. One way such a material can be physically realized is with thin perforated plates, stacked with air gaps in between, as shown in the left panels of Fig. 8.8. The thickness of these plates and the size of the circular perforations control the effective mass density and enable the needed values to be realized with high precision.

The acoustic scattering from a triangular scatterer on a flat surface was then measured with and without the cloaking shell. The measured scattered field, i.e. the sound field after subtracting the incident field and the reflection from the flat surface, for both of these cases is shown in the right panels of Fig. 8.8. With the object on the surface, significant scattering is observed in two directions. One of these scattered beams is the specular reflection from the tilted surface of the object, and the other is forward scattering from the lack of a reflected signal in the specular direction for a flat plate. With the object and cloaking shell on the flat surface, both of these scattered field components are significantly reduced, meaning that sound energy reflects from the cloaked object on the reflecting surface essentially as if there were only a flat surface. Thus, this object is hidden from acoustic scattering.

8.7 Related Theories and Implications

Transformation acoustics theory also has some interesting consequences for other fields. The equations of linear acoustics, (8.2)–(8.3), can be reduced to the well-known scalar Helmholtz equation, which means that the transformation concept can be applied to any other wave system that can be reduced to the scalar Helmholtz equation. This includes surface water waves [12], waves on thin plates [13], and even quantum mechanical matter waves [42]. The latter is particularly interesting and suggests that if one can control the effective mass of a particle (which has to be anisotropic) and the potential field in which the particle moves, then one can arbitrarily manipulate the particle wavefunction and thus the statistical particle position. Physically realizing this latter phenomenon will be a challenge but suggests the very far-out possibility of cloaking matter.

It should also be noted that the above sections all focus on a formulation of transformation acoustics that builds out of the initial work in the field [3, 9, 10] and that maintains the basic fluid nature of the required materials. It turns out, however, that this is not the only way in which transformation acoustics can be made to work. Theoretical work first reported by Norris [23] and then later expanded and elucidated [24] has shown that there is a non-fluid class of materials that can also emerge from the fundamental transformation acoustics theory. These materials are solid materials with an anisotropic stiffness but isotropic mass. In some ways these materials are fluid-like, for instance their inability to support a shear stress, but they are fundamentally different from fluids because of the anisotropic stiffness. How to design and construct this type of material is not well-described in the literature at the time of this writing, but it is a very active area of research given the interesting devices that could be constructed from this approach.

8.8 Summary

In this chapter we have presented a concise summary of the development of the concept of transformation acoustics. First conceived only 4 years before the time of this writing, this design paradigm offers the possibility of creating novel acoustic materials and devices that are difficult if not impossible to design by other techniques. The main challenge for the field for the field at present is devising techniques to fabricate composite materials with the complex acoustic properties needed to realize transformation acoustic devices. Initial work in this area has developed several approaches that appear promising, and full experimental demonstrations can probably be expected soon.

References

1. Andkjaer, J., Sigmund, O.: Topology optimized low-contrast all-dielectric optical cloak. Appl. Phys. Lett. **98**, 021112 (2011)

2. Cai, W., et al.: Designs for optical cloaking with high-order transformations. Opt. Express **16**(8), 5444–5452 (2008)
3. Chen, H., Chan, C.T.: Acoustic cloaking in three dimensions using acoustic metamaterials. Appl. Phys. Lett. **91**, 183518 (2007)
4. Chen, H., Chan, C.T.: Acoustic cloaking and transformation acoustics. J. Phys. D **43**, 113001 (2010)
5. Cheng, Y., et al.: A multilayer structured acoustic cloak with homogeneous isotropic materials. Appl. Phys. Lett. **92**, 151913 (2008)
6. Climente, A., et al.: Sound focusing by gradient index sonic lenses. Appl. Phys. Lett. **97**, 104103 (2010)
7. Cummer, S.A., et al.: A rigorous and nonsingular two dimensional cloaking coordinate transformation. J. Appl. Phys. **105**, 056102 (2009)
8. Cummer, S.A., et al.: Full-wave simulations of electromagnetic cloaking structures. Phys. Rev. E **74**(3), 036621 (2006)
9. Cummer, S.A., et al.: Material parameters and vector scaling in transformation acoustics. New J. Phys. **10**, 115025 (2008)
10. Cummer, S.A., Schurig, D.: One path to acoustic cloaking. New J. Phys. **9**, 45 (2007)
11. Fang, N., et al.: Ultrasonic metamaterials with negative modulus. Nat. Mater. **5**, 452–456 (2006)
12. Farhat, M., et al.: Broadband cylindrical acoustic cloak for linear surface waves in a fluid. Phys. Rev. Lett. **101**, 134501 (2008)
13. Farhat, M., et al.: Ultrabroadband elastic cloaking in thin plates. Phys. Rev. Lett. **103**, 024301 (2009)
14. Greenleaf, A., et al.: Anisotropic conductivities that cannot be detected by EIT. Physiol. Meas. **24**, 413–419 (2003)
15. Knupp, P., Steinberg, S.: Fundamentals of Grid Generation. CRC Press, Boca Raton (1994)
16. Lai, Y., et al.: Illusion optics: the optical transformation of an object into another object. Phys. Rev. Lett. **102**, 253902 (2009)
17. Lee, S.H., et al.: Acoustic metamaterial with negative density. Phys. Lett. A **373**, 4464–4469 (2009)
18. Lee, S.H., et al.: Acoustic metamaterial with negative modulus. J. Phys. Condens. Matter **21**, 175704 (2009)
19. Li, J., Chan, C.T.: Double-negative acoustic metamaterial. Phys. Rev. E **70**(5), 055602 (2004)
20. Li, J., Pendry, J.B.: Hiding under the carpet: A new strategy for cloaking. Phys. Rev. Lett. **101**, 203901 (2008)
21. Liu, R., et al.: Broadband ground-plane cloak. Science **323**, 366 (2009)
22. Milton, G.W., et al.: On cloaking for elasticity and physical equations with a transformation invariant form. New J. Phys. **8**, 248 (2006)
23. Norris, A.N.: Acoustic cloaking theory. Proc. R. Soc. A **464**, 2411–2434 (2008)
24. Norris, A.N.: Acoustic metafluids. J. Acoust. Soc. Am. **464**, 839–849 (2008)
25. Padilla, W.J., et al.: Negative refractive index metamaterials. Mater. Today **9**, 28 (2006)
26. Pendry, J.B., et al.: Controlling electromagnetic fields. Science **312**, 1780–1782 (2006)
27. Plebanski, J.: Electromagnetic waves in gravitational fields. Phys. Rev. **118**, 1396–1408 (1960)
28. Popa, B.-I., Cummer, S.A.: Cloaking with optimized homogeneous anisotropic layers. Phys. Rev. A **79**, 023806 (2009)
29. Popa, B.-I., Cummer, S.A.: Design and characterization of broadband acoustic composite metamaterials. Phys. Rev. B **80**, 174303 (2009)
30. Popa, B.-I., Cummer, S.A.: Homogeneous and compact acoustic ground cloaks. Phys. Rev. B. In review (2011)
31. Popa, B.-I., et al.: Experimental acoustic ground cloak in air. Phys. Rev. Lett. **106**, 253901 (2011)
32. Rahm, M., et al.: Optical design of reflectionless complex media by finite embedded coordinate transformations. Phys. Rev. Lett. **100**, 063903 (2008)

33. Rahm, M., et al.: Transformation-optical design of adaptive beam bends and beam expanders. Opt. Express **16**, 11555 (2008)
34. Rahm, M., et al.: Design of electromagnetic cloaks and concentrators using form-invariant coordinate transformations of Maxwell's equations. Photonics Nanostruct. **6**, 87–95 (2008)
35. Schoenberg, M., Sen, P.N.: Properties of a periodically stratified acoustic half-space and its relation to a Biot fluid. J. Acoust. Soc. Am. **73**, 61–67 (1983)
36. Schurig, D., et al.: Metamaterial electromagnetic cloak at microwave frequencies. Science **314**, 977–980 (2006)
37. Schurig, D., et al.: Calculation of material properties and ray tracing in transformation media. Opt. Express **14**, 9794–9804 (2006)
38. Tamm, I.Y.: Electrodynamics of an anisotropic medium and the special theory of relativity. J. Russ. Phys.-Chem. Soc. **56**, 248 (1924)
39. Torrent, D., Sanchez-Dehesa, J.: Acoustic metamaterials for new two-dimensional sonic devices. New J. Phys. **9**, 323 (2007)
40. Torrent, D., Sanchez-Dehesa, J.: Acoustic cloaking in two dimensions: A feasible approach. New J. Phys. **10**, 063015 (2008)
41. Wood, A.B.: A Textbook of Sound. Macmillan, New York (1955)
42. Zhang, S., et al.: Cloaking of matter waves. Phys. Rev. Lett. **100**, 123002 (2008)
43. Zhang, S., et al.: Broadband acoustic cloak for ultrasound waves. Phys. Rev. Lett. **106**, 024301 (2011)
44. Zigoneanu, L., et al.: Design and measurements of a broadband 2D acoustic lens. Phys. Rev. B **84**, 024305 (2011)
45. Zigoneanu, L., et al.: Design and measurements of a broadband 2D acoustic metamaterial with anisotropic effective mass density. J. Appl. Phys. **109**, 054906 (2011)

Chapter 9
Acoustic Cloaking via Homogenization

José Sánchez-Dehesa and Daniel Torrent

Abstract Acoustic cloaking is the mechanism representing the ideal acoustic stealth. We introduce and discuss the acoustic cloak, a material shell that renders an object acoustically 'invisible' thanks to its presence surrounding the object. It has been shown that cloaking shells require very complex parameters to be realized. This complexity comes from the fact that their acoustic parameters must be anisotropic, inhomogeneous and divergent near the cloaked object. This chapter explains how to engineer artificial structures, which have been called acoustic metamaterials or metafluids, that respond dynamically as anisotropic and inhomogeneous materials. The metafluids are made from arrays of isotropic and homogeneous elastic cylinders or by metallic plates cylindrically corrugated. We also propose solutions to remove the divergences appearing in the design of cloaking shells. It is therefore predicted that, although difficult to realize, cloaking shells are not impossible by using metafluids based on the homogenization of periodic structures.

9.1 Introduction: Acoustic Cloaking

The control and guiding of waves around a given object was studied for electromagnetic waves (EM) by Greenleaf, Lassas, and Uhlmann [15], Pendry, Schurig, and Smith [23], and Leonhardt [16], who applied transformation optics to design materials accomplishing those goals. The properties of these materials are not found naturally and a new class of artificial structures called metamaterials have been developed since then. Thus, EM metamaterials based on split ring resonators were employed by Schurig and coworkers [26] to experimentally demonstrate EM cloaking in the microwave regime.

Acoustic cloaking (see Fig. 9.1) was predicted in two dimensions (2D) by Cummer and Schurig [11] by exploiting the analogy existing between the differential

J. Sánchez-Dehesa (✉) · D. Torrent
Grupo de Fenómenos Ondulatorios, Departamento de Ingeniería Electrónica, Universidad Politécnica de Valencia, C/Camino de Vera s/n, Valencia, Spain
e-mail: jsdehesa@upvnet.upv.es

D. Torrent
e-mail: datorma1@upvnet.upv.es

R.V. Craster, S. Guenneau (eds.), *Acoustic Metamaterials*,
Springer Series in Materials Science 166, DOI 10.1007/978-94-007-4813-2_9,

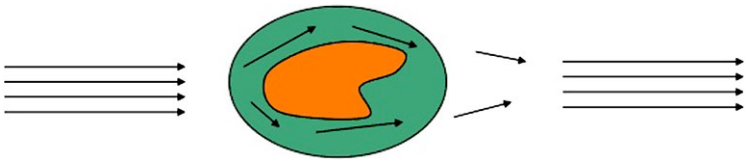

Fig. 9.1 Schematic representation of the acoustic cloaking phenomenon. The central area represents the object cloaked by acousticwaves. The surrounding zone represents the "cloaking shell" with some special properties such that, when an acoustic wave enters, this wave is guided around the central region and it is perfectly reconstructed outside the cloak (Color figure online)

wave equation for EM wave propagation of TE modes and that of pressure waves. The predicted 2D cloak consisted of an acoustic medium having a strong unnatural dynamical mass anisotropy. In further works by Chen and Chan [8] and Cummer *et al.* [12] acoustic cloaking in three dimensions (3D) was also envisaged thanks also to materials with mass anisotropy. In this regard, the work by Milton *et al.* [20] describes conceptually how the mass anisotropy could be made possible by spring loaded masses. Besides, Torrent and Sánchez-Dehesa [28] proposed that the physical realization of metamaterials with mass density anisotropy could be engineered using non-symmetric lattices of solid cylinders. However, no experimental demonstration of acoustic cloaking has been reported so far although cloaks based on layered structures made of two isotropic acoustic metamaterials have been introduced [9, 29]. Particularly, we also propose that the isotropic metamaterials could be engineered by using lattices of elastic cylinders [29]. The demonstration of acoustic cloaking awaits the practical realization of artificial structures (metafluids) having the dynamical properties required for cloaking.

Elastodynamic equations have non-invariance under coordinate transformations [20] and, therefore, cloaking for such types of waves should be of a different nature than that for EM and acoustic waves. However, a few works have reported 'quasi' elastic cloaks [2, 14] for reducing the scattering cross section of elastic waves for some polarizations. In fact, a layered structure was implemented to physically realize a 'quasi' elastic cloak [13]. For a full report on acoustic cloaking and transformation acoustics the reader is referred to the review of Chen and Chan [7].

This chapter gives a systematic account of the properties of the cloaking shells introduced by Cummer and Schurig [11] and demonstrates that, for example, they can be made possible by using arrays of elastic cylinders and for wavelengths large in comparison with the lattice separation between cylinders. We also describe another way to obtain mass anisotropy, which is by using corrugated structures. We will explain how to get the radial dependence required for the density $\rho(r)$ and bulk modulus $B(r)$.

For a cloaked region of circular shape and radius R_1 the predicted functional form is [11]

$$\frac{\rho_r(r)}{\rho_b} = \frac{r}{r - R_1}, \tag{9.1a}$$

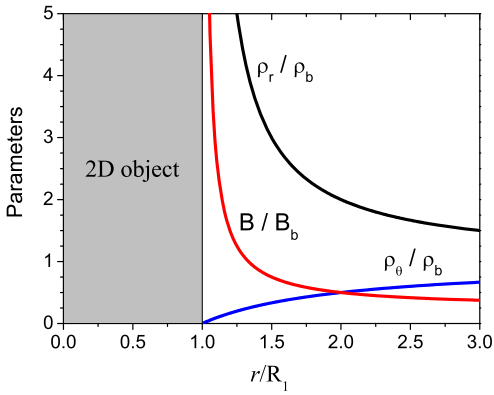

Fig. 9.2 Acoustic parameters of an ideal cloaking shell. The inner and outer radius of the cloak are R_1 and $R_2 = 2R_1$, respectively. Note that parameters diverge at the object's surface following the functional form in (9.1a)–(9.1c) (Color figure online)

$$\frac{\rho_\theta(r)}{\rho_b} = \frac{r - R_1}{r}, \tag{9.1b}$$

$$\frac{B(r)}{B_b} = \left(\frac{R_2 - R_1}{R_2}\right)^2 \frac{r}{r - R_1}, \tag{9.1c}$$

where R_1 and R_2 are the inner and outer radii of the cloaking shell, ρ_r and ρ_θ define the diagonal components of the mass density tensor. Parameters with subscript b represent the surrounding background that is a fluid or a gas. Figure 9.2 plots these parameters so their divergent behavior near the cloaked region can be clearly seen. Materials with such uncommon properties do not exist in nature and, therefore, some artificial material needs to be created with the same dynamical performance.

The chapter is organized as follows. After this introduction, in Sect. 9.2, we recall that dynamical mass anisotropy is easily obtained by using multilayers of two fluidlike materials and show how this property can be translated to cylindrical coordinates. In Sect. 9.3 we report the homogenization properties of 2D arrays of elastic cylinders. These structures are called sonic crystals and for large wavelengths they behaves as homogeneous fluidlike materials whose acoustic properties can be tailored up to some extend. Afterwards, in Sect. 9.4, the engineering of cloaks made by arrays of elastic materials and by corrugated structures are described. The issues associated with the practical realization of metafluids based cloaks are discussed in Sect. 9.5, where we also give proposal for solving them by introducing imperfect cloaks. Finally, the work is summarized in Sect. 9.6.

9.2 Dynamical Mass Anisotropy from One Dimensional Fluid-Fluid Systems

Anisotropic mass density is a property not found in ordinary fluids, mainly due to the 'disordered' nature of fluid materials. In this chapter we explain that this unusual

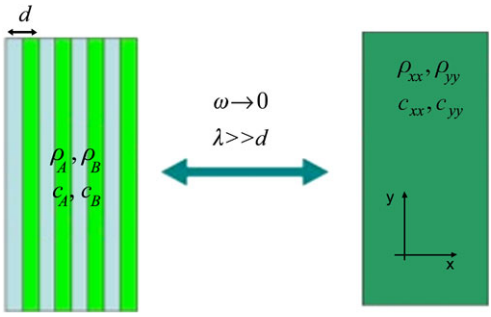

Fig. 9.3 One dimensional fluid-fluid multilayer (*left panel*). For wavelengths larger than the period d this structure behaves as a homogeneous and anisotropic fluidlike material (*right panel*) (Color figure online)

property can be obtained from fluid-fluid periodic composites in the homogenization limit; that is, at frequencies low enough that the composite can be represented as an uniform medium. In the following sections it will be shown how to realize such types of fluid-fluid composites.

Schoenberg and Sen [25] demonstrated that a one dimensional (1D) periodic multilayered fluid-fluid system (see Fig. 9.3) behaves, at wavelengths larger than the lattice constant d, as a fluidlike material with dynamical mass anisotropy. Then, by using their result, the cylindrical mass anisotropy required for 2D cloaking can be easily obtained by twisting the 1D structure around the cloaked object as shown in Fig. 9.4 and by changing locally the acoustic parameters of fluid materials in order to satisfy (9.1a)–(9.1c). The derivation of the expressions for the effective mass density tensor is straightforward and is based on the analysis of the band structure of the 1D periodic structure at very low frequencies [33].

Let us consider a 1D fluid-fluid periodic structure made of two alternating layers of materials A and B, respectively, as it is depicted in Fig. 9.3. For any periodic system the bulk modulus (in the homogenization limit) does not depend on the type of lattice (isotropic or anisotropic); in fact, the effective bulk modulus at large wavelength, B_{eff}, can be determined by a volume average of its reciprocal [28]. This volume averaging is

$$\frac{1}{B_{eff}} = \frac{1}{d_A + d_B}\left[\frac{d_A}{B_A} + \frac{d_B}{B_B}\right], \tag{9.2}$$

where B_A (B_B) is the bulk modulus of material A (B) and d_A (d_B) is the thickness of layer A (B).

To obtain the effective mass density tensor, ρ_{ij}^2, we need to calculate first the dispersion relation $K(\omega)$ of the system; i.e., the wavenumber as a function of the frequency, in the low frequency limit. Once $K(\omega)$ is known we derive the effective sound speed tensor c_{ij}^2. Afterwards, the mass density is directly related to this quantity through the bulk modulus [28]

$$\rho_{ij}^{-1} = c_{ij}^2 / B_{eff}. \tag{9.3}$$

The dispersion relation is obtained by solving the wave propagation for 1D periodic systems [33],

$$\cos K_x d = \cos k_{Ax} d_A \cos k_{Bx} d_B - \frac{1}{2}\left[\frac{\rho_A k_{Bx}}{\rho_B k_{Ax}} + \frac{\rho_B k_{Ax}}{\rho_A k_{Bx}}\right] \sin k_{Ax} d_A \sin k_{Bx} d_B, \tag{9.4}$$

where

$$K_{ix}^2 = \frac{\omega^2}{c_i^2} - K_y^2, \tag{9.5}$$

for $i = A, B$.

The effective sound speed is defined as the ratio between angular frequency ω and wavenumber K in the low frequency limit. This ratio is obtained by making a power series expansion of the trigonometric functions up to second order in their arguments. It is easy to show that the effective sound speed tensor that follows is

$$c_{xx}^2 = B_{eff} \frac{d_A + d_B}{d_A \rho_A + d_B \rho_B}, \tag{9.6a}$$

$$c_{yy}^2 = B_{eff} \frac{d_A \rho_A^{-1} + d_B \rho_B^{-1}}{d_A + d_B}, \tag{9.6b}$$

where c_{xx} and c_{yy} define the diagonal components giving the propagation along the perpendicular and parallel directions, respectively, inside the layered structure.

From (9.6a), (9.6b) and (9.3) the components of the mass density tensor are deduced,

$$\rho_{xx} = \frac{1}{d_A + d_B}(d_A \rho_A + d_B \rho_B), \tag{9.7a}$$

$$\rho_{yy}^{-1} = \frac{1}{d_A + d_B}\left(d_A \rho_A^{-1} + d_B \rho_B^{-1}\right). \tag{9.7b}$$

Note that the principal directions of anisotropy in this medium are along Cartesian coordinates. Now, if this structure is transformed to that in Fig. 9.4, the new tensor will have its principal axis along the cylindrical coordinates,

$$\rho_{xx} \to \rho_r,$$
$$\rho_{yy} \to \rho_\theta.$$

But, in order to satisfy conditions in (9.1a)–(9.1c), we need inhomogeneous components of the tensor; that is, $\rho_r = \rho_r(r)$ and $\rho_\theta = \rho_\theta(r)$. This property can be obtained by using fluidlike materials A and B with values of density and modulus, (ρ_A, B_A) and (ρ_B, B_B), that are functions of their position in the layered shell. This leads to fluidlike structures and, consequently, to cloaking shells impossible to build by using natural materials. However, in the section that follows we will explain how to engineer artificial materials (metafluids) with the dynamical properties required to get the acoustic cloaking phenomenon.

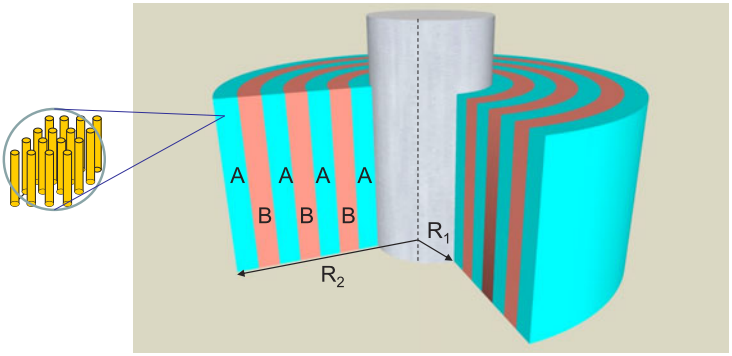

Fig. 9.4 Schematic view of a cloaking shell based on a multilayered structure made of two different isotropic fluidlike materials with the same thicknesses. Each layer consists of arrays of elastic cylinders as explained in Sect. 9.3. Reproduced from [29] with permission of IOP Publishing (Color figure online)

9.3 Homogenization of Two Dimensional Sonic Crystals

The concept of a metafluid is schematically described in Fig. 9.5. An array of elastic cylinders embedded in a fluid background behaves at low frequencies as an effective medium with fluid like properties. The homogenization of these type of structures has been widely employed for ordered and disordered systems [6, 17, 19, 27, 30, 31]. Recently, homogenization has been extended to scatterers with different shapes and the resulting effective media are called acoustic metamaterials or metafluids [21, 22, 24]. Here we present the basic idea and equations necessary to design cloaking shells based on these artificial structures.

The homogenization method is based on the assumption that, in the low frequency limit, the scattered field by a given cluster of cylinders can be fairly well reproduced by a homogeneous fluidlike object if its acoustic parameters ρ_{eff}, c_{eff} are properly chosen. This condition is completely general and can be applied to clusters with any external shape. However, for simplicity, we henceforth take clusters with cylindrical external shape. Then, the homogenization condition for a circular cluster is expressed mathematically as

$$\lim_{\lambda\to\infty} \frac{P^{sc}_{cluster}(\boldsymbol{r}) - P^{sc}_{cyl}(\boldsymbol{r})}{P^{sc}_{cyl}(\boldsymbol{r})} = 0. \tag{9.8}$$

The scattered field by the cluster, $P^{sc}_{cluster}(\boldsymbol{r})$, can be cast in terms of its T-matrix, which is a linear relation between some incident field and the scattered one by [34]

$$P^{sc}_{cluster}(\boldsymbol{r}) = \sum_q \sum_s T^{cluster}_{qs} A^0_s H_q(kr) e^{iq\theta}, \tag{9.9}$$

also, for the cylinder

$$P^{sc}_{cyl}(\boldsymbol{r}) = \sum_q \sum_s T^{eff}_{qs} A^0_s H_q(kr) e^{iq\theta}. \tag{9.10}$$

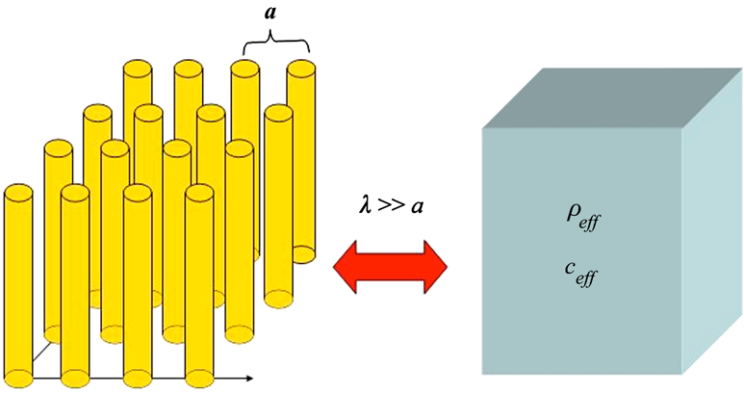

Fig. 9.5 A two dimensional metafluid. An array of elastic cylinders (*left panel*) behaves, for large enough wavelengths, like an effective acoustic material or metafluid with parameters ρ_{eff}, c_{eff}. These parameters can be tailored by modifying the radii and physical parameters of cylinders in the lattice (Color figure online)

With these definitions one can demonstrate that the homogenization condition on the scattered fields in (9.8) becomes the following condition on the matrix elements

$$\lim_{\lambda\to\infty} \frac{T_{qs}^{cluster}}{T_{qs}^{eff}} = 1. \tag{9.11}$$

Since we are considering clusters with nearly circular shape, it is expected that the homogeneous fluidlike object having the same dynamical properties will have also a circular shape. Moreover, only clusters with embedded isotropic lattices (square and hexagonal) are considered here because non-isotropic lattices would require a more complex analysis within this approach. In other words, we will be dealing with diagonal T-matrices only and, therefore, the homogenization conditions are

$$\widehat{T}_q^{cluster} = \widehat{T}_q^{eff}, \quad q = 0, \pm 1, \pm 2, \ldots, \tag{9.12}$$

where $\widehat{X}$ represent the coefficient of the lower order term in the Taylor expansion of X in powers of wavevector k.

The T-matrix elements of the cluster are the inputs of the problem and they are obtained numerically; they depend on the position and size of cylinders as well as on their elastic parameters. However, the T-matrix elements of the effective fluidlike cylinder is a function of the acoustic parameters to be determined. For example, the diagonal elements are:

$$\widehat{T}_{00}^{eff} = \frac{i\pi R_{eff}^2}{4}\left[\frac{\rho_b c_b^2}{\rho_{eff} c_{eff}^2} - 1\right], \tag{9.13a}$$

$$\widehat{T}_{11}^{eff} = \frac{i\pi R_{eff}^2}{4}\frac{\rho_{eff} - \rho_b}{\rho_{eff} + \rho_b}, \tag{9.13b}$$

$$\widehat{T}_{qq}^{eff} = \frac{i\pi R_{eff}^{2|q|}}{4^{|q|}} \frac{1}{(|q|-1)!|q|!} \frac{\rho_{eff}-\rho_b}{\rho_{eff}+\rho_b} k^{|q|}. \tag{9.13c}$$

Within this approach, it is possible to determine not only the effective acoustic parameters (bulk modulus and dynamical mass density) of the fluidlike cylinder but also its radius. These three unknowns can be obtained by using the first three conditions in (9.11). But, in practice, the following simple procedure is employed:

- We obtain first the radius of the effective homogeneous cylinder, R_{eff}, by imposing the condition that the fraction of the volume occupied by cylinders in the cluster is equal to that of the embedded lattice.
- We use the condition for the diagonal term $q = 0$ in (9.11) to determine $B_{eff} = \rho_{eff} c_{eff}^2$.
- We use the condition for the diagonal term $q = 1$ in (9.11) to determine ρ_{eff}.
- The effective sound speed is determined from the relationship $c_{eff} = \sqrt{B_{eff}/\rho_{eff}}$.
- Conditions for $q > 1$ are used to check the consistency of previous results.

Therefore, diagonal elements $\widehat{T}_0$ and $\widehat{T}_1$ are sufficient to characterize the homogenization of sonic crystals based on fluid or elastic cylinders. It has also been shown [31] that elements $\widehat{T}_0$ and $\widehat{T}_1$ of an elastic cylinder are equal to those of a fluid-like cylinder with effective sound speed given by

$$c_a \equiv \sqrt{c_\ell^2 - c_t^2}, \tag{9.14}$$

where c_ℓ and c_t are, respectively the longitudinal and transversal velocities of the actual elastic cylinder.

Therefore, the homogenized parameters of sonic crystals made of 2D binary solid (cylinders)-fluid (background) composites are calculated by using the general expressions reported in Refs. [27, 30], where full details are given. Here we report results for the case in which the sonic crystal is made of two different types of cylinders, because this mixture is employed to design the layers of the cloaking shell, as explained in the next section.

Let us consider periodic arrangements of two different elastic cylinders of radii R_1 and R_2, respectively, in a square lattice of parameter a (see inset in Fig. 9.6). The respective filling fractions are $f_1 = \pi R_1^2/(2a^2)$ and $f_2 = \pi R_2^2/(2a^2)$. If their fluidlike parameters are ρ_1, B_{a1} and ρ_2, B_{a2}, the resulting metafluid has parameters:

$$\zeta_{eff} = \zeta_1 f_1 + \zeta_2 f_2, \tag{9.15a}$$

$$\eta_{eff} = \eta_1 f_1 + \eta_2 f_2, \tag{9.15b}$$

where $\zeta_i \equiv (1 - B_b/B_{ai})$ and $\eta_i \equiv (\rho_i - \rho_b)/(\rho_i + \rho_b)$, for $i = 1, 2$. Moreover, $\zeta_{eff} \equiv (1 - B_b/B_{eff})$ and $\eta_{eff} \equiv (\rho_{eff} - \rho_b)/(\rho_{eff} + \rho_b)$.

From these expressions the following effective parameters are derived

$$\frac{1}{B_{eff}} = \frac{1-f}{B_b} + \frac{f_1}{B_{a1}} + \frac{f_2}{B_{a2}}, \tag{9.16}$$

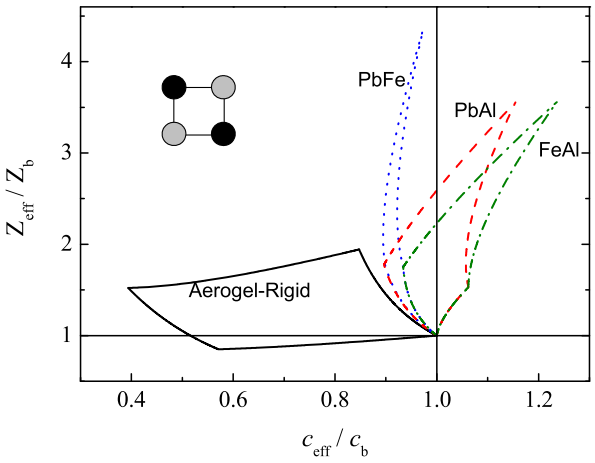

Fig. 9.6 Zc phase diagram of acoustic metafluids based on sonic crystals made of square arrangements of two types of solid cylinder in a background. A square lattice configuration like that displayed in the inset generates an isotropic metafluid. The range of available relative acoustic impedances, Z_{eff}, and sound speed, c_{eff} in the given background are defined by the area enclosed by lines with equal style. The calculations corresponding to combinations of two metals have employed water as the background. Instead, the mixture of aerogel and rigid cylinders are embedded in air. Note that mixtures of aerogel and rigid cylinders lead to metafluids that perfectly match the air impedance. The *horizontal* (*vertical*) *line* is a guide for the eye and defines the condition $\overline{Z}_{eff} = 1$ ($\overline{c}_{eff} = n_{eff}^{-1} = 1$). Reproduced from [31] with permission of IOP Publishing (Color figure online)

$$\rho_{eff} = \frac{1 + f_1\eta_1 + f_2\eta_2}{1 - f_1\eta_1 - f_2\eta_2}\rho_b, \tag{9.17}$$

$$c_{eff} = \sqrt{\frac{B_{eff}}{\rho_{eff}}}, \tag{9.18}$$

where f is the total volume fraction occupied by both cylinders, $f = f_1 + f_2$.

The advantage of having two types of cylinders in the structure is that, with fixed parameters for the cylinders, we can change the effective parameters of the medium simply by changing the radii (filling fractions) of the cylinders. Thus, as we have two parameters (f_1 and f_2) we can choose them in order to tailor B_{eff} and ρ_{eff}.

This approach was used in [31] to design a fully transparent gradient index (GRIN) lens, that is, a device having a position dependent speed of sound $c_{eff} = c_{eff}(y)$ and simultaneously having an acoustic impedance $Z_{eff} = \rho_{eff}c_{eff}$ that perfectly matches with that of the background.

To understand how the proposed GRIN lens is possible, let us look at Fig. 9.6, where the effective impedance Z_{eff} is plotted against c_{eff} for several sonic crystals made of pairs of selected materials. The calculations involving two types of metal cylinders (PbFe, PbAl and FeAl) are embedded in water while the sonic crystals made of Gel and rigid cylinders are in air. On the Zc diagram, each point on the curve obtained for a certain value f, which has associated a corresponding f_1 and

f_2, represents a possible metamaterial. The curves with the same color, which are obtained by changing f_1 and f_2, define an area enclosed by the parametric lines $Z_{eff}(f_1, f_2)$ and $c_{eff}(f_1, f_2)$. Since the larger cylinders considered have radii $R_i = a/2$, the four corners of a selected area correspond to values $(f_1 = 0, f_2 = \pi/8)$, $(f_1 = \pi/8, f_2 = \pi/8)$, $(f_1 = \pi/8, f_2 = 0)$ and $(f_1 = 0, f_2 = 0)$. The last one is always centered at the point (1, 1) in the phase diagram. Note that only the combination of Gel and rigid cylinders in air leads to a metafluid that passes through the line $Z_{eff} = 1$. In other words, only this composite system is able to create a metafluid with perfect matching of impedance with the background, which is air in this case. Moreover, note that this remarkable property is accomplished over a broad range of filling fractions (f_1, f_2), which opens the possibility of having metafluids transparent to airborne sound but with different refractive index n. Thus, this mixture was the one employed to design the GRIN lens previously described. Recently, two proof-of-concept demonstrations have been reported for GRIN lens with mismatching of impedance with the background [10, 18].

The same procedure can be followed to efficiently design cloaking shells in which the properties of the individual layers A and B will be achieved by using two types of cylinders. This is the topic of the next section.

9.4 Realization of Acoustic Cloaks with Sonic Crystals

Section 9.2 has described how to obtain the mass anisotropy required for an acoustic cloak by using a multilayer of two alternating homogeneous and isotropic fluidlike materials A and B, respectively. The properties of these materials are here determined and we also explain how to get them by using sonic crystals.

The following system of equations have to be solved

$$\rho_r(r) = \frac{1}{d_A + d_B}(d_A\rho_A + d_B\rho_B), \tag{9.19a}$$

$$\rho_\theta^{-1}(r) = \frac{1}{d_A + d_B}\left(d_A\rho_A^{-1} + d_B\rho_B^{-1}\right), \tag{9.19b}$$

$$B^{-1}(r) = \frac{1}{d_A + d_B}\left[\frac{d_A}{B_A} + \frac{d_B}{B_B}\right], \tag{9.19c}$$

where $\rho_r(r)$, $\rho_\theta(r)$ and $B(r)$ have the functional dependence given by (9.1a)–(9.1c). Note that we have three equations to determine six parameters: ρ_A, ρ_B, d_A, d_B, B_A and B_B. These parameters are obtained here by following the procedure described in [29].

First, we use the simplifying assumption of a cloaking shell in which both layers have the same thicknesses; i.e., $d_A = d_B = d/2$. Second, we also assume that both layers have the same speed of sound $c_L = c_A = c_B$ although they have different densities. With these two assumptions only three parameters remain, that are, the

layer densities, ρ_A and ρ_B, and their common sound speed c_L. Equations (9.19a)–(9.19c) are now

$$\rho_r(r) = \frac{1}{2}(\rho_A + \rho_B), \tag{9.20a}$$

$$\rho_\theta^{-1}(r) = \frac{1}{2}\left(\rho_A^{-1} + \rho_B^{-1}\right), \tag{9.20b}$$

$$c_L(r) = \sqrt{\frac{B(r)}{\rho_\theta(r)}}, \tag{9.20c}$$

where the last equation follows directly from the definition of the bulk modulus $B_A = \rho_A c_A^2$ and $B_B = \rho_B c_B^2$. So, the two first equations provide the solution for the layer densities:

$$\rho_A(r) = \rho_r(r) + \sqrt{\rho_r^2(r) - \rho_r \rho_\theta}, \tag{9.21a}$$

$$\rho_B(r) = \rho_r(r) - \sqrt{\rho_r^2(r) - \rho_r \rho_\theta}. \tag{9.21b}$$

These expressions together with (9.20c) describe the radial dependence of the acoustic parameters defining the layers such that the cloaking shell made with them (see Fig. 9.4) verifies (9.1a)–(9.1c). The performance of the proposed multilayered cloak has been demonstrated by numerical simulations based on the multiple scattering method [3–5]. A 2D map of the total pressure field, which is represented by the real part of the complex amplitude p, is shown in Fig. 9.7 for the case of a rigid core of radius R_1 that is surrounded by a cloaking shell of radius $R_2 = 2R_1$. A point source placed near the cloak's surface is radiating a field of wavelength $\lambda = R_1/2$. The shell is made of 50 double layers, where each double-layer of thickness d consists of two homogeneous layers made of isotropic materials A and B, respectively, having the same thicknesses; i.e., $d = d_A + d_B = d/2 + d/2$. The cloaking effect is clearly observed; the field is distorted inside the cloak to surround the object and it is almost perfectly reconstructed outside the cloak; better performance can be obtained by increasing the number of layers in the cloak. Reference [29] reports examples of pressure maps when the impinging sound has a plane wavefront.

It is interesting to analyze the cloaking effect as a function of the number of layers employed in the fabrication of the cloak. The resulting behavior is important in order to simplify as much as possible the fabrication of the cloaking shell. The backscattered field is used as a typical parameter characterizing the cloak's performance and it is represented (in a logarithmic scale) in Fig. 9.8 as a function of the frequency for several number of layers. Note that by using just 50 double-layers the backscattered field is reduced by more than one order of magnitude for a wide range of frequencies in comparison with that obtained for the case of a rigid cylinder without cloak. Other interesting cases like a penetrable and a void regions are not reported here but we expect results analogous to those already discussed in Ref. [5].

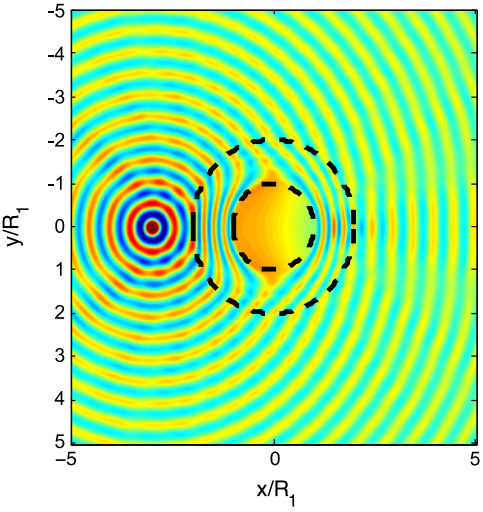

Fig. 9.7 Pressure map (amplitude) produced by the scattering of the field generated by a punctual sound source and a rigid cylinder surrounded by a multilayered cloaking shell made of 50 layers. The cylinder is placed at the origin of coordinates and the radius of the shell is two times the radius of the cylindrical core ($R_2 = 2R_1$). The wavelength of the emitted field is $\lambda = R_1/2$ (Color figure online)

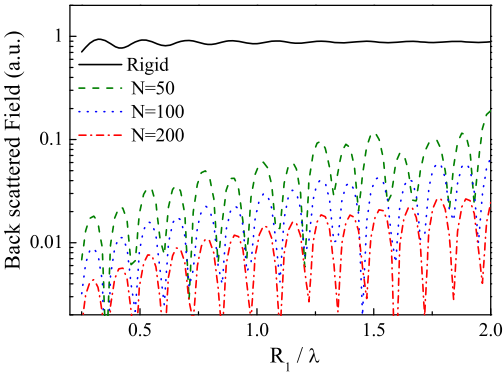

Fig. 9.8 Frequency response of the field backscattered by a rigid cylinder surrounded by a cloaking shell like that described in Fig. 9.4. N is the number of layers in the structure. The case of a bare rigid cylinder is also represented (*continuous line*). Reproduced from [29] with permission of IOP Publishing

9.4.1 Metafluids Engineering by Using Sonic Crystals

It has been demonstrated that the acoustic parameters of acoustic cloaks can be exactly obtained by using a set of N double-layers, each one made of two isotropic metafluids A and B, respectively, whose parameters are given by conditions (9.20c), (9.21a) and (9.21b). Here, we show that the required metafluids can be engineered by using sonic crystals, the artificial structures described in Fig. 9.5 and whose homogenization properties have been obtained in Sect. 9.3.

Let us assume that metafluids A and B consist of two types of cylinders with acoustic parameters: $(\rho_{A\alpha}, c_{A\alpha})$ and $(\rho_{A\beta}, c_{A\beta})$ for metamaterial A, and $(\rho_{B\alpha}, c_{B\alpha})$, and $(\rho_{B\beta}, c_{B\beta})$ for metamaterial B. The parameters of metafluids A and B can be

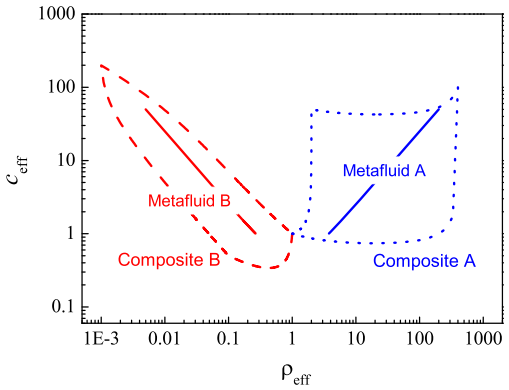

Fig. 9.9 Phase diagram showing that the acoustic properties for materials 1 and 2 can be satisfied with only two different materials. The *straight lines* represent the range of values for metafluids A and B. The *curves* enclosed the area representing the range of values that is possible to obtain with the corresponding two-composite sonic crystal. Reproduced from [29] with permission of IOP Publishing (Color figure online)

tailored with the filling fractions $f_{A\alpha}$, $f_{A\beta}$, $f_{B\alpha}$ and $f_{B\beta}$ of the components involved in their fabrication. Thus,

$$\frac{1}{B_A} = \frac{1 - f_{A\alpha} - f_{A\beta}}{B_b} + \frac{f_{A\alpha}}{B_{A\alpha}} + \frac{f_{A\beta}}{B_{A\beta}}, \tag{9.22a}$$

$$\eta_A = \eta_{A\alpha} f_{A\alpha} + \eta_{A\beta} f_{A\beta}, \tag{9.22b}$$

$$\frac{1}{B_B} = \frac{1 - f_{B\alpha} - f_{B\beta}}{B_b} + \frac{f_{B\alpha}}{B_{B\alpha}} + \frac{f_{B\beta}}{B_{B\beta}}, \tag{9.22c}$$

$$\eta_B = \eta_{B\alpha} f_{B\alpha} + \eta_{B\beta} f_{B\beta}, \tag{9.22d}$$

where $\eta_i = (\rho_i - \rho_b)/(\rho_i + \rho_b)$ for $i = A, B$.

Figure 9.9 represents a (ρ_{eff}, c_{eff}) phase diagram, similar to that reported in Sect. 9.3 for the Z, c parameters. This diagram has been obtained by considering cylinders made of materials whose parameters are given in Table 9.1. Lines of the same color enclose the area in which a metafluid with parameters (ρ_{eff}, c_{eff}) can be engineered by just changing the filling fractions associated with the materials employed in the composite. For instance, the area enclosed by dotted lines defines the range of parameters that can be tailored using materials $A\alpha$ and $A\beta$ in the composition of metafluid A. Within this area, the straight line represents the variation in (ρ_{eff}, c_{eff}) required by material A in order to accomplish the cloaking by the multilayered structure. So, the parameters for material A described by (9.21a), (9.21b) and (9.20c) can be fully accomplished by using materials $A\alpha$ and $A\beta$ in Table 9.1. For the case of material B, the straight line in Fig. 9.9 represent the range of variation requested for cloaking. The set of materials in Table 9.1 used for the acoustic metafluids, used in the construction of the cloaking shell, are just one possible set. In

Table 9.1 Acoustic parameters of the materials forming the composites. The third column reports the effective velocity of the elastic cylinder $c = \sqrt{c_\ell^2 - c_t^2}$, where c_ℓ and c_t are the longitudinal and transversal velocities, respectively

Material	ρ/ρ_b	c/c_b
$A\alpha$	400	100
$A\beta$	2	50
$B\alpha$	0.1	0.5
$B\beta$	0.001	200

order to make the cloak practically viable a more appropriate set should be chosen to match naturally available materials.

We remark that the present fabrication proposal of 2D cloaks can be extended to the case of acoustic cloaks in 3D, where the parameter conditions of the corresponding cloaking shell have been recently reported [8, 12]. Then, by following an analogous approach, we foresee that the corresponding 3D shell could be made of multilayers of two different isotropic metafluids, which could be engineered by using spheres made of different elastic materials.

9.4.2 Metafluids Engineering by Using Corrugated Structures

One main drawback associated with the fabrication of cloaks based on sonic crystals is that its actual realization needs to handle an enormous amount of cylinders. Also, it is expected that there will be strong sound attenuation due to losses. We present here an alternative to such an approach that consists of multilayered structures made of two fluidlike materials with different dynamical mass densities.

The proposed 2D multilayered fluid-fluid structure is obtained inside a planar wave guide made of Aluminum, where a circular cavity is drilled with an embedded corrugated structure, as shown in Fig. 9.10. In this cavity two alternating regions of heights h_1 and h_2 and widths d_1 and d_2 are defined. This height discontinuity in a waveguide can be described, as a first approximation, by assuming that regions 1 and 2 are two different fluids with the same sound speed as that of the background (i.e., $c_1 = c_2 = c_b$) and a mass density mismatch given by [1]

$$\frac{\rho_1}{\rho_2} = \frac{h_2}{h_1}. \tag{9.23}$$

This expression is valid only for the fundamental mode. Though a better description could be obtained by considering coupling through evanescent modes, for our purposes here the simple approach based on (9.23) is enough.

The multilayered structures considered are made of two alternating air regions of height h_1 and h_2. The Aluminum is used here just as a container and, due to the huge impedance mismatch with air, no sound propagation inside the Aluminum is considered. Then, a corrugated structure such as the one shown in Fig. 9.10 can be described by a cylindrical periodic multilayer of two alternating materials, where

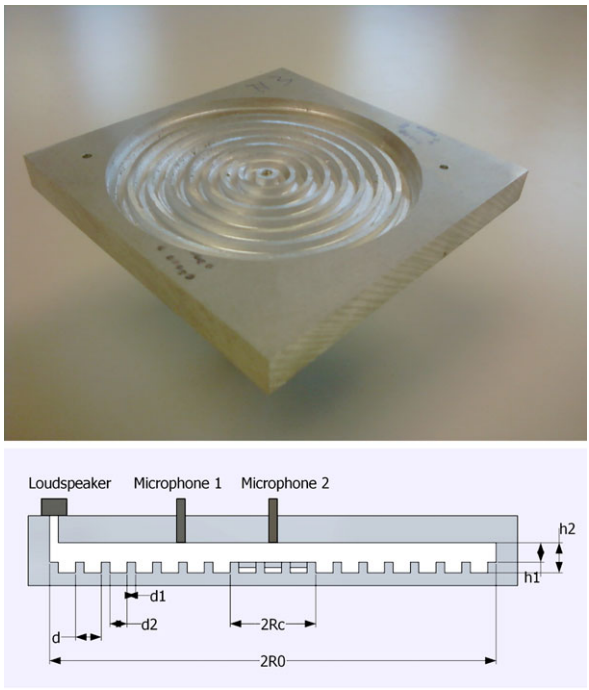

Fig. 9.10 Picture of a sample built and acoustically characterized. It consists of a periodic distribution of grooves that effectively behaves as a periodic fluid-fluid composite. The *lower panel* depicts a schematic view of the experimental setup employed in its characterization. The excited resonances are used to determine the effective parameters of the metafluid defined by this artificial structure. Reproduced from [32] with permission of American Physical Society (Color figure online)

material 1 (2) is a homogeneous and isotropic fluid of width d_1 (d_2) and acoustic parameters ρ_1, B_1 (ρ_2, B_2), where ρ_i and B_i are the density and bulk modulus of material i, respectively. At frequencies low enough this structure behaves as an anisotropic fluid-like material whose effective parameters are given by (9.19a)–(9.19c):

$$\rho_r = \frac{1}{d}[d_A\rho_A + d_B\rho_B] = \frac{\rho_1}{d}\left[d_1 + d_2\frac{h_1}{h_2}\right], \tag{9.24a}$$

$$\rho_\theta^{-1} = \frac{1}{d}\left[d_A\rho_A^{-1} + d_B\rho_B^{-1}\right] = \frac{\rho_1^{-1}}{d}\left[d_1 + d_2\frac{h_2}{h_1}\right], \tag{9.24b}$$

$$B^{-1} = \frac{1}{d}\left[d_A B_A^{-1} + d_B B_B^{-1}\right] = \frac{\rho_\theta^{-1}}{c_b^2}, \tag{9.24c}$$

where A and B materials represent now the regions 1 and 2 with the two different thicknesses h_1 and h_2, respectively. The last expression has been obtained by using $B_i = \rho_i c_i^2$ and $c_1 = c_2 = c_b$.

Sound propagation inside this medium is determined by the radial component of the sound speed c_r and the anisotropy factor γ defined by

$$c_r^2 \equiv B/\rho_r = c_b^2\frac{d^2}{[d_1 + d_2\frac{h_1}{h_2}][d_1 + d_2\frac{h_2}{h_1}]}, \tag{9.25}$$

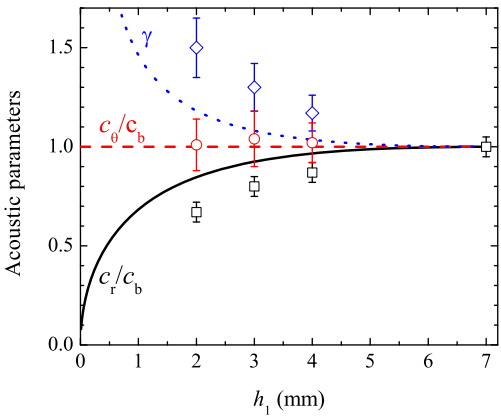

Fig. 9.11 Symbols with error bars represent experimental data for the components of the sound speed tensor relative to that of the background (*circles* and *squares*) and the anisotropy factor (*diamonds*). The *lines* describe the corresponding theoretical values. Reproduced from [32] with permission of American Physical Society (Color figure online)

$$\gamma^2 \equiv \rho_r \rho_\theta^{-1} = \frac{1}{d^2}\left[d_1 + d_2\frac{h_1}{h_2}\right]\left[d_1 + d_2\frac{h_2}{h_1}\right]. \tag{9.26}$$

From these relations the angular component of the sound speed is trivially obtained,

$$c_\theta = \gamma c_r = c_b. \tag{9.27}$$

To demonstrate these predictions we built and characterized four samples similar to that shown in Fig. 9.10. All the samples have the same cavity radius $R_0 = 52$ mm, the same layer thicknesses $d_1 = 2$ mm and $d_2 = 4$ mm, and the same height of region 2, $h_2 = 7$ mm. The only parameter that changes from sample to sample is the height h_1 of region 1, which takes the values $h_1 = 2, 3, 4$ and 7 mm for the samples 1, 2, 3 and 4, respectively. Note that the sample 4 has $h_1 = h_2 = 7$ mm, which makes it an isotropic cylindrical cavity, employed here to obtain the background speed of sound c_b.

The experimental set up is shown in the lower panel of Fig. 9.10: A loudspeaker excites a sound field inside the cavity through a hole drilled on the upper tap. Two microphones were used to measure the excited field; Mic1 is located at $r = 0$ and Mic2 at $r \neq 0$. The excited sound field is a band-limited white noise covering the range 1.5 kHz up to 5.5 kHz, because the fundamental resonances of the different samples are expected in this frequency range. The fact that the larger height is $h_2 =$ 7 mm for all the samples grants no z oscillations for propagating modes up to a frequency of $\nu_c \approx 25$ kHz, which is larger than the maximum working frequency $\nu_{\max} = 5$ kHz. Therefore the structure can be considered as 2D.

The characterization consists of measuring the frequencies of the resonances inside the cavity [32]. The monopolar modes are used to obtain the radial component of the sound speed, c_r, while those with higher order are employed to derive the anisotropy parameter γ. The angular component, c_θ, is obtained by using (9.28).

The results are summarized in Fig. 9.11 and confirm that structures of circular grooves effectively respond as fluid-like materials with anisotropic mass density. Therefore, these artificial structures are a class of metafluids with mass anisotropy

that can be employed to fabricate acoustic cloaks. The local variation of density can be achieved by locally changing the heights of grooves. Unfortunately, dynamical mass density with large values is not possible with this approach according to the results shown in Fig. 9.11. However, in the following section we will discuss how divergent values of ρ_r can be avoided by constructing 'imperfect' cloaks.

9.5 Problems Regarding the Physical Realization of Acoustic Cloaks

In previous sections it has been shown that an acoustic cloak should be, in principle, realizable by a multilayered shell made of elastic cylinders with properly chosen elastic parameters. This structure solves the problem of realizing an anisotropic and inhomogeneous fluidlike shell that, at the beginning, seemed impossible to realize.

Besides the mass anisotropy and the inhomogeneity of the parameters, there is another parameter which is difficult to achieve: the angular component of the sound speed tensor ρ_θ. It is easy to check that ρ_θ is always higher than the sound speed in the background c_b,

$$c_\theta^2 = \frac{B}{\rho_\theta} = \left(\frac{b-a}{a}\right)^2 \left(\frac{r}{r-a}\right)^2 c_b \geq c_b. \tag{9.28}$$

This functional form has been plotted in Fig. 9.2. It implies that sound speed in layer A or B (or both) must be also higher than that of the background. That is, as a function of the homogeneous layers parameters the angular component of the sound speed tensor is

$$c_\theta^2 = \frac{\delta \rho_A^{-1} + (1-\delta)\rho_B^{-1}}{\delta B_A^{-1} + (1-\delta) B_B^{-1}} \geq c_b^2, \tag{9.29a}$$

where $\delta = d_A/d$ and $1-\delta = d_B/d$. And this expression implies that

$$\frac{\delta}{\rho_A}\left(1 - c_b^2/c_A^2\right) + \frac{1-\delta}{\rho_B}\left(1 - c_b^2/c_B^2\right) \geq 0. \tag{9.29b}$$

Obviously this condition is only satisfied when either of c_A or c_B is larger than c_b. This is one of the hard points of acoustic cloaking shells. In principle there is no limitation of the speed of sound in acoustic materials (as there is in electromagnetic materials), however, if the background medium is water, it is difficult to find materials with speeds of sound much higher than that of water, and if the background is air, it is difficult to couple sound between the background and the material. Moreover, it is also required that the material with very high speed of sound has also very low density, which is a very strange property in common materials. This is due to

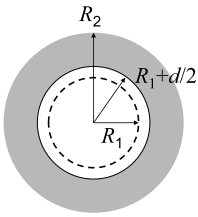

Fig. 9.12 A cloaking shell requires acoustic materials with properties that diverge near the surface of the cloaked object. These divergences can be avoided by designing shells for smaller objects. The resulting cloak is 'imperfect' but it is still capable of producing a substantial reduction of the scattering cross section. The imperfect cloak is here represented by the gray region $R_1 + d/2 \leq r \leq R_2$

the fact that as we are closer to the object's surface, ρ_θ goes to zero, thus we need a very soft layer, but the bulk modulus approaches to a divergent value, then

$$\frac{1}{B} \sim \frac{1}{\rho_B c_B^2} \to 0, \tag{9.30}$$

which obviously cannot be possible unless c_A^2 goes to ∞ faster than ρ_A goes to 0.

These divergences can be avoided with the multilayered structure of the shell. In practice the multilayered shell will have the minimum number of layers required for its correct behavior. Therefore, although the shell requires divergent material properties at the object's surface, a discrete multilayered shell will not require them.

Given a number of layers N, the spacing between them in the shell will be

$$d = \frac{R_2 - R_1}{N}, \tag{9.31}$$

and the position of the nth layer is defined as

$$r_n = R_1 + (n - 1/2)d, \tag{9.32}$$

thus the closest layer to the object surface is located at a distance

$$r_{\min} = R_1 + d/2. \tag{9.33}$$

With this configuration (see Fig. 9.12) the acoustic parameters are not divergent, but they have extremal values given by

$$\rho_r^{\max} \approx \frac{2R_1}{d}\rho_0, \tag{9.34a}$$

$$\rho_\theta^{\min} \approx \frac{d}{2R_1}\rho_0, \tag{9.34b}$$

$$B^{\max} \approx \left(\frac{R_2 - R_1}{R_2}\right)^2 \frac{2R_1}{d} B_0. \tag{9.34c}$$

The smaller the distance d (or the larger the number of layers N) the better the behavior of the cloaking shell, but also the acoustic parameters of the constituent materials become more extremal. The objective in any design will be the equilibrium between the correct number of layers and the feasibility of the materials acoustic properties.

Although acoustic cloaks can be realized by metafluids based on homogenized sonic crystals the material parameters required to engineer them are difficult to achieve, mainly due to the divergence required near the cloaked region. The discrete nature of the proposed cloak given here makes these divergences smaller, but as we demand better functionality of the cloaking shell, the number of layers is larger and the metafluids become more and more difficult to engineer. Moreover, the losses associated with the sound scattering by the cylinders in the metafluid could also be an issue since the transmitted sound could be extremely weak. This problem is under current research in our laboratory.

9.6 Summary

Acoustic cloaks are advanced fluid-like devices that allow ideal acoustic stealth. They can be realized only by using artificial structures called metafluids such that their acoustic parameters present three main characteristics that must be designed step by step. Firstly, the cloaks must have anisotropic dynamical mass density and scalar bulk modulus. Secondly, the acoustic parameters are also inhomogeneous, that is, they depend on the distance to the object to be cloaked. And thirdly, near to the object's surface the parameters become divergent, that is, they present infinite or null values relative to the background parameters.

The problem of having a fluid-like material with anisotropic mass density is solved using a multilayer of two homogeneous metafluids whose properties are obtained by arrays of elastic cylinders. Also, mass anisotropy can be obtained by using structures with radially corrugated surfaces. For both cases, it has been shown that, for wavelengths larger than the typical spacing between cylinders or corrugations, these structures can work as homogeneous fluid-like materials.

Also, if the properties of cylinders or grooves are changed locally according to some given equations, it is possible to obtain the required radial dependence of acoustic parameters in the cloaking shell; this resolves the problem of the cloak inhomogeneity.

However the acoustic parameters still present divergent behavior that cannot be easily avoided. Imperfect cloaks have been suggested as an alternative to overcome the divergent behavior; they are designed to render 'invisible' smaller object and then, the divergent region is not created. Though imperfect cloaks have a non-ideal performance they still produce a sufficient reduction of the object dimensions so that they can be useful in actual applications.

Acknowledgements The authors thank partial financial support by the US Office of Naval Research (Grant N000140910554) and by the Spanish Ministerio de Ciencia e Innovación (Grants

TEC2010-19751 and CSD2009-0066 (CONSOLIDER program). D.T. also acknowledges the contract provided by the program Campus de Excelencia Internacional 2010 UPV.

References

1. Bradley, C.E.: Time-harmonic acoustic Bloch wave-propagation in periodic wave-guides. 1. Theory. J. Acoust. Soc. Am. **96**, 1844–1853 (1994)
2. Brun, M., Guenneau, S., Movchan, A.B.: Achieving control of in-plane elastic waves. Appl. Phys. Lett. **94**, 061903 (2009)
3. Cai, L.W.: Multiple scattering in single scatterers. J. Acoust. Soc. Am. **115**, 986–995 (2004)
4. Cai, L.W., Sánchez-Dehesa, J.: Acoustical scattering by radially stratified scatterers. J. Acoust. Soc. Am. **124**, 2715–2726 (2008)
5. Cai, L.W., Sánchez-Dehesa, J.: Analysis of Cummer-Schurig acoustic cloaking. New J. Phys. **9**, 450 (2007)
6. Cervera, F., Sanchis, L., Sánchez-Pérez, J.V., Martínez-Sala, R., Rubio, C., Caballero, D., Sánchez-Dehesa, J.: Refractive acoustic devices for airborne sound. Phys. Rev. Lett. **88**, 023902 (2002)
7. Chen, H., Chan, C.T.: Acoustic cloaking and transformation acoustics. J. Phys. D, Appl. Phys. **43**, 11301 (2010)
8. Chen, H., Chan, C.T.: Acoustic cloaking in three dimensions using acoustic metamaterials. Appl. Phys. Lett. **91**, 183518 (2007)
9. Cheng, Y., Yang, F., Xu, J.Y., Liu, X.J.: A multilayer structured acoustic cloak with homogeneous isotropic materials. Appl. Phys. Lett. **92**, 151913 (2008)
10. Climente, A., Torrent, D., Sánchez-Dehesa, J.: Acoustic metamaterials for new two-dimensional sonic devices. Appl. Phys. Lett. **9**, 323 (2010)
11. Cummer, S.A., Schurig, D.: One path to acoustic cloaking. New J. Phys. **9**, 45 (2007)
12. Cummer, S.A., Popa, B.-I., Schurig, D., Smith, D.R., Pendry, J., Rahm, M., Starr, A.: Scattering theory derivation of a 3D acoustic cloaking shell. Phys. Rev. Lett. **100**, 024301 (2008)
13. Farhat, M., Guenneau, S., Enoch, S.: Ultrabroadband elastic cloaking in thin plates. Phys. Rev. Lett. **103**, 024301 (2009)
14. Farhat, M., Guenneau, S., Enoch, S., Movchan, A.B.: Cloaking bending waves propagating in thin elastic plates. Phys. Rev. B **79**, 033102 (2009)
15. Greenleaf, A., Lassas, M., Uhlmann, G.: On nonuniqueness for Calderon's inverse problem. Math. Res. Lett. **10**, 685–693 (2003)
16. Leonhard, U.: Optical conformal mapping. Science **312**, 1777–1779 (2006)
17. Krokhin, A.A., Arriaga, J., Gumen, L.: Speed of sound in periodic elastic composites. Phys. Rev. Lett. **91**, 264302 (2003)
18. Martin, T., Nicholas, M., Orris, G., Cai, L.W., Torrent, D., Sánchez-Dehesa, J.: Sonic gradient index lens for aqueous applications. Appl. Phys. Lett. **97**, 113503 (2010)
19. Mei, J., Liu, Z., Wen, W., Sheng, P.: Effective mass density of fluid-solid composites. Phys. Rev. Lett. **96**, 024301 (2006)
20. Milton, G.M., Briane, M., Willis, J.R.: On cloaking for elasticity and physical equations with a transformation invariant form. New J. Phys. **8**, 248 (2006)
21. Norris, A.N.: Acoustic metafluids. J. Acoust. Soc. Am. **125**, 839–849 (2009)
22. Pendry, J.B., Li, J.: An acoustic metafluid: Realizing a broadband acoustic cloak. New J. Phys. **10**(11), 115032 (2008)
23. Pendry, J.B., Schurig, D., Smith, D.R.: Controlling electromagnetic fields. Science **312**, 1780–1782 (2006)
24. Popa, B.I., Cummer, S.A.: Design and characterization of broadband acoustic composite metamaterials. Phys. Rev. B **80**, 174303 (2009)
25. Schoenberg, M., Sen, P.N.: Properties of a periodically stratified acoustic half-space and its relation to a Biot fluid. J. Acoust. Soc. Am. **73**, 61–67 (1983)

26. Schurig, D., Mock, J.J., Justice, B.J., Cummer, S.A., Pendry, J.B., Starr, A.F., Smith, D.R.: Metamaterial electromagnetic cloak at microwave frequencies. Science **314**, 977–980 (2006)
27. Torrent, D., Håkansson, A., Cervera, F., Sánchez-Dehesa, J.: Homogenization of two-dimensional clusters of rigid rods in air. Phys. Rev. Lett. **96**, 204302 (2006)
28. Torrent, D., Sánchez-Dehesa, J.: Anisotropic mass density by two-dimensional acoustic metamaterials. New J. Phys. **9**, 023004 (2008)
29. Torrent, D., Sánchez-Dehesa, J.: Acoustic cloaking in two dimensions: A feasible approach. New J. Phys. **10**, 063015 (2008)
30. Torrent, D., Sánchez-Dehesa, J.: Effective parameters of clusters of cylinders embedded in a non viscous fluid or gas. Phys. Rev. B **74**, 224305 (2006)
31. Torrent, D., Sánchez-Dehesa, J.: Acoustic metamaterials for new two-dimensional sonic devices. New J. Phys. **9**, 323 (2007)
32. Torrent, D., Sánchez-Dehesa, J.: Anisotropic mass density by radially periodic fluid structures. Phys. Rev. Lett. **105**, 174301 (2010)
33. Tretyakov, S.: Analytical Modeling in Applied Electromagnetism. Artech House, Norwood (2000)
34. Waterman, P.C.: New formulation of acoustic scattering. J. Acoust. Soc. Am. **45**, 1417–1429 (1969)

Chapter 10
Acoustic Cloaking with Plasmonic Shells

Michael R. Haberman, Matthew D. Guild, and Andrea Alù

Abstract This chapter presents an overview of the scattering cancellation approach applied to acoustic waves, inspired by the use of plasmonic cloaks for electromagnetic waves. Using an analogous analytical approach, we show here that isotropic and homogeneous acoustic metamaterial covers may provide strong scattering reduction over moderately broad bandwidths of operation in a variety of acoustic scenarios of interest. This chapter outlines the basic physics of this approach, along with numerical examples for moderately sized elastic and fluid objects, thereby providing insights into the anomalous suppression of acoustic scattering produced by this cloaking technique.

10.1 Introduction

Recent interest in acoustic metamaterial cloaking has been primarily focused on the transformation method approach, as outlined in the previous chapter. This technique consists of a mathematical transformation of the acoustic wave equation that maps the acoustic field at a single point in space onto a surface that completely encloses a given region of space to be cloaked. Any arbitrary object placed in such a region would not disturb the field impinging on it [23–30], making it acoustically invisible to any observer placed around the cloak. In so doing, the method determines the material properties of the cloaking region that are needed to reroute incident

M.R. Haberman · M.D. Guild
Applied Research Laboratories and Department of Mechanical Engineering, The University of Texas at Austin, Austin, TX, USA

M.R. Haberman
e-mail: haberman@arlut.utexas.edu

M.D. Guild
e-mail: mdguild@arlut.utexas.edu

A. Alù (✉)
Department of Electrical and Computer Engineering, The University of Texas at Austin, Austin, TX, USA
e-mail: alu@mail.utexas.edu

R.V. Craster, S. Guenneau (eds.), *Acoustic Metamaterials*,
Springer Series in Materials Science 166, DOI 10.1007/978-94-007-4813-2_10,

acoustic waves around the object. Though theoretically exciting, the transformation approach present some challenges to its practical implementation. These challenges are inherently rooted in the necessity for the cloaking region to be acoustically matched to the surrounding medium at the outer cloak boundary while displaying zero normal phase velocity and infinite tangential phase velocity at the inner cloak boundary [24]. These requirements translate into the need for material properties that have drastic spatial gradations from its outer to inner boundary, and simultaneously have extreme values at its inner surface. In addition, this technique requires the occurrence of precise anisotropic response for the stiffness and density tensors of the cloak, making its practical realization quite challenging. Several approximate transformation approaches have been suggested to surmount these difficulties [25–30], with the objective of relaxing the requirement of an identically zero scattering cross-section, thereby increasing the likelihood of realizing an acoustic cloak using available acoustic materials.

An alternative approach to the transformation method for acoustic cloaking is known as the scattering cancellation method. This technique is an adaptation of the theoretical framework first introduced by Alù and Engheta [2, 4] in the electromagnetic (EM) domain to acoustic wave phenomena. Conceptually, the scattering cancellation method exploits the property of some metamaterials, typically 'plasmonic' in nature, to produce a 'negative' scattering effect that somehow cancels the wave disturbance resulting from the presence of an object in an acoustic medium. In the case of canonical shapes, such as cylinders or spheres, the method employs classical scattering formulation for the composite object-cloak system to solve the inverse problem of determining the dimensions and properties of a cloaking layer (or layers) that minimize the field scattered in all directions. This process results in the specification of properties and dimensions for cloaking layers that may be macroscopically homogeneous, isotropic, and are sometimes available in nature or that could be easily realized using composite materials [17, 18]. In addition to cloaking layers made from less exotic material properties, the scattering cancellation method applied in the EM domain has been shown to produce robust and moderately broadband response in the case of electromagnetic waves [2]. Similar and even superior performance is expected for acoustic waves [5–8, 11, 16–18]. Furthermore, the scattering cancellation approach is readily generalizable to consider cases of multiple and/or anisotropic layers. It therefore opens the door to producing acoustic cloaks that are functional over larger bandwidths and for objects of widely varying geometries [31].

10.1.1 Overview

This chapter discusses the design of 'plasmonic' acoustic cloaking shells. Section 10.2 introduces the mathematical and numerical framework that describes the scattering cancellation approach as applied here to spherical objects and it defines the metrics used to evaluate the effectiveness of acoustic plasmonic cloaking shells. The section begins with an introduction of the field equations for the scattering problem of interest; a spherical object covered by a spherical shell immersed in a fluid,

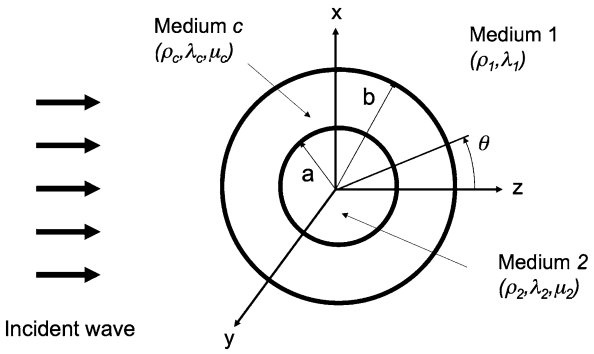

Fig. 10.1 Geometry of the cloaking problem. *Medium 1* represents the surrounding fluid, *medium 2* the sphere to be cloaked, and *medium c* is the cloaking layer. The density of each medium is denoted as ρ, while the Lamé constants are denoted as λ and μ

which is illustrated in Fig. 10.1. It provides the mathematical formulation describing the scattering problem for this geometry in the most general isotropic scenario: an elastic sphere covered by an elastic shell, a problem that also encompasses the simpler situation for which the shell, the sphere, or both are fluids. This formulation provides the equations that will be used to search the parameter space for the most suitable elastic shell to eliminate the scattered field and therefore produce an acoustic cloak. As explained in Sect. 10.2, this is done using a search algorithm that varies the parameters of the metamaterial shell to minimize the total scattering cross-section of the composite elastic object. In Sect. 10.3, we show that two parameter regions for the cloak material may support robust scattering cancellation. The first region may be regarded as the 'plasmonic' region, for which the cloak density and compressibility are the dual of the electromagnetic permittivity and permeability of plasmonic metamaterials used to cloak EM waves. The plasmonic region is the case most often studied in EM scattering cancellation, because it has been shown to ensure robust cloaking response [2]. The second region of interest is the 'anti-resonant' region, which arises near scattering resonances of the cloaking layer and offers more moderate bandwidth and less robust cloaking performance, but which may be achievable using naturally available acoustic materials. The physical behavior of these two types of cloaking shells is thoroughly discussed, and the benefits and drawbacks of each type are highlighted. The section continues by employing the methodology described in Sect. 10.2 to investigate several numerical examples that clearly illustrate the phenomenon of acoustic scattering cancellation. Finally, the chapter closes with a discussion of the benefits and drawbacks of plasmonic cloaking, and points out several potential applications of this cloaking technique in acoustic scenarios of interest.

10.2 Theoretical Formulation and Numerical Evaluation

An investigation of the phenomenon of plasmonic cloaking is best understood by considering the acoustic scattering problem for a canonical shape. In this chapter, an elastic sphere covered by an elastic shell and immersed in a fluid medium, as

already proposed in references [17, 18] and shown in Fig. 10.1, serves this purpose. The covered sphere is insonified by a longitudinal time-harmonic plane wave of frequency f propagating in the positive z-direction. The material properties of each medium are defined by the density ρ and Lamé constants λ and μ, while the geometry is defined by the inner and outer radii of the cloak, denoted as a and b, respectively. We stress here that this choice of geometry is quite arbitrary and only simplifies the notation and the scattering problem. As shown in the EM scenario, geometrical modifications of this ideal shape do not sensibly affect the cloaking performance and arbitrary shapes can be cloaked using a similar approach [31].

For isotropic linear elastic materials, time-harmonic wave motion may be described with two displacement potentials, ϕ and $\boldsymbol{\psi}$, and two decoupled Helmholtz equations [1]

$$\nabla^2\phi + \frac{\omega^2}{c_d^2}\phi = \nabla^2\phi + k_d^2\phi = 0, \tag{10.1}$$

$$\nabla^2\boldsymbol{\psi} + \frac{\omega^2}{c_s^2}\boldsymbol{\psi} = \nabla^2\boldsymbol{\psi} + k_s^2\boldsymbol{\psi} = 0, \tag{10.2}$$

where

$$c_d = \sqrt{\frac{\lambda + 2\mu}{\rho}}, \qquad c_s = \sqrt{\frac{\mu}{\rho}}, \tag{10.3}$$

with ω representing the radial frequency, c_d and c_s the longitudinal and shear wave speeds, respectively, k_d and k_s the longitudinal and shear wave numbers, respectively, and λ and μ corresponding to the Lamé constants of the material in which the wave propagates. Note that λ will always represent the Lamé constant in this chapter and that all wavelength information is conveyed in terms of the non-dimensional parameter ka to avoid confusion between the material property and wavelength.

The displacement potentials are related to the displacement vector $\mathbf{u}$ by

$$\mathbf{u} = \nabla\phi + \nabla \times \boldsymbol{\psi}, \tag{10.4}$$

where the vector potential $\boldsymbol{\psi}$ can be written in terms of two scalar Debye potentials ψ and χ and [14]

$$\boldsymbol{\psi} = r\psi\hat{\mathbf{e}}_\mathrm{r} + \nabla \times (r\chi\hat{\mathbf{e}}_\mathrm{r}), \tag{10.5}$$

with $\hat{\mathbf{e}}_\mathrm{r}$ denoting the unit vector in the radial direction. Considering the geometry illustrated in Fig. 10.1 with an incident compressional plane wave ϕ_inc propagating in the z-direction, the potential ψ is zero due to the azimuthal symmetry. Therefore, the field can be completely described by the two scalar potentials ϕ and χ. Using this approach, the Rayleigh expansion for the displacement potentials in each medium is given by [9]

$$\phi_\mathrm{inc} = \phi_0 e^{-i\omega t} \sum_{n=0}^{\infty} i^n (2n+1)\, j_n(k_{d1}r)\, P_n(\cos\theta), \tag{10.6}$$

$$\phi_1 = \phi_0 e^{-i\omega t} \sum_{n=0}^{\infty} i^n (2n+1) A_n^{(1)} h_n^{(1)}(k_{d1} r) P_n(\cos\theta), \tag{10.7}$$

$$\phi_c = \phi_0 e^{-i\omega t} \sum_{n=0}^{\infty} i^n (2n+1) \times \left[A_n^{(c)} j_n(k_{d,c} r) + B_n^{(c)} n_n(k_{d,c} r) \right] P_n(\cos\theta), \tag{10.8}$$

$$\phi_2 = \phi_0 e^{-i\omega t} \sum_{n=0}^{\infty} i^n (2n+1) A_n^{(2)} j_n(k_{d2} r) P_n(\cos\theta), \tag{10.9}$$

$$\chi_c = \phi_0 e^{-i\omega t} \sum_{n=0}^{\infty} i^n (2n+1) \times \left[C_n^{(c)} j_n(k_{s,c} r) + D_n^{(c)} n_n(k_{s,c} r) \right] P_n(\cos\theta), \tag{10.10}$$

$$\chi_2 = \phi_0 e^{-i\omega t} \sum_{n=0}^{\infty} i^n (2n+1) C_n^{(2)} j_n(k_{s2} r) P_n(\cos\theta), \tag{10.11}$$

where $A_n^{(m)}$, $B_n^{(m)}$, $C_n^{(m)}$, and $D_n^{(m)}$ are the nth scattering coefficients in the mth medium. Note that the Rayleigh expansion for the displacement potentials given by (10.6)–(10.11) is simply an implementation of a classic approach to calculate acoustic scattering from an elastically coated elastic sphere which can be found in the literature dating back to the 1950's [9, 10, 12–15, 19, 20].

To satisfy the boundary conditions using these equations it is first necessary to define the stress in each medium as a function of the displacement field and then formulate the requirements on the stress and displacement fields at the interfaces between media. This is achieved by noting that the stress tensor $\mathbf{T}$ is related to the displacement field through the stress-strain and strain-displacement relations for a linear elastic material shown in (10.12) and (10.13), respectively, and that the displacement is related to the displacement potentials via (10.4) [1]

$$\mathbf{T} = \lambda \, \mathrm{tr}(\varepsilon) + 2\mu\varepsilon, \tag{10.12}$$

$$\varepsilon = \frac{1}{2}\left[\nabla \mathbf{u} + (\nabla \mathbf{u})^{\mathrm{T}} \right]. \tag{10.13}$$

The boundary conditions on $\mathbf{T}$ and $\mathbf{u}$ at the radial elastic interfaces depend on the behavior of each medium. For different material interfaces, the boundary conditions are as follows: (i) for a solid-solid interface continuity of radial and tangential stress and displacement are required, (ii) for a fluid-solid interface the requirements are continuity of radial displacement and stress and zero tangential stress in the elastic solid, and (iii) for a fluid-fluid interface the continuity of radial stress (pressure) and radial displacement are required. To simplify the field equations given by (10.6)–(10.11) when one medium is not a solid, it suffices to set the shear modulus of the medium, μ, to zero and simplify all associated expressions, thereby eliminating shear deformation and stress fields.

Applying the appropriate boundary conditions to (10.6)–(10.11) yields a linear system of equations in the form

$$\mathbf{D} \cdot \mathbf{A} = \mathbf{r}, \tag{10.14}$$

where $\mathbf{D}$ is a system matrix that depends on sphere and shell geometry and material properties of each medium, $\mathbf{r}$ is the input vector describing the incident wave, and $\mathbf{A}$ is a vector containing the unknown scattering coefficients. When both sphere and shell are fluids, $\mathbf{D}$ is 4×4, when the sphere is elastic but the shell is a fluid $\mathbf{D}$ becomes 5×5, when the sphere is a fluid enclosed by an elastic shell, $\mathbf{D}$ is a 6×6 matrix, and when the shell and sphere are elastic, $\mathbf{D}$ is a 7×7 matrix. The components of the $\mathbf{D}$ matrix and $\mathbf{r}$ vector as functions of the material properties and geometry are given for the case of a solid sphere and solid shell in Ref. [17] and for the case of a fluid sphere and fluid shell in Ref. [18]. Regardless of the exact size of the linear system, it is very straightforward to use this formulation to determine the scattering coefficients up to order n when the properties of *medium 1*, *medium 2*, and *medium c* are known. The condition for cloaking coincides, as in the EM case, with the elimination of the scattering coefficients in the surrounding fluid (*medium 1*). In this case, the problem is reduced to a search for the dimensions and material properties of *medium c* that render the coefficient $A_n^{(1)}$ zero for all non-negligible scattering orders. The scattering coefficients of interest can then be calculated in a straightforward manner using Kramer's rule as

$$A_n^{(1)} = -\frac{U_n}{U_n + iV_n}, \tag{10.15}$$

where U_n and V_n are determinants whose elements are dictated by $\mathbf{D}$ and $\mathbf{r}$ [18]. This expression indicates that scattering cancellation of a given mode is achieved by finding cloak properties that lead to $U_n = 0$, provided that $V_n \neq 0$ since $V_n = 0$ corresponds to a modal resonance.

For low ka geometries, and the simple case of a fluid sphere and shell immersed in a fluid medium, it is possible to find closed form quasistatic solutions for the compressibility and density of a fluid shell that lead to substantial scattering suppression [2, 9]. In the more general scenario of larger ka the optimal cloak parameters are found using numerical minimization techniques, since several multipolar scattering orders contribute to the total acoustic cross-section of the object. The numerical procedure employed to minimize $A_n^{(1)}$, which employs the scattering strength metric given in the following section, is described in more detail in Sect. 10.2.2.

10.2.1 Definition of Scattering Strength and Approaches to Acoustic Cloaking

A determination of the material properties of the cloaking layer using numerical minimization requires the definition of a metric that describes the overall strength

of the scattered field. For the work reported in this chapter, the metric chosen for this evaluation is the scattering gain σ_{gain}, which relates the intensity of the field scattered from the sphere-cloak object to the scattered field from a reference sphere of same size. A judicious selection of the proper reference sphere is very important to ensure efficient numerical minimization and to eliminate the presence of misleading minima of the scattering gain associated with the resonances of the reference object.

To properly determine the scattering gain, it is first necessary to relate the linear system of (10.14) to the scattered acoustic intensity. To do so, the scattering coefficients for all frequencies of interest are found for a given sphere-cloak combination by inverting (10.14), $\mathbf{A} = \mathbf{D}^{-1}\mathbf{r}$. These coefficients are then employed in (10.7) to determine the spatial variation of the total scattered pressure field in the surrounding fluid $p_{\mathrm{sc}}(r,\theta)$ by summing the contributions from each mode. Since conservation of momentum requires that $p = \rho_1 \omega^2 \phi_1$, the pressure amplitude is shown to be related to the scattering coefficients through

$$p_{\mathrm{sc}}(r,\theta) = \rho_1 \omega^2 \sum_{n=0}^{\infty} A_n^{(1)} (2n+1)\, j_n(k_1 r)\, P_n(\cos\theta), \tag{10.16}$$

where $P_n(\cos\theta)$ represents the Legendre polynomials, $j_n(k_1 r)$ is the nth order spherical Bessel function of the first kind, k_1 is the wave number in the surrounding fluid, and the subscript n refers to the nth scattering mode. From this expression for the pressure, the scattered acoustic intensity in the radial direction I_{sc} is then calculated from (10.17)

$$I_{\mathrm{sc}}(r,\theta) = p_{\mathrm{sc}}(r,\theta)\dot{\mathbf{u}}(r,\theta)\cdot\hat{\mathbf{e}}_{\mathrm{r}}, \tag{10.17}$$

where $\dot{\mathbf{u}}$ is the time derivative of the particle displacement in *medium 1* defined by (10.4), and $\hat{\mathbf{e}}_{\mathrm{r}}$ is the unit vector pointing the radial direction. This expression for the scattered intensity can then be used to calculate the total scattering cross-section σ_{sc} [28]

$$\sigma_{\mathrm{sc}} = \int_S \frac{\langle I_{\mathrm{sc}}\rangle}{\langle I_{\mathrm{inc}}\rangle} dS, \tag{10.18}$$

where S represents a surface that fully encloses the cloaked object, $\langle\cdot\rangle$ represents the time average of the quantity in brackets, and $\langle I_{\mathrm{inc}}\rangle = |p_{\mathrm{inc}}|^2/2\rho_1 c_1$ is the intensity of the incident time-harmonic plane wave. Similarly, the scattering cross-section from an uncovered reference sphere having the same dimensions as the uncovered sphere can be calculated and denoted as $\sigma_{\mathrm{sc}}^{(\mathrm{ref})}$.

The scattering gain is then defined as the ratio between the scattering cross-section of the cloaked object and that of a reference sphere:

$$\sigma_{gain} = 10\log_{10}\left[\frac{\sigma_{\mathrm{sc}}}{\sigma_{\mathrm{sc}}^{(\mathrm{rigid})}}\right] = 10\log_{10}\left[\int_S \frac{\langle I_{\mathrm{sc}}\rangle}{\langle I_{\mathrm{sc}}^{(\mathrm{rigid})}\rangle} dS\right]. \tag{10.19}$$

In this chapter, we consider as reference a rigid sphere of the same size as the uncloaked object, rather than using the uncloaked object itself. The reason for this

choice is motivated by the fact that some of the objects considered support sharp modal resonances in the frequency range of interest when uncloaked since their size is comparable to the wavelength of excitation. Near such resonances, the scattering gain may appear artificially low, not necessarily due to a strong cloaking effect, but rather due to the suppression of the associated resonance. By comparing the scattering with an ideal rigid sphere of same size these issues are avoided.

As stated at the outset, the optimized cloak parameters are found by employing the scattering cancellation approach, which seeks to find the proper coating that leads to the minimization of the scattered field. This is achieved numerically through the minimization of the scattering gain of (10.19), by searching for the appropriate combination of material parameters and thickness of the shell material.

To better understand the peculiarities of the scattering cancellation approach to acoustic cloaking compared to alternative approaches to acoustic stealth, it is instructive to consider a simplified expression for the total scattering cross-section in terms of the scattering coefficients $A_n^{(1)}$. Consider first a cloak designed using the scattering cancellation approach. This technique aims to eliminate the total scattering cross-section at a given frequency or in a frequency band. From the relations in the previous section it is straightforward to show that $\sigma_{\rm sc}$ relates to the scattering coefficients and the wavenumber through the expression

$$\sigma_{\rm sc} = \frac{4\pi}{|k_1|^2} \sum_{n=0}^{\infty} (2n+1) \left| A_n^{(1)} \right|^2. \tag{10.20}$$

Due to the structure of this relationship, it is clear that $\sigma_{\rm sc}$ can only be drastically reduced if $A_n^{(1)} \to 0$ for all relevant multi-poles excited by the incident wave. This approach ensures that acoustic scattering is suppressed at all angles and for all types of observers and forms of excitation. This may be contrasted with a more traditional monostatic or bistatic stealth approach, which simply requires the elimination of the scattered field in a prescribed direction. As an example, consider the expression for the backscattered strength,

$$\sigma_{\rm back} = \frac{4\pi}{|k|^2} \left| \sum_{n=0}^{\infty} (-1)^n (2n+1) A_n \right|^2, \tag{10.21}$$

which quantifies the degree of monostatic detection effectiveness. It is clear from expression (10.21) that the backscattered field can be eliminated when $\sigma_{\rm back} \to 0$ which only requires that the summation approaches zero at the design frequency(ies). The condition $\sigma_{\rm back} \to 0$ may be achieved in a number of different ways, such as the total absorption of the incident field or matching techniques. However, these solutions tend to suppress the scattering in one direction by redirecting and enhancing the magnitude of the scattered field in other directions (typically in the forward direction, where large shadows are produced). This is clearly a less demanding requirement than the cloaking condition $A_n^{(1)} \to 0$, which leads to $\sigma_{\rm sc} \to 0$ and minimum detectability for arbitrary location of the observer.

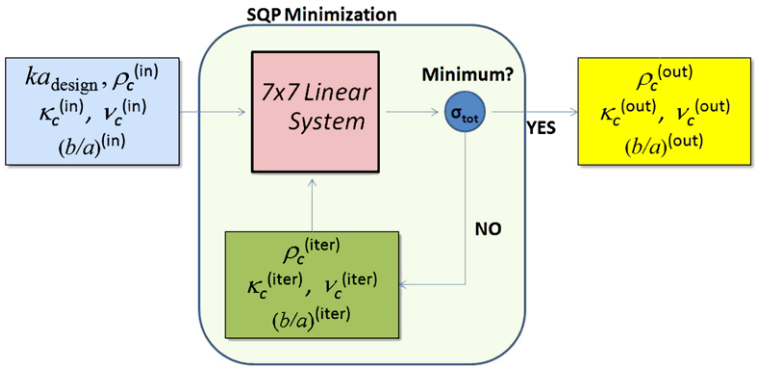

Fig. 10.2 Schematic of the minimization algorithm used to find the properties and geometry of the cloak using the scattering cancellation approach (Color figure online)

It is interesting to notice that, among the cloaking approaches, scattering cancellation is a less restrictive technique than transformation methods for the attainment of significant acoustic cloaking. This is primarily due to the fact that scattering cancellation places no requirement on the acoustic field inside the cloak. The transformation approach, due to the manner in which it is derived, requires the absence of acoustic disturbances inside the cloaked region. In terms of the scattering coefficients of (10.7)–(10.11), the scattering cancellation only requires that $A_n^{(1)} \to 0$, while a single frequency quasi-transformation cloak could be obtained if we further required $A_n^{(2)}, C_n^{(2)} \to 0$, and if one allowed the cloaking layer to be anisotropic and inhomogeneous. In this sense, the transformation approach places more requirements on the allowable acoustic fields, suggesting a physical rationale for the observation that the scattering cancellation approach achieves acoustical cloaking while utilizing less stringent requirements on the parameters of the cloak material. In addition, requiring the field to be zero in the cloaked region inherently restricts the operational bandwidth and frequency dispersion of the cloaking mechanism [5].

10.2.2 Minimization of the Scattered Field

Implementation of the scattering cancellation technique to the acoustic scenario requires a robust multidimensional numerical minimization scheme to search the cloaking layer parameter space in order to determine the set of parameter values that render the covered object acoustically invisible at the frequency(ies) of interest. For the work presented in this chapter, the minimization algorithm represented in Fig. 10.2 was implemented in Matlab using the scattering formulation described in preceding sections and detailed in references [17, 18]. The approach is a straightforward multivariable numerical minimization scheme that employs matrix equation (10.14) and relation (10.20) defining scattering strength to find the set of cloaking layer parameters that minimize the σ_{sc}. The user supplies an initial guess of the

cloak properties, in this case, the design frequency ka, ratio of radii b/a, bulk modulus κ_c, density ρ_c, and Poisson's ratio ν_c, where $\nu = \lambda/2(\lambda + \mu)$ for an isotropic elastic solid. The scattering gain is then calculated by finding the scattering coefficients, $A_n^{(1)}$, for the n significant modes at the design frequency and uses those coefficients to calculate σ_{sc}. A quasi-Newton minimization algorithm that employs sequential quadratic programming (SQP) is then utilized to vary the cloak parameters until σ_{sc} is minimized while simultaneously obeying constraints on allowable parameter values [22].

The authors have found that initial guesses leading to efficient evaluation of the numerical algorithm can be determined by calculating the density and bulk modulus that satisfy the condition of zero scattering for low ka approximations of the scattered field [17]. These values are found using (10.22) and (10.23):

$$\frac{\kappa_c}{\kappa_1} = \bar{\kappa}\frac{1-\varphi}{\bar{\kappa}-\varphi}, \tag{10.22}$$

$$\frac{\rho_c}{\rho_1} = \frac{1}{2(1-\varphi)}\left[\alpha + \sqrt{\alpha^2 + 8\bar{\rho}(1-\varphi)^2}\right], \tag{10.23}$$

where the constant α is given by

$$\alpha = (2+\varphi)\bar{\rho} - (1+2\varphi), \tag{10.24}$$

and $\bar{\kappa} = \kappa_2/\kappa_1$, $\bar{\rho} = \rho_2/\rho_1$, and $\varphi = (a/b)^3$. When the shell of a composite sphere-shell object has these parameters, the effective bulk modulus and the effective density of the composite object is the same as the surrounding fluid [33] in the quasistatic limit [10]. It should be noted, however, that for finite frequencies the optimized properties of the cloak for scattering minimization may be substantially different than these initial guesses, as the contribution of dynamic terms and higher-order multipoles become rapidly significant, even for moderate values of ka.

10.3 Plasmonic and Anti-Resonant Cloaking

As we show in the following, acoustic cloaking using the scattering cancellation approach may be achieved utilizing two distinct principles, and require materials of quite different acoustic properties. The two regimes of interest may be categorized as the 'plasmonic' and the 'anti-resonant' cloaking regimes. This section discusses shells that achieve acoustic cloaking using both of these regimes by highlighting three canonical examples: (i) cloaking a rigid sphere (Sect. 10.3.1), (ii) acoustic fluid cloaking (Sect. 10.3.2), and (iii) isotropic elastic sphere cloaking (Sect. 10.3.3). Being of primary interest for this chapter, the physical response and the required material parameters of plasmonic cloaks are described in more detail in the following examples.

10.3.1 Cloaking of a Rigid, Immovable Sphere

One potential hurdle to an efficient implementation of the scattering cancellation approach is the susceptibility of the numerical minimization scheme to return cloaking layer parameter sets associated with local, rather than global, minima, which either require difficult-to-realize material properties or that do not provide the desired degree of acoustic cloaking. For this reason, it is of interest to find a reliable and efficient means to inspect the parameter space of representative configurations before implementing the minimization code, in order to better understand the physical phenomena leading to scattering cancellation. One possible approach is the creation of two-dimensional contour plot depicting the scattering gain as a function of two relevant cloak parameters, while the others are held constant. Figure 10.3 shows such a plot for the variation of the scattering gain as a function of the shell material parameters ρ_c/ρ_1 and κ_c/κ_1, for a covered rigid sphere with $ka = 0.5$ and a fixed shell radius ratio of $b/a = 1.10$. The scattering gain in the figure is denoted by a scale in which light shading correspond to suppression of the scattered field, and dark shading correspond to stronger scattering regions.

The maxima and minima of the scattering strength are related to those of the scattering coefficients, according to (10.15) and, based on (10.24), are associated with $V_n = 0$ and $U_n = 0$, respectively, which are notated in Fig. 10.3. Two distinct regions within the parameter space may be identified as potentially of interest for strong scattering suppression. The first region is located at lower density ratios and higher bulk modulus ratios, compared to the values associated with the first modal resonance of the sphere where $V_0 = 0$. This region is characterized by a lack of sharp neighboring resonances and a broad, distinct minimum in the scattering gain. The location of this point in the parameter space identifies the material properties of a 'plasmonic' acoustic cloak, in analogy with the dual properties of plasmonic metamaterial cloaks in the EM scenario [2, 18]. The second region is located at higher density ratios and lower bulk modulus ratios than those supporting the first

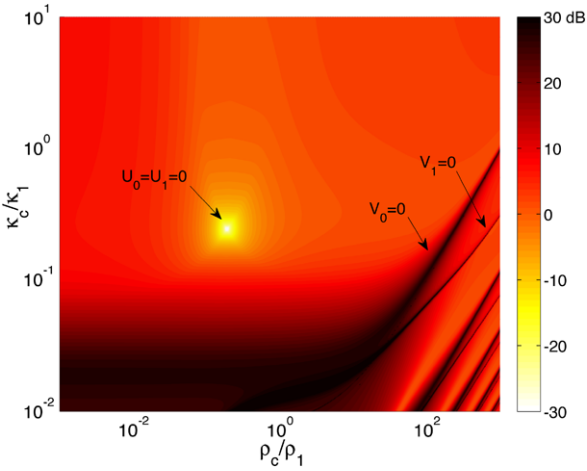

Fig. 10.3 Contour plot showing the scattering gain of an immovable rigid sphere having a cloaking layer with $ka = 0.50$, $b/a = 1.10$ and varying cloaking layer material properties. *Dark areas* correspond to material properties where the scattered field is minimized (Color figure online)

modal resonance, $V_0 = 0$. This region corresponds to material properties for which sharp modal resonances may occur within the shell. Although the scattering gain is large at or around these modal resonances, modal nulls or 'anti-resonances' may be found in between these resonances. A layer with these properties is referred to as an 'anti-resonant' acoustic cloak.

The 'plasmonic' region stems from the duality with the electromagnetic (EM) cloaking problem [2, 4], for which it was shown that plasmonic metamaterials with electric permittivity lower than free space may drastically suppress the scattering from moderately sized objects as a result of their local negative polarizability. The dual of this phenomenon in the acoustic domain corresponds to materials that have a density and bulk modulus less than that of the background fluid, when *medium 2* is denser and stiffer than the surrounding medium [18]. Indeed, the results of Fig. 10.3 show that an equivalent cloaking regime exists when the acoustic material properties of the cloaking layer are less than those of the host medium. Nature offers an abundance of materials whose compressibility and density are lower than water and, as a general rule, plasmonic cloaks are typified by their ability to push all resonant behavior to higher frequencies and lead to moderately broadband cloaking behavior and strong scattering suppression [18]. Plasmonic cloaking is of particular interest since EM cloaks have been shown to offer robust cloaking performance even when covering collections of objects [3] and objects with imperfections [4].

Using the optimized cloaking layer properties for the plasmonic acoustic cloak presented in Fig. 10.3, it is now possible to investigate the scattering reduction as a function of frequency for this specific cloaked system. Section 10.2 and the previous parametric study showed that the characteristic feature of the scattering cancellation technique consists of the ability of determining the optimal cloaking layer parameters that lead to an alignment of the zeros of $A_n^{(1)}$ at the ka of interest. To highlight this effect and further investigate the influence of each cloak parameter, a comparison of the scattering coefficient magnitudes of the uncloaked and cloaked rigid sphere has been performed. The results of this study are shown in Fig. 10.4. As is evident from the middle panel of Fig. 10.4, the scattering cancellation method has found cloaking layer parameters that effectively have aligned the nulls of the monopole and dipole scattering terms (corresponding to $n = 0$ and $n = 1$ multipoles), which dominates the scattering in the uncloaked scenario. The resulting scattered field will have a residual quadrupolar ($n = 2$) pattern and, as illustrated in the bottom panel of the same figure, have a scattered field whose scattering cross-section is 40 dB below the field scattered from an uncovered rigid sphere of same size. The effectiveness of the cloak and the benefit of employing a full dynamic formulation is reinforced by the results shown in the bottom panel of Fig. 10.4, which shows the scattering gain of the cloaked rigid sphere for values of ka up to 1. This curve demonstrates that, although the solution was optimized at a single design frequency ($ka = 0.5$), a minimum of 20 dB in scattering reduction is obtained over the entire band, from $ka = 0$ to $ka = 1$. Indeed, unity scattering gain for this example does not occur until near $ka = 3.0$, 6 times larger than the target frequency.

In Figs. 10.3 and 10.4, the effectiveness of plasmonic cloaking was highlighted for a constant cloaking shell thickness. The sensitivity to changes in shell thickness of the material properties of the cloaking layer, ρ_c and κ_c, required to achieve

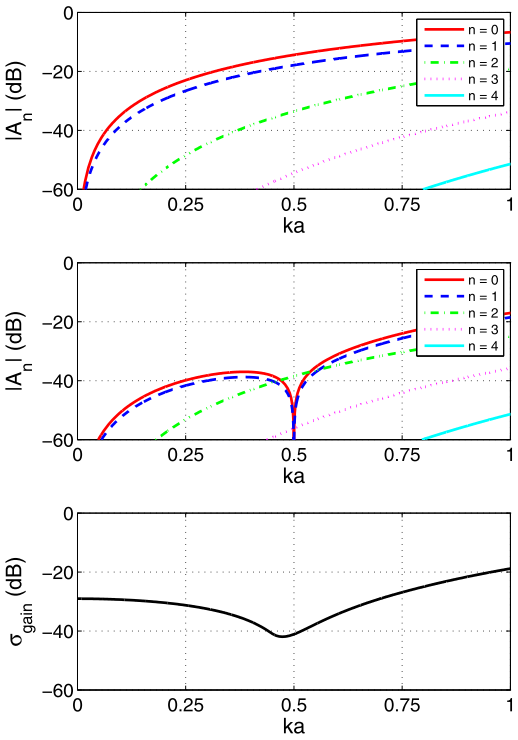

Fig. 10.4 Scattering coefficients of an uncloaked and cloaked rigid sphere are shown in *top* and *middle panels*, respectively. The resulting scattering gain σ_{gain} of the cloaked configuration is shown in the *bottom panel*. The cloaking layer thickness ratio is $b/a = 1.10$, and was optimized to cancel the first two scattering coefficients at $ka = 0.5$ (Color figure online)

cloaking can be shown by letting the thickness ratio vary and numerically determining the solution where U_0 and U_1 are zero. Doing so produces the trace of the optimized cloaking layer density and bulk modulus ratios as a function of b/a shown in Fig. 10.5. The scattering gain occurring at these optimal points is shown in the bottom panel. From these results, it is apparent that the properties necessary to produce a plasmonic cloak may be quite sensitive to the thickness of the cloaking layer, especially for ultrathin cloaking layers. Still, the achievable values of scattering suppression are consistently very large, and it is preferable to keep the overall cloak thickness small, whenever possible. It is important to point out that, when compared with the quasistatic solution given by (10.22) and (10.23) (dashed lines in the figure), the results are almost overlapping, due to the small size of the scatterer in this example. This shows that a 'plasmonic' cloaking layer designed to operate in this low-ka regime supports a non-resonant scattering cancellation, consistent with quasistatic considerations. For larger objects, the dynamic scattering effects become more relevant, and full-wave solutions become significantly different from their quasistatic analogs. Using an anti-resonant cloaking layer, on the other hand, one would not expect to find this similarity to the quasistatic solution even in the low ka regime, due to the inherently dynamic response of the cloak material, which leads to a cancellation of the scattered field due to its anti-resonant response [17]. It should also be noted that, despite the low value of ka in this example, non-resonant

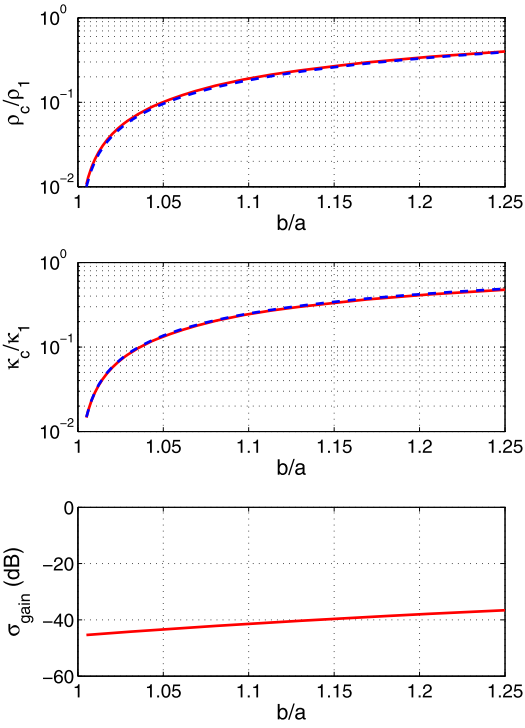

Fig. 10.5 Variation in optimized plasmonic cloaking layer density (*top panel*), bulk modulus (*middle panel*) and scattering gain (*bottom panel*) as a function of cloaking layer thickness for a rigid sphere with $ka = 0.5$. *Curves* are calculated using the full wave solution (*solid lines*) and quasistatic approximations given by (10.22) and (10.23) in *dashed lines* (Color figure online)

plasmonic cloaking may be achieved for higher values of ka with similar performance, in particular when multiple layers are considered [16], as discussed below.

10.3.2 Cloaking of a Penetrable Fluid Sphere

In Sect. 10.3.1, the behavior of plasmonic and anti-resonant cloaks were discussed for an immovable, rigid sphere. That discussion showed that one unique aspect of plasmonic and anti-resonant cloaks is that they must be tailored to the specific object that one desires to cloak. For the case of a lossless fluid sphere, the material properties can be completely described by ρ_2/ρ_1, and κ_2/κ_1, the density and bulk modulus, respectively, relative to the same parameters of the surrounding fluid.

To produce a plasmonic cloak for an arbitrary fluid sphere that is similar to the one discussed in the previous section, the cloaking layer properties will be a function of ρ_2/ρ_1 and κ_2/κ_1 for a fixed design frequency and layer thickness. It is therefore possible to construct a surface plot depicting the required value of ρ_c/ρ_1 and κ_c/κ_1 to yield a plasmonic metamaterial cloak for any given combination of ρ_2/ρ_1 and κ_2/κ_1. Consider, for example, the case of $ka = 0.5$ and $b/a = 1.10$ for a penetrable fluid sphere whose parametric plot is shown in Fig. 10.6. In this figure, the necessary cloaking layer material properties of ρ_c/ρ_1 (top panel) and κ_c/κ_1 (middle panel) are

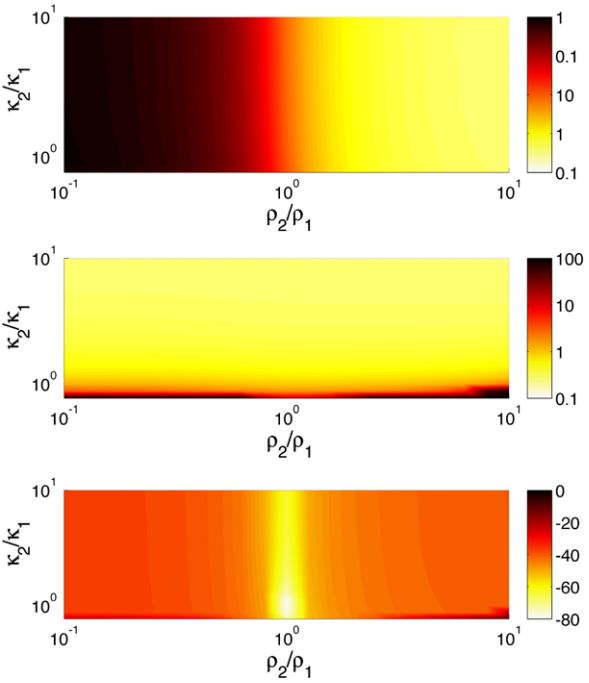

Fig. 10.6 Parametric plot of the optimized cloaking layer density (*top panel*), cloaking layer bulk modulus (*middle panel*) and scattering gain (*bottom panel*) as a function of the density and bulk modulus of a penetrable fluid scatterer relative to the external fluid. The results are given for a cloaking layer with a thickness ratio of $b/a = 1.10$ at $ka = 0.5$ (Color figure online)

denoted by a change in shade, with values less than unity being represented by light shading and values greater than unity represented by dark shading. Note that a logarithmic scale has been used to demonstrate the required parameters over a very large range of possible interior sphere values. For a given ρ_2/ρ_1 and κ_2/κ_1 combination, the minimum scattering gain achieved by the plasmonic cloak designed using the scattering cancellation method is illustrated in the bottom panel, with the scattering gain being given in dB and referenced to the scattering strength of a rigid scatterer of the same size.

Although virtually all regions throughout the parameter space show a scattering gain of -30 dB or less in the bottom panel of Fig. 10.6, there are some regions in the vicinity of ρ_2/ρ_1 and κ_2/κ_1 near unity which exhibit significantly more scattering reduction. This is to be expected, since the point where both parameters are identically equal to 1 is the trivial solution where the fluid sphere is the same as the surrounding fluid. When only one of these two fluid sphere material parameters matches the surrounding fluid, it is apparent that the reduction in scattering gain is much more significant for values near $\rho_2/\rho_1 = 1$.

From the top and middle panels of Fig. 10.6, it can be seen that the variation in each of the cloaking layer properties is governed largely by only one of the two fluid sphere parameters. Specifically, the variation in ρ_c/ρ_1 is dominated by ρ_2/ρ_1 while changes in the required κ_c/κ_1 are primarily influenced by κ_2/κ_1. This behavior is expected in the quasistatic regime considered here, since the lowest order scattering modes are relevant, and they are directly affected by the local bulk modulus and den-

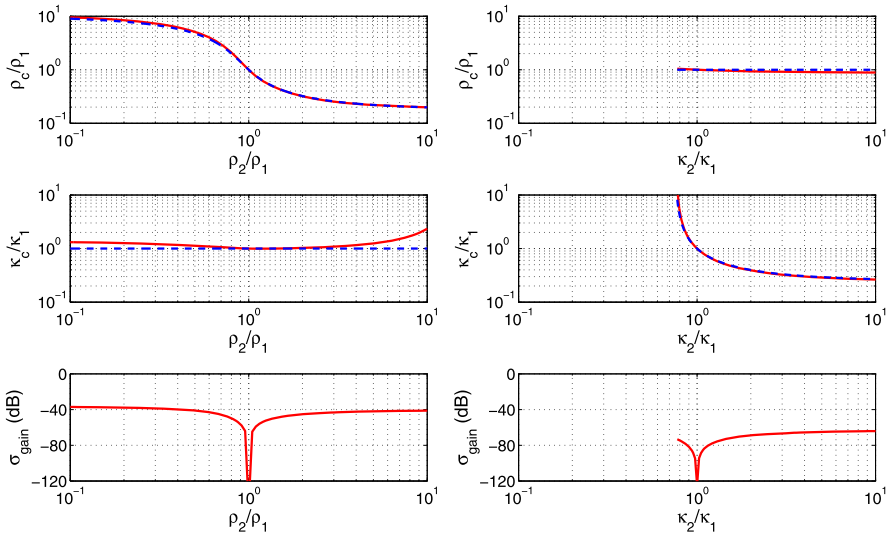

Fig. 10.7 Slices of the parametric plots of Fig. 10.6 for constant scatterer bulk modulus of $\kappa_2/\kappa_1 = 1$ (*left column*) and scatterer density of $\rho_2/\rho_1 = 1$ (*right column*). The *rows* depict resulting changes in the cloaking layer density (*top row*), cloaking layer bulk modulus (*middle row*) and scattering gain (*bottom row*) (Color figure online)

sity [18]. To further explore this behavior, Fig. 10.7 shows two slices taken from the contour plots of Fig. 10.6. The results in the left column depict changes in required values of ρ_c/ρ_1 and κ_c/κ_1 along with the resulting optimized σ_{gain} as a function of ρ_2/ρ_1 at $\kappa_2/\kappa_1 = 1$. Conversely, the right column shows those same parameters for the case where κ_2/κ_1 is varied but ρ_2/ρ_1 is held constant at unity. The quasistatic results of (10.22) and (10.23) are plotted with dashed lines for comparison to those predicted by the full-wave expansion. It is obvious that quasistatic predictions of shell density and modulus will lead to significant reductions in the scattered field, but the full-wave expansion is required for increased values of ka and even when the sphere and surrounding fluid have drastic parameter value contrast, as shown in the middle panel of the left column.

For constant κ_2/κ_1, the variation of ρ_c/ρ_1 with ρ_2/ρ_1 follows that of the quasistatic results very well. As expected, the cloaking layer density ratio is equal to unity at $\rho_2/\rho_1 = \kappa_2/\kappa_1 = 1$, and the resulting scattering gain at this point approaches negative infinity. With regards to the variation of κ_c/κ_1 with respect to ρ_2/ρ_1, the quasistatic results follow the same trend but do not capture the behavior away from ρ_2/ρ_1, especially for $\rho_2/\rho_1 \gg 1$ and to lesser degree when $\rho_2/\rho_1 \ll 1$. Although these deviations may seem relatively modest, even small changes in the plasmonic cloak properties can lead to misalignment at the design frequency, as will be discussed in Sect. 10.3.3.

For the case of constant ρ_2/ρ_1 shown in the right column of Fig. 10.7, there is little variation in the value of ρ_c/ρ_1 required for cloaking behavior, which is in excellent agreement with the quasistatic results. The behavior of κ_c/κ_1 is also captured in

the quasistatic expression given by (10.22), which increases rapidly for decreasing values of κ_2/κ_1. Looking at this equation, it is possible to identify the source of this behavior, since the denominator is zero when $\kappa_2/\kappa_1 = (a/b)^3$. For $b/a = 1.10$, this corresponds to the point where $\kappa_2/\kappa_1 = 0.7513$. For κ_2/κ_1 below this critical value, the required κ_c/κ_1 is negative. This presents a significant challenge in cloaking a compliant target. To overcome this problem using materials with positive κ_c/κ_1, one possible solution is using a thicker shell, since the critical value of κ_2/κ_1 scales with $(a/b)^3$. Alternatively, an anti-resonance cloak could be used, which has been shown to be very effective for the case of an air bubble in water, which represents a target that is several orders of magnitude more compliant than the surrounding fluid [17].

10.3.3 Cloaking an Isotropic Elastic Sphere

In many applications, the object to be cloaked will be an isotropic elastic solid, not a simple fluid. For the frequency range under consideration in this chapter, for which the wavelength in the surrounding fluid is on the order of the diameter or larger, the effects of a non-zero shear modulus in the target does not significantly affect the ability to design an effective plasmonic cloak using a single fluid layer. Although the non-zero shear modulus does change the modal behavior to some degree, the effect of shear is predominantly manifested for scattering orders $n = 2$ and higher. To show the effectiveness of an acoustic plasmonic metamaterial cloak in this scenario, an elastic sphere with low ka is now considered for illustrative purposes. Parameters of a single fluid layer are determined to cancel the first two scattering orders ($n = 0$ and $n = 1$), and we can expect no major differences in the trends and behaviors described thus far for cloaks tailored to rigid and fluid objects.

To demonstrate the robustness of the plasmonic cloaking technique in this scenario, three cases of isotropic elastic scatters in water will be considered, composed of stainless steel, aluminum and glass, respectively. The material properties for each example are listed in Table 10.1. These three examples represent three commonly used materials in scientific and engineering applications, which span a broad range of densities and elastic moduli. These material properties are significantly different than those of the surrounding water, and thus each of these cases also represents objects with significant scattering strength.

For each of these targets, plasmonic cloaks using three different design frequencies are examined: $ka = 0.5$, 0.75 and 1. The material properties of a plasmonic cloak for each sphere material are listed in Table 10.2, where the cloak thickness ratio is $b/a = 1.05$ for all cases. The scattering gain as a function of ka for each example is shown in Fig. 10.8. All the plasmonic cloaks show similar trends in the overall performance, achieving at least 30 dB reduction in scattering gain at the design frequency, and significant reductions over a large bandwidth around the design frequency. In each case, the scattering strength is reduced by 10–15 dB at $ka = 1.5$, and extends up to a ka of 2.5–3.0. An important feature of these plasmonic cloaks,

Table 10.1 Properties of elastic spheres to be cloaked for the three examples considered in Sect. 10.3.3 [21]

Parameter	Steel	Aluminum	Glass
Density, ρ (kg/m^3)	8000	2700	2300
Bulk modulus, κ (GPa)	170	75	39
Poisson's ratio, ν	0.28	0.33	0.24

Table 10.2 Properties of single fluid layer plasmonic cloak for $ka = 0.5$, 0.75, and 1.00 considered in Sect. 10.3.3

	Steel			Aluminum			Glass		
ka	0.50	0.75	1.00	0.50	0.75	1.00	0.50	0.75	1.00
Density, ρ (kg/m^3)	103.53	98.30	91.28	138.55	129.28	117.25	152.13	141.10	126.86
Bulk modulus, κ (MPa)	295.85	287.80	276.25	300.83	293.34	282.38	307.41	299.87	288.67

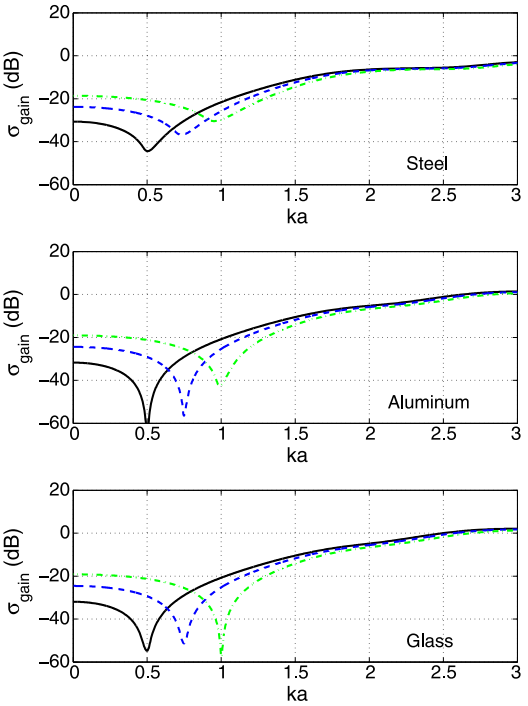

Fig. 10.8 Scattering gain as a function of ka for a cloaked sphere of stainless steel (*top*), aluminum (*middle*) and glass (*bottom*). Three plasmonic cloaking layers are presented for each case, optimized for $ka = 0.5$ (*solid line*), $ka = 0.75$ (*dashed line*) and $ka = 1.0$ (*dash-dotted line*). The cloaking layer material properties for each case are listed in Table 10.2. The cloaking layer thickness ratio in all cases was $b/a = 1.05$ (Color figure online)

as illustrated in these examples, is that the addition of a cloaking layer does not lead to an increase in the scattering gain, even when the bandwidth is extended to several octaves above the design frequency.

Comparing the response of each cloaked target, it can be seen that a larger decrease in the scattering gain is obtained for the aluminum and glass objects compared to the stainless steel case. Based on the analysis in the previous section for the results presented in Fig. 10.6, this is expected since the density of stainless steel is significantly larger than that of water, and is several times denser than that of the other two elastic targets. For each case except the cloaked glass at a design $ka = 1$, an increase in ka leads to reduced cloaking performance. This is due to the fact that the plasmonic cloaks were designed to cancel the first two scattering orders and, as the frequency increases, contributions from higher order modes become more significant. In the case of cloaked glass target with $ka = 1$, the reason for improved scattering reduction resides in the fact that the quadrupolar mode happens to be significantly reduced by the optimal combination of parameters. Although this does not happen in general for a single fluid layer plasmonic cloak, this is an additional benefit that may occur in particular for penetrable targets.

It should be recalled that the criteria used to optimize the cloak performance have been entirely based on the minimization of the overall scattering gain of the composite object, which is simply a relative measure of the total scattering cross-section of the cloak-sphere system. Although this is an excellent measure of the value of the scattered acoustic intensity averaged over all scattering angles, and provides a single metric to describe the scattered field at a given frequency, it may not fully show the phenomena underlying the functionality of these cloaks.

To illustrate additional features of this cloaking technique, the real part of the total pressure field in the sphere, shell and external fluid is plotted in Fig. 10.9 for the uncloaked (top row) and cloaked (bottom row) cases of stainless steel, aluminum and glass spheres in water. The illustrations are shown for a time-harmonic incident plane wave passing from left to right at $ka = 1$, which is also the frequency at which the cloaks are optimized. The length scale r in the figure is normalized to the uncloaked sphere radius a, and the scale of the pressure field is normalized by the amplitude of the incident pressure wave. Lines of constant phase are shown solid lines to highlight the effects of the scatterer and the cloak.

From the top row of Fig. 10.9, which shows the uncloaked spheres, the perturbation of incident wave by the isolated scatterer may clearly be seen. By comparison with the corresponding cloaked spheres in the bottom row, the addition of a thin plasmonic cloaking layer (only 5 % the radius of the sphere) effectively restores the pressure field in the surrounding fluid to that of the incident field, which passes by the cloaked sphere undisturbed. In addition, it should be stressed that our primary design criteria for cloaking have focused on the cancellation of the exterior scattered field, but one of the major differences between transformation-based and scattering cancellation cloaks is the difference in behavior of the interior fields. This is apparent in Fig. 10.9, in which a look at the interior pressure field shows that it retains high fidelity with that of the magnitude and phase of the incident wave passing through the surrounding fluid. Although the resulting scattering cancellation in the surrounding fluid is the same as one could attain using either a transformation-based cloak or an anti-resonance cloak, this interior wave structure is a unique feature of the plasmonic cloak. Combined with its isotropic properties, non-resonant behavior

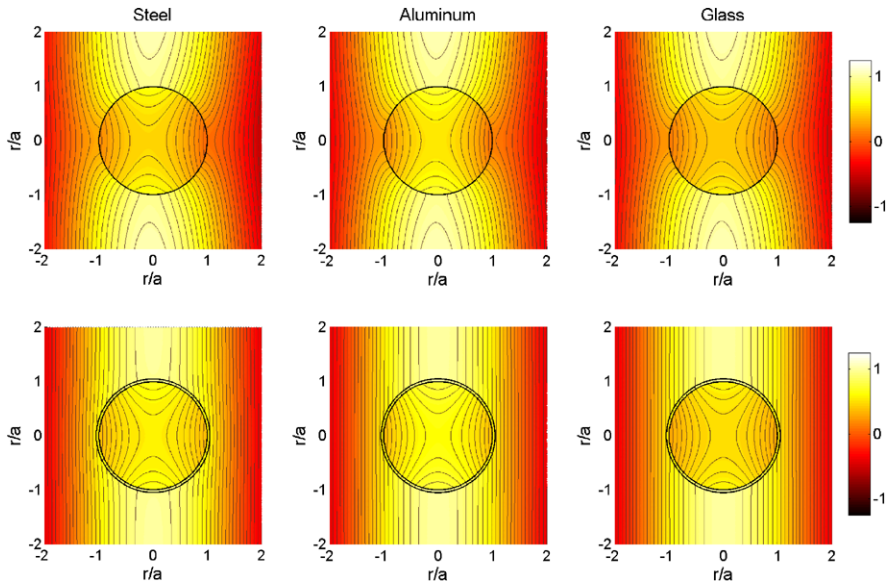

Fig. 10.9 Real part of total pressure field for an isotropic sphere of stainless steel (*left column*), aluminum (*middle column*) and glass (*right column*). For each case, the uncloaked sphere is presented in the *top row*, and with a plasmonic cloak with a thickness ratio of $b/a = 1.05$ presented in the *bottom row*. The scale for the pressure is normalized to the amplitude of the incident wave, which is a time-harmonic plane wave traveling from left to right with a frequency of $ka = 1$ (Color figure online)

and small thickness relative to the uncloaked sphere, this fidelity with the incident pressure wave allows for possible applications of ideal acoustic sensors which can detect a signal without disruption of the surrounding field, analogous to similar applications for electromagnetic waves [6, 7].

One practical issue currently being investigated is the significant disruption of the modal behavior of the sphere and cloaking layer combination when an isotropic elastic solid is used as a plasmonic cloak. This problem is due to the mismatch in the shear moduli of the surrounding fluid and the elastic layer coating an elastic sphere. Just as the design of a plasmonic cloaking layer can benefit from significant reduction or cancellation of the quadrupole mode, it can also be significantly disrupted by a large quadrupolar response, even at relatively low frequencies, which can be introduced when the cloaking layer has a non-zero shear modulus. Despite this limitation, promising results have been reported by using multiple thin lubricated elastic layers to construct plasmonic cloaks for optimized performance for the cancellation of higher order modes [16].

Though previous examples were limited to the low ka regime in order to demonstrate the physical principles leading to scattering cancellation, it is of interest to investigate the possibility of finding plasmonic cloaks when higher order multipoles are non-negligible. An illustrative example of the promising possibilities using multiple alternating elastic and fluid layers is presented in Fig. 10.10. This figure depicts

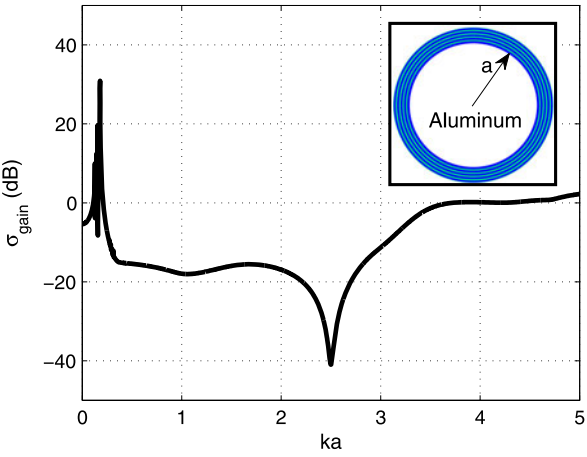

Fig. 10.10 Scattering gain as a function of ka for a cloaked sphere of aluminum in water. The plasmonic cloak is constructed with 10 isotropic layers, consisting of alternating elastic (*light*) and fluid (*dark*) layers. The cloaking layer material properties for each case are listed in Table 10.3 (Color figure online)

the scattering gain of an aluminum sphere in water that is coated with a multilayer plasmonic cloak optimized at $ka = 2.5$, a frequency at which the wavelengths are on the order of the diameter of the uncloaked sphere. The plasmonic cloak is constructed of two constituent materials: an elastic material (shown in light) that is denser and more compliant than water, and a fluid (shown in dark) with a lower density and a higher bulk modulus than water [16]. This type of cloak could be realized with a lubricated elastic layer construction and is therefore a realistic practical venue to produce acoustic plasmonic cloaks. These two materials are arranged in an alternating pattern, starting with the elastic material on the outside, such that a total of 10 layers (5 elastic and 5 fluid) yield a total cloak thickness of approximately 26 % of the uncloaked radius a. The material properties and shell thicknesses for each layer are given in Table 10.3.

At the design ka, a scattering reduction of 40 dB is achieved, which is comparable to the performance of a single fluid layer at lower ka shown in Fig. 10.8. This reduction in the scattered acoustic field is further illustrated in Fig. 10.11, which

Table 10.3 Properties of the multilayered plasmonic cloak illustrated in Fig. 10.10. The layers of the cloak are numbered starting from the outermost layer. The shell thickness values listed are relative to the uncloaked sphere radius, a. The total cloak thickness is the sum of all shell thicknesses and is equal to $0.2585a$

Material	Density, ρ (kg/m^3)	Bulk modulus, κ (GPa)	Poisson's ratio, ν
Water	1000	2.2	0.50
Fluid layers	251	11.7	0.50
Elastic layers	10521	0.516	0.25

Layer No.	1	2	3	4	5	6	7	8	9	10
Shell thickness	0.0078	0.0301	0.0215	0.0344	0.0213	0.0313	0.0202	0.0343	0.0192	0.0385

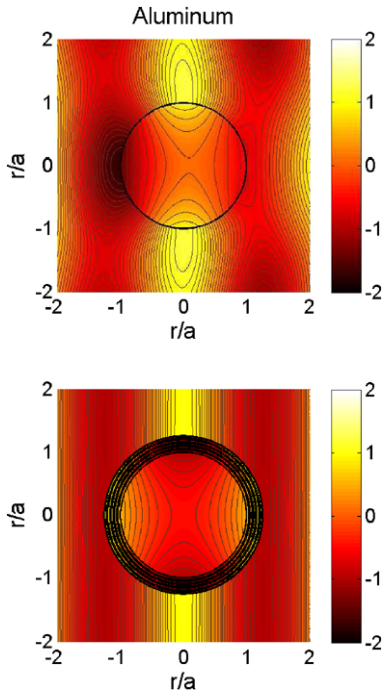

Fig. 10.11 Real part of total pressure field for an uncloaked (*top*) and cloaked (*bottom*) aluminum sphere in water at $ka = 2.5$. The plasmonic acoustic cloak is constructed using 10 isotropic layers with material properties given in Table 10.3. The scale for the pressure is normalized to the amplitude of the incident wave, which is a time-harmonic plane wave traveling from left to right (Color figure online)

shows the real part of the total acoustic pressure for the uncloaked and cloaked aluminum sphere in water at the design frequency of $ka = 2.5$. From this figure, it is clear that the time-harmonic incident wave (traveling from left to right) is significantly disrupted by the uncloaked aluminum sphere. With the addition of the multilayer plasmonic cloak, the incident wave passes nearly undisturbed around the aluminum sphere. As was observed with the single fluid plasmonic cloak, the interior wave structure retains a high fidelity with the incident wave in the water, except for the phase, which is 180 degrees out of phase. This change in phase is due to the construction of the plasmonic cloak for this particular example, due to the choice of using an even number of layers.

In a similar manner to the lower ka scattering cancellation results obtained using a single fluid layer, this multilayered plasmonic cloak exhibits a significant bandwidth over which the scattering gain is reduced. Above the design frequency, the reduction in scattering extends to $ka = 3.5$, and remains near zero scattering gain beyond this point. Below the design frequency, there is a region of broadband scattering reduction of 15–20 dB, but unlike the single fluid layer plasmonic cloak, this does not extend down to the static limit of $ka = 0$. Instead, there is a lower limit where scattering gain is actually increased as a result of a coupled response of the resistance to shear deformation offered by the plasmonic layer and the rigid body motion of the aluminum sphere. The result is a low frequency dipole resonance seen near $ka \approx 0.15$ in this example. Such an effect does not appear in an inviscid fluid cloak, since it does not support any type of shear motion. Although the results illus-

trated in Fig. 10.10 are only for a single representative example, they demonstrate that plasmonic cloaks have the potential to offer a robust means of acoustic cloaking for scatterers with significantly different properties than that of the surrounding fluid and under conditions where the wavelength of the incident field is on the order of the length scale of the scatterer.

10.4 Conclusion

This chapter has highlighted two main types of cloak designs, obtained by applying the scattering cancellation approach to acoustic waves: plasmonic cloaks and anti-resonance cloaks. Unlike acoustic cloaks developed using a transformation based approach, these types of cloaks are developed by prescribing a condition only on the scattered field in the surrounding fluid, without restricting interaction with the scatterer. In doing so, scattering cancellation cloaks allow for isotropic and homogeneous layers to be effectively utilized. Since the incident field is allowed to interact with the scatterer, improved bandwidth response is obtained, at the price of requiring each cloak design to be tailored to the specific scatterer.

A detailed analysis of the acoustic scattering cancellation approach has been presented, starting with the design of a plasmonic cloak for a rigid immovable sphere. An investigation of the parameter space revealed the existence of a non-resonant plasmonic cloaking region, and an anti-resonance cloaking region. The bandwidth and variations in cloaking layer thickness were also discussed. Using these ideas, the parameter space was expanded to include the range of penetrable fluid spheres. The variations in the necessary cloaking layer parameters with the target fluid properties were investigated, and a comparison with quasistatic behavior provided insight into some of these behaviors. It was shown that the precision needed to obtain a finely tuned plasmonic cloak ultimately requires a dynamic solution of the scattering problem, even at low ka.

The final section of the chapter illustrated the practical aspects of a plasmonic cloak by presenting a detailed analysis of three low ka examples of plasmonic cloaks using a single homogeneous and isotropic layer for spheres made of stainless steel, aluminum and glass in water, which are practical examples of scatterers of interest, for which this technique may provide interesting potentials. In addition, the results of a 10 layer plasmonic cloak for an aluminum sphere in water which was designed to cancel scattering at $ka = 2.5$ showed robust cloaking from $ka \approx 0.3$–3. The examples illustrate the generalizability of the scattering cancellation approach to consider the use of multiple layers to produce significant cloaking at increased ka. These results are of interest in a variety of applications, including suppression of scattering from air filled cavities and small to moderate sized scatterers in water as well as non-invasive acoustic field probing.

Acknowledgements Funding for this work was provided by the Applied Research Laboratories, The University of Texas at Austin, through an Independent Research and Development grant. A. Alù was partially supported by the NSF CAREER award with grant No. ECCS-0953311.

References

1. Achenbach, J.D.: Wave Propagation in Elastic Solids. North-Holland, Amsterdam (1993)
2. Alù, A., Engheta, N.: Achieving transparency with plasmonic and metamaterial coatings. Phys. Rev. E **72**, 016623 (2005)
3. Alù, A., Engheta, N.: Polarizabilities and effective parameters for collections of spherical nano-particles formed by pairs of concentric double-negative (dng), single negative (sng) and/or double-positive (dps) metamaterial layers. J. Appl. Phys. **97**, 094310 (2005)
4. Alù, A., Engheta, N.: Plasmonic materials in transparency and cloaking problems: Mechanism, robustness and physical insights. Opt. Express **15**, 3318–3332 (2007)
5. Alù, A., Engheta, N.: Effects of size and frequency dispersion in plasmonic cloaking. Phys. Rev. E **78**, 045602 (2008)
6. Alù, A., Engheta, N.: Cloaking a sensor. Phys. Rev. Lett. **102**(23), 233901 (2009)
7. Alù, A., Engheta, N.: Cloaked near-field scanning optical microscope tip for non-invasive near-field imaging. Phys. Rev. Lett. **105**, 263906 (2010)
8. Alù, A., Engheta, N.: Cloaking a receiving antenna or a sensor with plasmonic metamaterials. Metamaterials **4**, 153–159 (2010)
9. Baird, A.M., Kerr, F.H., Townend, D.J.: Wave propagation in a viscoelastic medium having fluid-filled microspheres. J. Acoust. Soc. Am. **105**, 1527–1538 (1999)
10. Berryman, J.G.: Long-wavelength propagation in composite elastic media I. Spherical inclusions. J. Acoust. Soc. Am. **68**, 1809–1819 (1980)
11. Cummer, S.A., Popa, B.I., Schurig, D., Smith, D.R., Pendry, J.B., Rahm, M., Starr, A.: Scattering theory derivation of a 3d acoustic cloaking shell. Phys. Rev. Lett. **74**, 024301 (2008)
12. Faran, J.J.: Sound scattering by solid cylinders and spheres. J. Acoust. Soc. Am. **23**, 405–418 (1951)
13. Gaunaurd, G.C.: Elastic and acoustic resonance wave scattering. Appl. Mech. Rev. **42**, 143–192 (1989)
14. Gray, C.G., Nickel, B.G.: Debye potential representation of vector fields. Am. J. Phys. **46**, 735–736 (1978)
15. Greenleaf, A., Lassas, M., Uhlmann, G.: On nonuniqueness for Calderon's inverse problem. Math. Res. Lett. **10**, 685–693 (2003)
16. Guild, M.D., Alù, A., Haberman, M.R.: Cancellation of the acoustic field scattered from an elastic sphere using periodic isotropic layers. J. Acoust. Soc. Am. 2374 (2010)
17. Guild, M.D., Alù, A., Haberman, M.R.: Cancellation of acoustic scattering from an elastic sphere. J. Acoust. Soc. Am. **129**(3), 1355–1365 (2011)
18. Guild, M.D., Haberman, M.R., Alù, A.: Plasmonic cloaking and scattering cancellation for electromagnetic and acoustic waves. Wave Motion **48**, 468–482 (2011)
19. Hickling, R.: Analysis of echos from a solid elastic sphere in water. J. Acoust. Soc. Am. **34**, 1582–1592 (1962)
20. Hickling, R.: Analysis of echos from a hollow metallic sphere in water. J. Acoust. Soc. Am. **34**, 1124–1137 (1964)
21. Kinsler, L.E., Frey, A.R., Coppens, A.B., Sanders, J.V.: Fundamentals of Acoustics, 4th edn. Wiley, New York (2000)
22. The Mathworks, Inc.: Optimization Toolbox (2009)
23. Milton, G.W., Briane, M., Willis, J.R.: On cloaking for elasticity and physical equations with a transformation invariant form. New J. Phys. **8**(248) (2006)
24. Norris, A.N.: Acoustic cloaking theory. Proc. R. Soc. A **464**, 2411–2434 (2008)
25. Norris, A.N., Nagy, A.J.: Acoustic metafluids made from three acoustic fluids. J. Acoust. Soc. Am. **128**, 1606 (2010)
26. Pendry, J.B., Li, J.: An acoustic metafluid: Realizing a broadband acoustic cloak. New J. Phys. **10**, 115032 (2008)
27. Pendry, J.B., Schurig, D., Smith, D.R.: Controlling electromagnetic fields. Science **312**(5781), 1780–1782 (2006)

28. Pierce, A.D.: Acoustics: An Introduction to Its Physical Principles and Applications. Acoustical Soc. of America (1989)
29. Scandrett, C.L., Boisvert, J.E., Howarth, T.R.: Acoustic cloaking using layered pentamode materials. J. Acoust. Soc. Am. **127**, 2856 (2010)
30. Torrent, D., Sánchez-Dehesa, J.: Acoustic cloaking in two dimensions: A feasible approach. New J. Phys. **10**, 063015 (2008)
31. Tricarico, S., Bilotti, F., Alù, A., Vegni, L.: Plasmonic cloaking for irregular objects with anisotropic scattering properties. Phys. Rev. E **81**, 026602 (2010)
32. Vasquez, F.G., Milton, G.W., Onofrei, D.: Active exterior cloaking. Appl. Math. Sci. 1–4 (2009)
33. Zhou, X., Hu, G., Lu, T.: Elastic wave transparency of a solid sphere coated with metamaterials. Phys. Rev. B **77**, 024101 (2008)

Chapter 11
Cloaking Liquid Surface Waves and Plasmon Polaritons

M. Kadic, M. Farhat, S. Guenneau, R. Quidant, and S. Enoch

Abstract In this chapter, we use analogies between the governing equations for linear surface liquid waves (LSWs) and surface plasmon polaritons (SPPs) in order to control their trajectories using geometric transforms. These two routes towards cloaking are emerging areas of physics known as transformational acoustics and plasmonics. We first analyze cloaking of LSWs propagating through a circular cloak, which consists of concentric layers cut into a large number of small sectors with rigid pillars. This water wave cloak behaves as an effective anisotropic fluid. We experimentally observe the decreased backscattering around the frequency 10 Hertz of a fluid with low viscosity and finite density (Methoxynonafluorobutane) from a cylindrical rigid obstacle surrounded by the cloak when it is located a couple of wavelengths away from the acoustic source. We then study theoretically, and numerically, the cloaking of SPPs propagating on a structured metal surface, and we manufacture and experimentally validate a plasmonic carpet working in the visible spectrum using dielectric plots of TiO_2 arranged along a quasi-conformal grid on a metal plate.

11.1 Introduction

During the last few years, research groups from all over the world have demonstrated the possibilities offered by metamaterials thanks to their ability to control

M. Kadic · S. Guenneau · S. Enoch (✉)
Institut Fresnel, CNRS, Aix-Marseille Universite, Campus Universitaire de Saint-Jerome, 13013 Marseille, France
e-mail: stefan.enoch@fresnel.fr

M. Farhat
Institute of Condensed Matter Theory and Solid State Optics, Friedrich-Schiller-Universitat Jena, D-07743 Jena, Germany
e-mail: mohamed.farhat@uni-jena.de

R. Quidant
ICFO-Institut de Ciéncies Fotóniques, Mediterranean Technology Park, 08860 Castelldefels, Barcelona, Spain
e-mail: romain.quidant@icfo.es

R.V. Craster, S. Guenneau (eds.), *Acoustic Metamaterials*,
Springer Series in Materials Science 166, DOI 10.1007/978-94-007-4813-2_11,

electromagnetic waves (and other types of waves, e.g. acoustic and elastic). After negative refraction and sub-wavelength imaging, it has appeared possible to hide some objects to electromagnetic radiation and to make them invisible. A first path to invisibility was investigated by Engheta and Alù [2] in 2005 and is based on plasmonic materials designed in order to cloak dielectric or conducting objects. This technique relies heavily on a scattering cancellation phenomenon, based on the negative local polarizability of a cover made of low electric permittivity materials. It appears to be relatively robust to changes in the design parameters, geometry and frequency of operation.

The only drawback of this process is the lack of experimental confirmation and its requirement of a priori knowledge of electromagnetic properties of the objects to hide. The use of space-time transformations as a design tool for new materials was subsequently introduced as an alternative path towards invisibility. A basic idea of this concept is that a metamaterial mimics a transformed empty space. The light rays follow straight trajectories according to Fermat's principle in this transformed (virtual electromagnetic) space, and are curved in a desired way in the (real) laboratory space. This allows one to design, in an efficient way, materials with various characteristics such as invisibility cloaks, whereby light is detoured smoothly around an object.

In 2006, Pendry, Schurig and Smith theorized that a finite size object surrounded by a coating consisting of a meta-material might become invisible for electromagnetic waves [28]. An international team involving these authors subsequently implemented this idea using a meta-material consisting of concentric layers of Splir Ring Resonantors (SRR) [32], which makes a copper cylinder invisible to an incident plane wave at a specific microwave frequency (8.5 GHz). The smooth behaviour of the electromagnetic field in the far field limit could be expected in view of the numerical evidence given [28] using a geometrical optics based software. Importantly, Leonhardt proposed, in parallel to this development of transformational optics, a conformal optics route towards invisibility [18], which is however constrained by the two-dimensional geometry, as it relies heavily on complex analysis, and the ray optics limit i.e. far field. To date, the only evidence that invisibility is preserved in the intense near field limit is purely numerical [37].

A very different route to invisibility was proposed by McPhedran, Nicorovici and Milton the same year. This grouping studied a countable set of line sources using anomalous resonance when the sources lie in the close neighbourhood of a cylindrical coating filled with negative permittivity material, which is nothing but a cylindrical version of the poor mans lens of Pendry [26]. These researchers attribute this cloaking phenomenon to anomalous localized resonances [23, 24], which is reminiscent of the field of plasmonics.

One of the most famous paradigms of plasmonics is the extraordinary physics of the transmission of light through holes small compared with the wavelength publicized by Ebbesen et al. [8] in the late nineties. However, some heralding earlier work is less well known (for example combining both theory and experiment [5]). Pendry, Martin-Moreno and Garcia-Vidal showed in 2004 that one can manipulate surface plasmon ad libitum via homogenization of structured surfaces [27]. In the

same vein, pioneering approaches to invisibility relying upon plasmonic metamaterials have already led to fascinating results [3, 4, 10, 33]. These include plasmonic shells with a suitable out-of-phase polarizability in order to compensate the scattering from the knowledge of the electromagnetic parameters of the object to be hidden, and external cloaking, whereby a plasmonic resonance cancels the external field at the location of a set of electric dipoles. In 2008, Smolyaninov, Hung and Davis achieved a noticeable reduction in the scattering of SPPs incident upon a cloak consisting of polymethylmethacrylate at a wavelength of 532 nm [33]. More recently, Baumeier, Leskova and Maradudin have demonstrated theoretically and experimentally that it is possible to reduce significantly the scattering of an object by an SPP at a wavelength of 632.8 nm when it is surrounded by two concentric rings of point scatterers [4]. However these two experiments rely upon the resonant features of the plasmonic cloak.

In the first section of this chapter, we show that it is possible to design a cylindrical acoustic cloak for linear surface liquid waves (LSWs). We construct a structured material which bends surfaces waves over a finite interval of Hertz frequencies. The cloak behaves as an effective fluid characterized by a transversely anisotropic shear viscosity. In the second section of this chapter, we design a structured metal plate which bends surface plasmon polaritons (SPPs) in the visible and near infrared spectrum. Such an invisibility carpet is deduced from a quasi-conformal grid and is therefore nearly isotropic. Such an enhanced control of water and electron wave trajectories, which used techniques developed in the emerging fields of transformational and conformal optics opens new vistas in transformational surface physics.

11.2 Acoustic Cloaking for Liquid Surface Waves

In this section, we describe an effective medium approach to cloaking for liquid surface waves, which works over a finite frequency bandwidth, unlike for cloaking using resonant metamaterials, such displaying spatially varying artificial magnetism [32]. Before we embark on our invisibility journey, we find it useful to recall under which hypotheses one can consider water waves satisfy governing equations reminiscent of those familiar to scientists working in the field of linear optics, or put in other words, how can one get rid of non-linearities in Navier-Stokes equations?

11.2.1 From Navier-Stokes to Helmholtz

Let us denote by Ω the open bounded domain in the space $\mathbb{R}^3$ occupied by a fluid. The conservation of momentum leads to the Navier-Stokes equation:

$$\frac{\partial \mathbf{u}}{\partial t} + (\mathbf{u} \cdot \nabla)\mathbf{u} + \frac{1}{\rho}\left(\nabla p - \mu \nabla^2 \mathbf{u}\right) = \mathbf{g} \quad \text{in } \Omega, \tag{11.1}$$

where $\mathbf{u}$ is the velocity field, p is the pressure, ρ the fluid density, $\mu\nabla^2\mathbf{u}$ accounts for the fluid's viscosity, and $\mathbf{g}$ is the vector of gravity force: $\mathbf{g} = -g\mathbf{e}_3$, where g denotes the acceleration caused by gravity and $\mathbf{e}_i$ are the basis vectors of the Euclidean space.

To start with the simplification process, we neglect the viscosity $\mu\nabla^2\mathbf{u}$. Such an hypothesis will bring a strong constraint on the choice of the liquid in the experimental setup. Further assuming that the velocity field $\mathbf{u}$ is curl-free, we show in the sequel that it derives from a potential Φ which is related to the vertical displacement of the liquid surface ξ through a reduced potential ϕ such that $\Phi(x_1, x_2, x_3, t) = \Re(\phi(x_1, x_2)\cosh(\kappa x_3)e^{-i\omega t})$ and $\xi(r, \theta, t) = \mathscr{R}(-\frac{i\omega}{g}\phi(r, \theta)e^{-i\omega t})$, where ω is the wave frequency and ϕ satisfies the Helmholtz's equation (11.10), with κ the spectral parameter [1].

Let $x_3 = \xi(x_1, x_2, t)$ be the equation of the free surface. The pressure is prescribed to be equal to the constant atmospheric pressure p_0 on $x_3 = \xi(x_1, x_2, t)$, and the surface tension is neglected. Hence, (11.1) leads to the well known Bernoulli's equation

$$\frac{\partial\Phi}{\partial t} + \frac{|\nabla\Phi|^2}{2} + \frac{p_0}{\rho} + g\xi = f(t) \quad \text{on } x_3 = \xi. \tag{11.2}$$

Assuming that $f(t)$ is incorporated into ϕ and that liquid fluctuations are small, i.e., $|\xi - h| \ll 1$, where h denotes the mean value of ξ, and also $|\frac{\partial\xi}{\partial x_j}| \ll 1$, $j = 1, 2$, differentiation of (11.2) with respect to t leads to the linearized equation

$$\frac{\partial^2\Phi}{\partial t^2} + g\frac{\partial\xi}{\partial t} = 0 \quad \text{on } x_3 = h. \tag{11.3}$$

Using the small-slope ansatz

$$u_3 = \frac{dx_3}{dt} = \frac{\partial\xi}{\partial t} + \frac{\partial\xi}{\partial x_1}\frac{\partial x_1}{\partial t} + \frac{\partial\xi}{\partial x_2}\frac{\partial x_2}{\partial t} \sim \frac{\partial\xi}{\partial t}, \tag{11.4}$$

the divergence-free condition $\nabla\cdot\mathbf{u} = 0$ (i.e. incompressible fluid) and (11.3) lead to Poisson's condition

$$\frac{\partial^2\phi}{\partial t^2} + g\frac{\partial\phi}{\partial x_3} = 0 \quad \text{on } x_3 = h. \tag{11.5}$$

Altogether, Φ is solution of the following system

$$\begin{cases} \nabla^2\Phi = 0 \quad \text{for } x_3 \in]0, h[, \\ \frac{\partial^2\Phi}{\partial t^2} + g\frac{\partial\Phi}{\partial x_3} = 0 \quad \text{for } x_3 = h, \\ \mathbf{n}\cdot\nabla\Phi = 0 \quad \text{for } x_3 = 0, \end{cases} \tag{11.6}$$

where the last boundary condition accounts for a no-flow condition through the plane $x_3 = 0$ (this stands for the fixed surface at the bottom of the water tank). If one looks for a harmonic ansatz for the potential $\Phi(x_1, x_2, x_3, t) = f(x_3)e^{-i(\omega t - \kappa_1 x_1 - \kappa_2 x_2)}$, Laplace's equation in (11.6) gives $f''(x_3) - \kappa^2 f(x_3) = 0$, where $\kappa^2 = \kappa_1^2 + \kappa_2^2$ is by inspection of the Neumann boundary condition in (11.6),

a parameter which forces the evanescence of the potential Φ away from the free boundary in the form $f(x_3) = \cosh(\kappa x_3)$. This means that the physics of the problem can be described by a governing equation on the free interface between liquid and air. Linear liquid surface waves (LSWs) are indeed governed by the Helmholtz's equation

$$\nabla^2\phi + \kappa^2\phi = 0, \tag{11.7}$$

on the free surface, where ϕ is the reduced potential related to the potential Φ via $\Phi(x_1, x_2, x_3, t) = \Re(\phi(x_1, x_2)\cosh(\kappa x_3)e^{-i\omega t})$. We note that if the free surface is perforated by rigid cylinders immersed in the liquid, this equation is valid in the liquid region outside the rigid cylinders and is supplied with a no-flow condition $\frac{\partial\phi}{\partial n}$ on each cylinder's boundary. This will be used in our model of a structured cloak for LSWs. Furthermore, from the Poisson's condition in (11.6), the spectral parameter κ in (11.7) is linked to the wave frequency via the dispersion relation [1]

$$\omega^2 = g\kappa\left(1 + d_c^2\kappa^2\right)\tanh\kappa h, \tag{11.8}$$

with $d_c = \sqrt{\sigma/(\rho g)}$ the liquid capillarity. Note that surface waves propagating at the liquid-air interface are thus always dispersive, unlike pressure waves within the liquid. This dispersive feature of surface waves is also found in the context of plasmonics, whereby electron waves propagate at a metal interface, and will be discussed in the next section.

11.2.2 Effective Anisotropic Shear Viscosity Through Homogenization

Our aim is now to extend this principle to the LSW waves governed by the Helmholtz equation (11.7) and the Neumann boundary conditions. The goal is to homogenize the micro-structured cloak shown in Fig. 11.1 which reveals an effective anisotropic shear viscosity underpinning the cloaking effect. Having in mind that when the shear viscosity matrix is large enough in the tangential θ direction, LSW waves will be bent around the central region of the cloak and thus make its interior almost invisible to any exterior observer.

For this, we note that when the fluid penetrates the micro-structure of Fig. 11.1 (whose cross-section Ω_c is evenly divided into a large number of small curved sectors ηY of radial length $\eta(R_2 - R_1)$ and azimuthal length $2\pi\eta$, where η is a small positive real parameter), it undergoes fast periodic oscillations. To filter these oscillations, we consider an asymptotic expansion of the potential field solution of the Helmholtz equation (11.7) in terms of a macroscopic (slow) variable $\mathbf{x} = (r, \theta)$ and a microscopic (fast) variable $\mathbf{x}/\eta$ [12]:

$$\forall \mathbf{x} \in \Omega_c, \quad \phi_\eta(\mathbf{x}) = \phi_0\left(\mathbf{x}, \frac{\mathbf{x}}{\eta}\right) + \eta\phi_1\left(\mathbf{x}, \frac{\mathbf{x}}{\eta}\right) + \eta^2\phi_2\left(\mathbf{x}, \frac{\mathbf{x}}{\eta}\right) + \cdots \tag{11.9}$$

where each term $\phi^{(i)}(\mathbf{x}, \cdot)$ is Y-periodic.

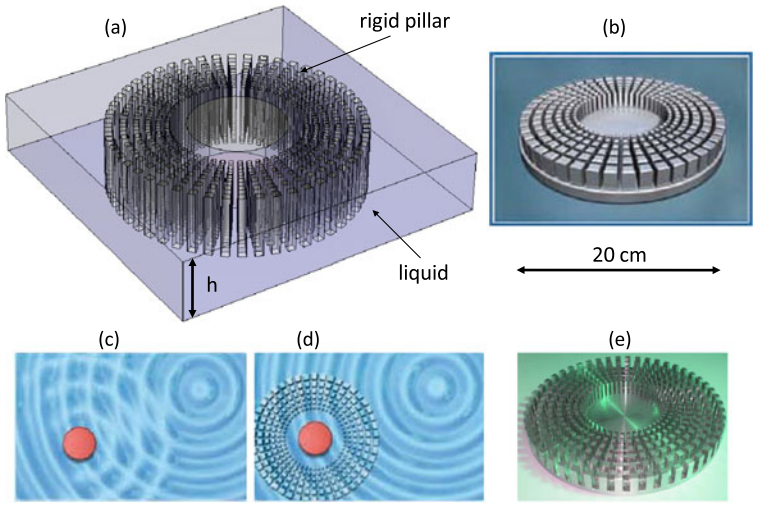

Fig. 11.1 *Principle of water wave cloak*: **(a)** Geometry of the structured cloak consisting of concentric arrays of rigid pillars immersed in a vessel of liquid of depth h; **(b)** Diagrammatic view of the cloak; **(c)–(d)** Scattering of water waves on a rigid obstacle (*dark disc*) without **(c)** and with **(d)** the water wave cloak; **(e)** Photo of the micro-structured cloak used in experiments around 10 Hertz

The differential operator is rescaled accordingly as $\nabla = \nabla_{\mathbf{x}} + \frac{1}{\eta}\nabla_{\mathbf{y}}$, and collecting terms of same powers of η, we obtain the following homogenized problem in the limit when η tends to zero (see also [12]):

$$\nabla \cdot \left([\mu_{hom}]\nabla\phi_{hom}(\mathbf{x})\right) = \kappa^2\phi_{hom}(\mathbf{x}) \quad \text{in } \Omega_c. \tag{11.10}$$

This homogenized equation shows that the velocity field is now a solution of (11.7) with an anisotropic matrix of viscosity with non-trivial part (transverse shear)

$$[\mu_{hom}] = \frac{1}{\mathscr{A}(Y^*)}\begin{pmatrix} \mathscr{A}(Y^*) - \psi_{rr} & \psi_{r\theta} \\ \psi_{\theta r} & \mathscr{A}(Y^*) - \psi_{\theta\theta} \end{pmatrix}. \tag{11.11}$$

Here, $\mathscr{A}(Y^*)$ denotes the area of the region Y^* surrounding a rigid inclusion S (subject to Neumann boundary conditions) in an elementary cell Y of the periodic array, and ψ_{ij} represent corrective terms derived from an integral over the boundary ∂S:

$$\forall i, j \in \{r, \theta\}, \quad \psi_{ij} = -\int_{\partial S} \Psi_i n_j \, ds, \tag{11.12}$$

where $\mathbf{n}$ is the unit outward normal to ∂S, and Ψ_j, $j \in \{r, \theta\}$, are Y-periodic potentials, which are unique solutions (up to an additive constant) of the following two Laplace equations $(\mathscr{L}_j)$:

$$(\mathscr{L}_j): \quad \nabla^2\Psi_j = 0 \quad \text{in } Y^*. \tag{11.13}$$

These so-called annex problems are supplied with the effective boundary condition $\frac{\partial \Psi_j}{\partial n} = -\mathbf{n} \cdot \mathbf{e}_j$ on the boundary ∂S of the inclusion. Here, $\mathbf{e}_r$ and $\mathbf{e}_\theta$ denote the vectors of the basis in polar coordinates (r, θ).

Altogether, this shows that the velocity field is solution of (11.1) with an anisotropic matrix of viscosity whose nontrivial part (transverse shear) could be calculated as

$$[\mu_{hom}] = \frac{1}{\mathscr{A}(Y^*)} \begin{pmatrix} \mathscr{A}(Y^*) + 0.7 & 0 \\ 0 & \mathscr{A}(Y^*) + 7.2 \end{pmatrix}, \tag{11.14}$$

which shows that the effective fluid is strongly anisotropic along the θ-direction.

11.2.3 Numerical Analysis of LSW Cloaking

In this section, we give some numerical illustrative examples of cloaking of an acoustic vibration (radiated by a cylindrical point source) located close to an obstacle through the phononic crystal fibre making the cloak (see Figs. 11.1 and 11.2). As detailed in the previous section, we first replace the micro-structured cloak immersed in the liquid by an effective transversely anisotropic fluid whose homogenized shear viscosity is deduced from the numerical solution (11.14) of the two annex problems (11.13). This provides us with a qualitative picture of the cloaking mechanism shown in the lower right panel of Fig. 11.2. We then compare this asymptotic theory against the numerical solutions of the same scattering problems when we model the complete micro-structured cloak, as shown in the upper right panel of Fig. 11.2. We notice the strong similarities between the asymptotic solution and the numerical solution.

According to transformation acoustics, the effective fluid should be characterized by a varying density ρ, as well as a varying radial and azimuthal shear viscosities μ_{rr} and $\mu_{\theta\theta}$ (reduced parameters inspired by that of the groupings of Cummer and Shalaev [6, 7]). These requirements seem to be beyond the actual experimental possibilities. Nevertheless, we can introduce some variation in the radial length of the sectors for which it seems reasonable to assume that the improved cloak is characterized by an effective anisotropic fluid whose shear viscosity (a diagonal matrix in polar basis) is

$$\mu'_{rr} = \left(\frac{R_2(r - R_1)}{(R_2 - R_1)r} \right)^2, \qquad \mu'_{\theta\theta} = \left(\frac{R_2}{R_2 - R_1} \right)^2, \tag{11.15}$$

where R_1 and R_2 are, respectively, the inner and outer radii of the ring. Importantly, the effective fluid's density $\rho' = \rho$; i.e., it does not play any prominent role. Figure 11.3 shows simulations performed for the ideal case when the obstacle is cloaked and for a vacuum for comparison.

The upper-right panel of Fig. 11.3 clearly shows that the structured cloak consisting of a very large number (100) of identical curved sectors small compared to

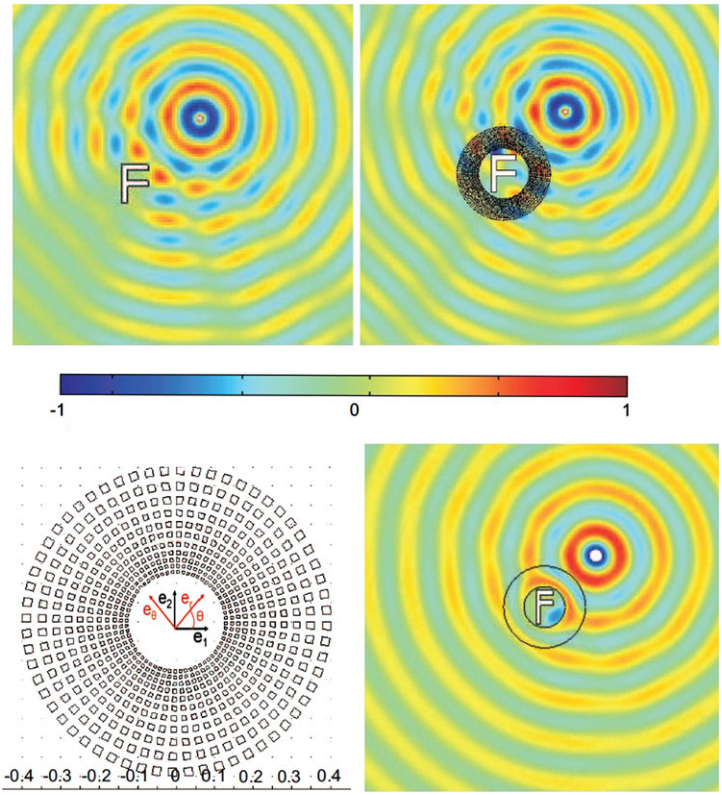

Fig. 11.2 *Upper panel*: 2D plot of the real part $\mathscr{R}e(\phi)$ of the potential of velocity **u** radiated by an acoustic point source of normalized wavelength, $\lambda = c/\nu = c/2.5$ in presence of an F-shaped obstacle (*left*) and a micro-structured cloak surrounding the obstacle (*right*); *Lower panel*: Zoom on the geometry of the micro-structured cloak (*left*) and diffraction by a cloak (with inner and outer boundaries $r = R_1 = 0.164$ and $r = R_2 = 0.4$) whose electromagnetic parameters are given by (5–10). The similarities between the *upper right* and *lower right panels* are noted. Importantly, the radii are normalized here and are related to those of Fig. 11.3 through a factor 2.5 (for meters)

the working wavelength and regularly arranged along the radial and azimuthal directions, will enable one to gain control over surface waves. We have also verified the effect of varying the size of sectors along the radial direction and numerically checked that the cloaking is thus further improved: It is enough to design a cloak with identical sectors to gain a good control of the velocity field, but the azimuthal shear wave speed of liquid particles will increase linearly with their distance to the center of the cloak only in the case of sectors with increasing size. We numerically checked that in the case of a cloak with identical sectors, this shear wave speed does not vary; hence, a shadow region revealing the presence of the hidden object is observed behind the cloak (through phase shift). We checked also that such a structured cloak with 256 curved sectors (Fig. 11.2 upper-right panel) is more appropriate for

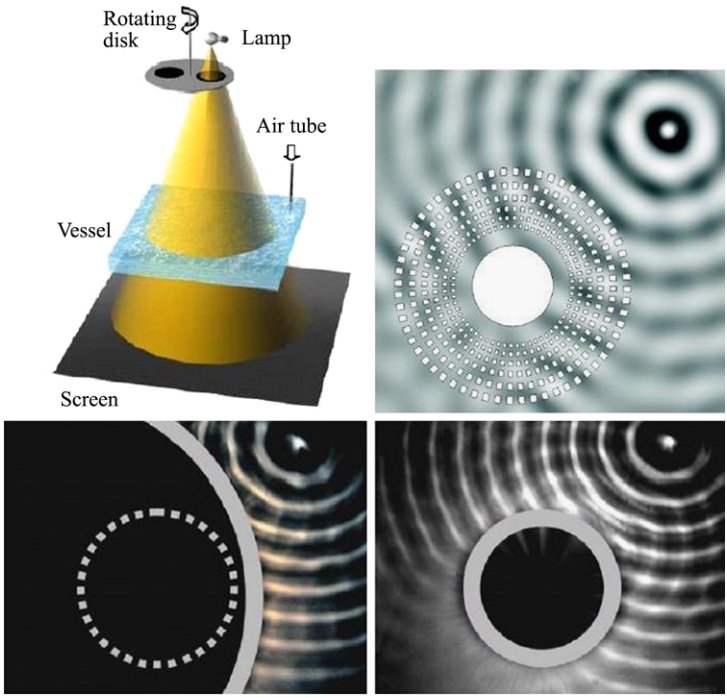

Fig. 11.3 *Upper-left* (experimental setup): A halogen lamp modulated by a perforated rotating disc illuminates a transparent vessel containing the liquid (methoxynonafluorobutane). The surface waves are excited by a localized pressure thanks to air pulsed in a small tube at the same frequency as the modulation of the light (stroboscopic effect); *Upper-right* (simulation): Diffraction pattern of the surface waves generated by an harmonic acoustic source at frequency 10 Hz for a cloak with 100 rigid sectors. The depth of liquid in the vessel is $h = 9$ mm and its capillarity is $d_c = 0.95$ mm; *Lower-left*: Snapshot of diffraction pattern by a rigid cylinder of radius 38 mm surrounded by the structured cloak (outlined as the gray coating) of Fig. 11.2 with inner and outer radii $R_1 = 41$ mm and $R_2 = 100$ mm. *Lower-right*: Snapshot of diffraction pattern by the rigid cylinder on its own (outlined by a *dashed gray circle* in the *left panel* for comparison)

the cloaking than with 100 curved sectors. But we had to find a compromise between the realizable structures using conventional machining, the limits imposed by the viscosity of the liquids, and the constraints imposed by homogenization.

11.2.4 Experimental Measurements of LSW Cloaking

Regarding the experimental setup, we refer the reader to Fig. 11.3, which clearly demonstrates a reduced backscattering for an acoustic source generating LSW at 10 Hertz a couple of wavelengths away from a structured cloak consisting of 100 rigid pillars arranged as in the lower left panel of Fig. 11.2.

The liquid used for the experiments was Methoxynonafluorobutane chosen for its physical properties and especially for having a low kinematic viscosity [1] ($\nu = \mu/\rho = 0.61$ mm^2/s) so that $\mu\nabla^2\mathbf{u}$ can be neglected outside the cloak in (11.1), a small surface tension $\sigma = 13.6$ N/cm and a large density ($\rho = 1.529$ g/mL), ensuring a small capillarity length $d_c = \sqrt{\sigma/(\rho g)} = 0.95$ mm. The vessel is filled with a depth of liquid $h = 9$ mm.

The basic principle behind the experiments is very simple: the light of a halogen lamp modulated by a perforated rotating disc illuminates a transparent vessel containing the liquid. The surface waves are excited by a localized pressure thanks to air pulsed in a small tube at the same frequency as the modulation of the light (to take advantage of the stroboscopic effect for the observation). The surface waves create local curvatures of the liquid and the light is refracted when crossing the surface. Thus, on the screen the dark and light zones allow for visualizing the liquid surface waves. Note that the low viscosity of the liquid is important for such experiments and we were unable to produce similar results with water: due to its larger viscosity, the water profile flattens within the micro-structured cloak, much like in thin channels [1], and water cannot flow.

11.3 Optical Cloaking for Surface Plasmon Polaritons

In this section, we adapt the tools of transformational optics to surface plasmon polaritons (SPPs) propagating at the interface between two anisotropic media of opposite permittivity sign. We identify the role played by entries of anisotropic heterogeneous tensors of permittivity and permeability deduced from a coordinate transformation in the dispersion relation governing propagation of SPPs. Using this concept and the idea of quasi-conformal mapping, we apply this concept to mimick a flat Bragg mirror by a curved Bragg mirror with a heterogeneous structure, thereafter caller plasmonic carpet, in front of the curved one. This novel concept is verified by an experimental characterization using one step lithography to realize the structure. The measurement of the propagation of the SPP in both structures has been achieved by the leakage radiation setup.

11.3.1 Introduction to Surface Plasmon Polaritons (SPPs)

The theory of Maxwell shows that electromagnetic waves can propagate at the interface between a metal and a dielectric. These waves are associated with plasma oscillations of free electrons on the surface of the metal. They are known as surface plasmon polaritons [29]. The maximum intensity of the field associated with this wave is confined at the metal-dielectric interface. The electromagnetic field decreases exponentially in the two media in the direction perpendicular to the interface, which is a characteristic of surface waves also encountered in very different

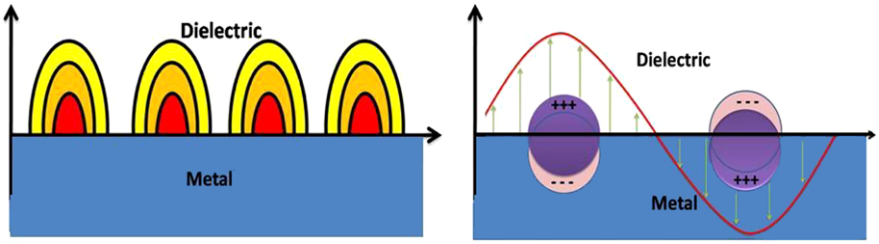

Fig. 11.4 Schematic representation of the electromagnetic field spreading at the metal-dielectric interface: (*left*) The maximum intensity of the magnetic field corresponds to the *dark color*, that is near the interface; (*right*) Polarization of the electric field and associated distribution of electric charges

physical contexts such as hydrodynamics (e.g. linear surface liquid waves as described in the previous section), or elastodynamics (e.g. Rayleigh seismic waves propagating at the surface of the Earth). Figure 11.4 is a schematic representation of the oscillations and the exponential dependence on the associated electric fields. These surface modes, introduced by Wood [36] in the beginning of the last century, have been studied intensively by spectroscopic loss of energy (attenuated total reflection: ATR) of electrons [17, 31]. The plasmons are extremely sensitive to the refractive index in contact with the metal surface or the roughness of the surfaces. For that reason, they find many applications in physics, chemistry and biology.

Considering the surface plasmons as an electromagnetic wave spreading at a plane interface between a dielectric and a metal, we will look at the relation between the energy of the oscillation and the wave vector. This wave is linked to the wave vector $\mathbf{k}$ by a dispersion relation. We consider two semi-infinite media (see Fig. 11.4), one consisting of a dielectric environment and the other of a metal. The xy-plane is defined as the interface and the z-direction is perpendicular to the interface. The plasmon spreads along the x-direction, which means that the system is invariant to translation along the y-direction. We find the existence conditions of surface plasmons from the Maxwell equations and boundary conditions.

Under these circonstances we show, that SPPs can only exist for TM polarized light. In this case we have the general form of the magnetic field propagating along the x direction above and below the interface $z = 0$ is:

$$\begin{cases} \mathbf{H}_2 = (0, H_{y2}, 0)\exp\{\mathrm{i}(k_{x2}x - \omega t) - k_{z2}z\}, & z > 0, \\ \mathbf{H}_1 = (0, H_{y1}, 0)\exp\{\mathrm{i}(k_{x1}x - \omega t) + k_{z1}z\}, & z < 0, \end{cases} \tag{11.16}$$

with $\Re(k_{z1})$ and $\Re(k_{z1})$ strictly positive numbers in order to maintain evanescent fields above and below the interface $z = 0$. Here ω denotes the wave frequency, t the time variable and k_{xi} and k_{zi} the (possibly complex) components of the wavevector along x and z directions above ($i = 2$) and below ($i = 1$) the interface.

For this field to be a solution of Maxwell's equations, continuity of its tangential components is required across the interface $z = 0$ and this requires $k_{x1} = k_{x2} = k_x$ and the dispersion relations

$$k_{zi} = \sqrt{k_x^2 - \varepsilon_i \left(\frac{\omega}{c}\right)^2}, \qquad \frac{k_{z1}}{\varepsilon_1} + \frac{k_{z2}}{\varepsilon_2} = 0, \tag{11.17}$$

where c is the celerity of light in vacuum, ε_1 is the permittivity in the upper-half plane (dielectric medium) and ε_2 is the permittivity in the lower-half plane (metal).

The dispersion relation of the propagative vector along the x-axis follows as:

$$k_x = \frac{\omega}{c}\left(\frac{\varepsilon_2 \varepsilon_1}{\varepsilon_2 + \varepsilon_1}\right)^{1/2}, \tag{11.18}$$

and if we consider now the dielectric function of the metal as complex, it results in k_x being complex. We note that a SPP can only exist between a metal and a dielectric and for a finite range of frequencies and has to satisfy the existing relation $\Re(\varepsilon_1)\Re(\varepsilon_2) < 0$. Importantly, we notice that the propagating length of SPPs can be easily computed from:

$$L = \frac{1}{2k_x''} = \frac{c}{\omega}\left|\frac{\varepsilon_1' + \varepsilon_2}{\varepsilon_1' \varepsilon_2}\right|^{3/2} \frac{\varepsilon_1'^2}{\varepsilon_1''}, \tag{11.19}$$

where c is the speed of light in vacuum, and primes (resp. double primes) denote real (resp. imaginary) parts of complex quantities. The evanescent behaviour of the surface plasmon for each medium depends on the dielectric constants. The penetration length is given in the metal by:

$$z_m = \frac{\lambda}{2\pi}\left(\frac{|\varepsilon_1' + \varepsilon_2|}{\varepsilon_1'^2}\right)^{1/2}, \tag{11.20}$$

and in the dielectric by:

$$z_d = \frac{\lambda}{2\pi}\left(\frac{|\varepsilon_1' + \varepsilon_2|}{\varepsilon_2'^2}\right)^{1/2}. \tag{11.21}$$

Using these relations, we note that a SPP at 700 nm $< \lambda <$ 900 nm propagating between an air-gold interface would have the following properties: penetration lengths respectively in metal and dielectric 20 nm $< z_m <$ 30 nm, 500 $< z_d <$ 800 nm, and the propagation length 30000 nm $< L <$ 50000 nm. It clearly appears that the main part of the electromagnetic energy is located in the dielectric region. We will make use of these properties in the last section of this chapter.

It should be noted that SPPs need be generated using an incident electromagnetic field, and this is in itself a non trivial task. Figure 11.5 shows the excitation of a SPP on a thin layer of metal by an incident plane wave at a critical angle depending upon the permittivity of the substrate. In this case the critical angle of SPP excitation corresponds to a glass substrate and can be easily found in [22].

Introduced in 2006, transformational optics was the pioneering idea of Sir John Pendry for electromagnetic waves [28]. This concept has been proposed for invis-

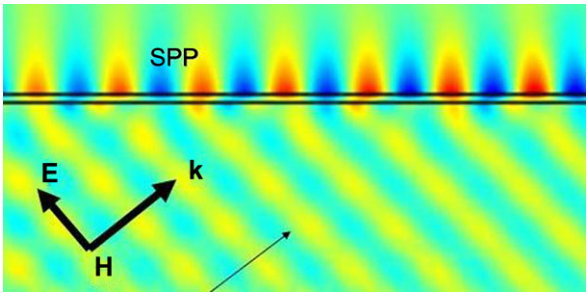

Fig. 11.5 Simulation of a SPP excitation on a thin metallic film with a plane electromagnetic wave incident through a glass substrate from below at a critical angle found using [22]

ibility and the idea of hiding under a carpet, which consists of mimicking a curved surface by a flat one. The basic idea consists of linking a space deformation to physical properties of that space (permittivity and permeability). This can be done by noticing that Maxwell's equations are invariant through a change of system of coordinates. In this way, one can obtain a relation between the change of coordinates and the physical properties (permittivity and permeability), which are encompassed in the Jacobian matrix [25, 35]. This leads to anisotropic and heterogeneous tensors of permittivity and permeability. An alternative route to the control of wave trajectories is that of optical conformal mapping, introduced by Ulf Leonhardt [18] in 2006, and published in the same issue of the Science magazine as the work of Pendry. Leonhardt's proposal, which was constrained to two-dimensional geometries as it heavily relied upon the mathematical theory of complex analysis, has been since then combined to the powerful tools of transformation optics by Li and Pendry [19] using the concept of quasi-conformal mapping in order to design invisibility carpets in two-dimensional [19, 20, 30, 34] and three-dimensional [9] geometries. In what follows, we extend this concept to plasmonics.

11.3.2 From Transformational Optics to Plasmonics

In this section, we would like to extend the control of electromagnetic fields using tools of geometric transforms, to the area of surface plasmons polaritons. For this, we first recall that when the original permittivity and permeability matrices are scalars in the coordinate system (x, y, z), their transformed counterparts in the new coordinate system (u, v, w) are given by [25]

$$\underline{\underline{\varepsilon'_j}} = \varepsilon_j \mathbf{T}^{-1}, \qquad \underline{\underline{\mu'_j}} = \mu_j \mathbf{T}^{-1}, \quad \text{where } \mathbf{T} = \frac{\mathbf{J}^T \mathbf{J}}{\det(\mathbf{J})}, \tag{11.22}$$

where $\det(\mathbf{J})$ is the determinant of the Jacobian matrix $\mathbf{J} = \partial(x, y, z)/\partial(u, v, w)$ of the map from coordinate system (u, v, w) to $(x(u, v, w), y(u, v, w), z(u, v, w))$. We emphasize the fact that it is the transformed domain and coordinate system that are mapped onto the initial domain with Cartesian coordinates, and not the opposite [25]. Moreover, in the context of plasmonics, $j = 1$ is the (transformed) metal region and $j = 2$ is the (transformed) dielectric region.

However, we have seen that the penetration depth in metal (11.20) is much smaller than in dielectric (11.21). Therefore, we can simplify the problem by assuming that only the dielectric medium needs to be transformed. Let us thus derive the dispersion relation for a surface plasmon at the interface between metal and a transformed medium described by diagonal tensors of relative permittivity and permeability $\underline{\underline{\varepsilon}}' = \mathrm{diag}(\varepsilon_{xx2}, \varepsilon_{yy2}, \varepsilon_{zz2})$ and $\underline{\underline{\mu}}' = \mathrm{diag}(\mu_{xx2}, \mu_{yy2}, \mu_{zz2})$. From the first Maxwell equation, we know that

$$\begin{cases} \nabla \times \mathbf{H}_2 = -\mathrm{i}\omega\varepsilon_0 \underline{\underline{\varepsilon}}' \mathbf{E}_2, & z > 0, \\ \nabla \times \mathbf{H}_1 = -\mathrm{i}\omega\varepsilon_0 \varepsilon_1 \mathbf{E}_1, & z < 0, \end{cases} \tag{11.23}$$

where $\varepsilon_0\mu_0 = c^{-2}$ and $\mathbf{H}_j$ is defined by:

$$\begin{cases} \mathbf{H}_2 = (0, H_{y_2}, 0)\exp\{\mathrm{i}(k_{x2}x - \omega t) - k_{z2}z\}, & z > 0, \\ \mathbf{H}_1 = (0, H_{y_1}, 0)\exp\{\mathrm{i}(k_{x1}x - \omega t) + k_{z1}z\}, & z < 0, \end{cases} \tag{11.24}$$

with $\Re(k_{z1})$ and $\Re(k_{z1})$ strictly positive in order to maintain evanescent fields above and below the interface $z = 0$. This leads to

$$\begin{cases} \mathbf{E}_2 = -\frac{c}{\omega} H_{y_2}(\frac{k_{z2}}{\varepsilon_{xx2}}, 0, \frac{k_{x2}}{\varepsilon_{zz2}})\exp\{\mathrm{i}(k_x x - \omega t) - k_{z2}z\}, & z > 0, \\ \mathbf{E}_1 = -\frac{c}{\omega} H_{y_1}(\frac{k_{z1}}{\varepsilon_1}, 0, \frac{k_{x2}}{\varepsilon_1})\exp\{\mathrm{i}(k_x x - \omega t) - k_{z1}z\}, & z < 0, \end{cases} \tag{11.25}$$

with $\mathbf{E}_j = (E_{xj}, 0, E_{zj})$. The transverse wavenumbers are found by invoking the other Maxwell equation

$$\begin{cases} \nabla \times \mathbf{E}_2 = \mathrm{i}\omega\mu_0 \underline{\underline{\mu}}' \mathbf{H}_2, & z > 0, \\ \nabla \times \mathbf{E}_1 = \mathrm{i}\omega\mu_0 \mathbf{H}_1, & z < 0, \end{cases} \tag{11.26}$$

which leads to

$$k_{zi} = \sqrt{\varepsilon_{xx2}\left(\frac{k_x^2}{\varepsilon_{zz2}} - \mu_{yy2}\left(\frac{\omega}{c}\right)^2\right)}, \quad j = 1, 2. \tag{11.27}$$

The boundary condition at the interface $z = 0$ requires continuity of the tangential components of the electromagnetic field, which brings

$$\frac{k_{z1}}{\varepsilon_1} + \frac{k_{z2}}{\varepsilon_{xx2}} = 0. \tag{11.28}$$

Substituting (11.27) into (11.28), we obtain the local dispersion relation for a surface plasmon at the interface between a metal and transformed heterogeneous anisotropic medium.

For the sake of simplicity, $\varepsilon_1 = 1 - \frac{\omega_p^2}{\omega^2 + \mathrm{i}\gamma\omega}$ has the usual Drude form in the metal ($z < 0$), for which ω_p is the plasma frequency (2175 THz) of the *free electron gas* and γ is a characteristic collision frequency of about 4.35 THz.

We have therefore shown that in the simple case where the varying tensors of permittivity $\underline{\underline{\varepsilon'}}$ and permeability $\underline{\underline{\mu'}}$ are assumed to be represented in a diagonal basis i.e. $\underline{\underline{\varepsilon'}} = \mathrm{diag}(\varepsilon_{xx2}, \varepsilon_{yy2}, \varepsilon_{zz2})$ and $\underline{\underline{\mu'}} = \mathrm{diag}(\mu_{xx2}, \mu_{yy2}, \mu_{zz2})$, the dispersion relation for the surface polariton at such an anisotropic interface takes the form [30]

$$k_x = \frac{\omega}{c}\sqrt{\frac{\varepsilon_{zz2}\varepsilon_1(\mu_{yy2}\varepsilon_1 - \varepsilon_{xx2})}{\varepsilon_1^2 - \varepsilon_{xx2}\varepsilon_{zz2}}}. \tag{11.29}$$

This necessary and sufficient condition for existence of a SPP is richer than the usual one (11.18), and importantly only requires some magnetism along the y direction, which is parallel to the polarization of the magnetic component of the SPP field.

11.3.3 Numerical Analysis of Plasmonic Cloaking

In this section we wish to analyze the interaction of this SPP with a specific anisotropic heterogeneous structure, in the present case a three-dimensional invisibility carpet [9, 30], deduced from the following geometric transformation:

$$\begin{cases} x' = \frac{x_2(y)-x_1(y)}{x_2(y)}x + x_1(y), & 0 < x < x_2(y), \\ y' = y, \quad a < y < b, \\ z' = z, \quad 0 < z < +\infty, \end{cases} \tag{11.30}$$

where x' is a stretched vertical coordinate. It is easily seen that this linear geometric transform maps the segment (a, b) of the horizontal axis $x = 0$ onto the curve $x' = x_1(y)$, and it leaves the curve $x = x_2(y)$ unchanged. Importantly, there is a one-to-one correspondence between the segment and x_1. The curves x_1 and x_2 are assumed to be differentiable, and this ensures that the carpet won't display any singularity on its inner boundary.

The symmetric tensors $\underline{\underline{\varepsilon'}}$ and $\underline{\underline{\mu'}}$ are fully described by five non vanishing entries in a Cartesian basis:

$$\underline{\underline{\varepsilon'}} = \underline{\underline{\mu'}} = \begin{pmatrix} \alpha(1 + (\frac{\partial x}{\partial y'})^2) & -\frac{\partial x}{\partial y'} & 0 \\ -\frac{\partial x}{\partial y'} & \alpha^{-1} & 0 \\ 0 & 0 & \alpha^{-1} \end{pmatrix}, \tag{11.31}$$

where $\alpha = (x_2 - x_1)/x_2$ and with $\mathbf{J}$ the Jacobian matrix of the transformation. Furthermore, the derivative of x with respect to y' is given by:

$$\frac{\partial x}{\partial y'} = x_2 \frac{x' - x_2}{(x_2 - x_1)^2}\frac{\partial x_1}{\partial y'} + x_1 \frac{x_1 - x'}{(x_2 - x_1)^2}\frac{\partial x_2}{\partial y'}. \tag{11.32}$$

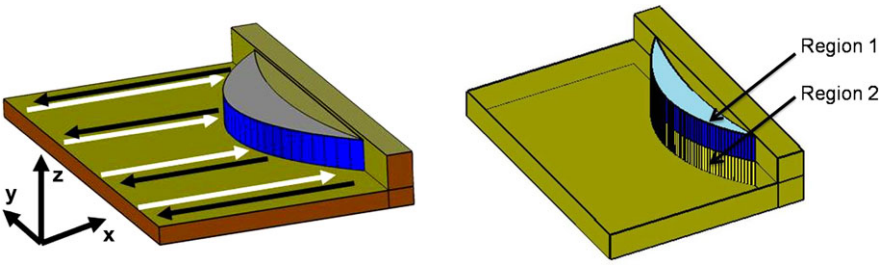

Fig. 11.6 *Left*: Diagrammatic representation of the diffraction of a SPP incident from the left (*white lines*). The SPP hits the curved reflector and is reflected (*black lines*) as if it was a flat mirror through the transformed medium (*grey and dark blue*), which is the plasmonic carpet. *Right*: Diagrammatic representation of the different media needed to be transformed if one wants a full control of SPP above and below the interface (Color figure online)

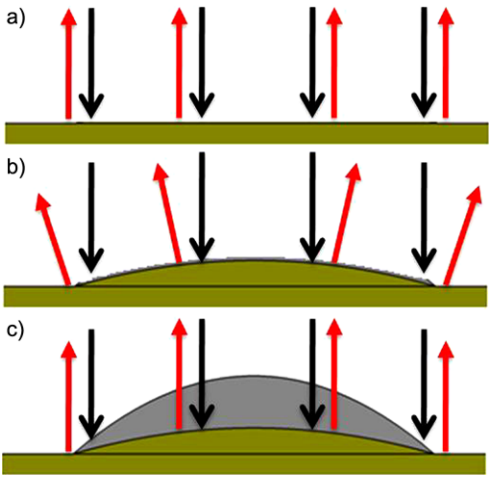

Fig. 11.7 Schematic diffraction of a SPP incident from the top. **(a)** The SPP hits the straight reflector. **(c)** The SPP hits the curved reflector. **(b)** Cloak in front of the curved reflector compensates for the curved reflector

We stress that such carpets work equally well for electromagnetic and plasmonic fields, as is intuitively the case when looking at the limit of ray optics, see Figs. 11.6 and 11.7. The numerical simulation with finite elements is shown in Fig. 11.8.

It is obvious that the wavefront is exactly the same for a flat mirror (a) and a curved mirror dressed with a carpet (b). This is due to the fact that the transformed medium is valid for any field solution of the Maxwell's equations. We note that new material inside the carpet is not only heterogeneous anisotropic, see Fig. 11.9, but also magnetic, which seems far fetched regarding the current technological progress.

However, these constraints can be further relaxed using some quasi-conformal grids in the spirit of Li and Pendry's work for two-dimensional carpets [19]. We show in Fig. 11.10 the quasi-conformal grid associated with the previous carpet. Then, keeping in mind an experimental realization requires a specific type of dielectric, in the present case TiO_2, we place particles on nodes of the quasi-grid and

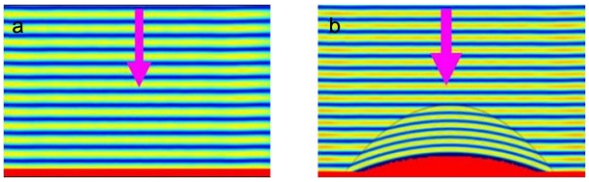

Fig. 11.8 Numerical simulation for the diffraction of a SPP incident from the top (magnetic field): **(a)** The SPP hits the straight reflector; **(b)** The SPP hits a carpet obtained by the geometrical transformation placed in front of the curved reflector

$$T^{-1} = \begin{bmatrix} T_{11}^{-1} & T_{12}^{-1} & 0 \\ T_{12}^{-1} & T_{22}^{-1} & 0 \\ 0 & 0 & T_{33}^{-1} \end{bmatrix} = \begin{bmatrix} \text{m=1.498, M=1.5} & \text{m=-0.42 , M=0.42} & 0 \\ \text{m=-0.42 , M=0.42} & \text{m=0.665, M=0.67} & 0 \\ 0 & 0 & \text{m=1.498, M=1.5} \end{bmatrix}$$

$$ {}_dT^{-1} = \begin{bmatrix} {}_dT_{11}^{-1} & 0 & 0 \\ 0 & {}_dT_{22}^{-1} & 0 \\ 0 & 0 & {}_dT_{33}^{-1} \end{bmatrix} = \begin{bmatrix} \text{m=1.498, M=1.5} & 0 & 0 \\ 0 & \text{m=0.59, M=0753} & 0 \\ 0 & 0 & \text{m=1.33, M=1.69} \end{bmatrix}$$

Fig. 11.9 *Top*: Variation of the metric tensor in the plasmonic carpet; *Bottom*: Diagonalized metric tensor for the plasmonic carpet, which could be used in an experimental implementation

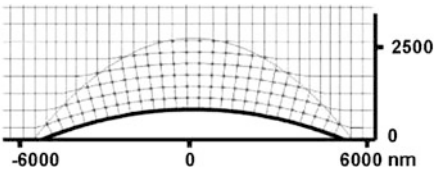

Fig. 11.10 Quasi-conformal grid associated with the geometrical transformation of the carpet. It should be noted that the right angles are preserved at the nodes of the mesh, which indicates that the associated transformed medium is nearly isotropic

we optimize the size of these particles to minimize the scattering and to maximize the flatness of the reflected SPP wavefront.

The numerical simulations in two-dimensions, see Fig. 11.11, and three-dimensions, see Fig. 11.12, validate our quasi-conformal approach to plasmonic cloaking.

11.3.4 Experimental Measurements of Plasmonic Cloaking

In order to meet experimentally the parameters found in our simulations, we chose a configuration in which a gold surface is structured with TiO_2 nanostructures. The

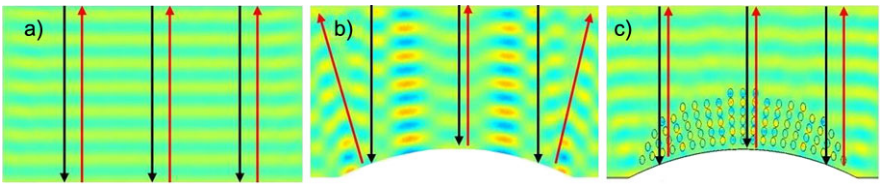

Fig. 11.11 Two-dimensional numerical simulations for the diffraction of a SPP: **(a)** On a flat mirror; **(b)** On a curved mirror; **(c)** On the curved mirror in presence of the metamaterial (cylindrical dielectric pillars of TiO_2) for a wavelength of 800 nm

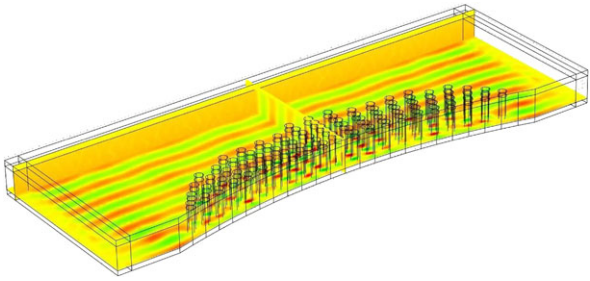

Fig. 11.12 Three-dimensional numerical simulation for the diffraction of a SPP on the curved mirror in presence of the metamaterial (cylindrical dielectric pillars of TiO_2) for a wavelength of 800 nm

TiO_2 pillars forming the crescent-moon-like carpet were first fabricated on top of a 60 nm-thin Au film by combining electron-beam lithography and reactive ion etching. In a second lithography step, we added a curved Bragg-type reflector (formed by 15 gold lines (section = 150 nm × 150 nm) periodically separated by half the SPP wavelength), acting as the object to be hidden behind the carpet (see Fig. 11.13, right panel). The shape of the obtained TiO_2 particles is conical ($h = 200$ nm, $r = 210$ nm) as a consequence of the etching anisotropy.

The SPP was launched at a ripple-like, 200-nm-wide TiO_2-line placed 44 μm away from the reflector as shown in Fig. 11.13, left panel. SPPs propagating on thin metal films deposited on dielectric substrate have radiative losses into the substrates. This leakage radiation was collected using a high-numerical aperture objective to map the SPP fields. Additionally for the sake of clarity, we employed spatial filtering in the conjugated (Fourier-) plane to suppress the direct transmitted light from the excitation spot and scattered light in order to isolate the carpet properties. Original attempts at reflecting SPPs with flat and curved homogeneous metallic step-like mirror turned out being inefficient because the SPPs tend to radiate in open space. We therefore decided to consider instead flat and curved Bragg mirrors, formed by periodically arranged metal ridges, which show a much higher reflectivity.

The leakage radiation microscopy (LRM), see Fig. 11.14, images map the distribution of the SPPs propagating at the gold/air interface and interacting with the different structures fabricated at the gold surface. In the case of a bare curved Bragg-reflector, the reflected SPPs are propagating into different directions depending on their relative angle to the normal to the mirror lines (see green arrows in Fig. 11.15(c)), thus leading to a curved wave front. Conversely, adding the crescent-moon-like TiO_2 carpet re-establishes a fringe pattern with a nearly straight wave

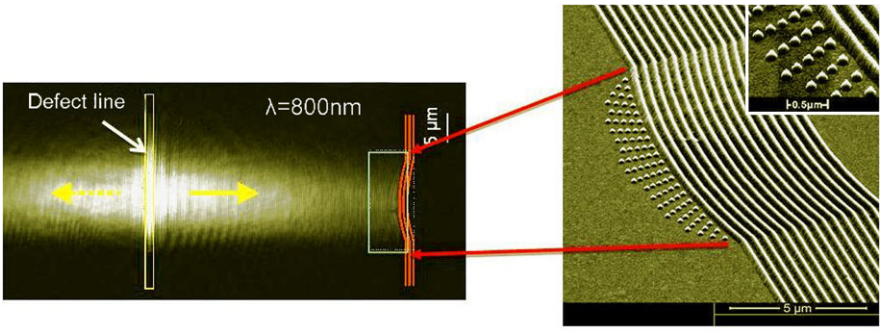

Fig. 11.13 SEM micrograph of the structure realized by single-step electron-beam-lithography. The *defect line* is used to lunch the SPP from the left to the structure (bump with carpet) (*right*). The carpet is made of TiO_2 cones as shown in the zoom (*right*)

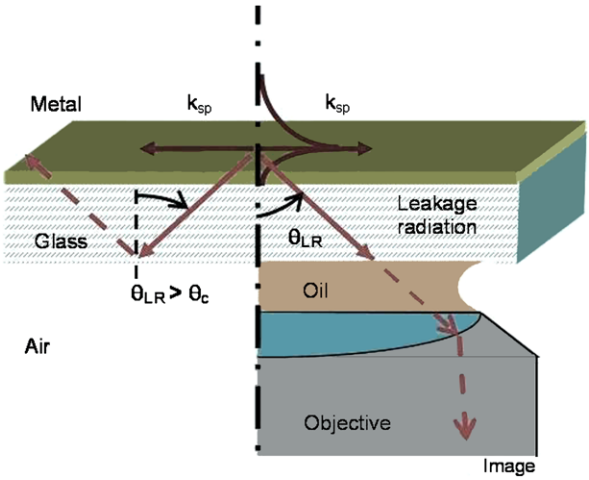

Fig. 11.14 Leakage radiation principle. By reciprocity, a SPP propagating at the surface of thin film leaks into the substrate. Mapping the leakage provides a direct information about the intensity of the surface field propagating at the interface

front (see Fig. 11.15(b)) very similar to the case of a flat Bragg-mirror. The remaining small lateral modulations are attributed to imperfections in the manufacturing. Further, data analysis has been used to quantify the modification in the wave front curvature induced by the presence of the crescent-moon-like TiO_2 carpet. Comparing the areas under the numerically averaged curves (b) (curved mirror with carpet) and (c) (curved mirror without carpet) leads to reduction by a factor 3.7 as shown in Fig. 11.15(d).

11.4 Concluding Remarks on LSW and SPP Cloaking

In the first part, we have proposed an original route towards Liquid Surface Waves (LSWs) cloaking. We studied theoretically and numerically the extension of elec-

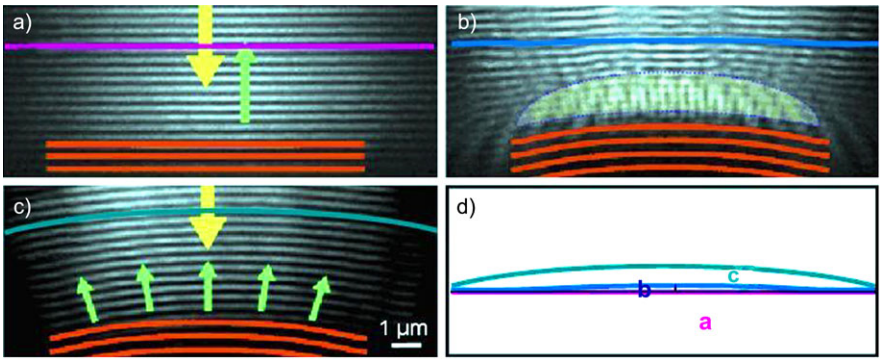

Fig. 11.15 Experimental diffraction of a SPP incident from the top (magnetic field). **(a)** The SPP hits the straight reflector. **(c)** The SPP hits the curved reflector. **(b)** Cloak in front of the curved reflector nearly compensates for the curved reflector. **(d)** Comparison between cases a), b) and c) (Color figure online)

tromagnetic and acoustic cloaking mechanisms to the domain of waves propagating at the free interface between fluids and air. We have proposed a design of a broadband micro-structured cloak consisting of a large number of small sectors arranged in a quasi-periodic manner on the surface of the liquid. For this, we have derived the homogenized linearized Navier-Stokes equations using a multi-scale asymptotic approach. We found that the homogenized fluid could be described by a rank-2 tensor (a generalized shear viscosity) and a scalar density that we took constant to simplify the experiment realization. We then performed numerical computations based on the finite elements method, which proved that a rigid obstacle surrounded by a coating consisting of concentric layers with 100 and 200 periodic perforations is almost invisible for LSW waves. This design could be used to protect off-shore platforms or coastlines from ocean waves such as tsunamis on a larger scale.

In the second part, we have studied numerically and experimentally the extension of the carpet of Li and Pendry to Surface Plasmon Polariton (SPPs). Our theoretical predictions, based on transformational plasmonics and quasi-conformal mapping, have been validated numerically and experimentally at visible wavelengths.

Our results show that strong analogies exist between the physics of linear liquid waves at free air-fluid interfaces and electron waves at metal surfaces. Advances in one field might fuel research in the other one. Actually, it is cloaking for LSWs, which prompted the work on transformational plasmonics [11, 13–16, 21, 30].

References

1. Acheson, D.J.: Elementary Fluid Dynamics. Oxford University Press, Oxford (1990)
2. Alù, A., Engheta, N.: Achieving transparency with plasmonic and metamaterial coatings. Phys. Rev. E **72**, 016623 (2005)
3. Alù, A., Engheta, N.: Achieving transparency with plasmonic and metamaterial coatings. Phys. Rev. E **72**, 016623 (2005)

4. Baumeier, B., Leskova, T.A., Maradudin, A.A.: Cloaking from surface plasmon polaritons by a circular array of point scatterers. Phys. Rev. Lett. **103**, 246809 (2009)
5. Bliek, P.J., Deleuil, R., Botten, L.C., McPhedran, R.C., Maystre, D.: Inductive grids in the region of diffraction anomalies – Theory, experiment, and applications. IEEE Microw. Theory Tech. **28**(10), 1119–1125 (1980)
6. Cai, W., Chettiar, U.K., Kildiev, A.V., Shalaev, V.M.: Optical cloaking with metamaterials. Nat. Photonics **1**, 224 (2007)
7. Cummer, S.A., Schurig, D.: One path to acoustic cloaking. New J. Phys. **9**, 45 (2007)
8. Ebbesen, T.W., Lezec, H.J., Ghaemi, H.F., Thio, T., Wolff, P.A.: Extraordinary optical transmission through sub-wavelength hole arrays. Nature **391**, 667–669 (1998)
9. Ergin, T., Stenger, N., Brenner, P., Pendry, J.B., Wegener, M.: Three-dimensional invisibility cloak at optical wavelengths. Science **328**, 337–339 (2010)
10. Garcia de Abajo, F.J., Gomez-Santos, G., Blanco, L.A., Borisov, A.G., Shabanov, S.V.: Tunneling mechanism of light transmission through metallic films. Phys. Rev. Lett. **95**, 067403 (2005)
11. Huidobro, P.A., Nesterov, M.L., Martin-Moreno, L., Garca-Vidal, F.J.: Transformation optics for plasmonics. Nano Lett. **10**, 1985–1990 (2010)
12. Jikhov, V.V., Kozlov, S.M., Oleinik, O.A.: Homogenization of Differential Operators and Integral Functionals. Springer, New York (1994)
13. Kadic, M., Dupont, G., Guenneau, S., Enoch, S.: Controlling surface plasmon polaritons in transformed coordinates. J. Mod. Opt. **58**(12), 994–1003 (2011)
14. Kadic, M., Dupont, G., Guenneau, S., Enoch, S.: Plasmonic wormholes: Defeating the early bird. http://arxiv.org/abs/1102.2372
15. Kadic, M., Dupont, G., Chang, T.M., Guenneau, S., Enoch, S.: Curved trajectories on transformed metal surfaces: Beam-splitter, invisibility carpet and black hole for surface plasmon polaritons. Photonics Nanostruct. **9**(4), 302–307 (2011)
16. Kadic, M., Guenneau, S., Enoch, S.: Transformational plasmonics: Cloak, concentrator and rotator for SPPs. Opt. Express **18**(11), 12027–12032 (2010)
17. Kretschmann, E., Raether, H.: Radiative decay of nonradiative surface plasmons excited by light. Z. Naturforsch. A **23**, 2135–2136 (1968)
18. Leonhardt, U.: Optical conformal mapping. Science **312**, 1777–1780 (2006)
19. Li, J., Pendry, J.B.: Hiding under the carpet: A new strategy for cloaking. Phys. Rev. Lett. **101**, 203901 (2008)
20. Liu, R., Ji, C., Mock, J.J., Chin, J.Y., Cui, T.J., Smith, D.R.: Broadband ground-plane cloak. Science **323**, 366 (2008)
21. Liu, Y., Zentgraf, T., Bartal, G., Zhang, X.: Transformational plasmon optics. Nano Lett. **10**, 1991–1997 (2010)
22. Maier, S.: Plasmonics: Fundamentals and Applications. Springer, New York (2007)
23. Milton, G.W., Nicorovici, N.A.P.: On the cloaking effects associated with anomalous localised resonance. Proc. R. Soc. Lond. A **462**, 3027 (2006)
24. Nicorovici, N.A.P., Milton, G.W., McPhedran, R.C., Botten, L.C.: Quasistatic cloaking of two-dimensional polarizable discrete systems by anomalous resonance. Opt. Express **15**, 6314–6323 (2007)
25. Nicolet, A., Remacle, J.F., Meys, B., Genon, A., Legros, W.: Transformation methods in computational electromagnetics. J. Appl. Phys. **75**, 6036–6038 (1994)
26. Pendry, J.B.: Negative refraction makes a perfect lens. Phys. Rev. Lett. **85**, 3966 (2000)
27. Pendry, J.B., Martin-Moreno, L., Garcia-Vidal, F.J.: Mimicking surface plasmons with structured surfaces. Science **305**, 847 (2004)
28. Pendry, J.B., Schurig, D., Smith, D.R.: Controlling electromagnetic fields. Science **312**, 1780–1782 (2006)
29. Rather, H.: Surface Plasmons. Springer, Berlin (1988)
30. Renger, J., Kadic, M., Dupont, G., Acimovic, S., Guenneau, S., Quidant, R., Enoch, S.: Hidden progress: Broadband plasmonic invisibility. Opt. Express **18**(15), 15757–15768 (2010)
31. Ritchie, R.H.: Plasma losses by fast electrons in thin films. Phys. Rev. **106**, 874–881 (1957)

32. Schurig, D., Mock, J.J., Justice, J.B., Cummer, S.A., Pendry, J.B., Starr, A.F., Smith, D.R.: Metamaterial electromagnetic cloak at microwave frequencies. Science **314**, 977–980 (2006)
33. Smolyaninov, I.I., Hung, Y.J., Davis, C.C.: Two-dimensional metamaterial structure exhibiting reduced visibility at 500 nm. Opt. Lett. **33**, 1342–1344 (2008)
34. Valentine, J., Li, J., Zentgraf, T., Bartal, G., Zhang, X.: An optical cloak made of dielectrics. Nat. Mater. **8**, 569–571 (2009)
35. Ward, A.J., Pendry, J.B.: Refraction and geometry in Maxwell's equations. J. Mod. Opt. **43**, 773–793 (1996)
36. Wood, R.W.: On a remarkable case of uneven distribution of light in a diffraction grating spectrum. Philos. Mag. **4**, 396 (1902)
37. Zolla, Z., Guenneau, S., Nicolet, A., Pendry, J.B.: Electromagnetic analysis of cylindrical invisibility cloaks and the mirage effect. Opt. Lett. **32**, 1069 (2007)

Chapter 12
Transformation Elastodynamics and Active Exterior Acoustic Cloaking

Fernando Guevara Vasquez, Graeme W. Milton, Daniel Onofrei, and Pierre Seppecher

Abstract This chapter consists of three parts. In the first part we recall the elastodynamic equations under coordinate transformations. The idea is to use coordinate transformations to manipulate waves propagating in an elastic material. Then we study the effect of transformations on a mass-spring network model. The transformed networks can be realized with "torque springs", which are introduced here and are springs with a force proportional to the displacement in a direction other than the direction of the spring terminals. Possible homogenizations of the transformed networks are presented, with potential applications to cloaking. In the second and third parts we present cloaking methods that are based on cancelling an incident field using active devices which are exterior to the cloaked region and that do not generate significant fields far away from the devices. In the second part, the exterior cloaking problem for the Laplace equation is reformulated as the problem of polynomial approximation of functions. An explicit solution is given that allows cloaking of larger objects at a fixed distance from the cloaking device, compared to previous explicit solutions. In the third part we consider the active exterior cloaking problem for the Helmholtz equation in 3D. Our method uses the Green's formula and an addition theorem for spherical outgoing waves to design devices that mimic the effect of the single and double layer potentials in Green's formula.

F. Guevara Vasquez · G.W. Milton · D. Onofrei
Department of Mathematics, University of Utah, Salt Lake City, UT 84112, USA

F. Guevara Vasquez
e-mail: fguevara@math.utah.edu

G.W. Milton (✉)
e-mail: milton@math.utah.edu

D. Onofrei
e-mail: onofrei@math.utah.edu

P. Seppecher
Institut de Mathématiques de Toulon, Université de Toulon et du Var, BP 132-83957
La Garde Cedex, France
e-mail: seppecher@imath.fr

R.V. Craster, S. Guenneau (eds.), *Acoustic Metamaterials*,
Springer Series in Materials Science 166, DOI 10.1007/978-94-007-4813-2_12,

Coordinate transformations can be used to manipulate fields in a variety of ways for the Maxwell and Helmholtz equations. In Sect. 12.1 we focus on transformation elastodynamics. The idea is to manipulate waves in an elastic medium by designing appropriate transformations of the coordinates and the displacements. As opposed to the Maxwell and Helmholtz equations, the elastodynamic equations are not invariant under these transformations. Here we recall the transformed elastodynamic equations, and then move to the effect of space transformations on a mass-spring network model. In order to realize the transformed networks we introduce "torque springs", which are springs with a force proportional to the displacement in a direction other than the direction dictated by the spring terminals. We discuss some possible homogenizations of transformed networks that could have applications to manipulating waves in an elastic medium for e.g. cloaking.

Then we look at an approach to cloaking which is based on cancelling the incident field using active devices (rather than passive composite materials) which are exterior to the cloaked region. Exterior means that the cloaked region is not completely surrounded by the cloak, as is the case in most transformation based methods. We present here active exterior cloaking methods for both the Laplace equation in dimension two (Sect. 12.2) and the Helmholtz equation in dimension three (Sect. 12.3).

The cloaking method for the Laplace equation we present in Sect. 12.2 applies also to the quasi-static (low frequency) regime and was in part presented in [19, 23]. We first reformulate the problem of designing an active cloaking device as the classic problem of approximating functions with polynomials. This theoretical approach shows that it is possible to cloak an object from an incident field with one single exterior device. Then we give an explicit solution to the problem in terms of a polynomial and determine its convergence region as the degree of the polynomial increases. This convergence region limits the size of the cloaked region, and for the new solution we propose here it allows one to cloak larger objects at a fixed distance from the device compared to the explicit polynomial solution given in [19, 23]. Following the ideas of [55] we also discuss how our approach can be modified to simultaneously hide an object and give the illusion of another object, in the same spirit as illusion optics [28].

Next in Sect. 12.3 we consider the Helmholtz equation and use the same techniques as in [22] to show that in dimension three it is possible to cloak an object using four devices and yet leaving the object connected with the exterior. Our method is based on Green's formula, which ensures that an analytic field can be reproduced inside a volume by a carefully chosen single and double layer potential at the surface of the volume. Then we use addition theorems for spherical outgoing waves to concentrate the single and double layer potential at a few multipolar sources (cloaking devices) located outside the cloaked region. We determine the convergence region of the device's field and include an explicit geometric construction of a cloak with four devices.

The three sections of this chapter can be read essentially independently of each other.

12.1 Transformation Elastodynamics

Transformation based cloaking was first discovered by Greenleaf, Lassas and Uhlmann [17, 18] in the context of the conductivity equations. Independently, Leonhardt realized that transformation based cloaking applies to geometric optics [29] and Pendry, Schurig and Smith [47] realized that transformation based cloaking applies to Maxwell's equations at fixed frequency, and this led to an explosion of interest in the field. It was found that transformation based cloaking also applies to acoustics [5, 9, 15, 43], which is governed by the Helmholtz equation, provided one permits anisotropic density [36, 49] or pentamode materials [25, 37, 43]. These developments, reviewed in [1, 4, 6, 16] rely on the invariance of the conductivity equations, Maxwell's equations, and the Helmholtz equation under coordinate transformations, and have been substantiated by rigorous proofs [15, 26, 27]. The invariance of Maxwell's equations under coordinate transformations has led to other envisaged applications such as field concentrators [48], field rotators [7], lenses [50], superscatterers [54] (see also [41]) and the name "transformation optics" is now used to describe this research: see, for example, the special issue in the New Journal of Physics [31] devoted to cloaking and transformation optics. The perfect lens of Pendry [46] can be viewed as the result of using a transformation which unfolds space [30] and associated with such folding transformations is cloaking due to anomalous resonance [38, 39, 42].

A largely open question is how to construct metamaterials with the required combination of anisotropic electrical permittivity $\boldsymbol{\varepsilon}(\mathbf{x})$ and anisotropic magnetic permeability $\boldsymbol{\mu}(\mathbf{x})$ needed in transformation optics designs, frequently with $\boldsymbol{\varepsilon}(\mathbf{x}) = \boldsymbol{\mu}(\mathbf{x})$. Only recently was it shown [35], building upon work of Bouchitté and Schweizer [2], that any combination of real tensors $(\boldsymbol{\varepsilon}, \boldsymbol{\mu})$ is approximately realizable, at least in theory.

Curiously, the usual elastodynamic equations do not generally keep their form under coordinate transformations. Either new terms enter the equations [36], so they take the form of equations Willis introduced [53] to describe the ensemble averaged elastodynamic behavior of composite materials (which are the analog of the bianisotropic equations of electromagnetism [51]), or the elasticity tensor field does not retain its minor symmetries [3, 44]. Nevertheless, as shown in [34] and as is explored further here, there is some hope that metamaterials can be constructed with a response corresponding approximately with that required by the new equations.

12.1.1 Continuous Transformation Elastodynamics

Following the work of Norris and Shuvalov, [44], let us show that the equation of elastodynamics

$$-\nabla \cdot \big(\mathbf{C}(\mathbf{x})\nabla \mathbf{u}\big) = \omega^2 \rho(\mathbf{x})\mathbf{u} \tag{12.1}$$

changes under the transformation

$$\mathbf{x}' = \mathbf{x}'(\mathbf{x}), \qquad \mathbf{u}'\big(\mathbf{x}'(\mathbf{x})\big) = \big(\mathbf{B}^T(\mathbf{x})\big)^{-1}\mathbf{u}(\mathbf{x}) \tag{12.2}$$

to the equation

$$-\nabla' \cdot \big(\mathbf{C}'(\mathbf{x}')\nabla'\mathbf{u}' + \mathbf{S}'(\mathbf{x}')\mathbf{u}'\big) + \mathbf{D}'(\mathbf{x}')\nabla'\mathbf{u}' - \omega^2\big(\boldsymbol{\rho}'(\mathbf{x}')\mathbf{u}'\big) = 0 \tag{12.3}$$

where the tensors $\mathbf{C}'$, $\mathbf{S}'$, $\mathbf{D}'$, $\boldsymbol{\rho}'$ are given in terms of the functions $\mathbf{x}'$, $\mathbf{B}$ and their derivatives. Here the transformation of the displacement is governed by $\mathbf{B}(\mathbf{x})$ which can be chosen to be any invertible matrix valued function. (The inverse and transpose in $(\mathbf{B}^T(\mathbf{x}))^{-1}$ have been introduced to simplify subsequent formulae.)

Indeed let us first note that

$$\begin{aligned}\nabla\mathbf{u} &= \frac{\partial u_j}{\partial x_i} = \frac{\partial(u'_p B_{pj})}{\partial x_i} = \frac{\partial x'_m}{\partial x_i}\frac{\partial u'_p}{\partial x'_m}B_{pj} + \frac{\partial B_{pj}}{\partial x_i}u'_p \\ &= \mathbf{A}^T(\nabla'\mathbf{u}')\mathbf{B} + \mathbf{G}'\mathbf{u}'\end{aligned} \tag{12.4}$$

in which $\mathbf{A}$ and $\mathbf{G}$ are the tensors with elements

$$A_{mi} = \frac{\partial x'_m}{\partial x_i}, \qquad G_{ijp} = \frac{\partial B_{pj}}{\partial x_i}. \tag{12.5}$$

Now (12.1) implies that for all smooth vector-valued test functions $\mathbf{v}(\mathbf{x})$ with compact support in a domain Ω,

$$\begin{aligned}0 &= \int_\Omega \big[-\nabla\cdot\big(\mathbf{C}(\mathbf{x})\nabla\mathbf{u}\big) - \omega^2\rho(\mathbf{x})\mathbf{u}\big]\cdot\mathbf{v}\,\mathrm{d}\mathbf{x} \\ &= \int_\Omega \big[\mathbf{C}(\mathbf{x})\nabla\mathbf{u} : \nabla\mathbf{v} - \omega^2\rho(\mathbf{x})\mathbf{u}\cdot\mathbf{v}\big]\,\mathrm{d}\mathbf{x} \\ &= \int_{\Omega'} \big[\mathbf{C}(\mathbf{x})\big(\mathbf{A}^T(\nabla'\mathbf{u}')\mathbf{B} + \mathbf{G}\mathbf{u}'\big) : \big(\mathbf{A}^T(\nabla'\mathbf{v}')\mathbf{B} + \mathbf{G}\mathbf{v}'\big) \\ &\quad - \omega^2\rho(\mathbf{x})\big(\mathbf{B}^T\mathbf{u}'\big)\cdot\big(\mathbf{B}^T\mathbf{v}'\big)\big]a^{-1}\,\mathrm{d}\mathbf{x}' \\ &= \int_{\Omega'} \big[\mathbf{C}'(\mathbf{x}')\nabla'\mathbf{u}' : \nabla'\mathbf{v}' + \mathbf{S}'(\mathbf{x}')\mathbf{u}' : \nabla'\mathbf{v}' + \big(\mathbf{D}'(\mathbf{x}')\nabla'\mathbf{u}'\big)\cdot\mathbf{v}' \\ &\quad - \omega^2\big(\boldsymbol{\rho}'(\mathbf{x}')\mathbf{u}'\big)\cdot\mathbf{v}'\big]\,\mathrm{d}\mathbf{x}' \\ &= \int_{\Omega'} \big[-\nabla'\cdot\big(\mathbf{C}'(\mathbf{x}')\nabla'\mathbf{u}' + \mathbf{S}'(\mathbf{x}')\mathbf{u}'\big) + \mathbf{D}'(\mathbf{x}')\nabla'\mathbf{u}' - \omega^2\big(\boldsymbol{\rho}'(\mathbf{x}')\mathbf{u}'\big)\big]\cdot\mathbf{v}'\,\mathrm{d}\mathbf{x}'\end{aligned} \tag{12.6}$$

in which the test function $\mathbf{v}(\mathbf{x})$ has been transformed, similarly to $\mathbf{u}(\mathbf{x})$, to

$$\mathbf{v}'\big(\mathbf{x}'(\mathbf{x})\big) = \big(\mathbf{B}^T(\mathbf{x})\big)^{-1}\mathbf{v}(\mathbf{x}), \tag{12.7}$$

and $a(\mathbf{x}'(\mathbf{x})) = \det \mathbf{A}(\mathbf{x})$ while $\mathbf{C}'(\mathbf{x}')$, $\mathbf{S}'(\mathbf{x}')$, $\mathbf{D}'(\mathbf{x}')$ and $\boldsymbol{\rho}'(\mathbf{x}')$ are the tensors with elements

$$\begin{aligned} C'_{ijk\ell} &= a^{-1} A_{ip} B_{jq} A_{kr} B_{\ell s} C_{pqrs}, \\ S'_{ijk} &= a^{-1} A_{ip} B_{jq} G_{rsk} C_{pqrs} = a^{-1} A_{ip} B_{jq} \frac{\partial B_{ks}}{\partial x'_r} C_{pqrs}, \\ D'_{kij} &= a^{-1} G_{pqk} A_{ir} B_{js} C_{pqrs} = S'_{ijk}, \\ \rho'_{ij} &= a^{-1} B_{ik} B_{jk} \rho - a^{-1} \omega^{-2} G_{pqi} G_{rsj} C_{pqrs} \\ &= a^{-1} B_{ik} B_{jk} \rho - a^{-1} \omega^{-2} \frac{\partial B_{iq}}{\partial x'_p} \frac{\partial B_{js}}{\partial x'_r} C_{pqrs}. \end{aligned} \tag{12.8}$$

From (12.6) we see directly that (12.1) transforms to (12.3).

Remark 12.1 The transformed elastodynamic equation (12.3) can be written in the equivalent form of Willis-type equations [53]

$$\begin{aligned} \nabla' \cdot \boldsymbol{\sigma}' &= -i\omega \mathbf{p}', \\ \boldsymbol{\sigma}' &= \mathbf{C}'(\mathbf{x}') \nabla' \mathbf{u}' + (i/\omega) \mathbf{S}'(\mathbf{x}')(-i\omega \mathbf{u}'), \\ \mathbf{p}' &= \boldsymbol{\rho}'(\mathbf{x}')(-i\omega \mathbf{u}') + (i/\omega) \mathbf{D}'(\mathbf{x}') \nabla \mathbf{u}', \end{aligned} \tag{12.9}$$

in which the stress $\boldsymbol{\sigma}'$, which is not necessarily symmetric, depends not only upon the displacement gradient $\nabla' \mathbf{u}'$ but also upon the velocity $-i\omega \mathbf{u}'$, and the momentum $\mathbf{p}'$ depends not only upon the velocity $-i\omega \mathbf{u}'$, but also on the displacement gradient $\nabla' \mathbf{u}'$.

Remark 12.2 If we desire the transformed elasticity tensor $\mathbf{C}'(\mathbf{x}')$ to have all the usual symmetries of elasticity tensors, namely that

$$C'_{ijk\ell} = C'_{jik\ell} = C'_{k\ell ij}, \tag{12.10}$$

then we need to restrict the transformations to those with $\mathbf{B} = \mathbf{A}$. This was the case analyzed by Milton, Briane and Willis [36].

Remark 12.3 As observed by Norris and Shuvalov [44], in the particular case where $\mathbf{B} = \mathbf{I}$ the transformation (12.9) reduces to

$$C'_{ijk\ell} = a^{-1} A_{ip} A_{kr} C_{pjr\ell}, \qquad \mathbf{S}' = \mathbf{D}' = 0, \qquad \boldsymbol{\rho}' = a^{-1} \rho \mathbf{I}, \tag{12.11}$$

corresponding to normal elastodynamics, with an isotropic density matrix $\boldsymbol{\rho}'$, but with an elasticity tensor $\mathbf{C}'$ only satisfying the major symmetry $C'_{ijk\ell} = C'_{k\ell ij}$. This was the case analyzed by Brun, Guenneau and Movchan [3] in a particular two-dimensional example.

Having derived the rules of transformation elasticity, one can then apply the same variety of transformations as used in transformation optics, including cloaking and folding transformations. The point is that a wave propagating classically in the classical medium can have a strange behavior in the new abstract coordinate system $\mathbf{x}'$. If we are able to design a real medium following a system of equations equivalent to the transformed system, then we are able to force a strange behavior for waves in real physical space.

12.1.2 Discrete Transformation Elastodynamics

There is a discrete version of the transformation (12.11). Suppose we have a network of springs, possibly a lattice infinite in extent, with a countable number of nodes at positions $\mathbf{x}_1, \mathbf{x}_2, \mathbf{x}_3, \ldots, \mathbf{x}_n \ldots$, at which there are masses $M_1, M_2, M_3, \ldots, M_n \ldots$, and at which the displacements are $\mathbf{u}_1, \mathbf{u}_2, \mathbf{u}_3, \ldots, \mathbf{u}_n \ldots$. Let k_{ij} denote the spring constant of the spring connecting node i to node j. There is no loss of generality in assuming that all pairs of nodes are joined by a spring, taking $k_{ij} = 0$ if there is no real spring joining node i and j. Let $\mathbf{F}_{i,j}$ denote the force which the spring joining nodes i and j exerts on node i. Hooke's law implies

$$\mathbf{F}_{i,j} = -\mathbf{F}_{j,i} = k_{i,j}\mathbf{n}_{i,j}\big[\mathbf{n}_{i,j} \cdot (\mathbf{u}_j - \mathbf{u}_i)\big], \tag{12.12}$$

where

$$\mathbf{n}_{i,j} = \frac{\mathbf{x}_j - \mathbf{x}_i}{|\mathbf{x}_j - \mathbf{x}_i|}, \tag{12.13}$$

is the unit vector in the direction of $\mathbf{x}_j - \mathbf{x}_i$. In the absence of any forces acting on the nodes, apart from inertial forces, Newton's second law implies

$$\sum_j \mathbf{F}_{i,j} = -M_i\omega^2\mathbf{u}_i. \tag{12.14}$$

Now let us consider a transformation $\mathbf{x}' = \mathbf{x}'(\mathbf{x})$ with an associated inverse transformation $\mathbf{x} = \mathbf{x}(\mathbf{x}')$. Under this transformation the position of the nodes transform to $\mathbf{x}'_1, \mathbf{x}'_2, \mathbf{x}'_3, \ldots, \mathbf{x}'_n \ldots$, where $\mathbf{x}'_i = \mathbf{x}'(\mathbf{x}_i)$. We focus, for simplicity, on the case corresponding to $\mathbf{B} = \mathbf{I}$ where the forces, masses and displacements transform according to

$$\mathbf{F}'_{i,j} = \mathbf{F}_{i,j}, \qquad M'_i = M_i, \qquad \mathbf{u}'_i = \mathbf{u}_i. \tag{12.15}$$

After the transformation, Newton's second law clearly keeps its form,

$$\sum_j \mathbf{F}'_{i,j} = -M'_i\omega^2\mathbf{u}'_i, \tag{12.16}$$

while (12.12) transforms to

$$\mathbf{F}'_{i,j} = -\mathbf{F}'_{j,i} = k'_{i,j}\mathbf{v}'_{i,j}\left[\mathbf{v}'_{i,j} \cdot (\mathbf{u}'_j - \mathbf{u}'_i)\right] \tag{12.17}$$

where

$$k'_{i,j} = k_{i,j}, \qquad \mathbf{v}'_{i,j} = \frac{\mathbf{x}(\mathbf{x}'_j) - \mathbf{x}(\mathbf{x}'_i)}{|\mathbf{x}(\mathbf{x}'_j) - \mathbf{x}(\mathbf{x}'_i)|}. \tag{12.18}$$

Hence in the new coordinates $\mathbf{x}'_i$ the system is governed by equations similar to the classical system of equations for a network of masses joined by springs, but the response of the springs does not anymore correspond to normal springs. While the action-reaction principle $\mathbf{F}'_{j,i} = -\mathbf{F}'_{i,j}$ remains valid, the force $\mathbf{F}'_{i,j}$ is not generally parallel to the line joining $\mathbf{x}'_j$ with $\mathbf{x}'_i$.

Now we desire to construct a real network having a behavior governed at a fixed frequency, by the system of equations (12.16) and (12.17). To that aim we need to construct a two-terminal network made of classical masses and springs which has the response (12.17) for any unit vector $\mathbf{v}'_{i,j}$. We call these two-terminal networks "torque springs" since they exert a torque in addition to the usual spring force. We show how they can be constructed for fixed frequency ω in the next section.

12.1.3 Torque Springs

A torque spring, being a two-terminal network with a response of the type (12.17), is characterized by two terminal nodes $\mathbf{x}_1$, $\mathbf{x}_2$, the direction of exerted forces $\mathbf{v}_{1,2}$ which can be different from the direction of the line joining $\mathbf{x}_1$ and $\mathbf{x}_2$ and the constant of the spring $k_{1,2}$. The existence of torque springs is guaranteed by the work of Milton and Seppecher [40] which provides a complete characterization of the response of multiterminal mass-spring networks at a single frequency. The complete characterization of the response of multiterminal mass-spring networks as a function of frequency was subsequently obtained by Guevara Vasquez, Milton, and Onofrei [21]. Here we are just interested in constructing two terminal networks with the response of a torque spring. In this case a simpler construction, than provided by the previous work, is possible.

Consider the network of Fig. 12.1. For its design we start with $\mathbf{x}_1$, $\mathbf{x}_2$ and a unit vector $\mathbf{v} = \mathbf{v}_{12}$ not parallel to $\mathbf{x}_1 - \mathbf{x}_2$. (A normal spring can be used if $\mathbf{v}$ is parallel to $\mathbf{x}_1 - \mathbf{x}_2$.) Choose $\rho > 0$ and define $\mathbf{y}_1 = \mathbf{x}_1 + \rho\mathbf{v}$, $\mathbf{y}_2 = \mathbf{x}_2 + \rho\mathbf{v}$, and choose a vector $\mathbf{w} \neq 0$ in a direction different from $\mathbf{v}$ and $\mathbf{x}_2 - \mathbf{x}_1$. Define $\mathbf{z}_1 = \mathbf{y}_1 + \mathbf{w}$, $\mathbf{z}_2 = \mathbf{y}_2 + \mathbf{w}$, $\mathbf{t}_1 = \mathbf{z}_1 + \mathbf{v}$, $\mathbf{t}_2 = \mathbf{z}_2 + \mathbf{v}$. The pairs $(\mathbf{x}_1, \mathbf{y}_1)$, $(\mathbf{x}_2, \mathbf{y}_2)$, $(\mathbf{y}_1, \mathbf{y}_2)$, $(\mathbf{y}_1, \mathbf{z}_1)$, $(\mathbf{y}_2, \mathbf{z}_2)$, $(\mathbf{z}_1, \mathbf{z}_2)$, $(\mathbf{z}_1, \mathbf{t}_1)$, $(\mathbf{z}_2, \mathbf{t}_2)$ are joined with normal springs of constant k. Masses (with mass m, where the lower case m is used to identify them as internal masses of torque springs) are attached to the nodes $\mathbf{t}_1$ and $\mathbf{t}_2$ only. All nodes but $\mathbf{x}_1$ and $\mathbf{x}_2$ are interior nodes which means that no external forces are exerted on them.

Let us denote by T the tension in the spring $(\mathbf{x}_1, \mathbf{y}_1)$, taken to be positive if the spring is under extension and negative if it is under compression, i.e. the spring

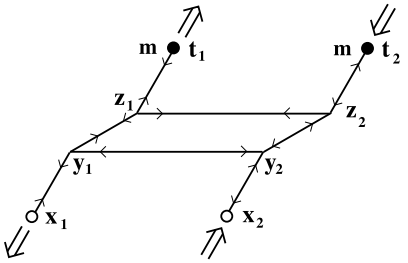

Fig. 12.1 Sketch of a torque spring. The *open circles* represent terminal nodes, and the *closed circles* could be either terminal nodes or interior nodes with masses attached. The *straight lines* represent springs. The *large arrows* represent external or inertial forces acting on the nodes at one instant in time. The *two small arrows* on each spring give the direction of the force which the spring exerts on the node nearest to the arrow

exerts a force $\mathbf{v}T$ on the terminal at $\mathbf{x}_1$ and a force $-\mathbf{v}T$ on the node at $\mathbf{y}_1$. Then the balance of forces at node $\mathbf{y}_1$ fixes the tensions T', T'' in the springs $(\mathbf{y}_1, \mathbf{y}_2)$, $(\mathbf{y}_1, \mathbf{z}_1)$ in a purely geometrical way. It is easy to check that the balance of forces at $\mathbf{y}_2$, $\mathbf{z}_1$, and $\mathbf{z}_2$ gives tensions $-T$, $-T''$, $-T'$, T, $-T$ in the springs $(\mathbf{x}_2, \mathbf{y}_2)$, $(\mathbf{y}_2, \mathbf{z}_2)$, $(\mathbf{z}_1, \mathbf{z}_2)$, $(\mathbf{z}_1, \mathbf{t}_1)$, $(\mathbf{z}_2, \mathbf{t}_2)$ respectively.

All the tensions being determined when one is known, the truss is rank one: there is only one scalar linear combination of the displacements $\mathbf{u}_1$, $\mathbf{u}_2$, $\mathbf{w}_1$, $\mathbf{w}_2$ of nodes $\mathbf{x}_1$, $\mathbf{x}_2$, $\mathbf{t}_1$, $\mathbf{t}_2$ which influences T, and $T = 0$ if and only if this scalar linear combination vanishes. It is easy to check that this combination is $(\mathbf{u}_2 - \mathbf{u}_1 - \mathbf{w}_2 + \mathbf{w}_1) \cdot \mathbf{v}$ since displacements leaving this zero (floppy modes) do not produce any tension in the springs, as they leave the spring lengths invariant to first order in the displacements. Hence there exists a constant K (proportional to k) such that $T = K(\mathbf{u}_2 - \mathbf{u}_1 - \mathbf{w}_2 + \mathbf{w}_1) \cdot \mathbf{v}$. Finally Newton's law (12.14) gives at nodes $\mathbf{t}_1$, $\mathbf{t}_2$ respectively $T = m\omega^2 \mathbf{w}_1 \cdot \mathbf{v}$ and $-T = m\omega^2 \mathbf{w}_2 \cdot \mathbf{v}$ and so $T = K(\mathbf{u}_2 - \mathbf{u}_1) \cdot \mathbf{v} + 2TKm^{-1}\omega^{-2}$ from which we conclude that

$$T = \frac{Km\omega^2}{m\omega^2 - 2K}(\mathbf{u}_2 - \mathbf{u}_1) \cdot \mathbf{v}. \tag{12.19}$$

The forces $\mathbf{F}_1$ and $\mathbf{F}_2$ which this torque spring exerts on terminals 1 and 2, respectively, are therefore

$$\mathbf{F}_1 = -\mathbf{F}_2 = T\mathbf{v} = k'\mathbf{v}\big[\mathbf{v} \cdot (\mathbf{u}_2 - \mathbf{u}_1)\big], \quad \text{with } k' = \frac{Km\omega^2}{m\omega^2 - 2K}, \tag{12.20}$$

which is exactly of the required form (12.17). If we want k' to be positive then we should choose m and K so that $m\omega^2 - 2K > 0$.

There are many other constructions which produce torque springs. Another configuration, which is closer in design to a normal spring, is that given in Fig. 12.2. In two-dimensions this type of construction may be preferable to that in Fig. 12.1 to reduce the number of spring intersections when assembling a network of torque

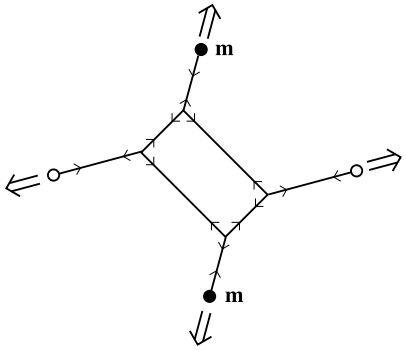

Fig. 12.2 An alternative construction of a torque spring. The *straight lines* represent springs and the *circles*, *large arrows*, and *small arrows* have the same meaning as in Fig. 12.1

springs. It also may be preferable if we wish to attach a torque spring say between two parallel interfaces.

The torque springs described here are quite floppy. To give them some structural integrity one would need to add a scaffolding of additional springs, extending out of the plane if the torque springs are going to be used in a three dimensional network. Provided the spring constants of these additional springs are sufficiently small, this can be done with only a small perturbation to the response of the torque spring, as shown in [21].

In assembling a network of torque springs it may happen that an interior spring or interior node of one torque spring intersects with an interior spring or interior node or interior node of another torque spring. Since we have the flexibility to move the interior nodes of each torque spring we only need be concerned with the intersection of two springs, or between the intersection of one spring and a node. In three dimensions if a spring intersects with another spring or a node we can replace one or both springs by an equivalent truss of springs to avoid this situation. In two dimensions if a spring intersects with a node we can again replace the spring by an equivalent truss to avoid this situation. Then if two springs intersect in two dimensions they must either overlap or cross: if they overlap we can replace each by an equivalent truss of springs, while if they cross we can (within the framework of linear elasticity) place a node at the intersection point and appropriately choose the spring constants of the joining springs so that they respond like two non-interacting springs—see Example 3.15 in Milton and Seppecher [40].

12.1.4 Homogenization of a Discrete Network of Torque Springs

As shown in Sect. 12.1.2, the original network of springs with nodes at positions $\mathbf{x}_1, \mathbf{x}_2, \mathbf{x}_3, \ldots, \mathbf{x}_n \ldots$ and spring constants k_{ij} responds in an equivalent manner to the new network of torque springs with nodes at positions $\mathbf{x}'_1, \mathbf{x}'_2, \mathbf{x}'_3, \ldots, \mathbf{x}'_n \ldots$ and

torque spring parameters given by (12.18). If the original network of springs homogenizes to an effective elasticity tensor field $\mathbf{C}(\mathbf{x})$ then the new network of torque springs homogenizes to an effective elasticity tensor field $\mathbf{C}'(\mathbf{x})$ given by (12.11), assuming the transformation $\mathbf{x}'(\mathbf{x})$ only has variations on the macroscopic scale. In particular the stress field in the homogenized network of torque springs is not be symmetric, and is influenced not just by the local strain, but also by the field of microrotations.

There are some practical barriers to this homogenization. Suppose, for simplicity, that we are in two dimensions, that the original network consists of a triangular network of identical springs with bond length h under uniform loading so that the tension is the same in all springs, and that the transformation is a rigid rotation $\mathbf{x}' = \mathbf{R}\mathbf{x}$ where $\mathbf{R}^T\mathbf{R} = \mathbf{I}$. The displacement $\mathbf{u}_i$ of the nodes $\mathbf{x}_i$ is, up to a translation, that of uniform dilation, $\mathbf{u}_i = \alpha\mathbf{x}_i$. It follows that if i and j are adjacent nodes on the network, then $\mathbf{u}'_i - \mathbf{u}'_j$ scales in proportion to h. On the other hand, in order that the traction force per unit length on a line remains constant the tension T in each torque spring must also scale in proportion to h. Therefore the torque spring constant $k' = Km\omega^2/(m\omega^2 - 2K)$ must be essentially independent of h. Also we don't want the density of mass per unit area associated with the torque springs to be too large (otherwise gravitational forces would be very significant). This would be ensured if m scales as h^β where $\beta \geq 2$. Since

$$K = \frac{k'm\omega^2}{2k' + m\omega^2} \tag{12.21}$$

we see that K should also scale as h^β, and that $2K$ would be close $m\omega^2$ when h is small. Thus each torque spring is very close to resonance. If this is satisfied at one frequency, it will not be satisfied at nearby frequencies. Thus the metamaterial is operational only within an extremely narrow band of frequencies. The situation is similar in three dimensions in a network having bond lengths of the order of h. Then $\mathbf{u}'_i - \mathbf{u}'_j$, T, k' and m need to scale as h, h^2, h, and h^β, respectively, with $\beta \geq 3$ to avoid an infinite mass density in the limit $h \to 0$. (T must scale as h^2 to maintain a constant traction per unit area on a surface). Again K given by (12.21) must be close to $m\omega^2/2$ when h is small.

In three dimensions an alternative is to avoid the use of masses within each torque spring altogether. This can be achieved by pinning the internal nodes of the torque springs, where there would be masses (such as at the nodes $\mathbf{t}_1$ and $\mathbf{t}_2$ in Fig. 12.1), to a rigid lattice (designed in a way which avoids intersection with the springs inside the torque springs). Such a pinning corresponds to setting $m = \infty$ and each torque spring has then a spring constant $k' = K$ which is independent of frequency. The resulting metamaterial is operational at all frequencies. Note that within the framework of linear elasticity each torque spring exerts a torque but not a net force on the underlying rigid lattice. If the rigid lattice (which might have only finite extent) itself is not pinned we require that the external forces on the metamaterial to be such that there is no net overall torque on the rigid lattice.

A more serious concern is the validity of linear elasticity, at least using the torque spring designs proposed here. A characteristic feature of the designs involving masses is that the internal masses m do not move when the springs are translated, to first order in the displacement. This accounts for the balance of forces $\mathbf{F}'_{j,i} = -\mathbf{F}'_{i,j}$. However the masses do move significantly if the terminals are translated a distance which is comparable to the size of the torque spring. Alternatively, if we pin the internal nodes of the torque springs, where there would be masses, to a rigid lattice then this restricts the motion of the torque spring terminals relative to the lattice. Clearly for the operation of the metamaterial the displacements $\mathbf{u}'_i$ must be small compared to h, assuming the size of each torque spring is of order h. When h is very small this severely limits the amplitude of waves propagating in the metamaterial for which linear elasticity applies. Thus the only metamaterials of the type described here that might possibly be of practical interest are those for which h is not too small. This is in contrast to homogenization of a normal elastodynamic network where linear elasticity may apply when only the displacement differences $\mathbf{u}'_i - \mathbf{u}'_j$, between adjacent nodes i and j, are small compared to h.

12.2 Active Exterior Cloaking in the Quasistatic Regime

We show that for the Laplace equation, it is possible for a device to generate fields that cancel out the incident field in a region while not interfering with the incident field far away from the device. Our results generalize to the quasistatic (low frequency) regime. Thus any (non-resonant) object located inside the region where the fields are negligible interacts little with the fields and is for all practical purposes invisible. Here we relate the problem of designing a cloaking device to the classic problem of approximating a function with polynomials. Then we propose a cloak design that is based on a family of polynomials. We also show that our solution can be easily modified to give cloak objects while giving the illusion of another object (illusion optics as in [28]).

12.2.1 Active Exterior Cloak Design

Following the ideas presented in [19], we first state the requirements that the field generated by a device (source) needs to satisfy in order to cloak objects inside a predetermined region. Here we denote by $B(\mathbf{x}, r) \subset \mathbb{R}^2$ the open ball of radius $r > 0$ centered at $\mathbf{x} \in \mathbb{R}^2$.

Let $B(\mathbf{c}, a)$ with $a > 0$ and $\mathbf{c} \in \mathbb{R}^2$ be the region where we want to hide objects (the cloaked region). The cloaking device is an active source (antenna) located (for simplicity) inside $B(0, \delta)$ with $\delta \ll 1$. Assuming a priori knowledge of the incident (probing) potential u_0, we say that the device is an active exterior cloak for the region $B(\mathbf{c}, a)$ if the device generates a potential u such that

i. The total potential $u + u_0$ is very small in the cloaked region $B(\mathbf{c}, a)$.
ii. The device potential u is very small outside $B(0, R)$, for some large $R > 0$.

Therefore, if the incoming (probing) field is known in advance, an active exterior cloak hides both itself and any (non-resonant) object placed in the region $B(\mathbf{c}, a)$. Indeed any object inside $B(\mathbf{c}, a)$ only interacts with very small fields and the device field is very small far away from the device.

After a suitable rotation of axes, we may assume, without loss of generality, that $\mathbf{c} = (p, 0)$ with $p > 0$. As in [19], we require the following conditions in our cloak design,

$$\begin{aligned} p &> a + \delta, \quad \text{the active device is outside the region } B(\mathbf{c}, a), \\ R &> a + p, \quad \text{the cloaking effect is observed in the far field.} \end{aligned} \tag{12.22}$$

12.2.2 The Conductivity Equation

Next, in the spirit of [19, 23] we give a more rigorous formulation of the exterior cloaking problem for the two-dimensional conductivity equation and prove its feasibility. The results extend easily to the quasistatic regime.

Theorem 12.1 *Let a, $\mathbf{c}$, R and δ satisfy (12.22), then for any $\varepsilon > 0$ and any harmonic potential u_0, there exists a function $g_0 : \mathbb{R}^2 \to \mathbb{R}$ and a potential $u : \mathbb{R}^2 \to \mathbb{R}$, satisfying*

$$\begin{cases} \Delta u = 0, & \text{in } \mathbb{R}^2 \setminus \overline{B(0, \delta)}, \\ u = g_0, & \text{on } \partial B(0, \delta), \\ |u| < \varepsilon & \text{in } \mathbb{R}^2 \setminus B(0, R), \\ |u + u_0| < \varepsilon & \text{in } \overline{B(\mathbf{c}, a)}. \end{cases} \tag{12.23}$$

Proof By applying the inversion (or Kelvin) transformation $w \doteq 1/z$, the geometry of problem (12.23) transforms as follows,

- $\mathbb{R}^2 \setminus B(0, \delta)$ transforms to $B(0, 1/\delta)$,
- $\mathbb{R}^2 \setminus B(0, R)$ transforms to $B(0, 1/R)$,
- $B(\mathbf{c}, a)$ transforms to $B(\mathbf{c}^*, \alpha)$, with

$$\alpha = \frac{a}{|p^2 - a^2|}, \qquad \mathbf{c}^* = (\beta, 0), \quad \text{and} \quad \beta = \frac{p}{p^2 - a^2}.$$

The different regions and their transforms are illustrated in Fig. 12.3. Thus the problem (12.23) is equivalent to finding $\tilde{g}_0$ and $\tilde{u}$ such that

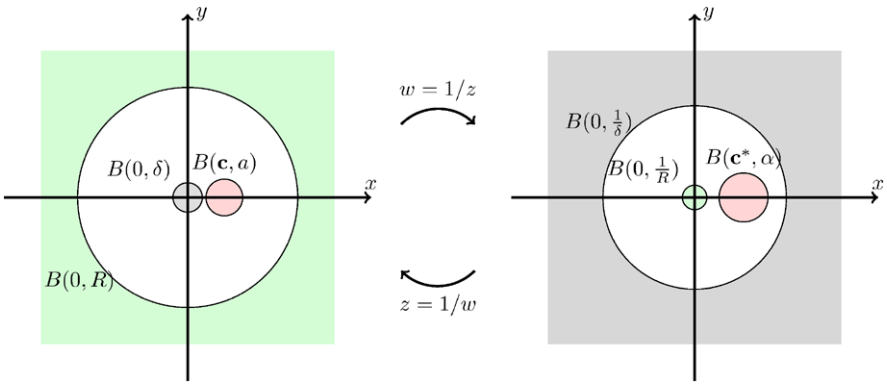

Fig. 12.3 The regions of Theorem 12.1 (*left*) and their transforms under the Kelvin or inversion transformation (*right*). The device field is harmonic everywhere except in the *gray areas*, is close to minus the incident field in the *red region* and is close to zero in the *green region*. Reprinted from [23] with permission of Springer-SBM

$$\begin{cases} \Delta\tilde{u} = 0, & \text{in } B(0, 1/\delta), \\ \tilde{u} = \tilde{g}_0, & \text{on } \partial B(0, 1/\delta), \\ |\tilde{u}| < \varepsilon, & \text{in } \overline{B(0, 1/R)}, \\ |\tilde{u} + \tilde{u}_0| < \varepsilon, & \text{in } \overline{B(\mathbf{c}^*, \alpha)}. \end{cases} \tag{12.24}$$

Relating to the functions g_0 and u_0 from (12.23), we get $\tilde{g}_0(z) = g_0(1/z)$ and $\tilde{u}_0(z) = u_0(1/z)$, so that $\tilde{u}_0$ is harmonic in the whole space except the origin. Next, we observe that the inversion transforms the necessary conditions (12.22) to

$$\begin{aligned} \frac{1}{R} < \beta - \alpha, &\quad \text{the two balls } B(0, 1/R) \text{and } B(\mathbf{c}^*, \alpha) \text{ do not touch,} \\ \beta + \alpha < \frac{1}{\delta}, &\quad \text{the two balls } B(0, 1/\delta) \text{ and } B(\mathbf{c}^*, \alpha) \text{ do not touch.} \end{aligned} \tag{12.25}$$

Let $\widetilde{U}_0$ be the analytic extension of $\tilde{u}_0$ in $B(\mathbf{c}^*, \alpha)$, obtained with the harmonic conjugate such that $\tilde{u}_0$ is the real part of $\widetilde{U}_0$. Because of analyticity of $\widetilde{U}_0$, we can approximate $\widetilde{U}_0$ with a polynomial Q_0 (e.g. by truncating the series expansion of $\widetilde{U}_0$) such that

$$|\widetilde{U}_0 - Q_0| < \frac{\varepsilon}{2} \quad \text{in } \overline{B\left(\mathbf{c}^*, \alpha\right)}. \tag{12.26}$$

This immediately yields the approximation for $\tilde{u}_0$

$$|\tilde{u}_0 - q_0| < \frac{\varepsilon}{2} \quad \text{in } \overline{B\left(\mathbf{c}^*, \alpha\right)}, \tag{12.27}$$

where $q_0 \doteq \Re(Q_0)$, i.e., the real part of Q_0. Since $\widetilde{U}_0$ can be approximated arbitrarily well by a polynomial, it is enough to consider (12.24) when $\tilde{u}_0$ is the real part of a polynomial, i.e.

$$\begin{cases} \Delta\tilde{u} = 0, & \text{in } B(0, 1/\delta), \\ \tilde{u} = \tilde{g}_0, & \text{on } \partial B(0, 1/\delta), \\ |\tilde{u}| < \varepsilon, & \text{in } \overline{B(0, 1/R)}, \\ |\tilde{u} + q_0| < \varepsilon/2, & \text{in } \overline{B(\mathbf{c}^*, \alpha)}. \end{cases} \tag{12.28}$$

In other words, problem (12.28) is equivalent to finding a function $\tilde{u}$, harmonic inside $B(0, 1/\delta)$ that approximates q_0 well inside $B(\mathbf{c}^*, \alpha)$ but is practically zero in $B(0, 1/R)$.

Let us now recall a classic result in harmonic approximation theory due to Walsh (see [14, p. 8]).

Lemma 12.1 (Walsh) *Let K be a compact set in $\mathbb{R}^2$ such that $\mathbb{R}^2 \setminus K$ is connected. Then for each function w, harmonic on an open set containing K, and for each $d > 0$, there is a harmonic polynomial q such that $|w - q| < d$ on K.*

Walsh's lemma implies the existence of a harmonic solution to problem (12.28). Indeed, from the design requirements (12.25) there exists $0 < \xi \ll 1$ such that

$$\frac{1}{R} + \xi < \beta - \alpha - \xi. \tag{12.29}$$

Then applying Lemma 12.1 with $K = \overline{B(0, 1/R)} \cup \overline{B(\mathbf{c}^*, \alpha)}$, we obtain that for an arbitrary small parameter $0 < d \ll 1$ and for the function w satisfying

$$w = \begin{cases} 0 & \text{in } B(0, \frac{1}{R} + \xi), \\ -q_0 & \text{in } B(\mathbf{c}^*, \alpha + \xi), \end{cases} \tag{12.30}$$

there exists a harmonic polynomial q such that $|q - w| < d$ on K. We conclude that there exists a harmonic solution to problem (12.28), which implies the statement of Theorem 12.1. □

12.2.3 Explicit Polynomial Solution in the Zero Frequency Regime

Although mathematically rigorous, the existence result of Theorem 12.1 (which follows from Walsh's lemma) does not give an explicit expression for the required potential at the active device (antenna). In [19] (see also [23]) we give a polynomial solution to problem (12.24). Unfortunately the radius a of the cloaked region in the polynomial solution of [19, 23] is limited by the distance from the origin p according to $a < (2 + 2\sqrt{2})^{-1} p$. Thus in [19, 23] we can only cloak large objects if they are sufficiently far from the origin. Here we state a conjecture that extends our

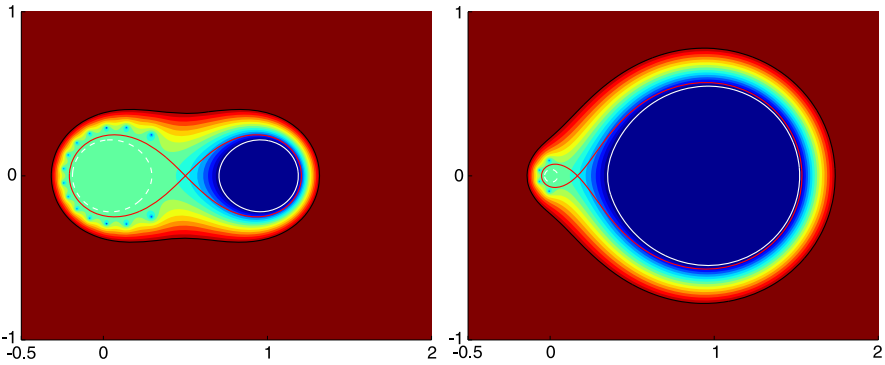

(a) $n = s = 15$ (b) $n = 5, s = 25$

Fig. 12.4 Contour plot for the polynomial $P_{n,s}$ with $\beta = 1$. The *solid white line* is the level-set $|P_{n,s}(z)| = 10^{-2}$, thus the cloaked region could be any disk inside this level-set. The *dashed white line* is the level-set $|P_{n,s}(z) - 1| = 10^{-2}$. The device field is small in any circle inside this level-set. The *red curve* is the boundary of $D_{\beta,L}$, the conjectured region of convergence of $P_{n,s}$ as both $n \to \infty$ and $s \to \infty$ with $s/n = 1$ and 5, respectively. (This is proved in the case $n = s$ in [23].) The *color scale* is logarithmic from 0.01 (*dark blue*) to 100 (*dark red*), with *light green* representing 1

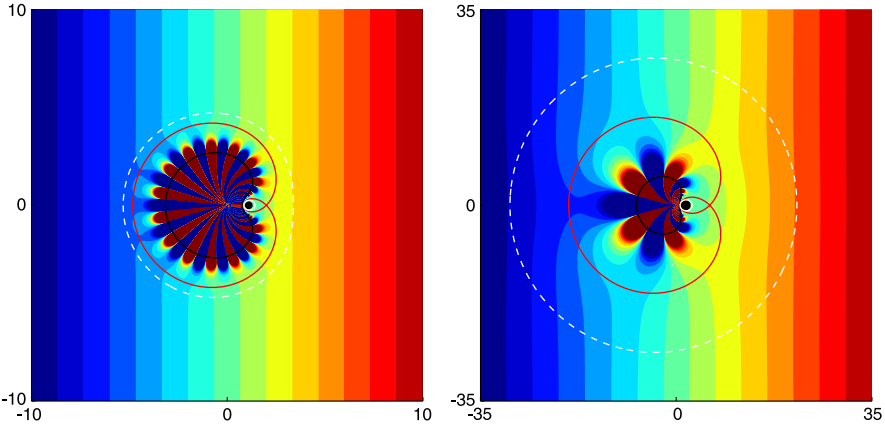

(a) $n = s = 15$ (b) $n = 5, s = 25$

Fig. 12.5 Real part of the total field with the cloaking device active, incident field $u_0(x, y) = x$ and $\beta = 1$. The *solid white*, *dashed white* and *red lines* are the inversion (Kelvin) transforms of their counterparts in Fig. 12.4. The *small black scatterer* inside the *cloaked region* is an almost resonant disk centered at $(p, 0)$ with radius r and dielectric constant ε given by: (**a**) $p = 1.1$, $r = 0.2$ and $\varepsilon = -0.99$; (**b**) $p = 1.7$, $r = 0.9$ and $\varepsilon = -0.998$. In (**a**) the *color scale* is linear from -10 (*dark blue*) to 10 (*dark red*). In (**b**) the scale is linear from -35 to 35

previous results [19, 23] and that gives more freedom on the choice of the cloaked region location and size. This is supported by numerical evidence (see Figs. 12.4 and 12.5).

Conjecture 12.1 *Let* $\mathbf{c}^* = (\beta, 0)$ *be as in the proof of Theorem* 12.1. *For any* $L > 0$, *any disk* S_1 *in the connected component containing the origin of the set*

$$D_{\beta,L} \doteq \left\{ z \in \mathbb{C}, |z-\beta|^L |z| < \frac{\beta^{L+1} L^L}{(L+1)^{L+1}} \right\}, \tag{12.31}$$

any disk S_2 *in the connected component of the set* $D_{\beta,L}$ *containing the point* $\mathbf{c}^*$ *and any* $\varepsilon > 0$, *there exists two positive integers* s *and* n *such that* $|s/n - L| < \varepsilon$ *and the polynomial* $P_{n,s} : \mathbb{C} \to \mathbb{C}$ *defined by*

$$P_{n,s}(z) = \left(1 - \frac{z}{\beta}\right)^s \sum_{j=0}^{n-1} \left(\frac{z}{\beta}\right)^j \binom{s+j-1}{j}, \tag{12.32}$$

satisfies

$$|P_{n,s} - 1| < \varepsilon \quad \text{on } \partial S_1 \quad \text{and} \quad |P_{n,s}| < \varepsilon \quad \text{on } \partial S_2. \tag{12.33}$$

Moreover the approximation property (12.33) *is not satisfied when either* S_1 *or* S_2 *is not contained in* $D_{\beta,L}$.

Remark 12.4 To see why we expect that the polynomial $P_{n,s}$ satisfies (12.33), notice that $z = \beta$ is a root of multiplicity s of the polynomial $P_{n,s}$. From the Taylor expansion of $P_{n,s}$ around $z = \beta$, we can expect that $P_{n,s} \approx 0$ in a sufficiently small disk around β. (The symbol $\approx$ denotes an approximation with respect to the supremum norm.) Now the function

$$g(z) = \left[\sum_{j=0}^{n-1} \left(\frac{z}{\beta}\right)^j \binom{s+j-1}{j} \right] - \left(1 - \frac{z}{\beta}\right)^{-s},$$

has a root of multiplicity n at $z = 0$, i.e. $g^{(k)}(0) = 0$ for $k = 0, \ldots, n-1$. This is because the sum in the definition of $g(z)$ corresponds to the first n terms in the Taylor expansion around $z = 0$ of $(1 - z/\beta)^{-s}$. Thus by Leibniz rule, $z = 0$ is a root of multiplicity n of the polynomial $P_{n,s} - 1 = (1 - z/\beta)^s g(z)$, and we can expect $P_{n,s} \approx 1$ in a sufficiently small disk around the origin. This suggests an alternative definition of $P_{n,s}$ as the unique Hermite interpolation polynomial (see e.g. [52]) satisfying:

$$\begin{aligned} P_{n,s}(0) &= 1, \\ P_{n,s}^{(k)}(0) &= 0, \quad \text{for } k = 1, \ldots, n-1, \\ P_{n,s}^{(k)}(\beta) &= 0, \quad \text{for } k = 0, \ldots, s-1. \end{aligned}$$

Remark 12.5 To motivate our belief that the region $D_{\beta,L}$ is the region of convergence of $P_{n,s}$ as $n \to \infty$ and $s \to \infty$ with $s/n \to L$, consider the special case

where $L > 0$ is an integer and $s = nL$. Then the last term in the sum (12.32) defining $P_{n,nL}(z)$ is

$$\left(1 - \frac{z}{\beta}\right)^{nL} \left(\frac{z}{\beta}\right)^{n-1} \binom{n(L+1)-1}{n-1},$$

which diverges outside of $D_{\beta,L}$ as $n \to \infty$ because

$$\binom{n(L+1)-1}{n-1}^{\frac{1}{n-1}} \to \frac{(L+1)^{L+1}}{L^L}, \quad \text{as } n \to \infty,$$

which follows from Stirling's formula, see e.g. [45, §5.11]. Therefore the region of divergence of $P_{n,Ln}$ contains the complement of $D_{\beta,L}$.

For some polynomial Q_0 we can deduce from (12.33) that

$$Q_0 P_{n,s} - Q_0 \approx 0 \quad \text{on } \partial S_1 \quad \text{and} \quad Q_0 P_{n,s} - Q_0 \approx -Q_0 \quad \text{on } \partial S_2, \tag{12.34}$$

Thus, by construction, the real part of $W = Q_0 P_{n,s} - Q_0$ is a solution of (12.28) with $S_1 = B(0, 1/R)$ and $S_2 = B(\mathbf{c}^*, \alpha)$. In the particular case when $n = s$ (i.e. $L = 1$), Conjecture 12.1 was proved in [23], see also [19].

In Fig. 12.4 we present a contour plot of the polynomial $P_{n,s}$ when $\beta = 1$ for different values of n and s. The region bounded by the peanut shaped red curve represents the conjectured domain of convergence $D_{\beta,L}$ of the functions $P_{n,s}$ when $n \to \infty$, $s \to \infty$ and $s/n \to L$. In the left side of $D_{\beta,L}$, $P_{n,s}$ is conjectured to converge to one, while in the right side of $D_{\beta,L}$, $P_{n,s}$ is conjectured to converge to zero. The area within the solid white circle on the right represents the region to be cloaked and the area within the dashed white circle in the left represents the location of the observer. We now present an active cloak design based on Conjecture 12.1.

Remark 12.6 Let u_0 be an a priori determined incoming harmonic potential. Let n and s be such that the real part of $W = Q_0 P_{n,s} - Q_0$ is a solution of (12.28) (recall Q_0 is a polynomial approximation of $\widetilde{U}_0$ in $B(\mathbf{c}^*, \alpha)$). Let S be a bounded region in the complex plane compactly including the two disks $S_1 = B(0, \frac{1}{R})$ and $S_2 = B(\mathbf{c}^*, \alpha)$. Then, the cloaking strategy we propose consists of an active device (antenna) located inside $B(0, \delta)$ and capable of generating a potential equal to the real part of $W(\frac{1}{z})$ on the set $\{z \in \mathbb{C}, \frac{1}{z} \in \partial S\}$. By (12.27), the total potential in the original physical configuration (the field from the antenna plus u_0) is well approximated by the real part of $(W + Q_0)(1/z)$ which ensures an almost zero field region in $B(\mathbf{c}, a)$ with negligible perturbations on the field outside $B(0, R)$.

Figure 12.5 illustrates how the cloaking device (represented by the solid black curve) works after applying the back-inversion to the configurations presented in Fig. 12.4. Here the incident field is $u_0(x, y) = x$ and the objects we want to hide are almost resonant disks. Clearly, the active device generates the necessary field to cancel the field in the cloaked region while having a very small effect in the

far field (outside the white dashed circle). With a polynomial of the same degree, when $s = 5n$ (Fig. 12.5(b)) we can hide an object roughly four times larger than when $s = n$ (Fig. 12.5(a)). Thus using the polynomials $P_{n,s}$ allows us to cloak large objects without restrictions on the distance from the origin β as was the case in [19, 23]. The disadvantage is that cloaking is enforced on $\partial B(0, R)$ (dotted white line in Fig. 12.5) with a larger R in the asymmetric $L > 1$ case than in the symmetric $L = 1$ case. For example to get a device field such that $|u| < 10^{-2}$, R needs to be roughly five times larger when $s = 5n$ (Fig. 12.5(b)) than when $s = n$ (Fig. 12.5(a)).

12.2.4 Extensions and Applications

We now extend the previous results to the case of an incoming field having sources in $\mathbb{R}^2 \setminus \overline{B(0, R)}$.

Remark 12.7 The case studied in Theorem 12.1 (with an explicit solution in Conjecture 12.1) corresponds to an incoming field u_0 generated by a source located at infinity. The more general case corresponding to an incoming field having sources in $\mathbb{R}^2 \setminus \overline{B(0, R)}$ can be treated similarly. Indeed, the problem remains to find g_0 and u satisfying (12.23), or equivalently $\tilde{g}_0$ and $\tilde{u}$ satisfying (12.24) where inside $B(0, 1/R)$, $\tilde{u}_0(z) = u_0(1/z)$ is harmonic. We can still approximate its analytic extension $\widetilde{U}_0$ by a polynomial in $B(\mathbf{c}^*, \alpha)$ and the proof goes as in Theorem 12.1.

Although our main focus here is cloaking, the same ideas can be applied to illusion optics, where one wants to conceal an object by imitating the response (scattering) of a completely different object.

Remark 12.8 Let u_1 be the response of an object we wish to imitate, i.e. an arbitrary potential harmonic in a set $D_1 \subset \mathbb{R}^2$ such that $\mathbb{R}^2 \setminus B(0, R) \Subset D_1$. Assuming the same notations as before, for any (known a priori) probing field u_0, harmonic in $\mathbb{R}^2$, there exists a function $g \in C(\partial B(0, \delta))$ so that the field u generated by the active device (antenna) located in $B(0, \delta)$ satisfies:

i. The total field $u + u_0$ is very small in the cloaked region $B(\mathbf{c}, a)$.
ii. The device field u is close to u_1 in $\mathbb{R}^2 \setminus B(0, R)$.

Remark 12.8 follows from the inversion (Kelvin) transform and Lemma 12.1 by using an argument similar to the proof of Theorem 12.1. Using ideas similar to those in Remark 12.7, the result of Remark 12.8 can be generalized to the case of an incoming field with sources in $\mathbb{R}^2 \setminus \overline{B(0, R)}$.

To illustrate Remark 12.8 assume that the field u_1 is chosen to be the response field of an inhomogeneity $\mathscr{I}$ when probed with the incident field u_0. Then Remark 12.8 means that when probing with the field u_0, an observer located in the far field detects the inhomogeneity $\mathscr{I}$ regardless of the inclusion inside $B(\mathbf{c}, a)$ and without detecting the active illusion device. This creates the illusion that the object inside $B(\mathbf{c}, a)$ is the inhomogeneity $\mathscr{I}$.

12.3 Active Exterior Cloaking for the Helmholtz Equation in Three Dimensions

Previously in [19, 20] we designed cloaking devices generating fields close to minus the incident field in the region to be cloaked and vanishing far away from the devices. Miller [33] proposed an active cloak based on Green's identities: a single and double layer potential is applied to the boundary of the cloaked region to cancel out the incident field inside the cloaked region, while not radiating waves. The idea of using Green's identities to cancel out waves in a region is well known in acoustics (see e.g. [13, 24, 32]). Jessel and Mangiante [24] showed that it is possible to achieve a similar effect to Green's identities (and thus cloaking) by replacing the single and double layer potentials on a surface by a source distribution in a neighborhood of the surface. What makes our approach different is that the cloaking devices are multipolar sources *exterior* to the cloaked region and thus do not completely enclose the cloaked region. In [19, 20] the cloaking devices are determined by solving numerically a least-squares problem with linear constraints. Our cloaking approach easily generalizes to several frequencies [20] but requires a priori knowledge of the incident field. Zheng, Xiao, Lai and Chan [55] used the same principle to achieve illusion optics [28] with active devices, i.e. making an object appear as another one. Then in [22] we showed Green's identity can be used to design devices which can cloak or give the illusion of another object, i.e. achieving an effect similar to the active devices in [19, 20, 55]. The single and double layer potential needed to reproduce a smooth field inside a region while being zero outside is given by Green's identity and can be replaced by a few multipolar sources using addition formulas for spherical outgoing waves. If in addition we want to imitate the scattered field from an object as in [55], a similar procedure applies.

The active cloaking devices we designed in [19, 20, 22] are two dimensional. Here we extend the result in [22] to the Helmholtz equation in three dimensions. The wave pressure field $u(\mathbf{x})$ solves the Helmholtz equation,

$$\Delta u + k^2 u = 0, \quad \text{for } \mathbf{x} \in \mathbb{R}^3,$$

where $k = 2\pi/\lambda$ is the wavenumber, $\lambda = 2\pi c/\omega$ is the wavelength, c is the wave propagation speed (assumed to be constant) and ω is the angular frequency. Recall for future reference that the radiating Green's function for the Helmholtz equation in three dimensions is

$$G(\mathbf{x}, \mathbf{y}) = \frac{\exp[ik|\mathbf{x} - \mathbf{y}|]}{4\pi|\mathbf{x} - \mathbf{y}|}. \tag{12.35}$$

Another underlying assumption is that the frequency ω is not a resonant frequency of the scatterer we wish to hide.

12.3.1 Green's Formula Cloak

As pointed out by Miller [33], it is possible to cloak an object inside a bounded region $D \in \mathbb{R}^3$ from an incident wave (probing field) u_i by generating a cloaking

device field using monopole and dipole sources (single and double layer potential) on ∂D. The device field u_d can be defined using Green's formula

$$\begin{aligned} u_d(\mathbf{x}) &= \int_{\partial D} \mathrm{d}S_{\mathbf{y}} \big\{ -\big(\mathbf{n}(\mathbf{y}) \cdot \nabla_{\mathbf{y}} u_i(\mathbf{y})\big) G(\mathbf{x}, \mathbf{y}) + u_i(\mathbf{y}) \mathbf{n}(\mathbf{y}) \cdot \nabla_{\mathbf{y}} G(\mathbf{x}, \mathbf{y}) \big\} \\ &= \begin{cases} -u_i(\mathbf{x}), & \text{if } \mathbf{x} \in D \\ 0, & \text{otherwise,} \end{cases} \end{aligned} \tag{12.36}$$

so that the total field $u_i + u_d$ is a solution to Helmholtz equation for $\mathbf{x} \notin \partial D$ that vanishes inside D while being indistinguishable form u_i outside D. Since the waves reaching a scatterer inside the cloaked region D are practically zero, the resulting scattered field is also practically zero. For clarity we assume the region D is a polyhedron. The arguments we give here can be easily modified for other domains with Lipschitz boundary, as Green's identity (12.36) is valid for these domains [11].

Remark 12.9 The Green representation formula (12.36) requires that u_i be a C^2 solution to the Helmholtz equation inside D. A similar identity holds when u_i is a C^2 radiating solution to the Helmholtz equation *outside* D. In this case, the device field u_d vanishes inside D and is identical to $-u_i$ outside D. The exterior cloak we present here can in principle be used to conceal a known active source and possibly accompanying scatterers inside D. If the radiating wave u_i is taken to be the scattered field from a known object, the same principle can be used for illusion optics [28, 55].

12.3.2 Active Exterior Cloak

The main idea here is to achieve a similar effect to the Green's identity cloak but without completely surrounding the cloaked region by monopoles and dipoles on ∂D. We "open the cloak" by replacing the single and double layer potential on each face ∂D_l of ∂D by a corresponding multipolar device located at some point $\mathbf{x}_l$. Each device produces a linear combination of outgoing spherical waves of the form

$$u_d(\mathbf{x}) = \sum_{l=1}^{n_{dev}} \sum_{n=0}^{\infty} \sum_{m=-n}^{n} b_{l,n,m} V_n^m(\mathbf{x} - \mathbf{x}_l), \tag{12.37}$$

where n_{dev} is the number of devices (or faces of ∂D) and $V_n^m(\mathbf{x})$ is a radiating, spherical wave defined for $\mathbf{x} \neq 0$ by

$$V_n^m(\mathbf{x}) = h_n^{(1)}\big(k|\mathbf{x}|\big) Y_n^m(\hat{\mathbf{x}}).$$

Here $h_n^{(1)}(t)$ is a spherical Hankel function of the first kind (see e.g. [45, §10.47]) and $Y_n^m(\hat{\mathbf{x}})$ is a spherical harmonic evaluated at the point $\hat{\mathbf{x}} \equiv \mathbf{x}/|\mathbf{x}|$ of the unit sphere

$S(0,1)$. In spherical coordinates, the spherical harmonics we use are defined as in [8, §2.3] by

$$Y_n^m(\theta,\phi) = \sqrt{\frac{2n+1}{4\pi}\frac{(n-|m|)!}{(n+|m|)!}}P_n^{|m|}(\cos\theta)e^{im\phi}, \tag{12.38}$$

where the elevation angle is $\theta \in [0,\pi]$ and the azimuth angle is $\phi \in [0,2\pi]$. Here $P_n^{|m|}(t)$ are the associated Legendre functions

$$P_n^m(t) = \left(1-t^2\right)^{m/2}\frac{d^m P_n(t)}{dt^m},$$

defined for $n = 0, 1, 2, \ldots$ and $m = 0, 1, \ldots, n$ in terms of the Legendre polynomials P_n of degree n with normalization $P_n(1) = 1$. The definition (12.38) ensures that the spherical harmonics Y_n^m have unit $L^2(S(0,1))$ norm.

The main tool to replace the fields generated by a face is the addition formula (see e.g. Theorem 2.10 in [8])

$$G(\mathbf{x},\mathbf{y}) = ik\sum_{n=0}^{\infty}\sum_{m=-n}^{n} V_n^m(\mathbf{x})\overline{U_n^m(\mathbf{y})} \tag{12.39}$$

which means we can mimic a point source located at $\mathbf{y}$ by a multipolar source located at the origin. The coefficients in the multipolar expansion are values of entire spherical waves

$$U_n^m(\mathbf{x}) = j_n\left(k|\mathbf{x}|\right)Y_n^m(\hat{\mathbf{x}}),$$

where $j_n(t)$ are spherical Bessel functions [45, §10.47]. The series in the multipolar expansion (12.39) converges uniformly on compact sets of $|\mathbf{x}| > |\mathbf{y}|$.

We are now ready to state the main result of this section.

Theorem 12.2 *Multipolar sources located at the points $\mathbf{x}_l \notin \partial D$, $l = 1, \ldots, n_{dev}$ can be used to reproduce the Green's formula cloak outside of the region*

$$A = \bigcup_{l=1}^{n_{dev}} B\left(\mathbf{x}_l,\ \sup_{\mathbf{y}\in\partial D_l}|\mathbf{y}-\mathbf{x}_l|\right),$$

where $B(\mathbf{x},r)$ is the closed ball of radius r centered at $\mathbf{x}$. The coefficients $b_{l,n,m}$ in (12.37) such that $u_d^{(ext)}(\mathbf{x}) = u_d(\mathbf{x})$ for $\mathbf{x} \notin A$ are

$$\begin{aligned} b_{l,n,m} = ik\int_{\partial D_l} \mathrm{d}S_{\mathbf{y}}\Big\{&\left(-\mathbf{n}(\mathbf{y})\cdot\nabla_{\mathbf{y}}u_i(\mathbf{y})\right)\overline{U_n^m(\mathbf{y}-\mathbf{x}_l)} \\ &+ u_i(\mathbf{y})\mathbf{n}(\mathbf{y})\cdot\nabla_{\mathbf{y}}\overline{U_n^m(\mathbf{y}-\mathbf{x}_l)}\Big\}. \end{aligned} \tag{12.40}$$

Moreover the convergence of (12.37) is uniform on compact sets outside A.

Proof Splitting the integral in (12.36) into integrals over each of the faces ∂D_l of the polyhedron ∂D and applying the addition theorem (12.39) with center at the corresponding $\mathbf{x}_l$ we obtain:

$$u_d(\mathbf{x}) = ik \sum_{l=1}^{n_{dev}} \int_{\partial D_l} \mathrm{d}S_{\mathbf{y}}\big(-\mathbf{n}(\mathbf{y}) \cdot \nabla_{\mathbf{y}} u_i(\mathbf{y})\big) \sum_{n=0}^{\infty} \sum_{m=-n}^{n} V_n^m(\mathbf{x}-\mathbf{x}_l)\overline{U_n^m(\mathbf{y}-\mathbf{x}_l)}$$

$$+ u_i(\mathbf{y})\mathbf{n}(\mathbf{y}) \cdot \nabla_{\mathbf{y}} \sum_{n=0}^{\infty} \sum_{m=-n}^{n} V_n^m(\mathbf{x}-\mathbf{x}_l)\overline{U_n^m(\mathbf{y}-\mathbf{x}_l)}. \tag{12.41}$$

The result (12.40) follows for $\mathbf{x} \notin A$ by switching the order of the sum and the integral in (12.41). For the first term in the integrand of (12.41), this switch is justified by the uniform convergence of the series (12.39) (for all devices) in compact sets outside of A.

For the second term in the integrand of (12.41), we shall show that the series converges uniformly on compact sets outside A, so it is also valid to switch the integral and the series in (12.41). To see the uniform convergence, it is useful to split the products $V_n^m(\mathbf{x}-\mathbf{x}_l)\nabla_{\mathbf{y}}\overline{U_n^m(\mathbf{y}-\mathbf{x}_l)}$ into two terms corresponding to the two terms in the gradient

$$\nabla_{\mathbf{y}} U_n^m(\mathbf{y}) = k\hat{\mathbf{y}}\, j_n'\big(k|\mathbf{y}|\big) Y_n^m(\hat{\mathbf{y}}) + j_n\big(k|\mathbf{y}|\big)\frac{|\mathbf{y}|^2 I - \mathbf{y}\mathbf{y}^T}{|\mathbf{y}|^3}\big(\nabla Y_n^m\big)(\hat{\mathbf{y}})$$

$$= g_{n,m}^{(1)}(\mathbf{y}) + g_{n,m}^{(2)}(\mathbf{y}), \tag{12.42}$$

where I is the 3×3 identity matrix.

For the series involving the first term in the gradient (12.42) we bound with the triangle and Cauchy-Schwarz inequalities:

$$\left| \sum_{m=-n}^{n} V_n^m(\mathbf{x}-\mathbf{x}_l)\overline{g_{n,m}^{(1)}(\mathbf{y}-\mathbf{x}_l)} \right|$$

$$\leq k\big|h_n^{(1)}\big(k|\mathbf{x}-\mathbf{x}_l|\big) j_n'\big(k|\mathbf{y}-\mathbf{x}_l|\big)\big|$$

$$\times \left(\sum_{m=-n}^{n} \big|Y_n^m(\widehat{\mathbf{x}-\mathbf{x}_l})\big|^2 \right)^{\frac{1}{2}} \left(\sum_{m=-n}^{n} \big|Y_n^m(\widehat{\mathbf{y}-\mathbf{x}_l})\big|^2 \right)^{\frac{1}{2}}.$$

Using the summation theorem for spherical harmonics (see e.g. Theorem 2.8 in [8])

$$\sum_{m=-n}^{n} \big|Y_n^m(\hat{\mathbf{y}})\big|^2 = \frac{2n+1}{4\pi}, \quad \text{for any } \hat{\mathbf{y}} \in S(0,1) \text{ and } n = 0, 1, \ldots, \tag{12.43}$$

we get the estimate:

$$\begin{aligned}
&\left|\sum_{m=-n}^{n} V_n^m(\mathbf{x}-\mathbf{x}_l)\overline{g_{n,m}^{(1)}(\mathbf{y}-\mathbf{x}_l)}\right| \\
&\quad\le k\left|h_n^{(1)}\big(k|\mathbf{x}-\mathbf{x}_l|\big)\,j_n'\big(k|\mathbf{y}-\mathbf{x}_l|\big)\right|\frac{2n+1}{4\pi} \\
&\quad= \mathscr{O}\left(\frac{|\mathbf{y}-\mathbf{x}_l|^{n-1}}{|\mathbf{x}-\mathbf{x}_l|^{n+1}}\right), \qquad (12.44)
\end{aligned}$$

for large $n\to\infty$. The last equality comes from the asymptotic expansion of Bessel functions for fixed $t>0$ and large order n, (see e.g. [45, §10.19])

$$\begin{aligned}
\left|j_n'(t)\right| &= nt^{n-1}/(2n+1)!!\big(1+\mathscr{O}(1/n)\big) \quad \text{and} \\
\left|h_n^{(1)}(t)\right| &= (2n-1)!!t^{-n-1}\big(1+\mathscr{O}(1/n)\big),
\end{aligned}$$

where $(2n+1)!!\equiv 1\cdot 3\cdot\ldots\cdot(2n+1)$ is the double factorial.

For the series involving the second term in the gradient (12.42) we bound the sums

$$\begin{aligned}
&\left|\sum_{m=-n}^{n} V_n^m(\mathbf{x}-\mathbf{x}_l)\overline{g_{n,m}^{(2)}(\mathbf{y}-\mathbf{x}_l)}\right| \\
&\quad\le 2\left|h_n^{(1)}\big(k|\mathbf{x}-\mathbf{x}_l|\big)\frac{j_n(k|\mathbf{y}-\mathbf{x}_l|)}{|\mathbf{y}-\mathbf{x}_l|}\right| \\
&\qquad\times\left(\sum_{m=-n}^{n}\left|Y_n^m\big(\widehat{\mathbf{x}-\mathbf{x}_l}\big)\right|^2\right)^{\frac12}\left(\sum_{m=-n}^{n}\left|\big(\nabla Y_n^m\big)\big(\widehat{\mathbf{y}-\mathbf{x}_l}\big)\right|^2\right)^{\frac12}.
\end{aligned}$$

Using the summation theorem for spherical harmonics (12.43) and their gradients (see e.g. (6.56) in [8]),

$$\sum_{m=-n}^{n}\left|\big(\nabla Y_n^m\big)(\hat{\mathbf{y}})\right|^2=\frac{n(n+1)(2n+1)}{4\pi}, \quad \text{for any } \hat{\mathbf{y}}\in S(0,1), \qquad (12.45)$$

we get the asymptotic

$$\begin{aligned}
&\left|\sum_{m=-n}^{n} V_n^m(\mathbf{x}-\mathbf{x}_l)\overline{g_{n,m}^{(2)}(\mathbf{y}-\mathbf{x}_l)}\right| \\
&\quad\le 2\left|h_n^{(1)}\big(k|\mathbf{x}-\mathbf{x}_l|\big)\frac{j_n(k|\mathbf{y}-\mathbf{x}_l|)}{|\mathbf{y}-\mathbf{x}_l|}\right|\left(\frac{2n+1}{4\pi}\right)^{\frac12}\left(\frac{n(n+1)(2n+1)}{4\pi}\right)^{\frac12} \\
&\quad= \mathscr{O}\left(\frac{|\mathbf{y}-\mathbf{x}_l|^{n-1}}{|\mathbf{x}-\mathbf{x}_l|^{n+1}}\right). \qquad (12.46)
\end{aligned}$$

Here we have used that for $t > 0$ fixed and as $n \to \infty$, (see e.g. [45, §10.19])

$$|j_n(t)| = t^n/(2n+1)!!\big(1+\mathscr{O}(1/n)\big) \quad \text{and} \quad \big|h_n^{(1)}(t)\big| = (2n-1)!!t^{-n-1}\big(1+\mathscr{O}(1/n)\big).$$

The estimates (12.44) and (12.46) give uniformly convergent majorants for the series in the second term of (12.41), since when $\mathbf{x} \notin A$ we have $|\mathbf{y} - \mathbf{x}_l| < |\mathbf{x} - \mathbf{x}_l|$, for $l = 1, \ldots, n_{dev}$. The proof is now completed. □

12.3.3 A Family of Exterior Cloaks with Four Devices

Nothing in Theorem 12.2 guarantees that the cloaked region $D \setminus A$ is non-empty. We show here how to construct a family of cloaks with non-empty $D \setminus A$ based on Green's identities applied to a regular tetrahedron D. We also determine what is the position of the devices that gives the largest cloaked region within this family.

Consider a regular tetrahedron with circumsphere $S(0, \sigma)$ and vertices $\mathbf{a}_1, \ldots, \mathbf{a}_4$. We locate the devices $\mathbf{x}_1, \ldots, \mathbf{x}_4$ on $S(0, \delta)$, with $\delta > \sigma$, such that $\mathbf{x}_l$ replaces the face opposite to vertex $\mathbf{a}_l$, that is $\mathbf{x}_l$ and $\mathbf{a}_l$ are on opposite sides of the plane formed by the face of the tetrahedron not containing $\mathbf{a}_l$. For simplicity we also require that $\mathbf{x}_l - \mathbf{a}_l$ is normal to this plane. The configuration is sketched in Fig. 12.6. Simple geometric arguments show that the radii of the balls that define the region A are all equal to

$$r(\sigma, \delta) = \left(\left(\sigma - \frac{\delta}{3}\right)^2 + \frac{8}{9}\delta^2\right)^{\frac{1}{2}}. \tag{12.47}$$

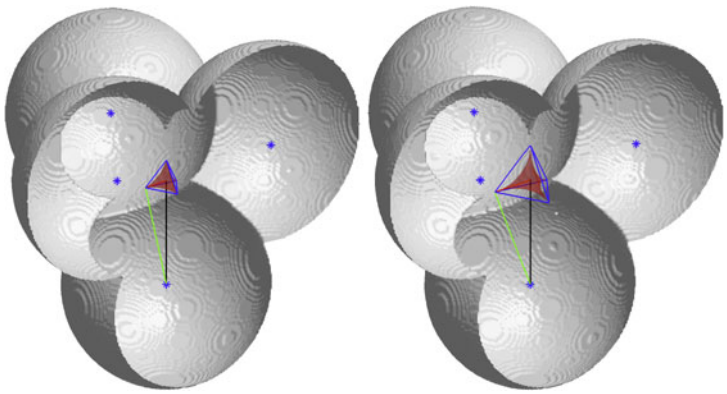

(a) suboptimal, $\sigma = \delta/5$ (b) optimal, $\sigma = \delta/3$

Fig. 12.6 The configuration for the tetrahedron based cloak of Sect. 12.3.3. The distance in *red* is the radius σ of the circumsphere to the tetrahedron D. The distance in *black* is the distance δ from the origin to a device. The distance $r(\sigma, \delta)$ (in *green*) is the distance from a device to the closest vertex of D. The exterior surface of the region A of Theorem 12.2 is in *gray* and has been cut to reveal the cloaked region $D \setminus A$ in *red*. The four devices are shown with *stars*

Moreover the radius of the largest sphere fitting inside the cloaked region is

$$r_{\text{eff}}(\sigma, \delta) = \delta - r(\sigma, \delta). \tag{12.48}$$

For fixed δ, the largest possible cloaked region is obtained when $\sigma = \delta/3$ which corresponds to the case when every triplet of balls in the definition of region A touch at a vertex $\mathbf{a}_l$ of the tetrahedron. Thus for fixed δ, the largest sphere we can fit inside the cloaked region has radius,

$$r^*_{\text{eff}} = \left(1 - \frac{2\sqrt{2}}{3}\right)\delta \approx 0.057\delta. \tag{12.49}$$

12.3.4 Numerical Experiments

We report in Fig. 12.7 simulations of this cloaking method with the setup described in Sect. 12.3.3. The incident field we take is the plane wave $u_i(\mathbf{x}) = \exp[ik\hat{\mathbf{k}} \cdot \mathbf{x}]$ with direction vector $\hat{\mathbf{k}} = [1, 1, 1]/\sqrt{3}$. We first compute the device field of Theorem 12.2 by truncating the sum in n of (12.37) to $n \leq N$. Throughout our numerical experiments we determine N with the heuristic (found by numerical experimentation)

$$N(\delta) = \lceil 1.5k\delta \rceil, \tag{12.50}$$

where $\lceil x \rceil$ is the smallest integer larger than or equal to x. The integrals in (12.40) were evaluated with a simple quadrature rule that is exact for piecewise linear functions on a uniform triangulation of the faces of the tetrahedron D, we chose the number of quadrature points so that there are at least eight points per wavelength. The scattered field by a ball was computed by first evaluating the incident field (or device field depending on the case) on a grid with equal number of points in ϕ and θ and then finding its first few spherical harmonic decomposition coefficients using the sampling theorem [10].

As can be seen in the first row of Fig. 12.7 the device field u_d is virtually zero far from A while being close to the incident field in the cloaked region $D \setminus A$. In the second and third rows of Fig. 12.7 we display the total field in the presence of a sound-soft (homogeneous Dirichlet boundary condition) ball centered at the origin and of radius $3r^*_{\text{eff}}(\delta)$ (i.e. a larger scatterer than what we expected from Sect. 12.3.3). The scattered field from the ball reveals the ball's position when the devices are inactive (third row). The scattered field is essentially suppressed when the cloaking devices are active (second row), as the field is indistinguishable from a plane wave far from A.

Since as $t \to 0$, $h^{(1)}_n(t) = \mathcal{O}(t^{-n-1})$ (see e.g. [45, §10.52]), we expect the device field u_d to blow up as we get close to the device locations $\mathbf{x}_l$. This blow up corresponds to the "urchins" in the first and second rows of Fig. 12.7 where even with the truncation of the series (12.37), we observe very large wave amplitudes which

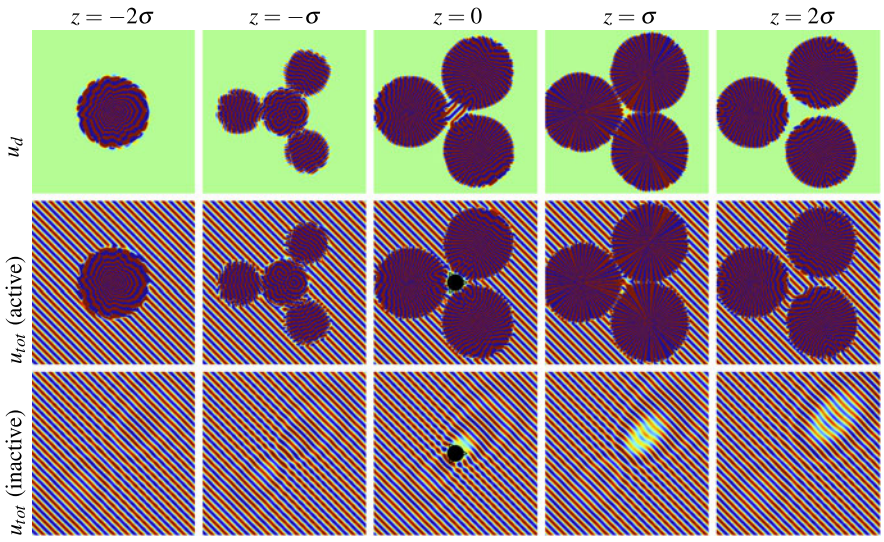

Fig. 12.7 Constant z slices of the real part of different fields, for the optimal case $\delta = 3\sigma$ and with $\delta = 6\lambda$. The *first row* shows the device field u_d which is close to zero far from the devices and close to $-u_i$ in a small region close to the origin. The *second* and *third rows* show the total field when the devices are active and inactive in the presence of a scatterer. The scatterer is a sound-soft ball centered at the origin and of radius $3r^*_{\text{eff}}(\delta)$. Even though this ball is not completely contained inside the tetrahedron D, the scattered field is greatly suppressed when the devices are active, making the ball harder to detect far from the devices. The *color scale* is linear from -1 (*dark blue*) to 1 (*dark red*) and each box is $10\lambda \times 10\lambda$, with the z-axis at the center

would be hard to realize in practice. Fortunately we can enclose the regions with very large fields by a surface and apply Green's formula (12.36) to replace these large fields by (hopefully) more manageable single and double layer potentials on the surface of some "extended" cloaking devices.

We illustrate these "extended" devices in Fig. 12.8 where we display the level sets where the device field amplitude is 5 (or 100) times the amplitude of the incident field. At least for the particular configuration ($\delta = 6\lambda$) considered in Fig. 12.8, these surfaces resemble spheres surrounding each device location $\mathbf{x}_l$. The "extended" devices still leave the cloaked region (in red in Fig. 12.8) communicating (connected) with the background medium. This is why we call our cloaking method "exterior cloaking".

We also consider the extended devices for larger values of δ in Fig. 12.9. Here we look at the cross-section of the extended devices on $S(0, \sigma)$, which in the construction of Sect. 12.3.3 is the circumsphere to the tetrahedron D. In the optimal case $\delta = 3\sigma$, the predicted cloaked region $D \setminus A$ and the exterior $\mathbb{R}^3 \setminus A$ meet on $S(0, \sigma)$ at the vertices of the tetrahedron D. We see that the extended devices (in black in Fig. 12.9) grow as δ increases, and leave gorges communicating the cloaked region with the exterior. The centers of the gorges appear to agree with the vertices of the tetrahedron D. The percentage area of $S(0, \sigma)$ that is not covered by the

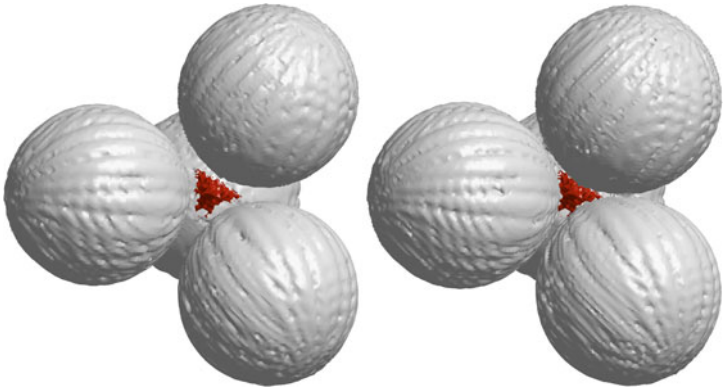

(a) $|u_d| = 100$ (b) $|u_d| = 5$

Fig. 12.8 Contours of $|u_d|$ (*gray*) and $|u_d + u_i| = 10^{-2}$ (*dark red*). Here the vector $(0, 0, 1)$ is perpendicular to plane of the page. By Green's identity it is possible to replace the large fields inside the gray surfaces by a single and double layer potential at the gray surfaces. These "extended devices" need only to generate fields that are at most the fields on the contours that we plot and they cloak the red region without completely surrounding it

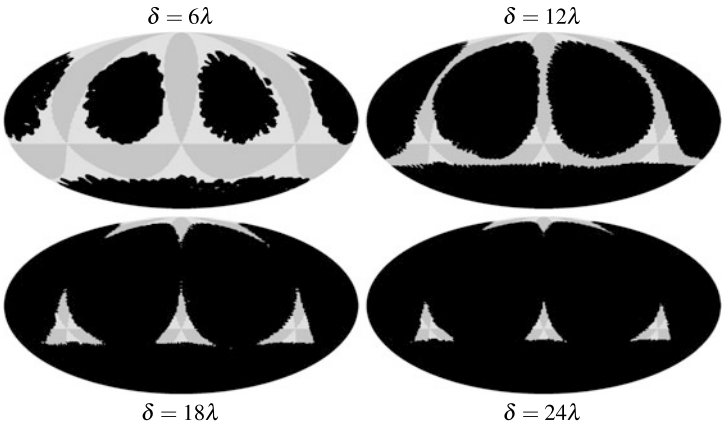

Fig. 12.9 Cross-section of level set $|u_d| \geq 10^2$ (*black*) and of the region A (*shades of gray*) on the sphere $|\mathbf{x}| = \sigma$ for the optimal $\sigma = \delta/3$. Here we used the equal area Mollweide projection (see e.g. [12]). In the optimal case, each triplet out of the four balls forming A meets at a single point which is a vertex of the tetrahedron D. Note that for the cases in the first row there are four distinct extended devices. The leftmost and rightmost spots correspond to one single device split in two by the projection

cross-section of the extended devices on $S(0, \sigma)$ is also quantified in Fig. 12.10(b). Since the relative area of the openings appears to decrease monotonically with δ/λ, Fig. 12.10(b) suggests the gorges close for large enough δ/λ. Further investigation is needed to find out whether the shrinking openings in the cloak is due to our choice of N with heuristic (12.50).

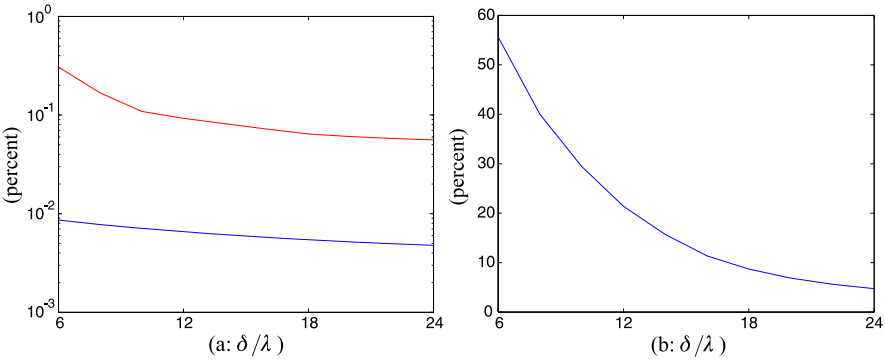

Fig. 12.10 (**a**) Cloak performance. In *red*: $\|u_i + u_d\|/\|u_i\|$, where the norm is the $L^2(S(0, r^*_{\text{eff}}(\delta)))$ norm, which measures how well we approximate the incident field inside the cloaked region. In *blue*: $\|u_d\|/\|u_i\|$, where the norm is the $L^2(S(0, 2\delta))$ norm, which measures how small is the device field far away from the devices. (**b**) Percentage of the area outside the cross-section of the extended devices on the sphere $S(0, \sigma = \delta/3)$ for different values of δ

Finally we give in Fig. 12.10(a) quantitative measures of the cloak performance for different values of δ. These measures show that the device field is close to minus the incident field inside the cloaked region and that it is very small outside of the cloaked region.

Acknowledgements We are thankful to Michael Bentley for noticing an error in an early version of this chapter. GWM is grateful for support from the University of Toulon-Var. GWM and DO are grateful to the National Science Foundation for support through grant DMS-0707978. FGV is grateful to the National Science Foundation for support through grant DMS-0934664. FGV, GWM and DO are grateful to the Mathematical Sciences Research Institute where parts of this manuscript were completed. The computations of the device and scattered fields in Sect. 12.3 were facilitated by the freely available spherical harmonics library SHTOOLS by Mark Wieczorek, available at http://www.ipgp.fr/~wieczor/SHTOOLS/SHTOOLS.html.

References

1. Alú, A., Engheta, N.: Plasmonic and metamaterial cloaking: Physical mechanisms and potentials. J. Opt. A, Pure Appl. Opt. **10**, 093002 (2008)
2. Bouchitté, G., Schweizer, B.: Homogenization of Maxwell's equations in a split ring geometry. Multiscale Model. Simul. **8**(3), 717–750 (2010)
3. Brun, M., Guenneau, S., Movchan, A.: Achieving control of in-plane elastic waves. Appl. Phys. Lett. **94**, 061903 (2009)
4. Cai, W., Shalaev, V.: Optical Metamaterials: Fundamentals and Applications. Springer, Dordrecht (2010)
5. Chen, H., Chan, C.T.: Acoustic cloaking in three dimensions using acoustic metamaterials. Appl. Phys. Lett. **91**, 183518 (2007)
6. Chen, H., Chan, C.T.: Acoustic cloaking and transformation acoustics. J. Phys. D, Appl. Phys. **43**(11), 113001 (2010). doi:10.1088/0022-3727/43/11/113001

7. Chen, H., Hou, B., Chen, S., Ao, X., Wen, W., Chan, C.T.: Design and experimental realization of a broadband transformation media field rotator at microwave frequencies. Phys. Rev. Lett. **102**, 183903 (2009)
8. Colton, D., Kress, R.: Inverse Acoustic and Electromagnetic Scattering Theory. Applied Mathematical Sciences, 2nd edn. vol. 93. Springer, Berlin (1998)
9. Cummer, S.A., Schurig, D.: One path to acoustic cloaking. New J. Phys. **9**, 45 (2007)
10. Driscoll, J.R., Healy, D.M. Jr.: Computing Fourier transforms and convolutions on the 2-sphere. Adv. Appl. Math. **15**(2), 202–250 (1994). doi:10.1006/aama.1994.1008
11. Evans, L.C., Gariepy, R.F.: Measure Theory and Fine Properties of Functions. Studies in Advanced Mathematics. CRC Press, Boca Raton (1992)
12. Feeman, T.G.: Portraits of the Earth. Mathematical World, vol. 18. Am. Math. Soc., Providence (2002)
13. Ffowcs Williams, J.E.: Review lecture: Anti-sound. Proc. R. Soc. A **395**, 63–88 (1984)
14. Gardiner, S.J.: Harmonic Approximation. London Mathematical Society Lecture Note Series, vol. 221. Cambridge University Press, Cambridge (1995). doi:10.1017/CBO9780511526220
15. Greenleaf, A., Kurylev, Y., Lassas, M., Uhlmann, G.: Full-wave invisibility of active devices at all frequencies. Commun. Math. Phys. **275**, 749–789 (2007)
16. Greenleaf, A., Kurylev, Y., Lassas, M., Uhlmann, G.: Cloaking devices, electromagnetic wormholes, and transformation optics. SIAM Rev. **51**(1), 3–33 (2009)
17. Greenleaf, A., Lassas, M., Uhlmann, G.: Anisotropic conductivities that cannot be detected by EIT. Physiol. Meas. **24**, 413–419 (2003)
18. Greenleaf, A., Lassas, M., Uhlmann, G.: On non-uniqueness for Calderón's inverse problem. Math. Res. Lett. **10**, 685–693 (2003)
19. Guevara Vasquez, F., Milton, G.W., Onofrei, D.: Active exterior cloaking for the 2D Laplace and Helmholtz equations. Phys. Rev. Lett. **103**, 073901 (2009). doi:10.1103/PhysRevLett.103.073901
20. Guevara Vasquez, F., Milton, G.W., Onofrei, D.: Broadband exterior cloaking. Opt. Express **17**, 14800–14805 (2009). doi:10.1364/OE.17.014800
21. Guevara Vasquez, F., Milton, G.W., Onofrei, D.: Complete characterization and synthesis of the response function of elastodynamic networks. J. Elast. **102**(1), 31–54 (2011). doi:10.1007/s10659-010-9260-y
22. Guevara Vasquez, F., Milton, G.W., Onofrei, D.: Exterior cloaking with active sources in two dimensional acoustics. Wave Motion **48**, 515–524 (2011). arXiv:1009.2038[math-ph]
23. Guevara Vasquez, F., Milton, G.W., Onofrei, D.: Mathematical analysis of two dimensional active exterior cloaking in the quasistatic regime. Anal. Math. Phys. **2**, 231–246 (2012)
24. Jessel, M.J.M., Mangiante, G.A.: Active sound absorbers in an air duct. J. Sound Vib. **23**(3), 383–390 (1972)
25. Kadic, M., Bückmann, T., Stenger, N., Thiel, M., Wegener, M.: On the practicability of pentamode mechanical metamaterials. Appl. Phys. Lett. **100**(19), 191901 (2012)
26. Kohn, R.V., Onofrei, D., Vogelius, M.S., Weinstein, M.I.: Cloaking via change of variables for the Helmholtz equation. Commun. Pure Appl. Math. **63**(8), 973–1016 (2010)
27. Kohn, R.V., Shen, H., Vogelius, M.S., Weinstein, M.I.: Cloaking via change of variables in electric impedance tomography. Inverse Probl. **24**, 015016 (2008)
28. Lai, Y., Ng, J., Chen, H., Han, D., Xiao, J., Zhang, Z.Q., Chan, C.T.: Illusion optics: The optical transformation of an object into another object. Phys. Rev. Lett. **102**(25), 253902 (2009). doi:10.1103/PhysRevLett.102.253902
29. Leonhardt, U.: Optical conformal mapping. Science **312**, 1777–1780 (2006)
30. Leonhardt, U., Philbin, T.G.: General relativity in electrical engineering. New J. Phys. **8**, 247 (2006)
31. Leonhardt, U., Smith, D.R.: Focus on cloaking and transformation optics. New J. Phys. **10**, 115019 (2008)
32. Malyuzhinets, G.D.: One theorem for analytic functions and its generalizations for wave potentials. In: Third All-Union Symposium on Wave Diffraction, Tbilisi, 24–30 September 1964, abstracts of reports. (1964)

33. Miller, D.A.B.: On perfect cloaking. Opt. Express **14**, 12457–12466 (2006)
34. Milton, G.W.: New metamaterials with macroscopic behavior outside that of continuum elastodynamics. New J. Phys. **9**, 359 (2007)
35. Milton, G.W.: Realizability of metamaterials with prescribed electric permittivity and magnetic permeability tensors. New J. Phys. **12**, 033035 (2010)
36. Milton, G.W., Briane, M., Willis, J.R.: On cloaking for elasticity and physical equations with a transformation invariant form. New J. Phys. **8**, 248 (2006)
37. Milton, G.W., Cherkaev, A.V.: Which elasticity tensors are realizable? ASME J. Eng. Mater. Technol. **117**, 483–493 (1995)
38. Milton, G.W., Nicorovici, N.A.P.: On the cloaking effects associated with anomalous localized resonance. Proc. R. Soc. A, Math. Phys. Sci. **462**, 3027–3059 (2006)
39. Milton, G.W., Nicorovici, N.A.P., McPhedran, R.C., Cherednichenko, K., Jacob, Z.: Solutions in folded geometries, and associated cloaking due to anomalous resonance. New J. Phys. **10**, 115,021 (2008)
40. Milton, G.W., Seppecher, P.: Realizable response matrices of multiterminal electrical, acoustic, and elastodynamic networks at a given frequency. Proc. R. Soc. A, Math. Phys. Sci. **464**(2092), 967–986 (2008)
41. Nicorovici, N.A., McPhedran, R.C., Milton, G.W.: Optical and dielectric properties of partially resonant composites. Phys. Rev. B **49**, 8479–8482 (1994)
42. Nicorovici, N.A.P., Milton, G.W., McPhedran, R.C., Botten, L.C.: Quasistatic cloaking of two-dimensional polarizable discrete systems by anomalous resonance. Opt. Express **15**, 6314–6323 (2007)
43. Norris, A.N.: Acoustic cloaking theory. Proc. R. Soc. A **464**, 2411–2434 (2008)
44. Norris, A.N., Shuvalov, A.L.: Elastic cloaking theory. Wave Motion **48**, 525–538 (2011)
45. Olver, F.W.J., Lozier, D.W., Boisvert, R.F., Clark, C.W. (eds.) NIST Handbook of Mathematical Functions, U.S. Department of Commerce National Institute of Standards and Technology, Washington (2010)
46. Pendry, J.B.: Negative refraction makes a perfect lens. Phys. Rev. Lett. **85**, 3966–3969 (2000)
47. Pendry, J.B., Schurig, D., Smith, D.R.: Controlling electromagnetic fields. Science **312**, 1780–1782 (2006)
48. Rahm, M., Schurig, D., Roberts, D.A., Cummer, S.A., Smith, D.R., Pendry, J.B.: Design of electromagnetic cloaks and concentrators using form-invariant coordinate transformations of Maxwell's equations. Photonics Nanostruc. **6**, 87–95 (2008). doi:10.1016/j.photonics.2007.07.013
49. Schoenberg, M., Sen, P.N.: Properties of a periodically stratified acoustic half-space and its relation to a Biot fluid. J. Acoust. Soc. Am. **73**(1), 61–67 (1983)
50. Schurig, D.: An aberration-free lens with zero F-number. New J. Phys. **10**, 115034 (2008)
51. Serdikukov, A., Semchenko, I., Tretkyakov, S., Sihvola, A.: Electromagnetics of Bi-anisotropic Materials, Theory and Applications. Gordon & Breach, Amsterdam (2001)
52. Stoer, J., Bulirsch, R.: Introduction to Numerical Analysis, 3rd edn. Texts in Applied Mathematics, vol. 12. Springer, New York (2002). Translated from the German by Bartels, R., Gautschi, W. and Witzgall, C.
53. Willis, J.R.: Variational principles for dynamic problems for inhomogeneous elastic media. Wave Motion **3**, 1–11 (1981)
54. Yang, T., Chen, H., Luo, X., Ma, H.: Superscatterer: Enhancement of scattering with complementary media. Opt. Express **16**, 18545–18550 (2008). doi:10.1364/OE.16.018545
55. Zheng, H.H., Xiao, J.J., Lai, Y., Chan, C.T.: Exterior optical cloaking and illusions by using active sources: A boundary element perspective. Phys. Rev. B **81**(19), 195116 (2010). doi:10.1103/PhysRevB.81.195116

Index

R.V. Craster, S. Guenneau (eds.), *Acoustic Metamaterials*,
Springer Series in Materials Science 166, DOI 10.1007/978-94-007-4813-2,